Modeling and numerics of anisotropic and inelastic materials: Plasticity, damage and growth

Von der Fakultät für Bauingenieurwesen
der Rheinisch-Westfälischen Technischen Hochschule Aachen
zur Erlangung des akademischen Grades eines Doktors der Ingenieurwissenschaften
genehmigte Dissertation

vorgelegt von

Hagen Hanns Holthusen, M. Sc.

Berichter*innen: Prof. Dr.-Ing. habil. Stefanie Reese
Prof. Dr.-Ing. habil. Ellen Kuhl

Tag der mündlichen Prüfung: 15. August 2023

"Denn weil Wissen nur belastet, wolln wir nicht Mitwisser sein
Wir lassen es unangetastet – das Gewissen, es bleibt rein
Porentief rein"
– Dirk Felsenheimer, NichtWissen (Geräusch)

"Even if we found a complete theory of the universe,
it wouldn’t remove the need for music"
– Stephen Hawking

"Ich bin dagegen, denn ihr seid dafür"
– Jan Vetter, Rebell (13)

Acknowledgements

This cumulative dissertation represents the result of my scientific work at the Institute of Applied Mechanics (IFAM) at the RWTH Aachen University. I would like to take this opportunity to thank all the people who supported me and contributed in some way or another to the successful completion of this work. The English-speaking reader may forgive me my decision to write the following personal acknowledgements in German.

Zunächst möchte ich mich herzlichst bei der Betreuerin meiner Arbeit, Frau Prof. Dr.-Ing. habil. Stefanie Reese, für die wunderbare Zeit am Institut und besonders für die Möglickeit ein Teil dieses außergewönlichen Teams in Aachen zu sein bedanken. Die mir hier gebotenen Freiheiten bezüglich meiner Forschung haben mir immer viel bedeutet, ihre kontinuierliche Förderung war dabei ein stetiger Antrieb noch besser zu werden. Dabei war ihr Vertrauen in meine Arbeit als auch in der Lehre mir stets ein hohes Gut, wobei letzteres nicht unterschätzt werden sollte, hilft es doch jedem und jeder jungen WissenschaftlerIn die eigene Forschung besser zu erklären und somit auch besser zu verstehen.

Weiterhin git mein Dank Prof. Dr.-Ing. habil. Ellen Kuhl die sich bereit erklärt hat ein Zweitgutachten für meine Dissertation anzufertigen und dafür den weiten Weg aus Kalifornien auf sich zu nehmen. Während meines Forschungsaufenthaltes in ihrem Team in Stanford haben mich ihr stets ansteckender Enthusiasmus für die Forschung sowie ihre schnelle und clevere Art über Fragestellungen nachzudenken sehr begeitert und mir den Aufenthalt zu einem großen Vergnügen gemacht.

Darüber hinaus gilt mein Dank Prof. Dr.-Ing. habil. Sven Klinkel für die Übernahme des Vorsitzes meiner Promotionskommission. Ich möchte ihm auch ganz herzlich für meine Zeit als studentische Hilfskraft an seinem Institut während meines Studiums danken. Besonders hervorzuheben sind meine damaligen Betreuer Florian (Efka) Kieser und Dr.-Ing. Thomas Kubalski, die mich betreut und gefördert haben. Besonders Efka gilt mein tiefster Dank, hat er mir doch eine Weise beigebracht über Probleme in unserem Bereich nachzudenken von der ich bis heute äußerst profitiere. Ohne die Zeit, die er in mich investiert hat, wäre ich sicherlich nicht da wo ich bin. Auch bei all meinen damaligen KollegInnen Philipp Alder, Leonie Mester, Dr.-Ing. Philipp Michel, Jessica Mundt, Dr.-Ing. Maximilian Praster und Dr.-Ing. Simon Schleiter, die ich glücklicherweise heute als meine Freunde zählen darf, möchte ich mich bedanken. Ohne sie würde ich vermutlich immer noch in einer der Kneipen Aachens schlafen. Ich möchte die Zeit als studentische Hilfskraft nicht missen, hätte ich doch ohne sie mit Gewissheit nicht den Weg zur Promotion eingeschlagen. Ganz besonders wertschätzend hervorheben möchte ich den vielen Blödsinn um, während und nach der Arbeit mit Leo. Im

Hinblick auf diese Dissertation und mich selbst ist das mit Gewissheit viel wichtiger als so manch kluge Idee, sei es auch nur ein Kaffee um den Bau oder (zwei) brillante Skiseminare!

Meinen Übergang ans IFAM verdanke ich Prof. Dr.-Ing. habil. Jaan-Willem Simon, der mit seiner inspirierenden Art zu lehren mir in dieser Hinsicht ein Vorbild war. Mit Beginn am IFAM sei zuallererst Dr.-Ing. Tim Brepols zu nennen, von dem ich wie von keinem anderen in fachlicher Hinsicht lernen durfte und nach wie vor darf. Dass er mir seine Expertise und Zeit in zahllosen Diskussionen schenkte, werde ich ihm nicht vergessen! Auch gegenüber meinen Freunden Dr.-Ing. Sebastian Felder sowie Dr.-Ing. Oliver Barfusz empfinde ich große Dankbarkeit für wertvolle Ratschläge in und um die Promotionen. Beide haben mir gerade in der Anfangszeit geholfen meinen Weg in der Forschung zu finden. Neben diesen beiden sind zudem Lukas Lamm, Domen Macek und Tim van der Velden zu nennen, welche mit ihren spannenden Fragen und Ideen mich immer auf Trab gehalten haben. Letzterem gilt zudem mein Dank als meinem Bürokollegen für eine tolle, verpflegungsreiche, aber leider viel zu kurze Zeit in 309.b und für unseren Aufenthalt in Südafrika.

In diesem Sinne empfinde ich auch große Dankbarkeit gegenüber all den Studierenden die ich während meiner Promotion betreuen durfte. Explizit zu nennen sind hier Christiane Rothkranz, Greta Kloppenburg, Ahmad Awad, Njomza Pacolli, Marcelle van der Sande und Skadi Bögershausen. Hervorheben möchte ich dabei zum einen Christiane, welche ich zu meinem Glück nicht nur während ihrer Bachelor- und Masterarbeit betreuen durfte, sondern auch als studentische Hilfskraft gewinnen konnte. Ihre stets cleveren und kreativen Einfälle haben mir meine Arbeit erheblich erleichtert und ich selbst habe eine Menge durch die Zusammenarbeit gelernt. Zum anderen ist noch Greta zu nennen, die mir eine gute Freundin wurde und mit der ich das Vergnügen hatte das Fach Mechanik I zu betreuen.

Zudem möchte ich mich auch bei allen KollegInnen am IFAM sowie allen Ehemaligen während meiner Zeit am Institut für unvergässliche und prägende Erfahrungen bedanken. Der stets kollegiale und humorvolle Umgang haben den täglichen Weg zur Arbeit definitiv zu einem freudigen gemacht, die immer offenen Türen um über Probleme aller Art zu sprechen kamen gerade mir auf dem Weg zur Kaffeemaschine und Teekocher zu Gute. Ich kann allen nachfolgenden KollegInnen nur raten dieses Arbeitsklima sorgsam aufrecht zu halten und zu pflegen, da dadurch – meiner bescheidenen Meinung nach – sich auch wunderbare Freundschaften entwickelen können!

Dennoch sind auch abseits der Arbeit – manch einer möge sogar so weit gehen und glücklicherweise sagen – Freundschaften unverzichtbar. In diesem Sinne möchte ich meinen engen Freundeskreis aus Mülheim an der Ruhr nennen. Es steht außer Frage, dass, auch wenn man sich über die Jahre sicherlich seltener sieht, ich mich jedesmal auf ein Wiedersehen freue und

es die Seele baumelen lässt wie es vielleicht nur so alte Freundschaften können. Danke euch allen dafür! Vor allem aber Max Muscharski für viele stille bis sehr wertvolle Gespräche, die sich zum Glück um alles andere als Arbeit drehten, voll mit überragender Musik!

Es steht außer Frage, dass mein ganzes Studium als auch Promotion nicht möglich gewesen wäre ohne meine beiden Eltern Ursula und Holger Holthusen sowie meine beiden außergewöhnlichen Schwestern Ira und Katharina. Sie haben mich mein ganzes Leben lang begleitet, mich gefördert, in schwierigen Situationen beraten und standen mir stets zur Seite.

Diese Danksagung wäre keine Danksagung ohne meine langjährige Partnerin Freya Paintner, die mich immer unterstützt hat als auch mir Rückhalt bot wenn ich nicht weiter wusste. Ihr prägender Einfluss auf mich ist nicht in Worte zu fassen, hat er doch dafür gesorgt, dass ich mich auf einen viel wichtigeren Bereich als die Arbeit konzentriere – das Leben und alles drum herum. Ohne sie würde ich vermutlich immer noch bis spät in die Nacht irgendwelche Paper oder wissenschaftlichen Bücher lesen. Auch wenn mich das gegebenenfalls zu einem schlaueren Wissenschaftler gemacht hätte, dann doch sicher nicht zu einem besseren Menschen – und wer will das schon?

Hagen Holthusen
Aachen, 2023

P.S. Was uns der Autor damit sagen will: Das Leben ist schöner und spannender, wenn man von glücklichen Menschen umgeben ist. Seid nett zueinander, es macht das eigene Leben viel lebenswerter. Kann das so schwierig sein?

P.P.S. Wie der oder die eifrige LeserIn bemerket haben wird, war diese Danksagung – ganz im Stil dieser Dissertation – sehr lang. Es sei aber betont, dass zumindest in der Danksagung kein Wort zu viel verloren wurde.

P.P.P.S. Wer es bis hier her geschafft hat und vielleicht sogar bereits erwähnt wurde, darf sich frei fühlen auch den gesamten Rest zu lesen.

Summary

There has been tremendous technological progress, both in the manufacturing of ever more sophisticated materials and in the steadily increasing computational power. Thus, materials showing a pronounce kind of anisotropy – initially and/or induced – found their way into various fields of engineering applications. On the one hand, for example, fusion deposition modeling as used in 3D printing creates materials that behave anisotropically to increase load-bearing capacity. On the other hand, the power of modern computers enables numerical simulations that provide deeper insights into the underlying material behavior. However, in order to accurately predict material behavior while keeping the computational time cost relatively low, continuum mechanical models are needed that are capable of capturing a broad spectrum of anisotropy, in particular those anisotropic effects caused by various inelastic material behaviors.

In this regard, almost all materials, regardless of whether they are non-living or living, undergo inelastic deformation at some point. May it be irreversible deformation, rate dependence, degradation up to failure or even growth of living organisms. Macroscopically, all of these phenomena can cause the material to behave anisotropically if it did not already do so initially. For instance, the material's stiffness might fail completely in one direction due to microcracks, while being less degraded in another direction. Further well-known inelastic effects might be caused by anisotropic yield criteria such as Hill's one, or even by kinematic (plastic strain) hardening. In addition, one of the currently most challenging topics in continuum mechanics is the modeling of (direction-dependent) growth of biological tissues. From a continuum mechanical point of view, all these phenomena are modeled based on two essential concepts: The multiplicative decomposition of the deformation gradient and structural tensors.

Besides theoretical modeling, numerical implementation can be highly challenging as well and is known to be error-prone due to the complexity typically associated with such models. Therefore, the continuum mechanical framework employed should be designed in such a way that it can be easily implemented in algorithmic differentiation (AD) tools to enable robust and efficient computations.

This cumulative dissertation is intended to make a valuable contribution in this regard. The overall objective is to develop generic continuum mechanical formulations for inelastic phenomena associated with anisotropy in a geometrically nonlinear context. Therefore, a compilation of several publications by the author (and his co-authors) is presented. These should contribute to the development of more advanced material models in the future. In the beginning of this thesis the motivation, the research relevant questions and a comprehensive literature overview regarding the state-of-the-art are presented. After this introductory part,

the first paper deals with initially anisotropic materials such as fiber reinforced plastics. For the fiber, different failure mechanisms under tensile or compressive loadings are taken into account, while for the matrix isotropic damage coupled to plasticity is considered. Therefore, in addition to the initial anisotropy, further anisotropic effects arise due to the involved tension-compression asymmetry as well as the change in the stiffness ratio between fiber and matrix. Since three scalar (local) damage variables are used in this work, each of them is gradient-extended using the micromorphic approach to obtain mesh-independent results. The entire framework is formulated in a geometrically nonlinear sense and investigated using several numerical simulations.

Thereafter, the following three articles address the anisotropy induced by plasticity and anisotropic damage within initially isotropic materials. As in the first work, a 'two-surface' approach is employed to treat plasticity and damage as independent but strongly coupled mechanisms. The governing equations are described in logarithmic strain space using an additive split, while damage is represented by a symmetric second order tensor. Moreover, the proposed framework satisfies the damage growth criterion, which prevents the model from artificial stiffening effects. Once again, the micromorphic approach is used, whereas the damage tensor's invariants are gradient-extended. Several representative structural examples are examined to investigate the model's ability to provide mesh-independent results in uniaxial and multiaxial settings, as well as two- and three-dimensional boundary value problems.

The last two articles of this dissertation deal with the combination of the multiplicative decomposition and AD in the context of biomechanics. For this purpose, a co-rotated configuration of the intermediate configuration is introduced, which shares the same characteristics with the intermediate configuration, but is uniquely defined. Thus, it can be implemented using AD in an efficient and physically sound manner. In addition, the concept of structural tensors, an additional split of the inelastic part of the deformation gradient and hardening effects are discussed in a thermodynamically consistent manner. The stress-driven kinematic growth model, which is formulated in terms of the co-rotated configuration, utilizes the concept of homeostatic surfaces to describe growth and remodeling processes of soft biological tissues. In this regard, two parallel decompositions of the deformation gradient are employed, in order to treat direction-dependent and independent constituents separately. Moreover, remodeling of collagen fibers is taken into account in a stress-driven manner. The model is fully implemented using AD using an implicit approach. The predicted growth and remodeling behavior is compared with experiments found in literature and agrees qualitatively well with these data.

Zusammenfassung

Die technologischen Fortschritte sind enorm, sowohl bei der Herstellung von immer ausgefeilteren Materialien als auch in der stetig wachsenden Rechenleistung. Dadurch haben anisotrope Materialien – initial und/oder induziert – ihren Weg in verschiedene Bereiche der Ingenieursanwendungen gefunden. Einerseits werden beispielsweise durch die Schmelzschichtung im 3D-Druck Materialien geschaffen, die sich anisotrop verhalten, um die Tragfähigkeit zu erhöhen. Andererseits ermöglicht die Leistungsfähigkeit moderner Computer tiefere Einblicke in das zugrunde liegende Materialverhalten. Um jedoch das Materialverhalten vorhersagen zu können und gleichzeitig die Rechenzeit relativ gering zu halten, werden kontinuumsmechanische Modelle benötigt, die in der Lage sind anisotropes und inelastisches Verhalten zu beschreiben.

Nahezu alle Materialien, unabhängig ob sie nicht-lebendig oder lebendig sind, erfahren inelastische Verformungen. Dabei kann es sich um irreversible Verformung, Ratenabhängigkeit, Degradation bis hin zum Versagen oder um das Wachstum von lebenden Organismen handeln. Makroskopisch gesehen können all diese Phänomene dazu führen, dass sich das Material zusätzlich anisotrop verhält. So kann die Steifigkeit des Materials in einer Richtung aufgrund von Mikrorissen vollständig versagen, während sie in einer anderen Richtung weniger stark beeinträchtigt wird. Weitere bekannte inelastische Effekte können durch anisotrope Fließkriterien wie das von Hill oder auch durch kinematische Verfestigung verursacht werden. Darüber hinaus ist die Modellierung des (richtungsabhängigen) Wachstums von biologischem Gewebe eine der derzeit anspruchsvollsten Herausforderungen. Aus kontinuumsmechanischer Sicht werden all diese Phänomene mittels zwei wesentliche Konzepte modelliert: Die multiplikative Zerlegung des Deformationsgradienten und Strukturtensoren.

Neben der Modellierung kann auch die numerische Umsetzung eine große Herausforderung darstellen und ist aufgrund der Komplexität, die mit solchen Modellen verbunden ist, fehleranfällig. Daher sollte das kontinuumsmechanische Modell leicht mit algorithmischer Differenzierung (AD) kombinierbar sein, um robuste und effiziente Berechnungen zu ermöglichen.

Diese kumulative Dissertation soll einen wertvollen Beitrag dazu leisten. Das übergeordnete Ziel besteht darin, allgemeine kontinuumsmechanische Formulierungen für inelastische Phänomene mit Anisotropie bei großen Deformationen zu entwickeln. Dazu werden mehrere Veröffentlichungen des Autors (und seiner KoautorInnen) präsentiert. Damit soll auch in Zukunft die Entwicklung anspruchsvoller Materialmodelle ermöglicht werden.

Zu Beginn werden die Motivation, die forschungsrelevanten Fragestellungen und ein Lite-

raturüberblick zum Stand der Technik vorgestellt. Danach beschäftigt sich der erste Artikel mit initial anisotropen Materialien wie faserverstärkten Kunststoffen. Für die Faser werden unterschiedliche Versagensmechanismen unter Zug- oder Druckbelastung berücksichtigt, während für die Matrix isotrope Schädigung gekoppelt mit Plastizität betrachtet wird. Zusätzlich zur ursprünglichen Anisotropie treten weitere anisotrope Effekte aufgrund der involvierten Zug-Druck-Asymmetrie sowie der Änderung des Steifigkeitsverhältnisses zwischen Faser und Matrix auf. Es werden drei skalare (lokale) Schädigungsvariablen verwendet, welche mittels des mikromorphen Ansatzes gradientenerweitert werden, um netzunabhängige Ergebnisse zu erhalten. Das Modell wird geometrisch nichtlinear formuliert und anhand mehrerer numerischer Simulationen untersucht.

Die folgenden drei Arbeiten befassen sich mit der durch Plastizität und anisotrope Schädigung induzierten Anisotropie in ursprünglich isotropen Materialien. Wie im ersten Artikel wird ein Zwei-Flächen-Ansatz verwendet, um Plastizität und Schädigung als unabhängige, aber stark gekoppelte Phänomene zu behandeln. Die maßgebenden Gleichungen werden im logarithmischen Dehnungsraum durch eine additive Zerlegung beschrieben, während die Schädigung durch einen symmetrischen Tensor zweiter Ordnung beschrieben wird. Darüber hinaus wird das Damage Growth Criterion erfüllt, wodurch künstliche Versteifungseffekte vermieden werden. Die Invarianten des Schädigungstensors werden mittels des mikromorphen Ansatzes gradientenerweitert. Mehrere repräsentative Strukturbeispiele untersuchen, ob das Modell in der Lage ist netzunabhängige Ergebnisse in ein- und mehrachsigen Anwendungen sowie bei zwei- und dreidimensionalen Randwertproblemen zu liefern.

Die letzten beiden Artikel befassen sich mit der Kombination von multiplikativer Zerlegung und AD im Kontext der Biomechanik. Zu diesem Zweck wird die Zwischenkonfiguration ko-rotiert formuliert, wodurch die physikalischen Eigenschaften erhalten bleiben, aber mit AD auf effiziente und physikalisch fundierte Weise kombiniert werden kann. Darüber hinaus werden das Konzept der Strukturtensoren, eine zusätzliche Zerlegung des inelastischen Anteils des Deformationsgradienten und Verfestigungseffekte in einer thermodynamisch konsistenten Weise diskutiert. Das spannungsgetriebene Wachstumsmodell, das in Bezug auf die korotierte Konfiguration formuliert ist, nutzt das Konzept der homöostatischen Oberflächen zur Beschreibung von Wachstums- und Umbauprozessen weicher biologischer Gewebe. In diesem Zusammenhang werden zwei parallele Zerlegungen des Deformationsgradienten verwendet, um richtungsabhängige und unabhängige Konstituenten getrennt zu behandeln. Außerdem wird das Remodeling von Kollagenfasern spannungsgetrieben berücksichtigt. Das Modell wird vollständig implizit mittels AD implementiert. Das vorhergesagte Materialverhalten wird mit Experimenten aus der Literatur verglichen und stimmt qualitativ gut mit diesen überein.

Contents

1 Introduction

1.1 Motivation and research-relevant questions

Nature is anisotropic. Nature is inelastic. But nature is in equilibrium.

Mechanical behavior in nature is far from being simple, since it is in general neither isotropic nor elastic. However, as nature has been optimized over millions of years of evolution following the principle of *survival of the fittest*, it is not surprising that some of the best solutions to biochemical processes and for load-bearing mechanisms can be found there.

In fauna, there are countless examples of biological materials that are subject to growth and behave initially or induced anisotropically, as e.g. teeth and bones, but also soft tissues and blood vessels. An example for initial anisotropy is the helical arrangement of collagen fibers in arteries, which is optimal for achieving the highest possible resilience and strength while keeping the tissue flexible at the same time. Contrary to this, an isotropically behaving material would result in a much too high stiffness in radial direction of the vessels, which would significantly reduce the vessel's flexibility. This example vividly underlines the advantage of directionally dependent material behavior.

In flora, similar components can be found, which provide the plants with nutrients and stability. Here, the material behaves strongly anisotropic like e.g. wood fibers in the wood tissue or also the transport tissue consisting of xylem. Sclerenchyma cells, which are usually grouped into bundles, serve as supporting and strengthening tissue at the periphery of plant organs. Only in this way is it possible, for instance, for thin leaf stems to carry flat leaf blades and for stems to bear leaves, flowers and fruit, as well as for trees to withstand strong winds.

Due to mutations, selection and isolation in the course of evolution, highly optimized and perfectly adapted load-bearing structures have evolved, which nowadays serve as inspiration in the engineering of large structures or plant-based designs. In addition, modern and precise manufacturing processes make it possible to design components with preferred directions in order to increase resistance while at the same time reducing material consumption. Apart from these non-living applications, *in-silico* therapy in the context of patients' healthcare requires (among other things) a deep understanding of the (anisotropic) mechanical behavior of all

types of tissues. Computer-aided therapy can be used to preoperatively estimate diseases such as coronary in-stent restenosis and to adapt the design of drug-eluting stents to patient-specific needs.

No material found in nature behaves in an absolute elastic manner, since all materials exceeding a certain threshold either behave rate-dependently (viscous), undergo irreversible deformations (plasticity), grow in the case of living organisms, or fatigue and/or even fail (damage). From an evolutionary perspective, this proofed advantageous. During the forming of tissue, water stored in the tissue can lead to locally increased internal pressures, which, due to its visco-elastic behavior, are reduced over time and an (almost) uniform pressure is restored. Moreover, large deformations can occur (locally) in the affected living soft tissues. Furthermore, most non-living materials show significant inelastic behavior due to the underlying microstructure, e.g., metals and polymeric materials. The former undergo plastic deformations due to both dislocations of crystallographic planes and twinning, while in the latter polymer chains in the amorphous phase can cause the material to behave visco-elastically or crystalline phases may slip and cause irreversible deformations. This does not even require the component to be overstressed during its application, since inelastic deformations at large deformations can already be observed during manufacture as a result of forming (mechanical, thermo-mechanical or electro-chemical).

Although large deformations do not always occur globally, finite strains can certainly be observed locally in the process zone in addition to finite rotations, for instance, considering forming, (continuously smeared out) cracks as well as growth and remodeling. Thus, an in-depth understanding of inelastic material behavior at large deformations in a continuum mechanical context is essential.

None of the above challenges in today's engineering applications, ranging from automotive and aerospace to civil and mechanical engineering or computer-aided medical therapy, could be handled without powerful numerical simulations, most of which are conducted by means of the finite element method (FEM). The accuracy and prediction capabilities of these simulations strongly depend on the element formulation, but especially on the material model employed. Although multiscale models can be used that resolve the microstructure in a discrete manner, these methods suffer from high computational cost (see e.g. Geers et al. [2010], Matouš et al. [2017], Praster et al. [2019], Gierden et al. [2022], Kloppenburg et al. [2023] and Mester et al. [2021, 2023]). Therefore, efficient continuum mechanical models that account for the microstructural effects in a smeared and phenomenological sense are desirable, as they drastically reduce computation time while providing reliable results.

In order to address also the aforementioned ambitious challenges, it is necessary to gain

a deeper understanding of the underlying mechanisms of inelastic phenomena in the context of anisotropic material behavior. Especially in the regime of finite deformations, there is a growing need for research in recent years, since there is no unified concept to treat the combination of anisotropy and inelastic material behavior in a continuum mechanical way. Therefore, in the following, the phenomena of plasticity, anisotropic damage and its gradient-extension, and growth and remodeling of living organisms that are considered in this work are introduced, as well as the scientific questions that arise in the context of continuum mechanical formulations.

Plasticity. As one the oldest inelastic phenomena investigated at large deformations, the first contributions to the field of finite elasto-plasticity were made in the 1960s. Two famous theories, which are still widely used in the continuum mechanics community, are hypo- and hyperelastic based material models. The former assume the rate of deformation tensor (symmetric part of the spatial velocity gradient) to be additively decomposable into an elastic rate tensor and a plastic rate tensor. The latter theory suggests the multiplicative decomposition of the deformation gradient into an elastic (recoverable) part and plastic (irreversible) part (see, e.g., Eckart [1948], Kröner [1959], Lee and Liu [1967], Lee [1969] and Mandel [1973]). This decomposition introduces a stress-free intermediate configuration, which is essential to state the elastic law. Further, it is assumed that a specific (and differentiable) strain energy exists that is a potential for the stress. In line with the procedure of Coleman and Noll [1963], the free energy serves as such a potential.

It is worth noting that only hyperelastic based material formulations are considered in this dissertation, i.e. all proposed material models assume that the stress is derivable from the Helmholtz free energy.

Moreover, reference is made to the pioneering works of Coleman and Gurtin [1967] and Rice [1971] as well as Germain et al. [1983] for a mathematically sound and thermodynamically consistent derivation of inelastic materials based on the concept of internal variables. In particular, the latter comments on the thermodynamically consistent use of inelastic- or pseudo-potentials – a concept used throughout this dissertation – to derive the evolution equations of these variables.

In case of pure hyperelasticity, i.e. no irreversible strains occur, the deformed body is fully described by the boundary value problem applied as well as a specific expression for the Helmholtz free energy function. Contrary, in most common approaches nowadays, plasticity requires at least a set of internal variables as well as the definition of a (convex) yield criterion, which indicates the elastic limit. Usually, the thermodynamic driving forces associated with the internal variables serves as an argument for the yield criterion/function, which is topologically

decomposed into its interior (elastic) and its surface (plastic). As the evolution of the internal variables is determined neither by the boundary value problem nor the strain energy, evolution equations for those must be prescribed. Following the principle of maximum plastic dissipation, the evolution of plastic strains might be prescribed by the gradient of the yield criterion, which is suitable for most metals and is called associative flow rule. However, most soil materials such as clay behave differently. These materials require the introduction of an inelastic potential, where the (non-associative) flow rule is prescribed by the gradient of the inelastic potential.

Unfortunately, the employed multiplicative decomposition suffers from an inherent rotational non-uniqueness of the intermediate configuration. As a result, constitutive relations cannot be implemented directly in numerical softwares. Pull-back operations are required, making the numerical implementation more challenging and error-prone.

Therefore, elegant formulations of the constitutive relations are of invaluable importance for modern computational mechanics as well as for the application of sophisticated material models.

Damage. While plasticity is usually associated with dislocations on the microscopic level, damage is typically characterized by microdefects. These defects can roughly be classified into (spherical or elliptical) microvoids and microcracks. After nucleation, these microdefects grow and coalesce with each other until a macroscopic crack can be observed, whose propagation is referred to as fracture. Compared to modeling approaches for elasto-plasticity or visco-elasticity, there is a large number of approaches for the description of damage and fatigue existing, but until today, no universally valid concept has emerged.

Nevertheless, describing damage in a smeared sense according to the concept of continuum damage mechanics has steadily gained popularity in recent decades. Within this approach, scalar- or tensor-valued internal variables accounting for the degree of degradation are introduced. In case of a linear relationship between the strain and the work conjugated stress, these variables may degrade the stiffness tensor. More general, the Helmholtz free energy is degraded by the damage variables such that the energy tends to zero as the material is considered ‘fully broken’. In their most simplified version, damage approaches assume the microdefects to be only spherical microvoids. Hence, the overall damage behavior is isotropic, i.e. the material is degraded directionally independent, and thus, only a scalar damage variable is required.

However, it is known that the underlying damage mechanisms are much more complex. Due to elliptical microvoids and orientated microcracks, the behavior at the macroscopic level cannot be considered isotropic anymore. Especially non-proportional loading or highly directional loading are known to cause the material to behave anisotropic, although it may behaved initially isotropic. Therefore, it seems natural to model damage as a direction dependent phenomenon.

If the material behaves brittle, introducing damage variables as internal variables is sufficient to describe the inelastic material behavior. Analogous to plasticity, the evolution equations can then be set up, for example, based on the dissipation inequality and the principle of maximum dissipation. In the case of ductile material behavior, i.e. plasticity coupled to damage, the modeling is much more challenging. There exist approaches in the literature which assume a simultaneous evolution of damage and plasticity (so-called 'one-surface' approaches) or independent evolution ('two-surface' approaches). The latter approaches allow a much more flexible modeling, but are more complex in terms of multiple loading scenarios comparable to multi-surface plasticity. In addition, the evolution of plasticity is often assumed to take place in the so-called effective continuum, i.e. the material is virgin. Thus, the plastic evolution is strongly coupled to damage, since the mapping to the effective continuum depends on the approach chosen to incorporate damage.

In summary, the scientific debate on how to couple anisotropic damage to plasticity is still not conclusively settled and of greatest interest.

Gradient-extension. Unfortunately, as continuum damage models belong to the class of so-called conventional 'local' damage models, they suffer from a mesh size dependence in case of softening. This results, among others deficiencies, in an undesirable and unphysical decrease of energy dissipation with increasing mesh density. Moreover, the width of the damage zone does not remain finite. In addition, not only the mesh density but also the orientation of the finite elements may influence the direction of the macroscopic crack within a numerical simulation. This pathological dependence is caused by a loss of ellipticity (at least for static problems) of the boundary value problem, resulting in an ill-posed problem. Remarkably, the reason for this does not lie in the FEM, but is rather an inherent problem of the material model formulation itself. Hence, using a different numerical approach to solve the boundary value problem would not solve the aforementioned problems.

In order to overcome these issues, several techniques have been developed, of which the two most prominent are the nonlocal integral- and gradient-type method. The idea of both methods is to include the neighborhood of the material point into the calculation of the material response and not only the physical state present at the point itself.

In integral-type approaches, for example, a local material quantity is replaced by its nonlocal and averaged counterpart. By taking the integral over the domain, a nonlocal character is incorporated into the material formulation. However, with regard to the numerical implementation within the FEM, this approach contradicts the local character of the finite element method, since a spatial averaging necessarily requires information of the neighboring elements. This also complicates the linearization in case of a global Newton-Raphson iteration for solving the

boundary value problem.

Contrary to this, gradient-type approaches usually introduce another partial differential equation as well as a 'nonlocal' variable associated with this differential equation at the global level. Since these approaches require only the variable itself as well as its gradient (higher order gradients can also be used), these approaches are easy to implement into standard finite element codes and fit perfectly with the local character of the FEM. In addition to the differential equation, the constitutive relations for the mechanical stress response are enriched by a contribution of the 'nonlocal' variable. This relationship introduces a nonlocal character into the material formulation by considering an internal length scale at the material point level.

However, since the 'nonlocal' variables do not necessarily have a clear physical interpretation, it is not straightforward to determine the interplay between them and the constitutive framework. In particular, for anisotropic damage, how to choose the constitutive framework using gradient-type approaches as well as the number of 'nonlocal' variables remain open scientific questions.

Growth and remodeling. Aiming to improve patients' healthcare by providing patient-specific medical therapy to enable preoperative estimates of therapeutic success, computer-aided simulations are becoming an indispensable tool in modern medicine. In addition, multiphysical simulations, which include the inelastic material behavior of biological tissues, allow predictions to be made about the successful insertion of implants and, based on this, their improvement to bioadaptive designs. To address these challenges, profound and interdiscipline knowledge regarding the complex physiological, chemical, biological, and mechanical interactions are inevitable. From a continuum mechanical point of view, especially residual stresses evolving in soft biological tissues are of particular interest, as they strongly influence the deformation of the body even in the absence of external loadings. Nowadays, rise in these stresses is assumed to be caused by growth (addition and/or removal of mass) and remodeling (adaption of internal structure).

While earlier approaches employed, for example, pseudo-thermal loading to cause the observed residual stresses, more recently two approaches have become particularly popular for describing the two phenomena: Constrained mixture models and the kinematic growth approach.

Although constrained mixture models will not be employed to model soft tissues within this dissertation, their main idea will be briefly discussed, however, the interested reader is referred to the following works as well as the literature cited therein. Motivated by e.g. individual half-lives in the extracellular matrix of each constituent, constrained mixture models for soft tissues (see Humphrey and Rajagopal [2002]) assume each volume element to be a mixture of

several constituents, for example, elastin, collagen, and smooth muscle cells. While all of them undergo the same deformation, this approach enables to take into account individual turn-over rates, deposition times and stress-free configurations. Since all constituents are resolved within the governing equations, an extension to include the interstitial fluids, such as was done by Ateshian and Ricken [2010], can be easily considered. However, the drawback of this method is its mathematically challenging description of soft tissues as well as its complex computational implementation. Therefore, more recent models perform a homogenization in time such that only a single reference configuration is required (see Cyron et al. [2016]), which significantly reduces the computational cost.

In contrast to constrained mixture models, the fundamentals of kinematic growth approaches rely on the multiplicative decomposition of the deformation gradient. Although the underlying mechanisms of growth and remodeling are far from understood, it is widely assumed that both are triggered by mechanical stimuli. Hence, in order to reach the so-called 'homeostatic stress' throughout the tissue, causing the above mentioned residual stresses, the tissue grows and remodels itself. Therefore, from a modeling point of view, the inelastic part of the deformation gradient must be designed in such a way that this condition is met at each material point. The simplest approach is to assume isotropic growth, i.e. the inelastic part is proportional to the identity tensor multiplied by one or more growth factors. The latter are usually a function of the stress tensor. Since the results obtained by these isotropic growth models are generally inconsistent with experimental observations, more sophisticated approaches take into account the local stress state and define the (tensorial) evolution of growth and remodeling as a function of the stress tensor. Such kind of models are referred to as anisotropic growth models and are much more flexible with regard to the particular boundary value problem. Noteworthy, the type of growth is independent of the underlying or initial macroscopic material behavior, i.e. anisotropic growth may also be present in initially isotropic material.

In the literature, a variety of approaches can be found to describe anisotropic growth. Some of them are limited to specific components (and their idealized geometries such as e.g. cylinders) in the human body, for instance, blood vessels and in particular arteries. However, it seems more appropriate to choose a stress-like growth criterion based only on the state at the local material point rather than on the geometry.

This raises scientific questions about the choice of such a growth criterion, the choice of the associated stress tensor, the incorporation of a time scale since growth and remodeling are not instantaneous, and a flexible but physically reasonable formulation of the evolution equations.

Fiber reorientation. A major constituent of soft biological tissues is collagen fibers, which are responsible for optimized carrying of mechanical loadings. Due to these fibers, the overall

material behavior is initially anisotropic.

In contrast to non-living materials, collagen fibers are remodeled by the cells due to a complex interplay between resorption and production of those fibers, which is commonly referred to as fiber reorientation. Macroscopically, these processes can be described by a reorientation of the structural vector aligned with the (averaged) direction of collagen. While it is generally accepted that reorientation takes place towards a principal direction, for instance, by minimizing the angle between the structural vector and the principal direction, it is controversial whether this principal direction is defined by strain- or stress-like quantities.

For elastic material behavior, both approaches lead to the same result, since the thermodynamically conjugated strain and stress measures are coaxial, but due to growth and remodeling, this is no longer necessarily the case. In the context of this dissertation, stress-driven remodeling is pursued, as this seems reasonable to reduce the mechanical loading of the tissue.

Scientifically interesting is the question of how to choose a time-dependent and physically reasonable evolution equation, especially with regard to the associated stress tensor in the case of inelastic material behavior.

Fundamental questions are still open in various fields of material modeling in a continuum mechanical sense, ranging from classical elasto-plasticity to modern biomechanics. Although the materials to be modeled are both living and non-living, from a continuum mechanics point of view they can be subsumed as inelastic and anisotropic materials. Therefore, the dissertation aims at developing thermodynamically consistent material models that are not only applicable to various anisotropic and inelastic materials, but are also numerically efficient and can be easily implemented by means of AD, as modern material models are accompanied by challenging numerical implementations.

To begin with, anisotropic (transversely isotropic) materials consisting of fibers embedded in a matrix are discussed. Conceptually, the anisotropy is captured through structural tensors, where the matrix is modeled elasto-plastically based on the multiplicative decomposition of the deformation gradient. Different failure mechanisms (fiber breakage, fiber kinking, matrix failure) are accounted for by multiple scalar-valued damage variables. To avoid mesh sensitivity, each of them is gradient-extended using the micromorphic approach by Forest [2009, 2016], which provides a straightforward and conventional way to extend ‘local’ models to ‘nonlocal’ ones.

Subsequently, anisotropic damage using a second order tensor coupled to elasto-plasticity at finite strains is presented. For conceptual reasons, the constitutive framework is stated with respect to the logarithmic strain space. Within this approach, both phenomena are treated

as independent but strongly coupled dissipative mechanisms. Noteworthy, the damage tensor can be interpreted as an evolving structural tensor. Furthermore, it is appealing to recognize that the proposed model does not suffer from artificial stiffening, since the damage growth criterion by Wulfinghoff et al. [2017] is fulfilled. As for initially anisotropic materials, the micromorphic approach is employed to overcome mesh dependence in case of softening. To this end, the three invariants of the damage tensor are gradient-extended.

Finally, concerning the questions related to the rotational non-uniqueness of the multiplicative decomposition as well as growth and remodeling, a co-rotated formulation of the intermediate configuration is proposed. This allows a conceptually straightforward combination of inelastic and anisotropic materials with AD. In this way, the proposed stress-driven kinematic growth model for soft biological tissues can be efficiently implemented. Thereby, tensional homeostasis is accounted for by homeostatic surfaces introduced by Lamm et al. [2022], which describe the preferred stress with respect to the principal stress space. Additionally, production and resorption of collagen fibers is modeled in a smeared sense by a reorientation of the associated structural vector towards the principal stress direction in the current configuration.

1.2 State-of-the-art in geometrically nonlinear anisotropic inelasticity

In order to contextualize the aforementioned questions and issues with already published papers and to further motivate this dissertation, a review of the relevant literature is provided. Plasticity based on the multiplicative decomposition is already well established in the continuum mechanics community and a variety of standard literature exists (e.g. Haupt [2002] and Bertram [2012]), including its numerical treatment (see e.g. Weber and Anand [1990], Cuitiño and Ortiz [1992], Miehe [1996] and Sielenkämper et al. [2022]). Thus, the following will mainly focus on the fields of anisotropic damage and its regularization as well as soft tissue modeling.

The following literature review is not meant to be complete, but rather serves as an introduction to the different topics based on their origins as well as to current challenges that are of particular interest to the scope of this dissertation.

1.2.1 Continuum mechanical modeling of anisotropic damage

As mentioned above, damage modeling can be divided into isotropic and anisotropic damage, the latter of which also causes initially isotropic materials to behave in a direction-dependent manner.

Since its micromechanical motivation, also in a phenomenological and smeared sense, goes back to various works dealing with isotropic damage, this topic will be introduced in the following paragraph.

Furthermore, as this thesis deals with ductile damage, i.e. coupled damage and plasticity, works that are of particular interest in this regard will be mentioned. In this context, only 'coupled' models in the case of ductile damage will be discussed. In contrast to the 'uncoupled' models, these models are able to consider e.g. a stiffness reduction or a reduction of the plastic threshold in time, since damage is incorporated into the constitutive modeling.

Microstructure. As mentioned above, dislocations are associated with plasticity, while nucleation of microdefects, their growth and coalescence are the underlying mechanisms to cause material degradation. The experimental investigation of these mechanisms is of particular interest in Scheyvaerts et al. [2011], Shang et al. [2020] and Liu et al. [2021].

In this regard, Lemaitre and Dufailly [1987] proposed several techniques to measure the degree of degradation. These techniques can be classified into direct and non-direct methods. The former evaluate e.g. micrographic pictures, while the latter measure the influence of degradation on other material properties such as stiffness, thermal conductivity or electric potential. This already gives rise to the requirements for continuum mechanical modeling, since all these quantities must be considered as influenced by damage. For instance, Celentano and Chaboche [2007] investigated and characterized ductile damage of steel in an experimental study using non-direct methods.

Moreover, it is found that the stress state, especially the stress triaxiality, has a significant influence on the nucleation, growth and coalescence of microvoids. Over the years, several studies have investigated this influence, e.g. the works of Benzerga et al. [2004], Brünig et al. [2008], Mirone and Corallo [2010], Malcher et al. [2014]. Benzerga et al. [2004] concluded that all stages of damage should be considered inherent anisotropic. In order to measure anisotropic damage, for instance, the direction dependent stiffness reduction can be measured (see Hao et al. [1985] and Lemaitre et al. [2000]). More recently, either biaxial loading scenarios are utilized to study the effect of damage anisotropy due to different stress states applied (see e.g. Brünig et al. [2008, 2013] and Schemmann et al. [2018]) or the specimen is subjected to non-proportional loading paths (see Brünig et al. [2019]). In this context, Gerke et al. [2020] provided a collection of specimen geometries to study damage anisotropy.

Isotropic damage. Although most of the existing approaches to model damage are based on the above described mechanisms of damage growth, they can be roughly differentiated into micromechanically and phenomenologically motivated ones.

A popular subgroup of the first approach are Gurson-type models (see Gurson [1977]), which are based on the observations for void evolution of McClintock [1968] and Rice and Tracey [1969]. Within these models, the internal variables are associated with the void volume fraction, which, in turn, reduces the yield threshold of plasticity. In a series of publications (see Tvergaard [1981, 1982*a*,*b*]), the original formulation of the Gurson-type model was adapted and made more flexible. Finally, Tvergaard and Needleman [1984] chose a type of damage threshold based on the void volume fraction, which is probably the most popular and is often referred to as the Gurson-Tvergaard-Needleman (GTN) model. The GTN model was then enhanced to include, for example, the shear damage evolution (see e.g. Wu et al. [2019]), plastic anisotropy (see e.g. Morin et al. [2015]), yield criteria for intergranular ductile void growth (see Sénac et al. [2023]) and kinematic hardening (see e.g. Klingbeil et al. [2016]). For a comprehensive literature review and a comparison between micromechanically and phenomenologically motivated models, the interested reader is referred to Besson [2010].

Models belonging to the second group are consistent with the concept of Continuum Damage Mechanics, which goes back to the pioneering work of Kachanov [1958] and describes degradation in a smeared sense. To this end, a scalar-valued variable associated with the material integrity was introduced, which was slightly exchanged by Rabotnov [1963, 1969] with a scalar-valued variable related to the damage state rather than the integrity. Furthermore, an interpretation as the reduced cross-sectional area was provided.

In contrast to micromechanically motivated models, the damage variable in Continuum Damage Mechanics (CDM) considers the underlying mechanisms only in a phenomenological and smeared sense, and further usually reduces the stiffness of the material. Hence, its evolution is derived from irreversible thermodynamic principles, and, most of the time, the concept of either ‘effective stress’ or ‘effective variables’ as well as the hypothesis of strain (see Lemaitre [1971] and Lemaitre and Chaboche [1978]) or energy equivalence (Cordebois and Sidoroff [1982]). In Skrzypek and Ganczarski [1999], a comprehensive overview about different phenomenological models and the underlying behavior (e.g. ductile or brittle) is provided. Due to its versatility, the CDM serves as an inspiration in various fields of material modeling, for instance, for the modeling of material dissolution in electro-chemical machining (see van der Velden et al. [2021] and van der Velden et al. [2023]).

As one of the first contributions to derive a thermodynamically sound damage model, the work of Chaboche [1978] is to be mentioned. Lemaitre [1984, 1985*a*,*b*] went on to develop

one of the first ductile isotropic damage models, which is still widely used in the mechanics community. Since then, various effects were included into the original formulation, e.g., aging (Marquis and Lemaitre [1988]), crack-closure (Andrade Pires et al. [2003] and Bouchard et al. [2011]), Lode's angle (Lian et al. [2014]) and finite strains (de Souza Neto et al. [1998] and Saanouni and Lestriez [2009]).

Most of these models utilize 'single-surface' approaches, i.e., damage can only evolve simultaneously with plasticity. Contrary, 'two-surface' approaches treat damage and plasticity as independent and irreversible but strongly coupled mechanisms (see the early works of Ju [1989], Hansen and Schreyer [1994] and Zhu and Cescotto [1995]). This makes it possible to model damage behavior ranging from brittle to ductile within a single material model (see e.g. Vignjevic et al. [2012], Brepols et al. [2017, 2018*b*, 2020], Kiefer et al. [2018], Dittmann et al. [2018] and Sprave and Menzel [2020]). Some recent contributions to this field have already derived thermo-mechanically coupled 'two-surface' models (see e.g. Dittmann et al. [2020] and Felder et al. [2022]). In this dissertation, only these types of approaches are used to model coupled damage and plasticity.

Anisotropic damage. Isotropic damage is to be considered an extreme exception, since microdefects occurring only in the shape of spherical microvoids are practically excluded, regardless of the degree of ductility. Experimentally, it can be observed that the stiffness depends on the loading direction, which means that in the case of a hyperleastic material, the Helmholtz free energy also depends on the loading direction. For phenomenological modeling, a variety of approaches can be found in the literature. These can be broadly classified according to their tensorial order:

- **Scalar-valued/zeroth order.** Conceptually, the simplest extension to include anisotropic damage might be to use a set of scalar-valued (tensors of zeroth order) damage variables. These variables are associated either with the failure of individual constituents in case of composites or with different failure mechanisms of one constituent. For instance, the volumetric/deviatoric response for small strains can be degraded by individual damage variables (see e.g. Neilsen and Schreyer [1993] and Carol et al. [2002]) or in case of finite deformations for the volumetric/isochoric parts (see e.g. Rolfes et al. [2006]) as well as tension-compression asymmetry can be accounted for by several damage variables (see e.g.Mazars et al. [1990], Papa [1996], Comi [2001] and Comi and Perego [2001]). Continuum damage mechanical modeling of composites is investigated using several variables, among others, by Maimí et al. [2007], Holthusen et al. [2020] and Poggenpohl et al. [2021]. For completeness, micro-plane models also belong to this group of scalar-valued damage models (see e.g. Bažant and Gambarova [1984], Bažant and Oh [1985]

and Kuhl et al. [2000, 2001]). Here, anisotropic damage is incorporated using multiple micro-planes, all of which are degraded by individual damage variables.

- **First order.** Due to non-spherical voids and microcracks, the cross-sectional area parallel to these cracks is reduced. Mathematically, the area in a given direction can be described by an outward normal vector of that plane and its magnitude, which represents the area. Therefore, the use of a first order damage tensor can be motivated and have been used, for example, by Davison and Stevens [1973] and Krajcinovic and Fonseka [1981]. The recent publication of Dorn and Wulfinghoff [2021] introduces a (first order) crack orientation director in order to describe normal and shear cracking. In addition, a multiplicative split of the deformation gradient is applied into elastic and crack parts. Thus, the model may also be classified in the second subgroup of second order tensors, cf. below.

- **Second order.** Using a second order damage tensors seems to be a natural extension compared to the modeling of elasto-plasticity, visco-elasticity or growth. These inelastic phenomena are modeled by introducing second order tensors in addition to the total strain tensor. Therefore, and due to their easier interpretation compared to higher order tensors, second order anisotropic damage models are widely used today. These models can be divided into two groups:

  (i) In analogy to isotropic damage, the second order damage tensor is treated as an additional internal variable, which can be considered 'decoupled' from the deformation. Additionally, the second order damage tensor is usually assumed to be symmetric. Most models existing (small and finite strains) follow this type of approach, among many others, see the models of Dragon and Mróz [1979], Murakami [1981], Cordebois and Sidoroff [1982], Hansen and Schreyer [1994], Murakami and Kamiya [1997], Voyiadjis et al. [2008], Badreddine et al. [2015] and Fassin et al. [2019*b*,*a*]. Since the Helmholtz free energy is usually considered to be a scalar-valued isotropic function of its arguments, it is modeled using (mixed) invariants (see Spencer [1971] and Zheng [1994]). Thus, an isotropic degradation results from the principal invariants of the damage tensor itself, while damage anisotropy is caused by mixed invariants of the strain and the damage tensor (see e.g. Kuna-Ciskał and Skrzypek [2004] and Challamel et al. [2005]). More generally, this allows to interpret the damage tensors as a structural tensor (see Reese et al. [2021], Holthusen, Brepols, Reese and Simon [2022*a*], Holthusen, Brepols, Reese and Simon [2022*b*], and Holthusen, Brepols, Simon and Reese [2022]).

  (ii) The total strain is decomposed into elastic strains and damage strains (and plastic,

viscous and growth strains, if required). Consequently, damage enters the Helmholtz free energy indirectly through the amount of elastic strain. Models based on this approach can be found, for instance, in Lehmann [1989], Brünig [2003] and Menzel et al. [2005].

- **Fourth order.** In case of a linear relationship between the strain and the work conjugated stress, the constitutive law can be equivalently expressed by double contracting the (second order) strain tensor with the (fourth order) elasticity tensor. Hence, it seems reasonable to modify the (effective) elasticity tensors, and thus, to incorporate damage anisotropy through the stiffness tensor (see e.g. Chaboche et al. [1995] and Pituba and Fernandes [2011]). More generally, there are also irreducible sets of invariants for fourth order tensors (Betten [1987]), which may allow constitutive modeling of damage similar to the approach described for second order tensors. Compared to models using a second order tensor, a higher degree of damage anisotropy can be realized using a fourth order damage tensor.

- **Eighth order.** For completeness, damage tensors of eighth order are mentioned. As described by Chaboche [1978] and subsequent works, the highest degree of damage anisotropy is achieved using eighth order damage tensors. However, from a continuum mechanical modeling point of view, these tensors are not practical for constitutive modeling.

It should be noted that for ductile damage modeled by a second order damage tensor, the question of how to define the 'effective' stress as well as the mapping between the 'real' and 'effective' stresses is by no means trivial to answer. In addition, Murakami [2012] mentioned that using a second order damage tensor, damage orthotropy is the most complex damage anisotropy representable, however, Kachanov [1987] emphasized its accuracy even for high crack densities. Therefore, and due to the large amount of available literature using second order damage tensors, a second order damage tensor is employed in the models presented in Chapters 3-5.

The model for transversely isotropic materials (matrix with embedded fibers) presented in Chapter 2 uses several scalar-valued damage variables both for the individual components and to account for different failure mechanisms of the fibers (fiber breakage and kinking). The latter split accounts for asymmetric behavior between tension and compression.

1.2.2 Mesh regularization techniques

All damage models outlined in the previous Chapter 1.2.1, regardless of whether they are micromechanically or phenomenologically motivated (including the micro-plane approaches), are so-called 'local' models, and thus, unfortunately suffer from a pathological mesh dependency. Although damage is perhaps the most well-known inelastic phenomena causing mesh dependence, this dependence can also generally occur due to softening behavior, such as plasticity. Since reported in the literature by Bažant et al. [1984] and de Borst et al. [1993], the issue of mesh sensitivity has been intensively studied and a wide variety of approaches to solving it have been developed. Additionally, for instance, Jirásek and Grassl [2008] reported an undesired dependence between the propagation of the localization zone and the orientation of the finite elements. Loosely, the techniques to cure the pathological mesh dependence can be categorized into three groups.

The first group contains so-called crack band models (see e.g. Bažant [1982] and Bažant [1985]). As these models only require an adaption of the material parameters, they are easy to implement. However, although these models provide the correct amount of dissipated energy, the remaining issues are not solved.

Models belonging to the second group account for cracks in a discrete manner, i.e., discontinuities such as a jump in the displacement field are allowed. Cohesive zone models (Dugdale [1960] and Barenblatt [1962]) resolve the crack by a separation between finite element surfaces. Hillerborg et al. [1976] introduced the fracture energy into the formulation of traction-separation laws, in order to define the threshold of crack initiation and propagation. Until today, the cohesive zone approach is subject of several contribution to the field of discrete damage modeling (see e.g. Bayat et al. [2020], Chen et al. [2021] and Rezaei et al. [2021]). Unfortunately, the crack path must be known in advance, since its propagation is restricted along the elements' surfaces. Therefore, the extended finite element method (Belytschko and Black [1999]) was developed. In the field of damage modeling, the energetic approach of Moës and Belytschko [2002] can be mentioned, since this allows to model arbitrary cracks.

Continuous modeling approaches represent the third group. While continuum mechanics accounting for the microstructure, for instance, by means of the Cosserat continuum theory (see e.g. de Borst [1991]), nonlocal continuum formulations such as kinematics-inspired peridynamics (Javili et al. [2019] and Laurien et al. [2023]) as well as viscous regularization techniques (see e.g. Needleman [1988] and Niazi et al. [2013]) can be subsumed in this group, two established approaches are of particular interest here: Nonlocal integral and gradient-extended formulations.

Nonlocal integral-type. First introduced by Pijaudier-Cabot and Bažant [1987] and Bažant

and Pijaudier-Cabot [1988] in field of inelastic, especially damage, material modeling, the nonlocal integral-type approach. Since then, nonlocal integral-type models were further developed and applied to various structural problems (see e.g. Ganghoffer et al. [1999] and Borino et al. [2003]). However, as already indicated, the combination of nonlocal integral formulation and the FEM is obstructive from the numerical implementation point of view, since the general characteristics (nonlocal integrals and local finite elements) oppose each other.

Gradient-extended. Contrary to nonlocal integral-type models, gradient-enhanced formulations incorporate an internal length scale by an additional partial differential equation (PDE). This PDE includes gradients of the newly introduced field variable, and both the variable itself and the gradients enter the material formulation. Consequently, the 'local' material model is enriched by a nonlocal character through the PDE on the global level. For 'local' plasticity models, gradient-enhanced formulations were proposed, for instance, by Svendsen and Bargmann [2010], Wulfinghoff and Böhlke [2012] and Miehe [2014]. A comprehensive review paper on gradient-enhanced plasticity theories was presented by Voyiadjis and Song [2019].

In analogy to these enhanced formulations, 'local' damage(-plasticity) models were enhanced by incorporating an internal length scale via an additional PDE. Particular subclasses of those are the phase field of fracture (see Francfort and Marigo [1998] and Bourdin et al. [2000]) and the micromorphic approach (see Forest [2009, 2016]).

In the phase field approach, a field order parameter as well as a corresponding PDE is introduced on the global level. Within the 'local' material model, the 'local' damage variable is replaced by the field order parameter. Hence, the formulation is rendered nonlocal. Important contribution to the phase field of fracture approach are its thermodynamically consistent derivation presented by Miehe et al. [2010*a*] and its robust implementation in the context of the FEM (see Miehe et al. [2010*b*]).

The micromorphic approach, and the conceptually similar but less general formulation of Dimitrijevic and Hackl [2008, 2011], introduces a 'micromorphic' or 'nonlocal' variable on the global level similar to the phase field of fracture. In contrast to phase field models, this variable is not directly incorporated into the formulation of, for instance, the elastic stored energy, but rather a 'local' counterpart is still utilized. Thus, material point studies are still possible without spatial discretization. In order to ensure a strong coupling between both variables, a penalty energy is usually added to the Helmholtz free energy, which penalizes the difference between these variables. The advantage of the micromorphic framework definitely lies in its rigorous thermodynamically consistent derivation and its unified applicability to a

wide range of material phenomena. Noteworthy, the micromorphic approach is not limited to damage and/or plasticity models. Consequently, a very general procedure to gradient-enhance any variable on the 'local' material point level is proposed.

In the field of (ductile) damage modeling, the micromorphic approach was successfully applied by various authors: Micromorphic-extended isotropic (ductile) damage is considered e.g. by Aslan et al. [2011], Saanouni and Hamed [2013], Brepols et al. [2017, 2018*b*, 2020], Sprave and Menzel [2020] and Friedlein et al. [2023], among many others. For instance, Fassin et al. [2019*b*,*a*], Holthusen et al. [2020], Holthusen, Brepols, Reese and Simon [2022*b*], Poggenpohl et al. [2021] and Langenfeld and Mosler [2020] cured mesh sensitivity in the case of anisotropic damage using the micromorphic approach. Due to the above mentioned advantages in terms of consistency and generality, the regularization technique chosen in Chapters 2-5 is the micromorphic approach.

1.2.3 Growth and remodeling of soft biological tissues

The simulation of growth and remodeling processes are two of the most prominent subfields of biomechanics and mechanobiology. In this regard, growth deals with the change of mass and/or volume, while remodeling is associated with the adaptation of internal structure. Since new findings in these two fields and all peripherally related subfields are being explored on a daily basis, it would be foolish to assume that all aspects could be introduced here. One of the reasons for this is that the macroscopic effects and relationships are somewhat understood, but the underlying mechanisms are far from understood.

A detailed characterization of growth and remodeling would require modeling in a multi-physics context, including fluid-structure interactions and various advection-reaction-diffusion equations for the transport of hormones and nutrients. These are extremely challenging scientific problems in themselves and are the subject of ongoing research (see, among many others, Yoshihara et al. [2014], Thon et al. [2017], Escuer et al. [2019] and Manjunatha et al. [2022*a*]). However, it is common sense that a major factor influencing growth and remodeling is mechanical stimulation, regardless of whether the biological material of interest is hard or soft tissue. Since the growth and remodeling model proposed in this thesis is limited to mechanically-driven inelastic deformations, the following focuses on the mechanical influence on tissues.

First of all, the variety of different types of tissues found in nature is enormous, but a rough classification can be made between plant and animal tissues. The continuum mechanical modeling of the former is treated, for example, in Macek et al. [2023]. In this dissertation, the focus is on animal tissues.

Animal tissues can be categorized into connective, muscle, nervous, and epithelial tissues (cf. Pawlina and Ross [2018]). These tissues are a mixture of cells and the extracellular matrix, which consists mainly of elastin, collagen, and ground substance. The latter two are most commonly produced by fibroblasts cells. A much deeper insight into the hierarchical structure of tissues, tissue types, the cells involved, the interactions at the cellular level, and generally into biomechanics with special emphasis on tissue mechanics is provided in the textbook by Cowin and Doty [2007]. In addition, the interested reader may find more detailed introductions to biomechanics and the mechanical modeling of biological growth in the textbooks by Humphrey and Delange [2004] and Goriely [2017], respectively.

A common categorization in biomechanics and/or mechanobiology distinguishes between hard and soft tissues. On the one hand, hard tissues and their continuum mechanical modeling such as, for example, bones (see e.g. Cowin and Hegedus [1976], Hegedus and Cowin [1976], Cowin and Nachlinger [1978], Cowin [1999], Cowin [2001], Nackenhorst and Hartung [2001] and Floerkemeier et al. [2010]), horns (see Skalak et al. [1997]) and teeth already received greater consideration from the modeling point of view. On the other hand, the physiologically specific material modeling of soft tissues includes brain tissues (see e.g. Budday et al. [2015], Mihai et al. [2017], Budday et al. [2017] and Budday et al. [2020]), the skin (see e.g. Buganza Tepole et al. [2011]), arteries (Holzapfel et al. [2000], Holzapfel and Ogden [2010]), the cardiovascular system (see e.g. Humphrey [2002], Hoskins et al. [2017] and Quarteroni et al. [2017]), the heart (see e.g. Dal et al. [2013], Baillargeon et al. [2014]), muscles (see e.g. Böl et al. [2014] and Wisdom et al. [2014]), tendons (see e.g. Böl et al. [2015] and Burgio et al. [2022]) and many more. In contrast to hard tissues, soft biological tissues are subject to both finite rotations and finite strains, while hard tissues are usually only exposed to finite rotations. In this dissertation, special attention is paid to the continuum mechanical modeling of soft tissues.

Non-living materials behave only in a *passive* way, i.e. all elastic and inelastic deformations are caused by the natural dissipation mechanisms. Thus, no entropy source or sink has to be introduced to be in agreement with physics. With respect to inelastic behavior, besides degradation, viscoelastic behavior is quite pronounced for soft tissues, e.g. in the case of brain tissues (Reiter et al. [2021] and Ricker et al. [2023]) and the heart (Tikenoğulları et al. [2022]). These processes usually occur on a much smaller time scale than *active* deformations (cf. Goriely [2017]). Active deformations refer to processes in which the dissipation of the system is reduced, which only occurs in living materials and is most prominent in growth and remodeling. Obviously, this violates the rules of physics if the living organism is modeled as a closed system. To this end, living organisms are mechanically considered an open system and

additional entropy sources and/or sinks are introduced (see Kuhl and Steinmann [2003*a*,*b*]). Furthermore, due to the large time scale of growth processes, the balance of mass is considered to be implicitly satisfied, and thus, the balance of linear momentum is reduced to the quasi-static case, which is known as the *slow-growth assumption* (cf. Goriely [2017]).

Since active deformations are not necessarily driven by thermodynamically consistent driving forces, it is appropriate to mention the most common modeling approaches to drive (active) growth and remodeling:

- Active forces extend the body forces in the strong form of linear momentum by an active force term. Thus, in order to be in equilibrium, the stress state is altered with respect to the load state of the external loads.
- The existence of active stresses is postulated in addition to the stresses derived from the elastic stored energy (see e.g. Guccione and McCulloch [1993]).
- Typically, all strain energies are designed so that a stretch of one corresponds to the zero-value minimum of the energy. However, shifting the minimum of the collagen fibers toward a stretch of zero, the fibers actively desire to contract themselves. Of course, a minimum at zero is forbidden, as this would result in a contraction to zero. This approach is called active fibers (see e.g. Moulton et al. [2016]).
- An active metric known from differential geometry is utilized (see e.g. Yavari and Goriely [2014]). Here, the distance between material points is changed such that stresses arise caused by a change of the reference configuration.
- The deformation gradient is decomposed multiplicatively into an elastic as well as a growth and remodeling part, sometimes referred to as active strains or kinematic growth approach, which will be used in the present thesis. Although it may seem similar to the previous approach, active strains should not be confused with an active metric, since the multiplicative decomposition suffers from inherent rotational non-uniqueness, unlike the active metric.

For a brief but extremely insightful overview that is well worth reading, see the overview by Goriely [2018]. In this regard, the purpose of soft biological tissues to grow and remodel themselves can be attributed to several reasons, but one established reason is the ability to achieve, maintain, and restore a state of homeostasis.

Homeostasis. Homeostasis is an essential factor in ensuring healthy tissues. According to the definition of Cannon [1929], homeostasis describes the ability of tissues to respond to

physiological influences in such a way that a similar mechanical state is maintained and restored (cf. e.g. Cyron and Humphrey [2016]). However, this does not specify the mechanical quantity describing the homeostasis, be it strain, stress, force or stiffness. Wolinsky and Glagov [1967] went on to study the aorta and found that tension seemed to drive homeostasis regardless of the size of the specimen.

Subsequently, Brown et al. [1998] introduced the term tensional homeostasis to account for the hypothesis that soft tissues seem to prefer a tensile stress state. However, since 'tensional homeostasis' is only a hypothesis, the term 'mechanical homeostasis' can also be used more generally (see Humphrey et al. [2014]). Considering that growth and remodeling might be mainly driven by mechanical stimuli, additional limiting factors such as the availability of hormones and nutrients should be mentioned. Thus, 'mechanical homeostasis' may also emphasize that most (continuum mechanical) modeling approaches consider only the influence of mechanical fields. One of the few works that combines growth and remodeling with the diffusion and availability of nutrients is the contribution of Soleimani et al. [2020].

In order to gain more knowledge about the underlying mechanisms and to understand what drives homeostasis, an excessive number of experimental studies have been conducted in the recent past. Uniaxially constrained experiments of tissue equivalents were conducted, for example, by Marenzana et al. [2006] and Ezra et al. [2010]. Both a contraction of the tissue, indicating tensional homeostasis, and a restoration of homeostasis were observed. However, tissues are generally not exposed to uniaxial conditions, but are practically always subject to multiaxial conditions. In order to close this gap in experimental terms and the deeper understanding of homeostasis, a large number of multiaxial experiments, including perturbation to observe the recovery of homeostasis, have been performed by Eichinger et al. [2020], Eichinger, Grill, Kermani, Aydin, Wall, Humphrey and Cyron [2021] and Eichinger, Paukner, Aydin, Wall, Humphrey and Cyron [2021] in the recent past. For a broader description and a more detailed explanation of the mechanisms associated with homeostasis at the cellular level, the interested reader is kindly referred to the review article by Eichinger, Haeusel, Paukner, Aydin, Humphrey and Cyron [2021] and the thesis by the same author (Eichinger [2021]).

Kinematic growth. The variety of approaches that have been developed over the years to simulate soft tissue is as diverse as soft tissue is complex. As alluded to in the previous Chapter 1.1, constrained mixture models have become popular for several reasons mentioned. In addition, since the behavior of soft tissues is mainly controlled by cells, it seems natural to resolve the cells' behavior as well as the cell-cell interactions in a discrete manner (see e.g. Mogilner et al. [2012]). In this way, new knowledge about the cells can be directly

incorporated into the simulation. However, this approach suffers from a lack of connection from this microscale to the macroscopic tissue scale (see Goriely [2017]). Therefore, continuum mechanical models are still preferable, and the multiplicative decomposition (active strains) is employed here.

The multiplicative decomposition of the deformation gradient in the field of growth and remodeling goes back to the work of Rodriguez et al. [1994]. The models developed on the basis of the multiplicative split may be classified into isotropic and anisotropic growth models. Note that anisotropic growth does not refer to the initial material behavior, i.e., initially isotropic materials may grow anisotropically and vice versa.

Isotropic growth models assume that the growth tensor itself or its evolution is proportional to the identity tensor multiplied by some growth factor (see Lubarda and Hoger [2002]). The growth factor can then be chosen as a function of some scalar quantity, say the trace of the elastic Mandel-like stress tensor relative to the homeostatic stress. If both are equal, no further evolution of growth and remodeling should take place. Consequently, all eigenvalues of the inelastic part of the deformation gradient are equal at all times. Such kind of isotropic growth models were proposed, for instance, by Himpel et al. [2005] and Kuhl et al. [2007]. However, isotropic models imply that an extremely restrictive assumption about growth and remodeling is made a priori, which in itself does not seem very flexible from a modeling point of view. It is therefore not surprising that the comparison between isotropic growth models and experiments conducted by Braeu et al. [2017] showed a large number of limitations and no satisfactory agreement between simulation and experiment.

In contrast, anisotropic growth models are able to grow and remodel directionally. The straightforward extension of isotropic growth models is to introduce more than one growth factor and multiply it by a specific direction (structural tensor), similar to modeling anisotropic thermal expansion at finite deformations (see Vujosevic and Lubarda [2002]). The sum of all growth factors gives the direction of the evolution of the total growth tensor. In the spirit of this method, Göktepe et al. [2010] developed an anisotropic growth model including three growth factors associated with specific muscle fiber orientation in the heart. Similarly, Sáez et al. [2014] and Rahman et al. [2023] modeled growth in a hypertensive human carotid artery using a transversally isotropic growth approach (cf. Goriely [2017] for different categories of growth tensors).

Since growth and remodeling are assumed to be related to tensile stresses, it seems reasonable to define the evolution of growth in terms of the local stress field. This is the basic idea of the models proposed, for example, by Zahn and Balzani [2017, 2018] and Liu et al. [2019]. The former introduce a general growth tensor that is multiplicatively decomposed into three

individual parts. Each part can account for a different preferred direction of growth.

An idea reminiscent of plasticity is presented by Soleimani et al. [2020]. A scalar function similar to a yield criterion is introduced to capture the over- and understress between the current stress state and the homeostatic stress state. However, the tensor describing the direction of growth is not derived from a potential, but rather is chosen based on the eigenvectors of the Cauchy stress tensor. The idea of using a concept already known from plasticity was presented by Lamm et al. [2021, 2022]. A so-called 'homeostatic surface' is postulated, which describes the preferred stress state in the principal stress state of the thermodynamically consistent driving force associated with growth. The evolution might then be derived associatively or non-associatively by postulating another growth potential. In addition, since growth and remodeling do not occur instantaneously, time-dependent approaches motivated by the theory of visco-plasticity are used to introduce a time scale into the model. Holthusen et al. [2023] followed this approach and extended it for initially anisotropic materials, in particular considering collagen fibers.

Remodeling. The inelastic part of the deformation gradient generally contains both growth and remodeling. Thus, according to Cyron et al. [2016] and Braeu et al. [2017], it seems reasonable to multiplicatively decompose the inelastic part of the deformation gradient into a part related to growth and a second part related to remodeling. Since remodeling refers only to a change in the internal structure, the evolution of the remodeling related part must be volume preserving. This can be achieved, for example, by a deviatoric evolution direction of the remodeling related part, cf. von Mises plasticity (see e.g. Vladimirov et al. [2008]).

An example of remodeling in hard tissues (bones) is their adaptation to external loads by some kind of reinforcement. From a modeling point of view, this can be achieved by adjusting the density. Although this involves a change in volume associated with growth, it can also be considered as remodeling (see Goriely [2017]). However, the most well-known remodeling phenomenon is certainly the remodeling of collagen fibers or their reorientation. The purpose of this reorientation is to optimally carry external (tensile) loads. This topic will be discussed in more detail in the following Chapter 1.2.4.

The growth and remodeling model presented in Chapters 6-7 is based on the kinematic growth approach and further postulates the existence of homeostatic surfaces. A 'one-surface' approach based on the Cauchy stress of the entire tissue and a 'two-surface' model, where one surface describes the homeostatic state of the collagen and a second surface is responsible for the homeostasis of the matrix are investigated. In order to elegantly implement the material model through algorithmic differentiation, a novel framework is proposed using a uniquely defined co-rotated intermediate configuration.

1.2.4 Fiber reorientation

Collagen is one of the major constituents of, for instance, the extracellular matrix and tendons. These collagen fibers are composed of collagen fibrils, which are produced by fibroblasts within the cells. While they are perfectly suited to carry (tensile) mechanical loads, their contribution under compressive conditions is negligible in most cases. For an overview of the molecular structure, mechanical properties, and assembly process of collagen fibers, at least in tendons, see the comprehensive article by Silver et al. [2003] and the literature cited therein.

A collagen fiber bundle does not contain completely parallel oriented fibers, rather the orientation of all collagen fibers can be described by an average (major) direction. To account for this dispersion within the continuum mechanical modeling, Gasser et al. [2006] proposed different approaches to consider the fiber dispersion. The identification of the fiber dispersion parameter is the subject of e.g, Schriefl, Reinisch, Sankaran, Pierce and Holzapfel [2012] and Schriefl, Zeindlinger, Pierce, Regitnig and Holzapfel [2012].

As mentioned in the previous chapters, a change in internal structure – referred to as remodeling – distinguishes living from non-living materials. Remodeling allows the organism to dynamically adapt its material response to, for example, mechanical loading. Fiber reorientation can be considered a prominent remodeling process within soft biological tissues. Although far from being understood, the interplay between resorption and production (proliferation) of collagen fibrils and the fibroblasts involved is assumed to be mainly driven by mechanical stimuli (see the review article by Wells [2013]), which is supported by experimental evidence (see e.g. Stopak and Harris [1982], Eastwood et al. [1998] and Hu et al. [2009]).

From a mechanical modeling point of view, these mechanical stimuli can be divided into strain- and stress-driven approaches. The former usually assume that the averaged direction of collagen coincides with the principal direction of (tensile) strain, while stress-driven approaches proceed analogously with the principal direction of (tensile) stress.

Strain-driven. Cowin [1984] argued that baroreceptors sensing mechanical stimulation are merely stretch/strain receptors. Therefore, fiber reorientation can only be a strain-driven process. This argument culminates in the statement of Cowin [2004] that the concept of stress is a purely fictitious and man-made concept (a statement that the author of this dissertation shares in principle) Therefore, physiologically, only the measurable quantity stretch/strain can influence reorientation. It is interesting to note that Wang et al. [2001] observed the fibers' reorientation mainly depends on the magnitude of the applied strain rather than its rate.

Driessen et al. [2004] defined the evolution equation for fiber reorientation in terms of the angle between the collagen fibers and the target vector towards the collagen fibers should be reoriented. The model was then extended to include fiber dispersion (see Driessen et al. [2008])

and successfully applied in the context of (idealized) arteries and aortic valves. A patient-specific simulation including fiber remodeling was presented by Creane et al. [2011], who assumed that the mean fiber direction is at an angle between the first and second highest positive strain vectors. A constitutive framework for strain-driven fiber remodeling for transversely isotropic materials has been proposed by Menzel [2005]. Here, an evolution equation is set for the structural vector aligned with the averaged direction of collagen fibers, which rotates the vector in the direction of the principal eigenvector of the right Cauchy-Green tensor. This evolution equation is beneficial since it naturally preserves the orthogonality condition, i.e., the structural vector remains a vector of unit length. This approach was pursued, for example, by Kuhl et al. [2005] and Himpel et al. [2008] in the context of structural simulations. Later, Menzel [2007] extended the constitutive framework to two families of fibers included. The interested reader is referred to the introductory part of the latter article for an overview of the physiological background and continuum mechanical modeling of fiber reorientation.

Stress-driven. Since the strain energy in a hyperleastic material takes an extremum if the strain tensor and the work conjugated stress tensor are coaxial (cf. Sgarra and Vianello [1997]), one may motivate a stress-driven fiber reorientation. However, for inelastic materials the right Cauchy-Green tensor and the second Piola-Kirchhoff stress tensor are generally not coaxial, since the second Piola-Kirchhoff stress is a tensor-valued isotropic function of the right Cauchy-Green tensor as well as the inelastic part of the deformation gradient. Thus, for inelastic materials, the stress-driven approach will lead to a different orientation compared to the results for a strain-driven approach in general.

In Imatani and Maugin [2002], an evolution equation for the structural vector is introduced, where the driving force involved is of Mandel-stress-type and its principal directions, respectively. Johansson et al. [2005] followed a similar approach as well. Hariton et al. [2007*a*,*b*] proposed an iterative scheme in which the boundary value problem is computed several times to obtain the final orientation of the collagen fibers. In their work, they considered two families of fibers in an arterial wall. To increase efficiency and to reduce computational cost, Fausten et al. [2016] developed an incremental algorithm, where they averaged the principal stresses over all Gaussian points and chose the loaded state for the computation. Although for most applications the orientation of collagen at the end of fiber remodeling is of interest, incremental approaches may suffer from abrupt changes in the direction of anisotropy, and thus, lead to numerical instabilities. Therefore, Zahn and Balzani [2017, 2018] introduced a continuous reorientation algorithm based on the angles enclosed between the actual orientation of collagen fibers and the target vector. Similarly, Holthusen et al. [2023] adopted the approach presented by Menzel [2005], however, the structural vectors with respect to the current configuration ori-

ents towards the principal direction of the Cauchy stress tensor. Here, a continuous remodeling approach is utilized with decreasing remodeling rate for decreasing angle enclosed between collagen fibers and the principal direction.

Additionally, the recent approach of Ciambella and Nardinocchi [2019, 2022] and Ciambella et al. [2022] can be considered stress-driven. Instead of evolving the referential structural vector towards a preferred direction, they introduced a (second order) rotation tensor and multiplied it with the second order structural tensor, which is the dyadic product of the structural vector with itself. This rotated structural tensor then enters the Helmholtz free energy. After a rigorous thermodynamic evaluation, an evolution equation only for the rotation tensor is obtained. Thus, the structural vector remains unaltered. Since the driving force used to derive the evolution equation for this rotation tensor is in fact its thermodynamically consistent driving force, the approach can be classified as stress-driven.

Besides the question whether fiber reorientation is strain- or stress-driven, there is an ongoing debate about the deformation of the structural vector between the reference and the current configuration, and thus, also to the intermediate one. Most models for soft biological tissues found in literature assume an affine deformation, however, as investigated by Stracuzzi et al. [2022] affine mappings might not be appropriate in each case. A non-affine continuum mechanical approach can be found, for instance, in Raina and Linder [2014].

However, this question is out of the scope of this dissertation and an affine mapping is chosen. Furthermore, the remodeling of the structural vector is stress-driven and an evolution equation for the current structural vector is introduced (see Chapters 6-7). The target vector is equivalent to the (tensile) principal direction of the Cauchy stress tensor.

1.3 Outline of the dissertation

The present cumulative dissertation consists of three peer-reviewed journal articles (Chapters 2, 3 and 6) as well as three contributions to conference proceedings (Chapters 4, 5 and 7). The dissertation is structured as follows:

- **Article 1** (Chapter 2) deals with the modeling of initially anisotropic materials, for instance fiber-reinforced plastics, which undergo plastic deformations and damage. The entire framework is derived in a thermodynamically consistent manner. To account for the anisotropy resulting from the embedded fibers, the concept of structural tensors is used. Furthermore, both damage of the fibers and damage coupled to plasticity of the matrix constituent are considered at finite strains. A ‘two-surface’ approach for coupled damage-plasticity is utilized for the matrix part. Moreover, three scalar

damage variables associated with fiber damage under tensile loading, fiber kinking under compressive loading, and a variable accounting for the damage of the matrix material are used. As a result, based on the stretch in fiber direction, crack-closure of fibers can be taken into account, providing a tension-compression asymmetry of the overall model. Since the damage variables are employed in a local sense, the model would suffer from pathological mesh dependence. To overcome this issue, each local damage variable is gradient-extended using the micromorphic approach. In addition, the numerical implementation of the evolution equations, the finite element formulation, and the solution procedure are presented in a fully implicit manner. Finally, material point studies and structural examples are used to examine the various inelastic effects of the proposed formulation and highlight its ability to provide mesh-independent results.

- **Article 2** (Chapter 3) is concerned with initially isotropic materials, which, due to damage anisotropy coupled to plasticity, become anisotropic with respect to their overall response. For the kinematics, logarithmic strains are considered, where an additive split into elastic and plastic parts is utilized. Once more, a 'two-surface' approach for coupled damage-plasticity equips the model with greater flexibility with regard to the degree of ductility and allows an independent constitutive modeling of each inelastic phenomenon. In addition, isotropic and kinematic hardening effects are considered for both inelastic phenomenon. Furthermore, anisotropic damage is modeled in line with Continuum Damage Mechanics, where a symmetric second order damage tensor is utilized to account for the induced anisotropy. Since the framework is derived in the logarithmic strain space, its transformation into the Lagrangian strain space is presented not only for the consitutively dependent quantities, but also for the material tangent operators, to be applicable in the finite element formulation described in Chapter 2. Besides these constitutive modeling related considerations, the question on how to address mesh sensitivity using the micromorphic approach arises again. Contrary to scalar isotropic damage, the choice of nonlocal variables is non-trivial as there are several ways to incorporate an internal length scale into the model. Therefore, the invariants of the damage tensor are gradient-extended. Moreover, the entire numerical implementation on a local material point level and on the structural finite element level is presented. Several single element tests as well as three structural examples show the effect of damage anisotropy, anisotropic damage coupled to plasticity, and that the novel invariant-based gradient-extension can provide mesh-independent results.

- **Article 3** (Chapter 4) presents a condensed version of the material model derived in

Chapter 3. Here, the difference is the incorporation of anisotropic damage into the elastic strain energy. The final material formulation to be implemented is analogous to Chapter 3. Moreover, the choice of most energy contributions to the Helmholtz free energy is not presented in a generic way, but rather simplified to the most appropriate version. However, another structural example of an asymmetrically notched specimen that undergoes both plasticity and anisotropic damage is examined. The results again illustrate both the effect of damage anisotropy on a structural level and the robust numerical framework.

- In **Article 4** (Chapter 5) addresses additional theoretical aspects of the anisotropic damage model coupled to plasticity that were discussed neither in Chapter 3 nor in Chapter 4. First, it is shown that due to the chosen mapping of the second order damage tensor from the reference to the intermediate configuration, the formulation is invariant with respect to superimposed rotations of the intermediate configuration. Second, another possible gradient-extension is suggested based on the volumetric and deviatoric part of the damage tensor, respectively. Hence, the number of additional nonlocal variables is reduced to two. The framework is similarly condensed as in Chapter 4. Moreover, and in contrast to the examples from Chapters 3 and 4, the material model is studied in a three-dimensional setting using a 'dog-bone' specimen.

- **Article 5** (Chapter 6) presents both a novel co-rotated formulation of the intermediate configuration and a new stress-driven kinematic growth model for soft biological tissues. Due to the inherent rotational non-uniqueness of the intermediate configuration, it is not straightforward to implement the constitutive equations stated with respect to the intermediate configurations into an AD tool. Moreover, all derivatives with respect to variables of this very configuration cannot be calculated using AD. Therefore, a co-rotated formulation is presented, which shares the same physical interpretation with the intermediate configuration, but is uniquely defined. Especially in case of highly anisotropic materials undergoing inelastic effects, this approach proved helpful. Next, this co-rotated approach then serves as the theoretical framework for the novel stress-driven growth model. Within this model, two parallel multiplicative decompositions of the deformation gradient are used to distinguish between growth and remodeling of either direction-independent constituents or direction-dependent constituents such as collagen. Furthermore, the approach of homeostatic surfaces introduced by Lamm et al. [2022] is employed to describe the inelastic evolution equations, where both a 'one-' and a 'two-surface' approach are discussed. Since growth and remodeling are a

time-dependent processes, a Perzyna-type approach is employed to incorporate a time scale into the model. In addition, remodeling of collagen fibers is included in a stress-driven manner with respect to the co-rotated current configuration. The latter avoids the usage of objective rates. In order to study the proposed material model, the model is validated using several experimental data for uniaxial and multiaxial loading taken from the literature.

- **Article 6** (Chapter 7) considers a condensed version of the stress-driven growth model developed in the previous chapter. The model is derived with respect to the co-rotated intermediate configuration, however, contrary to Chapter 6, no inelastic hardening effects are taken into account. Furthermore, only the 'one-surface' approach based on the overall Cauchy stress is used to derive the evolution equations in an associative manner. As in the previous article, fiber remodeling is included in a stress-driven manner based on the overall Cauchy stress. Due to the co-rotated formulation, the entire model is implemented using an algorithmic differentiation tool. Lastly, another structural example of a cylindrical specimen with a hole, which is subjected to internal pressure, is examined. Here, special attention is paid to both the overall growth and remodeling rate and remodeling of collagen fibers towards the major tensile stress direction.

Finally, in Chapter 8 an overall conclusion of the present work as well as an outlook on further topics with respect to current trends in material modeling is given.

2 Article 1: An anisotropic constitutive model for fiber-reinforced materials including gradient-extended damage and plasticity at finite strains

This article was published as:

Holthusen, H., Brepols, T., Reese, S., and Simon, J.-W. [2020], 'An anisotropic constitutive model for fiber-reinforced materials including gradient-extended damage and plasticity at finite strains', *Theoretical and Applied Fracture Mechanics* **108**, 102642.

Disclosure of the individual authors' contributions to the article:

H. Holthusen reviewed the relevant existing literature, derived the constitutive framework and implemented the material model and the element routine into the finite element software *FEAP*. He set up and performed all simulations, interpreted the results and wrote the preliminary version of the article. It was his idea to employ the finite strain elasto-plasticity framework coupled to gradient-extended damage by Brepols et al. [2020] as the basis for the model development. Moreover, T. Brepols, S. Reese, and J.-W. Simon gave conceptual advice, contributed to the discussion of the results, read the current version of the article, and gave valuable suggestions for improvement. All authors approved the preliminary publication of the article in the present dissertation.

2.1 Abstract

An anisotropic, in particular transversal isotropic, thermodynamically consistent material model for unidirectional fiber composite layers at finite strain is proposed. To account for the anisotropy, the concept of structural tensors is used. Tension-compression asymmetric fiber damage as well as an elasto-plastic-damage matrix material are discussed, whereas plasticity and damage are modeled by a two-surface approach. Anisotropic damage is modeled by utilizing three scalar, local damage variables. In this context, mesh-independent damage evolution is achieved using the micromorphic approach presented by Forest [2009, 2016], separately for the fiber and the matrix part. Further, an element formulation including the additional micromorphic degrees of freedom and its linearization for the global Newton-Raphson scheme are presented. Numerical examples show the behavior of the presented material model at the Gauss point and structural level.

Nomenclature

a	Scalar	$\mathbf{A}$	Matrix $n \times m$
$\boldsymbol{a}$	First order tensor	$\mathcal{A}$	Third order tensor
$\mathbf{a}$	Tuple $n \times 1$	$\mathbb{A}$	Fourth order tensor
$\boldsymbol{A}$	Second order tensor	$\boldsymbol{e}_i$	Cartesian basis vector
$\mathbf{0}$	Zero tensor/matrix of any order	$\boldsymbol{I}$	Second order identity tensor
δ_{ij}	Kronecker delta	$\otimes$	Dyadic product
ψ	Specific free Helmholtz energy	$\|(*)\|$	Frobenius norm
Ψ	Free Helmholtz energy	$\boldsymbol{A}^T$	Transpose of $\boldsymbol{A}$
$(*)_F$	Fiber associated value	$\boldsymbol{A}^{-1}$	Inverse of $\boldsymbol{A}$
$(*)_M$	Matrix associated value	$\mathrm{tr}\,(\boldsymbol{A})$	Trace of $\boldsymbol{A}$
$(*)_e$	Elastic quantity	$\mathrm{dev}\,(\boldsymbol{A})$	Deviator of $\boldsymbol{A}$
$(*)_p$	Plastic quantity	$\mathrm{sym}\,(\boldsymbol{A})$	Symmetric part of $\boldsymbol{A}$
$(*)_d$	Local damage quantity	$\mathrm{Grad}\,(*)$	Lagrangian gradient
$(*)_{\bar{d}}$	Nonlocal damage quantity	$\mathrm{Div}\,(*)$	Lagrangian divergence
$(*)_t$	Tension quantity of fiber	$\dot{(*)}$	Total time derivative
$(*)_c$	Compression quantity of fiber	$\mathrm{diag}\,(*)$	Diagonal matrix

$\cdot$	Single contraction ($=: \boldsymbol{AB}$)	$(*)^{\overset{ik}{T}}$	Exchange ith and kth basis vector
$:$	Double contraction	$\hat{(*)}$	Nye notation $(11, 22, 33, 12, 13, 23)$

2.2 Introduction

The growing demand for fiber-reinforced materials in both automotive and aerospace industries makes efficient numerical calculations necessary. Due to the fibers, this class of materials behaves no longer isotropic. Instead, they are dependent on the direction of the fibers, resulting in an anisotropic, for unidirectional layers transversal isotropic, material response. In addition to the consideration of anisotropic material behavior, the calculation of the complex failure of the composite is especially needed to optimize the structural design. In most cases a polymer is used for the matrix material, whereas carbon, aramid or glass fibers are often used for the fiber material, which explains the high strength as well as stiffness ratio to weight. Nevertheless, also fiber materials such as steel, nylon or organic materials (e.g. wood fibers) and ceramic or metals for the matrix are applied (see e.g. Harris [1999]).

Over the last decades, fiber-reinforced composites have undergone intensive research, with particular attention being paid to structural failure. This has resulted in a multitude of criteria for the description of such a behavior. Among others, well-known failure analyses are based on the work of Puck [1996], Puck and Schürmann [2002], Tsai and Wu [1971], Hashin and Rotem [1973] and Cuntze [2006]. The latter, for example, has identified several failure modes that can be associated with either the matrix or fiber failure and further depend on the loading. The kinking of the composite under compressive stress parallel to the fiber direction was investigated in detail in the work of Evans and Adler [1978] and Chung and Weitsman [1995]. Kinking is to be seen as a separate failure mode, whereby this is not to be mistaken with instability phenomena as investigated e.g. in Dow and Gruntfest [1960]. Based on the numerical findings by Harich et al. [2009], Läufer [2018] developed a scalar three damage variable model, which associates kinking with one of those.

Furthermore, Chaboche et al. [1995] and Chaboche and Maire [2002] reported crack-closure effects for Ceramic Matrix Composites, whereby the initial stiffness is nearly regained after damage in the case that the loading regime is changed from e.g. tension to compression. Modeling of this effect can be found e.g. in Desmorat and Cantournet [2008]. Further investigations of fiber-reinforced polymers especially regarding the epoxy matrix material have been done by González and LLorca [2007] and Totry et al. [2008, 2010], who reported plastic deformations

within the matrix material. Pure epoxy specimens were tested in detail by Littell et al. [2008], who measured remaining deformations even after failure. This behavior was also observed by Rocha et al. [2019]. In this context, the work of Basu et al. [2006] and Ji et al. [2011] are mentioned, who model the behavior of the matrix plastically within fiber composites.
Besides the anisotropic and plastic behavior, a realistic material model for this kind of composite materials needs to model the decreasing stiffness from the point of loss of the material integrity. The discipline of Continuum Damage Mechanics (CDM) (cf. Kachanov [1958], Rabotnov [1963]) is one possible way to account for these effects. Here, the damage is modeled by extending the constitutive equations by a set of damage variables, often referred as local damage variables. Nevertheless, it is well known that in the framework of Finite Element Method (FEM) localization effects occur for local damage models (cf. Bažant et al. [1984], de Borst et al. [1993]). As a result, mesh-independence is not guaranteed anymore and a efficient numerical investigation can not be performed. In literature, several ways to overcome this problem are discussed, whereas one possible way is to use nonlocal damage models (cf. e.g. Bazant [1991]). One possibile nonlocal method is the gradient-extension. For the gradient extension, the 'micromorphic' approach introduced by Forest [2009, 2016] can be used. This framework adds additional degrees of freedom to the global system, often referred as 'micromorphic' or 'nonlocal' damage variables.
Due to the intrinsically anisotropic, in unidirectional layers transversally isotropic, behavior of fiber composites an anisotropic damage formulation of the CDM is required. Based on the work of Lemaitre et al. [2000], second order damage tensors are mostly used for this purpose. A general and sufficient formulation is still an ongoing subject of research, currently investigated by e.g. Desmorat [2016], Alliche [2016], Simon et al. [2017], Wulfinghoff et al. [2017], He [2019], Jin and Arson [2018], Nasab and Mashayekhi [2019], Fassin et al. [2019*b*,*a*]. Although the mentioned works consider anisotropic damage evolution, not all formulated material models behave initially anisotropic, which is the case for fiber-reinforced materials. In addition, scalar damage variables seem to be sufficient enough for fiber composites as they can be associated with the several damage modes. Hence, the presented model in this paper uses only scalar damage variables associated with the noted damage modes. Similar approaches have been exploited by the already mentioned works of Läufer [2018] and Reinoso et al. [2017]. The latter account for damage with three variables and their tension-compression split, which leads to six variables in total. They further consider Puck's criterion in a thermodynamically consistent manner, which is e.g. also applied by Kerschbaum and Hopmann [2016]. Several publications that are also dealing with fiber-reinforced material modeling and taking either damage or plasticity or even both into account are for instance the works by Matzenmiller et al.

[1995], Maimí et al. [2007], Vogler et al. [2013], Dean et al. [2017, 2019] and Jha et al. [2019], to give a short extract from the literature.

An efficient construction with fiber-reinforced materials requires a macroscopic material model considering the mentioned effects and a stable numerical implementation. Therefore, this paper is concerned with the thermodynamically consistent derivation of a CDM model for general transversally isotropic materials, in particular for unidirectional fiber-reinforced layers. The free Helmholtz energy is splitted into the matrix material and the additional fiber contribution. The matrix is assumed to be elasto-plastic, whereby isotropic hardening is assumed. This is modeled with a modification of the isotropic elasto-plastic model of Vladimirov et al. [2008] which was further extended to plastic anisotropy by Vladimirov et al. [2010].

In order to take material anisotropy into account, structural tensors are applied in connection with the free energy of the fiber. For both material parts, the damage is modeled separately by means of scalar damage variables. These damage variables are associated with the matrix failure as well as fiber tension and fiber compression failure, resulting in three scalar damage variables. Although coupling between the fiber tension and fiber compression damage is captured due to coupling damage functions, a direct coupling between matrix damage and fiber failure e.g. fiber pull-out is not considered. Thus, indirect anisotropic damage evolution is achieved by the corresponding stiffness reduction of the matrix and fiber part, respectively. In order to differentiate between tension and compression failure, tension-compression asymmetry is used. In addition, it is thus possible to capture crack-closure effects. To describe all the above mentioned failure modes, three scalar damage variables are certainly not enough. Nevertheless, these variables and the damage modes associated are assumed to capture the main damage modes that are necessary to describe the basic damage mechanisms within fiber-reinforced materials. The matrix part can be considered as a two-surface elasto-plastic-damage model, whereas the elasto-damage fiber part is a one-surface model. Furthermore, to prevent localization, the scalar, isotropic framework of Brepols et al. [2017, 2018*a*, 2020] is applied to all three damage variables. Since this framework is based on the micromorphic approach, three additional degrees of freedom are required in the presented model. Hence, this paper also deals with the implementation into the FEM and presents an element formulation and its consistent linearization as well as some numerical investigations at the Gauss point level and structural examples.

2.3 Constitutive modeling

The material model for fiber-matrix composites presented in the following is derived thermo-mechanically consistent in this Section. The damage of both the fiber and the matrix is based on the micromorph approach of Forest [2009, 2016], whereas the framework used here is based on the work of Brepols et al. [2018*a*, 2020]. As in these works, the concept of 'micromorphic' degrees of freedom is used. For a better understanding of the modeling strategy, see the schematic illustration Fig. 2.1.

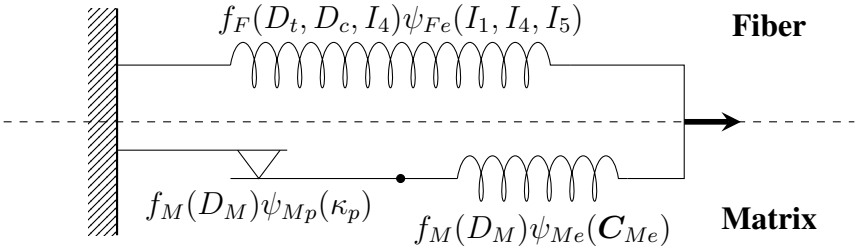

Figure 2.1: Schematic illustration of the fiber-reinforced model

2.3.1 Kinematics

Fiber. To describe the anisotropic material behavior induced by the fiber direction, the concept of structural tensors is widely used. Since the composite model behaves transversally isotropic, only the introduction of a single structural tensor $\boldsymbol{M}_F$ is necessary. This is described by $\boldsymbol{M}_F = \boldsymbol{m}_F \otimes \boldsymbol{m}_F$, where $\boldsymbol{m}_F$ is oriented in the fiber direction and is defined as

$$\boldsymbol{m}_F = \begin{pmatrix} \cos\varphi_{xy}\cos\varphi_z & \sin\varphi_{xy}\cos\varphi_z & \sin\varphi_z \end{pmatrix}_a \boldsymbol{e}_a. \tag{2.1}$$

Figure 2.2 shows the definition of the angles φ_{xy} and φ_z. Based on this structural tensor, two additional mixed invariants (2.3) to the classical ones (2.2) can be formulated to describe a transversal isotropic material (see e.g. Spencer [1971, 1984], Balzani [2006] and Holzapfel [2010])

$$I_1 = \operatorname{tr}(\boldsymbol{C}), \quad I_2 = \frac{1}{2}\left(\operatorname{tr}(\boldsymbol{C})^2 - \operatorname{tr}\left(\boldsymbol{C}^2\right)\right), \quad I_3 = \det(\boldsymbol{C}) \tag{2.2}$$

$$I_4 = \operatorname{tr}(\boldsymbol{C}\boldsymbol{M}_F) = \lambda_F^2, \quad I_5 = \operatorname{tr}\left(\boldsymbol{C}^2\boldsymbol{M}_F\right), \tag{2.3}$$

since $\boldsymbol{M}_F = \boldsymbol{M}_F^2$. In the above, $\boldsymbol{C} = \boldsymbol{F}^T\boldsymbol{F}$ is the right Cauchy-Green stretch tensor and λ_F is the stretch in fiber direction. Since only elasticity and damage is considered for the fiber, no further discussion regarding the deformation gradient $\boldsymbol{F}$ is necessary.

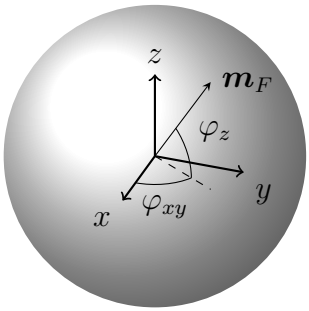

Figure 2.2: Definition of the structural vector $\boldsymbol{m}_F$

Matrix. The elasto-plastic-damage model for the matrix presented here is mainly based on the work of Vladimirov et al. [2008], which use a widely accepted multiplicative split of the deformation gradient in its elastic and plastic part (cf. Eckart [1948], Kröner [1959], Lee and Liu [1967])

$$\boldsymbol{F} = \boldsymbol{F}_{Me}\boldsymbol{F}_{Mp}. \tag{2.4}$$

Vladimirov et al. [2008] further decompose $\boldsymbol{F}_{Mp}$ to account for nonlinear kinematic hardening. Since only isotropic hardening is assumed here, this decomposition is not necessary. However, the presented framework is still valid and therefore only a brief summary of the kinematic relations will be presented

$$\boldsymbol{C}_{Me} = \boldsymbol{F}_{Me}^T\boldsymbol{F}_{Me} = \boldsymbol{F}_{Mp}^{-T}\boldsymbol{C}\boldsymbol{F}_{Mp}^{-1}, \quad \dot{\boldsymbol{C}}_{Me} = \boldsymbol{F}_{Mp}^{-T}\dot{\boldsymbol{C}}\boldsymbol{F}_{Mp}^{-1} - \boldsymbol{L}_{Mp}^T\boldsymbol{C}_{Me} - \boldsymbol{C}_{Me}\boldsymbol{L}_{Mp}, \tag{2.5}$$

where $\boldsymbol{L}_{Mp} = \dot{\boldsymbol{F}}_{Mp}\boldsymbol{F}_{Mp}^{-1}$. Furthermore, the plastic right Cauchy-Green tensor $\boldsymbol{C}_{Mp} = \boldsymbol{F}_{Mp}^T\boldsymbol{F}_{Mp}$ is introduced.

2.3.2 Free Helmholtz energy

The aim of this section is to provide the general form of the specific Helmholtz free energy. First, the total energy can be split using the rule of mixtures into a fiber-associated and a matrix part using the fiber volume fraction V_F

$$\psi = (1 - V_F)\psi_M + V_F\,\psi_F. \tag{2.6}$$

The above assumed Helmholtz free energy is approached from a phenomenological perspective (see e.g. Stier et al. [2015], Simon et al. [2015], Stapleton et al. [2015]). In the case presented here, a Voigt type model is considered, which results in the assumption of equal strains, but

different stresses for the fiber and matrix (cf. Section 2.3.3). However, for e.g. transverse loading this approach is known to be not the most suitable, since the stress within the matrix and the fiber are equal in this case. For the specific application, this choice of mixture must be carefully examined and, if necessary, replaced by a more proper choice. A more advanced approach, which also considers Reuss type bounds can be found in e.g. Li et al. [2016].
In the literature, the fiber part is often referred as the 'anisotropic' part and the matrix as the 'isotropic' part (cf. Holzapfel et al. [2000], Reese et al. [2001], Reese [2003]). In this paper, the interpretation is rather from a practical point of view, in which the matrix material is seen as isotropic in itself and behaves macroscopically anisotropic only due to the additional fibers. Hence, the energy of the fiber does not mean the real fiber energy, rather the additional contribution due to the anisotropy to the isotropic stiffness.

Fiber. As mentioned above, for the fiber an elasto-damage model is used. A widely used approach to model tension-compression asymmetry is the spectral decomposition of the strain or stretch tensors, e.g. for small deformations $\boldsymbol{\varepsilon} = \boldsymbol{\varepsilon}_t + \boldsymbol{\varepsilon}_c$, discussed e.g. by Ladeveze and Lemaitre [1984] and Simo and Ju [1987] and has been used by e.g. Comi [2001]. Furthermore, by utilizing tension-compression asymmetry, it is possible to model the damage behavior in the tension regime different to those in the compression regime and also account for any crack-closure effects.
Therefore, the additive split of $\boldsymbol{C}$ into a tension and compression part $\boldsymbol{C} = \boldsymbol{C}_t + \boldsymbol{C}_c$ is discussed. Based on this, the invariants (2.3) would result in $I_4 = \operatorname{tr}(\boldsymbol{C}_t \boldsymbol{M}_F) + \operatorname{tr}(\boldsymbol{C}_c \boldsymbol{M}_F)$ and $I_5 = \operatorname{tr}(\boldsymbol{C}_t^2 \boldsymbol{M}_F) + \operatorname{tr}(\boldsymbol{C}_c^2 \boldsymbol{M}_F)$, since $\boldsymbol{C}_t \boldsymbol{C}_c = \boldsymbol{C}_c \boldsymbol{C}_t = \boldsymbol{0}$ holds (see Appendix 2.7.1). However, this approach would lead to problems for the specific choices of the several energy terms, which will be discussed in Section 2.3.7. Also a spectral decomposition of e.g. $\boldsymbol{C}\boldsymbol{M}_F$ is not useful, since the tensors are both symmetric, however, not coaxial in general. Therefore, a new approach is presented based on the fiber stretch (2.3), which is beneficial as there is no need for a spectral decomposition

$$\begin{aligned}\psi_F = &\overbrace{\left(\underbrace{f_t(D_t) f_{tc}(D_c) \langle I_4 - 1 \rangle}_{\text{tension part}} + \underbrace{f_c(D_c) f_{ct}(D_t) \langle 1 - I_4 \rangle}_{\text{compression part}}\right)}^{=: f_F(D_t, D_c, I_4)} \psi_{Fe}\left(I_1, I_4, I_5\right) \\ &+ \psi_{Fd}(\kappa_t, \kappa_c) + \psi_{F\bar{d}}\left(D_t, \bar{D}_t, \operatorname{Grad}\left(\bar{D}_t\right), D_c, \bar{D}_c, \operatorname{Grad}\left(\bar{D}_c\right)\right).\end{aligned} \tag{2.7}$$

In the above, the Heaviside function was used

$$\langle(*)\rangle = \begin{cases} 1 & ,(*) \geq 0 \\ 0 & ,\text{else.} \end{cases} \tag{2.8}$$

The presented approach is very similar to those presented in e.g. Holzapfel et al. [2000]; Holzapfel and Ogden [2010], Reese et al. [2001]. However, two main points should be mentioned. First, none of the mentioned works consider damage, which can be easily accounted for with the presented approach. Second, all works assume no stiffness contribution of the fiber due to soft behavior in the compression regime. Since the damage variable D_c should account for e.g. kink band damage modes, neglecting the fiber in the compression regime would not be suitable.

The first term in (2.7) represents the tension-compression asymmetry with the damage functions f_t and f_c as well as the coupling functions for tension and compression f_{tc} and f_{ct} (cf. Fassin et al. [2019*a*]), which is multiplied with the elastic strain energy associated with the fiber ψ_{Fe}. This term is both dependent on the first invariant of $\boldsymbol{C}$ and the mixed invariants (2.3). Moreover, D_t and D_c are the scalar fiber damage variables for tension and compression, respectively. Furthermore, the term ψ_{Fd}, depending on the damage hardening variables for tension κ_t and compression κ_c, accounts for the energy stored by fiber damage hardening. At last, $\psi_{F\bar{d}}$ is associated with the micromorphic fiber damage and depends on the micromorphic damage variables $\bar{D}_t$ and $\bar{D}_c$.

Matrix. In contrast to the fiber part, for the matrix plasticity is also considered. Since the matrix model used here is mainly based on Vladimirov et al. [2008] and Brepols et al. [2020], a detailed discussion can be found in these works

$$\psi_M = f_M(D_M)\left(\psi_{Me}\left(\boldsymbol{C}_{Me}\right) + \psi_{Mp}(\kappa_p)\right) + \psi_{Md}(\kappa_M) + \psi_{M\bar{d}}\left(D_M, \bar{D}_M, \mathrm{Grad}\left(\bar{D}_M\right)\right). \tag{2.9}$$

It should be emphasized that the plastic energy term ψ_{Mp} only denotes the energy stored by isotropic hardening without any kinematic hardening. Furthermore, κ_p can be interpreted as the accumulated plastic strain. The remaining energies are to be interpreted analogously to the fiber part. Furthermore it should be mentioned that $\boldsymbol{C}_{Me}$ can be expressed indirectly in terms of the invariants (2.2) (cf. Appendix 2.7.2). Thus, all required invariants to describe a transversally isotropic material are included. Unlike for the fiber part, no tension-compression asymmetry is assumed for the matrix. Therefore, f_M is the matrix damage function and D_M the scalar matrix damage variable associated with both tension and compression.

2.3.3 Derivation based on the isothermal Clausius-Duhem inequality

In order to avoid unphysical behavior, the derivation of the constitutive dependent quantities is based on the local form of the second law of thermodynamics

$$-\rho_0\dot{\psi} + \boldsymbol{S} : \frac{1}{2}\dot{\boldsymbol{C}} + \underbrace{\boldsymbol{\xi}_{0\mathfrak{I}} \cdot \dot{\bar{\boldsymbol{d}}} + \boldsymbol{\Xi}_{0\mathfrak{I}} : \mathrm{Grad}\left(\dot{\bar{\boldsymbol{d}}}\right)}_{\text{micromorphic extension}} \geq 0, \tag{2.10}$$

where $\boldsymbol{S}$ is the second Piola-Kirchhoff stress tensor and ρ_0 is the density with respect to the reference configuration. It can be observed that due to the micromorphic approach, additional terms $\boldsymbol{\xi}_{0\mathfrak{I}}$ and $\boldsymbol{\Xi}_{0\mathfrak{I}}$ appear in the usual Clausius-Duhem inequality, accounting for the internal damage forces. A detailed discussion of the contribution of the micromorphic extension to the Clausius-Duhem inequality can be found in Forest [2009, 2016]. The first order tensor $\bar{\boldsymbol{d}} = (\bar{D}_t\ \bar{D}_c\ \bar{D}_M)_a\ \boldsymbol{e}_a$ contains the micromorphic damage variables.
First the derivative of the specific free Helmholtz energy (2.6) with respect to time is derived

$$\begin{aligned}\dot{\psi} = &\overbrace{\left(\frac{\partial\psi}{\partial I_1}\frac{\partial I_1}{\partial \boldsymbol{C}} + \frac{\partial\psi}{\partial I_4}\frac{\partial I_4}{\partial \boldsymbol{C}} + \frac{\partial\psi}{\partial I_5}\frac{\partial I_5}{\partial \boldsymbol{C}}\right) : \dot{\boldsymbol{C}}}^{\text{Part I } g_1} + \overbrace{\frac{\partial\psi}{\partial \boldsymbol{C}_{Me}} : \dot{\boldsymbol{C}}_{Me}}^{\text{Part II } g_2} + \frac{\partial\psi}{\partial\kappa_p}\dot{\kappa}_p \\ &+ \sum_i \frac{\partial\psi}{\partial D_i}\dot{D}_i + \sum_i \frac{\partial\psi}{\partial\kappa_i}\dot{\kappa}_i + \frac{\partial\psi}{\partial\bar{\boldsymbol{d}}} \cdot \dot{\bar{\boldsymbol{d}}} + \frac{\partial\psi}{\partial \mathrm{Grad}\left(\bar{\boldsymbol{d}}\right)} : \mathrm{Grad}\left(\dot{\bar{\boldsymbol{d}}}\right)\end{aligned} \tag{2.11}$$

where the index $i = (t, c, M)$ is used. In the following, the parts **I** and **II** will be treated separately.

Part I. Having in mind relation (2.6) and (2.7), the first part can be reformulated as

$$g_1 = V_F\ f_F(D_t, D_c, I_4)\left(\frac{\partial\psi_{Fe}}{\partial I_1}\frac{\partial I_1}{\partial \boldsymbol{C}} + \frac{\partial\psi_{Fe}}{\partial I_4}\frac{\partial I_4}{\partial \boldsymbol{C}} + \frac{\partial\psi_{Fe}}{\partial I_5}\frac{\partial I_5}{\partial \boldsymbol{C}}\right) : \dot{\boldsymbol{C}}. \tag{2.12}$$

At this point, it has already been utilized that $\partial f_F/\partial I_4 = 0$ holds. Introducing the partial derivatives of the invariants

$$\frac{\partial I_1}{\partial \boldsymbol{C}} = \boldsymbol{I}, \quad \frac{\partial I_4}{\partial \boldsymbol{C}} = \boldsymbol{M}_F, \quad \frac{\partial I_5}{\partial \boldsymbol{C}} = \left(\boldsymbol{C}\boldsymbol{M}_F + \boldsymbol{M}_F\boldsymbol{C}\right), \tag{2.13}$$

equation (2.12) can be further transformed

$$g_1 = V_F\ f_F(D_t, D_c, I_4)\left(\frac{\partial\psi_{Fe}}{\partial I_1}\boldsymbol{I} + \frac{\partial\psi_{Fe}}{\partial I_4}\boldsymbol{M}_F + \frac{\partial\psi_{Fe}}{\partial I_5}\left(\boldsymbol{C}\boldsymbol{M}_F + \boldsymbol{M}_F\boldsymbol{C}\right)\right) : \dot{\boldsymbol{C}}. \tag{2.14}$$

As a result, a new second Piola-Kirchhoff stress tensor for the fiber is introduced

$$\boldsymbol{S}_F := f_F(D_t, D_c, I_4)\, 2\rho_0 \left(\frac{\partial \psi_{Fe}}{\partial I_1} \boldsymbol{I} + \frac{\partial \psi_{Fe}}{\partial I_4} \boldsymbol{M}_F + \frac{\partial \psi_{Fe}}{\partial I_5} \left(\boldsymbol{C}\boldsymbol{M}_F + \boldsymbol{M}_F \boldsymbol{C} \right) \right). \tag{2.15}$$

Part II. First, relation (2.5) is to be inserted into g_2 as well as relation (2.6) and (2.9) are utilized

$$g_2 = (1 - V_F)\, f_M(D_M) \frac{\partial \psi_{Me}}{\partial \boldsymbol{C}_{Me}} : \left(\boldsymbol{F}_{Mp}^{-T} \dot{\boldsymbol{C}} \boldsymbol{F}_{Mp}^{-1} - \boldsymbol{L}_{Mp}^T \boldsymbol{C}_{Me} - \boldsymbol{C}_{Me} \boldsymbol{L}_{Mp} \right). \tag{2.16}$$

With the application of invariance of the trace operator under cyclic permutation, the scalar product rule of two general second order tensors $\mathrm{sym}\,(\boldsymbol{A}) : \boldsymbol{B} = \mathrm{sym}\,(\boldsymbol{A}) : \mathrm{sym}\,(\boldsymbol{B})$ and both the symmetry as well as the coaxiality of $\boldsymbol{C}_{Me}(\partial \psi_{Me}/\partial \boldsymbol{C}_{Me})$, two further stress measures can be defined

$$\boldsymbol{S}_M := f_M(D_M)\, 2\rho_0 \boldsymbol{F}_{Mp}^{-1} \frac{\partial \psi_{Me}}{\partial \boldsymbol{C}_{Me}} \boldsymbol{F}_{Mp}^{-T} \tag{2.17}$$

$$\boldsymbol{\Sigma}_{Mp} := f_M(D_M)\, 2\rho_0 \boldsymbol{C}_{Me} \frac{\partial \psi_{Me}}{\partial \boldsymbol{C}_{Me}}, \tag{2.18}$$

which can be referred as the second Piola-Kirchhoff stress tensor associated with the matrix and a Mandel stress tensor, accounting for the plasticity in the matrix model. A more detailed derivation and discussion of these quantities can be found in Vladimirov et al. [2008].

For further simplification, the thermodynamically conjugated forces are introduced

$$R_t := -\rho_0 \frac{\partial \psi_{Fd}}{\partial \kappa_t}, \quad R_c := -\rho_0 \frac{\partial \psi_{Fd}}{\partial \kappa_c}, \quad R_M := -\rho_0 \frac{\partial \psi_{Md}}{\partial \kappa_M}, \quad R_p := -f_M(D_M)\, \rho_0 \frac{\partial \psi_{Mp}}{\partial \kappa_p} \tag{2.19}$$

$$Y_t := -\rho_0 \frac{\partial f_F(D_t, D_c, I_4)}{\partial D_t} \psi_{Fe} - \rho_0 \frac{\partial \psi_{F\bar{d}}}{\partial D_t},\; Y_c := -\rho_0 \frac{\partial f_F(D_t, D_c, I_4)}{\partial D_c} \psi_{Fe} - \rho_0 \frac{\partial \psi_{F\bar{d}}}{\partial D_c},$$
$$Y_M := -\rho_0 \frac{\mathrm{d} f_M(D_M)}{\mathrm{d} D_M} (\psi_{Me} + \psi_{Mp}) - \rho_0 \frac{\partial \psi_{M\bar{d}}}{\partial D_M}. \tag{2.20}$$

With the equations (2.15), (2.17), (2.18), (2.19) and (2.20) at hand, the Clausius-Duhem inequality (2.10) can be rewritten as

$$\begin{aligned}&(\boldsymbol{S}-(1-V_F)\boldsymbol{S}_M-V_F\boldsymbol{S}_F):\frac{1}{2}\dot{\boldsymbol{C}}+\left(\boldsymbol{\xi}_{0_\mathfrak{I}}-\rho_0\frac{\partial\psi}{\partial\bar{\boldsymbol{d}}}\right)\cdot\dot{\bar{\boldsymbol{d}}}\\&+\left(\boldsymbol{\Xi}_{0_\mathfrak{I}}-\rho_0\frac{\partial\psi}{\partial\mathrm{Grad}\left(\bar{\boldsymbol{d}}\right)}\right):\mathrm{Grad}\left(\dot{\bar{\boldsymbol{d}}}\right)+V_F\left(Y_t\dot{D}_t+R_t\dot{\kappa}_t+Y_c\dot{D}_c+R_c\dot{\kappa}_c\right)\\&+(1-V_F)\left(Y_M\dot{D}_M+R_M\dot{\kappa}_M+\boldsymbol{\Sigma}_{Mp}:\boldsymbol{D}_{Mp}+R_p\dot{\kappa}_p\right)\geq 0.\end{aligned}\tag{2.21}$$

By using the standard arguments of Coleman and Noll [1961], main conclusions are the following

$$\boldsymbol{S}=(1-V_F)\boldsymbol{S}_M+V_F\boldsymbol{S}_F,\quad \boldsymbol{\xi}_{0_\mathfrak{I}}=\rho_0\frac{\partial\psi}{\partial\bar{\boldsymbol{d}}},\quad \boldsymbol{\Xi}_{0_\mathfrak{I}}=\rho_0\frac{\partial\psi}{\partial\mathrm{Grad}\left(\bar{\boldsymbol{d}}\right)}.\tag{2.22}$$

2.3.4 Evolution equations

It remains to be shown that the dissipation of the internal effects (damage and plasticity) can never be negative to obtain a physically meaningful behavior. Accordingly, evolution equations should be chosen for both damage and plasticity that satisfy this condition.

2.3.4.1 Evolution for the plastic regime

To present a general framework for modeling plasticity within the matrix, the evolution equation for $\boldsymbol{D}_{Mp}$ is based on a convex plastic potential, g_p, defined in the stress space

$$\boldsymbol{D}_{Mp}=\dot{\lambda}_p\frac{\partial g_p}{\partial\boldsymbol{\Sigma}_{Mp}},\tag{2.23}$$

in which $\dot{\lambda}_p$ is the plastic multiplier. Further, the evolution of the accumulated plastic strain κ_p is usually based on either the plastic dissipation potential or the norm of the plastic strain rate $\boldsymbol{D}_{Mp}$, whereas both include the plastic multiplier (see de Souza Neto et al. [2011]). The yield criterion in connection with the Karush-Kuhn-Tucker (KKT) (Karush [1939], Kuhn and Tucker [1951]) conditions

$$\dot{\lambda}_p\geq 0,\quad \Phi_p\leq 0,\quad \dot{\lambda}_p\Phi_p=0,\tag{2.24}$$

close the set of constitutive equations. In most applications of fiber-reinforced materials, the matrix material behaves non-associative, in particular polymeric matrices are known to be pressure dependent (see e.g. Fiedler et al. [2001]). In the literature, various works deal with

suitable modeling especially in the context of fiber-reinforced polymers, e.g. the works of Melro et al. [2012, 2013], Vogler et al. [2013], Mehdipour et al. [2019], Dean et al. [2019] and Rocha et al. [2019], to name a few.

Since the aim of this paper is to present a thermodynamically consistent model, two assumptions are made: (i) associative plasticity ($g_p = \Phi_p$) for the plastic strains and the accumulated plastic strain, (ii) a von Mises type yield criterion is chosen and (iii) no plastic tension-compression asymmetry is observed for the matrix due to the yield criterion. In addition, it should be emphasized that these assumptions are e.g. only valid for metallic matrix materials, however thermodynamical consistency can be directly ensured if Φ_p is a homogeneous function. Based on the already mentioned works by Vladimirov et al. [2008] and Brepols et al. [2020], the yield criterion is defined as

$$\Phi_p = \sqrt{\frac{3}{2}} \left\| \mathrm{dev}\left(\tilde{\boldsymbol{\Sigma}}_{Mp}\right) \right\| - (\sigma_{y0} - \tilde{R}_p) \tag{2.25}$$

with the stress like quantity σ_{y0}, denoting the constant initial yield stress. In the above formulation, plasticity is considered to act only on the undamaged part (cf. Brepols et al. [2018*a*])

$$\tilde{(*)} = \frac{(*)}{f_M(D_M)}. \tag{2.26}$$

With these relations at hand, the evolution equations read as follows

$$\boldsymbol{D}_{Mp} = \dot{\lambda}_p \frac{\partial \Phi_p}{\partial \boldsymbol{\Sigma}_{Mp}} = \dot{\lambda}_p \frac{\sqrt{3/2}}{f_M(D_M)} \frac{\mathrm{dev}\left(\tilde{\boldsymbol{\Sigma}}_{Mp}\right)}{\left\| \mathrm{dev}\left(\tilde{\boldsymbol{\Sigma}}_{Mp}\right) \right\|} \tag{2.27}$$

$$\dot{\kappa}_p = \dot{\lambda}_p \frac{\partial \Phi_p}{\partial R_p} = \frac{\dot{\lambda}_p}{f_M(D_M)}. \tag{2.28}$$

2.3.4.2 Evolution for the damage regime

As already stated in Section 2.3.4.1, in this Section the framework for the damage evolution should be derived in a general manner. The following general remarks apply separately to each damage variable, but are shown for the sake of brevity for only one variable. Therefore, a convex damage potential g_d and a corresponding damage yield criterion Φ_d is introduced. In the literature it is common practice to formulate the damage potential or the damage yield criterion in terms of stresses or energy-based. However, for instance Hansen and Schreyer [1994] discuss disadvantages of a stress-based damage criterion. In the present model, the energy-based version comes naturally into play due to the driving force Y derived for each damage variable in equation (2.21).

Analogously to equation (2.23), the evolution of the damage variable D can be defined as

$$\dot{D} = \dot{\lambda}_d \frac{\partial g_d}{\partial Y}. \tag{2.29}$$

For the corresponding accumulated variable κ_d similar formulations are conceivable as for the plastic counterpart. A variety of possibilities exist to formulate both Φ_d and g_d, which in turn consider different aspects of damage mechanisms. At this point the work of Barbero [2013], Bednarcyk et al. [2015] and Simon et al. [2017] should be exemplary mentioned, since these works consider scalar damage variables as well. In their formulations, coupling matrices are used in the formulation of g_d and Φ_d, in order to take into account the interaction of the different damage variables during their evolution. For similar reasons as for the plastic evolution equations, several simplifications are made at this point: (i) associative damage evolution ($g_d = \Phi_d$) is assumed, (ii) no direct interaction, as e.g. achieved by coupling matrices, is included in the several yield criterions and (iii) at the development state of the present model, an extensive study to determine the most suitable criterion has not been carried out. Instead, the damage evolutions of the three independent damage variables are each described by a similar damage yield criterion (cf. Brepols et al. [2018*a*]). These assumptions restrict the model, of course, but the presented framework is sufficient to investigate the essential mechanisms.
The structure of the damage criterion is very similar to the plastic one. Therefore, the equations are given without further discussion

$$\Phi_t = \langle I_4 - 1 \rangle Y_t - (Y_{t0} - R_t) \tag{2.30}$$

$$\Phi_c = \langle 1 - I_4 \rangle Y_c - (Y_{c0} - R_c) \tag{2.31}$$

$$\Phi_M = Y_M - (Y_{M0} - R_M). \tag{2.32}$$

The prefactor of the tension part $\langle I_4 - 1 \rangle$ and the compression part $\langle 1 - I_4 \rangle$, ensures evolution of the damage variable only in the tension regime and analogously for the compression regime. At the same time, this implies that the tension and compression damage variables can never evolve simultaneously. The scalars Y_{t0}, Y_{c0} and Y_{M0} are the corresponding damage thresholds. Thus, the several evolution equations read

$$\dot{D}_i = \dot{\lambda}_i \frac{\partial \Phi_i}{\partial Y_i} = \dot{\lambda}_i, \quad \dot{\kappa}_i = \dot{\lambda}_i \frac{\partial \Phi_i}{\partial R_i} = \dot{\lambda}_i \qquad i = (t, c, M). \tag{2.33}$$

It should be emphasized that the prefactor of equation (2.30) and (2.31) is omitted for the derivatives, since the specific damage variable only evolves if the prefactor is equal to one and thus does not change the derivative. At last, the KKT conditions are introduced for the damage

regime

$$\dot{\lambda}_i \geq 0, \quad \Phi_i \leq 0, \quad \dot{\lambda}_i \Phi_i = 0 \qquad i = (t, c, M). \tag{2.34}$$

2.3.5 Proof of thermodynamic consistency

With the evolution equations just introduced in Section 2.3.4, it now remains to prove the thermodynamic consistency. This will only be done in a shortened way, because the basic procedure was shown in the already noted works. Nevertheless, some remarks need to be made. For this purpose, the remaining part of equation (2.21) is first used and the equations (2.25), (2.27), (2.28), (2.32) and (2.33) are to be inserted, which results in

$$V_F \left((Y_t + R_t)\dot{\lambda}_t + (Y_c + R_c)\dot{\lambda}_c \right) + (1 - V_F) \left((\Phi_M + Y_{M0})\dot{\lambda}_M + (\Phi_p + \sigma_{y0})\dot{\lambda}_p \right) \geq 0. \tag{2.35}$$

Due to the prefactor in equations (2.30) and (2.31) it is not possible to directly transform the above stated equation. Nevertheless, consistency can be shown by means of a case differentiation. In the case that the prefactor is equal to one, then e.g. $Y_t + R_t = \Phi_t + Y_{t0}$ holds true. If the prefactor is equal to zero, there is no dissipation due to damage evolution, which implicitly fulfills the Clausius-Duhem inequality. Thus, taking into account the KKT conditions ((2.24) and (2.34)) and that the material parameters Y_{t0}, Y_{c0}, Y_{M0} and σ_{y0} are greater than or equal to zero as well as $0 \leq V_F < 1$, the inequality is satisfied.

2.3.6 Representation of the constitutive relations in the reference configuration

For the previous derivation, the fact that the different quantities within the plastic model were related to different configurations did not matter. In the course of an efficient numerical implementation, however, these should all be related to the reference configuration. Again, no explicit derivations are given here and the reader is referred to the already above mentioned literature.

Stress-like quantity: $$\boldsymbol{Y}_{Mp} = \boldsymbol{C}\boldsymbol{S}_M \tag{2.36}$$

Evolution: $$\dot{\boldsymbol{C}}_{Mp} = 2\dot{\lambda}_p \frac{\sqrt{3/2}}{f_M(D_M)} \frac{\operatorname{dev}\left(\tilde{\boldsymbol{Y}}_{Mp}\right)\boldsymbol{C}_{Mp}}{\sqrt{\operatorname{dev}\left(\tilde{\boldsymbol{Y}}_{Mp}\right) : \operatorname{dev}\left(\tilde{\boldsymbol{Y}}_{Mp}\right)^T}} \tag{2.37}$$

Strain-like quantity: $$\boldsymbol{T}_{Mp} = 2\frac{\sqrt{3/2}}{f_M(D_M)} \frac{\operatorname{dev}\left(\tilde{\boldsymbol{Y}}_{Mp}\right)\boldsymbol{C}_{Mp}}{\sqrt{\operatorname{dev}\left(\tilde{\boldsymbol{Y}}_{Mp}\right) : \operatorname{dev}\left(\tilde{\boldsymbol{Y}}_{Mp}\right)^T}} \tag{2.38}$$

Yield-function: $$\Phi_p = \sqrt{\frac{3}{2}}\sqrt{\operatorname{dev}\left(\tilde{\boldsymbol{Y}}_{Mp}\right) : \operatorname{dev}\left(\tilde{\boldsymbol{Y}}_{Mp}\right)^T} - (\sigma_{y0} - \tilde{R}_p) \tag{2.39}$$

For reasons presented in Vladimirov et al. [2008] the strain-like quantity $\boldsymbol{T}_{Mp}$ is symmetric.

2.3.7 Specific choice of free Helmholtz energies

To this point, the derivation is completely independent of the specific form of the free Helmholtz energy. In the following it is necessary to find meaningful forms for the different energies. Thereby, the matrix material should behave isotropic and the transversal isotropy purely depends on the fiber. Nevertheless, the total energy is to be understood as a scalar isotropic function of the tensors $\boldsymbol{C}$, $\boldsymbol{C}_{Mp}$ (or $\boldsymbol{C}_{Me}$) and $\boldsymbol{M}_F$, since the Helmholtz energy does not change under a rotation of the tensors (see Holzapfel [2010]).

Fiber. The elastic strain energy for the fiber is mainly based on the function introduced by Reese et al. [2001] with slight modifications and just for one fiber direction

$$\Psi_{Fe} = \frac{1}{\alpha}K_{ani1}(I_4 - 1)^\alpha + \frac{1}{\beta}K_{ani2}(I_5 - 1)^\beta + \frac{1}{\gamma}K_{coup}(I_1 - 3)^\gamma(I_4 - 1)^\gamma. \tag{2.40}$$

In the above, K_{ani1}, K_{ani2} and K_{coup} as well as α, β and γ are material parameters. To guarantee a stress free state for $\boldsymbol{C} = \boldsymbol{I}$ the exponents have to be chosen to $\alpha, \beta, \gamma \geq 2$. However, to reduce the model to linear elasticity the parameters are $\alpha = 2$, $\beta = 1$ and $\gamma = 1$. In order to keep a stress free state, one could either add a term to the energy function (cf. Reese et al. [2001]) or use the relation $\hat{\boldsymbol{S}}_F = \hat{\mathbb{C}}_F^{lin}\hat{\boldsymbol{E}}$ in which $\boldsymbol{E}$ is the Green-Lagrange strain tensor and $\hat{\mathbb{C}}_F^{lin}$ is the material tangent (see Appendix 2.7.3). It should also be noted that this choice of exponents means that polyconvexity can no longer be ensured. The interested reader can find a detailed discussion of polyconvexity in the context of transversal isotropy in Schröder and

Neff [2003].

Remark 1. *In Section 2.3.2 it was mentioned that the split of $\boldsymbol{C}$ into a tension and a compression part causes issues for the specific energies. Taking for example the term $(I_4-1)^2$ into account (where the exponent has been already chosen equal to two) the split of the fourth invariant $I_4 = I_{4t} + I_{4c}$ would lead to $(I_{4t}+I_{4c}-1)^2$. Since $I_{4t}I_{4c}$ is not equal to zero in general, a split into both a pure tension and a pure compression part is not possible. This split may work for other strain energy functions, however it is not suitable for the type chosen here.*

Matrix. In the present material model formulation a compressible Neo-Hookean description of the elastic strain energy function is chosen as well as a combination of Voce type and linear hardening for the plastic energy

$$\Psi_{Me} = \frac{\mu}{2}\left[\operatorname{tr}\left(\boldsymbol{C}_{Me}\right) - 3 - \ln\left(\det\left(\boldsymbol{C}_{Me}\right)\right)\right] + \frac{\Lambda}{4}\left[\det\left(\boldsymbol{C}_{Me}\right) - 1 - \ln\left(\det\left(\boldsymbol{C}_{Me}\right)\right)\right] \tag{2.41}$$

$$\Psi_{Mp} = r_p\left(\kappa_p + \frac{\exp(-s_p\kappa_p)-1}{s_p}\right) + \frac{1}{2}H_p\kappa_p^2. \tag{2.42}$$

The material parameters Λ and μ are the Lamé constants. In addition, H_p is the linear hardening modulus and r_p as well as s_p describe the Voce type hardening Voce [1955].

Remark 2. *Considering the case of linear elasticity also for the matrix contribution, the total material tangent can be written as*

$$\hat{\mathbb{C}}^{lin} = (1-V_F)\hat{\mathbb{C}}_M^{lin} + V_F\hat{\mathbb{C}}_F^{lin}, \tag{2.43}$$

with the linear elastic material tangent of the matrix $\hat{\mathbb{C}}_M^{lin}$ (see Appendix 2.7.3). For a physically meaningful behavior it is necessary that the material tangent is positive definite, whereby different restrictions can be derived for the Young's modulus in fiber-parallel as well as fiber-perpendicular direction as for the counterpart shear moduli and the Poisson's ratio for tension in fiber direction (cf. Altenbach [2015]). The several restrictions can be found in Appendix 2.7.4. Since the material tangent of the fiber has two eigenvalues equal to zero and taking equation (2.84) *into account, it is obvious that no material can be described purely by the fiber part. Furthermore, the conversion formulas based on equation* (2.43) *in Appendix 2.7.4 lead to the unusual case that some material parameters of equation* (2.40) *can result in negative values.*

Damage. It remains to choose energy functions for the local damage function ψ_{Fd} and ψ_{Md} along with their micromorphic counterparts $\psi_{F\bar{d}}$ and $\psi_{M\bar{d}}$. For the local ones, a structure

similar to the Voce type hardening is chosen

$$\Psi_{Fd} = r_t \left(\kappa_t + \frac{\exp(-s_t \kappa_t) - 1}{s_t} \right) + r_c \left(\kappa_c + \frac{\exp(-s_c \kappa_c) - 1}{s_c} \right) \tag{2.44}$$

$$\Psi_{Md} = r_M \left(\kappa_M + \frac{\exp(-s_M \kappa_M) - 1}{s_M} \right). \tag{2.45}$$

The several material parameters are to be interpreted analogously to the plastic Voce type hardening. For reasons that become more clear in the later course, the energies for the micromorphic parts are expressed together in an equation

$$\Psi_{F\bar{d}} + \Psi_{M\bar{d}} = \frac{1}{2} \left(\boldsymbol{d} - \bar{\boldsymbol{d}} \right) \cdot \boldsymbol{H}_{\bar{d}} \cdot \left(\boldsymbol{d} - \bar{\boldsymbol{d}} \right) + \frac{1}{2} \mathrm{Grad} \left(\bar{\boldsymbol{d}} \right) : \left(\boldsymbol{A}_{\bar{d}} \cdot \mathrm{Grad} \left(\bar{\boldsymbol{d}} \right) \right), \tag{2.46}$$

where the tensors $\boldsymbol{H}_{\bar{d}} = \mathrm{diag} \left(H_t \; H_c \; H_M \right)_{ab} \boldsymbol{e}_a \otimes \boldsymbol{e}_b$ and $\boldsymbol{A}_{\bar{d}} = \mathrm{diag} \left(A_t \; A_c \; A_M \right)_{ab} \boldsymbol{e}_a \otimes \boldsymbol{e}_b$ contain the so-called micromorphic moduli.

2.3.7.1 Specific forms of conjugated driving forces

Now, with the just chosen specific forms of the free Helmholtz energy parts, the thermodynamic driving forces can be expressed. First, using the relations (2.15) and (2.17) the second Piola-Kirchhoff stress tensors for the fiber and matrix read as follows

$$\begin{aligned} \boldsymbol{S}_F = f_F(D_t, D_c, I_4) \; 2 \big[& K_{ani1} (I_4 - 1)^{\alpha - 1} \boldsymbol{M}_F + K_{ani2} (I_5 - 1)^{\beta - 1} \left(\boldsymbol{C} \boldsymbol{M}_F + \boldsymbol{M}_F \boldsymbol{C} \right) \\ & + K_{coup} \left((I_1 - 3)^{\gamma - 1} (I_4 - 1)^{\gamma} \boldsymbol{I} + (I_1 - 3)^{\gamma} (I_4 - 1)^{\gamma - 1} \boldsymbol{M}_F \right) \big] \end{aligned} \tag{2.47}$$

$$\boldsymbol{S}_M = f_M(D_M) \left[\mu \left(\boldsymbol{C}_{Mp}^{-1} - \boldsymbol{C}^{-1} \right) + \frac{\Lambda}{2} \left(\frac{\det \left(\boldsymbol{C} \right)}{\det \left(\boldsymbol{C}_{Mp} \right)} - 1 \right) \boldsymbol{C}^{-1} \right]. \tag{2.48}$$

With these equations at hand, the total stress can be calculated according to equation (2.22). Furthermore, the driving forces for the local damage variables (2.20) are defined as

$$\begin{aligned} Y_t = -\frac{\partial f_F(D_t, D_c, I_4)}{\partial D_t} \Psi_{Fe} - H_t (D_t - \bar{D}_t), \; Y_c = -\frac{\partial f_F(D_t, D_c, I_4)}{\partial D_c} \Psi_{Fe} - H_c (D_c - \bar{D}_c), \\ Y_M = -\frac{\mathrm{d} f_M(D_M)}{\mathrm{d} D_M} (\Psi_{Me} + \Psi_{Mp}) - H_M (D_M - \bar{D}_M). \end{aligned} \tag{2.49}$$

The additional scalar driving forces are as follows

$$R_i = -r_i(1 - \exp(-s_i\kappa_i)) \qquad i = (t, c, M) \tag{2.50}$$

$$R_p = -f_M(D_M)\left(r_p(1 - \exp(-s_p\kappa_p)) + H_p\kappa_p\right). \tag{2.51}$$

It is further necessary to find expressions for $\boldsymbol{\xi}_{0_\mathfrak{I}}$ and $\boldsymbol{\Xi}_{0_\mathfrak{I}}$. Considering the equations (2.6), (2.22) and (2.46), the quantities can be expressed as

$$\boldsymbol{\xi}_{0_\mathfrak{I}} = -\boldsymbol{V}_F \cdot \boldsymbol{H}_{\bar{d}} \cdot \left(\boldsymbol{d} - \bar{\boldsymbol{d}}\right) \tag{2.52}$$

$$\boldsymbol{\Xi}_{0_\mathfrak{I}} = \boldsymbol{V}_F \cdot \boldsymbol{A}_{\bar{d}} \cdot \mathrm{Grad}\left(\bar{\boldsymbol{d}}\right), \tag{2.53}$$

with $\boldsymbol{V}_F = \mathrm{diag}\left(V_F\, V_F\, (1 - V_F)\right)_{ab}\, \boldsymbol{e}_a \otimes \boldsymbol{e}_b$ containing the fiber volume fraction. Table 2.1 gives a short overview of the constitutive equations needed in the reference configuration.

2.3.8 Strong and weak forms of the field equations

Since this paper is less concerned with the theoretical derivation of the field equations than with their numerical implementation in the context of the presented material model, reference is again made to the relevant literature (e.g. Forest [2009, 2016] and Brepols et al. [2020]). In the current context, the following strong forms of linear momentum and micromorphic balance equation with their Dirichlet and Neumann boundary conditions are stated

Linear momentum:		Micromorphic balance:	
$\mathrm{Div}\left(\boldsymbol{F}\boldsymbol{S}\right) + \boldsymbol{f}_0 = \boldsymbol{0}$	in Ω_0	$\mathrm{Div}\left(\boldsymbol{\Xi}_{0_\mathfrak{I}} - \boldsymbol{\Xi}_{0_\mathfrak{E}}\right) - \boldsymbol{\xi}_{0_\mathfrak{I}} + \boldsymbol{\xi}_{0_\mathfrak{E}} = \boldsymbol{0}$	in Ω_0
$\boldsymbol{F}\boldsymbol{S} \cdot \boldsymbol{n}_0 = \boldsymbol{t}_0$	on $\partial_t\Omega_0$	$\left(\boldsymbol{\Xi}_{0_\mathfrak{I}} - \boldsymbol{\Xi}_{0_\mathfrak{E}}\right) \cdot \boldsymbol{n}_0 = \boldsymbol{\xi}_{0_\mathfrak{E}}$	on $\partial_c\Omega_0$
$\boldsymbol{u} = \breve{\boldsymbol{u}}$	on $\partial_u\Omega_0$	$\bar{\boldsymbol{d}} = \breve{\bar{\boldsymbol{d}}}$	on $\partial_{\bar{d}}\Omega_0$

In the above, $\partial_t\Omega_0$ and $\partial_c\Omega_0$ describe the Neumann boundaries in the reference configuration and $\partial_u\Omega_0$ and $\partial_{\bar{d}}\Omega_0$ the Dirichlet boundaries. The terms indicated by $\breve{(*)}$ describe the prescribed values at the Dirichlet boundaries.

Remark 3. *Noteworthy, the boundary of Ω_0 is composed of the union of $\partial_c\Omega_0$ and $\partial_{\bar{d}}\Omega_0$ with $\partial_c\Omega_0 \cap \partial_{\bar{d}}\Omega_0 = \emptyset$ for the micromorphic extension. However, in the case of micromorphic damage no prescribed values for the Dirichlet boundary are considered. Hence, the boundary of Ω_0 is equal to $\partial_c\Omega_0$.*

Table 2.1: Constitutive equations in reference configuration

Fiber	**Matrix**
Stress $\boldsymbol{S}_F = f_F(D_t, D_c, I_4)\, 2\rho_0 \left(\dfrac{\partial \psi_{Fe}}{\partial I_1}\boldsymbol{I} + \dfrac{\partial \psi_{Fe}}{\partial I_4}\boldsymbol{M}_F + \dfrac{\partial \psi_{Fe}}{\partial I_5}\left(\boldsymbol{C}\boldsymbol{M}_F + \boldsymbol{M}_F\boldsymbol{C}\right)\right)$	Stresses $\boldsymbol{S}_M = f_M(D_M)\, 2\rho_0 \boldsymbol{F}_{Mp}^{-1} \dfrac{\partial \psi_{Me}}{\partial \boldsymbol{C}_{Me}} \boldsymbol{F}_{Mp}^{-T}$ $\boldsymbol{\Sigma}_{Mp} = f_M(D_M)\, 2\rho_0 \boldsymbol{C}_{Me} \dfrac{\partial \psi_{Me}}{\partial \boldsymbol{C}_{Me}}$
Damage driving forces $Y_t = -\dfrac{\partial f_F(D_t, D_c, I_4)}{\partial D_t}\Psi_{Fe} - H_t(D_t - \bar{D}_t)$ $Y_c = -\dfrac{\partial f_F(D_t, D_c, I_4)}{\partial D_c}\Psi_{Fe} - H_c(D_c - \bar{D}_c)$	Damage and plastic driving forces $Y_M = -\dfrac{\mathrm{d}f_M(D_M)}{\mathrm{d}D_M}(\Psi_{Me} + \Psi_{Mp}) - H_M(D_M - \bar{D}_M)$ $\boldsymbol{Y}_{Mp} = \boldsymbol{C}\boldsymbol{S}_M$
Damage evolution equations $\dot{D}_t = \dot{\lambda}_t, \qquad \dot{\kappa}_t = \dot{\lambda}_t$ $\dot{D}_c = \dot{\lambda}_c, \qquad \dot{\kappa}_c = \dot{\lambda}_c$	Damage and plastic evolution equations $\dot{D}_M = \dot{\lambda}_M, \qquad \dot{\kappa}_M = \dot{\lambda}_M$ $\dot{\boldsymbol{C}}_{Mp} = 2\dot{\lambda}_p \dfrac{\sqrt{3/2}}{f_M(D_M)} \dfrac{\mathrm{dev}\left(\tilde{\boldsymbol{Y}}_{Mp}\right)\boldsymbol{C}_{Mp}}{\sqrt{\mathrm{dev}\left(\tilde{\boldsymbol{Y}}_{Mp}\right) : \mathrm{dev}\left(\tilde{\boldsymbol{Y}}_{Mp}\right)^T}}$ $\dot{\kappa}_p = \dfrac{\dot{\lambda}_p}{f_M(D_M)}$
Damage yield functions $\Phi_t = \langle I_4 - 1\rangle Y_t - (Y_{t0} - R_t)$ $\Phi_c = \langle 1 - I_4\rangle Y_c - (Y_{c0} - R_c)$	Damage and plastic yield functions $\Phi_M = Y_M - (Y_{M0} - R_M)$ $\Phi_p = \sqrt{\dfrac{3}{2}} \left\| \mathrm{dev}\left(\tilde{\boldsymbol{\Sigma}}_{Mp}\right) \right\| - (\sigma_{y0} - \tilde{R}_p)$
Damage hardening forces $R_t = -\rho_0 \dfrac{\partial \psi_{Fd}}{\partial \kappa_t}$ $R_c = -\rho_0 \dfrac{\partial \psi_{Fd}}{\partial \kappa_c}$	Damage and plastic hardening forces $R_M = -\rho_0 \dfrac{\partial \psi_{Md}}{\partial \kappa_M}$ $R_p = -f_M(D_M)\rho_0 \dfrac{\partial \psi_{Mp}}{\partial \kappa_p}$

In addition, the test functions $\delta\boldsymbol{u} \in \{H^1 \mid \delta\boldsymbol{u} = \boldsymbol{0} \text{ on } \partial_u\Omega_0\}$ together with $\delta\bar{\boldsymbol{d}} \in \{H^1 \mid \delta\bar{\boldsymbol{d}} = \boldsymbol{0} \text{ on } \partial_{\bar{d}}\Omega_0\}$ are introduced. By further simplifications, in particular neglecting all contact and external forces associated with the micromorphic damage ($\boldsymbol{\xi}_{0_{\mathfrak{C}}} = \boldsymbol{\xi}_{0_{\mathfrak{E}}} = \boldsymbol{0}$ and $\boldsymbol{\Xi}_{0_{\mathfrak{E}}} = \boldsymbol{0}$), the micromorphic balance can be rewritten using equation (2.52) and (2.53)

$$\boldsymbol{V}_F \cdot \boldsymbol{H}_{\bar{d}} \cdot \left(\boldsymbol{d} - \bar{\boldsymbol{d}}\right) + \boldsymbol{V}_F \cdot \boldsymbol{A}_{\bar{d}} \cdot \operatorname{Div}\left(\operatorname{Grad}\left(\bar{\boldsymbol{d}}\right)\right) = \boldsymbol{0} \tag{2.54}$$

$$\left(\boldsymbol{V}_F \cdot \boldsymbol{A}_{\bar{d}} \cdot \operatorname{Grad}\left(\bar{\boldsymbol{d}}\right)\right) \cdot \boldsymbol{n}_0 = \boldsymbol{0}. \tag{2.55}$$

Further mathematical operations finally lead to

$$\boldsymbol{H}_{\bar{d}} \cdot \left(\boldsymbol{d} - \bar{\boldsymbol{d}}\right) + \boldsymbol{A}_{\bar{d}} \cdot \operatorname{Div}\left(\operatorname{Grad}\left(\bar{\boldsymbol{d}}\right)\right) = \boldsymbol{0} \tag{2.56}$$

$$\operatorname{Grad}\left(\bar{\boldsymbol{d}}\right) \cdot \boldsymbol{n}_0 = \boldsymbol{0}, \tag{2.57}$$

which is very similar to the structure for one scalar damage variable, e.g. presented in Brepols et al. [2020], and besides does not depend on the volume fiber fraction. Of course $0 < V_F < 1$ has to hold at this point to avoid a division by zero.
By following the standard procedure (multiply by the test function, integrate over the domain and apply the divergence theorem), the following weak forms are obtained under the consideration of the Neumann boundaries

$$g_u := \int_{\Omega_0} \boldsymbol{S} : \delta\boldsymbol{E} \, \mathrm{d}V - \int_{\Omega_0} \boldsymbol{f}_0 \cdot \delta\boldsymbol{u} \, \mathrm{d}V - \int_{\partial_t\Omega_0} \boldsymbol{t}_0 \cdot \delta\boldsymbol{u} \, \mathrm{d}A = 0 \tag{2.58}$$

$$g_{\bar{d}} := \int_{\Omega_0} \delta\bar{\boldsymbol{d}} \cdot \boldsymbol{H}_{\bar{d}} \cdot \left(\boldsymbol{d} - \bar{\boldsymbol{d}}\right) \, \mathrm{d}V - \int_{\Omega_0} \operatorname{Grad}\left(\delta\bar{\boldsymbol{d}}\right) : \left(\boldsymbol{A}_{\bar{d}} \cdot \operatorname{Grad}\left(\bar{\boldsymbol{d}}\right)\right) \, \mathrm{d}V = 0. \tag{2.59}$$

2.4 Finite Element implementation

A brief summary of the implementation scheme following the framework of Brepols et al. [2020] is presented. However, since there are three instead of one independent damage variable, the framework has to be extended and particular attention must be paid to the arrangement of the different matrices to ensure an efficient implementation, which is presented in the following.

2.4.1 Linearization

In the course of the Newton-Raphson scheme, the equations (2.58) and (2.59) are to be linearized at the global level with respect to the increments $\Delta\boldsymbol{u}$ and $\Delta\bar{\boldsymbol{d}}$. For this purpose, the Gâteaux derivative $\mathscr{D}[(*)]$ in the direction of the displacement increment $\Delta\boldsymbol{u}$ and the

micromorphic damage increment $\Delta\bar{\boldsymbol{d}}$ has to be performed for each weak form. For short hand notation, the resulting increments $\Delta g_u := \mathscr{D}_{\boldsymbol{u}}[g_u] \cdot \Delta\boldsymbol{u} + \mathscr{D}_{\bar{\boldsymbol{d}}}[g_u] \cdot \Delta\bar{\boldsymbol{d}}$ as well as $\Delta g_{\bar{d}} := \mathscr{D}_{\boldsymbol{u}}[g_{\bar{d}}] \cdot \Delta\boldsymbol{u} + \mathscr{D}_{\bar{\boldsymbol{d}}}[g_{\bar{d}}] \cdot \Delta\bar{\boldsymbol{d}}$ of the weak forms are introduced (a more precise definition can be found in Appendix 2.7.5.1). Under the assumption that the body force $\boldsymbol{f}_0$ as well as the traction vector $\boldsymbol{t}_0$ are independent of the actual displacement state, the following increments are obtained

$$\Delta g_u = \int_{\Omega_0} \Delta\boldsymbol{S} : \delta\boldsymbol{E} \, \mathrm{d}V + \int_{\Omega_0} \boldsymbol{S} : \Delta\delta\boldsymbol{E} \, \mathrm{d}V \tag{2.60}$$

$$\Delta g_{\bar{d}} = \int_{\Omega_0} \delta\bar{\boldsymbol{d}} \cdot \boldsymbol{H}_{\bar{d}} \cdot \left(\Delta\boldsymbol{d} - \Delta\bar{\boldsymbol{d}}\right) \, \mathrm{d}V - \int_{\Omega_0} \mathrm{Grad}\left(\delta\bar{\boldsymbol{d}}\right) : \left(\boldsymbol{A}_{\bar{d}} \cdot \mathrm{Grad}\left(\Delta\bar{\boldsymbol{d}}\right)\right) \, \mathrm{d}V. \tag{2.61}$$

In the linearized terms, $\Delta\boldsymbol{S} = \mathbb{C} : \Delta\boldsymbol{E} + \boldsymbol{\mathcal{L}}_{\bar{d}} \cdot \Delta\bar{\boldsymbol{d}}$ and $\Delta\boldsymbol{d} = \boldsymbol{\mathcal{L}}_E : \Delta\boldsymbol{E} + \boldsymbol{Q}_{\bar{d}} \cdot \Delta\bar{\boldsymbol{d}}$ can be expressed in terms of the required increments. In order to achieve quadratic convergence during the solution procedure, the several material tangents have to be treated carefully and will be therefore discussed in more detail in Section 2.4.4.

2.4.2 Numerical approximation

For the numerical approximation, the two dimensional scheme present in Klinkel and Reichel [2019] is applied and extended to the three dimensional case. In the present context this scheme has the advantage that due to the same number of degrees of freedom for the displacement as for the micromorphic damage the same trilinear shape function matrices and their derivatives can be used for the displacement and damage field. First, the exact domain is approximated and then divided into subdomains

$$\Omega_0 \approx \Omega_0^h = \bigcup_{e=1}^{n_{el}} \Omega_0^e. \tag{2.62}$$

Based on these subdomains, the several approximations of the field variables are as follows

$$\boldsymbol{u}^e = \mathbf{N}(\xi,\eta,\zeta)\mathbf{U}^e, \quad \delta\boldsymbol{u}^e = \mathbf{N}(\xi,\eta,\zeta)\delta\mathbf{U}^e, \quad \Delta\boldsymbol{u}^e = \mathbf{N}(\xi,\eta,\zeta)\Delta\mathbf{U}^e \tag{2.63}$$

$$\bar{\boldsymbol{d}}^e = \mathbf{N}(\xi,\eta,\zeta)\bar{\mathbf{D}}^e, \quad \delta\bar{\boldsymbol{d}}^e = \mathbf{N}(\xi,\eta,\zeta)\delta\bar{\mathbf{D}}^e, \quad \Delta\bar{\boldsymbol{d}}^e = \mathbf{N}(\xi,\eta,\zeta)\Delta\bar{\mathbf{D}}^e, \tag{2.64}$$

with the shape function matrix $\mathbf{N}(\xi,\eta,\zeta)$ defined in the isoparametric space (see Appendix 2.7.5.2) as well as the nodal values $\mathbf{U}^e$ and $\bar{\mathbf{D}}^e$. It remains to introduce the approximation of

the derivatives

$$\hat{\boldsymbol{F}}^e = \hat{\boldsymbol{I}} + \mathbf{B}(\xi,\eta,\zeta)\mathbf{U}^e, \qquad \delta\hat{\boldsymbol{F}}^e = \mathbf{B}(\xi,\eta,\zeta)\delta\mathbf{U}^e, \qquad \Delta\hat{\boldsymbol{F}}^e = \mathbf{B}(\xi,\eta,\zeta)\Delta\mathbf{U}^e \tag{2.65}$$

$$\mathrm{Grad}\left(\bar{\boldsymbol{d}}\right)^e = \mathbf{B}(\xi,\eta,\zeta)\bar{\mathbf{D}}^e, \mathrm{Grad}\left(\delta\bar{\boldsymbol{d}}\right)^e = \mathbf{B}(\xi,\eta,\zeta)\delta\bar{\mathbf{D}}^e, \mathrm{Grad}\left(\Delta\bar{\boldsymbol{d}}\right)^e = \mathbf{B}(\xi,\eta,\zeta)\Delta\bar{\mathbf{D}}^e. \tag{2.66}$$

These approximations now allow the equations (2.58) (neglecting the body and external forces), (2.59) as well as the incremental equations (2.60) and (2.61), in connection with the abbreviations introduced in Section 2.4.1, to be suitably adapted for the FEM implementation

$$\begin{aligned} g_u^h &= \bigcup_{e=1}^{n_{el}} \delta\mathbf{U}^{eT} \overbrace{\left(\int_{\Omega_0^e} \mathbf{B}^T\mathbf{F}_m^T\hat{\boldsymbol{S}}^e \,\mathrm{d}V^e - \int_{\Omega_0^e} \mathbf{N}^T\boldsymbol{f}_0^e \,\mathrm{d}V^e - \int_{\partial_t\Omega_0^e} \mathbf{N}^T\boldsymbol{t}_0^e \,\mathrm{d}A^e\right)}^{\mathbf{r}_u^e} \\ g_{\bar{d}}^h &= \bigcup_{e=1}^{n_{el}} \delta\bar{\mathbf{D}}^{eT} \underbrace{\int_{\Omega_0^e} \left(\mathbf{N}^T\hat{\boldsymbol{H}}_{\bar{d}}\left(\boldsymbol{d}^e - \bar{\boldsymbol{d}}^e\right) - \mathbf{B}^T\hat{\boldsymbol{A}}_{\bar{d}}\mathrm{Grad}\left(\bar{\boldsymbol{d}}^e\right)\right) \mathrm{d}V^e}_{\mathbf{r}_{\bar{d}}^e} \end{aligned} \tag{2.67}$$

$$\begin{aligned} \Delta g_u^h = &\bigcup_{e=1}^{n_{el}} \delta\mathbf{U}^{eT} \overbrace{\left(\int_{\Omega_0^e} \mathbf{B}^T\mathbf{F}_m^T\hat{\mathbb{C}}\mathbf{F}_m\mathbf{B} \,\mathrm{d}V^e + \int_{\Omega_0^e} \mathbf{B}^T\mathbf{S}_m\mathbf{B} \,\mathrm{d}V^e\right)}^{\mathbf{K}_{uu}^e} \Delta\mathbf{U}^e \\ &+ \bigcup_{e=1}^{n_{el}} \delta\mathbf{U}^{eT} \underbrace{\left(\int_{\Omega_0^e} \mathbf{B}^T\mathbf{F}_m^T\hat{\mathcal{L}}_{\bar{d}}\mathbf{N} \,\mathrm{d}V^e\right)}_{\mathbf{K}_{u\bar{d}}^e} \Delta\bar{\mathbf{D}}^e \end{aligned} \tag{2.68}$$

$$\begin{aligned} \Delta g_{\bar{d}}^h = &\bigcup_{e=1}^{n_{el}} \delta\bar{\mathbf{D}}^{eT} \overbrace{\left(\int_{\Omega_0^e} \mathbf{N}^T\hat{\boldsymbol{H}}_{\bar{d}}\left(\hat{\boldsymbol{Q}}_{\bar{d}} - \hat{\boldsymbol{I}}\right)\mathbf{N} \,\mathrm{d}V^e - \int_{\Omega_0^e} \mathbf{B}^T\hat{\boldsymbol{A}}_{\bar{d}}\mathbf{B} \,\mathrm{d}V^e\right)}^{\mathbf{K}_{\bar{d}\bar{d}}^e} \Delta\bar{\mathbf{D}}^e \\ &+ \bigcup_{e=1}^{n_{el}} \delta\bar{\mathbf{D}}^{eT} \underbrace{\left(\int_{\Omega_0^e} \mathbf{N}^T\hat{\boldsymbol{H}}_{\bar{d}}\hat{\boldsymbol{\mathcal{L}}}_E\mathbf{F}_m\mathbf{B} \,\mathrm{d}V^e\right)}_{\mathbf{K}_{\bar{d}u}^e} \Delta\mathbf{U}^e. \end{aligned} \tag{2.69}$$

In the latter equations the relations $\Delta\hat{\boldsymbol{E}} = \mathbf{F}_m\Delta\hat{\boldsymbol{F}}$ and $\delta\hat{\boldsymbol{E}} = \mathbf{F}_m\delta\hat{\boldsymbol{F}}$ have been exploited. The approximation of $\bar{\boldsymbol{d}}^e$ holds also true for the local counterpart. Furthermore, the matrices $\mathbf{F}_m$ and $\mathbf{S}_m$ can be found in Appendix 2.7.5.2. Finally, applying the Dirichlet boundary conditions

and assembling both the element residuals ($\mathbf{r}_u^e$, $\mathbf{r}_{\bar{d}}^e$) and the element stiffness matrices ($\mathbf{K}_{uu}^e$, $\mathbf{K}_{u\bar{d}}^e$, $\mathbf{K}_{\bar{d}u}^e$ and $\mathbf{K}_{\bar{d}\bar{d}}^e$), one obtains the coupled global boundary value problem

$$\begin{pmatrix} \mathbf{K}_{uu} & \mathbf{K}_{u\bar{d}} \\ \mathbf{K}_{\bar{d}u} & \mathbf{K}_{\bar{d}\bar{d}} \end{pmatrix} \begin{pmatrix} \Delta\mathbf{U} \\ \Delta\bar{\mathbf{D}} \end{pmatrix} = - \begin{pmatrix} \mathbf{r}_u \\ \mathbf{r}_{\bar{d}} \end{pmatrix}. \tag{2.70}$$

2.4.3 Implicit time integration of the evolution equations

The local evolution equations are generally discretized in the time interval $[t_n, t_{n+1}]$. Therefore, the Backward Euler method within the numerical implementation on the Gaussian level is used. An exception is the equation for $\dot{\boldsymbol{C}}_{Mp}$ (2.37), which is based on the modified exponential mapping algorithm presented in Vladimirov et al. [2008], Reese and Christ [2008] and Dettmer and Reese [2004]. This approach directly guarantees volume preserving and preserves the symmetry of $\dot{\boldsymbol{C}}_{Mp}$. For the damage part one is again referred to Brepols et al. [2020]. The several residuals are then defined as

$$r_1 = \Phi_t = 0, \qquad r_2 = \Phi_c = 0 \tag{2.71}$$

$$r_3 = \Phi_M = 0, \qquad r_4 = \Phi_p = 0 \tag{2.72}$$

$$\boldsymbol{R}_5 = -\boldsymbol{C}_{Mp_n}^{-1} + \boldsymbol{U}_{Mp}^{-1} \exp\left(\Delta\lambda_p \boldsymbol{U}_{Mp}^{-1} \boldsymbol{T}_{Mp} \boldsymbol{U}_{Mp}^{-1}\right) \boldsymbol{U}_{Mp}^{-1} = \boldsymbol{0}. \tag{2.73}$$

Note that the index $n+1$ was omitted. Furthermore, the plastic stretch tensor is defined as $\boldsymbol{C}_{Mp} = \boldsymbol{U}_{Mp}^2$. Several possible loading/unloading scenarios for the residuals defined in (2.72) and (2.73) have to be considered (see Brepols et al. [2020]), which influence the size of the equation system (2.76) shown later. In addition, a case differentation regarding the damage evolution of the fiber part can be made. Due to the specific structure of Φ_t (2.30) and Φ_c (2.31) only one damage criterion can be exceeded, since the fiber is either stretched or compressed.

2.4.4 Consistent tangent operators

As mentioned in Section 2.4.1 the material tangents have to be defined in a consistent manner to achive quadratic convergence. Therefore, one should bear in mind that the stress is a function of the several local damage variables, the plastic Cauchy-Green tensor and the total Cauchy-Green tensor. Taking into account the relation $1/2\Delta\boldsymbol{C} = \Delta\boldsymbol{E}$ and using the chain rule, the following expressions are obtained

$$\mathbb{C} = 2\left(\frac{\partial \boldsymbol{S}}{\partial \boldsymbol{C}} + \frac{\partial \boldsymbol{S}}{\partial \boldsymbol{U}_{Mp}^{-1}} : \frac{\partial \boldsymbol{U}_{Mp}^{-1}}{\partial \boldsymbol{C}} + \frac{\partial \boldsymbol{S}}{\partial \boldsymbol{d}} \cdot \frac{\partial \boldsymbol{d}}{\partial \boldsymbol{C}}\right), \quad \boldsymbol{Q}_{\bar{d}} = \frac{\partial \boldsymbol{d}}{\partial \bar{\boldsymbol{d}}} \tag{2.74}$$

$$\mathcal{L}_{\bar{d}} = \frac{\partial \boldsymbol{S}}{\partial \boldsymbol{d}} \cdot \frac{\partial \boldsymbol{d}}{\partial \bar{\boldsymbol{d}}} + \frac{\partial \boldsymbol{S}}{\partial \boldsymbol{U}_{Mp}^{-1}} : \frac{\partial \boldsymbol{U}_{Mp}^{-1}}{\partial \bar{\boldsymbol{d}}}, \quad \mathcal{L}_E = 2\frac{\partial \boldsymbol{d}}{\partial \boldsymbol{C}}. \tag{2.75}$$

The derivatives of the stress tensor $\partial \boldsymbol{S}/\partial \boldsymbol{C}$, $\partial \boldsymbol{S}/\partial \boldsymbol{d}$, $\partial \boldsymbol{S}/\partial \boldsymbol{U}_{Mp}^{-1}$ can be found in Appendix 2.7.6. The remaining partial derivatives are computed based on the converged values for the residuals of the previous Section. To gain these derivatives, an additional local Newton-Raphson step is performed. In Nye notation the following system of equations has to be solved

$$\begin{pmatrix} \frac{\partial r_1}{\partial \boldsymbol{d}} & \frac{\partial r_1}{\partial \Delta\lambda_p} & \frac{\partial r_1}{\partial \hat{\boldsymbol{U}}_{Mp}^{-1}} \\ \frac{\partial r_2}{\partial \boldsymbol{d}} & \frac{\partial r_2}{\partial \Delta\lambda_p} & \frac{\partial r_2}{\partial \hat{\boldsymbol{U}}_{Mp}^{-1}} \\ \frac{\partial r_3}{\partial \boldsymbol{d}} & \frac{\partial r_3}{\partial \Delta\lambda_p} & \frac{\partial r_3}{\partial \hat{\boldsymbol{U}}_{Mp}^{-1}} \\ \frac{\partial r_4}{\partial \boldsymbol{d}} & \frac{\partial r_4}{\partial \Delta\lambda_p} & \frac{\partial r_4}{\partial \hat{\boldsymbol{U}}_{Mp}^{-1}} \\ \frac{\partial \hat{\boldsymbol{R}}_5}{\partial \boldsymbol{d}} & \frac{\partial \hat{\boldsymbol{R}}_5}{\partial \Delta\lambda_p} & \frac{\partial \hat{\boldsymbol{R}}_5}{\partial \hat{\boldsymbol{U}}_{Mp}^{-1}} \end{pmatrix}_{10\times 10} \begin{pmatrix} \Delta \boldsymbol{d} \\ \Delta\Delta\lambda_p \\ \Delta \hat{\boldsymbol{U}}_{Mp}^{-1} \end{pmatrix} = - \begin{pmatrix} \frac{\partial r_1}{\partial \hat{\boldsymbol{C}}} & \frac{\partial r_1}{\partial \bar{\boldsymbol{d}}} \\ \frac{\partial r_2}{\partial \hat{\boldsymbol{C}}} & \frac{\partial r_2}{\partial \bar{\boldsymbol{d}}} \\ \frac{\partial r_3}{\partial \hat{\boldsymbol{C}}} & \frac{\partial r_3}{\partial \bar{\boldsymbol{d}}} \\ \frac{\partial r_4}{\partial \hat{\boldsymbol{C}}} & \frac{\partial r_4}{\partial \bar{\boldsymbol{d}}} \\ \frac{\partial \hat{\boldsymbol{R}}_5}{\partial \hat{\boldsymbol{C}}} & \frac{\partial \hat{\boldsymbol{R}}_5}{\partial \bar{\boldsymbol{d}}} \end{pmatrix}_{10\times 9} \begin{pmatrix} \Delta \hat{\boldsymbol{C}} \\ \Delta \bar{\boldsymbol{d}} \end{pmatrix}. \tag{2.76}$$

Here, the abbreviation $\Delta\lambda_p = \Delta t\, \dot{\lambda}_{p_{n+1}}$ was introduced. To end up with the form presented above, several things should be noted: (i) the symmetry of $\boldsymbol{U}_{Mp}^{-1}$ was used, (ii) κ_p is defined directly based on the plastic multiplier, (iii) similar to the last point the several $\kappa_{t,c,M}$ and D values can be defined explicitly based on the corresponding evolution equation and thus no additional residuals are required to calculate these values. Hence, these variables just have to be updated after the local Newton-Raphson iteration has converged and (iv) having equation (2.33) in mind it can be shown that $\partial\Delta\lambda_i/\partial D_{i_{n+1}} = 1$ holds true. Therefore, the damage variables D can be chosen as the independent variable.
Due to the fact that the material model is still under development and that the evolution equations can still change (e.g. by Puck's criterion), the derivatives of the residuals are determined numerically. Also, the above mentioned scenarios reduce the size of the equation system (2.76) immensely in some cases.

2.5 Numerical examples

For a better understanding of this quite complex model, numerical examples are presented to examine different aspects of the model. Due to the lack of own experimental data at the present time, the material parameters for the numerical studies are freely chosen in each example. First, the asymmetric damage evolution of the fiber is to be investigated with a cyclic uniaxial tensile compression test. In order to obtain only the response of the material, a single element

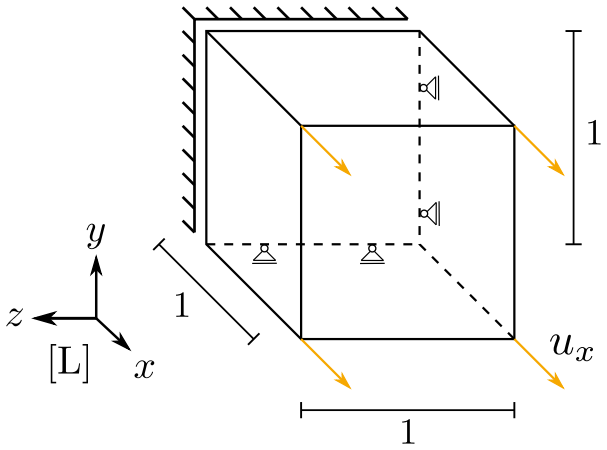

Figure 2.3: Cube: Boundary and loading conditions

is used. Second, the influence of the fiber direction on the matrix is investigated, however using different mesh refinements. Here, the focus is on the fiber direction influence on the plastic and matrix damage behavior. These two examples are discussed using a unit cube. The last example investigates mainly the interaction of the fiber and matrix damage under various conditions. For this purpose, a plate with hole specimen is used.
For the numerical examples, both the presented material model and the element formulation were implemented into the *MATLAB* based FEM code *DAEdalon* (see Baaser [2014]).

2.5.1 Tension-compression asymmetric fiber damage

First, the model is investigated in the small strain regime. The purpose of the investigation is the fiber elasto-damage behavior. Therefore, Y_{M0} and σ_{y0} were set to infinity. The remaining needed material parameters are listed in Table 2.2. In addition, the damage functions have been chosen to $f_t = (1 - D_t)^2$, $f_c = (1 - D_c)^2$ as well as the coupling functions f_{ct}, f_{tc} are set to one and the fiber exponents α, β, γ are equal to two.

Table 2.2: Material parameters for small strain study

	Λ	μ	K_{ani1}	K_{ani2}	K_{coup}	$r_{t/c}$	$s_{t/c}$	$Y_{t0/c0}$	$\varphi_{xy/z}$	V_F
Unit	[F/L^2]	[F/L^2]	[F/L^2]	[F/L^2]	[F/L^2]	[FL/L^3]	[-]	[FL/L^3]	[°]	[%]
	750/13	500/13	800	50	70	0.0001	1000	1.0·10^{-12}	0	65

Figure 2.3 shows the loading and boundary conditions as well as the displacement is defined by the load program time t / displacement u_x (cf. Fig. 2.4): (A) 0/0, (C) 0.5/0.001, (D) 0.75/0, (F) 1/-0.001.
As expected, the chosen material parameters lead to a symmetric behavior in the tension and

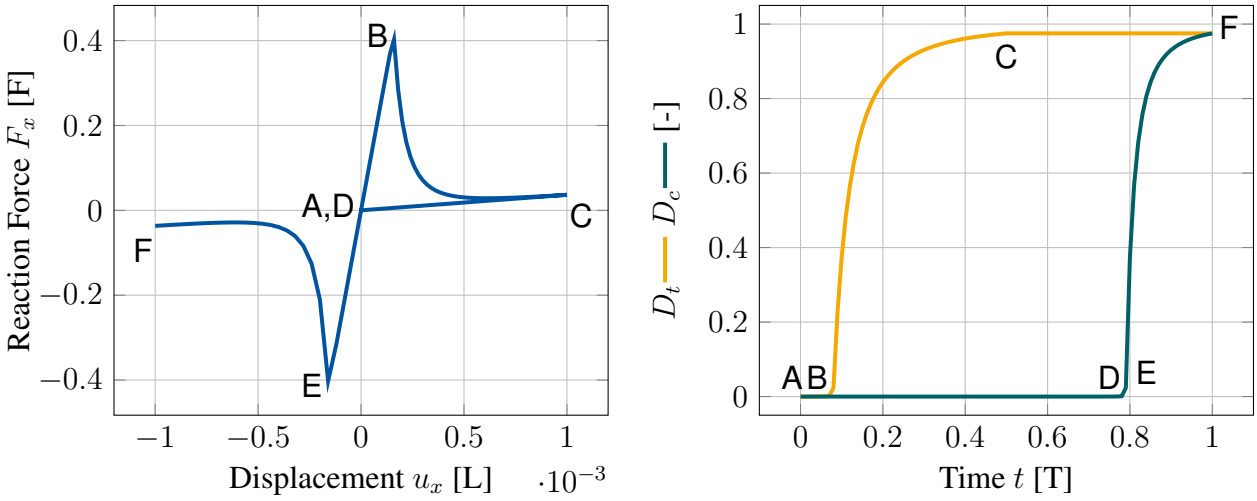

Figure 2.4: Force-displacement (left) and damage-time curves (right) at small strains

compression regime, since the strain energy Ψ_{Fe} leads to basically the same values at small strains. Figure 2.4 shows the observed results, which are reasonable. Having in mind that only the fiber damages, the remaining stiffness is caused by the matrix contribution.
Now, the material is investigated in the finite strain regime with the following load program (cf. Fig. 2.5): (A) 0/0, (C) 0.5/0.5, (D) 0.75/0, (F) 1/-0.5. In addition, the influence of a fiber direction, which is not parallel to the load direction, is to be investigated as well as different damage parameters for the tensile and compression domain. Since the same elastic material parameters as presented in Table 2.2 were chosen, Table 2.3 shows the modified parameters.

Table 2.3: Material parameters for finite strain study

	r_t	r_c	s_t	s_c	Y_{t0}	Y_{c0}	φ_z
Unit	[FL/L^3]	[FL/L^3]	[-]	[-]	[FL/L^3]	[FL/L^3]	[°]
	80	200	50	5	1	25	0

The obtained results are shown in Figure 2.5. Here, the advantage of the tension-compression asymmetry, besides the crack closure modeling, can be observed. The damage behavior in the tension regime behaves totally different from the compression part. Although the damage thresholds differ widely, the damage onset is within the same range.
The initial stiffness of the 30 degree angle investigation can be explained by the fact that the fibers first orient themselves in the tensile direction. Thus, it is mainly the matrix stiffness that can be observed at the beginning. This nonlinear behavior is similar to the ones observed by e.g. Reese et al. [2001] and Jha et al. [2019]. Although they discuss orthotropic behavior, the mechanism of fiber reorientation is comparable. Further, Puck and Schürmann [2002] named

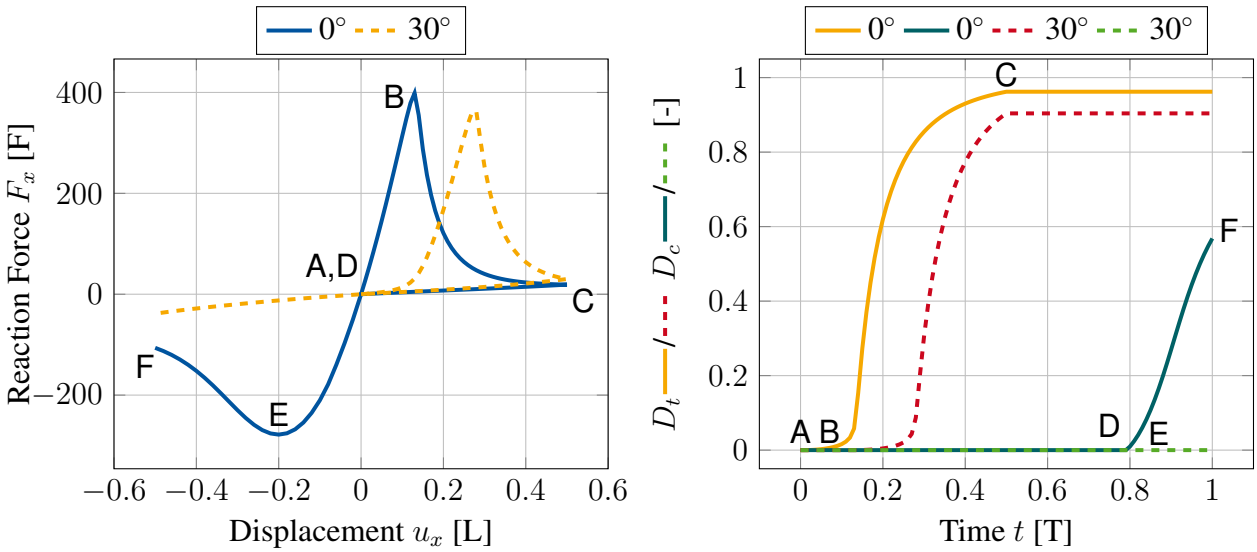

Figure 2.5: Force-displacement (left) and damage-time (right) curves for different fiber angles φ_{xy} at finite strains

fiber-reorientation as a source of nonlinearities. In the compression regime, however, the fibers are not aligned in the load direction, but shifted until they are perpendicular to the load direction. Only then they effectively contribute to the stiffness through transverse elongation. However, this state has not been reached yet. Thus, mainly the matrix stiffness can be observed again.

Despite the above discussion, the results of the 30 degree study may seem unexpected, especially in the compression regime. Two remarks should be made on this: (i) the stiffness of the matrix is extremely low compared to the fiber and in addition the value of K_{ani1} is very high compared to K_{ani2} and K_{coup}, whereby especially the strain in the fiber direction has a high influence on the stress in this direction, but less perpendicular to it, and (ii) nevertheless the stiffnesses at small deformations provide a linear response even for 30 degrees. The last point is examined in Figure 2.6, where also a linear relationship between strain and stress ($\beta = \gamma = 1$) has been investigated for the fiber part. Since a detailed study of the material parameters, in particular on the elastic response, is out of the scope of this paper, it is not further investigated.

2.5.2 Fiber influence on isotropic matrix material

To study the material model of the matrix, among others, structural examples with imperfections are commonly carried out. Such detailed investigations and also mesh convergence studies can be found in Brepols et al. [2020]. This work rather focuses on the indirect anisotropic

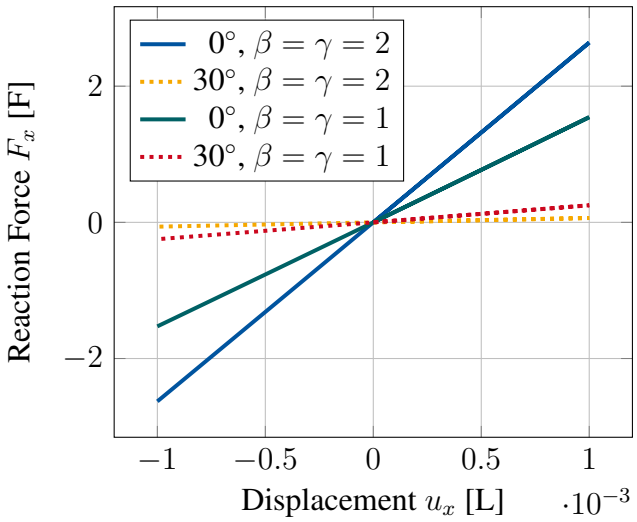

Figure 2.6: Force-displacement curves for different angles φ_{xy} at small strains

influence of the fiber on the isotropic matrix formulation. As in the previous chapter, a simple example will be chosen, whereby the spatial influence will be considered additionally. Again, this is a uniaxial tensile test in x-direction of a cube of edge length L, but with different mesh refinements.

In most cases, the material inelasticities of fiber-reinforced materials within the matrix occur before those of the fibers. Therefore, the fiber is considered purely elastic with the parameters $K_{ani1} = K_{ani2} = K_{coup} = 10$ [F/L^2] and $\alpha = \beta = \gamma = 2$ [-]. In Table 2.4 the material parameters describing the matrix material are listed. Furthermore, the parameters for the gradient-extended damage formulation are $A_M = 10$ [FL^3/L^3] and $H_M = 1 \cdot 10^5$ [FL/L^3], as well as the damage function $f_M = (1 - D_M)^2$. The fiber volume fraction was chosen to ten percent and φ_z is set to zero.

Table 2.4: Matrix material parameters

	Λ	μ	H_p	r_p	s_p	σ_{y0}	r_M	s_M	Y_{M0}
Unit	[F/L^2]	[F/L^2]	[F/L^2]	[F/L^2]	[-]	[F/L^2]	[FL/L^3]	[-]	[FL/L^3]
	15000/13	10000/13	450	20	10	40	8	0.1	100

Figure 2.7 shows the force-displacement curves for 512 elements as well as mesh convergence studies for the different fiber angles. For 0, 30 and 60 degrees a well converged mesh can be seen. Although the 90 degree convergence is less accurate, it is sufficient enough for the examples studied here. Due to the early onset of plasticity, in Figure 2.7 no major difference can be seen between the different curves at the onset. However, looking at Figure 2.8a, quasi-homogeneous plasticity can be seen for 0 degrees. In contrast, Figure 2.8b shows an

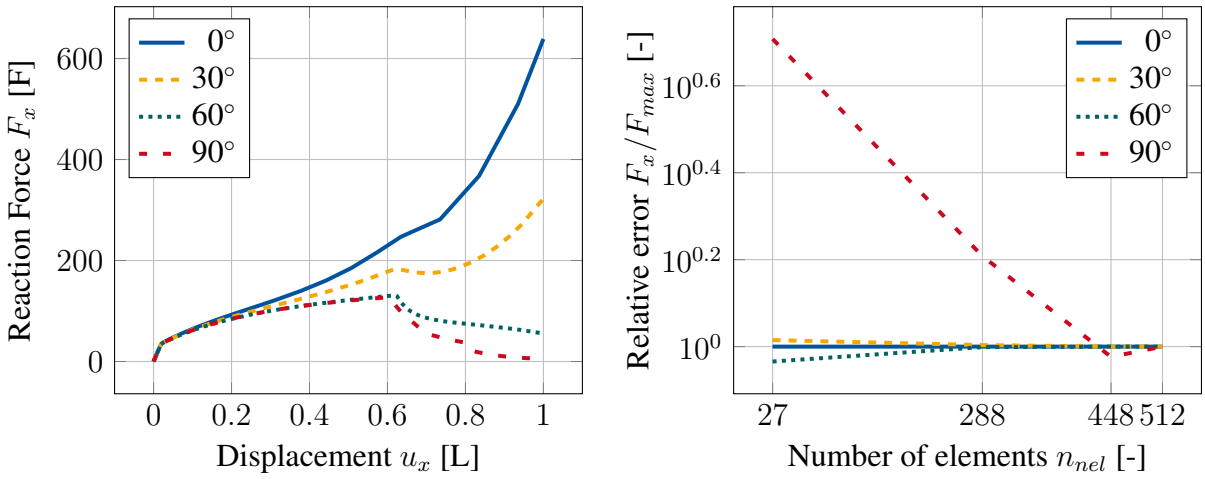

Figure 2.7: Force-displacement curves (left) and mesh convergence (right) for different fiber angles φ_{xy}

inhomogeneous field. This is due to the inhomogeneous strain state resulting from the fiber direction, which leads to strain peaks or relaxed areas. For other material parameters, the difference between the values can be even larger. However, this already gives an idea of the impact of the fiber direction.

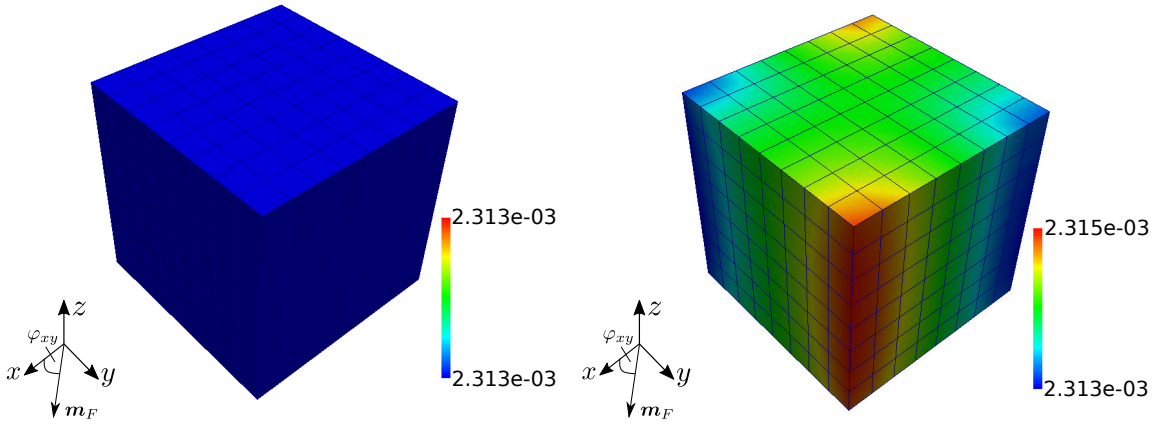

(a) κ_p [-] for $\varphi_{xy} = 0°$ (b) κ_p [-] for $\varphi_{xy} = 60°$

Figure 2.8: Initial accumulated plastic strain for different angles at $u_x = 0.023$ [L]

Considering the fact that for 0 and 30 degrees the curves are already dominated by the stiffness of the fibers, similar observations can be made for the beginning of the damage. Again, local strain peaks lead to a slight difference in the beginning. Remarkable is the earlier start for 90 degrees. This could be explained by the not identical transverse contraction ratios in y and z direction, in contrast to zero degrees. Furthermore, the jump is noticeable with a deformation

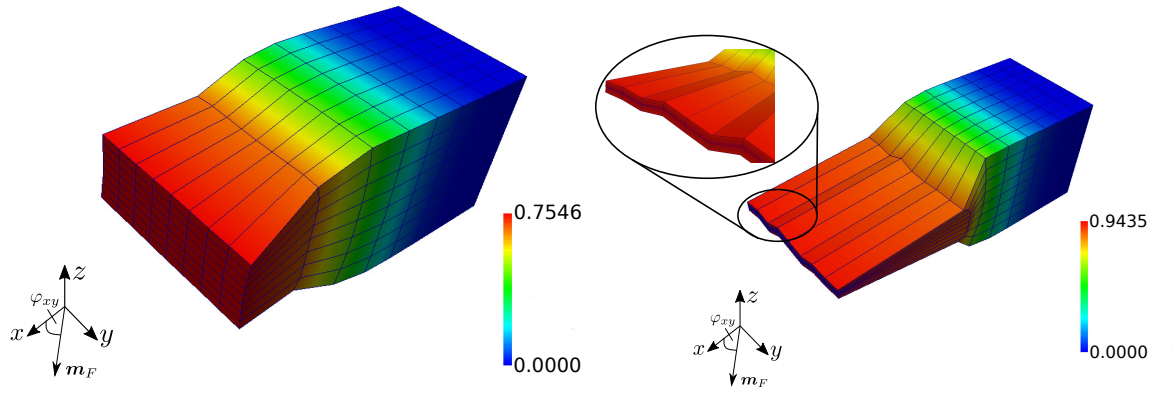

(a) Aspect ratio: D_M [-] at $u_x = 0.811$ [L] (b) Unstable behavior: D_M [-] at $u_x = 1.323$ [L]

Figure 2.9: Deformed structure for $\varphi_{xy} = 90°$

of approx. $u_x = 0.8$ [L]. If one looks at the deformed structure (Fig. 2.9a), this is due to the strongly changing aspect ratio caused by the different transverse contraction.

If a larger deformation is applied (Fig. 2.9b), a further interesting result is observed. Due to the nearly fully damaged matrix material, the structure has mainly a remaining stiffness in the fiber direction. Having the actual loading in mind, the fibers a compressed because of transverse elongation. Thus, in addition to the already very thin deformation state of the structure, it can be seen as a thin structure which is under compression loading. For such a case, it is known to behave unstable.

Nevertheless, this comparison should be substantiated by numerical investigations. For this purpose, a deformation $u_x = 1.19$ [L] was applied for which the instability could be recognized for the first time (see Appendix 2.7.7). In order to understand the underlying mechanisms in a better way, the eigenvalues of the material tangent of one element in the area of the instability are carried out. The results a presented in Table 2.5. Two interesting results can be observed: (i) for stretch parallel to the fiber (second row of the Green-Lagrange strain tensor), zero eigenvalues occur and (ii) for compression parallel to the fiber even negative ones are observed.

Under consideration that the matrix nearly does not contribute to the material response, it is mainly the contribution of the fiber part. As already discussed in Section 2.3.2, a physical reasonable material can not be described only by the fiber, since the corresponding material tangent is only semidefinite. However, it should be emphasized that these considerations were carried out for linear elasticity. Since in the actual case the material tangent depends on the deformation state (nonlinear elasticity), it is not surprising that also negative eigenvalues can be observed.

Hence, the unstable behavior can also be explained from a numerical point of view and is

further an interesting example of the theoretical considerations from Section 2.3.2. A more detailed discussion would be out of place here, as the focus is different. However, the interested reader can find a more detailed discussion in Appendix 2.7.7.

Table 2.5: Gaussian point investigation of element with center coordinate at (0.9375, 0.4375, 0.4375)

	GP 1	GP 2	GP 3	GP 4	GP 5	GP 6	GP 7	GP 8
D_M	9.248E-01	9.257E-01	8.723E-01	8.758E-01	9.258E-01	9.267E-01	8.727E-01	8.767E-01
$\hat{\boldsymbol{E}}$	2.33E+01	23.78	23.33	23.78	2.33E+01	2.38E+01	2.33E+01	2.38E+01
	8.33E-04	0	-0.01	-0.01	9.39E-04	9.39E-04	-7.51E-03	-7.51E-03
	-0.49	-0.49	-0.44	-0.44	-0.49	-0.49	-0.44	-0.44
	2.12E-01	2.00E-01	0.66	0.65	1.61E-01	1.48E-01	0.64	0.63
	2.80E-02	0.02	0.07	0.03	8.54E-04	-7.45E-03	0	-0.04
	4.29E-02	4.28E-02	1.29E-01	1.30E-01	4.27E-02	4.25E-02	1.29E-01	1.29E-01
Eigenvalues of $\hat{\mathbb{C}}$	49492.457	46569.341	8548.100	8870.943	48072.517	45045.226	8527.785	8870.883
	8382.404	8713.096	2941.651	2676.929	8364.726	8718.892	2916.566	2635.130
	270.645	251.925	2.029	1.936	262.824	243.316	1.872	1.789
	5.701	5.173	-0.095	-0.109	5.548	5.001	-0.094	-0.107
	0.366	0.325	-4.433	-4.822	0.251	0.216	-4.471	-4.785
	0.001	0.000	-239.111	-248.554	0.001	0.000	-242.424	-248.230

Finally, Figure 2.10 will be discussed, which shows the accumulated plastic strain κ_p as well as the damage variable of the matrix D_M at the end of the deformation. As expected, the material behaves quasi homogeneously for 0 degrees, since there is no anisotropy perpendicular to the loading direction. Due to the mentioned strain peaks for the other angles, locally, significantly higher values for κ_p and D_M along the fiber are obtained compared to the quasi isotropic case, at the same time with lower values for lower deformations. This emphasizes that even the purely elastic behavior of the fiber already has a significant influence on the isotropic matrix formulation, which should not be underestimated in real applications.
Further, it should be noted that all simulations were characterized by a quadratic convergence behavior. Only oscillating values during the Newton-Raphson scheme caused problems, which could be solved by halving the step size on appearance.

2.5.3 Plate with hole

In the following, several finite element structural computations will be performed. The main purpose is to investigate the interaction between matrix damage and fiber damage under various conditions. Therefore, a plate with hole (PWH) example is considered, which boundary conditions for the full structure 2.11a and the symmetric part 2.11b are shown in Figure 2.11. As it is illustrated, the structure is supported at the top and bottom. It is held fixed in x-direction and the top displacement in the y-direction is increased over time. Thus, a clamping of the

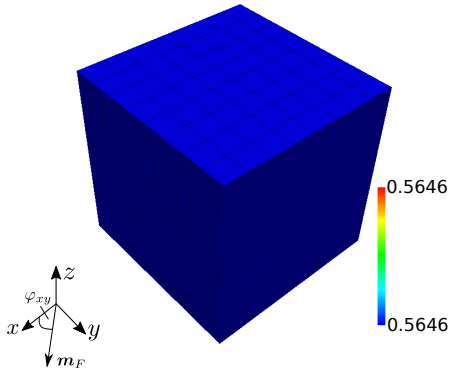

(a) κ_p [-] for $\varphi_{xy} = 0°$

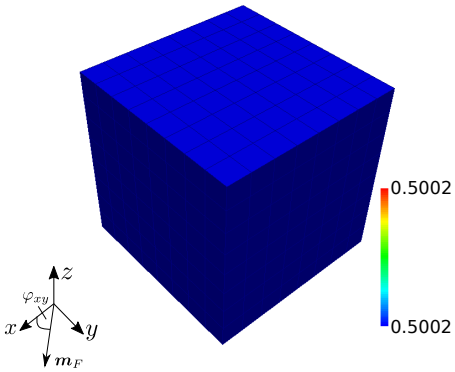

(b) D_M [-] for $\varphi_{xy} = 0°$

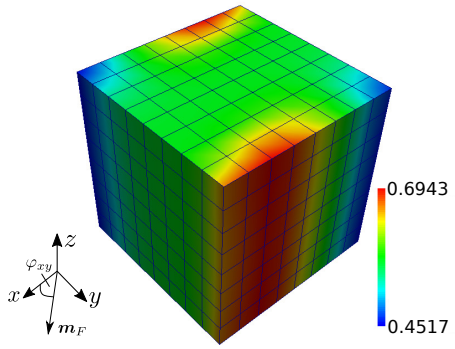

(c) κ_p [-] for $\varphi_{xy} = 30°$

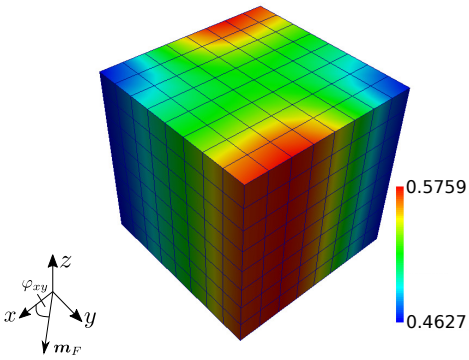

(d) D_M [-] for $\varphi_{xy} = 30°$

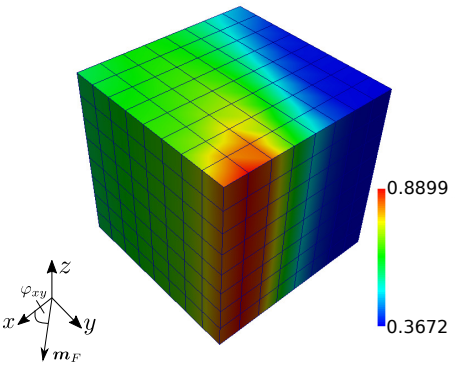

(e) κ_p [-] for $\varphi_{xy} = 60°$

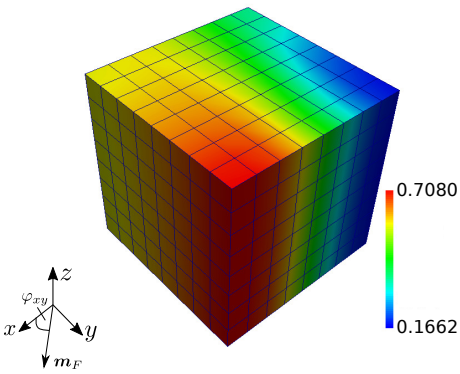

(f) D_M [-] for $\varphi_{xy} = 60°$

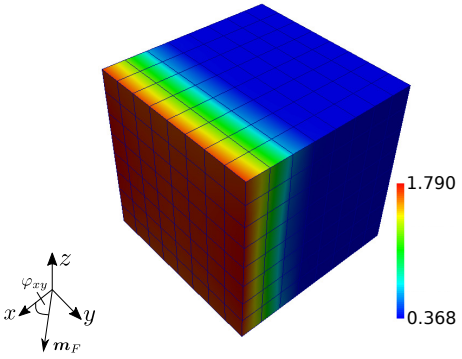

(g) κ_p [-] for $\varphi_{xy} = 90°$

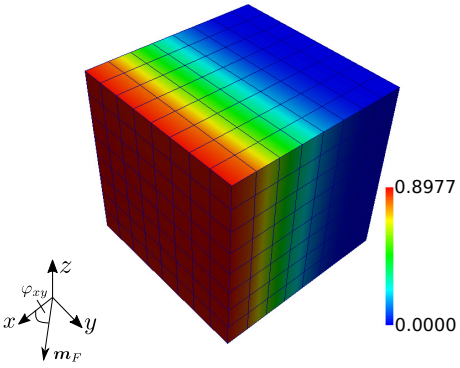

(h) D_M [-] for $\varphi_{xy} = 90°$

Figure 2.10: Accumulated plastic strain (left) and matrix damage (right) for different angles at $u_x = 1$ [L]

PWH is simulated. Note that for the symmetric part only half of the y-displacement is applied, since applying half the displacement at the top and bottom for the full structure is equivalent to the case shown here. However, the case illustrated is more common.

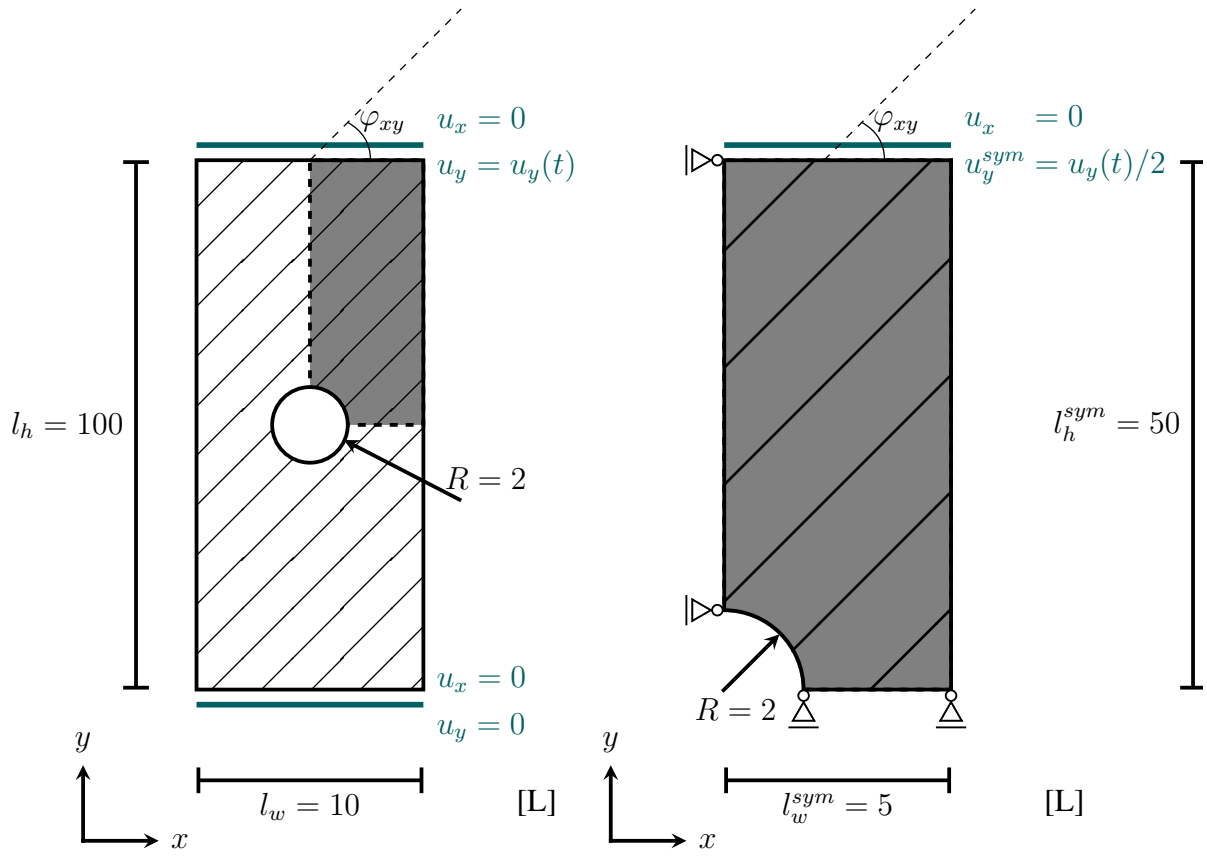

(a) Full structure (b) Symmetric part

Figure 2.11: Plate with hole and boundary conditions

For reasons of simplicity and numerical efficiency, respectively the more straightforward numerical implementation, a plane strain state is assumed. Even if a plane stress state would be more realistic for this type of testing, this does not harm the purpose of the investigation carried out here. For the realization, one element over the thickness is used, which is completely held fixed in z-direction. The thickness is set to $l_t = 0.1$ [L].The angle φ_z is always equal to zero.

The elastic and damage material parameters for the matrix and the fiber can be found in Table 2.6 and 2.8, respectively. The material parameters for the additional plastic investigations are listed in Table 2.7. Furthermore, the fiber volume fraction is set to $V_F = 30\%$. The degradation function for the fiber tension damage and matrix damage are chosen to $f_t = (1 - D_t)^2$ and $f_M = (1 - D_M)^2$. Again, the coupling functions f_{tc} and f_{ct} are set to one. Since no fiber

compression damage is expected for the following studies, no compression damage material parameters have to be chosen or the damage threshold Y_{c0} is set to infinity.
In addition, an artificial viscosity by means of $\boldsymbol{S}_v = v\dot{\boldsymbol{E}}$ is added to the overall second Piola-Kirchhoff stress tensor to overcome the severe snapback behavior in case of damage, which was also successfully applied by e.g. Fassin et al. [2019*b*,*a*]. The artificial parameter is set to $v = 1$ [FT/L^2].

Table 2.6: Material parameters for matrix material (PWH)

	Λ	μ	r_M	s_M	Y_{M0}	A_M	H_M
Unit	[F/L^2]	[F/L^2]	[FL/L^3]	[-]	[FL/L^3]	[FL^3/L^3]	[FL/L^3]
	40000	40000	8	10	10	30	1·10^5

Table 2.7: Plastic material parameters for matrix material (PWH)

	H_p	r_p	s_p	σ_{y0}
Unit	[F/L^2]	[F/L^2]	[-]	[F/L^2]
	20000	125	20	300

Table 2.8: Material parameters for fiber material (PWH)

	K_{ani1}	K_{ani2}	K_{coup}	$\alpha/\beta/\gamma$	r_t	s_t	Y_{t0}	A_t	H_t
Unit	[F/L^2]	[F/L^2]	[F/L^2]	[-]	[FL/L^3]	[-]	[FL/L^3]	[FL^3/L^3]	[FL/L^3]
	35000	2500	15000	2	5	1	275	200	1·10^5

In order to understand the interaction between fiber and matrix damage in more detail, the following investigations are to be performed:

1. Pure elasto-damage matrix (EDM) material
2. Pure elasto-plastic-damage matrix (EPDM) material
3. Elasto-damage matrix and elasto-damage fiber with $\varphi_{xy} = 90°$ (EDMF90)
4. Elasto-plastic-damage matrix and elasto-damage fiber with $\varphi_{xy} = 90°$
5. Elasto-damage matrix and elasto-damage fiber with $\varphi_{xy} = 45°$

As a result of the first two investigations it is possible to better identify the influence of the fiber. For the sake of completeness, Table 2.9 lists the maximum reaction forces $F_y^{\max}$ to which the force-displacement curves in the following Sections are normalized.

Table 2.9: Maximum reaction forces

Figure	2.13	2.15	2.17	2.20	2.23
$F_y^{\max}$ [F]	617.554	412.987	1020.869	1159.164	467.501

2.5.3.1 Pure elasto-damage matrix material

The aim of this first investigation is to be able to study the influence of the fiber and its damage evolution on the matrix material. Hence, the pure matrix material ($V_F = 0\%$) is investigated using the parameters presented in Table 2.6 and the symmetric part of the PWH (Figure 2.11b). Different mesh refinements with 1022, 2480, 3944 and 6739 finite elements are used to conduct a mesh convergence study. These meshes differ mainly in the area of the hole, since here the main inelastic effects are expected. The refinements are shown in Figure 2.12. As it can be seen, only regular hexahedral elements are used and further no strong mesh distortion is observed.

The global force-displacement curves obtained for the different meshes are presented in Figure 2.13. The curves are normalized to the maximum load of the 6739 mesh as well as the total length l_h of the specimen.
Measured are both the total reaction force in y-direction and the displacement in y-direction. Note that for both the values are multiplied by two to gain the answer of the full structure. The difference between the curves is negligible small. Therefore, the curve of the mesh with 1022 elements can be considered as already converged. Due to the small deformations applied compared to the total length of the structure, a linear relationship between the load and displacement can be observed in the elastic regime. Nevertheless, in the regions of high damage values large strains occur. Thus, finite strain theory is absolutely required.
In addition, Figure 2.14 gives different stages of the local matrix damage variable D_M. Shown is the mirrored, full and deformed structure for the 6739 element mesh. In black is the undeformed outline of the upper part of the full structure. The four snapshots are taken at different times that are indicated by black rectangles in the load displacement curve (Figure 2.13). The first three ones are taken during the decrease of the force-displacement curve. The last one belongs to the end of the simulation. As expected, the damage begins to evolve at the edge of the hole and then continues to rise to the outer edge of the structure.

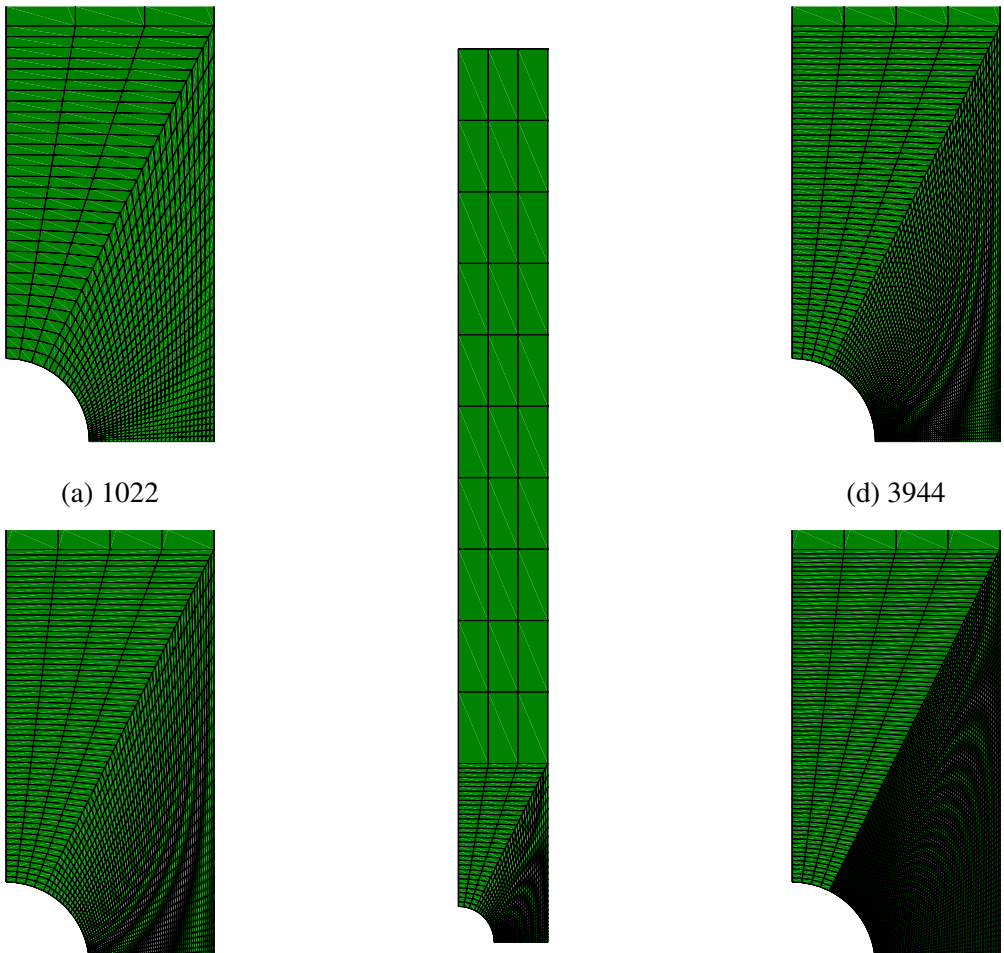

(a) 1022 (d) 3944

(c) Full mesh (1022)

(b) 2480 (e) 6739

Figure 2.12: Mesh refinements for symmetric PWH

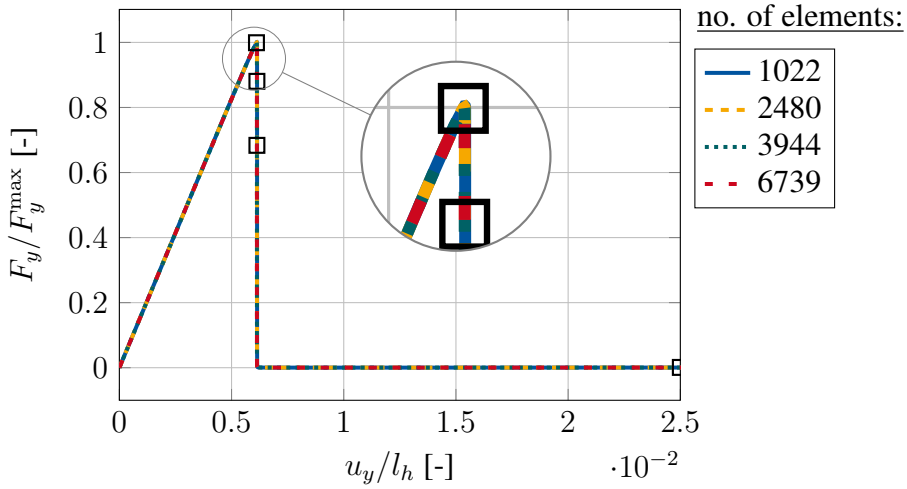

Figure 2.13: Force-displacement curves for pure elasto-damage matrix study

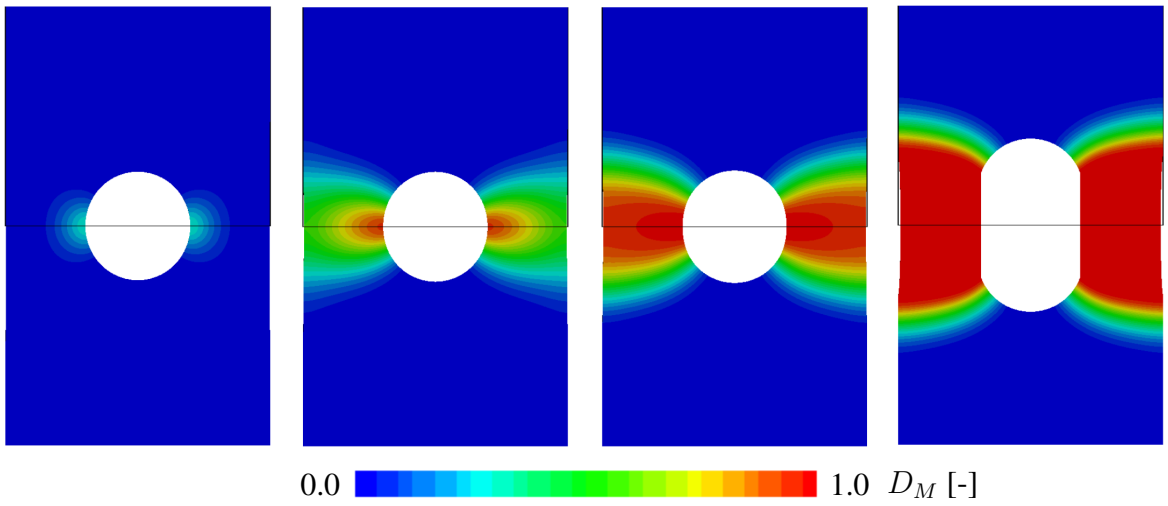

Figure 2.14: Four different stages of pure matrix damage (deformed structure)

2.5.3.2 Pure elasto-plastic-damage matrix material

It is the aim of this paper to present not only a model for an elasto-damage matrix material, but also for an elasto-plasti-damage matrix material. Thus, additionally to the last example the influence of plasticity is investigated. To further study the influence of the fiber, the pure elasto-plastic-damage matrix material is to be studied here. For this purpose, the same mesh refinements as in the last example (Figure 2.12) are used.

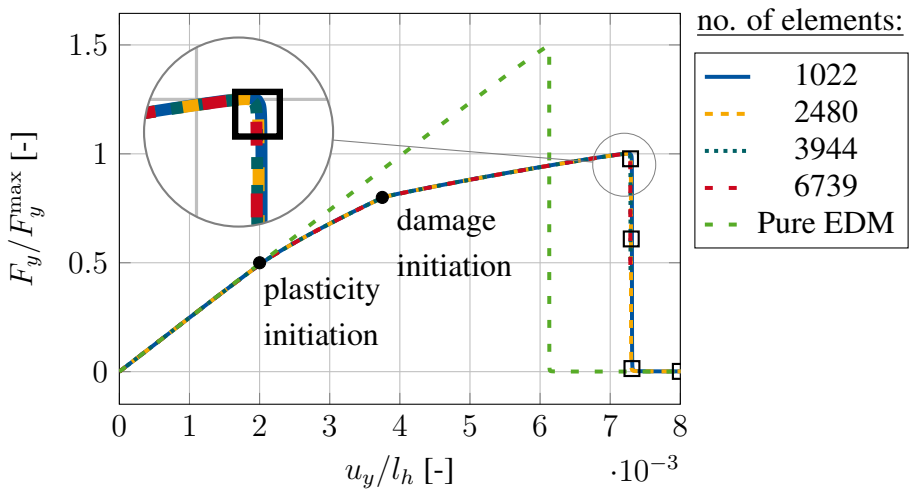

Figure 2.15: Force-displacement curves for pure elasto-plastic-damage matrix study

The force-displacement curves are presented in Figure 2.15, which are normalized to the maximum force of the 6739 mesh. Regarding the maximum force as well as the begin of the

degradation good convergence can be observed. However, it should be noted that for the 3944 and 6739 mesh no convergence could be achieved at $F_y/F_y^{\max} \approx 0.5$. This may could be explained by a too low artificial viscosity and the resulting snapback. Nevertheless, from a practical point of view the maximum reached forced and the beginning of degradation are far more interesting. Therefore, these convergence difficulties are not further investigated.
It should also be noted that the difference to the EDM curve coincides with the beginning of plasticity. The second kink in turn corresponds to the beginning of the damage. Although the maximum reached force is less compared to the EDM case, the displacement at the beginning of the degradation is higher.

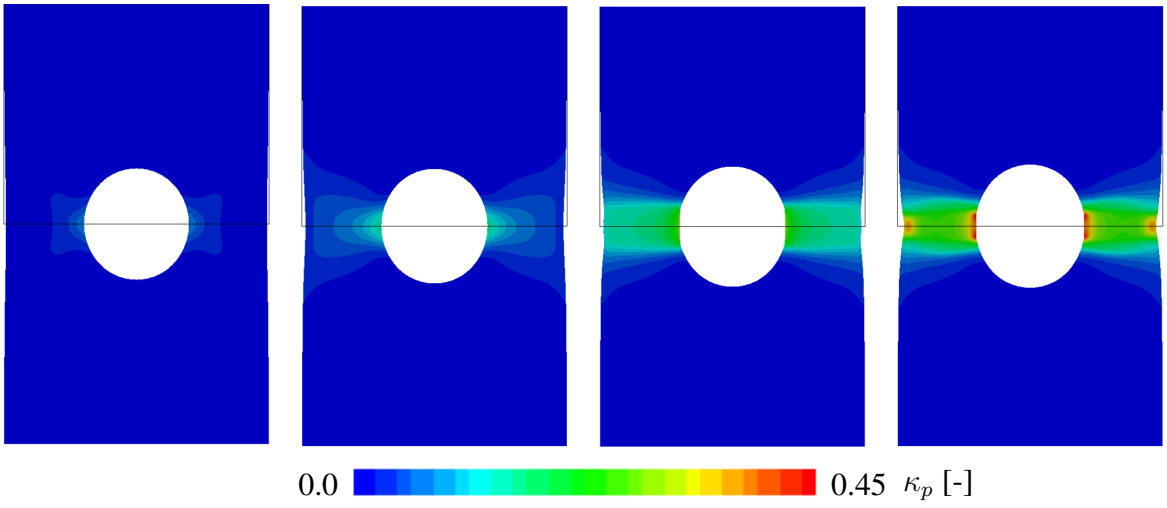

(a) Accumulated plastic strain κ_p

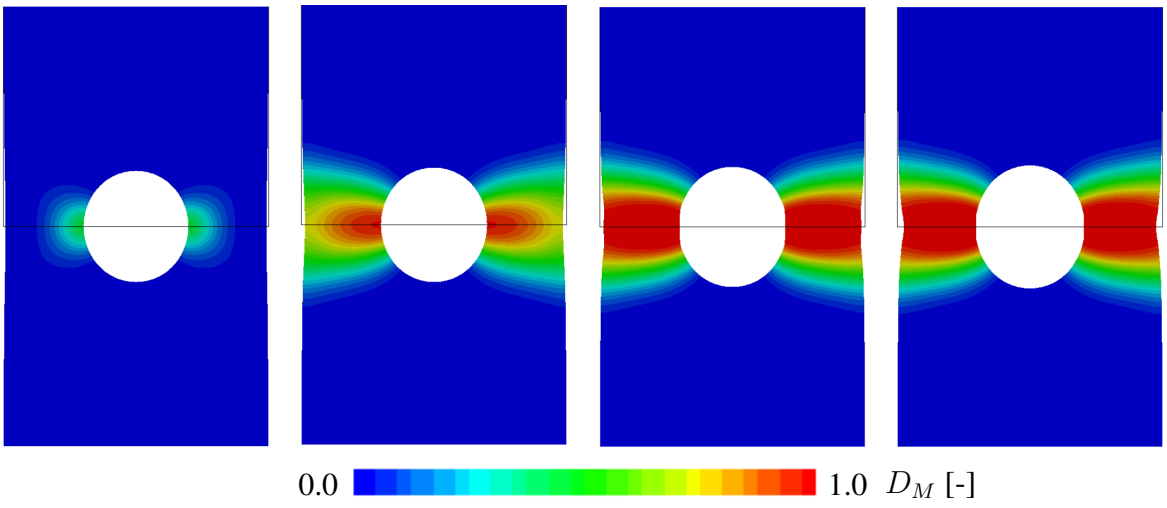

(b) Matrix damage D_M

Figure 2.16: Four different stages of pure matrix damage with plasticity (deformed structure)

In Figure 2.16 the accumulated plastic strain as well as the matrix damage at for different stages are presented, which are indicated by rectangles in Figure 2.15. These snapshots are taken from the 2480 mesh.
Compared to the results of Figure 2.14, the general evolution of the matrix damage is similar in both cases. However, due to the increasing plasticity, the observed necking of the specimen in the area of the hole is much stronger than in the pure elasto-damage case with at the same time lower applied deformation. The reasons for the differences compared to the pure elastic failure can be explained by the much more ductile behavior due to the plasticity.

2.5.3.3 Elasto-damage matrix and elasto-damage fiber with $\varphi_{xy} = 90°$

The next aim is to investigate the additional influence of the fiber, whose parameters are shown in Table 2.8. Since an angle of $\varphi_{xy} = 90°$ is chosen here, the symmetry with respect to both the x and the y axis is given. Therefore, as for the pure matrix analysis only a quarter of the structure has to be simulated. For the discretization, the same meshes as in the last example (Figure 2.12) are used.

First, a mesh convergence study is performed. The force-displacement curves for the various mesh discretizations are presented in Figure 2.17. These are normalized to the maximum load of the 6739 mesh and to the structure length l_h. A small but noticeable difference between the 1022 elements mesh and the other discretization suggests a non converged mesh. However, the next finer discretization can be considered to be converged.

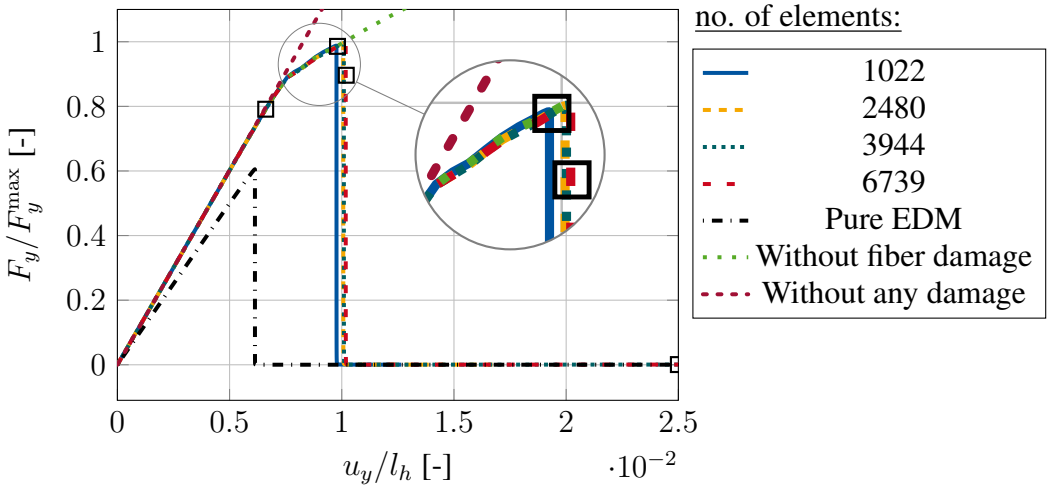

Figure 2.17: Force-displacement curves for elasto-damage matrix / elasto-damage fiber study with $\varphi_{xy} = 90°$

In addition, the force-displacement curve of the pure matrix behavior is plotted (6739 elements). It is worth mentioned that the maximum achieved load is only about 60 percent compared to the fiber reinforced material and further is less stiff, which is usually the case for fiber-reinforced materials.

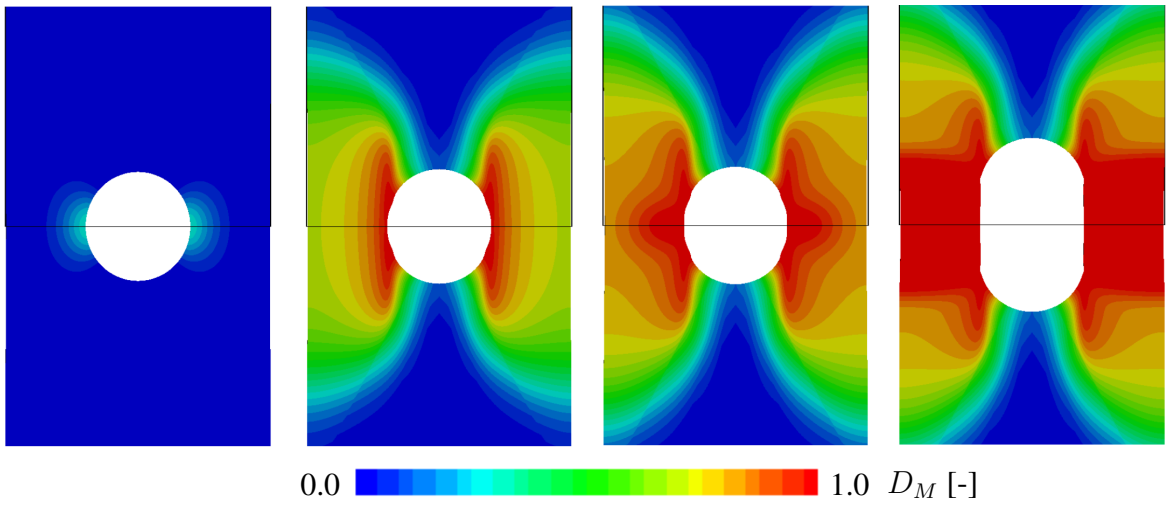

(a) Matrix damage D_M

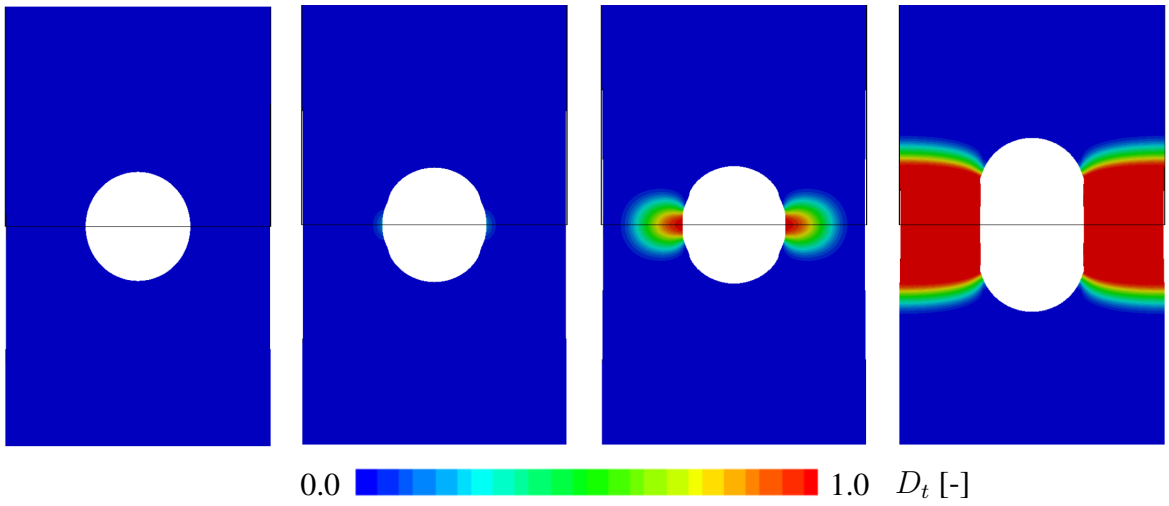

(b) Fiber damage D_t

Figure 2.18: Four different stages of fiber and matrix damage $\varphi_{xy} = 90°$ (deformed structure)

A further interesting observation is the kink at $u_y/l_h \approx 0.007$. To preclude that perhaps the fiber damage is mainly responsible for this effect, two further computation with the reinforced material but without any fiber damage and without neither fiber nor matrix damage are performed. The results are also added to the force-displacement curves in Figure 2.17. Since the

original curves and the curve without fiber damage look quite the same and further the curve without any damage does not show any nonlinearities, it can be suspected that it is mainly the matrix damage leading to these nonlinearities.

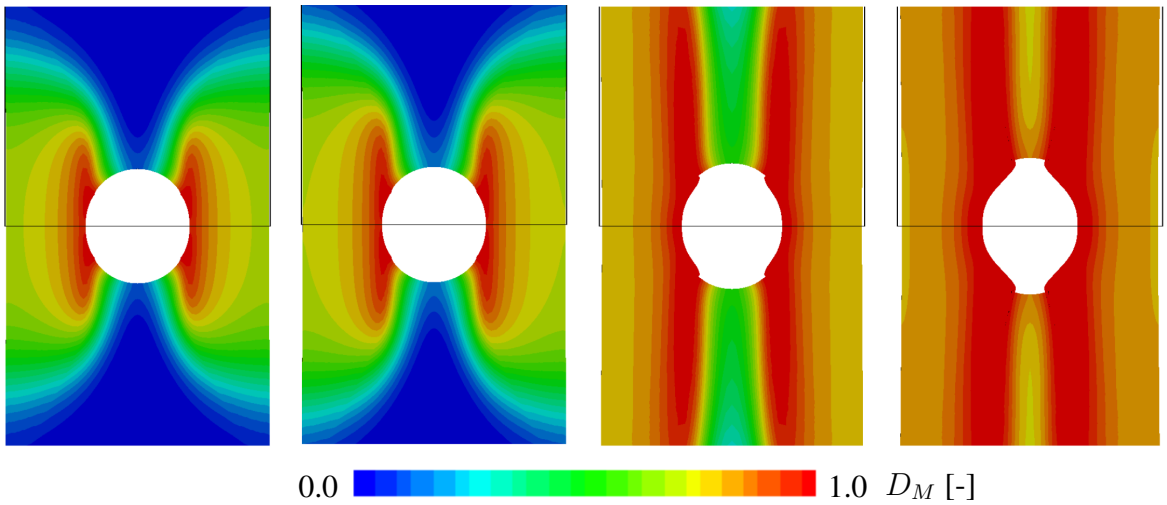

Figure 2.19: Four different stages of matrix damage without fiber damage $\varphi_{xy} = 90°$ (deformed structure)

In order to understand the local behavior better and to study the interaction between fiber and matrix damage, the damage evolutions of the fiber part D_t and the matrix part D_M at different snapshots will be discussed, which are indicated in Figure 2.17 by black rectangles. These snapshots for the matrix and the fiber are presented for the 6739 mesh in Figure 2.18. At first, it can be seen that the matrix damage starts way earlier than the fiber damage. Furthermore, due to the transversal isotropic behavior the damage of the isotropic matrix material does not evolve as in case of an material without reinforcement. In particular, having a look at the second snapshot of Figure 2.18a, it is clearly visible that the damage evolves parallel to the fiber direction. This influence was already studied in Section 2.5.2 and is further similar to the experimental observations of e.g. Hashin and Rotem [1973], Reifsnider and Lauraitis [1977]; Lauraitis [1981], Tsai [1979] or Kawai et al. [2001]. Although the structural example is not totally equal, since a plate *without* hole was investigated by the mentioned works, the basic mechanisms should stay the same as the influence of the fiber on the direction of matrix damage.

Since the second snapshot is taken nearly at the maximum load reached and the fact that the fiber damage has quite not start to evolve, the kink in the force-displacement curve can be fully explained by the matrix damage as already suggested above.

The interaction between fiber damage and matrix damage becomes particularly clear between

the second and third snapshot. If the matrix damage initially evolved parallel to the fiber, the direction starts to change with the beginning of the fiber damage. As expected, the fiber damage does not evolve along the fiber itself, but transversely. From a mechanical point of view this makes complete sense, since, due to the 'crack' of the fiber, the fiber does not contribute to the load transfer anymore. This effect causes the matrix to be loaded in such a way that it is also damaged along the fiber crack.
To give the reader an idea of how the matrix damage evolves at no or much later onset of fiber damage, Figure 2.19 shows different stages without fiber damage. The first two snapshots belong to the second and third snapshots in Figure 2.18a. If the same contour can be seen in the first, this changes with the next snapshot. This is due to the fact that the absence of fiber damage means that the matrix damage continues to evolve along the fiber. As shown in the last two snapshots, which are out of the range of the force-displacement curve 2.17, this progresses further towards the clamping.

2.5.3.4 Elasto-plastic-damage matrix and elasto-damage fiber with $\varphi_{xy} = 90°$

As a second variation of the 90 degree angle specimen, an elasto-plastic-damage matrix material is considered. Hence, the symmetry conditions are still fulfilled meaning that again the symmetric mesh (Figure 2.12) can be used for the investigation.

Figure 2.20 provides the force-displacement curve for the different mesh refinements with 1022, 2480, 3944 and 6739 finite elements, which are normalized to the ultimate force of the 6739 mesh. Similar to the example of Section 2.5.3.2 not all mesh refinements succeeded to converge during the degradation, in particular the 6739 mesh here. However, as convergence has been achieved for the same reasons as in Section 2.5.3.2 for the essential characteristics, this is not relevant in the following. Therefore, the results of the 3944 mesh are discussed below.
In order to allow a proper interpretation of the results, the force-displacement curves from Section 2.5.3.2 and 2.5.3.3 have also been added. First of all, it can be seen that the material response is stiffer than in the EPDM case and, secondly, that there are significantly nonlinear effects compared to the results of the EDMF90 tests at $u_y/l_h \approx 0.0035$. In contrast to the curve presented in Figure 2.15, it is not possible to differentiate between the onset of plasticity and damage. Indeed, both phenomena start to evolve at even this deformation state.

Several snapshots of the accumulated plastic strain, matrix damage and fiber damage taken during the process, which can be identified by rectangles in Figure 2.20, are shown in Figure

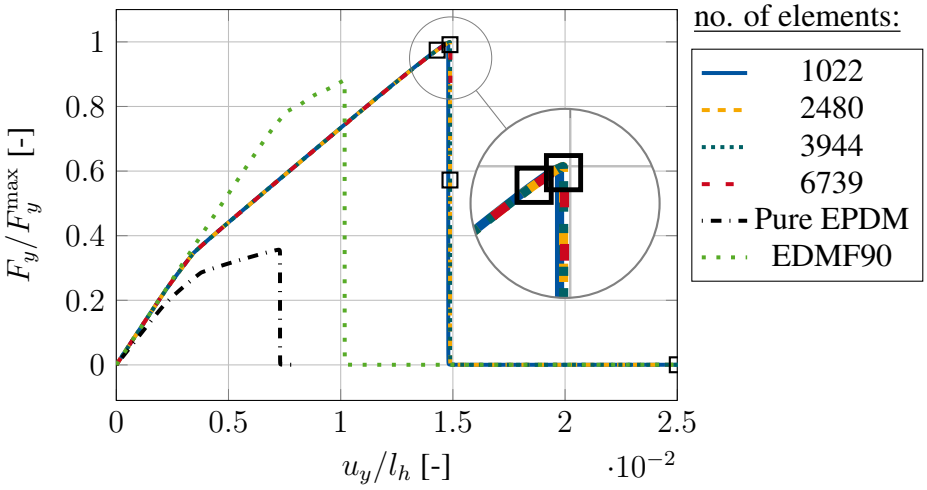

Figure 2.20: Force-displacement curves for elasto-plastic-damage matrix / elasto-damage fiber study with $\varphi_{xy} = 90°$

2.21. As the first snapshots of accumulated plastic strain (Figure 2.21a) and especially matrix damage (Figure 2.21b) show, both inelastic effects developed during the process up to the moment immediately before degradation. In particular, the matrix damage has reached a maximum value of $D_M \approx 0.7$. Furthermore, compared to the results of the EPDM case in Figure 2.16, it can easily be seen that similar to the last example the fiber has a notable influence on the direction of the evolution of both phenomena.

Finally, an interesting finding of the actual investigation shall be discussed, namely the higher reaction force than in the EDMF90 investigation. While it was the case for the pure matrix material that the testing without plasticity led to a lower reaction force compared to the brittle material (see Figure 2.15), this is quite the opposite here.
First of all, the damage mechanism of the brittle EDMF90 investigation should be remembered. Although the structure remained stable after the onset of matrix damage, as the fiber caused the matrix damage to develop parallel to the fiber and not onto the exterior, the matrix did no further contribute to the stiffness in the area of the hole. Hence, the fiber remains to carry the load and is therefore extremely loaded in especially this area, leading to an early onset of the fiber damage and the resulting failure of the structure.
The current investigation is contrary to this. As the investigations in Section 2.5.3.2 already demonstrated, the much more ductile behavior of the matrix, which can also be recognized by the stronger necking (Figure 2.18 and 2.21), entails its damage to develop but does not lead to sudden - or more precisely brittle - failure. In this way, the matrix does contribute

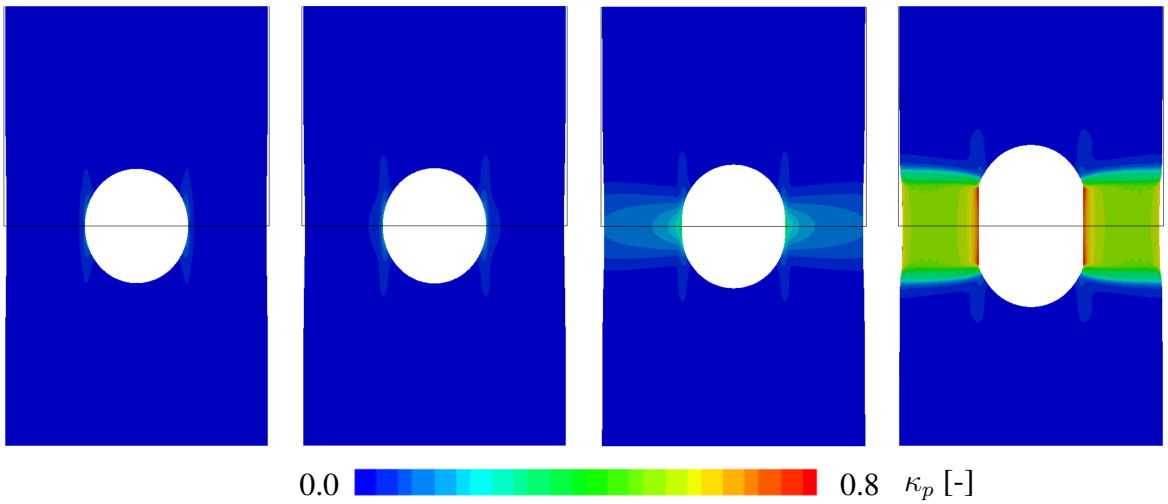

(a) Accumulated plastic strain κ_p

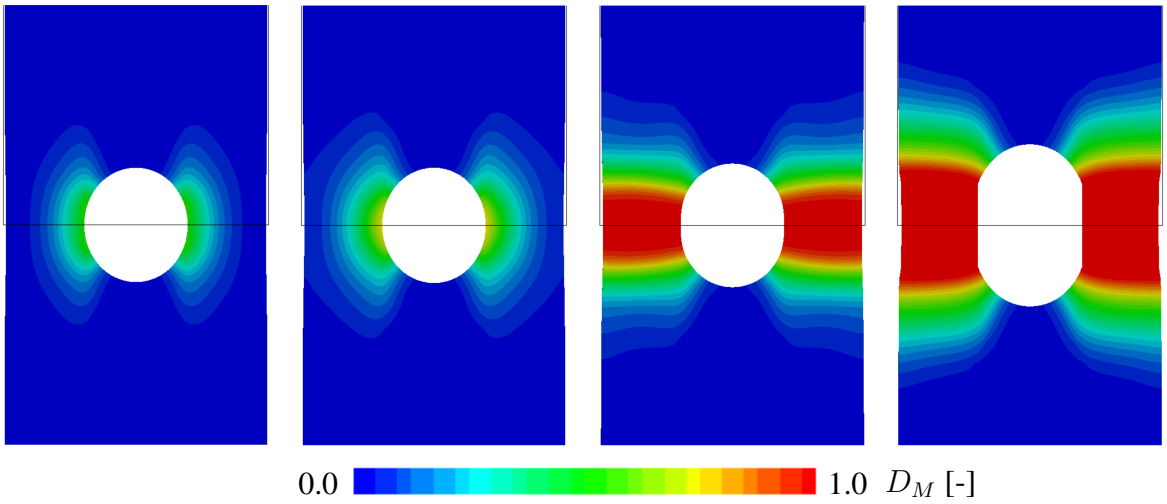

(b) Matrix damage D_M

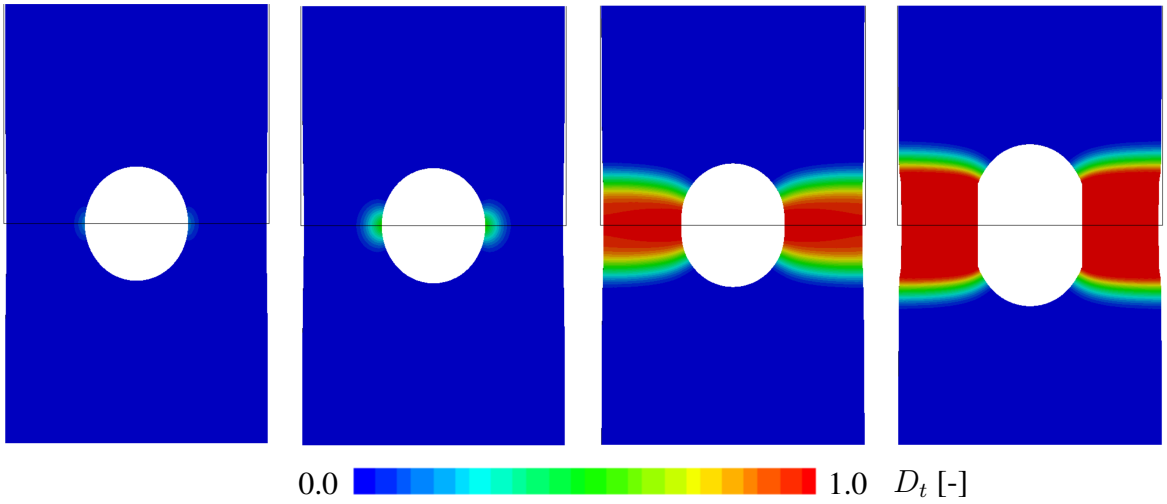

(c) Fiber damage D_t

Figure 2.21: Four different stages of fiber and matrix damage with plasticity $\varphi_{xy} = 90°$ (deformed structure)

to the stiffness much more in the area of the hole compared to the brittle case resulting in a lower loading of the fiber. For this reason, the onset of fiber damage is reached at a higher deformation state. Nevertheless, quite soon after this damage threshold is exceeded, the entire structure fails because a 'crack' runs from the interior to the exterior, which can be nicely observed by comparing the second and third snapshot in Figure 2.21b and 2.21c.

2.5.3.5 Elasto-damage matrix and elasto-damage fiber with $\varphi_{xy} = 45°$

The last example focuses on the interaction between matrix and fiber damage under off-axis angle ($\varphi_{xy} = 45°$) conditions. Thus, the symmetry with respect to neither the x nor the y axis is given. Consequently, the full structure is meshed.
For the mesh convergence study, three different mesh refinements are used which are presented in Figure 2.22. As already for the symmetric part, the inelastic effects are expected in the area of the hole, which is why the refinement is mainly in this region of the structure.

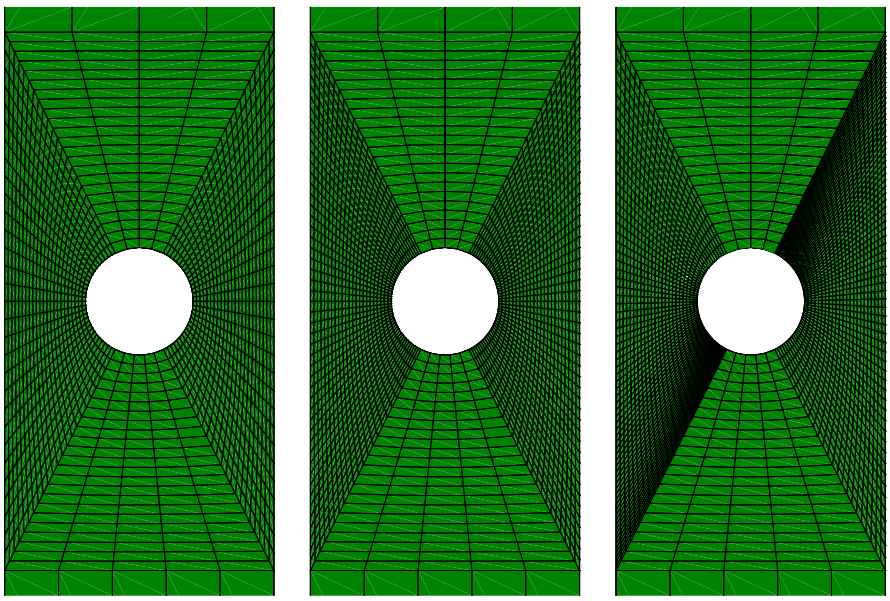

(a) 1677 (b) 2597 (c) 3517

Figure 2.22: Mesh refinements for full PWH

The gained force-displacement curves are shown in Figure 2.23. First of all, it can be nicely seen that already the 1677 finite element mesh is converged regarding the damage onset as well as the degradation.
Comparing the results of the off-axis analysis to the ones of both the pure matrix as well as the 90 degree angle investigation, a less stiff answer is observed. Regarding the latter, this is not surprising, but prima facie for the pure matrix case. Although in the case of pure matrix and

the off-axis study globally the structure is loaded under tension, locally the matrix is undergoes shear stresses for the off-axis study due to the fibers. Since in both cases it is mainly the matrix that contributes to the overall stiffness (the fibers reorient themselves for the off-axis study), it is not astonishing for the off-axis investigation to result in lower stiffness.
Furthermore, in contrast to the results of other investigations, it can be seen that force-displacement curves for the off-axis investigations increase at end. This effect is a result of the reorientation of the fibers. Although the matrix has reached a fully broken state, the fiber damage threshold is not excited. Thus, the fibers still contribute the stiffness and reorient themselves, as no fiber pull-out is considered.

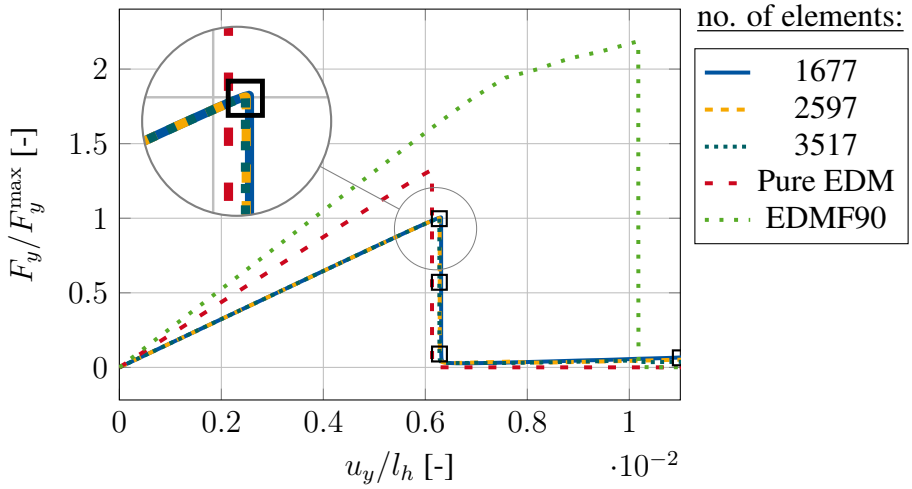

Figure 2.23: Force-displacement curves for elasto-damage matrix / elasto-damage fiber study with $\varphi_{xy} = 45°$

Having a look at Figure 2.24, several snapshots of the matrix damage can be seen, which are indicated by rectangles in Figure 2.23. In addition, the black lines illustrate the outline of the undeformed, full structure.
The evolution of the matrix damage is clearly different compared to the results presented in Figure 2.18a. This strong difference is only due to a different angle of the fiber.
Moreover, the reorientation of the fibers and thus the resulting increase of the force-displacement curve as discussed above can be observed in the last two snapshots. However, the last snapshot shows a kind of 'inflation' of the structure. This is partly due to the reorientation, but also because the matrix has practically no contribution to stiffness. Thus the material is again only described by the fiber, which can be rather problematic, as discussed above several times.

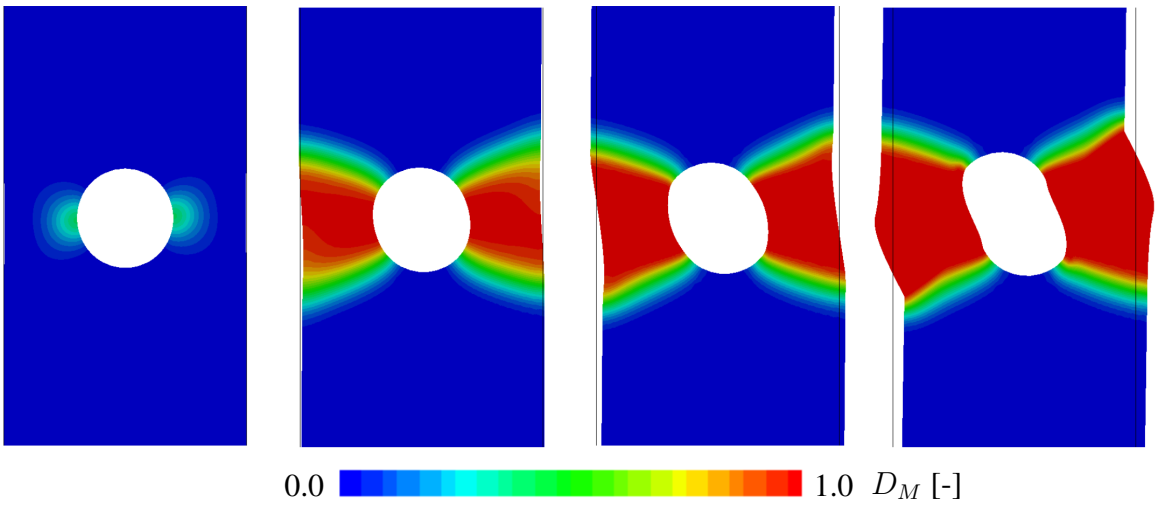

Figure 2.24: Four different stages of matrix damage $\varphi_{xy} = 45°$ (deformed structure)

Although the results so far obviously show that the angle of the fiber influences the matrix damage and its direction, the correlation is not fully understandable due to e.g. the early onset of matrix damage. Therefore, in Figure 2.25 the results for $\varphi_{xy} = 45°$ and $\varphi_{xy} = 60°$ are shown to the reader with an additional higher damage threshold $Y_M = 100$ [FL/L^3]. Comparing the contour plots of the undeformed structure, it can nicely be seen that the direction of the matrix damage corresponds much better with that of the fiber. With regard to the direction of matrix damage, these results are similar to the experimental observations of Hashin and Rotem [1973], Pipes and Cole [1973], Reifsnider and Lauraitis [1977]; Lauraitis [1981] and Kawai et al. [2001].

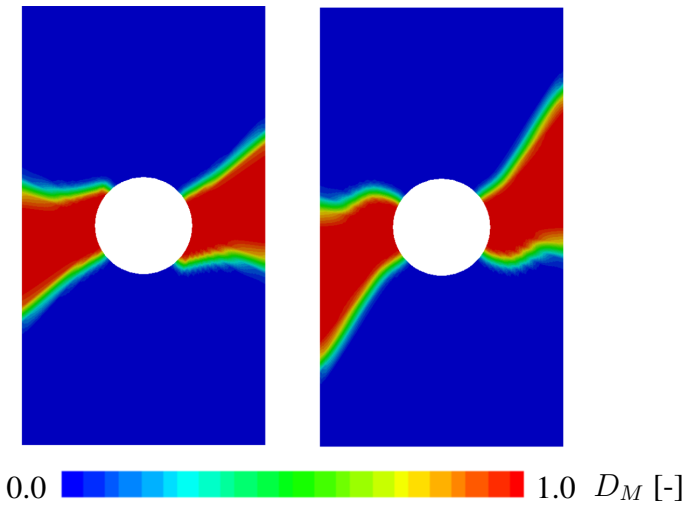

Figure 2.25: Matrix damage with $Y_M = 100$ [FL/L^3], $\varphi_{xy} = 45°$ (left) and $\varphi_{xy} = 60°$ (right) (undeformed structure)

2.6 Conclusion and outlook

A thermodynamically consistent material model for transversally isotropic materials with gradient-extended damage separately for the elasto-plastic, isotropic and elastic, anisotropic part at finite deformations was shown. Further, a new approach for the description of tension-compression asymmetry based on fiber stretch was developed, to capture two main mechanisms. On the one hand, the damage evolution in the tension and compression regime of the anisotropic part can be described differently in order to take, for example, kinking into account. On the other hand, the effect of crack closure can also be captured. Two scalar damage variables associated with the fiber damage are introduced for this purpose.
The isotropic matrix material is modeled by an elasto-plastic model, whereby nonlinear isotropic hardening was considered. In addition, for the matrix, isotropic damage was assumed. Therefore, a further damage variable was introduced. By a two-surface approach the plasticity and the damage are generally independent from each other, whereby greater flexibility of the model is achieved.
To avoid artificial mesh-sensitivity, the micromorphic approach was applied to each damage variable separately, which is why an efficient element formulation and its linearization were presented. In order to obtain quadratic convergence within the global Newton-Raphson scheme, the derivation of material tangents with respect to the global degrees of freedom was also discussed.

Various numerical examples have examined the different aspects of the model. Thus, it could be shown that the damage behavior of the fiber in the tension and compression regime is modeled completely independently of each other. Furthermore, the influence of the additional anisotropic fiber part on the isotropic elasto-plastic-damage part was studied. In these studies, the effect of local strain peaks has been observed, which leads to inhomogeneous plastic and damage fields even in the case of a uniaxial tensile test without any structural imperfection. Finally, the interaction between fiber and matrix damage and additionally plasticity was examined. It could be shown that the fiber does not only have an influence on both the matrix damage and plasticity but further the fiber damage results in an interaction with the matrix and its inelastic phenomena and vice versa.

Future works should concentrate on several points that had been mentioned in this work: First, a lot of work has to be done to determine a consistent set of material parameters. For this sake, the matrix material and the composite material have to be investigated separately, to avoid

any inconsistency in the context of the material parameter identification. By this experimental procedure the elastic, plastic and damage properties of the matrix can be determined first. In a further step, the parameters associated with the fiber can then be determined by investigating the composite.
Second, the formulation of the matrix damage used here is based on a scalar damage function without considering the influence of the actual stress state. However, some of the above mentioned works on failure analysis suggest that it is necessary to consider whether tension is applied in the direction of the fiber or transversely to it. To take this influence into account, alternative formulations like the puck criterion are a possibility. In addition, in the case of e.g. a fully broken matrix material state, it is not suitable to describe the material only by the fiber part. Therefore, a global failure criterion (to capture e.g. fiber pull-out) should be discussed. Third, the plasticity model used here is of a von Mises type. This assumption has to be validated for the used matrix material in the actual context and perhaps has to be adjusted. Last, attention has to be paid for delamination between the individual unidirectional layers. It can be expected that the impact on the structural response of the fiber-reinforced laminate and especially on its damage evolution is significant.
Apart from the material formulation, the FEM implementation has to be considered more closely. It should be studied whether the observed unstable behavior caused under compression is realistic or due to e.g. the Q1 element formulation. Furthermore, fiber-reinforced laminates are usually extremely thin structures, which can lead to locking phenomena. Various finite element technologies are conceivable to avoid these. In addition, this could reduce the computation time immensely.

2.7 Appendix

2.7.1 Tension-compression split of right Cauchy-Green tensor

A general right Cauchy-Green tensor with its eigenvalues ω_1, ω_2 and ω_3 and its eigenvectors $\boldsymbol{n}_1$, $\boldsymbol{n}_2$ and $\boldsymbol{n}_3$ is discussed. If, for example, ω_1 is larger or equal to one and both ω_2 and ω_3 are lower than one, the tension-compression split lead to

$$\boldsymbol{C}_t = \omega_1 \boldsymbol{n}_1 \otimes \boldsymbol{n}_1 \tag{2.77}$$

$$\boldsymbol{C}_c = \omega_2 \boldsymbol{n}_2 \otimes \boldsymbol{n}_2 + \omega_3 \boldsymbol{n}_3 \otimes \boldsymbol{n}_3. \tag{2.78}$$

Since $\boldsymbol{n}_1 \cdot \boldsymbol{n}_2 = \boldsymbol{n}_1 \cdot \boldsymbol{n}_3 = 0$ holds true, it is obvious that $\boldsymbol{C}_t \boldsymbol{C}_c = \boldsymbol{C}_c \boldsymbol{C}_t = \boldsymbol{0}$.

2.7.2 Relations between the invariants of the elastic and plastic parts

Using relation (2.5) and $\boldsymbol{C}_{Mp} = \boldsymbol{F}_{Mp}^T \boldsymbol{F}_{Mp}$, one can formulate the following

$$\mathrm{tr}\left(\boldsymbol{C}_{Me}\right) = \mathrm{tr}\left(\boldsymbol{F}_{Mp}^{-T}\boldsymbol{C}\boldsymbol{F}_{Mp}^{-1}\right) = \mathrm{tr}\left(\boldsymbol{C}\boldsymbol{C}_{Mp}^{-1}\right) \tag{2.79}$$

$$\mathrm{tr}\left(\boldsymbol{C}_{Me}^2\right) = \mathrm{tr}\left(\left(\boldsymbol{F}_{Mp}^{-T}\boldsymbol{C}\boldsymbol{F}_{Mp}^{-1}\right)^2\right) = \mathrm{tr}\left(\boldsymbol{F}_{Mp}^{-T}\boldsymbol{C}\boldsymbol{F}_{Mp}^{-1}\boldsymbol{F}_{Mp}^{-T}\boldsymbol{C}\boldsymbol{F}_{Mp}^{-1}\right) = \mathrm{tr}\left(\left(\boldsymbol{C}\boldsymbol{C}_{Mp}^{-1}\right)^2\right) \tag{2.80}$$

$$\det\left(\boldsymbol{C}_{Me}\right) = \det\left(\boldsymbol{C}\boldsymbol{C}_{Mp}^{-1}\right) = \det\left(\boldsymbol{C}\right)\det\left(\boldsymbol{C}_{Mp}^{-1}\right). \tag{2.81}$$

This shows that the invariants of $\boldsymbol{C}_{Me}$ can be expressed in terms of $\boldsymbol{C}$ and $\boldsymbol{C}_{Mp}$. In the case of no plasticity this further proves the equivalence of the invariants of $\boldsymbol{C}_{Me}$ and $\boldsymbol{C}$.

2.7.3 Linear elastic material tangents

The material tangent in Nye notation for the fiber material in the case of linear elasticity with respect to the fiber direction is

$$\hat{\mathbb{C}}_F^{lin} = 4\frac{\partial^2 \Psi_{Fe}^{lin}}{\partial \boldsymbol{C}\partial \boldsymbol{C}} = \begin{pmatrix} 4K_{ani1} + 8K_{ani2} + 8K_{coup} & 4K_{coup} & 4K_{coup} & 0 & 0 & 0 \\ 4K_{coup} & 0 & 0 & 0 & 0 & 0 \\ 4K_{coup} & 0 & 0 & 0 & 0 & 0 \\ 0 & 0 & 0 & 2K_{ani2} & 0 & 0 \\ 0 & 0 & 0 & 0 & 2K_{ani2} & 0 \\ 0 & 0 & 0 & 0 & 0 & 0 \end{pmatrix}. \tag{2.82}$$

For the matrix material the material tangent for pure linear elasticity reads

$$\hat{\mathbb{C}}_M^{lin} = 4\frac{\partial^2 \Psi_{Me}^{lin}}{\partial \boldsymbol{C}_{Me}\partial \boldsymbol{C}_{Me}} = \begin{pmatrix} \Lambda + 2\mu & \Lambda & \Lambda & 0 & 0 & 0 \\ \Lambda & \Lambda + 2\mu & \Lambda & 0 & 0 & 0 \\ \Lambda & \Lambda & \Lambda + 2\mu & 0 & 0 & 0 \\ 0 & 0 & 0 & \mu & 0 & 0 \\ 0 & 0 & 0 & 0 & \mu & 0 \\ 0 & 0 & 0 & 0 & 0 & \mu \end{pmatrix}. \tag{2.83}$$

2.7.4 Engineering constants

Material parameter restrictions.

$$E_{||}, E_{\perp}, G_{||}, G_{\perp} > 0, \quad |\nu_{\perp}| < 1, \quad \nu_{||} < \sqrt{E_{||}/E_{\perp}}$$
$$1 - \nu_{\perp} - 2\nu_{||}^2 \frac{E_{\perp}}{E_{||}} > 0$$

Conversion formulas.

$$E_{||} = \frac{Q}{((\Lambda + \mu)(V_F - 1))} \tag{2.84}$$

$$\begin{aligned} Q = &-3\Lambda\mu + 4V_F\mu^2 + 16K_{coup}^2 V_F^2 - 2\mu^2 - 2V_F^2\mu^2 \\ &- 4K_{ani1}V_F\Lambda - 8K_{ani2}V_F\Lambda - 4K_{ani1}V_F\mu - 8K_{ani2}V_F\mu - 8K_{coup}V_F\mu \\ &+ 6V_F\Lambda\mu + 4K_{ani1}V_F^2\Lambda + 8K_{ani2}V_F^2\Lambda + 4K_{ani1}V_F^2\mu + 8K_{ani2}V_F^2\mu \\ &+ 8K_{coup}V_F^2\mu - 3V_F^2\Lambda\mu \end{aligned}$$

$$E_{\perp} = \frac{Q_1}{Q_2} \tag{2.85}$$

$$\begin{aligned} Q_1 = &\ 3\Lambda\mu^2 - 6V_F\mu^3 + 2\mu^3 + 6V_F^2\mu^3 - 2V_F^3\mu^3 - 8K_{ani1}V_F^2\mu^2 \\ &+ 4K_{ani1}V_F^3\mu^2 - 16K_{ani2}V_F^2\mu^2 + 8K_{ani2}V_F^3\mu^2 \\ &- 16K_{coup}V_F^2\mu^2 - 16K_{coup}^2V_F^2\mu + 8K_{coup}V_F^3\mu^2 \\ &+ 16K_{coup}^2V_F^3\mu + 9V_F^2\Lambda\mu^2 - 3V_F^3\Lambda\mu^2 + 4K_{ani1}V_F\mu^2 \\ &+ 8K_{ani2}V_F\mu^2 + 8K_{coup}V_F\mu^2 - 9V_F\Lambda\mu^2 - 8K_{ani1}V_F^2\Lambda\mu \\ &+ 4K_{ani1}V_F^3\Lambda\mu - 16K_{ani2}V_F^2\Lambda\mu + 8K_{ani2}V_F^3\Lambda\mu \\ &+ 4K_{ani1}V_F\Lambda\mu + 8K_{ani2}V_F\Lambda\mu \\ Q_2 = &\ \Lambda\mu - 2V_F\mu^2 - 4K_{coup}^2V_F^2 + \mu^2 + V_F^2\mu^2 + K_{ani1}V_F\Lambda \\ &+ 2K_{ani2}V_F\Lambda + 2K_{ani1}V_F\mu + 4K_{ani2}V_F\mu + 4K_{coup}V_F\mu \\ &- 2V_F\Lambda\mu - K_{ani1}V_F^2\Lambda - 2K_{ani2}V_F^2\Lambda - 2K_{ani1}V_F^2\mu \\ &- 4K_{ani2}V_F^2\mu - 4K_{coup}V_F^2\mu + V_F^2\Lambda\mu \end{aligned}$$

$$G_{||} = \mu + 2K_{ani2}V_F - V_F\mu \tag{2.86}$$

$$G_{\perp} = \mu - V_F * \mu \tag{2.87}$$

$$\nu_{||} = \frac{\Lambda + 4K_{coup}V_F - V_F\Lambda}{2(\Lambda + \mu - V_F\Lambda - V_F\mu)} \tag{2.88}$$

With these lengthly equations at hand, the five engineering parameters can be determined. It is also visible that for $V_F = 0$ an isotropic material behavior is achieved.

2.7.5 Finite Element additions

2.7.5.1 Gâteaux derivative of the field equations

The Gâteaux or directional derivative of the multi-field problem about a known state $(\boldsymbol{u}^*, \bar{\boldsymbol{d}}^*)$ is defined as follows

$$\begin{aligned} \mathscr{D}_{\boldsymbol{u}}[g_u] \cdot \Delta\boldsymbol{u} &= \frac{\mathrm{d}}{\mathrm{d}\epsilon}\left(g_u(\boldsymbol{u}^* + \epsilon\,\Delta\boldsymbol{u}, \bar{\boldsymbol{d}}^*)\right)\Big|_{\epsilon=0} \quad \mathscr{D}_{\bar{\boldsymbol{d}}}[g_u] \cdot \Delta\bar{\boldsymbol{d}} = \frac{\mathrm{d}}{\mathrm{d}\epsilon}\left(g_u(\boldsymbol{u}^*, \bar{\boldsymbol{d}}^* + \epsilon\,\Delta\bar{\boldsymbol{d}})\right)\Big|_{\epsilon=0} \\ \mathscr{D}_{\boldsymbol{u}}[g_{\bar{d}}] \cdot \Delta\boldsymbol{u} &= \frac{\mathrm{d}}{\mathrm{d}\epsilon}\left(g_{\bar{d}}(\boldsymbol{u}^* + \epsilon\,\Delta\boldsymbol{u}, \bar{\boldsymbol{d}}^*)\right)\Big|_{\epsilon=0} \quad \mathscr{D}_{\bar{\boldsymbol{d}}}[g_{\bar{d}}] \cdot \Delta\bar{\boldsymbol{d}} = \frac{\mathrm{d}}{\mathrm{d}\epsilon}\left(g_{\bar{d}}(\boldsymbol{u}^*, \bar{\boldsymbol{d}}^* + \epsilon\,\Delta\bar{\boldsymbol{d}})\right)\Big|_{\epsilon=0} \end{aligned} \tag{2.89}$$

2.7.5.2 Approximations

$$\mathbf{N} = \begin{pmatrix} N_1\boldsymbol{I} & \dots & N_8\boldsymbol{I} \end{pmatrix} \tag{2.90}$$

$$\begin{aligned} \mathbf{B} &= \left(\mathbf{B}_\xi \frac{\partial}{\partial\xi} + \mathbf{B}_\eta \frac{\partial}{\partial\eta} + \mathbf{B}_\zeta \frac{\partial}{\partial\zeta}\right)\mathbf{N} \\ \mathbf{B}_{(*)} &= \begin{pmatrix} \mathrm{diag}\begin{pmatrix} \frac{\partial(*)}{\partial X_1} & \frac{\partial(*)}{\partial X_2} & \frac{\partial(*)}{\partial X_3} \end{pmatrix} & \mathrm{diag}\begin{pmatrix} \frac{\partial(*)}{\partial X_2} & \frac{\partial(*)}{\partial X_3} & \frac{\partial(*)}{\partial X_1} \end{pmatrix} & \mathrm{diag}\begin{pmatrix} \frac{\partial(*)}{\partial X_3} & \frac{\partial(*)}{\partial X_1} & \frac{\partial(*)}{\partial X_2} \end{pmatrix} \end{pmatrix}^T \end{aligned} \tag{2.91}$$

$$\mathbf{F}_m = \begin{pmatrix} F^e_{11} & 0 & 0 & 0 & 0 & F^e_{31} & 0 & F^e_{21} & 0 \\ 0 & F^e_{22} & 0 & F^e_{12} & 0 & 0 & 0 & 0 & F^e_{32} \\ 0 & 0 & F^e_{33} & 0 & F^e_{23} & 0 & F^e_{13} & 0 & 0 \\ F^e_{12} & F^e_{21} & 0 & F^e_{11} & 0 & F^e_{32} & 0 & F^e_{22} & F^e_{31} \\ F^e_{13} & 0 & F^e_{31} & 0 & F^e_{21} & F^e_{33} & F^e_{11} & F^e_{23} & 0 \\ 0 & F^e_{23} & F^e_{32} & F^e_{13} & F^e_{22} & 0 & F^e_{12} & 0 & F^e_{33} \end{pmatrix} \tag{2.92}$$

$$\mathbf{S}_m = \begin{pmatrix} S^e_{11} & 0 & 0 & S^e_{12} & 0 & 0 & S^e_{13} & 0 & 0 \\ 0 & S^e_{22} & 0 & 0 & S^e_{23} & 0 & 0 & S^e_{12} & 0 \\ 0 & 0 & S^e_{33} & 0 & 0 & S^e_{13} & 0 & 0 & S^e_{23} \\ S^e_{12} & 0 & 0 & S^e_{22} & 0 & 0 & S^e_{23} & 0 & 0 \\ 0 & S^e_{23} & 0 & 0 & S^e_{33} & 0 & 0 & S^e_{13} & 0 \\ 0 & 0 & S^e_{13} & 0 & 0 & S^e_{11} & 0 & 0 & S^e_{12} \\ S^e_{13} & 0 & 0 & S^e_{23} & 0 & 0 & S^e_{33} & 0 & 0 \\ 0 & S^e_{12} & 0 & 0 & S^e_{13} & 0 & 0 & S^e_{11} & 0 \\ 0 & 0 & S^e_{23} & 0 & 0 & S^e_{12} & 0 & 0 & S^e_{22} \end{pmatrix} \tag{2.93}$$

2.7.6 Partial derivatives of the second Piola-Kirchhoff stress tensor

$$\begin{aligned}
\frac{\partial \boldsymbol{S}}{\partial \boldsymbol{C}} &= (1-V_F)\frac{\partial \boldsymbol{S}_M}{\partial \boldsymbol{C}} + V_F \frac{\partial \boldsymbol{S}_F}{\partial \boldsymbol{C}} \\
\frac{\partial \boldsymbol{S}_M}{\partial \boldsymbol{C}} &= f_M(D_M)\left(-\frac{1}{2}\left(-\mu + \frac{\Lambda}{2}\frac{\det(\boldsymbol{C})}{\det(\boldsymbol{C}_{Mp})} - \frac{\Lambda}{2}\right)\left(\left(\boldsymbol{C}^{-1}\otimes\boldsymbol{C}^{-1}\right)^{\frac{23}{T}} + \left(\boldsymbol{C}^{-1}\otimes\boldsymbol{C}^{-1}\right)^{\frac{24}{T}}\right)\right. \\
&\quad \left. + \frac{\Lambda}{2}\frac{\det(\boldsymbol{C})}{\det(\boldsymbol{C}_{Mp})}\boldsymbol{C}^{-1}\otimes\boldsymbol{C}^{-1}\right) \\
\frac{\partial \boldsymbol{S}_F}{\partial \boldsymbol{C}} &= f_F(D_t, D_c, I_4)\, 2\left(K_{ani1}(\alpha-1)(I_4-1)^{\alpha-2}\boldsymbol{M}_F\otimes\boldsymbol{M}_F\right. \\
&\quad + K_{ani2}\left((\beta-1)(I_5-1)^{\beta-2}\frac{\partial I_5}{\partial \boldsymbol{C}}\otimes\frac{\partial I_5}{\partial \boldsymbol{C}} + (I_5-1)^{\beta-1}\mathbb{D}^{I_5}\right) \\
&\quad + K_{coup}\left((\gamma-1)(I_1-3)^{\gamma-2}(I_4-1)^{\gamma}\boldsymbol{I}\otimes\boldsymbol{I} + \gamma(I_1-3)^{\gamma-1}(I_4-1)^{\gamma-1}\right. \\
&\quad \left.\left.(\boldsymbol{M}_F\otimes\boldsymbol{I} + \boldsymbol{I}\otimes\boldsymbol{M}_F) + (\gamma-1)(I_1-3)^{\gamma}(I_4-1)^{\gamma-2}\boldsymbol{M}_F\otimes\boldsymbol{M}_F\right)\right) \\
\mathbb{D}^{I_5} &= \frac{1}{2}\left(\delta_{jk}M_{F_{il}} + \delta_{ik}M_{F_{jl}} + \delta_{il}M_{F_{jk}} + \delta_{jl}M_{F_{ik}}\right)\boldsymbol{e}_i\otimes\boldsymbol{e}_j\otimes\boldsymbol{e}_k\otimes\boldsymbol{e}_l
\end{aligned} \tag{2.94}$$

$$\begin{aligned}
\frac{\partial \boldsymbol{S}}{\partial \boldsymbol{U}^{-1}_{Mp}} &= (1-V_F)f_M(D_M)\frac{1}{2}\left(\frac{\mu}{2}\left(\delta_{jk}U^{-1}_{Mp_{il}} + \delta_{ik}U^{-1}_{Mp_{jl}} + \delta_{il}U^{-1}_{Mp_{jk}} + \delta_{jl}U^{-1}_{Mp_{ik}}\right)\right. \\
&\quad + \frac{\mu}{2}\left(\delta_{ik}U^{-1}_{Mp_{jl}} + \delta_{jk}U^{-1}_{Mp_{il}} + \delta_{jl}U^{-1}_{Mp_{ik}} + \delta_{il}U^{-1}_{Mp_{jk}}\right) \\
&\quad \left. + \Lambda\frac{\det(\boldsymbol{C})}{\det(\boldsymbol{C}_{Mp})}\left(C^{-1}_{ij}U_{Mp_{lk}} + C^{-1}_{ij}U_{Mp_{kl}}\right)\right)\boldsymbol{e}_i\otimes\boldsymbol{e}_j\otimes\boldsymbol{e}_k\otimes\boldsymbol{e}_l
\end{aligned} \tag{2.95}$$

$$\frac{\partial \boldsymbol{S}}{\partial D_t} = V_F \frac{\partial f_F(D_t, D_c, I_4)}{\partial D_t} 2 \left(K_{ani1}(I_4 - 1)^{\alpha-1} \boldsymbol{M}_F + K_{ani2}(I_5 - 1)^{\beta-1} \right.$$
$$\left. (\boldsymbol{C}\boldsymbol{M}_F + \boldsymbol{M}_F\boldsymbol{C}) + K_{coup} \left((I_1 - 3)^{\gamma-1}(I_4 - 1)^{\gamma} \boldsymbol{I} + (I_1 - 3)^{\gamma}(I_4 - 1)^{\gamma-1} \boldsymbol{M}_F \right) \right) \tag{2.96}$$

$$\frac{\partial \boldsymbol{S}}{\partial D_c} = V_F \frac{\partial f_F(D_t, D_c, I_4)}{\partial D_c} 2 \left(K_{ani1}(I_4 - 1)^{\alpha-1} \boldsymbol{M}_F + K_{ani2}(I_5 - 1)^{\beta-1} \right.$$
$$\left. (\boldsymbol{C}\boldsymbol{M}_F + \boldsymbol{M}_F\boldsymbol{C}) + K_{coup} \left((I_1 - 3)^{\gamma-1}(I_4 - 1)^{\gamma} \boldsymbol{I} + (I_1 - 3)^{\gamma}(I_4 - 1)^{\gamma-1} \boldsymbol{M}_F \right) \right) \tag{2.97}$$

$$\frac{\partial \boldsymbol{S}}{\partial D_M} = (1 - V_F) \frac{\mathrm{d} f_M(D_M)}{\mathrm{d} D_M} \left(\mu \left(\boldsymbol{C}_{Mp}^{-1} - \boldsymbol{C}^{-1} \right) + \frac{\Lambda}{2} \left(\frac{\det(\boldsymbol{C})}{\det(\boldsymbol{C}_{Mp})} - 1 \right) \boldsymbol{C}^{-1} \right) \tag{2.98}$$

2.7.7 Unstable behavior discussion

The observed unstable behavior in the numerical example (Section 2.5.2) should be investigated in a more focused way. In this Section, it was stated that the instability was observed first for a deformation of $u_x = 1.19$ [L]. The corresponding deformed structure as well as the matrix damage variable are presented in Figure 2.26.

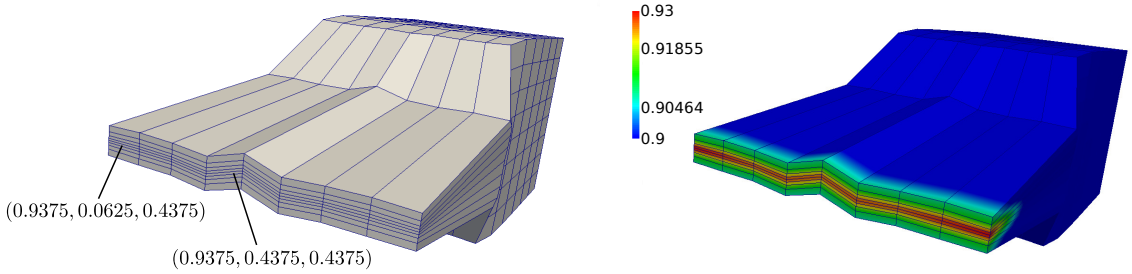

(a) Deformed structure (b) D_M [-]

Figure 2.26: First observed unstable behavior at $u_x = 1.19$ [L]

On the one hand, it can be observed that it is mainly the middle part of the structure beginning to deform into the z-Direction. On the other hand, the damage has reached a higher value at the edge. Thus, two elements and their material tangent eigenvalues are studied in addition to the element presented in Section 2.5.2. One element at the edge of the structure and second a element in the nearly undamaged area for comparison. The results are presented in Table 2.10 and 2.11.

The nearly undamaged element (Table 2.10) is positive definite for all deformation states, even for those where compression is applied in fiber direction. Thus, no unstable behavior is expected. In contrast to that, the element at the edge (Table 2.11) shows a similar behavior to

Table 2.10: Gaussian point investigation of element with center coordinate at (0.0625, 0.0625, 0.0625)

	GP 1	GP 2	GP 3	GP 4	GP 5	GP 6	GP 7	GP 8
D_M	2.207E-02	2.207E-02	2.207E-02	2.207E-02	2.207E-02	2.207E-02	2.207E-02	2.207E-02
$\hat{\boldsymbol{E}}$	5.83E-01	0.58	0.58	0.58	5.84E-01	5.84E-01	5.84E-01	5.84E-01
	-1.58E-01	-0.16	-0.16	-0.16	-1.58E-01	-1.58E-01	-1.58E-01	-1.58E-01
	-0.16	-0.16	-0.16	-0.16	-0.16	-0.16	-0.16	-0.16
	-6.05E-05	-5.20E-05	0	0	-8.85E-05	-8.85E-05	0	0
	-7.35E-05	0	0	0	-8.53E-05	-8.53E-05	0	0
	-1.71E-05	1.21E-05	-2.08E-05	-1.02E-05	1.14E-05	1.14E-05	1.22E-06	1.18E-05
Eigenvalues of $\hat{\mathbb{C}}$	7298.8	7299.7	7298.51	7299.32	7299.75	7300.64	7299.21	7300.01
	2861.14	2861.06	2860.84	2860.67	2861	2860.93	2860.42	2860.26
	1427.64	1427.6	1427.49	1427.41	1427.56	1427.53	1427.28	1427.2
	451.34	451.22	451.3	451.17	451.15	451.04	451.1	450.97
	444.55	444.4	444.52	444.36	444.41	444.26	444.33	444.18
	359.95	359.76	359.94	359.74	359.72	359.54	359.7	359.51

Table 2.11: Gaussian point investigation of element with center coordinate at (0.9375, 0.0625, 0.4375)

	GP 1	GP 2	GP 3	GP 4	GP 5	GP 6	GP 7	GP 8
D_M	9.282E-01	9.295E-01	8.784E-01	8.804E-01	9.291E-01	9.305E-01	8.791E-01	8.812E-01
$\hat{\boldsymbol{E}}$	2.43E+01	24.88	24.27	24.88	2.43E+01	2.49E+01	2.43E+01	2.49E+01
	2.73E-04	0	-0.01	-0.01	3.09E-04	3.09E-04	-5.41E-03	-5.41E-03
	-0.49	-0.49	-0.45	-0.45	-0.49	-0.49	-0.45	-0.45
	1.08E-01	9.88E-02	0.71	0.71	1.08E-01	9.82E-02	0.71	0.71
	1.15E-02	0.01	0	0	-1.30E-02	-1.43E-02	-0.06	-0.06
	-2.28E-03	-2.32E-03	-2.50E-04	-4.63E-05	-1.90E-03	-1.94E-03	-4.01E-05	1.63E-04
Eigenvalues of $\hat{\mathbb{C}}$	44337.062	47394.317	9200.926	9659.705	43084.527	45990.424	9217.390	9678.963
	9080.195	9545.862	2395.999	2345.221	9099.643	9568.170	2366.905	2312.999
	242.993	251.012	2.508	2.505	235.967	243.395	2.535	2.531
	4.877	4.926	-0.121	-0.116	4.733	4.773	-0.119	-0.114
	0.147	0.134	-4.084	-4.018	0.145	0.131	-4.021	-3.947
	0.000	0.000	-203.386	-205.032	0.000	0.000	-200.883	-202.182

the one discussed in Section 2.5.2, since also here negative eigenvalues are present in the case of compression parallel to the fiber direction. The reason for these observation is similar to the one already discussed in Section 2.5.2.

Although the edge element has reached a higher matrix damage state, the middle element is more interesting for two reasons: (i) the unstable behavior is obviously more crucial compared to the edge element and (ii) the absolute value of the negative eigenvalues is higher. Hence, a eigenvalue analysis of the resulting stiffness matrix is carried out. The key results are presented in Table 2.12.

Table 2.12: Eigenvalues of $\mathbf{K}_{uu}$ of element with center coordinate at (0.9375, 0.4375, 0.4375) at a displacement $u_x = 1.19$ [L]

Number of eigenvalue	Value
1	530.88
2	178.41
⋮	⋮
17	0.01
18	6.37E-15
19	1.72E-15
20	-4.37E-15
21	-2.88E-02
22	-3.84E-02
23	-5.84E-02
24	-3.27

In particular, the significant negative eigenvalue of -3.27 is critical with regard to the deformation behavior and especially in terms of the unstable behavior. For a better understanding of the related effects, the corresponding eigenvector is illustrated using a unit cube in Figure 2.27.

The observed deformation is very similar to the one globally observed within the structure in Figure 2.26a. Hence, it can be concluded that the deformation is mainly influenced by the negative eigenvalue. At last, it should be remarked that also for the edge element negative eigenvalues were observed, which will be also the case for the other unstable elements. Thus, it is not surprising that the deformation gets worse for larger displacements applied as seen in Figure 2.9b.

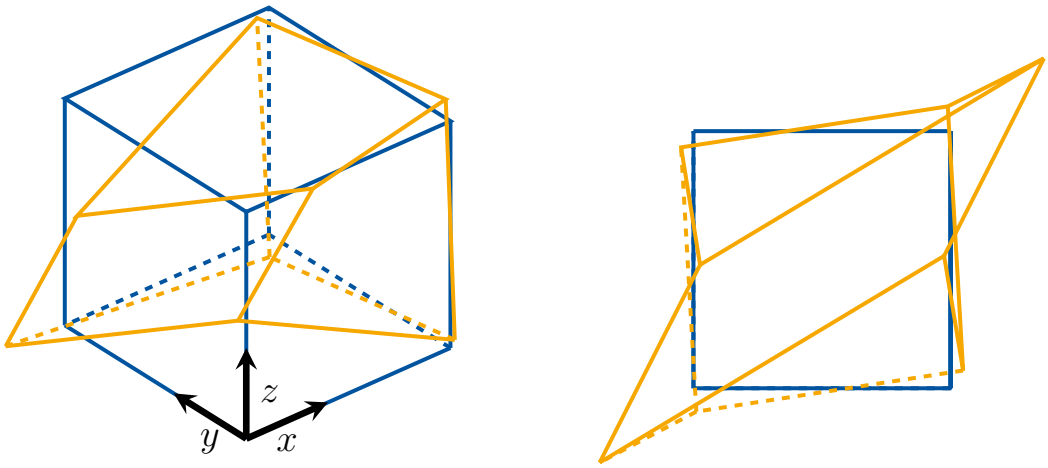

(a) Perspective view (b) YZ-Plane

Figure 2.27: Illustration of eigenvector (yellow) corresponding to eigenvalue -3.27

3 Article 2: A two-surface gradient-extended anisotropic damage model using a second order damage tensor coupled to additive plasticity in the logarithmic strain space

This article was published as:

Holthusen, H., Brepols, T., Reese, S., and Simon, J.-W. [2022], 'A two-surface gradient-extended anisotropic damage model using a second order damage tensor coupled to additive plasticity in the logarithmic strain space', *Journal of the Mechanics and Physics of Solids* **136**, 104833.

Disclosure of the individual authors' contributions to the article:

H. Holthusen reviewed the relevant existing literature, derived the constitutive framework and implemented the material model and the element routine into the finite element software *FEAP*. He set up and performed all simulations, interpreted the results and wrote the preliminary version of the article. It was his idea to employ the finite strain elasto-plasticity framework coupled to gradient-extended damage by Brepols et al. [2020] and the anisotropic damage model at small strains by Fassin et al. [2019*b*] as the basis for the model development. Moreover, T. Brepols, S. Reese, and J.-W. Simon gave conceptual advice, contributed to the discussion of the results, read the current version of the article, and gave valuable suggestions for improvement. All authors approved the preliminary publication of the article in the present dissertation.

3.1 Abstract

The objective of the present paper is to develop a thermodynamically consistent coupled damage-plasticity model at large deformations, which accounts for damage anisotropy. Moreover, a 'two-surface' approach allows modeling plasticity and damage independently. Thus, both phenomena are treated as separate dissipative mechanisms, making the model attractive for application to both brittle and ductile materials. The framework is based on Continuum Damage Mechanics. Furthermore, logarithmic strain measures - also known as Hencky strain - are considered for the kinematics, while the decomposition of the total deformation into elastic and plastic parts is based on the additive split. Hence, the derivation of the model and its conjugated quantities takes place in the logarithmic strain space, but these are subsequently transformed to their Lagrangian counterparts to be applicable in standard finite element formulations. Consequently, the transformation of constitutively dependent quantities such as stresses, but also the various associated material sensitivities, are addressed here. Another main aspect of this work is the gradient-extension of the presented model in order to cure mesh sensitivity in case of material softening. To this end, a novel gradient extension is derived using the invariants of the second order damage tensor, which is based on the micromorphic approach. In addition to the theoretical framework, special attention is paid to the finite element implementation, the formulation of the local residuals, and additionally the computation of the material tangents to achieve quadratic convergence rate within the Newton-Raphson scheme. Single element studies as well as representative structural examples investigate the model's response to various loading scenarios, the effect of damage anisotropy and further highlight its ability to provide mesh-independent results while undergoing large deformations.

Nomenclature

a, A	Scalar	$\otimes$	Dyadic product
$\boldsymbol{a}$	First order tensor	$\boldsymbol{A}^T$	Transpose of $\boldsymbol{A}^T$
$\boldsymbol{e}_i$	Cartesian basis	$\boldsymbol{A}^{-1}$	Inverse of $\boldsymbol{A}^{-1}$
$\mathbf{a}$	Tuple $n \times 1$	$\mathrm{tr}\,(\boldsymbol{A})$	Trace of $\boldsymbol{A}$
$\boldsymbol{A}$	Second order tensor	$\mathrm{dev}\,(\boldsymbol{A})$	Deviatoric part of $\boldsymbol{A}$
$\mathbf{A}$	Matrix $n \times m$	$\mathrm{vol}\,(\boldsymbol{A})$	Trace of $\boldsymbol{A}$
$\mathbb{A}$	Fourth order tensor	$\det(\boldsymbol{A})$	Determinant of $\boldsymbol{A}$

$\overset{n}{\mathbb{A}}$	Tensor of n-th order	$\ln(\boldsymbol{A})$	Logarithm of $\boldsymbol{A}$
$\mathrm{Sym}(\bullet)$	Symmetric group	$\mathrm{Grad}(\bullet)$	Lagrangian gradient
$\cdot$	Single contraction	$\mathrm{Div}(\bullet)$	Lagrangian divergence
$\boldsymbol{AB}$	$\boldsymbol{A} \cdot \boldsymbol{B} = A_{ik}B_{kj}\boldsymbol{e}_i \otimes \boldsymbol{e}_j$	$\mathrm{diag}(\bullet)$	Diagonal matrix
$:$	Double contraction (e.g. $\boldsymbol{A} : \boldsymbol{B} = A_{ij}B_{ij}$)	$(\bullet)^{\overset{ik}{T}}$	Interchange i-th and k-th basis vector

3.2 Introduction

Over the last decades, research in the field of material modeling of damage and in particular anisotropic damage has steadily increased. As observed in the course of, for instance, metal forming or natural engineering materials such as paperboard, isotropic models reach their limitations for such complex load paths and are not able to adequately represent reality anymore. Hence, accurate material models are essential for a proper prediction based on simulations and, thus, for the reduction of costs due to extensive experiments as well as for the general optimization of complex process flows. Besides brittle damage, characterized by an abrupt failure of the structure, ductile damage is of particular interest in this regard.
Micromechanically, ductile damage is characterized by dislocations and microdefects, the former being associated with plasticity. Microdefects, in turn, can be classified into (spherical or elliptical) microvoids and microcracks, where the degree, ratio, and orientation of at least microcracks depend on the material itself, but also strongly on the loading process. Due to such preferred directions of the microdefects, the microlevel can no longer be considered isotropic, which then becomes apparent at the macrolevel in the form of anisotropic damage. Nucleation and growth of these microdefects lead to a continuous loss of stiffness and, with further load increase, coalescence finally leads to a crack on the macroscopic level and thus to failure.
For a better understanding of these processes at the microlevel, excessive experimental investigations have been carried out, focusing not only on the growth of the microdefects but also, for example, on the stress state influence as well as the failure mechanism itself. In this context, the works of Mirone and Corallo [2010], Barsoum and Faleskog [2011], Li et al. [2011] and Malcher et al. [2014] who payed attention to stress triaxiality are exemplary mentioned. Nucleation, growth and coalescence of microdefects is of particular interest in e.g. Scheyvaerts et al. [2011], Shang et al. [2020], Liu et al. [2021]. In addition, the works of Brünig et al.

[2008], Brünig and Gerke [2011], Brünig et al. [2013, 2018, 2019] contributed a lot to the understanding of micromechanical damage processes, along with the comprehensive literature therein. Especially the latter, as well as the works of e.g. Kulawinski et al. [2011] and Song et al. [2017], studied the influence of non-proportional load paths on the macroscopic behavior. Gerke et al. [2020] provided an overview of possible specimen geometries and loading scenarios in order to study anisotropic damage.

The current work is based on the common approach of Continuum Damage Mechanics (CDM), which originates from the ongoing development of the works of Kachanov [1958] and Rabotnov [1963, 1969] by the pioneering contribution of Chaboche [1978]. CDM describes damage phenomenologically by means of scalar and/or tensorial quantities, which capture the loss of material integrity in a smeared sense. Among the first contributions in the field of ductile isotropic damage, the model of Lemaitre [1984, 1985*a*,*b*] is certainly one of the most important to be mentioned. This model treats damage and plasticity as strongly coupled phenomena rather than as separate mechanisms, and was continuously improved over the years to include various effects: Aging (Marquis and Lemaitre [1988]), crack-closure effect (e.g. Andrade Pires et al. [2003], Bouchard et al. [2011]), finite strains (e.g. de Souza Neto et al. [1998], Saanouni and Lestriez [2009]) and damage anisotropy (e.g. Lemaitre et al. [2000], Badreddine et al. [2010]).

The latter is of particular interest and will be briefly discussed.

In the case of initially anisotropic materials, the individual constituents usually show different failure behavior, which can be modeled by means of scalar damage variables (see, for example, Maimí et al. [2007], Bednarcyk et al. [2015], Reinoso et al. [2017], Simon et al. [2017], Holthusen et al. [2020], Dean et al. [2020], Poggenpohl et al. [2021]) and studied experimentally, for instance, by Reinoso et al. [2012]. In contrast, initially isotropic materials are much more challenging to model, since the degree of anisotropy is strongly related to the mentioned microdefects. Two approaches are most popular to model anisotropic damage. On the one hand, a fourth order tensor is utilized (e.g. Chaboche [1981, 1993], Chaboche et al. [1995], Ortiz [1985], Govindjee et al. [1995], Chow and Wei [1999]) which is beneficial in terms of formulating effective stresses. On the other hand, using a (symmetric) second order tensor (Dragon and Mróz [1979], Murakami [1981], Cordebois and Sidoroff [1982], Chaboche [1992, 1993], Hansen and Schreyer [1994], Murakami and Kamiya [1997], Abu Al-Rub and Voyiadjis [2003], Voyiadjis et al. [2008], Desmorat and Cantournet [2008]; Desmorat [2016], Fassin et al. [2017, 2019*b*,*a*], among many others) seems to be a natural extension in comparison to continuum mechanical modeling of e.g. visco-elasticity and elasto-plasticity and gained wide acceptance. In Chaboche [1984], a comparison between a fourth order tensor and

a second order tensor model is provided.
Over the last years, several approaches were developed to extend the classical infinitesimal damage theory and especially the case of anisotropic damage to finite strains. One particular approach introduces a damage metric tensor, while different kinematic assumptions are adopted for the finite deformation measure. For instance, the model of Brünig [2003], which was already validated in several experimental studies, is based on the theory of Lehmann [1989, 1991]. Menzel and Steinmann [2003], Menzel [2005], Bammann and Solanki [2010*a*] and Balieu and Kringos [2015] developed a material model which shares some similarities with the multiplicative decomposition of the deformation gradient in elasto-plasticity and was further extended to crystal plasticity (Ekh et al. [2004]) and viscous effects (Chen et al. [2017]). Another kind of finite anisotropic damage models accounts for damage by means of an additional second order damage tensor, which was already proposed by Murakami [1988]. Similar approaches are followed e.g. by Badreddine et al. [2015] , Badreddine and Saanouni [2015, 2017], Badreddine et al. [2017] and Voyiadjis and Kattan [1992*b*,*a*]. Also the model in the recently published work of Reese et al. [2021] is a representative of this type of modeling strategy. The model proposed within the current work follows this kind of modeling approach as well.
The literature review on various topics of CDM is by no means complete, nor does it claim to be. However, several textbooks, e.g. those by Lemaitre and Desmorat [2006], Voyiadjis and Katten [2005, 2006], Murakami [2012] and Saanouni [2013], which deal with the state of the art of CDM, provide a fairly deep insight into these topics. This variety of textbooks underscores the importance of CDM even nowadays.

Besides these various modeling strategies, so-called 'local' models, including the approaches named above, are ill-posed mathematical problems and thus suffer from the disadvantage of pathological mesh-dependence on a structural level in the context of finite element simulations (Bažant et al. [1984], de Borst et al. [1993] and de Borst [1996]). This leads to an artificial decrease of both energy dissipation and damage onset during mesh refinement. In order to counteract these problems, several regularization techniques were developed during the last decades. Three famous regularization methods are the viscous-type one (see e.g. Needleman [1988], Langenfeld et al. [2018]), the nonlocal integral-type formulation (see e.g. Pijaudier-Cabot and Bažant [1987], Bažant and Ožbolt [1990], Bažant and Jirásek [2002]), and gradient-enhanced models (see e.g. Peerlings et al. [1995, 1996] and Geers [2004]). A comprehensive and detailed comparison between the last two mentioned methods can be found in Peerlings et al. [2001]. One interesting subclass of gradient-enhanced models is the micro-

morphic approach suggested by Forest [2009, 2016], which was also used with considerable success in the field of damage in the recent past, for instance, by Aslan and Forest [2009], Aslan et al. [2011], Saanouni and Hamed [2013], Brepols et al. [2017, 2018*b*, 2020], Fassin et al. [2017, 2019*b*,*a*], Langenfeld and Mosler [2020] and Sprave and Menzel [2020]. In fact, the micromorphic approach offers a quite general way to introduce a nonlocal counterpart to any of the material model's local variables and, thus, offers a flexible way to account for internal length scales within the actual framework. Therefore, this very same approach to cure mesh-dependence is pursued.

From the literature review given, an ongoing demand for regularized elasto-plasticity models coupled to anisotropic damage at finite strains becomes evident. In particular, anisotropic damage models and their gradient extension are important topics of investigation in order to be able to make adequate predictions. Thus, the scope and key points of the present contribution can be summarized as follows:

- Conceptional treatment of an anisotropic damage framework in logarithmic strain space using the additive split for kinematics (Section 3.3 and 3.3.1).
- Development of a novel gradient-extension based on the micromorphic approach using the damage tensor's invariants, to overcome severe mesh-dependence (Section 3.3.2).
- Thermodynamically consistent derivation in the logarithmic strain space based on a 'two-surface' approach in order to treat damage and plasticity independently (Section 3.4).
- Fulfillment of the *damage growth criterion* proposed by Wulfinghoff et al. [2017] (Section 3.4.4).
- Derivation, linearization, and numerical implementation of the weak forms of linear momentum and micromorphic balance in the context of finite element simulations (Section 3.4.5 and 3.5).
- Presentation of transformation relationships of constitutively dependent quantities and material sensitivities between logarithmic and Lagrangian strain space (Section 3.5.4).

Finally, in Section 3.6 several single element studies and structural examples examine the model's response to different loading scenarios and the influence of anisotropic damage. Moreover, its ability to deliver mesh-independent results is investigated. A conclusion and outlook are given in Section 3.7.

3.3 Preliminaries

Nowadays, the multiplicative split of the deformation gradient $\boldsymbol{F}$ into its elastic part $\boldsymbol{F}_e$ and its plastic part $\boldsymbol{F}_p$ is widely accepted (see e.g. Eckart [1948], Kröner [1959], Lee and Liu [1967]) for modeling elasto-plastic behavior at finite strains

$$\boldsymbol{F} = \boldsymbol{F}_e \boldsymbol{F}_p. \tag{3.1}$$

Additionally, the polar decompositions of $\boldsymbol{F} = \boldsymbol{R}\boldsymbol{U}$, $\boldsymbol{F}_e = \boldsymbol{R}_e\boldsymbol{U}_e$ and $\boldsymbol{F}_p = \boldsymbol{R}_p\boldsymbol{U}_p = \boldsymbol{V}_p\boldsymbol{R}_p$ into their proper orthogonal and positive definite stretch parts are introduced. As a consequence of these decompositions, and in analogy to the right Cauchy-Green tensor $\boldsymbol{C} = \boldsymbol{F}^T\boldsymbol{F} = \boldsymbol{U}^2$, the following rotational-free right Cauchy-Green-like tensors are defined as

$$\boldsymbol{C}_e \coloneqq \boldsymbol{F}_e^T\boldsymbol{F}_e = \boldsymbol{U}_e^2 = \boldsymbol{F}_p^{-T}\boldsymbol{C}\boldsymbol{F}_p^{-1} = \boldsymbol{R}_p\,\boldsymbol{U}_p^{-1}\boldsymbol{C}\boldsymbol{U}_p^{-1}\boldsymbol{R}_p^{-1} \tag{3.2}$$

$$\boldsymbol{C}_p \coloneqq \boldsymbol{F}_p^T\boldsymbol{F}_p = \boldsymbol{U}_p^2 \tag{3.3}$$

where it is important to note that $\boldsymbol{C}_e$ and $\boldsymbol{U}_p^{-1}\boldsymbol{C}\boldsymbol{U}_p^{-1}$ share the same eigenvalues, while their eigenvectors are transformed by $\boldsymbol{R}_p$. In contrast to $\boldsymbol{C}_e$, $\boldsymbol{C}_p$ is defined with respect to the reference configuration. Therefore, the following left Cauchy-Green-like tensor

$$\boldsymbol{B}_p = \boldsymbol{F}_p\boldsymbol{F}_p^T = \boldsymbol{V}_p^2 = \boldsymbol{R}_p\,\boldsymbol{C}_p\,\boldsymbol{R}_p^{-1} \tag{3.4}$$

is introduced, in addition. However, since the constitutive framework will be stated in terms of logarithmic strains (Section 3.4), these strain tensors are defined based on $\boldsymbol{C}$ and Equations (3.2)-(3.4) as

$$\boldsymbol{\varepsilon} \coloneqq \ln(\boldsymbol{U}) \;= \frac{1}{2}\ln(\boldsymbol{C}) \tag{3.5}$$

$$\boldsymbol{\eta}_e \coloneqq \ln\left(\boldsymbol{U}_e\right) = \frac{1}{2}\ln\left(\boldsymbol{C}_e\right) = \frac{1}{2}\boldsymbol{R}_p \ln\left(\boldsymbol{U}_p^{-1}\boldsymbol{C}\boldsymbol{U}_p^{-1}\right)\boldsymbol{R}_p^{-1} =: \boldsymbol{R}_p\,\boldsymbol{\varepsilon}_e\,\boldsymbol{R}_p^{-1} \tag{3.6}$$

$$\boldsymbol{\eta}_p \coloneqq \ln(\boldsymbol{V}_p) \;= \frac{1}{2}\boldsymbol{R}_p \ln(\boldsymbol{C}_p)\boldsymbol{R}_p^{-1} =: \boldsymbol{R}_p\,\boldsymbol{\varepsilon}_p\,\boldsymbol{R}_p^{-1}. \tag{3.7}$$

It can be directly concluded that an isotropic function of $\boldsymbol{\eta}_e$ can be equivalently expressed in terms of $\boldsymbol{\varepsilon}_e$[1]. Unfortunately, $\dot{\boldsymbol{\varepsilon}}_e$ cannot be expressed generally in terms of $\dot{\boldsymbol{\varepsilon}}$ and $\dot{\boldsymbol{\varepsilon}}_p$ in a closed-form manner, which is considered a drawback. In this context, it is interesting to note that $\boldsymbol{\varepsilon}_e = \boldsymbol{\varepsilon} - \boldsymbol{\varepsilon}_p$ holds if and only if $\boldsymbol{C}$ and $\boldsymbol{U}_p$ commute and thus $\dot{\boldsymbol{\varepsilon}}_e = \dot{\boldsymbol{\varepsilon}} - \dot{\boldsymbol{\varepsilon}}_p$ (see Remark 4).

[1] The same holds for $\boldsymbol{\eta}_p$ and $\boldsymbol{\varepsilon}_p$.

From now on, it is assumed that the elastic strain is given by

$$\bar{\boldsymbol{\eta}}_e \coloneqq \boldsymbol{R}_p \left(\boldsymbol{\varepsilon} - \boldsymbol{\varepsilon}_p\right) \boldsymbol{R}_p^{-1} =: \boldsymbol{R}_p \, \bar{\boldsymbol{\varepsilon}}_e \, \boldsymbol{R}_p^{-1} \tag{3.8}$$

in general, and in analogy to Equation (3.6), which is known as the additive split. Although Itskov [2004] and Neff and Ghiba [2016] reported some disadvantages using this additive split, it is at least '*surprisingly close*' to Equation (3.6) as pointed out e.g. by Miehe et al. [2002]. Moreover, these disadvantages are usually outweighed in engineering applications as demonstrated in the literature by the successful usage across a wide range of material behaviors (see e.g. Papadopoulos and Lu [1998, 2001], Schröder et al. [2002], Sansour and Wagner [2003] and Miehe et al. [2002, 2009, 2011, 2017])[2].
Additionally, and for the sake of brevity, the following short hand notations for the integrity bases of an isotropic function for up to two tensors are introduced (see Spencer [1971, 1984], Boehler [1979], Zheng [1994])

$$\begin{aligned} \mathcal{E}(\boldsymbol{A}) &\coloneqq \{(\operatorname{tr}(\boldsymbol{A}), \operatorname{tr}\left(\boldsymbol{A}^2\right), \operatorname{tr}\left(\boldsymbol{A}^3\right)) \mid \boldsymbol{A} \in \operatorname{Sym}(3)\} \\ \mathcal{M}(\boldsymbol{A}, \boldsymbol{B}) &\coloneqq \{(\operatorname{tr}(\boldsymbol{A}\boldsymbol{B}), \operatorname{tr}\left(\boldsymbol{A}^2\boldsymbol{B}\right), \operatorname{tr}\left(\boldsymbol{A}\boldsymbol{B}^2\right), \operatorname{tr}\left(\boldsymbol{A}^2\boldsymbol{B}^2\right)) \mid \boldsymbol{A}, \boldsymbol{B} \in \operatorname{Sym}(3)\}. \end{aligned} \tag{3.9}$$

Remark 4. *Due to the property that* $\ln(\boldsymbol{A}\boldsymbol{B}) = \ln(\boldsymbol{A}) + \ln(\boldsymbol{B})$ *if* $\boldsymbol{A}$ *and* $\boldsymbol{B}$ *commute,* $\boldsymbol{\eta}_e$ *and* $\bar{\boldsymbol{\eta}}_e$ *coincide if and only if* $\boldsymbol{C}$ *and* $\boldsymbol{U}_p$ *commute. This is always the case when the principal axes of* $\boldsymbol{C}$ *do not rotate during loading (coaxial loading). For instance, pure stretch and pure shear fulfill this requirement. Nevertheless, as investigated by Itskov [2004] in a theoretical manner, non-coaxial loadings, e.g. simple shear, show a clear difference between the multiplicative and additive decomposition in general. Only the former is able to provide physically reasonable results for these deformations. However, under the additional assumption of small elastic strains, i.e.* $\boldsymbol{C}_e \to \boldsymbol{I}$*,* $\boldsymbol{C}$ *and* $\boldsymbol{U}_p$ *are 'nearly' coaxial, and thus, the additive decomposition is 'close' to the multiplicative version. This assumption is also made here. In this regard, the recent works of Friedlein et al. [2021, 2022] studied the performance of the additive split in case of excessive strains also on a structural level, revealing interesting insights into its structural response for coaxial and non-coaxial loadings. Of course, the assumption of small elastic strains restricts the model to, for instance, metals, however, this is not the main focus of this particular contribution.*

[2] All of them dealing with small elastic deformations.

3.3.1 Mapping of second order damage tensor

Going back to the work of Murakami [1981], anisotropic damage in the small strain regime can be modeled using a second order damage tensor. In further development, Murakami [1988] extended this to the finite strain regime by introducing a (positive semi-definite) damage tensor $\boldsymbol{D}_t \in \mathrm{Sym}(3)$ in the current configuration. While the virgin material is obtained if $\boldsymbol{D}_t = \boldsymbol{0}$, a fully broken state corresponds to $\boldsymbol{D}_t = \boldsymbol{I}$. As further argued in this work, the damage state should only depend on the *'irreversible change of internal structure'*, hence the constitutive framework is stated in terms of the *'elastically unloaded configuration'* (EUC) by means of a pull-back operation from the current configuration using $\boldsymbol{F}_e^{-1}$. However, as a consequence of this pull-back, the damage tensor $\boldsymbol{D}$ in the EUC is obtained by a mixed-variant mapping (cf. Sansour et al. [2007]) of the damage tensor $\boldsymbol{D}_t$, which means that $\boldsymbol{D}$ is not symmetric in general[3].

One possible symmetry-preserving mapping is presented by Reese et al. [2021], which is briefly discussed in the following. In contrast to Murakami [1988], the referential (positive semi-definite) damage tensor $\boldsymbol{D}_r \in \mathrm{Sym}(3)$ is used and pushed by $\boldsymbol{D} = \boldsymbol{F}_p \boldsymbol{D}_r \boldsymbol{F}_p^T$ to the EUC. The 'fully broken' state is characterized by $\boldsymbol{D}_r = \boldsymbol{I}$ and $\boldsymbol{D} = \boldsymbol{B}_p$, respectively. The subtle issue that $\boldsymbol{D} = \boldsymbol{I}$ is not correlated with the 'fully broken' state can be circumvented by working with

$$\boldsymbol{D} = \boldsymbol{R}_p \boldsymbol{D}_r \boldsymbol{R}_p^{-1} = \boldsymbol{R}_p \boldsymbol{D}_r \boldsymbol{R}_p^T = \boldsymbol{R}_p^{-T} \boldsymbol{D}_r \boldsymbol{R}_p^T \tag{3.10}$$

which naturally preserves both the symmetry of $\boldsymbol{D}$ as well as the same characteristic polynomial, such that $\mathcal{E}(\boldsymbol{D}) = \mathcal{E}(\boldsymbol{D}_r)$. Hence, $\boldsymbol{D} = \boldsymbol{I}$ corresponds to a 'fully broken' state and further the damage tensors reduce to $\boldsymbol{D}_r = \boldsymbol{D} = D\,\boldsymbol{I}$ with the scalar damage variable D in case of isotropic damage.

The mapping (3.10) will be used within this work and is similar to the one provided by Ganjiani et al. [2013][4]. In addition, the interested reader may find a more general treatment of this topic on transformations between different configurations, including the one defined in Equation (3.10), in the work of Latorre and Montáns [2016].

[3] Murakami [1988] mentioned that the skew-symmetric part of $\boldsymbol{D}$ can be excluded. However, this procedure is not followed here.

[4] They use the elastic rotation tensor $\boldsymbol{R}_e$ between the EUC and the current configuration.

3.3.2 Micromorphic approach and its application to gradient-extended damage

Based on the micromorphic approach introduced by Forest [2009, 2016] and due to the requirement that both the internal and the external virtual work have to be equal, the local forms of the balance equations are obtained as[5]

Balance of linear momentum:

$$\begin{aligned} \mathrm{Div}\,(\boldsymbol{F}\boldsymbol{S}) + \boldsymbol{f}_0 &= \boldsymbol{0} \quad \text{in } B_0 \\ \boldsymbol{F}\boldsymbol{S}\cdot\boldsymbol{n}_0 &= \boldsymbol{t}_0 \quad \text{on } \partial_t B_0 \\ \boldsymbol{u} &= \boldsymbol{u}' \quad \text{on } \partial_u B_0 \end{aligned} \tag{3.11}$$

Balance of micromorphic field:

$$\begin{aligned} \mathrm{Div}\,(\boldsymbol{\Xi}_{0_i} - \boldsymbol{\Xi}_{0_e}) - \boldsymbol{\xi}_{0_i} + \boldsymbol{\xi}_{0_e} &= \boldsymbol{0} \quad \text{in } B_0 \\ (\boldsymbol{\Xi}_{0_i} - \boldsymbol{\Xi}_{0_e})\cdot\boldsymbol{n}_0 &= \boldsymbol{\xi}_{0_c} \quad \text{on } \partial_c B_0 \\ \bar{\mathbf{d}} &= \bar{\mathbf{d}}' \quad \text{on } \partial_{\bar{d}} B_0 \end{aligned} \tag{3.12}$$

In the above equations, $\boldsymbol{S}$ denotes the second Piola-Kirchhoff stress tensor, $\boldsymbol{\xi}_{0_i}$ as well as $\boldsymbol{\Xi}_{0_i}$ refer to the conjugated internal forces related to the micromorphic tuple $\bar{\mathbf{d}} \coloneqq (\bar{d}_1, \ldots, \bar{d}_n)$ with n micromorphic variables $\bar{d}_i$. This tuple can be considered the nonlocal counterpart of the local tuple $\mathbf{d} \coloneqq (d_1, \ldots, d_n)$ with the same number n but local variables d_i given later on. Further, the external forces acting on the body are the volume force $\boldsymbol{f}_0$ and the micromorphic 'volume' forces $\boldsymbol{\xi}_{0_e}$, $\boldsymbol{\Xi}_{0_e}$. Surface loads acting on their corresponding boundary are introduced by the tractions $\boldsymbol{t}_0$ and $\boldsymbol{\xi}_{0_c}$. Furthermore, B_0 denotes the problem's referential domain, where its boundary is decomposed according to $\partial B_0 = \partial_u B_0 \cup \partial_t B_0 = \partial_{\bar{d}} B_0 \cup \partial_c B_0$ with $\partial_u B_0 \cap \partial_t B_0 = \partial_{\bar{d}} B_0 \cap \partial_c B_0 = \emptyset$. The outward normal vector in the reference configuration is denoted by $\boldsymbol{n}_0$ and prescribed values on the Dirichlet boundaries are indicated by $(\bullet)'$.

3.3.2.1 Invariant-based gradient-extension

There exist several approaches in the literature to account for gradient-extended material models in the case of anisotropic damage. For instance, the isotropic damage model developed by Titscher et al. [2019], based on the work of Peerlings et al. [1996], was extended by Yin et al. [2020] to the case of anisotropic damage. The latter authors chose three equivalent strain measures for the gradient-extension. In a similar way, Germain et al. [2007] introduced three additional fields for the anisotropic gradient-extension. In contrast, Abu Al-Rub and Voyiadjis [2003] chose the individual components of the damage tensor itself for the gradient-extension. In a recently published work, Fassin et al. [2019*b*] derived their gradient-extended model by means of the micromorphic approach (Forest [2009, 2016]). While this very last model is highly efficient from a computational point of view, since only the scalar damage hardening

[5] For more details, see Appendix 3.8.1.

variable is extended, the principle of maximum dissipation cannot be followed in every case for damage evolution.
In contrast, the present model follows this principle but uses the micromorphic approach for gradient-extension in connection with the damage tensor as well[6]. Choosing damage for the gradient-extension is based on the one hand on the good experiences made so far in other damage gradient-extended models such as tension-compression asymmetric, anisotropic damage (e.g. Fassin et al. [2019*a*]), isotropic damage coupled with (finite) elasto-plasticity (e.g. Brepols et al. [2017, 2018*b*, 2020]), and initially anisotropic materials (e.g. Holthusen et al. [2020], Poggenpohl et al. [2021]), and on the other hand an undesired artificial widening of the damage zone reported e.g. by Geers et al. [1998] and Saroukhani et al. [2013] could not be observed up to now.

As pointed out in Section 3.3.2, a set of local d_i and their corresponding nonlocal $\bar{d}_i$ variables is introduced. In order to ensure a strong coupling between them, the Helmholtz free energy is extended by a penalty energy h. In case of isotropic damage, a possible choice is $h = P/2\ (D - \bar{D})^2$, with the nonlocal damage variable $\bar{D}$ and penalty factor P (cf. Brepols et al. [2020]). In case of a second order damage tensor, a natural extension would be of the type $h = P/6 \sum_{i=1}^{3} (D_i - \bar{D}_i)^2$ with the eigenvalues D_i of the damage tensor, since this directly reduces to the penalty term for isotropic damage if all eigenvalues are equal. However, this approach implies that the 'correct' pair D_i and $\bar{D}_i$ must be connected at any time. Hence, the eigenvalues' evolutions must be known, which especially in a time discretized solution scheme and having in mind that eigenvalues are usually obtained using iterative solution methods does not seem very practical. Therefore, the invariants of $\boldsymbol{D}$ are gradient-extended, i.e. $\mathbf{d}$ reads

$$\mathbf{d} = (d_1,\ d_2,\ d_3) = \left(\mathrm{tr}\,(\boldsymbol{D}),\ \mathrm{tr}\left(\boldsymbol{D}^2\right),\ \mathrm{tr}\left(\boldsymbol{D}^3\right)\right) \tag{3.13}$$

which does not suffer from the just mentioned issues. Consequently, three additional degrees of freedom $\left(\bar{d}_1, \bar{d}_2, \bar{d}_3\right)$ are introduced.
To the authors' knowledge, a gradient-extension based on the invariants of the damage tensor in the context of the micromorphic approach has not been reported in the literature yet and, thus, represents a novel approach.

Remark 5. *Although the integrity basis* (3.13) *is chosen, one could also use the principal invariants, namely the trace of the damage tensor, the trace of the cofactor and the determinant of the damage tensor. However, as will be seen later, the derivative of* $\mathbf{d}$ *with respect to the dam-*

[6]Hence, a gradient-extended damage hardening variable is not used here.

age tensor itself is required. Since this tensor is positive semi-definite, the expression obtained would be more complicated compared to the one obtained in (3.13)*, see Appendix 3.8.2.*

3.4 Constitutive modeling in the logarithmic strain space

3.4.1 Helmholtz free energy

Following the concept of material isomorphism (see e.g. Bertram [1999] and Svendsen [2001] and the literature cited therein), the volume specific Helmholtz free energy depends on quantities stated in the EUC (intermediate configuration). Further, it is assumed to be an isotropic function (cf. Equation (3.9)), which can be additively decomposed as

$$\begin{aligned}\psi\left(\bar{\boldsymbol{\eta}}_e, \boldsymbol{\eta}_p, \boldsymbol{D}, \kappa_p, \kappa_d, \mathbf{d}, \bar{\mathbf{d}}, \operatorname{Grad}\left(\bar{\mathbf{d}}\right)\right) &= \psi_e(\bar{\boldsymbol{\eta}}_e, \boldsymbol{D}) + \psi_p(\boldsymbol{\eta}_p, \boldsymbol{D}, \kappa_p) + \psi_d(\kappa_d) \\ &\quad + \psi_h(\boldsymbol{D}) + \psi_{\bar{d}}\left(\mathbf{d}, \bar{\mathbf{d}}, \operatorname{Grad}\left(\bar{\mathbf{d}}\right)\right),\end{aligned} \tag{3.14}$$

The (damaged) elastic stored energy is given by ψ_e, the plastic hardening due to isotropic as well as kinematic hardening, which is also influenced by damage, is given by ψ_p. Furthermore, isotropic hardening is captured by the plastic hardening variable κ_p. Similar to the latter phenomenon, damage hardening is additionally considered by the damage hardening variable κ_d. The fourth term, namely ψ_h, is introduced in order to ensure that the eigenvalues of $\boldsymbol{D}$ and $\boldsymbol{D}_r$ do not exceed the value one, i.e. $0 \leq D_i \leq 1$ and so for D_{ri}, respectively[7]. Noteworthy, the hardening energy ψ_h and the driving force derived from it can be interpreted as a special kind of kinematic damage hardening (cf. Hansen and Schreyer [1994]), which was used in a similar manner by Fassin et al. [2017, 2019*b*,*a*] and Poggenpohl et al. [2021]. The energy $\psi_{\bar{d}}$ accounts for the micromorphic contribution (cf. Section 3.3.2 and 3.3.2.1). Furthermore, in the present work, the gradient influence is given by the Lagrangian gradient of $\bar{\mathbf{d}}$. It should be noted that choosing the Lagrangian gradient of $\bar{\mathbf{d}}$ is not a unique choice. Although other approaches exist, several authors made good experience working with the Lagrangian gradient (see e.g. Steinmann [1999], Wcisło et al. [2013], Brepols et al. [2020]). Moreover, as discussed in Section 3.3.2.1 and Equation (3.13), $\mathbf{d}$ is not an 'extra' internal variable, but can be expressed as a function of the damage tensor. Hence, the energy $\psi_{\bar{d}}$ is alternatively stated as

$$\psi_{\bar{d}} = \hat{\psi}_{\bar{d}}\left(\mathbf{d}(\boldsymbol{D}), \bar{\mathbf{d}}, \operatorname{Grad}\left(\bar{\mathbf{d}}\right)\right) = \breve{\psi}_{\bar{d}}\left(\boldsymbol{D}, \bar{\mathbf{d}}, \operatorname{Grad}\left(\bar{\mathbf{d}}\right)\right). \tag{3.15}$$

[7] Since this energy is chosen so that its influence is small until D_i tends towards one, material hardening caused by it is negligible (cf. Section 3.4.4)

Although both the elastic and the plastic energy are not necessarily influenced in the same way by the damage tensor (see Hansen and Schreyer [1994]), both have to approach zero if the damage tensor reaches $\boldsymbol{D} = \boldsymbol{I}$. Furthermore, as a consequence of the damage growth criterion[8], the individual energies have to be monotonically decreasing functions with respect to $\boldsymbol{D}$.

Remark 6. *Although ψ_h can generally be expressed in terms of $\mathcal{E}(\boldsymbol{D})$, it is more convenient to choose a form depending on the eigenvalues, i.e. $\psi_h = \breve{\psi}_h(D_1, D_2, D_3)$. Indeed, this still satisfies that ψ_h is an isotropic function of $\boldsymbol{D}$.*

3.4.2 Derivation based on the isothermal Clausius-Duhem inequality

In order to obtain the constitutive relations in a thermodynamically consistent manner, a derivation based on the (micromorphically extended) isothermal form of the Clausius-Duhem inequality (cf. Forest [2009, 2016]) is carried out, i.e.

$$-\dot{\psi} + \boldsymbol{T} : \dot{\boldsymbol{\varepsilon}} + \underbrace{\boldsymbol{\xi}_{0_i} \cdot \dot{\bar{\mathbf{d}}} + \boldsymbol{\Xi}_{0_i} : \mathrm{Grad}\left(\dot{\bar{\mathbf{d}}}\right)}_{\text{micromorphic extension}} \geq 0 \tag{3.16}$$

where the stress power is given in terms of the logarithmic strain and its conjugated force $\boldsymbol{T}$. Considering the assumed form of the Helmholtz free energy (3.14) and (3.15), the time derivative can be expressed as follows

$$\begin{aligned}\dot{\psi} = &\frac{\partial \psi_e}{\partial \bar{\boldsymbol{\eta}}_e} : \dot{\bar{\boldsymbol{\eta}}}_e + \frac{\partial \psi_p}{\partial \boldsymbol{\eta}_p} : \dot{\boldsymbol{\eta}}_p + \left(\frac{\partial \psi_e}{\partial \boldsymbol{D}} + \frac{\partial \psi_p}{\partial \boldsymbol{D}} + \frac{\partial \psi_h}{\partial \boldsymbol{D}} + \frac{\partial \psi_{\bar{d}}}{\partial \boldsymbol{D}}\right) : \dot{\boldsymbol{D}} \\ &+ \frac{\partial \psi_p}{\partial \kappa_p}\dot{\kappa}_p + \frac{\partial \psi_d}{\partial \kappa_d}\dot{\kappa}_d + \frac{\partial \psi_{\bar{d}}}{\partial \bar{\mathbf{d}}} \cdot \dot{\bar{\mathbf{d}}} + \frac{\partial \psi_{\bar{d}}}{\partial \mathrm{Grad}\left(\bar{\mathbf{d}}\right)} : \mathrm{Grad}\left(\dot{\bar{\mathbf{d}}}\right).\end{aligned} \tag{3.17}$$

For the following derivations, it should be noted that these are quite similar to the more detailed procedure presented in e.g. Dettmer and Reese [2004] and Vladimirov et al. [2008, 2010]. Starting with differentiating Equation (3.8) with respect to time results in

$$\dot{\bar{\boldsymbol{\eta}}}_e = \boldsymbol{R}_p\, \dot{\bar{\boldsymbol{\varepsilon}}}_e\, \boldsymbol{R}_p^{-1} - \underbrace{\boldsymbol{R}_p\, \bar{\boldsymbol{\varepsilon}}_e \boldsymbol{R}_p^{-1}}_{=\bar{\boldsymbol{\eta}}_e}\, \underbrace{\dot{\boldsymbol{R}}_p\, \boldsymbol{R}_p^{-1}}_{=:\boldsymbol{W}_R} - \underbrace{\boldsymbol{R}_p\, \dot{\boldsymbol{R}}_p^{T}}_{=\boldsymbol{W}_R^T}\, \underbrace{\boldsymbol{R}_p\, \bar{\boldsymbol{\varepsilon}}_e \boldsymbol{R}_p^{-1}}_{=\bar{\boldsymbol{\eta}}_e} \tag{3.18}$$

where it is important to note that $\boldsymbol{W}_R$ is skew-symmetric. Since the mappings between the EUC and reference configurations for $\boldsymbol{\eta}_p$ (3.7) and $\boldsymbol{D}$ (3.10) are chosen in a similar way, their

[8] For more details, see Appendix 3.8.3

rates are easily obtained as

$$\dot{\boldsymbol{\eta}}_p = \boldsymbol{R}_p\,\dot{\boldsymbol{\varepsilon}}_p\,\boldsymbol{R}_p^{-1} - \boldsymbol{\eta}_p\,\boldsymbol{W}_R - \boldsymbol{W}_R^T\,\boldsymbol{\eta}_p, \quad \dot{\boldsymbol{D}} = \boldsymbol{R}_p\,\dot{\boldsymbol{D}}_r\,\boldsymbol{R}_p^{-1} - \boldsymbol{D}\,\boldsymbol{W}_R - \boldsymbol{W}_R^T\,\boldsymbol{D}. \tag{3.19}$$

In the next step, the rate of the elastic energy ψ_e is considered while both rates (3.18) and $(3.19)_2$ as well as the additive split (3.8) are taken into account. In addition, the invariance of the trace operator under cyclic permutation leads to

$$\dot{\psi}_e = \boldsymbol{R}_p^{-1}\,\frac{\partial \psi_e}{\partial \bar{\boldsymbol{\eta}}_e}\,\boldsymbol{R}_p : (\dot{\boldsymbol{\varepsilon}} - \dot{\boldsymbol{\varepsilon}}_p) + \underbrace{\boldsymbol{R}_p^{-1}\,\frac{\partial \psi_e}{\partial \boldsymbol{D}}\,\boldsymbol{R}_p}_{=:-\boldsymbol{Y}_e} : \dot{\boldsymbol{D}}_r - 2\underbrace{\underbrace{\left(\bar{\boldsymbol{\eta}}_e \frac{\partial \psi_e}{\partial \bar{\boldsymbol{\eta}}_e} + \boldsymbol{D}\frac{\partial \psi_e}{\partial \boldsymbol{D}}\right)}_{\text{symmetric}} : \boldsymbol{W}_R}_{=0} \tag{3.20}$$

where $\boldsymbol{Y}_e$ denotes the damage driving force resulting from the elastic part of the energy. Moreover, the proof of symmetry is presented in Appendix 3.8.4 and holds analogously for the subsequent derivations. Continuing with the rate of the plastic energy ψ_p and under consideration of the rates (3.19), the following is obtained

$$\dot{\psi}_p = \underbrace{\boldsymbol{R}_p^{-1}\,\frac{\partial \psi_p}{\partial \boldsymbol{\eta}_p}\,\boldsymbol{R}_p}_{=:\boldsymbol{X}} : \dot{\boldsymbol{\varepsilon}}_p + \underbrace{\boldsymbol{R}_p^{-1}\,\frac{\partial \psi_p}{\partial \boldsymbol{D}}\,\boldsymbol{R}_p}_{=:-\boldsymbol{Y}_p} : \dot{\boldsymbol{D}}_r - 2\underbrace{\left(\boldsymbol{\eta}_p \frac{\partial \psi_p}{\partial \boldsymbol{\eta}_p} + \boldsymbol{D}\frac{\partial \psi_p}{\partial \boldsymbol{D}}\right) : \boldsymbol{W}_R}_{=0} + \underbrace{\frac{\partial \psi_p}{\partial \kappa_p}}_{=:-R_p}\,\dot{\kappa}_p. \tag{3.21}$$

In the above equation, the following conjugated driving forces are introduced: The plastic backstress $\boldsymbol{X}$, the plastic driving force for damage $\boldsymbol{Y}_p$ and the (plastic) isotropic hardening force R_p.

In what follows, it is essential to note that $(\partial \psi_h/\partial \boldsymbol{D})\,\boldsymbol{D} = \boldsymbol{D}\,(\partial \psi_h/\partial \boldsymbol{D})$ holds, since ψ_h is only dependent on the integrity basis $\mathcal{E}(\boldsymbol{D})$ and, thus, coaxial to $\boldsymbol{D}$. Hence, the following is found for the energies associated with damage hardening

$$\dot{\psi}_h + \dot{\psi}_d = \underbrace{\boldsymbol{R}_p^{-1}\,\frac{\partial \psi_h}{\partial \boldsymbol{D}}\,\boldsymbol{R}_p}_{=:\boldsymbol{Y}_h} : \dot{\boldsymbol{D}}_r - 2\underbrace{\boldsymbol{D}\frac{\partial \psi_h}{\partial \boldsymbol{D}} : \boldsymbol{W}_R}_{=0} + \underbrace{\frac{\partial \psi_d}{\partial \kappa_d}}_{=:-R_d}\,\dot{\kappa}_d. \tag{3.22}$$

Regarding the product of the damage tensor and the partial derivative of $\psi_{\bar{d}}$ with respect to $\boldsymbol{D}$, similar relations hold as for ψ_h, having in mind that the dependence of $\psi_{\bar{d}}$ on $\boldsymbol{D}$ is expressed in terms of $\mathcal{E}(\boldsymbol{D})$ as well (cf. Equation (3.13))

$$\dot{\psi}_{\bar{d}} = \underbrace{\boldsymbol{R}_p^{-1}\,\frac{\partial \psi_{\bar{d}}}{\partial \boldsymbol{D}}\,\boldsymbol{R}_p}_{=:\boldsymbol{Y}_{\bar{d}}} : \dot{\boldsymbol{D}}_r - 2\underbrace{\boldsymbol{D}\frac{\partial \psi_{\bar{d}}}{\partial \boldsymbol{D}} : \boldsymbol{W}_R}_{=0} + \frac{\partial \psi_{\bar{d}}}{\partial \bar{\mathbf{d}}} \cdot \dot{\bar{\mathbf{d}}} + \frac{\partial \psi_{\bar{d}}}{\partial \mathrm{Grad}\left(\bar{\mathbf{d}}\right)} : \mathrm{Grad}\left(\dot{\bar{\mathbf{d}}}\right). \tag{3.23}$$

As the above derivations showed, the rate of $\boldsymbol{W}_R$ and thus also of $\boldsymbol{R}_p$ never contributes to the rate of the Helmholtz free energy and is left undetermined, which is considered an advantage. Moreover, Appendix 3.8.5 proves that $\boldsymbol{R}_p$ is not required to compute the several conjugated driving forces, which are all defined in the reference configuration. Finally, inserting the different rates (3.20)-(3.23) into Equation (3.16) leads to

$$\begin{aligned}&\left(\boldsymbol{T}-\boldsymbol{R}_p^{-1}\frac{\partial\psi_e}{\partial\bar{\boldsymbol{\eta}}_e}\boldsymbol{R}_p\right):\dot{\boldsymbol{\varepsilon}}+\left(\boldsymbol{R}_p^{-1}\frac{\partial\psi_e}{\partial\bar{\boldsymbol{\eta}}_e}\boldsymbol{R}_p-\boldsymbol{X}\right):\dot{\boldsymbol{\varepsilon}}_p+\overbrace{(\boldsymbol{Y}_e+\boldsymbol{Y}_p-\boldsymbol{Y}_h-\boldsymbol{Y}_{\bar{d}})}^{=:\boldsymbol{Y}}:\dot{\boldsymbol{D}}_r\\&+R_p\,\dot{\kappa}_p+R_d\,\dot{\kappa}_d+\left(\boldsymbol{\xi}_{0_i}-\frac{\partial\psi_{\bar{d}}}{\partial\bar{\mathbf{d}}}\right)\cdot\dot{\bar{\mathbf{d}}}+\left(\boldsymbol{\Xi}_{0_i}-\frac{\partial\psi_{\bar{d}}}{\partial\mathrm{Grad}\left(\bar{\mathbf{d}}\right)}\right):\mathrm{Grad}\left(\dot{\bar{\mathbf{d}}}\right)\geq 0.\end{aligned}\tag{3.24}$$

Following the well-known arguments of Coleman and Noll [1961] and assuming zero dissipation resulting from the micromorphic variables as well (see Forest [2016]), the following state laws are obtained

$$\boldsymbol{T}=\boldsymbol{R}_p^{-1}\frac{\partial\psi_e}{\partial\bar{\boldsymbol{\eta}}_e}\boldsymbol{R}_p,\quad \boldsymbol{\xi}_{0_i}=\frac{\partial\psi_{\bar{d}}}{\partial\bar{\mathbf{d}}},\quad \boldsymbol{\Xi}_{0_i}=\frac{\partial\psi_{\bar{d}}}{\partial\mathrm{Grad}\left(\bar{\mathbf{d}}\right)}.\tag{3.25}$$

3.4.3 Onset criteria and evolution equations

In order to prove the fulfillment of Equation (3.24), onset criteria and evolution equations for both plasticity and damage have to be chosen. The evolution equations follow the principle of maximum dissipation. Nevertheless, the following particular choices certainly do not affect the generality of the model in any way.

3.4.3.1 Plastic yield criterion and evolution equations

Going back to the pioneering work of Kachanov [1958], plasticity takes place in the so-called effective continuum. Thus, the plastic yield criterion is expressed in terms of effective quantities, i.e.

$$\tilde{(\bullet)}=(\bullet)|_{\boldsymbol{D}=\boldsymbol{0}}.\tag{3.26}$$

A von Mises-type criterion is chosen and extended by kinematic and isotropic hardening

$$\Phi_p\coloneqq\sqrt{3\tilde{J}_2}-(\sigma_{y0}-\tilde{R}_p)\leq 0.\tag{3.27}$$

In the above, the second invariant of the stress deviator is used $J_2\coloneqq 1/2\ \mathrm{tr}\left(\mathrm{dev}\left(\boldsymbol{T}-\boldsymbol{X}\right)^2\right)$ and the initial yield stress is denoted by σ_{y0}. With these definitions at hand, the associative

flow rules for the plastic quantities read as follows

$$\dot{\boldsymbol{\varepsilon}}_p = \dot{\gamma}_p \, \frac{\partial \Phi_p}{\partial \boldsymbol{T}} = \dot{\gamma}_p \, \frac{3}{\sqrt{12 \tilde{J}_2}} \, \mathbb{M}^{-1} : \operatorname{dev}\left(\tilde{\boldsymbol{T}} - \tilde{\boldsymbol{X}}\right), \quad \dot{\kappa}_p = \dot{\gamma}_p \, \frac{\partial \Phi_p}{\partial R_p} = \frac{\dot{\gamma}_p}{f_d} \tag{3.28}$$

with the plastic multiplier $\dot{\gamma}_p$. Note that in the these equations, it is assumed that the following mappings between effective and damaged continuum hold: $\boldsymbol{T} = \mathbb{M} : \tilde{\boldsymbol{T}}$ and $R_p = f_d \, \tilde{R}_p$, where $\mathbb{M}$ possesses both minor and major symmetry and will further be specified in the following (cf. Section 3.4.4.1 and Appendix 3.8.6). To close the set of plastic constitutive equations, the Karush-Kuhn-Tucker conditions (KKT) (Karush [1939], Kuhn and Tucker [1951]) are introduced such that

$$\dot{\gamma}_p \geq 0, \quad \Phi_p \leq 0, \quad \dot{\gamma}_p \Phi_p = 0. \tag{3.29}$$

Remark 7. *In case that $\boldsymbol{T}$ and $\boldsymbol{\varepsilon}$ commute, it can be shown that $\boldsymbol{C}\boldsymbol{S} = \boldsymbol{T}$ holds true, and thus, $\boldsymbol{T}$ has the same eigenvalues as the (physical reasonable) Kirchhoff stress $\boldsymbol{F}\boldsymbol{S}\boldsymbol{F}^T$. Since the yield criterion* (3.27) *is provided in terms of effective quantities, this is always the case if $\boldsymbol{\varepsilon}$ and $\boldsymbol{\varepsilon}_p$ are coaxial.*

Remark 8. *In view of Equation* (3.28)*, the von Mises effective plastic strain rate $\sqrt{\frac{2}{3}\operatorname{tr}\left(\dot{\boldsymbol{\varepsilon}}_p^2\right)}$ is equivalent to $\dot{\kappa}_p$, at least for isotropic damage, since $\mathbb{M}^{-1}$ reduces to $\frac{1}{2\,f_d}\left(\delta_{ik}\delta_{jl} + \delta_{il}\delta_{kj}\right)$ with δ_{ij} being the Kronecker delta.*

3.4.3.2 Damage onset criterion and evolution equations

Since a two-surface approach is considered in this work, i.e. individual onset criteria are stated for plasticity and damage, the damage onset criterion is chosen as

$$\Phi_d \coloneqq \sqrt{3}\sqrt{\boldsymbol{Y}_+ : \mathbb{A}_d : \boldsymbol{Y}_+} - (Y_0 - R_d) \leq 0. \tag{3.30}$$

At this point, several things should be noted: (i) the pre-factor $\sqrt{3}$ is introduced in order to be in line with the scalar isotropic damage model of Brepols et al. [2020], (ii) $(\bullet)_+$ refers to the positive semi-definite part[9] of $\boldsymbol{Y}$ (cf. Fassin et al. [2019*b*]) and (iii) since the damage growth criterion (see Appendix 3.8.3) restricts the choice of the Helmholtz free energy and thus the damage driving force, the fourth order damage projection tensor $\mathbb{A}_d$ is introduced in line with Reese et al. [2021]. This tensor provides more flexibility and can be seen similar to

[9] In fact, $\boldsymbol{Y}_e$ and $\boldsymbol{Y}_p$ are positive (semi-)definite (cf. Section 3.4.4.1). In contrast, the hardening force $\boldsymbol{Y}_h$ can become so large that the overall driving force $\boldsymbol{Y}$ becomes (semi-)negative definite. This is only the case, if a eigenvalue of $\boldsymbol{D}$ tends to one.

the extension of the von Mises criterion by Hill and Orowan [1948]. Here, the following form is suggested

$$\mathbb{A}_d = \left((\boldsymbol{I} - \boldsymbol{D}_r)^{c_d} \otimes (\boldsymbol{I} - \boldsymbol{D}_r)^{c_d}\right)^{\overset{23}{T}}. \tag{3.31}$$

The material parameter Y_0 in (3.30) denotes the damage threshold, while c_d controls the degree of nonlinearity of $\mathbb{A}_d$. Further, in order to compute $(\boldsymbol{I} - \boldsymbol{D}_r)^{c_d}$, a spectral decomposition of $\boldsymbol{D}_r$ is required in general, however, since this is already necessary for $\boldsymbol{Y}_h$, no additional computational effort is needed. Nevertheless, it should be noted that the product $\mathbb{A}_d : \boldsymbol{Y}_+$ must yield a positive (semi-)definite tensor, in general, to ensure $\boldsymbol{Y}_+ : \mathbb{A}_d : \boldsymbol{Y}_+$ to be positive in (3.30). For $\mathbb{A}_d$ chosen in Equation (3.31), this can easily be shown (cf. Remark 10). With these equations at hand, the associative evolution equations are introduced as

$$\dot{\boldsymbol{D}}_r = \dot{\gamma}_d \frac{\partial \Phi_d}{\partial \boldsymbol{Y}} = \dot{\gamma}_d \frac{\sqrt{3}}{2} \frac{1}{\sqrt{\boldsymbol{Y}_+ : \mathbb{A}_d : \boldsymbol{Y}_+}} \left(\mathbb{P}_+ : \mathbb{A}_d : \boldsymbol{Y}_+ + \boldsymbol{Y}_+ : \mathbb{A}_d : \mathbb{P}_+\right), \; \dot{\kappa}_d = \dot{\gamma}_d \frac{\partial \Phi_d}{\partial R_d} = \dot{\gamma}_d \tag{3.32}$$

with the fourth order projection tensor $\mathbb{P}_+$ defined according to $\boldsymbol{Y}_+ = \mathbb{P}_+ : \boldsymbol{Y}$. Under consideration of the tensor's symmetries, $\mathbb{P}_+$ can be expressed following Ju [1989] as

$$\boldsymbol{Q}_+ = \sum_{i=1}^{3} \langle Y_i \rangle \, \boldsymbol{n}_i^{\boldsymbol{Y}} \otimes \boldsymbol{n}_i^{\boldsymbol{Y}}, \quad \mathbb{P}_+ = \frac{1}{2}\left(\left(\boldsymbol{Q}_+ \otimes \boldsymbol{Q}_+\right)^{\overset{23}{T}} + \left(\boldsymbol{Q}_+ \otimes \boldsymbol{Q}_+\right)^{\overset{24}{T}}\right). \tag{3.33}$$

In the above equation, the eigenvalues Y_i of $\boldsymbol{Y}$ and its eigenvectors $\boldsymbol{n}_i^{\boldsymbol{Y}}$ are introduced. Further, the Heaviside step function is denoted by $\langle \bullet \rangle$

$$\langle \bullet \rangle = \begin{cases} 1 & , (\bullet) \geq 0 \\ 0 & , (\bullet) < 0 \end{cases}. \tag{3.34}$$

In addition, since it is required in the local Newton-Raphson iteration, the derivative of $\boldsymbol{Q}_+$ with respect to $\boldsymbol{Y}$ can be obtained with the formula provided in Appendix 3.8.7 (which is non-zero only if $\boldsymbol{Y}$ is indefinite). The set of constitutive damage equations is closed by the corresponding KKT conditions, similar to Equation (3.29).

Remark 9. *Due to $\boldsymbol{Y}_h$, $\boldsymbol{Y}_+$ can turn out to be the zero tensor, in which case the onset criterion* (3.30) *is not differentiable anymore. Unfortunately, also during the Newton-Raphson iteration this can be the case. In order to avoid a division by zero, it is exploited that the onset criterion for a converged solution is zero due to the KKT conditions. Hence, the following relationship*

can be found

$$\frac{\sqrt{3}}{2}\frac{1}{\sqrt{\boldsymbol{Y}_+ : \mathbb{A}_d : \boldsymbol{Y}_+}} = \frac{3}{2}\frac{1}{Y_0 - R_d} \tag{3.35}$$

which is used for the numerical implementation and is similar to Challamel et al. [2005].

Remark 10. *The rate of the damage tensor* $(3.32)_1$ *must be positive semi-definite, since damage healing does not occur (non-reversible process). Therefore, taking into account Equation* (3.31)*, the following can be deduced for the damage rate*

$$\dot{\boldsymbol{D}}_r = \dot{\gamma}_d \, \frac{\sqrt{3}}{\sqrt{\boldsymbol{Y}_+ : \mathbb{A}_d : \boldsymbol{Y}_+}} \, \boldsymbol{Q}_+ \left(\boldsymbol{I} - \boldsymbol{D}_r\right)^{c_d} \boldsymbol{Y}_+ \left(\boldsymbol{I} - \boldsymbol{D}_r\right)^{c_d} \boldsymbol{Q}_+ \tag{3.36}$$

which is indeed positive semi-definite, since $\boldsymbol{Y}_+$ *is positive semi-definite.*

The remaining part of the reduced Clausius-Duhem inequality (3.24) can be proven to be fulfilled under consideration of the evolution equations (3.28) and (3.32), and the KKT conditions[10].

3.4.4 Specific form of Helmholtz free energy

The previous derivation was performed in a very general manner, without specifying the actual forms of the individual Helmholtz free energies. The main purpose was to show that the presented framework is not limited to specific expressions for these energies but is very flexible. Nevertheless, in order to study the model in a detailed manner and its behavior for different loading scenarios, concrete expressions are chosen in the following.

For the elastic energy, a quadratic form with respect to the elastic logarithmic strains is chosen. In addition, as considered e.g. by Lemaitre et al. [2000], Lemaitre and Desmorat [2006], Saanouni [2013], Badreddine et al. [2015], Badreddine and Saanouni [2015] and Desmorat [2016], the anisotropic nature of damage is assumed to affect only the isochoric part of the Helmholtz free energy. In contrast, the volumetric part is influenced by means of a scalar degradation function f_d. These considerations, and further the volumetric-isochoric decomposition of logarithmic strains (cf. Appendix 3.8.9), motivate to introduce the following elastic energy

$$\psi_e = \mu_e \, \mathrm{tr}\left(\mathrm{dev}\,(\bar{\boldsymbol{\eta}}_e)^2 (\boldsymbol{I} - \boldsymbol{D})\right) \vartheta + f_d \, \mu_e \, \mathrm{tr}\left(\mathrm{dev}\,(\bar{\boldsymbol{\eta}}_e)^2\right)(1 - \vartheta) + f_d \, \frac{K_e}{2} \mathrm{tr}\,(\bar{\boldsymbol{\eta}}_e)^2. \tag{3.37}$$

[10] For more details, see Appendix 3.8.8.

The elastic shear modulus is denoted by μ_e, the elastic bulk modulus by K_e, and the parameter $\vartheta \in [0,1]$ controls the degree of anisotropy (see Fassin et al. [2019*b*]). The degradation function $f_d = \breve{f}_d(\mathcal{E}(\boldsymbol{D})) = \bar{f}_d(\mathcal{E}(\boldsymbol{D}_r))$ captures isotropic damage and is chosen as

$$f_d = \left(1 - \frac{\operatorname{tr}(\boldsymbol{D})}{3}\right)^{e_d} = \left(1 - \frac{\operatorname{tr}(\boldsymbol{D}_r)}{3}\right)^{e_d} \tag{3.38}$$

with $e_d > 0$.

The energy contribution of plastic hardening is chosen analogously as follows

$$\begin{aligned}\psi_p = \mu_p \operatorname{tr}\left(\operatorname{dev}(\boldsymbol{\eta}_p)^2(\boldsymbol{I} - \boldsymbol{D})\right)\vartheta + f_d\,\mu_p \operatorname{tr}\left(\operatorname{dev}(\boldsymbol{\eta}_p)^2\right)(1-\vartheta) + f_d\,\frac{K_p}{2}\operatorname{tr}(\boldsymbol{\eta}_p)^2 \\ + f_d\,r_p\left(\kappa_p + \frac{\exp(-s_p\,\kappa_p) - 1}{s_p}\right)\end{aligned} \tag{3.39}$$

where the plastic material parameters have a similar meaning as their elastic counterparts. In addition, nonlinear isotropic hardening is modeled according to Voce [1955] with the corresponding material parameters r_p, s_p.

Isotropic damage hardening is chosen similar to isotropic plastic hardening, however, a quadratic term is added with hardening modulus H_d to account for linear damage hardening

$$\psi_d = r_d\left(\kappa_d + \frac{\exp(-s_d\,\kappa_d) - 1}{s_d}\right) + \frac{1}{2}H_d\,\kappa_d^2. \tag{3.40}$$

The additional damage hardening, limiting the eigenvalues of $\boldsymbol{D}$, follows from an integrated form of the Lorentz factor[11] and the requirement that it is equal to zero if no damage is present

$$\psi_h = K_h \sum_{i=1}^{3}\left(-\frac{(1-D_i)^{1-\frac{1}{n_d}}}{1-\frac{1}{n_d}} - D_i + \frac{1}{1-\frac{1}{n_d}}\right) \tag{3.41}$$

with hardening parameter K_h and n_d being a positive and even integer.

Finally, the micromorphic contribution to the Helmholtz free energy is chosen as a quadratic function of its arguments, i.e.

$$\psi_{\bar{d}} = \frac{1}{2}\sum_{i=1}^{3}\left(H_i\,(d_i - \bar{d}_i)^2\right) + \frac{1}{2}\sum_{i=1}^{3}\left(A_i\,\operatorname{Grad}(\bar{d}_i)\cdot\operatorname{Grad}(\bar{d}_i)\right). \tag{3.42}$$

The first term penalizes the difference between the local and nonlocal variable with the individual penalty factors H_1, H_2, H_3 (cf. h and P in Section 3.3.2.1). The second term represents

[11] Thus, the influence of $\boldsymbol{Y}_h$ is negligible small except then D_i tend to one.

the gradient-extension of the micromorphic approach. Via the material parameters A_1, A_2, A_3 internal length scales are introduced into the model. The choice of three distinct micromorphic moduli H_i and A_i is not mandatory but equips the model with a greater flexibility.

Remark 11. *As is frequently the case for coupled plasticity-damage models, the number of material parameters is relatively high. However, four different phenomena can be identified to which these parameters belong, namely: elastic (μ_e, K_e), plastic (μ_p, K_p, r_p, s_p, σ_{y0}), damage (ϑ, e_d, H_d, r_d, s_d, c_d, Y_0, A_i) and numerical (K_h, n_d, a_d, H_i) parameters, the latter are associated either with damage (K_h, n_d, a_d) or gradient extension (H_i). Furthermore, it should be noted that depending on the specific application or material, for instance, not all hardening mechanisms are needed, which would reduce the number of parameters. Nevertheless, the physically related parameters can be obtained most readily by monotonic and cyclic loading tests within the relevant regimes, with cyclic tests allowing the relationship between kinematic and isotropic hardening to be determined, as well as damage initiation and subsequent degradation. A similar procedure has already been successfully used for comparable models (e.g. by Dittmann et al. [2020], Sprave and Menzel [2020], Felder et al. [2022]). The numerical parameters are usually chosen such that a stable simulation is ensured.*

3.4.4.1 Specific forms of conjugated driving forces

The chosen expressions for the individual energies lead to the following conjugated driving forces

- State laws associated with $\dot{\boldsymbol{\varepsilon}}$, $\dot{\bar{\mathbf{d}}}$ and $\mathrm{Grad}\left(\dot{\bar{\mathbf{d}}}\right)$:

$$\begin{aligned}\boldsymbol{T} = \mu_e \Big[&(\boldsymbol{I} - \boldsymbol{D}_r)\bar{\boldsymbol{\varepsilon}}_e + \bar{\boldsymbol{\varepsilon}}_e(\boldsymbol{I} - \boldsymbol{D}_r) - \frac{2}{3}\mathrm{tr}\left((\boldsymbol{I} - \boldsymbol{D}_r)\bar{\boldsymbol{\varepsilon}}_e\right)\boldsymbol{I} - \frac{2}{9}\mathrm{tr}\left(\bar{\boldsymbol{\varepsilon}}_e\right)\mathrm{tr}\left(\boldsymbol{D}_r\right)\boldsymbol{I} \\ &+ \frac{2}{3}\mathrm{tr}\left(\bar{\boldsymbol{\varepsilon}}_e\right)\boldsymbol{D}_r \Big] \; \vartheta + f_d \, 2\mu_e \, \mathrm{dev}\left(\bar{\boldsymbol{\varepsilon}}_e\right)\left(1 - \vartheta\right) + f_d \, K_e \, \mathrm{tr}\left(\bar{\boldsymbol{\varepsilon}}_e\right)\boldsymbol{I}\end{aligned} \tag{3.43}$$

$$\left(\xi_{0_i}\right)_k = -H_k \, \left(d_k - \bar{d}_k\right), \quad k \in \{1,2,3\} \tag{3.44}$$

$$\left(\Xi_{0_i}\right)_k = A_k \, \mathrm{Grad}\left(\bar{d}_k\right), \quad k \in \{1,2,3\} \tag{3.45}$$

- Plastic driving forces associated with $\dot{\boldsymbol{\varepsilon}}_p$ and $\dot{\kappa}_p$:

$$\boldsymbol{X} = \mu_p \left[(\boldsymbol{I} - \boldsymbol{D}_r)\boldsymbol{\varepsilon}_p + \boldsymbol{\varepsilon}_p(\boldsymbol{I} - \boldsymbol{D}_r) - \frac{2}{3}\mathrm{tr}\left((\boldsymbol{I} - \boldsymbol{D}_r)\boldsymbol{\varepsilon}_p\right)\boldsymbol{I} - \frac{2}{9}\mathrm{tr}\left(\boldsymbol{\varepsilon}_p\right)\mathrm{tr}\left(\boldsymbol{D}_r\right)\boldsymbol{I} + \frac{2}{3}\mathrm{tr}\left(\boldsymbol{\varepsilon}_p\right)\boldsymbol{D}_r \right] \vartheta + f_d\, 2\mu_p\, \mathrm{dev}\left(\boldsymbol{\varepsilon}_p\right)(1-\vartheta) + f_d\, K_p\, \mathrm{tr}\left(\boldsymbol{\varepsilon}_p\right)\boldsymbol{I} \tag{3.46}$$

$$R_p = -f_d\, r_p(1 - \exp(-s_p\kappa_p)) \tag{3.47}$$

- Damage driving forces associated with $\dot{\boldsymbol{D}}_r$ and $\dot{\kappa}_d$:

$$\boldsymbol{Y}_e = \mu_e\, \mathrm{dev}\left(\bar{\boldsymbol{\varepsilon}}_e\right)^2 \vartheta - \mu_e\, \mathrm{tr}\left(\mathrm{dev}\left(\bar{\boldsymbol{\varepsilon}}_e\right)^2\right)(1-\vartheta)\frac{\partial f_d}{\partial \boldsymbol{D}_r} - \frac{K_e}{2}\mathrm{tr}\left(\bar{\boldsymbol{\varepsilon}}_e\right)^2\frac{\partial f_d}{\partial \boldsymbol{D}_r} \tag{3.48}$$

$$\boldsymbol{Y}_p = \mu_p\, \mathrm{dev}\left(\boldsymbol{\varepsilon}_p\right)^2 \vartheta - \mu_p\, \mathrm{tr}\left(\mathrm{dev}\left(\boldsymbol{\varepsilon}_p\right)^2\right)(1-\vartheta)\frac{\partial f_d}{\partial \boldsymbol{D}_r} - \frac{K_p}{2}\mathrm{tr}\left(\boldsymbol{\varepsilon}_p\right)^2\frac{\partial f_d}{\partial \boldsymbol{D}_r} - r_p\left(\kappa_p + \frac{\exp(-s_p\kappa_p) - 1}{s_p}\right)\frac{\partial f_d}{\partial \boldsymbol{D}_r} \tag{3.49}$$

$$\boldsymbol{Y}_h = K_h \sum_{i=1}^{3}\left(\left[\frac{1}{(1 - D_{r_i})^{\frac{1}{n_d}}} - 1\right]\boldsymbol{n}_i^{\boldsymbol{D}_r} \otimes \boldsymbol{n}_i^{\boldsymbol{D}_r}\right) \tag{3.50}$$

$$\boldsymbol{Y}_{\bar{d}} = \sum_{i=1}^{3}\left(H_i(\mathrm{tr}\left(\boldsymbol{D}_r^i\right) - \bar{d}_i)\; i\; \boldsymbol{D}_r^{i-1}\right) \tag{3.51}$$

$$R_d = -\left[r_d(1 - \exp(-s_d\kappa_d)) + H_d\,\kappa_d\right] \tag{3.52}$$

with the eigenvalues D_{r_i} and eigenvectors $\boldsymbol{n}_i^{\boldsymbol{D}_r}$ of $\boldsymbol{D}_r$. Further, it should be emphasized that in the above it was utilized that the eigenvectors of $\boldsymbol{D}$ and $\boldsymbol{D}_r$ transform according to $\boldsymbol{n}_i^{\boldsymbol{D}} = \boldsymbol{R}_p\, \boldsymbol{n}_i^{\boldsymbol{D}_r}$. Additionally, the fourth order damage tensor $\mathbb{M}$ (cf. Section 3.4.3.1) can be deduced from Equation (3.43) and is derived in Appendix 3.8.6.
Moreover, from a numerical point of view, $D_{r_i} \geq 1$ may occur during the iterative solution on the local level, which would result in 'not a number' for $\boldsymbol{Y}_h$. Therefore, it is approximated by a Taylor expansion for values of D_{r_i} close to one[12].

Remark 12. *The degradation function f_d must be a monotonically decreasing function with respect to $\mathcal{E}(\boldsymbol{D})$ (same holds for $\mathcal{E}(\boldsymbol{D}_r)$). Hence, $\partial f_d/\partial \boldsymbol{D}_r$ is negative semi-definite. Consequently, both the elastic $\boldsymbol{Y}_e$ and plastic $\boldsymbol{Y}_p$ driving forces are positive semi-definite tensors. Hence, the damage growth criterion (see Appendix 3.8.3) is fulfilled.*

[12]For more details, see Appendix 3.8.7.

3.4.5 Weak forms and their linearization

To solve the global field equations numerically, the weak forms of the balance relations (3.11) and (3.12) are derived. The micromorphic balance relation is therefore simplified, in particular all external and contact forces are neglected as well as no values on the Dirichlet boundary are prescribed, i.e. $\partial B \equiv \partial_c B_0$. Taking these simplifications and the relations for the generalized stresses (3.44)-(3.45) into account, the weak forms are obtained by following the standard procedure (multiplication by test functions, integration by parts and application of divergence theorem)

$$g_u(\boldsymbol{u}, \bar{\mathbf{d}}, \delta\boldsymbol{u}) \coloneqq \int_{B_0} \boldsymbol{S} : \delta\boldsymbol{E} \, \mathrm{d}V - \int_{B_0} \boldsymbol{f}_0 \cdot \delta\boldsymbol{u} \, \mathrm{d}V - \int_{\partial_t B_0} \boldsymbol{t}_0 \cdot \delta\boldsymbol{u} \, \mathrm{d}A = 0 \tag{3.53}$$

$$g_{\bar{d}}(\boldsymbol{u}, \bar{\mathbf{d}}, \delta\bar{\mathbf{d}}) \coloneqq \int_{B_0} \delta\bar{\mathbf{d}} \cdot \mathbf{H}_{\bar{d}} \cdot \left(\mathbf{d} - \bar{\mathbf{d}}\right) \mathrm{d}V - \int_{B_0} \mathrm{Grad}\left(\delta\bar{\mathbf{d}}\right) : \left(\mathbf{A}_{\bar{d}} \cdot \mathrm{Grad}\left(\bar{\mathbf{d}}\right)\right) \mathrm{d}V = 0 \tag{3.54}$$

with the test functions $\delta\boldsymbol{u}$ and $\delta\bar{\mathbf{d}}$ as well as $\mathbf{H}_{\bar{d}} = \mathrm{diag}(H_1\ H_2\ H_3)$ and $\mathbf{A}_{\bar{d}} = \mathrm{diag}(A_1\ A_2\ A_3)$. Since both weak forms are generally nonlinear functions, a Newton-Raphson iteration is used for numerical solution. For this purpose, the linearization of (3.53) and (3.54) is required, which is performed using the Gâteaux derivative $\mathfrak{D}[\bullet]$. The resulting increments are abbreviated $\Delta g_u \coloneqq \mathfrak{D}_u[g_u] \cdot \Delta\boldsymbol{u} + \mathfrak{D}_{\bar{d}}[g_u] \cdot \Delta\bar{\mathbf{d}}$ and $\Delta g_{\bar{d}} \coloneqq \mathfrak{D}_u[g_{\bar{d}}] \cdot \Delta\boldsymbol{u} + \mathfrak{D}_{\bar{d}}[g_{\bar{d}}] \cdot \Delta\bar{\mathbf{d}}$[13]. Furthermore, the body force $\boldsymbol{f}_0$ and the surface traction $\boldsymbol{t}_0$ are assumed to be independent of the field variables, resulting in the following increments

$$\Delta g_u = \int_{B_0} \Delta\boldsymbol{S} : \delta\boldsymbol{E} \, \mathrm{d}V + \int_{B_0} \boldsymbol{S} : \Delta\delta\boldsymbol{E} \, \mathrm{d}V \tag{3.55}$$

$$\Delta g_{\bar{d}} = \int_{B_0} \delta\bar{\mathbf{d}} \cdot \mathbf{H}_{\bar{d}} \cdot \left(\Delta\mathbf{d} - \Delta\bar{\mathbf{d}}\right) \mathrm{d}V - \int_{B_0} \mathrm{Grad}\left(\delta\bar{\mathbf{d}}\right) : \left(\mathbf{A}_{\bar{d}} \cdot \mathrm{Grad}\left(\Delta\bar{\mathbf{d}}\right)\right) \mathrm{d}V. \tag{3.56}$$

The first summands in (3.55)-(3.56) can further be reformulated in terms of the desired increments $\Delta\boldsymbol{u}$ and $\Delta\bar{\mathbf{d}}$, which leads to

$$\Delta\boldsymbol{S} = \left.\frac{\partial\boldsymbol{S}}{\partial\boldsymbol{E}}\right|_{\bar{\mathbf{d}}} : \Delta\boldsymbol{E} + \left.\frac{\partial\boldsymbol{S}}{\partial\bar{\mathbf{d}}}\right|_{\boldsymbol{E}} \cdot \Delta\bar{\mathbf{d}} =: \mathbb{C} : \Delta\boldsymbol{E} + \mathscr{K}_{\bar{d}} \cdot \Delta\bar{\mathbf{d}} \tag{3.57}$$

$$\Delta\mathbf{d} = \left.\frac{\partial\mathbf{d}}{\partial\boldsymbol{E}}\right|_{\bar{\mathbf{d}}} : \Delta\boldsymbol{E} + \left.\frac{\partial\mathbf{d}}{\partial\bar{\mathbf{d}}}\right|_{\boldsymbol{E}} \cdot \Delta\bar{\mathbf{d}} =: \mathscr{G}_u : \Delta\boldsymbol{E} + \mathbf{G}_{\bar{d}} \cdot \Delta\bar{\mathbf{d}} \tag{3.58}$$

[13] For more details, see Appendix 3.8.10.

where $\boldsymbol{E}$ denotes the Green-Lagrange strain tensor and the short hand notations

$$\Delta \boldsymbol{E} \coloneqq \frac{1}{2}\left(\mathrm{Grad}\,(\Delta \boldsymbol{u})^T \boldsymbol{F} + \boldsymbol{F}^T \mathrm{Grad}\,(\Delta \boldsymbol{u})\right) \tag{3.59}$$

$$\Delta\delta \boldsymbol{E} \coloneqq \frac{1}{2}\left(\mathrm{Grad}\,(\delta \boldsymbol{u})^T \mathrm{Grad}\,(\Delta \boldsymbol{u}) + \mathrm{Grad}\,(\Delta \boldsymbol{u})^T \mathrm{Grad}\,(\delta \boldsymbol{u})\right). \tag{3.60}$$

Analogously to (3.59), $\delta \boldsymbol{E} \coloneqq 1/2\left(\mathrm{Grad}\,(\delta \boldsymbol{u})^T \boldsymbol{F} + \boldsymbol{F}^T \mathrm{Grad}\,(\delta \boldsymbol{u})\right)$ is introduced. In order to obtain a quadratic convergence rate during the Newton-Raphson procedure, the (algorithmic) consistent tangent operators in (3.57)-(3.58) have to be computed, which will be discussed in Section 3.5.4.

3.5 Algorithmic implementation

3.5.1 Numerical approximation and discretization

First, the exact domain in the reference configuration B_0 is approximated (superscript h) and further divided into n_{el} number of finite elements

$$B_0 \approx B_0^h = \bigcup_{e=1}^{n_{el}} B_0^e. \tag{3.61}$$

The element types used in this work are trilinear hexahedral and bilinear quadrilateral Q1 standard elements, thus the approximations and consequently the numerical integration take place in the isoparametric space. Hence, the field variables, their increments as well as the test functions are approximated in the corresponding finite element domain (superscript e) and discretized according to

$$\boldsymbol{u}^e = \mathbf{N}_u(\boldsymbol{\xi})\ \underline{\mathbf{u}}^e, \qquad \delta\underline{\mathbf{u}}^e = \mathbf{N}_u(\boldsymbol{\xi})\ \delta\underline{\mathbf{u}}^e, \qquad \Delta\underline{\mathbf{u}}^e = \mathbf{N}_u(\boldsymbol{\xi})\ \Delta\underline{\mathbf{u}}^e \tag{3.62}$$

$$\bar{\mathbf{d}}^e = \mathbf{N}_{\bar{d}}(\boldsymbol{\xi})\ \underline{\bar{\mathbf{d}}}^e, \qquad \delta\bar{\mathbf{d}}^e = \mathbf{N}_{\bar{d}}(\boldsymbol{\xi})\ \delta\underline{\bar{\mathbf{d}}}^e, \qquad \Delta\bar{\mathbf{d}}^e = \mathbf{N}_{\bar{d}}(\boldsymbol{\xi})\ \Delta\underline{\bar{\mathbf{d}}}^e \tag{3.63}$$

where $\underline{\mathbf{u}}^e$ and $\underline{\bar{\mathbf{d}}}^e$ contain the nodal values of displacement and micromorphic variables, respectively. The shape function matrices $\mathbf{N}_u$ and $\mathbf{N}_{\bar{d}}$ contain the corresponding shape functions in terms of natural coordinates $\boldsymbol{\xi} = (\xi, \eta, \zeta)$. Next, based on (3.62)-(3.63), the spatial derivatives

of the field variables are expressed as

$$\hat{\boldsymbol{F}}^e = \hat{\boldsymbol{I}} + \mathbf{B}_u(\boldsymbol{\xi})\ \underline{\mathbf{u}}^e, \quad \mathrm{Grad}\,(\delta\boldsymbol{u})^e = \mathbf{B}_u(\boldsymbol{\xi})\ \delta\underline{\mathbf{u}}^e, \quad \mathrm{Grad}\,(\Delta\boldsymbol{u})^e = \mathbf{B}_u(\boldsymbol{\xi})\ \Delta\underline{\mathbf{u}}^e \tag{3.64}$$

$$\mathrm{Grad}\left(\bar{\mathbf{d}}\right)^e = \mathbf{B}_{\bar{d}}(\boldsymbol{\xi})\ \underline{\bar{\mathbf{d}}}^e, \qquad \mathrm{Grad}\left(\delta\bar{\mathbf{d}}\right)^e = \mathbf{B}_{\bar{d}}(\boldsymbol{\xi})\ \delta\underline{\bar{\mathbf{d}}}^e, \quad \mathrm{Grad}\left(\Delta\bar{\mathbf{d}}\right)^e = \mathbf{B}_{\bar{d}}(\boldsymbol{\xi})\ \Delta\underline{\bar{\mathbf{d}}}^e \tag{3.65}$$

where $\hat{(\bullet)}$ denotes Nye's notation of the corresponding quantity. Having these equations at hand, the (approximated) weak forms (3.53)-(3.54) as well as their linearizations (3.55)-(3.56) can be suitably discretized for the finite element procedure

$$g_u^h := \bigcup_{e=1}^{n_{el}} \delta\underline{\mathbf{u}}^{eT} \overbrace{\left(\int_{B_0^e} \mathbf{B}_u^T\ \mathbf{F}_m^T\ \hat{\boldsymbol{S}}^e\ \mathrm{d}V^e - \int_{B_0^e} \mathbf{N}_u^T\ \boldsymbol{f}_0^e\ \mathrm{d}V^e - \int_{\partial_t B_0^e} \mathbf{N}_u^T\ \boldsymbol{t}_0^e\ \mathrm{d}A^e \right)}^{=:\mathbf{r}_u^e} = 0 \tag{3.66}$$

$$g_{\bar{d}}^h := \bigcup_{e=1}^{n_{el}} \delta\underline{\bar{\mathbf{d}}}^{eT} \underbrace{\left(\int_{B_0^e} \mathbf{N}_{\bar{d}}^T\ \mathbf{H}_{\bar{d}}^e\ \left(\mathbf{d}^e - \bar{\mathbf{d}}^e\right)\ \mathrm{d}V^e - \int_{B_0^e} \mathbf{B}_{\bar{d}}^T\ \hat{\mathbf{A}}_{\bar{d}}^e\ \mathrm{Grad}\left(\bar{\mathbf{d}}\right)^e\ \mathrm{d}V^e \right)}_{=:\mathbf{r}_{\bar{d}}^e} = 0 \tag{3.67}$$

and, taking into account (3.57)-(3.58),

$$\begin{aligned} \Delta g_u^h = &\bigcup_{e=1}^{n_{el}} \delta\underline{\mathbf{u}}^{eT} \overbrace{\left(\int_{B_0^e} \mathbf{B}_u^T\ \mathbf{F}_m^T\ \hat{\mathbb{C}}^e\ \mathbf{F}_m\ \mathbf{B}_u\ \mathrm{d}V^e + \int_{B_0^e} \mathbf{B}_u^T\ \mathbf{S}_m\ \mathbf{B}_u\ \mathrm{d}V^e \right)}^{=:\mathbf{K}_{uu}^e} \Delta\underline{\mathbf{u}}^e \\ &+ \bigcup_{e=1}^{n_{el}} \delta\underline{\mathbf{u}}^{eT} \underbrace{\left(\int_{B_0^e} \mathbf{B}_u^T\ \mathbf{F}_m^T\ \hat{\mathscr{K}}_{\bar{d}}^e\ \mathbf{N}_{\bar{d}}\ \mathrm{d}V^e \right)}_{=:\mathbf{K}_{u\bar{d}}^e} \Delta\underline{\bar{\mathbf{d}}}^e \end{aligned} \tag{3.68}$$

$$\begin{aligned} \Delta g_{\bar{d}}^h = &\bigcup_{e=1}^{n_{el}} \delta\underline{\bar{\mathbf{d}}}^{eT} \overbrace{\left(\int_{B_0^e} \mathbf{N}_{\bar{d}}^T\ \mathbf{H}_{\bar{d}}^e\ \left(\mathbf{G}_{\bar{d}}^e - \boldsymbol{I}\right)\ \mathbf{N}_{\bar{d}}\ \mathrm{d}V^e - \int_{B_0^e} \mathbf{B}_{\bar{d}}^T\ \hat{\mathbf{A}}_{\bar{d}}^e\ \mathbf{B}_{\bar{d}}\ \mathrm{d}V^e \right)}^{=:\mathbf{K}_{\bar{d}\bar{d}}^e} \Delta\underline{\bar{\mathbf{d}}}^e \\ &+ \bigcup_{e=1}^{n_{el}} \delta\underline{\bar{\mathbf{d}}}^{eT} \underbrace{\left(\int_{B_0^e} \mathbf{N}_{\bar{d}}^T\ \mathbf{H}_{\bar{d}}^e\ \hat{\mathscr{G}}_u^e\ \mathbf{F}_m\ \mathbf{B}_u\ \mathrm{d}V^e \right)}_{=:\mathbf{K}_{\bar{d}u^e}} \Delta\underline{\mathbf{u}}^e \end{aligned} \tag{3.69}$$

where the relations $\delta\hat{\boldsymbol{E}}^e = \mathbf{F}_m\mathbf{B}_u\ \delta\underline{\mathbf{u}}^e$ and $\Delta\hat{\boldsymbol{E}}^e = \mathbf{F}_m\mathbf{B}_u\Delta\underline{\mathbf{u}}^e$ are exploited. The introduced terms $\mathbf{r}_{(\bullet)}^e$ and $\mathbf{K}_{(\bullet)(\bullet)}^e$ denote the element residuals and element stiffness matrices, respectively.

These element contributions are assembled finally, in order to obtain the global nonlinear system of equations, which can be solved using the Newton-Raphson scheme, i.e.

$$\begin{pmatrix} \mathbf{K}_{uu} & \mathbf{K}_{u\bar{d}} \\ \mathbf{K}_{\bar{d}u} & \mathbf{K}_{\bar{d}\bar{d}} \end{pmatrix} \begin{pmatrix} \Delta\underline{\mathbf{u}} \\ \Delta\underline{\bar{\mathbf{d}}} \end{pmatrix} = - \begin{pmatrix} \mathbf{r}_u \\ \mathbf{r}_{\bar{d}} \end{pmatrix} . \tag{3.70}$$

In the above nonlinear system of equations

$$\begin{aligned} \mathbf{K}_{uu} &= \mathop{\mathbf{A}}_{e=1}^{n_{el}} (\mathbf{K}^e_{uu}) \qquad \mathbf{K}_{u\bar{d}} = \mathop{\mathbf{A}}_{e=1}^{n_{el}} (\mathbf{K}^e_{u\bar{d}}) \qquad \mathbf{K}_{\bar{d}u} = \mathop{\mathbf{A}}_{e=1}^{n_{el}} (\mathbf{K}^e_{\bar{d}u}) \qquad \mathbf{K}_{\bar{d}\bar{d}} = \mathop{\mathbf{A}}_{e=1}^{n_{el}} (\mathbf{K}^e_{\bar{d}\bar{d}}) \\ \mathbf{r}_u &= \mathop{\mathbf{A}}_{e=1}^{n_{el}} (\mathbf{r}^e_u) \qquad \mathbf{r}_{\bar{d}} = \mathop{\mathbf{A}}_{e=1}^{n_{el}} (\mathbf{r}^e_{\bar{d}}) \end{aligned} \tag{3.71}$$

represent the assembled global stiffness matrices as well as the assembled residuals with the assembly operator $\mathop{\mathbf{A}}_{e=1}^{n_{el}} (\bullet)$.

Remark 13. *As pointed out by Holthusen et al. [2020], for the special case of three additional micromorphic field variables, the shape function matrices* $\mathbf{N}_u$ */* $\mathbf{N}_{\bar{d}}$ *as well as their corresponding* $\mathbf{B}$*-Operators can be chosen in the exact same way, which results in a more efficient element implementation. Nevertheless, for the sake of clarity, these operators were distinguished here. In addition, the explicit expressions for* $\mathbf{F}_m$*,* $\mathbf{S}_m$ *as well as the* $\mathbf{B}$*-Operators are provided there.*

3.5.2 Implicit time integration

Before the discretized evolution equations are introduced, some notes on the numerical implementation in the context of finite elasto-plasticity are briefly discussed. In case of volume preserving plasticity, i.e. $\det(\boldsymbol{C}_p) = 1$, the standard Backward Euler scheme usually does not preserve the volume when choosing the multiplicative decomposition. A problem which can be solved, for instance, by using additional constraint equations (see Vladimirov et al. [2008]). Another method to circumvent this issue - also in the case of anisotropic plasticity - is the usage of the exponential map integrator, which naturally preserves the volume (see e.g. Dettmer and Reese [2004], Reese and Christ [2008], Vladimirov et al. [2008, 2010])[14]. However, from a computational point of view, the exponential map integrator requires way more numerical effort compared to the Backward Euler method in each local Newton-Raphson step. In this regard, it is interesting to note that the requirement $\det(\boldsymbol{C}_p) = 1$ in terms of logarithmic strains

[14] Arghavani, Auricchio, Naghdabadi and Reali [2011]; Arghavani, Auricchio and Naghdabadi [2011] proposed a modification of the exponential map integrator based on the logarithm, which seems to be an improvement from a computational point of view.

is equivalent to $\mathrm{tr}\,(\boldsymbol{\varepsilon}_p) = 0$, as pointed out in Appendix 3.8.9. As will be seen, the Backward Euler scheme directly ensures this requirement without any further modifications.
All the evolution equations are discretized within the time interval $t \in [t_n, t_{n+1}]$ and are solved using a fully implicit scheme. Using the Backward Euler scheme for the evolution equations associated with plasticity, the following discretized formulas are obtained

$$\boldsymbol{\varepsilon}_p = \boldsymbol{\varepsilon}_{p_n} + \Delta\gamma_p \frac{3}{\sqrt{12\tilde{J}_2}}\, \mathbb{M}^{-1} : \mathrm{dev}\left(\tilde{\boldsymbol{T}} - \tilde{\boldsymbol{X}}\right), \quad \kappa_p = \kappa_{p_n} + \frac{\Delta\gamma_p}{f_d}. \tag{3.72}$$

Note that the index $n+1$ indicating values at time t_{n+1} is omitted. Both in the absence of damage and in case of isotropic damage, it becomes evident that Equation $(3.72)_1$ preserves the volume, since $\mathbb{M}$ is proportional to the fourth order symmetric identity tensor and so its inverse. In Appendix 3.8.6 it is shown that also the product $\mathbb{M}^{-1} : \mathrm{dev}\left(\tilde{\boldsymbol{T}} - \tilde{\boldsymbol{X}}\right)$ yields a deviatoric tensor in case of anisotropic damage, so that for a general elasto-plastic-damage loading step the plastic volume is preserved. The evolution equations for damage are discretized accordingly (under consideration of Remark 9)

$$\boldsymbol{D}_r = \boldsymbol{D}_{r_n} + \Delta\gamma_d \frac{3}{2}\frac{1}{Y_0 - R_d}\left(\mathbb{P}_+ : \mathbb{A}_d : \boldsymbol{Y}_+ + \boldsymbol{Y}_+ : \mathbb{A}_d : \mathbb{P}_+\right), \quad \kappa_d = \kappa_{d_n} + \Delta\gamma_d. \tag{3.73}$$

In the evolution equations for both plasticity $\Delta\gamma_p := \Delta t\ \dot{\gamma}_{p_{n+1}}$ and damage $\Delta\gamma_d := \Delta t\ \dot{\gamma}_{d_{n+1}}$ denote the individual incremental multipliers with time increment Δt.

Remark 14. *The evolution equations for κ_p $(3.72)_2$ and κ_d $(3.73)_2$ do not have to be treated as additional variables within the nonlinear system of equations at the material point level. Both can be obtained based on their converged values from the last step, the incremental multipliers and $\boldsymbol{D}_r$.*

3.5.3 Possible loading scenarios and corresponding residuals at the integration point level

On a material point level, more precisely on an integration point level, four different loading scenarios have to be distinguished: (i) elastic loading/unloading, (ii) elasto-plastic loading, (iii) elastic-damage loading and (iv) elasto-plastic-damage loading. Based on the KKT conditions, the restrictions for the onset criteria as well as the (incremental) multipliers are summarized in Table 3.1. For the identification of the active inelastic phenomena, a classical trial step procedure in combination with a active-set search strategy similar to multi-surface plasticity

(see e.g. Simo and Hughes [2006]) is followed[15,16].

Table 3.1: Possible loading/unloading scenarios at the integration point level

Loading scenarios	Multiplier		Onset criteria		Active residuals
	plasticity	damage	plasticity	damage	
elastic loading/unloading	$\Delta\gamma_p = 0$	$\Delta\gamma_d = 0$	$\Phi_p \leq 0$	$\Phi_d \leq 0$	-
elasto-plastic loading	$\Delta\gamma_p > 0$	$\Delta\gamma_d = 0$	$\Phi_p = 0$	$\Phi_d \leq 0$	r_1, $\boldsymbol{R}_2$
elastic-damage loading	$\Delta\gamma_p = 0$	$\Delta\gamma_d > 0$	$\Phi_p \leq 0$	$\Phi_d = 0$	r_3, $\boldsymbol{R}_4$
elasto-plastic-damage loading	$\Delta\gamma_p > 0$	$\Delta\gamma_d > 0$	$\Phi_p = 0$	$\Phi_d = 0$	r_1, $\boldsymbol{R}_2$, r_3, $\boldsymbol{R}_4$

Taking into account Equations (3.27), $(3.72)_1$, (3.30) and $(3.73)_1$ the full set of residual equations is defined as follows

$$\underbrace{\begin{pmatrix} r_1 \\ \boldsymbol{R}_2 \\ r_3 \\ \boldsymbol{R}_4 \end{pmatrix}}_{=:\mathbf{r}_{loc}} \coloneqq \begin{pmatrix} \sqrt{3\tilde{J}_2} - (\sigma_{y0} - \tilde{R}_p) \\ \boldsymbol{\varepsilon}_p - \boldsymbol{\varepsilon}_{p_n} - \Delta\gamma_p \, 3 \, \mathbb{M}^{-1} : \operatorname{dev}\left(\tilde{\boldsymbol{T}} - \tilde{\boldsymbol{X}}\right) / \sqrt{12\tilde{J}_2} \\ 3 \, \boldsymbol{Y}_+ : \mathbb{A}_d : \boldsymbol{Y}_+ - (Y_0 - R_d)^2 \\ \boldsymbol{D}_r - \boldsymbol{D}_{r_n} - \Delta\gamma_d \, 3 \, \left(\mathbb{P}_+ : \mathbb{A}_d : \boldsymbol{Y}_+ + \boldsymbol{Y}_+ : \mathbb{A}_d : \mathbb{P}_+\right) / (2(Y_0 - R_d)) \end{pmatrix} = \begin{pmatrix} 0 \\ \mathbf{0} \\ 0 \\ \mathbf{0} \end{pmatrix} \tag{3.74}$$

In addition, considering the symmetry of both $\boldsymbol{\varepsilon}_p$ and $\boldsymbol{D}_r$ the residual reduces to fourteen equations in the most complex case of elasto-plastic-damage loading. The set of updated unknowns during the iterative solution procedure is $\mathbf{x}_{loc} \coloneqq (\Delta\gamma_p \; \hat{\boldsymbol{\varepsilon}}_p \; \Delta\gamma_d \; \hat{\boldsymbol{D}}_r)^T$. In order to compute the Jacobian $\mathbf{J}_{loc} \coloneqq \partial\hat{\mathbf{r}}_{loc}/\partial\mathbf{x}_{loc}$ for the local iteration, the algorithmic differentiation software package *AceGen* is utilized (Korelc [2002], Korelc and Wriggers [2016]).

Remark 15. *In the local residual system of equations* (3.74)*, the residual for the damage criterion r_3 is different from Φ_d in Equation* (3.30)*. The reason for this is similar to the argumentation within Remark 9. Although setting $r_3 = \Phi_d$ would not result in any numerical problems, the Jacobian $\mathbf{J}_{loc}$ contains a division by zero if $\boldsymbol{Y}_+$ is equal to the zero tensor. To circumvent this issue, the form for r_3 provided in* (3.74) *is used, which results in the same solution for the unknowns.*

3.5.4 Algorithmic consistent tangent operators

The material moduli introduced in Equations (3.57) and (3.58) need to be computed with the same accuracy as the Jacobian $\mathbf{J}_{loc}$ in order to achieve quadratic convergence on a global level

[15] As investigated in detail e.g. by Brepols et al. [2017], a Fischer-Burmeister approach could be utilized alternatively, which has several advantages and disadvantages compared to the active-set search.

[16] In contrast to multi-surface plasticity, in the present case each multiplier describes a different phenomenon.

during the iterative solution procedure. These tangents have to be 'algorithmically consistent' with the chosen time integration algorithm, i.e. the Backward Euler method. However, since the material model is formulated in the logarithmic strain space, the Lagrangian derivatives cannot be obtained directly. Instead, first their logarithmic counterparts are computed and then transformed to the tangents (3.57)-(3.58) with the help of the formulas provided in Appendix 3.8.11. Therefore, the following tangent moduli are introduced in analogy to (3.57)-(3.58)

$$\mathbb{C}^{LOG} := \left.\frac{\partial \boldsymbol{T}}{\partial \boldsymbol{\varepsilon}}\right|_{\bar{\mathbf{d}}} = \left.\frac{\partial \boldsymbol{T}}{\partial \boldsymbol{\varepsilon}}\right|_{\substack{\boldsymbol{\varepsilon}_p \\ \boldsymbol{D}_r}} + \left.\frac{\partial \boldsymbol{T}}{\partial \boldsymbol{\varepsilon}_p}\right|_{\substack{\boldsymbol{\varepsilon} \\ \boldsymbol{D}_r}} : \left.\frac{\partial \boldsymbol{\varepsilon}_p}{\partial \boldsymbol{\varepsilon}}\right|_{\bar{\mathbf{d}}} + \left.\frac{\partial \boldsymbol{T}}{\partial \boldsymbol{D}_r}\right|_{\substack{\boldsymbol{\varepsilon} \\ \boldsymbol{\varepsilon}_p}} : \left.\frac{\partial \boldsymbol{D}_r}{\partial \boldsymbol{\varepsilon}}\right|_{\bar{\mathbf{d}}} \tag{3.75}$$

$$\mathscr{K}_{\bar{d}}^{LOG} := \left.\frac{\partial \boldsymbol{T}}{\partial \bar{\mathbf{d}}}\right|_{\boldsymbol{\varepsilon}} = \left.\frac{\partial \boldsymbol{T}}{\partial \boldsymbol{\varepsilon}_p}\right|_{\substack{\boldsymbol{\varepsilon} \\ \boldsymbol{D}_r}} : \left.\frac{\partial \boldsymbol{\varepsilon}_p}{\partial \bar{\mathbf{d}}}\right|_{\boldsymbol{\varepsilon}} + \left.\frac{\partial \boldsymbol{T}}{\partial \boldsymbol{D}_r}\right|_{\substack{\boldsymbol{\varepsilon} \\ \boldsymbol{\varepsilon}_p}} : \left.\frac{\partial \boldsymbol{D}_r}{\partial \bar{\mathbf{d}}}\right|_{\boldsymbol{\varepsilon}} \tag{3.76}$$

$$\mathscr{G}_{u}^{LOG} := \left.\frac{\partial \mathbf{d}}{\partial \boldsymbol{\varepsilon}}\right|_{\bar{\mathbf{d}}} = \frac{\partial \mathbf{d}}{\partial \boldsymbol{D}_r} : \left.\frac{\partial \boldsymbol{D}_r}{\partial \boldsymbol{\varepsilon}}\right|_{\bar{\mathbf{d}}} \tag{3.77}$$

$$\mathbf{G}_{\bar{d}}^{LOG} := \left.\frac{\partial \mathbf{d}}{\partial \bar{\mathbf{d}}}\right|_{\boldsymbol{\varepsilon}} = \frac{\partial \mathbf{d}}{\partial \boldsymbol{D}_r} : \left.\frac{\partial \boldsymbol{D}_r}{\partial \bar{\mathbf{d}}}\right|_{\boldsymbol{\varepsilon}} \tag{3.78}$$

Again, all partial derivatives of the constitutively dependent variable $\boldsymbol{T}$ are obtained with the help of *AceGen*. Since $\mathbf{d}$ depends only on $\mathcal{E}(\boldsymbol{D}_r)$, the partial derivatives are given in closed-form as

$$\frac{\partial d_1}{\partial \boldsymbol{D}_r} = \boldsymbol{I}, \qquad \frac{\partial d_2}{\partial \boldsymbol{D}_r} = 2\boldsymbol{D}_r, \qquad \frac{\partial d_3}{\partial \boldsymbol{D}_r} = 3\boldsymbol{D}_r^2. \tag{3.79}$$

It remains to compute the partial derivatives of the internal variables with respect to the 'global' ones. Therefore, and on the basis of the implicit function theorem[17], the following can be concluded

$$\frac{\partial \mathbf{x}_{loc}}{\partial \mathbf{x}_{glo}} = -\mathbf{J}_{loc}^{-1} \left.\frac{\partial \hat{\mathbf{r}}_{loc}}{\partial \mathbf{x}_{glo}}\right|_{\mathbf{x}_{loc}} \tag{3.80}$$

where $\mathbf{x}_{glo} := (\hat{\boldsymbol{\varepsilon}}\ \bar{\mathbf{d}})^T$ contains the 'global' nine variables (taking the symmetry of $\boldsymbol{\varepsilon}$ into account). The additional partial derivative of the residual on the right hand side is computed using *AceGen*. From the solution of the system of equations (3.80), the desired derivatives can be obtained by the corresponding submatrices.

Once the tangent moduli (3.75)-(3.78) are obtained, they have to be transformed to their Lagrangian counterparts. Considering the derivation presented in Appendix 3.8.11, the following

[17] In the current context, the implicit function theorem is expressed by $\mathbf{r}_{loc}(\mathbf{x}_{glo}, \mathbf{x}_{loc}(\mathbf{x}_{glo})) = \mathbf{0}$.

transformation relations hold between the logarithmic and Lagrangian tangent moduli

$$\mathbb{C} = \mathbb{Q} : \mathbb{C}^{LOG} : \mathbb{Q} + \boldsymbol{T} : \overset{6}{\mathbb{L}}, \qquad \mathscr{K}_{\bar{d}} = \mathbb{Q} : \mathscr{K}_{\bar{d}}^{LOG} \tag{3.81}$$

$$\mathscr{G}_u = \frac{\mathbf{d}}{\partial \boldsymbol{\varepsilon}}\bigg|_{\bar{\mathbf{d}}} : \frac{\partial \boldsymbol{\varepsilon}}{\partial \boldsymbol{E}} = \mathscr{G}_u^{LOG} : \mathbb{Q}, \quad \mathbf{G}_{\bar{d}} = \mathbf{G}_{\bar{d}}^{LOG} \tag{3.82}$$

where the major symmetry of $\mathbb{Q} \coloneqq (2\partial\boldsymbol{\varepsilon}/\partial\boldsymbol{C})$ is exploited. Further, it is important to note that the second Piola-Kirchhoff stress tensor is obtained by $\boldsymbol{S} = \boldsymbol{T} : \mathbb{Q}$, while no transformation is required for $\mathbf{d}$. With these transformation relations at hand, the finite element equations in Section 3.5.1 can be computed. Moreover, a pseudo-code of the numerical implementation is presented in Appendix 3.8.12.

3.6 Numerical examples

In the following, several numerical examples examine both the (local) material model itself as well as its behavior on a structural level with the proposed gradient-extension. Due to a current lack of experimental data, the material parameters are chosen in accordance to Brepols et al. [2020] and are summarized in Table 3.2. For simplicity, the gradient-extension parameters A_i and H_i are chosen to be the same for all studies. The material model as well as the element routine were implemented into the finite element software package *FEAP* (Taylor [2020]), where the commercial software tool *HyperMesh* and the open-source software *ParaView* (Ahrens et al. [2005]) were used for meshing and visualization of the structural examples, respectively.

3.6.1 Single element studies

In order to investigate the pure material response of this complex material model, several 3D and 2D single element studies, with an edge length of one millimeter, are performed. To avoid any influence resulting from gradient-extension, the material parameters A_i and H_i are set to zero and, additionally, the corresponding degrees of freedom for nonlocal damage are restrained. The material parameters correspond to 'set 1' in Table 3.2.

3.6.1.1 Ductile damage under uniaxial tension

This first example is concerned with the interaction between plasticity and isotropic ($\vartheta = 0$) as well as anisotropic damage ($\vartheta = 1$), respectively. For this purpose, a single 3D element

Table 3.2: Material parameter sets

Symbol	Material Parameter	set 1	set 2	Unit	Eq.
μ_e	Elastic shear modulus	7500	55000	MPa	(3.37)
K_e	Elastic bulk modulus	10000	$61666.\overline{6}$	MPa	(3.37)
ϑ	Anisotropy parameter	0.0-1.0	0.0/1.0	-	(3.37)
μ_p	1st kinematic hardening parameter	12.5	62.5	MPa	(3.39)
K_p	2nd kinematic hardening parameter	0	0	MPa	(3.39)
r_p	1st isotropic hardening parameter	12.5	125	MPa	(3.39)
s_p	2nd isotropic hardening parameter	8.5	5	-	(3.39)
σ_{y0}	Initial yield stress	20	100	MPa	(3.27)
e_d	Isotropic damage exponent	1	1	-	(3.38)
H_d	Linear damage hardening parameter	0.1	1	MPa	(3.40)
r_d	1st nonlinear damage hardening parameter	0	5	MPa	(3.40)
s_d	2nd nonlinear damage hardening parameter	0	100	-	(3.40)
K_h	Additional hardening parameter	1	0.1	MPa	(3.41)
n_d	Additional hardening exponent	2	2	-	(3.41)
a_d	Taylor series coefficient	0.999999	0.9999999	-	App. 3.8.7
c_d	Extended damage criterion	0	1	-	(3.31)
Y_0	Initial damage threshold	0.1/10	2.5	MPa	(3.30)
A_i	Internal length scale parameters	0	100/75	MPa mm^2	(3.42)
H_i	Penalty parameters	0	$10^4/10^5$	MPa	(3.42)

is subjected to uniaxial loading. The resulting force-displacement curves in loading direction for two different values of the initial damage threshold $Y_0 = \{0.1, 10\}$ [MPa] are shown in Figure 3.1a. Due to the loading applied, no shear terms are present for $\boldsymbol{D}_r$.
In case of $Y_0 = 0.1$ [MPa], there is hardly any difference visible between isotropic and anisotropic damage in Figure 3.1a, both with regard to the onset of damage and to the overall degradation. However, the rate of the (anisotropic) damage component in loading direction (D_{r_1}) is higher than for the isotropic version (D), while the rates of the other damage components corresponding to the perpendicular loading directions (D_{r_2}, D_{r_3}) are lower (Figure 3.1b). In contrast, a clear difference between the onset of damage and degradation becomes evident for $Y_0 = 10$ [MPa], while the same behavior for the damage rates as before is observed. Although a difference espcially in damage onset may seem counterintuitive for a virgin material, the reason for this lies in the different expressions between the isotropic and anisotropic versions of the damage driving forces $\boldsymbol{Y}_e$ (3.48) and $\boldsymbol{Y}_p$ (3.49). Due to these differences, the criterion of damage onset is reached 'earlier'.

Additionally, an effect due to finite strains can be recognized in Figure 3.1a. In contrast to a geometrically linear framework, the decreasing stiffness in a geometrically nonlinear framework can be caused not only by material softening, but is also influenced by the change

in cross section. This phenomenon is known as 'geometrical softening'. As a result, onset of damage or beginning of strong degradation may not necessarily coincide with reaching the maximum force, as is also the case in Figure 3.1a.

The influence of anisotropy parameter ϑ on the damage tensor's main components is studied in Figure 3.2. Increasing the anisotropy parameter, meaning that the damaged material behaves 'more anisotropic', the rates and values between these components differ more strongly. Choosing $\vartheta = 0$ leads to the very same evolution of each component, which is a natural requirement for isotropic damage.

3.6.1.2 Ductile damage under plane stretch and shearing

The second example investigates the material under shear loading, which, in general, results in an evolution of shear damage components in the case of anisotropic damage. However, since a 'fully broken' state corresponds to $\boldsymbol{D}_r = \boldsymbol{I}$, these shear terms must vanish with increasing loading. Moreover, the damage driving forces $\boldsymbol{Y}_e$ (3.48) and $\boldsymbol{Y}_p$ (3.49) are generally independent of $\boldsymbol{D}_r$, which could lead to an unphysical increase of $\boldsymbol{D}_r$ ($\boldsymbol{D}_r > \boldsymbol{I}$) even in a fully broken material. These latter effects are cured by the hardening force $\boldsymbol{Y}_h$ (3.50) and are demonstrated in the following. For this purpose, the deformation gradient acting on a single element is prescribed as

$$\boldsymbol{F} = \begin{pmatrix} 1+\omega & 0 & 0 \\ \omega & 1 & 0 \\ 0 & 0 & 1 \end{pmatrix} \boldsymbol{e}_i \otimes \boldsymbol{e}_j \tag{3.83}$$

with the stretch parameter ω and an initial damage threshold $Y_0 = 10$ [MPa]. For simplicity, a plane strain 2D element in the $\boldsymbol{e}_1$-$\boldsymbol{e}_2$-plane is used.
Figure 3.3 depicts the damage evolution of the main diagonal components $D_{r_{11}}$, $D_{r_{22}}$, and $D_{r_{33}}$ as well as the off-diagonal component $D_{r_{12}}$. All other shear components are zero during the entire loading. Both effects addressed above can be nicely observed. On the one hand, the shear component reaches its maximum with increasing main diagonal components, but tends to zero in further progress, i.e. $\boldsymbol{D}_r = \boldsymbol{I}$ is accomplished. On the other hand, an undesired and unphysical increase of the damage tensor after the material lost its stiffness is not observed. Without taking $\boldsymbol{Y}_h$ into account, these latter two behaviors would not be achieved, at least not without additional modifications[18].

[18] For instance, if c_d in $\mathbb{A}_d$ (3.31) is unequal to zero, the latter effect is also achieved. However, the choice for $\mathbb{A}$ in Equation (3.31) does not ensure a decrease in the shear components.

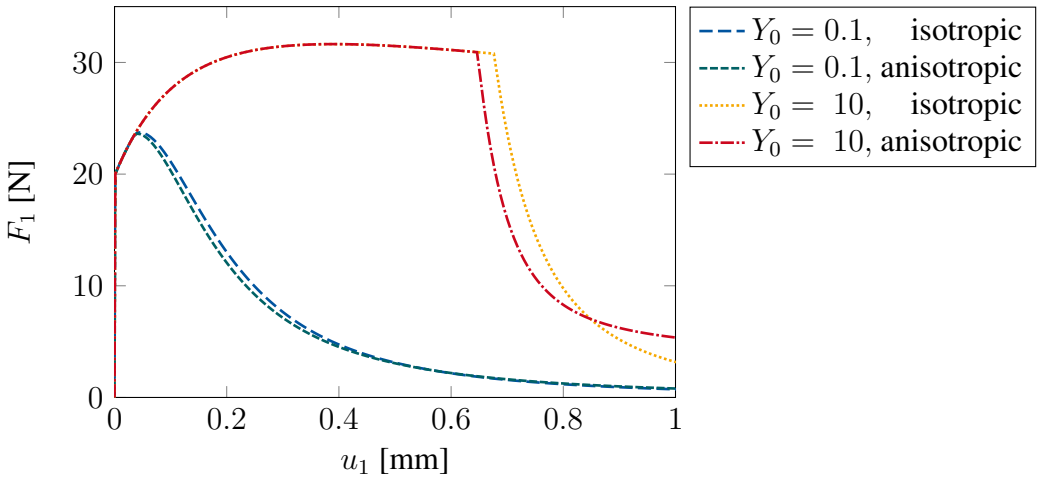

(a) Force-displacement curves

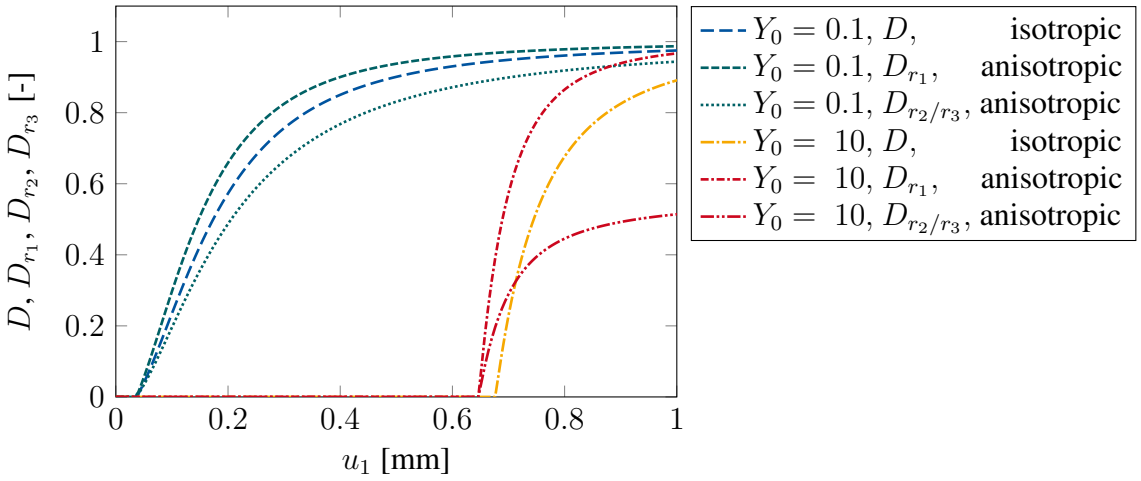

(b) Damage-displacement curves

Figure 3.1: Comparison between isotropic ($\vartheta = 0$) and anisotropic ($\vartheta = 1$) ductile damage for different damage thresholds Y_0 under uniaxial loading in $\boldsymbol{e}_1$-direction. In case of anisotropic damage, $\boldsymbol{D}_r$ is diagonal with equal components in $\boldsymbol{e}_2$- and $\boldsymbol{e}_3$-direction ($D_{r_2} = D_{r_3}$). For isotropic damage, $\boldsymbol{D}_r$ is spherical, i.e. $\boldsymbol{D}_r = D\boldsymbol{I}$.

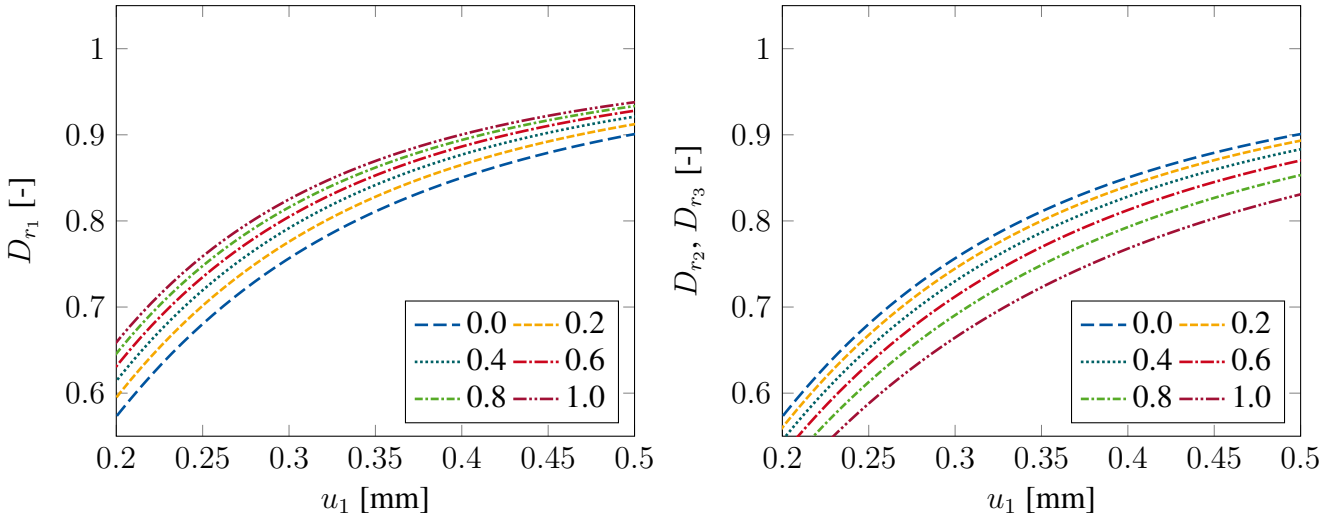

(a) Damage in $\boldsymbol{e}_1$-direction

(b) Damage in $\boldsymbol{e}_2$- and $\boldsymbol{e}_3$-direction

Figure 3.2: Influence of anisotropy parameter ϑ on damage evolution D_{r_1} in $\boldsymbol{e}_1$-direction (loading direction) and D_{r_2}, D_{r_3} ($D_{r_2} = D_{r_3}$) in $\boldsymbol{e}_2$- and $\boldsymbol{e}_3$-direction with damage threshold $Y_0 = 0.1$ [MPa]. For $\vartheta = 0$, the behavior is isotropic, i.e. $D_{r_1} = D_{r_2} = D_{r_3}$.

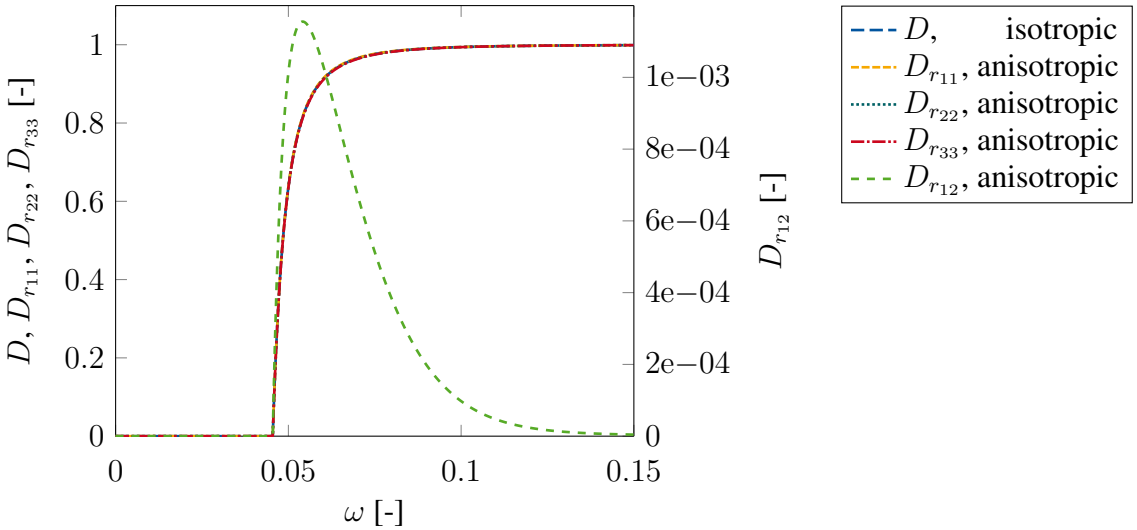

Figure 3.3: Evolution of damage components for stretch in $\boldsymbol{e}_1$-direction combined with shearing in $\boldsymbol{e}_1$-$\boldsymbol{e}_2$-plane for increasing stretch parameter ω in $\boldsymbol{F}$ (3.83) and damage threshold $Y_0 = 10$ [MPa]. After ω reaches 0.05 [-], the off-diagonal component $D_{r_{12}}$ tends to zero with increasing main diagonal components ($D_{r_{13}} = D_{r_{23}} = 0$). Isotropic damage ($D$) is shown for comparison.

3.6.1.3 Brittle damage under alternating loading direction

The last single 3D element study serves to illustrate the meaning of induced anisotropy on an initially isotropic material. For this purpose, the plastic yield stress is set to (nearly) infinity and a damage threshold $Y_0 = 0.1$ [MPa] is used. Consequently, and because of the resulting absence of plastic strains, the kinematics can be considered 'exact' since no additive split is assumed.
The displacements are prescribed as shown in Figure 3.4. The loading in each spatial direction is increased until all damage components reach the same value, here 0.985 (Figure 3.5b). Noteworthy, in order to achieve this requirement, different maximal displacement values must be prescribed in the present study. In addition, due to the uniaxial boundary conditions applied during each loading/unloading phase, no shear damage components evolve.

The resulting force-displacement curves in each direction are depicted in Figure 3.5a, while the damage evolution corresponding to the time points in Figure 3.4 are shown in Figure 3.5b. For a better understanding of induced anisotropy and its influence on the material, the isotropic case is briefly discussed. Therefore, ϑ is set to zero and the 3D element is loaded by the same loading program as shown in Figure 3.4. During the first loading/unloading phase, the damage threshold is exceeded, and thus, damage occurs. During reloading in the second phase, the reloading stiffness is the very same as the unloading stiffness during the first phase. Noteworthy, since u_2^{max} is less than u_1^{max}, degradation of the material does not further increase during the second loading phase. In the third loading phase, the same behavior with regard to the reloading stiffness is observed, but unlike the second loading phase, u_3^{max} is higher compared to u_1^{max} leading to further degradation. The fact that the reloading stiffness is always the same as the previous unloading stiffness illustrates the direction-independent behavior of an isotropically damaged material.

Contrary to the isotropic case, the anisotropic model ($\vartheta = 1$) depends on a specific direction. On the one hand, damage does not only occur when the displacement in the subsequent loading phase is higher than the previous one. An effect that can be explained by induced anisotropy, since anisotropic behavior generally changes the transversal elongation of the material and, thus, the damage driving force $\boldsymbol{Y}_e$ (3.48) is different in each loading phase. On the other hand, the reloading stiffness is higher compared to the previous one after the loading displacement direction is altered. Considering the damage rates and evolutions of the first example (Section 3.6.1.1), it is easier to understand the directional manner. Since the damage component (e.g. D_{r_1} for the first loading phase) corresponding to the spatial direc-

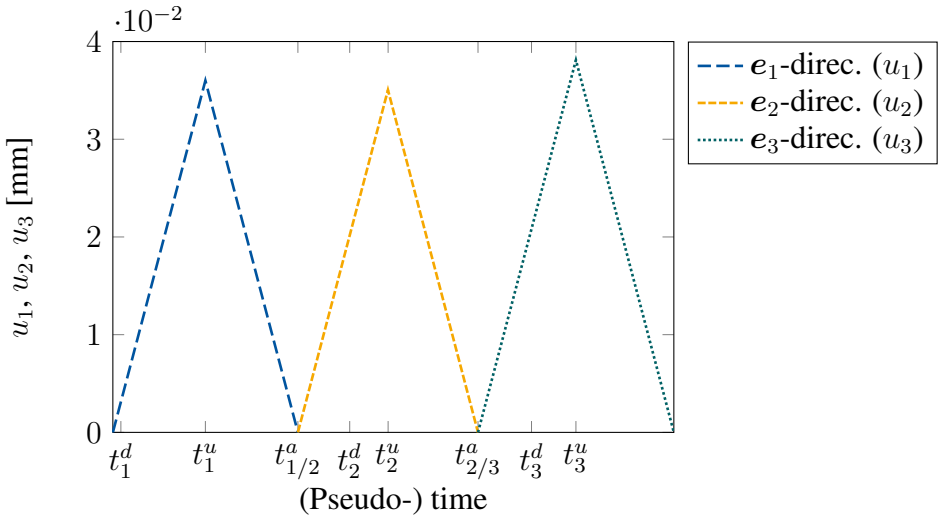

Figure 3.4: Prescribed displacements in each spatial direction until $D_{r_1} = D_{r_2} = D_{r_3} \approx 0.985$ [-] is reached (cf. Figure 3.5b). Thus, the maximum prescribed displacements are $u_1^{max} = 0.036$ [mm], $u_2^{\max} = 0.0354$ [mm], $u_3^{\max} = 0.0381$ [mm]. The time points correspond to t_i^d: Initiation of (anisotropic) damage (cf. Figure 3.5b), t_i^a: Alter uniaxial displacement loading direction, t_i^u: Unloading.

tion (u_1) increases under uniaxial loading at a higher rate than the other components (D_{r_2}, D_{r_3}) - which was demonstrated in the first example - the stiffness associated with this very direction is degraded the most. Thus, the reloading stiffness in another direction is less reduced.

In addition to these discrepancies, a significant higher load is reached for the isotropic version compared to the anisotropic one during the first loading phase. Reasons given for this are that (isotropic) damage occurs later under the applied loading (cf. Section 3.6.1.1) and further that κ_d evolves differently. In the present study, the latter results in more pronounced damage hardening and consequently a higher maximum force is gained in case of isotropic damage.

3.6.2 Structural examples

In the following, the proposed material model is investigated on a structural level. In particular, the ability of the invariant-based regularization to predict mesh-independent results is studied. For simplicity, 2D plane strain problems are considered using quadrilateral elements. The material parameters correspond to ‘set 2’ from Table 3.2 for all structural examples.

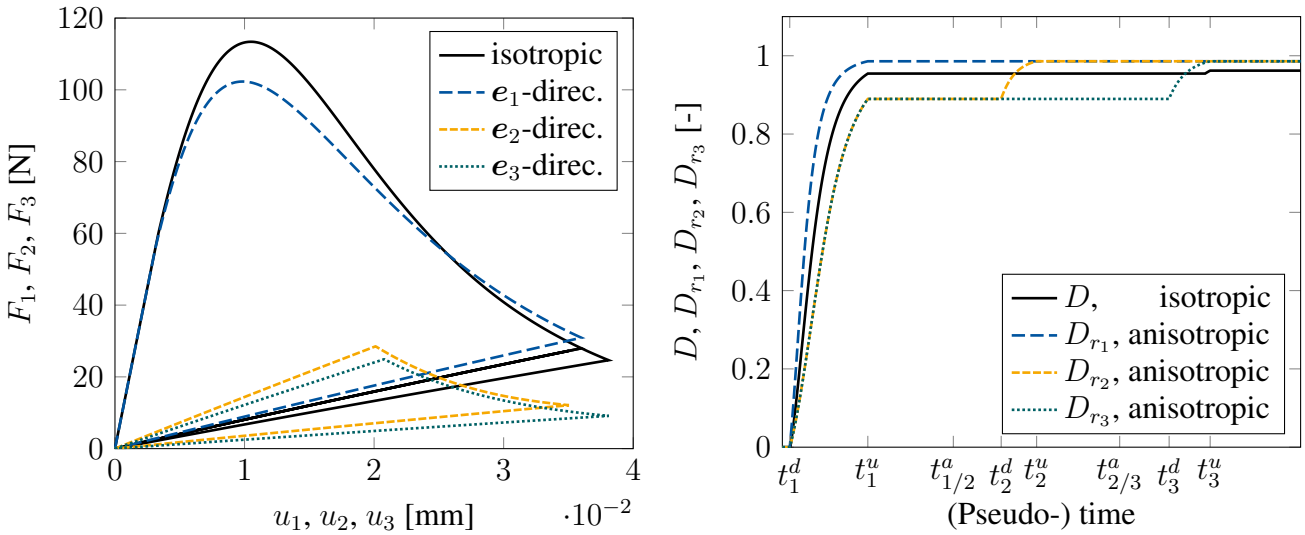

(a) Force-displacement curves

(b) Damage-time curves

Figure 3.5: Material response of anisotropic brittle damage in each spatial direction subjected to the loading in Figure 3.4 with damage threshold $Y_0 = 0.1$ [MPa]. Isotropic damage behavior obtained for the same loading is shown, in addition.

3.6.2.1 Asymmetrically notched specimen (brittle damage, monotonic loading)

The first structural example deals with an asymmetrically notched specimen undergoing monotonic loading in $\boldsymbol{e}_1$-direction. The main purpose is to prove that mesh-independent results are achieved by the proposed gradient-extension and further that mesh convergence is gained also for complex and shear dominated deformations. To exclude any influence of plasticity on the regularization, the material is considered 'brittle' for the time being, i.e. $\sigma_{y0} \to \infty$, and furthermore, the micromorphic moduli are set to $A_i = 100$ [MPa mm^2] and $H_i = 10^4$ [MPa]. The particular boundary value problem and geometry are taken from Brepols et al. [2017] and are depicted in Figure 3.6. The left edge is considered clamped, while the right edge is loaded by a single force in the middle and is also constrained to remain perpendicular to the load. However, the edge is allowed to deform perpendicular to the load.

Mesh refinement using 1624, 3592, 6651, 9667, 12704 and 13955 finite elements is mainly performed in the green highlighted area in Figure 3.6. The coarsest as well as the finest mesh are shown in Figure 3.7. The obtained force-displacement curves for the different meshes are shown in Figure 3.8 and are normalized to the maximum achieved load by the finest mesh. During degradation, severe snap-back behavior becomes visible. In order to follow the quasi-static solution path, an arc-length controlled solution procedure is utilized. Nevertheless, mesh

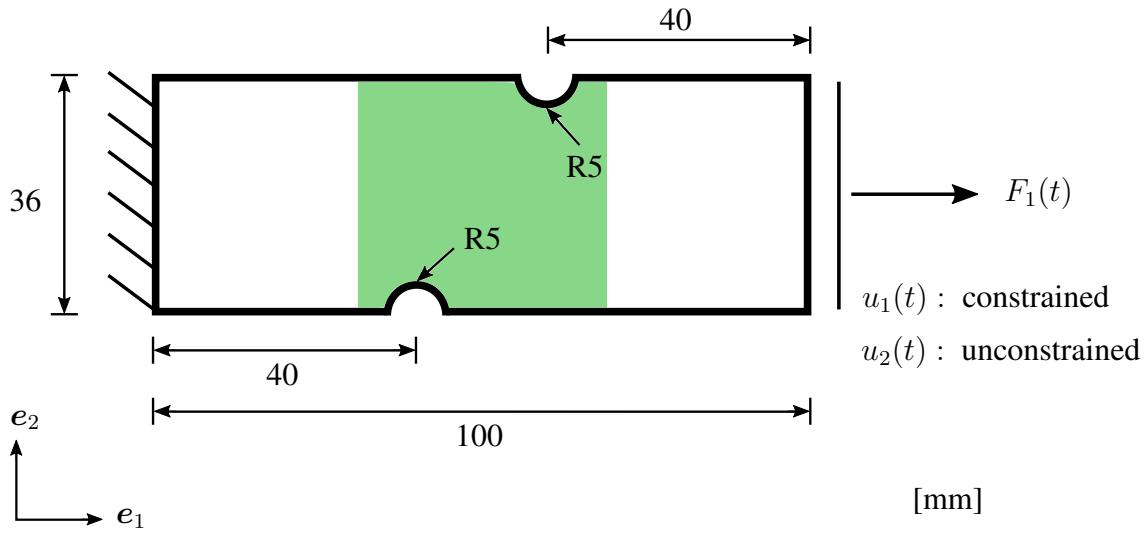

Figure 3.6: Geometry and boundary value problem. Left edge is completely fixed, right edge is loaded by a single force and is enforced to stay straight and perpendicular to the force. The green highlight indicates the area of mesh refinement. The thickness is one millimeter.

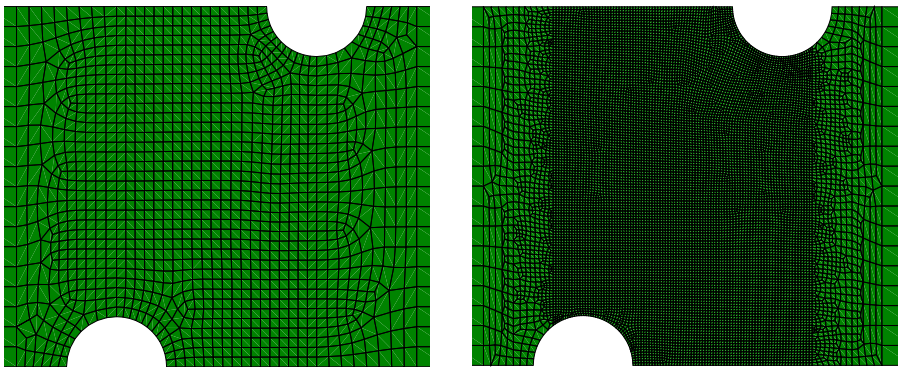

Figure 3.7: Mesh with 1624 (left) and 13955 finite elements (right). The area of refinement including mesh transition coincides with the green highlight in Figure 3.6.

convergence towards a solution with a finite amount of energy dissipation for decreasing mesh size is clearly visible. Thus, the ability of the proposed method to achieve mesh-independent results, also for complex solution paths, is well demonstrated.

In contrast to the degradation during snap-back, where most of material's integrity loss arises, the following degradation rate is slow. To explain this effect, a closer look at $D_{r_{33}}$ is needed. Although the contour plot of $D_{r_{33}}$ looks qualitatively the same as $D_{r_{11}}$ and $D_{r_{22}}$ in Figure 3.9 (not shown here), due to the plane strain conditions its evolution is quite slower. Having in mind that the volumetric response of $\boldsymbol{T}$ is influenced by a scalar degradation function f_d, which

is only zero if $\boldsymbol{D}_r = \boldsymbol{I}$, the stress component T_{11} is not necessarily zero even if $D_{r_{11}}$ tends to one. Thus, the remaining stiffness and the slow degradation can be explained. Nevertheless, the remaining force is about seven percent of the maximum force at $u_1 = 2$ [mm], which can be macroscopically considered 'fully broken'.

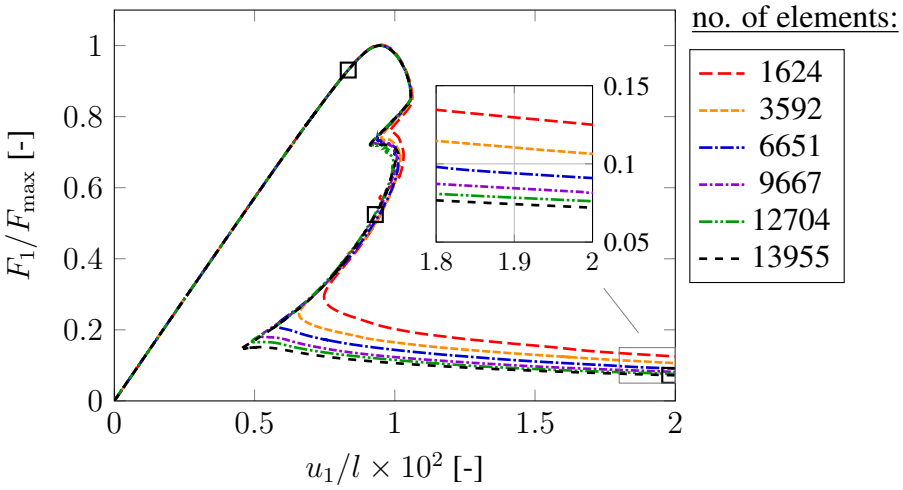

Figure 3.8: Normalized force-displacement curves with maximum load $F_{max} = 37.957$ [kN]. The displacement is normalized to the total length $l = 100$ [mm]. For 13955 elements, the final value is about 0.07 [-]. Black squares indicate three analyzed snaps.

To give the reader a better understanding of the underlying process, three contour snaps at different stages of the simulation, indicated in Figure 3.8, are provided in Figure 3.9. When reaching a certain state of deformation, $D_{r_{11}}$ starts to evolve at the lower notch first and progressively increases towards the upper edge. Right after damage initiation, $D_{r_{22}}$ evolves as well and 'follows' $D_{r_{11}}$, but the damage zone is smaller compared to $D_{r_{11}}$. Due to the asymmetrically arranged notches, the imposed shear band leads to a vertical movement of the right part of the specimen, which in its final broken state (3. snap) is completely separated.

Lastly, Figure 3.10 compares the final damage zones of three exemplary chosen meshes. All zones remain finite and do conform well between the different meshes. No artificial widening of the damage zones can be observed. Hence, the proposed regularization technique is able to control the range of localization and keeps it constant during refinement.

For a better understanding of the stress-strain state, various scalar stress and strain measures are given in Figure 3.11. In line with Voyiadjis et al. [2021], the strain state is described

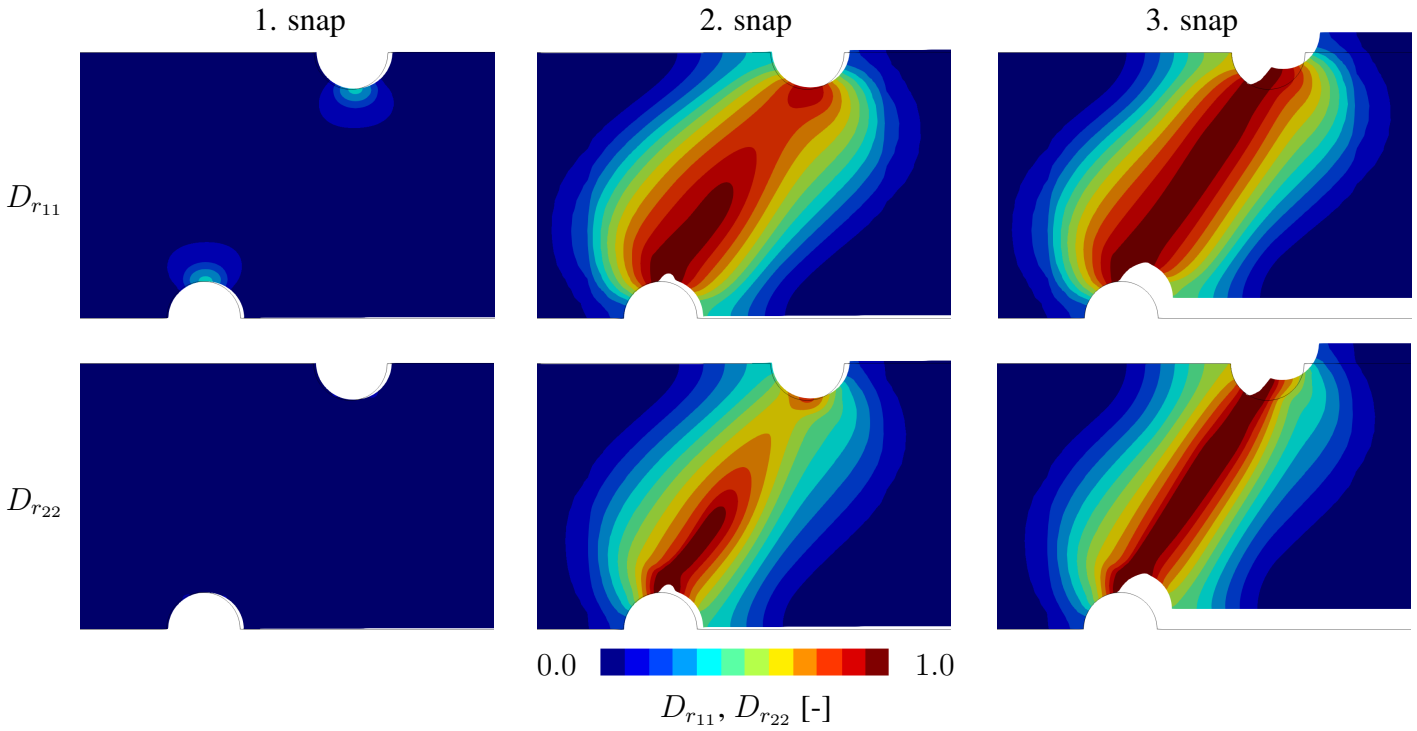

Figure 3.9: Damage contour plots of main diagonal components of $\boldsymbol{D}_r$. The third component $D_{r_{33}}$ behaves qualitatively similar. In Figure 3.8, the snaps are indicated by black squares. The undeformed geometry is illustrated by black lines.

by the effective Green-Lagrange strain $E_{eff} := \sqrt{\frac{2}{3}\mathrm{tr}\,(\boldsymbol{E}^2)}$, while the stress state is represented by several invariants, namely the von Mises stress σ_{eq}, the triaxiality ρ, and the Lode parameter r. All stress invariants are calculated with respect to the Cauchy stress tensor (see Appendix 3.8.13). As expected, the strain localizes in the severely damaged zone, indicating a rather high deformation in this region. Similarly, the von Mises stress at the notches is most pronounced at the first snap and drops to almost zero when the left and right parts are separated. Only at the upper notch, some stress peaks occur. In this context, it is interesting to note that Lode's parameter within the damaged area is minus one, which is contrary to the rest of the specimen. This is due to the negative stress component in the thickness direction (not shown here). The state of triaxiality allows a similar conclusion. Briefly, the transition from damaged to undamaged material is characterized by very high gradients in both the strain and stress contour plots, which can be seen most clearly in the first and second snap, respectively.

Table 3.3 is concerned with the global numerical stability. Shown are the global (normalized) residual norms. At the beginning of damage (1. snap), the convergence rate is perfectly quadratic and converges towards the solution within a few steps. With increasing degradation,

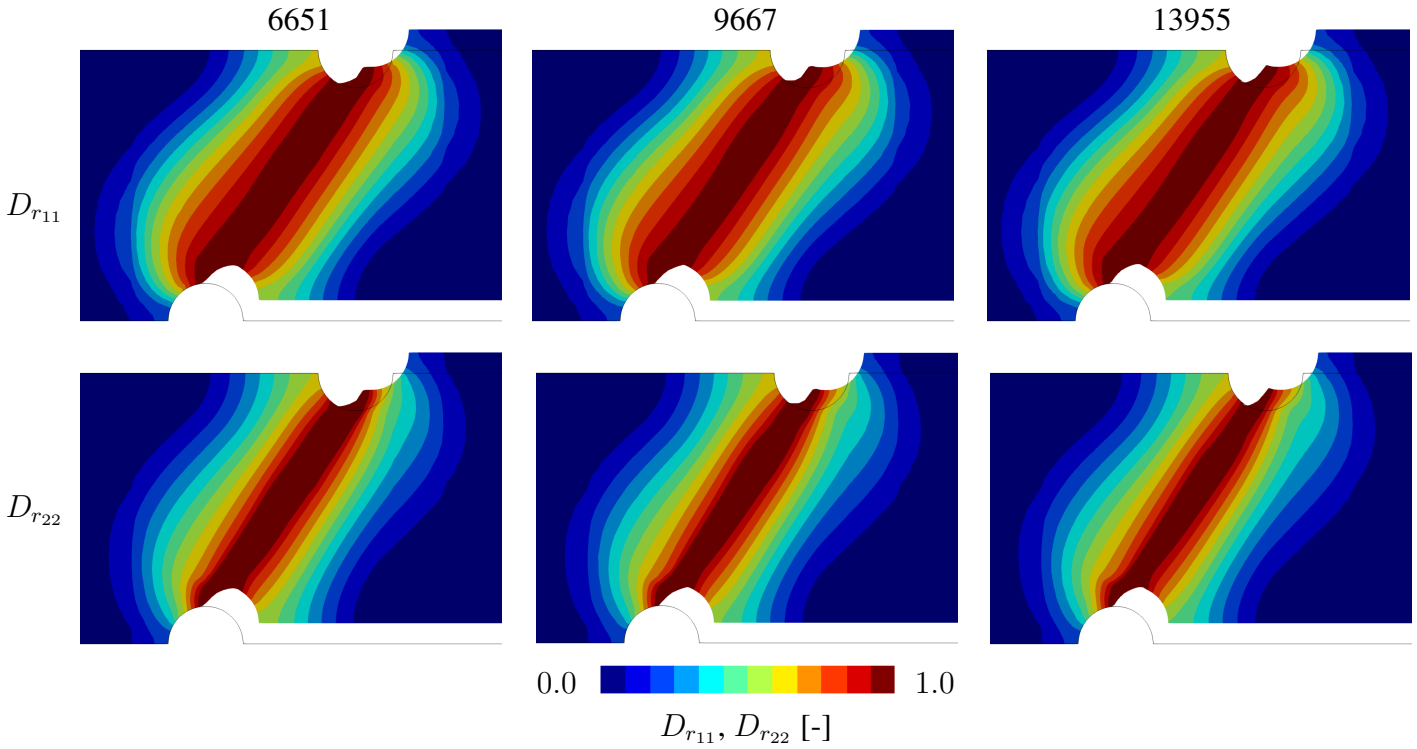

Figure 3.10: Comparison of the width of the final damage zone of $D_{r_{11}}$ and $D_{r_{22}}$ for three exemplary chosen meshes at $u_1 = 2$ [mm]. The width per damage component remains almost constant.

especially when the force-displacement curves are descending, the convergence is quite slower and loses its quadratic rate, even though the tangents are derived in a consistent manner (2. snap). However, similar observations were already reported in the literature, e.g. by Brepols et al. [2020] and Felder et al. [2022]. In addition to this loss of quadratic convergence and the accompanying increase in iterations, quite many restart files were needed during the snap-back. With each restart, the arc-length was adjusted. This high computational effort is only observed for brittle simulations, while ductile simulations do not require an extraordinary number of restart files. After the severe snap-back, the convergence behavior reaches a quadratic rate again, as shown at the end of the simulation (3. snap), which is associated with a much more stable numerical simulation.

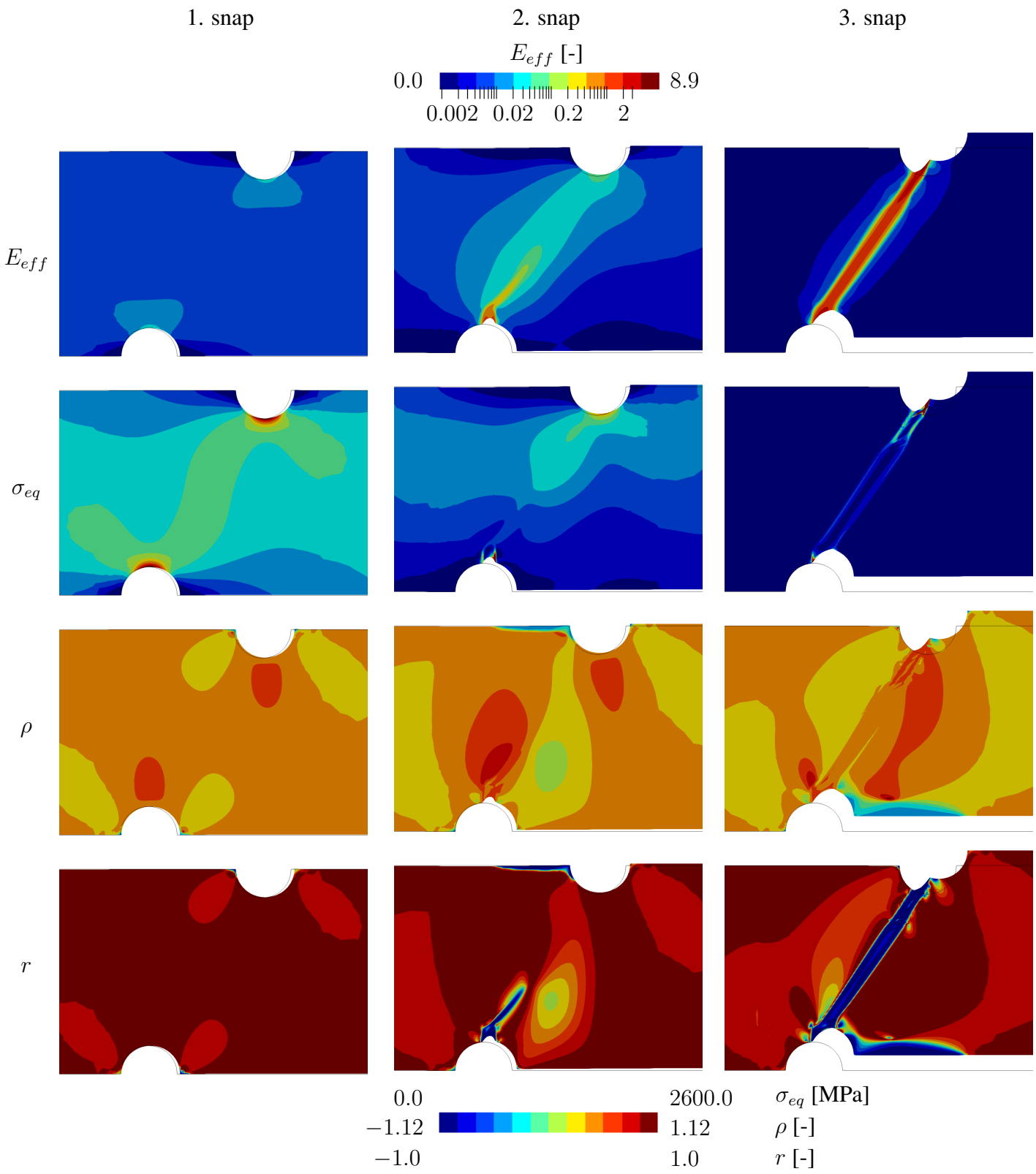

Figure 3.11: Stress-strain states at three different snaps indicated by black squares in Figure 3.8. First column: Effective Green-Lagrange strain E_{eff} (logarithmic scale), second column: Von Mises stress σ_{eq}, third column: Lode parameter r.

Table 3.3: Global convergence rates of the asymmetrically notched specimen at three different snaps. The snaps are indicated by black rectangles in Figure 3.8.

	1. snap		2. snap		3. snap	
iteration	residual	residual (normalized)	residual	residual (normalized)	residual	residual (normalized)
0	1.000E+03	1.000E+00	1.000E+03	1.000E+00	1.000E+03	1.000E+00
1	3.029E-03	3.0298E-06	1.789E-02	1.789E-05	3.527E-01	3.527E-04
2	7.414E-08	7.414E-11	5.313E-05	5.313E-08	7.960E-04	7.960E-07
3	-	-	9.176E-07	9.176E-10	2.403E-08	2.403E-11

3.6.2.2 Tensile specimen with imperfection (ductile damage, monotonic loading)

In contrast to the previous example, the following example takes plasticity also into account. The example's objective is the interaction between plasticity and isotropic/anisotropic damage on a structural level, as well as the ability to still provide mesh-independent results. Therefore, a tensile specimen is investigated, which is subjected to monotonic loading in $\boldsymbol{e}_2$-direction. The boundary value problem is taken from the literature (Ambati et al. [2016]) and was studied by Brepols et al. [2020] as well. However, the these papers did not consider an imperfection in their studies, as shown in Figure 3.12. The reason for the imperfection is that in a previous study without imperfection (not shown here), a nearly horizontal crack which resulted only in a vertical deformation of the specimen. In order to impose a horizontal deformation and, thus, a numerically more challenging simulation, the imperfection is added. Furthermore, the micromorphic moduli are chosen as $A_i = 75$ [MPa mm^2] and $H_i = 10^5$ [MPa].

For the anisotropic version, mesh convergence is studied by various mesh refinements using 892, 1908, 3722, 7066 and 9512 finite elements, where the refined areas of the 892 and 9512 meshes are shown in Figure 3.13. The corresponding force-displacement curves are illustrated in Figure 3.14 and show the desired convergence towards a solution with negligibly small differences. Moreover, the isotropic damage model is computed using the finest mesh. In addition to the last 'brittle' example, these results clearly demonstrate the model's regularization also in a 'ductile' framework.

Although not as significant in the present example, the slightly higher maximum force achieved as well as the later onset of degradation of the isotropic model compared to the anisotropic version, as visible in Figure 3.14, are consistent with the findings of the single element test

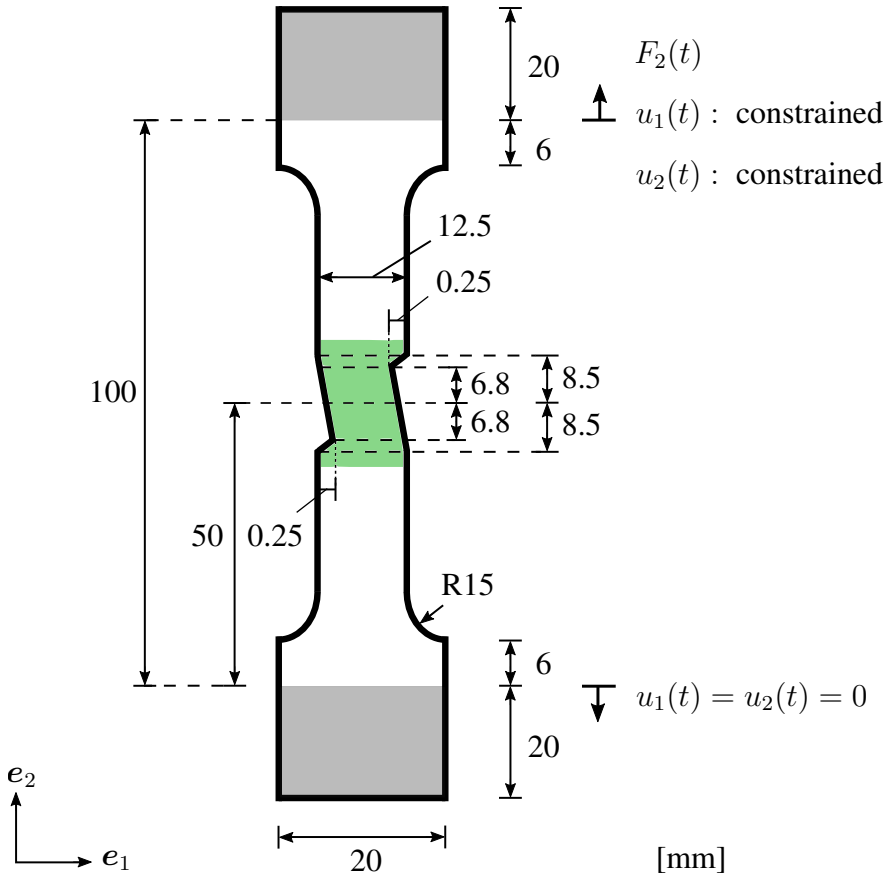

Figure 3.12: Geometry and boundary value problem with imperfection (not to scale). The gray highlight indicates clamping and is not simulated. Bottom edge is completely fixed, upper edge is loaded by a single force and is allowed to deform as a rigid body as well as stays perpendicular to the force. The green highlight indicates the area of mesh refinement. The thickness is one millimeter.

in Section 3.6.1.1. Moreover, the evolution of damage and accumulated plastic strain fields are investigated at discrete deformation states and illustrated in Figure 3.15. In line with the observed behavior in the force-displacement curves, damage initiation in the anisotropic model occurs earlier, resulting in a lower force and degradation. Although damage anisotropy is considered, the contour plots of $D_{r_{11}}$ and $D_{r_{22}}$ do not noticeably differ in terms of values or damage zone widths, the latter being in contrast to the previous example. Moreover, the final anisotropic state looks quite similar to isotropic damage.

In contrast, there is a clear difference between κ_p in case of isotropic and anisotropic damage. In view of its evolution Equation $(3.28)_2$, one notices that the rate of κ_p is strongly influenced by f_d. Considering that $D_{r_{33}}$ evolves much slower than $D_{r_{11}}$ and $D_{r_{22}}$, a slower decrease of f_d compared to f_d in the isotropic version can be comprehended for similar reasons as in the

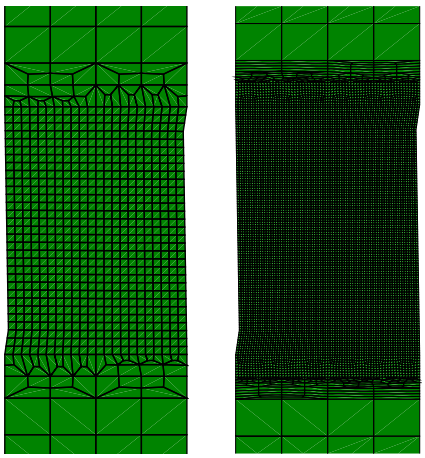

Figure 3.13: Mesh with 892 (left) and 9512 finite elements (right). The area of refinement including mesh transition coincides with the green highlight in Figure 3.12.

previous example. Thus, the rate of κ_p, and so its final value, is less in the anisotropic version in this particular example.

As intended, Figure 3.15 shows a clear horizontal movement of the upper part of the specimen, which can be considered separated from the lower part in its final state, demonstrating the robustness of the material model formulation and gradient-extension. Shear components in $\boldsymbol{D}_r$ for anisotropic damage might contribute to the larger horizontal movement than in case of isotropic damage, in addition. Furthermore, Figure 3.16 compares the final damage zones. Again no artificial widening is observed.

The stress and strain state is shown in Figure 3.17. Especially with regard to the differences between isotropic and anisotropic damage, these are interesting to investigate, since quite few differences can be identified in the force-displacement curves. Both models reach very high effective strain values in the highly notched center of the specimen. Only few differences can be observed in the contour plots. In contrast, the corresponding stress states differ clearly over time, which becomes best apparent from Lode's parameter. For the first two snaps, σ_{eq}, ρ and r already diverge between isotropic and anisotropic damage, but for the third snap, the difference is most evident. In particular, the maximum von Mises stress in the anisotropic case is much less localized than in the isotropic case, and the triaxiality also deviates from each other in the strongly notched area. It should be mentioned that the local peaks partly deviate even more significantly from each other, but are not shown here for the sake of better visualization. Finally, ρ and r reveal the reason for the differences. In the anisotropic case, r is minus one almost in the entire notched zone, whereas in the isotropic case plus one clearly prevails, high-

lighting a substantially different stress state only due to anisotropic damage. In fact, the stress in thickness direction is negative in case of anisotropic damage, while it is positive for isotropic damage. Reason for this might be that Poisson's ratio is initially direction-independent and remains direction-independent in case of isotropic damage, while anisotropic damage leads to a direction-dependence of Poisson's ratio, and thus, to a completely different transversal strain.

As for the last example, the numerical stability of the tensile specimen is briefly discussed. The corresponding (normalized) residual norms for both anisotropic and isotropic damage are shown in Table 3.4 and 3.5, respectively. A quadratic convergence rate was observed throughout the elasto-plastic regime until strong degradation occurs (1. snap), which is not shown in Table 3.4 and 3.5. At damage initiation (1. snap), the convergence rate for both cases is almost quadratic, with only one additional iteration for the anisotropic version. During the drop of the force-displacement curves (2. snap), both model version suffer from a lack of quadratic convergence, which is comparable to the asymmetrically notched specimen. However, it should be mentioned that throughout the degradation, no restart files were necessary, which is contrary to the last example. Only during the transition from the rise to the fall of the curves, a restart was necessary. With the curves flattening, both versions reach quadratic convergence rate again (3. snap). Noteworthy, the isotropic version performs quite well. Nevertheless, it is remarkable that the anisotropic version coupled with plasticity also achieves a quadratic convergence rate again. The observations for the last example (Section 3.6.2.3) are quite the same as for the tensile specimen.

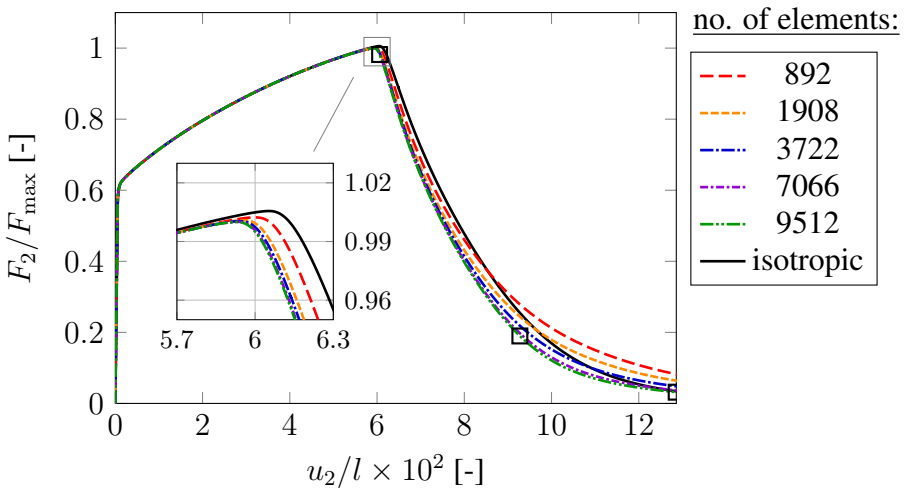

Figure 3.14: Normalized force-displacement curves with maximum load $F_{max} = 2.3285$ [kN]. The displacement is normalized to the total length $l = 140$ [mm]. For 9512 elements, the final value is about 0.03 [-]. Black squares indicate three analyzed snaps.

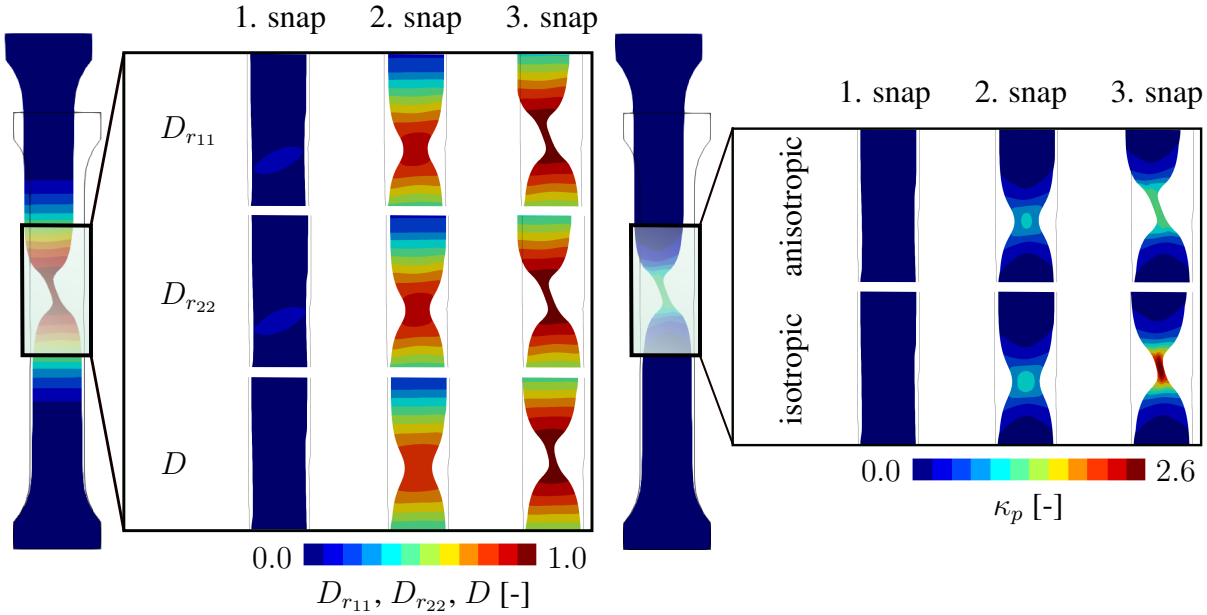

Figure 3.15: Left: Damage contour plots of $D_{r_{11}}$ and $D_{r_{22}}$ for anisotropic damage and D for isotropic damage. Right: Accumulated plastic strain contour plots in case of anisotropic and isotropic damage. Figure 3.14 indicates the snaps by black squares. The (full) deformed geometry corresponds to anisotropic damage.

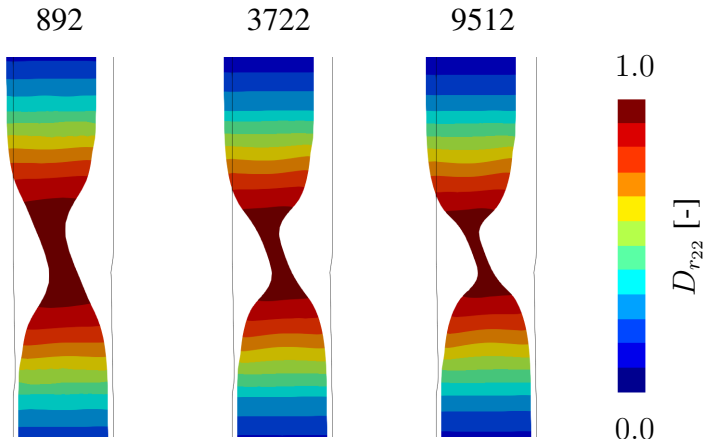

Figure 3.16: Comparison of the damage zone $D_{r_{22}}$ for three exemplary chosen mesh refinements at the end of the simulation $u_2 = 18$ [mm]. The widths remain almost constant.

Table 3.4: Global convergence rates of the tensile specimen (anisotropic damage) at three different snaps. The snaps are indicated by black rectangles in Figure 3.14.

	1. snap		2. snap		3. snap	
iteration	residual	residual (normalized)	residual	residual (normalized)	residual	residual (normalized)
0	1.000E+02	1.000E+00	1.000E+02	1.000E+00	1.000E+02	1.000E+00
1	1.313E+00	1.313E-02	9.859E-02	9.859E-04	9.863E-02	9.863E-04
2	2.585E-04	2.585E-06	6.217E-06	6.217E-08	7.390E-04	7.390E-06
3	2.611E-05	2.611E-07	1.047E-08	1.047E-10	1.558E-04	1.558E-06
4	6.702E-09	6.702E-11	-	-	1.419E-08	1.419E-10

Table 3.5: Global convergence rates of the tensile specimen (isotropic damage) at three different snaps. The snaps are indicated by black rectangles in Figure 3.14.

	1. snap		2. snap		3. snap	
iteration	residual	residual (normalized)	residual	residual (normalized)	residual	residual (normalized)
0	1.000E+02	1.000E+00	1.000E+02	1.000E+00	1.000E+02	1.000E+00
1	1.239E-01	1.239E-03	2.061E-01	2.061E-03	1.027E-02	1.027E-04
2	3.854E-05	3.854E-07	6.539E-05	6.539E-07	5.649E-07	5.649E-09
3	6.653E-09	6.653E-11	1.006E-08	1.006E-10	-	-

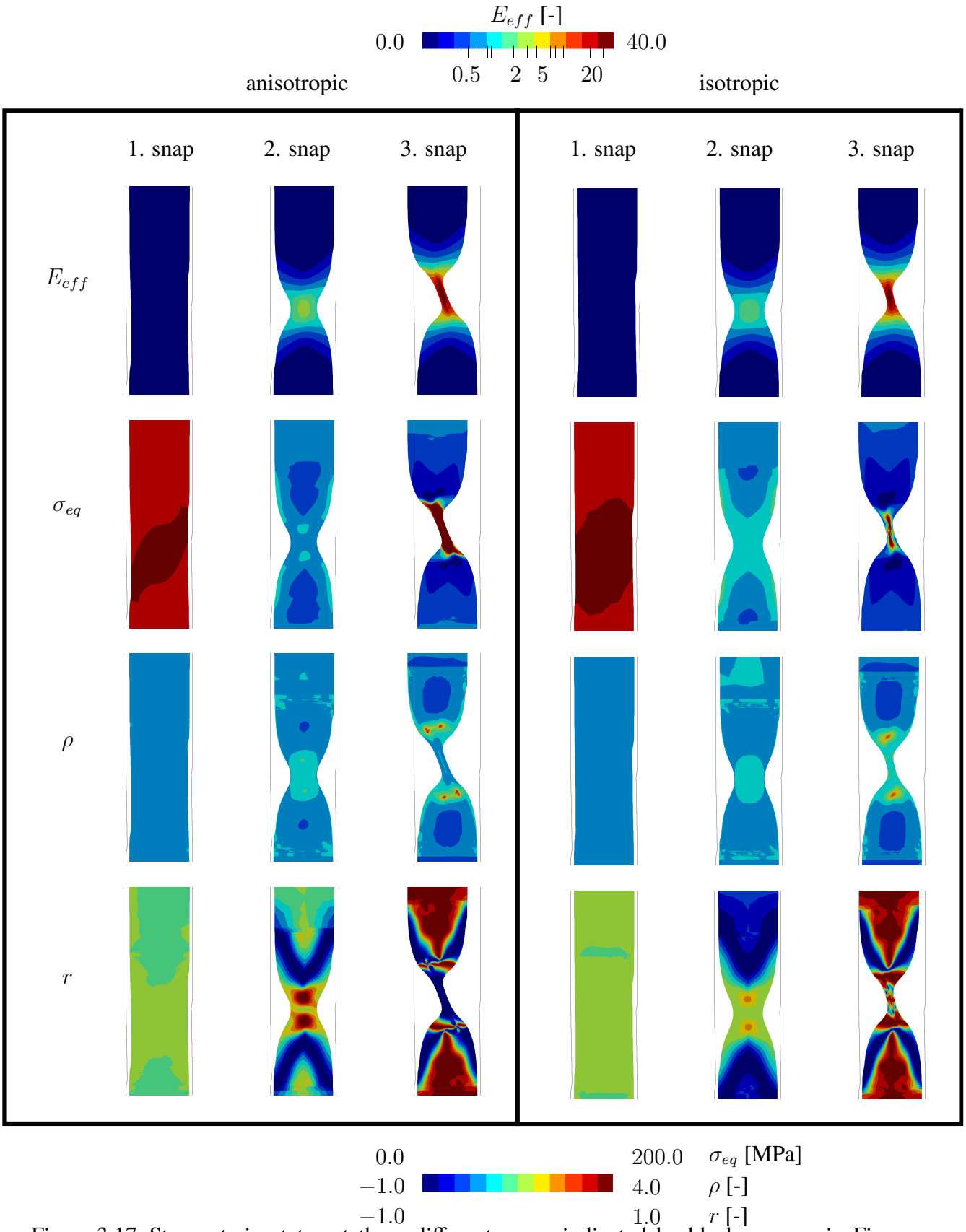

Figure 3.17: Stress-strain states at three different snaps indicated by black squares in Figure 3.14. First column: Effective Green-Lagrange strain E_{eff} (logarithmic scale), second column: Von Mises stress σ_{eq}, third column: Lode parameter r.

3.6.2.3 Cruciform specimen (ductile damage, non-proportional loading)

The last structural example serves to demonstrate the influence of damage anisotropy on a structural level, similar to the single element study in Section 3.6.1.3, but for 'ductile' material behavior. To this end, a cruciform specimen with slightly adopted geometry as inspired by Seymen et al. [2016] is considered and depicted in Figure 3.18. Due to symmetry, only one quarter is simulated and loaded as shown in Figure 3.19. Furthermore, $A_i = 75$ [MPa mm^2] and $H_i = 10^5$ [MPa] are chosen.
In the previous example, a clear difference between anisotropic and isotropic damage was hardly observed, neither in terms of the load-displacement curves nor in the contour plots of damage. Therefore, as described in some previously mentioned experimental works (cf. Section 3.2), a non-proportional load program is prescribed, where the two outer edges are biaxially loaded in a stepwise manner. The loading is shown in Figure 3.20, and two values for the intermediate displacement are investigated in the following, i.e. $\bar{u} = \{0.8, 1.75\}$ [mm]. For most of the following discussion, it is sufficient to consider only the results up to time t_2, but for completeness, the simulation is performed up to t_3 in order to achieve a 'fully broken' state. All simulations are performed fully displacement-driven.

Careful mesh convergence studies, until convergence for both edges A and B is observed, are performed using 1260, 2512, 5444, 10404, 17254, 21700, 32208 and 41836 finite elements (not shown here for brevity, see Appendix 3.8.14). The corresponding mesh sizes for the coarsest and finest mesh are shown in Figure 3.21, at least a detail due to the small mesh size for 41835 elements. All results presented in the following correspond to the finest mesh.

First, the results for $\bar{u} = 0.8$ [mm] are considered. Within interval $0 - t_0$, no differences between the isotropic and anisotropic force-displacement curves can be observed (Figure 3.22). Changing the loading direction at t_0 and increasing the displacement at edge B, a first deviation between isotropic and anisotropic behavior is noticeable within interval $t_0 - t_1$ (Figure 3.23), caused by both different damage onsets and different evolutions of damage. These two effects lead to the load drop at edge A between $t_0 - t_1$ (Figure 3.22). The following load increase in $\boldsymbol{e}_1$-direction then clearly highlights a discrepancy between both model versions. The underlying process is illustrated at specific snaps during the applied load program in Figure 3.24. In accordance with the mentioned observations in the force-displacement curves, no damage occurs during the first loading phase, but initiates during the second one. Furthermore, $D_{r_{11}}$ and $D_{r_{22}}$ reach a higher value compared to D, suggesting a more degraded state. Noteworthy, and in contrast to the previous structural examples, the component $D_{r_{33}}$ evolves quite differently

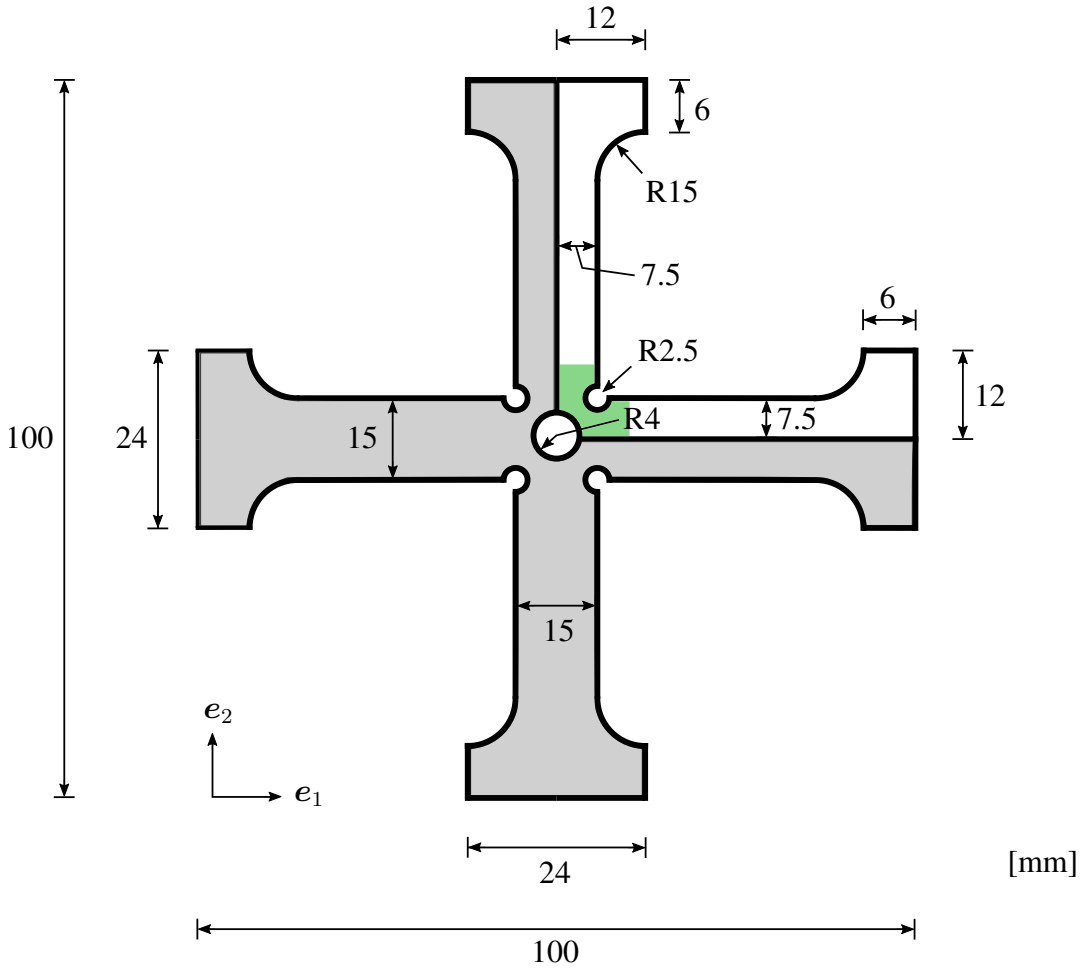

Figure 3.18: Geometry and boundary value problem. Due to symmetry, the gray highlighted parts are not simulated. Mesh refinement is mainly performed in the green highlighted area. The thickness is two millimeters.

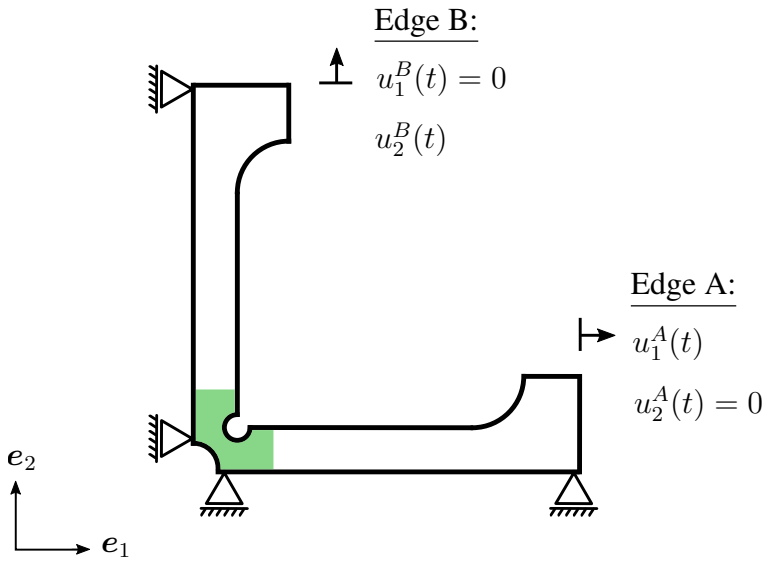

Figure 3.19: Symmetric part of boundary value problem and applied boundary conditions. The displacement perpendicular to each edge is set to zero. Displacement-driven calculations are conducted following the load program in Figure 3.20.

than $D_{r_{11}}$ and $D_{r_{22}}$.

Next, the simulation for $\bar{u} = 1.75$ [mm] is discussed in further detail. Contrary to $\bar{u} = 0.8$ [mm], the force-displacement curves between the isotropic and anisotropic version diverge

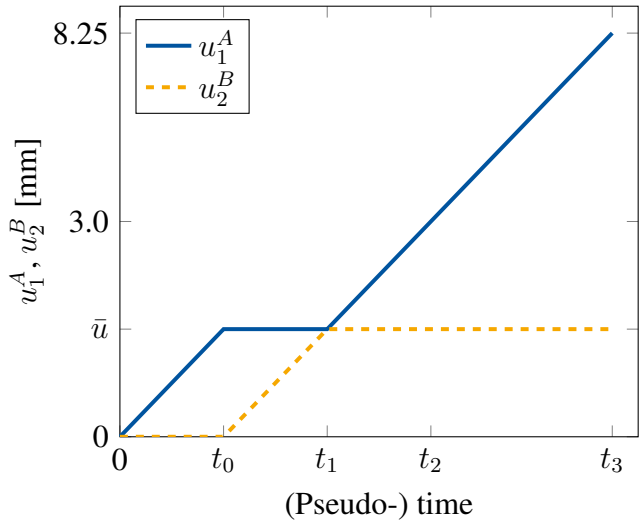

Figure 3.20: Prescribed non-proportional loading at edge A and B (cf. Figure 3.19). The slopes during loading are equal to one in each time interval. Two different values $\bar{u} = \{0.8, 1.75\}$ [mm] are investigated.

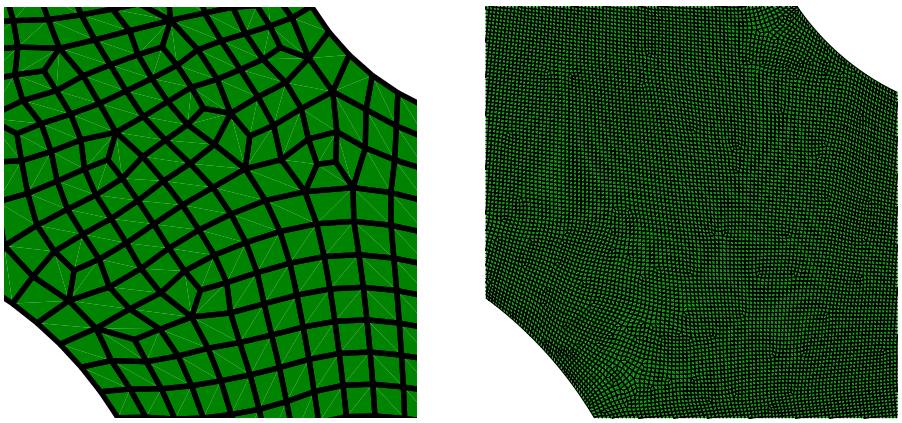

Figure 3.21: Detail of refined area (highlighted in green, cf. Figure 3.18) between the two notches. Mesh with 1260 (left) and 41836 finite elements (right).

strongly within interval $0 - t_0$, in particular after reaching their maximum loads and during material softening, respectively. Hence, the forces at edge B at t_0 differ significantly, but within $t_0 - t_1$ and $t_1 - t_2$, the curves diverge just slightly further. As before, three snaps are presented in Figure 3.25 to underpin the explanations for the differences compared to $\bar{u} = 0.8$ [mm]. In the actual case, damage initiates already within the first interval for all components. Again, components $D_{r_{11}}$ and $D_{r_{22}}$ are more pronounced than D and, moreover, all components gain higher values than their counterparts for $\bar{u} = 0.8$ [mm]. The latter explains why the forces for $\bar{u} = 1.75$ [mm] are lower than for $\bar{u} = 0.8$ [mm] at time t_2 (cf. Figure 3.22).

Figure 3.26 presents the crack shapes for the anisotropic and isotropic versions at t_3. It is interesting to note that the anisotropic crack shape looks quite sharper when the softening regime is not reached within $0 - t_0$ ($\bar{u} = 0.8$ [mm]), while for $\bar{u} = 1.75$ [mm] both shapes look almost the same. Despite the different crack shapes and differences in the force-displacement curves, the final crack contour plots for isotropic (D) and anisotropic damage ($D_{r_{11}}$, $D_{r_{22}}$) seem to closely match each other (cf. Figure 3.24, 3.25 and Appendix 3.8.14).
For completeness, contour plots of accumulated plastic strain are shown in Figure 3.27 at t_3[19]. As for the previous structural example, κ_p yields higher values in case of isotropic damage - independent of $\bar{u}$ - most likely due to the same argumentation as given in Section 3.6.2.2.

Lastly, the stress and strain responses of the various loading cases for both isotropic and anisotropic damage are discussed. Figures 3.28 and 3.29 illustrate the stress-strain states for $\bar{u} = 0.8$ [mm] of anisotropic damage and isotropic damage, respectively. At t_0 as well

[19]The corresponding damage contour plots are provided in Appendix 3.8.14.

as t_1, none of the different strain and stress measures differ significantly between isotropic and anisotropic damage. Having the corresponding force-displacement curves (Figures 3.22 and 3.23) as well as the damage contour plots (Figure 3.24) in mind, this might not be very surprising. In fact, at t_1 the state of degradation is more or less the same. As mentioned above, however, the structure at t_2 is more degraded in case of anisotropic damage, which explains why the von Mises stress is lower compared to isotropic damage, at least on average. Although the effective Green-Lagrange strain looks quite the same, the triaxiality and Lode's parameter show some differences. These results are consistent with the conclusion that the influence of anisotropic damage is not as significant when $\bar{u}$ is set to the lower of the two values.

For $u = 1.75$ [mm], a similar behavior is observed as also discussed above. Already at time t_1, the effective Green-Lagrange strain in the case of isotropic damage is localized to a much narrower range (Figures 3.30 and 3.31). Thus, the von Mises stress observed is higher within this region. Considering the fact that, roughly speaking, stiffness attracts loads and the isotropic model is less damaged at t_1, these observations can be well understood. Similar observations can be made for ρ and r. As the difference in the force-displacement curves increase over time, it is not surprising that the very same is the case for the stress-strain states. While both the strain and stress gradients are less sharp for anisotropic damage, a much narrower range is of interest in the case of isotropic damage with the corresponding gradients being higher. In particular, the effective Green-Lagrange strain and the Lode parameter clearly highlight these differences. One possible explanation is a different degradation state as already described for $u = 0.8$ [mm] and, as in the previous example, a continuously evolving directional dependence of Poisson's ratio with increasing degradation.

3.7 Conclusion and outlook

A gradient-extended coupled damage-plasticity model accounting for anisotropic damage by means of a second order damage tensor at large strains was presented. The model was derived in a thermodynamically consistent manner and accounts for both plastic and damage hardening, where the key points of the constitutive framework include the representation in the logarithmic strain space, the use of the additive split, the transformation to the Lagrangian space, and the fulfillment of the *damage growth criterion* for a generally elasto-plastic-damage loading step. The latter prevents the model from artificial stiffening. Moreover, in order to gain a flexible formulation with regard to the material's degree of ductility, a 'two-surface' approach was employed.

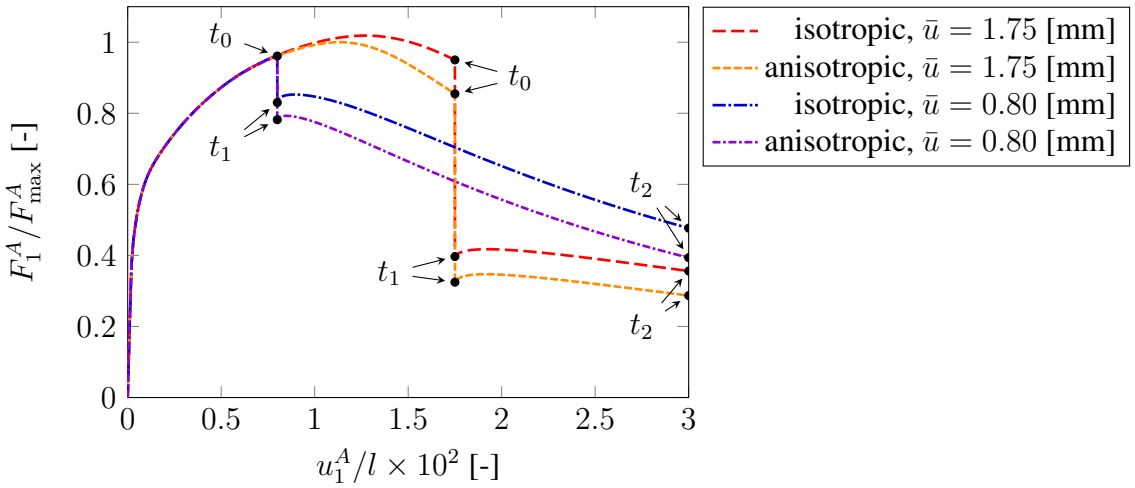

Figure 3.22: Normalized load-displacement curves (41836 elements, edge A) with maximum load $F^A_{max} = 1.5912$ [kN] ($\bar{u} = 1.75$ [mm], anisotropic model, finest mesh). The displacement is normalized to $l = 100$ [mm]. The time points correspond to the load program in Figure 3.20.

Although a symmetric second order damage tensor was used, the proposed gradient-extension, which is based on the micromorphic approach, requires only three 'nonlocal' variables associated with the damage tensor's invariants. The numerical solution procedure for the fully coupled system of equations, solving both the linear momentum in terms of Lagrangian quantities and the micromorphic balance, uses Newton-Raphon's method. Therefore, the composition of the algorithmically consistent tangent operators in the Lagrangian space was presented as well.

Single element studies were performed and demonstrated the difference between plasticity coupled to isotropic and anisotropic damage, as well as the effect of induced anisotropy. Finally, structural examples investigated the model's ability to achieve mesh-independent results. In order to exclude any influence of plasticity on the regularization, brittle simulations proved the applicability of the regularization technique. Moreover, the structural influence of damage anisotropy on the model's plastic evolution was investigated in ductile simulations. Although these simulation did not show a significant difference in the final crack path, a crucial difference in the load-displacement curves between isotropic and anisotropic damage was observed, especially for non-proportional loading. This clearly highlights the relevance of taking anisotropic damage into account in, for instance, forming processes.

Despite these promising numerical results, comprehensive experimental calibrations and val-

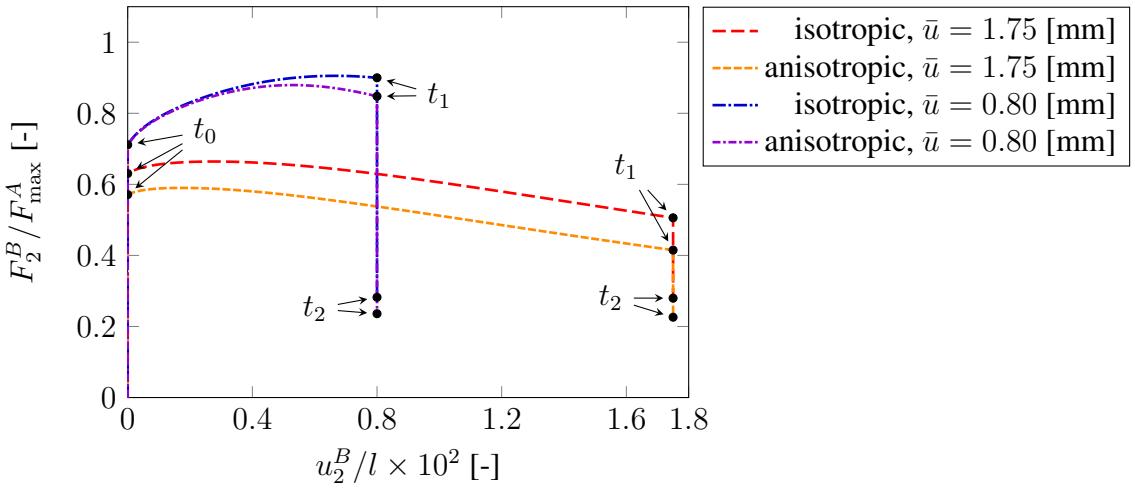

Figure 3.23: Normalized load-displacement curves (41836 elements, edge B) with maximum load $F^A_{max} = 1.5912$ [kN] (cf. edge A, Figure 3.22) and total length $l = 100$ [mm]. The time points correspond to the load program in Figure 3.20.

idations are highly desirable in the future. At least the plastic part was already validated in several mentioned works. In this context, the usage of the additive split in connection with anisotropic damage might be studied in more detail. Furthermore, a material formulation that does not make use of the additive split is of interest, as well as the comparison between multiplicative and additive decompositions in the presence of anisotropic damage. Moreover, due to the strong influence on the final crack path, the model should be equipped with anisotropic plasticity and - in this regard - additional (plastic) regularization should be considered (see e.g. Dimitrijevic and Hackl [2011], Lodygowski et al. [2011], Saanouni and Hamed [2013] and Miehe et al. [2017]) to counteract localizing shear bands. Moreover, numerical studies should investigate the possibility of reducing the set of 'nonlocal' variables in order to reduce the numerical effort. In this context, it is worth referring to the recently proposed developments of reduced integration elements for gradient-extended damage (see Barfusz, Brepols, van der Velden, Frischkorn and Reese [2021]; Barfusz, van der Velden, Brepols, Holthusen and Reese [2021]) based on Reese [2005] and Juhre and Reese [2010], which noticeably reduce the computational effort and make the structural simulations very robust against strong mesh distortions.

3.8 Appendix

3.8.1 Virtual work in the context of the micromorphic approach

The pathological mesh dependence in FE simulations and, in its absolute consequence, the shrinking of the damage zone to zero, can be remedied by various methods. Gradient-extension introduces an internal length scale, which additionally describes the material by means of a material parameter. In the present work, the micromorphic approach of Forest [2009, 2016] is followed, which in parts goes back to the work of Mindlin [1964]. Accordingly, the desired regularization is realized only indirectly via the micromorphic variable and the requirement that its local counterpart is constantly close to it.
The internal virtual work g_{int} as well as its external counterpart g_{ext} defined in terms of constitutively dependent quantities in the reference configuration are obtained as

$$g_{int} = \int_{B_0} \boldsymbol{S} : \delta \boldsymbol{E} \, \mathrm{d}V + \underbrace{\int_{B_0} \left(\boldsymbol{\xi}_{0_i} \cdot \delta \bar{\mathbf{d}} + \boldsymbol{\Xi}_{0_i} : \mathrm{Grad}\left(\delta \bar{\mathbf{d}}\right) \right) \mathrm{d}V}_{\text{micromorphic extension}} \tag{3.84}$$

$$\begin{aligned} g_{ext} = & \int_{B_0} \boldsymbol{f}_0 \cdot \delta \boldsymbol{u} \, \mathrm{d}V + \int_{\partial_t B_0} \boldsymbol{t}_0 \cdot \delta \boldsymbol{u} \, \mathrm{d}A \\ & \underbrace{+ \int_{B_0} \left(\boldsymbol{\xi}_{0_e} \cdot \delta \bar{\mathbf{d}} + \boldsymbol{\Xi}_{0_e} : \mathrm{Grad}\left(\delta \bar{\mathbf{d}}\right) \right) \mathrm{d}V + \int_{\partial_c B_0} \boldsymbol{\xi}_{0_c} \cdot \delta \bar{\mathbf{d}} \, \mathrm{d}A}_{\text{micromorphic extension}} \end{aligned} \tag{3.85}$$

A much more deep discussion as well as derivation of the above formulas and their detailed transformation to their strong forms can be found in Brepols et al. [2020].

3.8.2 Invariant-based approach in terms of principal invariants

Choosing the principal invariants $I_D = \mathrm{tr}\,(\boldsymbol{D})$, $II_D = 1/2\left((\mathrm{tr}\,(\boldsymbol{D}))^2 - \mathrm{tr}\,(\boldsymbol{D}^2)\right)$, $III_D = \det(\boldsymbol{D})$, the derivatives in Equation (3.79) are obtained as

$$\frac{\partial I_D}{\partial \boldsymbol{D}_r} = \boldsymbol{I}, \quad \frac{\partial II_D}{\partial \boldsymbol{D}_r} = I_D \, \boldsymbol{I} - \boldsymbol{D}_r, \quad \frac{\partial III_D}{\partial \boldsymbol{D}_r} = III_D \, \boldsymbol{D}_r^{-1}. \tag{3.86}$$

However, since $\boldsymbol{D}_r$ is positive semi-definite, the inverse cannot always be computed. Therefore, in order to obtain a closed-form expression for the third derivative, one rewrites the concerned term by applying the Cayley-Hamilton theorem

$$\frac{\partial III_D}{\partial \boldsymbol{D}_r} = II_D \boldsymbol{I} - I_D \boldsymbol{D}_r + \boldsymbol{D}_r^2. \tag{3.87}$$

Note that the above formula could also be obtained by a limit analysis. Although the advantage of always as many non-zero principal invariants as eigenvalues, the approach from Equation (3.13) is chosen due to its simpler structure.

3.8.3 Damage growth criterion

Damage, unless material healing is considered, is generally associated with a loss of material integrity and thus with a decrease of the material resistance. Consequently, if the damage tensor 'increases', i.e. one of its eigenvalues increases, the material stiffness must decrease. A more general (and mathematical) treatment of this topic can be found in Wulfinghoff et al. [2017], which derived the so-called *damage growth criterion*, an important contribution to the field of CDM. The fulfillment of this criterion prevents any kind of artificial stiffening. Although this requirement seems natural, many models in the literature suffer from violating it (see the discussion in Wulfinghoff et al. [2017]). In the case of anisotropic damage, the criterion has been successfully applied by e.g. Fassin et al. [2019*b*,*a*] and Reese et al. [2021]. Without going to much into detail, the main findings are summarized here. For simplicity, an elasto-plastic material without any kind of hardening is considered. Thus, the energy contributing to the overall stiffness of the material ψ_e has to decrease for evolving damage

$$\psi_e(\bar{\boldsymbol{\eta}}_e^*, \boldsymbol{D} + \mathrm{d}\boldsymbol{D}) \leq \psi_e(\bar{\boldsymbol{\eta}}_e^*, \boldsymbol{D}) \quad \forall\, \bar{\boldsymbol{\eta}}_e^* \in \mathrm{Sym}^+(3) \tag{3.88}$$

here expressed with respect to the intermediate configuration. Alternatively, Equation (3.88) can be expressed as

$$\frac{\partial \psi_e}{\partial \boldsymbol{D}} : \mathrm{d}\boldsymbol{D} \leq 0. \tag{3.89}$$

Since $\mathrm{d}\boldsymbol{D}$ is positive semi-definite, $\partial\psi_e/\partial\boldsymbol{D}$ must be at least negative semi-definite. The interested reader may found a more detailed discussion, also in the case of elasto-plasticity, in the work of Wulfinghoff et al. [2017].

3.8.4 Isotropic tensor function of two symmetric tensors

Considering ψ which is an isotropic function of $\boldsymbol{A}, \boldsymbol{B} \in \mathrm{Sym}(3)$, i.e. $\psi = \breve{\psi}(\boldsymbol{A}, \boldsymbol{B}) = \hat{\psi}(\mathcal{E}(\boldsymbol{A}), \mathcal{M}(\boldsymbol{A}, \boldsymbol{B}), \mathcal{E}(\boldsymbol{B}))$. Hence, one can show that the following holds

$$\boldsymbol{A}\frac{\partial \psi(\mathcal{E}(\boldsymbol{A}))}{\partial \boldsymbol{A}} = \frac{\partial \psi(\mathcal{E}(\boldsymbol{A}))}{\partial \boldsymbol{A}}\boldsymbol{A} = \alpha_0\, \boldsymbol{A} + \alpha_1\, 2\boldsymbol{A}^2 + \alpha_2\, 3\boldsymbol{A}^3 \tag{3.90}$$

which yields a symmetric tensor and moreover holds analogously for $\boldsymbol{B}$. Thus, in order to prove that $\boldsymbol{A}\ (\partial\psi/\partial\boldsymbol{A}) + \boldsymbol{B}\ (\partial\psi/\partial\boldsymbol{B})$ yields a symmetric tensor, it is only necessary to investigate the following

$$\begin{aligned}\boldsymbol{A}\frac{\partial\psi(\mathcal{M}(\boldsymbol{A},\boldsymbol{B}))}{\partial\boldsymbol{A}} + \boldsymbol{B}\frac{\partial\psi(\mathcal{M}(\boldsymbol{A},\boldsymbol{B}))}{\partial\boldsymbol{B}} &= \beta_0\ \boldsymbol{AB} + \beta_1\ \boldsymbol{A}^2\boldsymbol{B} + \beta_1\ \boldsymbol{ABA} + \beta_2\ \boldsymbol{AB}^2 \\ &+ \beta_3\ \boldsymbol{A}^2\boldsymbol{B}^2 + \beta_3\ \boldsymbol{AB}^2\boldsymbol{A} + \beta_0\ \boldsymbol{BA} + \beta_1\ \boldsymbol{BA}^2 \\ &+ \beta_2\ \boldsymbol{BAB} + \beta_2\ \boldsymbol{B}^2\boldsymbol{A} + \beta_3\ \boldsymbol{BA}^2\boldsymbol{B} + \beta_3\ \boldsymbol{B}^2\boldsymbol{A}^2\end{aligned} \tag{3.91}$$

which indeed yields a symmetric tensor, too. The several α_i and β_i denote the partial derivatives of the isotropic tensor function with respect to the invariants.

3.8.5 Representation of thermodynamic driving forces with respect to reference configuration

Taking the findings of Appendix 3.8.4 into account and further noticing $\mathcal{E}(\bar{\boldsymbol{\eta}}_e) = \mathcal{E}(\bar{\boldsymbol{\varepsilon}}_e)$, $\mathcal{M}(\bar{\boldsymbol{\eta}}_e, \boldsymbol{D}) = \mathcal{M}(\bar{\boldsymbol{\varepsilon}}_e, \boldsymbol{D}_r)$, $\mathcal{E}(\boldsymbol{\eta}_p) = \mathcal{E}(\boldsymbol{\varepsilon}_p)$, $\mathcal{M}(\boldsymbol{\eta}_p, \boldsymbol{D}) = \mathcal{M}(\boldsymbol{\varepsilon}_p, \boldsymbol{D}_r)$ and $\mathcal{E}(\boldsymbol{D}) = \mathcal{E}(\boldsymbol{D}_r)$, the following can be found for the driving forces

$$\begin{aligned}\boldsymbol{T} &= \boldsymbol{R}_p \left(\alpha_0\ \boldsymbol{I} + \alpha_1\ 2\bar{\boldsymbol{\eta}}_e + \alpha_2\ 3\bar{\boldsymbol{\eta}}_e^2 + \beta_0\ \boldsymbol{D} + \beta_1(\bar{\boldsymbol{\eta}}_e\boldsymbol{D} + \boldsymbol{D}\bar{\boldsymbol{\eta}}_e)\right. \\ &\quad \left. + \beta_2\boldsymbol{D}^2 + \beta_3(\bar{\boldsymbol{\eta}}_e\boldsymbol{D}^2 + \boldsymbol{D}^2\bar{\boldsymbol{\eta}}_e)\right) \boldsymbol{R}_p^{-1} \\ &= \alpha_0\ \boldsymbol{I} + \alpha_1\ 2\bar{\boldsymbol{\varepsilon}}_e + \alpha_2\ 3\bar{\boldsymbol{\varepsilon}}_e^2 + \beta_0\ \boldsymbol{D}_r + \beta_1(\bar{\boldsymbol{\varepsilon}}_e\boldsymbol{D}_r + \boldsymbol{D}_r\bar{\boldsymbol{\varepsilon}}_e) \\ &\quad + \beta_2\boldsymbol{D}_r^2 + \beta_3(\bar{\boldsymbol{\varepsilon}}_e\boldsymbol{D}_r^2 + \boldsymbol{D}_r^2\bar{\boldsymbol{\varepsilon}}_e)\end{aligned} \tag{3.92}$$

$$\begin{aligned}\boldsymbol{X} &= \boldsymbol{R}_p \left(\nu_0\ \boldsymbol{I} + \nu_1\ 2\boldsymbol{\eta}_p + \nu_2\ 3\boldsymbol{\eta}_p^2 + \tau_0\ \boldsymbol{D} + \tau_1(\boldsymbol{\eta}_p\boldsymbol{D} + \boldsymbol{D}\boldsymbol{\eta}_p)\right. \\ &\quad \left. + \tau_2\boldsymbol{D}^2 + \tau_3(\boldsymbol{\eta}_p\boldsymbol{D}^2 + \boldsymbol{D}^2\boldsymbol{\eta}_p)\right) \boldsymbol{R}_p^{-1} \\ &= \nu_0\ \boldsymbol{I} + \nu_1\ 2\boldsymbol{\varepsilon}_p + \nu_2\ 3\boldsymbol{\varepsilon}_p^2 + \tau_0\ \boldsymbol{D}_r + \tau_1(\boldsymbol{\varepsilon}_p\boldsymbol{D}_r + \boldsymbol{D}_r\boldsymbol{\varepsilon}_p) \\ &\quad + \tau_2\boldsymbol{D}_r^2 + \tau_3(\boldsymbol{\varepsilon}_p\boldsymbol{D}_r^2 + \boldsymbol{D}_r^2\boldsymbol{\varepsilon}_p)\end{aligned} \tag{3.93}$$

which shows that the driving forces can be fully expressed in terms of quantities located within the reference configuration. Similar expressions are obtained for $\boldsymbol{Y}_e$ and $\boldsymbol{Y}_p$ by interchanging $\bar{\boldsymbol{\eta}}_e|\boldsymbol{D}$ $(\bar{\boldsymbol{\varepsilon}}_e|\boldsymbol{D}_r)$ and $\boldsymbol{\eta}_p|\boldsymbol{D}$ $(\boldsymbol{\varepsilon}_p|\boldsymbol{D}_r)$, respectively. The driving forces $\boldsymbol{Y}_h$ and $\boldsymbol{Y}_{\bar{d}}$ are obtained in a quite similar way and thus are not shown here for brevity.

3.8.6 Fourth order damage mapping tensor

For the plastic evolution Equations (3.28), it is necessary to specify the relation between the effective stress $\tilde{\boldsymbol{T}}$ and its damaged counterpart $\boldsymbol{T}$, defined by $\mathbb{M}$, based on the energy chosen in (3.37). First, the effective stress is obtained by evaluating $\boldsymbol{T}$ for $\boldsymbol{D}_r = \boldsymbol{0}$

$$\tilde{\boldsymbol{T}} = 2\mu_e \operatorname{dev}(\bar{\boldsymbol{\varepsilon}}_e) + K_e \operatorname{tr}(\bar{\boldsymbol{\varepsilon}}_e)\, \boldsymbol{I}. \tag{3.94}$$

Next, the effective stress can be decomposed into its deviatoric and volumetric part as follows

$$\operatorname{vol}(\tilde{\boldsymbol{T}}) = \mathbb{P}_{vol} : \tilde{\boldsymbol{T}} = K_e \operatorname{tr}(\bar{\boldsymbol{\varepsilon}}_e)\, \boldsymbol{I}, \quad \operatorname{dev}(\tilde{\boldsymbol{T}}) = \mathbb{P}_{dev} : \tilde{\boldsymbol{T}} = 2\mu_e \operatorname{dev}(\bar{\boldsymbol{\varepsilon}}_e) \tag{3.95}$$

with the two fourth order projection tensors $\mathbb{P}_{vol} = 1/3\, \boldsymbol{I} \otimes \boldsymbol{I}$ and $\mathbb{P}_{dev} = (\boldsymbol{I} \otimes \boldsymbol{I})^{\overset{23}{T}} - \mathbb{P}_{vol}$. By comparing the deviatoric as well as volumetric parts of the effective and damaged stress, one can find the following relations: $\operatorname{vol}(\boldsymbol{T}) = \mathbb{N}_{vol} : \operatorname{vol}\left(\tilde{\boldsymbol{T}}\right)$ and $\operatorname{dev}(\boldsymbol{T}) = \mathbb{N}_{dev} : \operatorname{dev}\left(\tilde{\boldsymbol{T}}\right)$. These two additional mapping tensors read as follows

$$\mathbb{N}_{vol} = f_d\, (\boldsymbol{I} \otimes \boldsymbol{I})^{\overset{23}{T}} \tag{3.96}$$

$$\mathbb{N}_{dev} = \left(\frac{1}{2} \left((\boldsymbol{I} \otimes (\boldsymbol{I} - \boldsymbol{D}_r))^{\overset{23}{T}} + ((\boldsymbol{I} - \boldsymbol{D}_r) \otimes \boldsymbol{I})^{\overset{23}{T}} \right) + \frac{1}{3} \boldsymbol{I} \otimes \boldsymbol{D}_r \right) \vartheta + (1 - \vartheta)\, \mathbb{N}_{vol}. \tag{3.97}$$

Finally, under consideration of the several minor and major symmetries, the fourth order damage mapping tensor is deduced as

$$\mathbb{M} = \left(\frac{1}{2} \left((\boldsymbol{I} \otimes \boldsymbol{I})^{\overset{23}{T}} + (\boldsymbol{I} \otimes \boldsymbol{I})^{\overset{24}{T}} \right) \right) : (\mathbb{N}_{vol} : \mathbb{P}_{vol} + \mathbb{N}_{dev} : \mathbb{P}_{dev}) \tag{3.98}$$

while its inverse results in a somehow lengthy expression, and thus is not provided within this written part. Nevertheless, a *MATLAB* script is provided as supplementary material in the online version of this work. Within this script, the expression for $\mathbb{M}^{-1}$ is given with respect to the eigensystem of the damage tensor $\boldsymbol{D}_r$ in a symbolic manner. In addition, it is proven that $\mathbb{M}^{-1}$ maps a general deviatoric second order tensor $\boldsymbol{A}_{dev}$ onto a deviatoric second order tensor. Therefore, it is important to note that a deviatoric tensor keeps deviatoric under a proper orthogonal change of the basis system, such that

$$\operatorname{tr}\left(\left(\boldsymbol{Q}\boldsymbol{A}\boldsymbol{Q}^T - \frac{\operatorname{tr}\left(\boldsymbol{Q}\boldsymbol{A}\boldsymbol{Q}^T\right)}{3} \boldsymbol{I} \right) \right) = \operatorname{tr}\left(\boldsymbol{Q}\boldsymbol{A}_{dev}\boldsymbol{Q}^T\right) = \operatorname{tr}(\boldsymbol{A}_{dev}) = 0 \tag{3.99}$$

with $\boldsymbol{Q} \in \mathrm{SO}(3)$. Hence, the product $\mathbb{M}^{-1} : \boldsymbol{A}_{dev}$ can also be proven to yield a deviatoric tensor with respect to the eigensystem of $\boldsymbol{D}_r$.

3.8.7 Additional damage hardening

For simplicity, the additional damage hardening force $\boldsymbol{Y}_h$ (3.50) is rewritten in terms of the derivative with respect to D_{r_i}

$$\boldsymbol{Y}_h = K_h \sum_{i=1}^{3} \left(f(D_{r_i})\, \boldsymbol{n}_i^{\boldsymbol{D}_r} \otimes \boldsymbol{n}_i^{\boldsymbol{D}_r} \right) \tag{3.100}$$

$$f(D_{r_i}) = \frac{1}{(1 - D_{r_i})^{\frac{1}{n_d}}} - 1 \tag{3.101}$$

$$f'(D_{r_i}) = \frac{(1 - D_{r_i})^{-\frac{1}{n_d}-1}}{n_d} \tag{3.102}$$

As pointed out, during the local iteration it can not be excluded a priori that the values D_{r_i} do not exceed one, which would produce a 'not a number' error. In order to prevent this issue, a Taylor series up to the fourth term of the function $f(D_{r_i})$ at $a_d \in \mathbb{R}$ is carried out (cf. Fassin et al. [2019*b*]). The evaluation point a_d has to be lower than one but is usually very close it. The following polynomial approximation is used every time D_{r_i} is larger than a_d

$$\begin{aligned} T_4\, f(D_{r_i};\, a_d) = {} & \frac{1}{(1 - a_d)^{\frac{1}{n_d}}} - 1 + \frac{(1 - a_d)^{-\frac{1}{n_d}-1}}{n_d} (D_{r_i} - a_d) \\ & - \frac{\left(-\frac{1}{n_d} - 1\right)(1 - a_d)^{-\frac{1}{n_d}-2}}{2\, n_d} (D_{r_i} - a_d)^2 \\ & + \frac{\left(-\frac{1}{n_d} - 2\right)\left(-\frac{1}{n_d} - 1\right)(1 - a_d)^{-\frac{1}{n_d}-3}}{6\, n_d} (D_{r_i} - a_d)^3 \\ & + \frac{(n_d + 1)\,(2n_d + 1)\,(3n_d + 1)}{24\, n_d^4 (1 - a_d)^{\frac{1}{n_d}}\, (a_d - 1)^4} (D_{r_i} - a_d)^4 \end{aligned} . \tag{3.103}$$

For the Jacobian $\mathbf{J}_{loc}$ during the local Newton-Raphson iteration, the analytical derivative of $\boldsymbol{Y}_h$ with respect to $\boldsymbol{D}_r$ is required. This derivative is obtained according to the formula provided

in e.g. Ogden [1984]

$$\boldsymbol{A}(\boldsymbol{B}) = \sum_{i=1}^{3} f(B_i)\, \boldsymbol{n}_i^{\boldsymbol{B}} \otimes \boldsymbol{n}_i^{\boldsymbol{B}} \tag{3.104}$$

$$\frac{\partial \boldsymbol{A}}{\partial \boldsymbol{B}} = \sum_{i=1}^{3} f'(B_i)\, \boldsymbol{n}_i^{\boldsymbol{B}} \otimes \boldsymbol{n}_i^{\boldsymbol{B}} \otimes \boldsymbol{n}_i^{\boldsymbol{B}} \otimes \boldsymbol{n}_i^{\boldsymbol{B}} + \frac{1}{2} \sum_{i \neq j}^{3} \left(\overbrace{\left(\frac{f(B_j) - f(B_i)}{B_j - B_i} \right)}^{\overset{B_i \to B_j}{\Rightarrow} f'(B_i)} \right. \tag{3.105}$$

$$\left. \left(\boldsymbol{n}_i^{\boldsymbol{B}} \otimes \boldsymbol{n}_j^{\boldsymbol{B}} \otimes \boldsymbol{n}_i^{\boldsymbol{B}} \otimes \boldsymbol{n}_j^{\boldsymbol{B}} + \boldsymbol{n}_i^{\boldsymbol{B}} \otimes \boldsymbol{n}_j^{\boldsymbol{B}} \otimes \boldsymbol{n}_j^{\boldsymbol{B}} \otimes \boldsymbol{n}_i^{\boldsymbol{B}} \right) \right) .$$

3.8.8 Thermodynamic consistency

In order to prove the thermodynamic consistency of the model and under consideration of Equation (3.28), the plastic quantities within the reduced part of the Clausius-Duhem inequality are expressed as

$$(\boldsymbol{T} - \boldsymbol{X}) : \dot{\boldsymbol{\varepsilon}}_p = \dot{\gamma}_p \frac{3}{\sqrt{12 \tilde{J}_2}} \left(\tilde{\boldsymbol{T}} - \tilde{\boldsymbol{X}} \right) : \operatorname{dev} \left(\tilde{\boldsymbol{T}} - \tilde{\boldsymbol{X}} \right) = \dot{\gamma}_p \sqrt{3 \tilde{J}_2} \tag{3.106}$$

as well as the contribution of isotropic hardening with $R_p\, \dot{\kappa}_p = \dot{\gamma}_p\, \tilde{R}_p$. Hence, the plastic contribution to the overall dissipation is equal to

$$(\boldsymbol{T} - \boldsymbol{X}) : \dot{\boldsymbol{\varepsilon}}_p + R_p\, \dot{\kappa}_p = \dot{\gamma}_p \left(\Phi_p + \sigma_{y0} \right) \geq 0 \tag{3.107}$$

which is obviously fulfilled taking into account the KKT conditions (3.29) and $\sigma_{y0} \geq 0$. Analogously is proceeded for the damage part

$$\boldsymbol{Y} : \dot{\boldsymbol{D}}_r = \dot{\gamma}_d \frac{\sqrt{3}}{\sqrt{\boldsymbol{Y}_+ : \mathbb{A} : \boldsymbol{Y}_+}} \left(\boldsymbol{Y}_+ : \mathbb{A} : \boldsymbol{Y}_+ \right) = \dot{\gamma}_d \sqrt{3} \sqrt{\boldsymbol{Y}_+ : \mathbb{A} : \boldsymbol{Y}_+}. \tag{3.108}$$

Hence, the dissipation caused by damage is obtained as

$$\boldsymbol{Y} : \dot{\boldsymbol{D}}_r + R_d\, \dot{\kappa}_d = \dot{\gamma}_d \left(\Phi_d + Y_0 \right) \geq 0 \tag{3.109}$$

which is always positive for similar reasons as stated before.

3.8.9 Volumetric-isochoric decoupling

In classical continuum models, the isochoric-volumetric split is obtained by following the approach of Flory [1961], expressed in terms of the stretch tensor $\boldsymbol{U}$ as $\boldsymbol{U} = \det(\boldsymbol{U})^{-1/3}\boldsymbol{U}\ \det(\boldsymbol{U})^{1/3}\boldsymbol{I} =: \boldsymbol{U}_{iso}\boldsymbol{U}_{vol}$. The Helmholtz free energy depending on $\boldsymbol{U}$ is additively decomposed: $\psi(\boldsymbol{U}) = \psi_{iso}(\boldsymbol{U}_{iso}) + \psi_{vol}(\det(\boldsymbol{U}_{vol}))$. In e.g. Criscione et al. [2000] and Neff et al. [2015] as well as the literature cited therein, several properties of logarithmic strain measurements are discussed. A significant result in the context of the volumetric-isochoric split is the property that of all strain measures that are members of the Seth-Hill family (see Appendix 3.8.11), only the decomposition of logarithmic strains into a spherical and deviatoric part is directly related to the volumetric-isochoric split

$$\begin{aligned}\ln(\boldsymbol{U}) = \ln(\boldsymbol{U}\det(\boldsymbol{U})^{-1/3}\det(\boldsymbol{U})^{1/3}) &= \left(\ln(\boldsymbol{U}) - \frac{\ln(\det(\boldsymbol{U}))}{3}\boldsymbol{I}\right) + \frac{\ln(\det(\boldsymbol{U}))}{3}\boldsymbol{I} \\ &= \underbrace{\left(\ln(\boldsymbol{U}) - \frac{\operatorname{tr}(\ln(\boldsymbol{U}))}{3}\boldsymbol{I}\right)}_{=\operatorname{dev}(\ln(\boldsymbol{U}))} + \underbrace{\frac{\operatorname{tr}(\ln(\boldsymbol{U}))}{3}\boldsymbol{I}}_{=\operatorname{vol}(\ln(\boldsymbol{U}))},\end{aligned} \tag{3.110}$$

with $\ln(\det(\boldsymbol{A})) = \operatorname{tr}(\ln(\boldsymbol{A}))$. Further, the incompressibility condition $\det(\boldsymbol{U}) = 1$ is equivalent to $\operatorname{tr}(\ln(\boldsymbol{U})) = 0$, which holds analogously for $\boldsymbol{U}_p$ and is an essential statement in volume preserving plasticity.

3.8.10 Gâteaux derivative of the multi-field problem

The Gâteaux derivative applied in the context of the present multi-field problem is expressed as

$$\mathfrak{D}_u[g_u]\cdot\Delta\boldsymbol{u} = \frac{\mathrm{d}}{\mathrm{d}\epsilon}\left(g_u\left(\boldsymbol{u}^* + \epsilon\,\Delta\boldsymbol{u}, \bar{\mathbf{d}}^*, \delta\boldsymbol{u}\right)\right)\Big|_{\epsilon=0} \tag{3.111}$$

$$\mathfrak{D}_{\bar{d}}[g_u]\cdot\Delta\bar{\mathbf{d}} = \frac{\mathrm{d}}{\mathrm{d}\epsilon}\left(g_u\left(\boldsymbol{u}^*, \bar{\mathbf{d}}^* + \epsilon\,\Delta\bar{\mathbf{d}}, \delta\boldsymbol{u}\right)\right)\Big|_{\epsilon=0} \tag{3.112}$$

$$\mathfrak{D}_u[g_{\bar{d}}]\cdot\Delta\boldsymbol{u} = \frac{\mathrm{d}}{\mathrm{d}\epsilon}\left(g_{\bar{d}}\left(\boldsymbol{u}^* + \epsilon\,\Delta\boldsymbol{u}, \bar{\mathbf{d}}^*, \delta\bar{\mathbf{d}}\right)\right)\Big|_{\epsilon=0} \tag{3.113}$$

$$\mathfrak{D}_{\bar{d}}[g_{\bar{d}}]\cdot\Delta\bar{\mathbf{d}} = \frac{\mathrm{d}}{\mathrm{d}\epsilon}\left(g_{\bar{d}}\left(\boldsymbol{u}^*, \bar{\mathbf{d}}^* + \epsilon\,\Delta\bar{\mathbf{d}}, \delta\bar{\mathbf{d}}\right)\right)\Big|_{\epsilon=0} \tag{3.114}$$

where $(\boldsymbol{u}^*, \bar{\mathbf{d}}^*)$ denote a known state of the field variables in time. With the following definitions at hand

$$\boldsymbol{F}(\epsilon) \coloneqq \boldsymbol{I} + \operatorname{Grad}(\boldsymbol{u}^* + \epsilon\,\Delta\boldsymbol{u}) =: \boldsymbol{F}^* + \epsilon\,\operatorname{Grad}(\Delta\boldsymbol{u}) \tag{3.115}$$

$$\begin{aligned}
\boldsymbol{E}(\epsilon) &\coloneqq \frac{1}{2}\left(\left[\boldsymbol{F}^* + \epsilon\,\operatorname{Grad}(\Delta\boldsymbol{u})\right]^T\left[\boldsymbol{F}^* + \epsilon\,\operatorname{Grad}(\Delta\boldsymbol{u})\right] - \boldsymbol{I}\right) \\
&= \frac{1}{2}\left(\boldsymbol{F}^{*T}\boldsymbol{F}^* - \boldsymbol{I}\right) + \epsilon\,\frac{1}{2}\left(\boldsymbol{F}^{*T}\operatorname{Grad}(\Delta\boldsymbol{u}) + \operatorname{Grad}(\Delta\boldsymbol{u})^T\boldsymbol{F}^*\right) \\
&\quad + \epsilon^2\,\frac{1}{2}\operatorname{Grad}(\Delta\boldsymbol{u})^T\operatorname{Grad}(\Delta\boldsymbol{u}) \\
&=: \boldsymbol{E}^* + \epsilon\,\Delta\boldsymbol{E}^* + \epsilon^2\,\frac{1}{2}\operatorname{Grad}(\Delta\boldsymbol{u})^T\operatorname{Grad}(\Delta\boldsymbol{u})
\end{aligned} \tag{3.116}$$

$$\begin{aligned}
\delta\boldsymbol{E}(\epsilon) &\coloneqq \frac{1}{2}\left(\left[\boldsymbol{F}^* + \epsilon\,\operatorname{Grad}(\Delta\boldsymbol{u})\right]^T\operatorname{Grad}(\delta\boldsymbol{u}) + \operatorname{Grad}(\delta\boldsymbol{u})^T\left[\boldsymbol{F}^* + \epsilon\,\operatorname{Grad}(\Delta\boldsymbol{u})\right]\right) \\
&= \frac{1}{2}\left(\boldsymbol{F}^{*T}\operatorname{Grad}(\delta\boldsymbol{u}) + \operatorname{Grad}(\delta\boldsymbol{u})^T\boldsymbol{F}^*\right) \\
&\quad + \epsilon\,\frac{1}{2}\left(\operatorname{Grad}(\delta\boldsymbol{u})^T\operatorname{Grad}(\Delta\boldsymbol{u}) + \operatorname{Grad}(\Delta\boldsymbol{u})^T\operatorname{Grad}(\delta\boldsymbol{u})\right) \\
&=: \delta\boldsymbol{E}^* + \epsilon\,\Delta\delta\boldsymbol{E}
\end{aligned} \tag{3.117}$$

$$\bar{\mathbf{d}}(\epsilon) \coloneqq \bar{\mathbf{d}}^* + \epsilon\,\Delta\bar{\mathbf{d}} \tag{3.118}$$

the Gâteaux derivatives of g_u are obtained as

$$\begin{aligned}
\mathfrak{D}_u[g_u]\cdot\Delta\boldsymbol{u} &= \frac{\mathrm{d}}{\mathrm{d}\epsilon}\left(\int_{B_0}\boldsymbol{S}\left(\boldsymbol{E}(\epsilon),\bar{\mathbf{d}}^*\right):\delta\boldsymbol{E}(\epsilon)\,\mathrm{d}V - \int_{B_0}\boldsymbol{f}_0\cdot\delta\boldsymbol{u}\,\mathrm{d}V - \int_{\partial_t B_0}\boldsymbol{t}_0\cdot\delta\boldsymbol{u}\,\mathrm{d}A\right)\Bigg|_{\epsilon=0} \\
&= \left(\int_{B_0}\left[\delta\boldsymbol{E}(\epsilon):\frac{\partial\boldsymbol{S}}{\partial\boldsymbol{E}}:\frac{\partial\boldsymbol{E}}{\partial\epsilon} + \boldsymbol{S}\left(\boldsymbol{E}(\epsilon),\bar{\mathbf{d}}^*\right):\frac{\partial\delta\boldsymbol{E}}{\partial\epsilon}\right]\,\mathrm{d}V\right)\Bigg|_{\epsilon=0} \\
&= \int_{B_0}\left[\delta\boldsymbol{E}^*:\frac{\partial\boldsymbol{S}}{\partial\boldsymbol{E}}:\Delta\boldsymbol{E}^* + \boldsymbol{S}\left(\boldsymbol{E}^*,\bar{\mathbf{d}}^*\right):\Delta\delta\boldsymbol{E}\right]\,\mathrm{d}V
\end{aligned} \tag{3.119}$$

and

$$\begin{aligned}
\mathfrak{D}_{\bar{d}}[g_u]\cdot\Delta\bar{\mathbf{d}} &= \frac{\mathrm{d}}{\mathrm{d}\epsilon}\left(\int_{B_0}\boldsymbol{S}\left(\boldsymbol{E}^*,\bar{\mathbf{d}}(\epsilon)\right):\delta\boldsymbol{E}^*\,\mathrm{d}V - \int_{B_0}\boldsymbol{f}_0\cdot\delta\boldsymbol{u}\,\mathrm{d}V - \int_{\partial_t B_0}\boldsymbol{t}_0\cdot\delta\boldsymbol{u}\,\mathrm{d}A\right)\Bigg|_{\epsilon=0} \\
&= \left(\int_{B_0}\delta\boldsymbol{E}^*:\frac{\partial\boldsymbol{S}}{\partial\bar{\mathbf{d}}}\cdot\frac{\partial\bar{\mathbf{d}}}{\partial\epsilon}\,\mathrm{d}V\right)\Bigg|_{\epsilon=0} \\
&= \int_{B_0}\delta\boldsymbol{E}^*:\frac{\partial\boldsymbol{S}}{\partial\bar{\mathbf{d}}}\cdot\Delta\bar{\mathbf{d}}\,\mathrm{d}V.
\end{aligned} \tag{3.120}$$

In a similar fashion, $\mathfrak{D}_u[g_{\bar{d}}] \cdot \Delta \boldsymbol{u}$ and $\mathfrak{D}_{\bar{d}}[g_{\bar{d}}] \cdot \Delta \bar{\mathbf{d}}$ are calculated

$$\begin{aligned}
\mathfrak{D}_u[g_{\bar{d}}] \cdot \Delta \boldsymbol{u} &= \frac{\mathrm{d}}{\mathrm{d}\epsilon} \left(\int_{B_0} \delta \bar{\mathbf{d}} \cdot \mathbf{H}_{\bar{d}} \cdot \left(\mathbf{d}\left(\boldsymbol{E}(\epsilon), \bar{\mathbf{d}}^* \right) - \bar{\mathbf{d}}^* \right) \mathrm{d}V \right. \\
&\qquad \left. - \int_{B_0} \operatorname{Grad}\left(\delta \bar{\mathbf{d}}\right) : \left(\mathbf{A}_{\bar{d}} \cdot \operatorname{Grad}\left(\bar{\mathbf{d}}^* \right) \right) \mathrm{d}V \right) \Big|_{\epsilon=0} \\
&= \left(\int_{B_0} \delta \bar{\mathbf{d}} \cdot \mathbf{H}_{\bar{d}} \cdot \frac{\partial \mathbf{d}}{\partial \boldsymbol{E}} : \frac{\partial \boldsymbol{E}}{\partial \epsilon} \, \mathrm{d}V \right) \Big|_{\epsilon=0} \\
&= \int_{B_0} \delta \bar{\mathbf{d}} \cdot \mathbf{H}_{\bar{d}} \cdot \frac{\partial \mathbf{d}}{\partial \boldsymbol{E}} : \Delta \boldsymbol{E}^* \, \mathrm{d}V
\end{aligned} \tag{3.121}$$

as well as

$$\begin{aligned}
\mathfrak{D}_{\bar{d}}[g_{\bar{d}}] \cdot \Delta \bar{\mathbf{d}} &= \frac{\mathrm{d}}{\mathrm{d}\epsilon} \left(\int_{B_0} \delta \bar{\mathbf{d}} \cdot \mathbf{H}_{\bar{d}} \cdot \left(\mathbf{d}\left(\boldsymbol{E}^*, \bar{\mathbf{d}}(\epsilon) \right) - \bar{\mathbf{d}}(\epsilon) \right) \mathrm{d}V \right. \\
&\qquad \left. - \int_{B_0} \operatorname{Grad}\left(\delta \bar{\mathbf{d}}\right) : \left(\mathbf{A}_{\bar{d}} \cdot \operatorname{Grad}\left(\bar{\mathbf{d}}(\epsilon) \right) \right) \mathrm{d}V \right) \Big|_{\epsilon=0} \\
&= \left(\int_{B_0} \delta \bar{\mathbf{d}} \cdot \mathbf{H}_{\bar{d}} \cdot \left(\frac{\partial \mathbf{d}}{\partial \bar{\mathbf{d}}} \cdot \frac{\partial \bar{\mathbf{d}}}{\partial \epsilon} - \frac{\partial \bar{\mathbf{d}}}{\partial \epsilon} \right) \mathrm{d}V \right. \\
&\qquad \left. - \int_{B_0} \operatorname{Grad}\left(\delta \bar{\mathbf{d}}\right) : \left(\mathbf{A}_{\bar{d}} \cdot \operatorname{Grad}\left(\Delta \bar{\mathbf{d}} \right) \right) \mathrm{d}V \right) \Big|_{\epsilon=0} \\
&= \left(\int_{B_0} \delta \bar{\mathbf{d}} \cdot \mathbf{H}_{\bar{d}} \cdot \left(\frac{\partial \mathbf{d}}{\partial \bar{\mathbf{d}}} \cdot \Delta \bar{\mathbf{d}} - \Delta \bar{\mathbf{d}} \right) \mathrm{d}V - \int_{B_0} \operatorname{Grad}\left(\delta \bar{\mathbf{d}}\right) : \left(\mathbf{A}_{\bar{d}} \cdot \operatorname{Grad}\left(\Delta \bar{\mathbf{d}} \right) \right) \mathrm{d}V \right)
\end{aligned} \tag{3.122}$$

where $\operatorname{Grad}\left(\bar{\mathbf{d}}(\epsilon)\right) = \operatorname{Grad}\left(\bar{\mathbf{d}}^*\right) + \epsilon \operatorname{Grad}\left(\Delta \bar{\mathbf{d}}\right)$ was exploited.

3.8.11 Derivation of transformation law between logarithmic and Lagrangian strain space

For the following discussion, the generalized family of strain tensors also known as the Seth-Hill strain tensors (see Seth [1961], Hill [1968]) is introduced

$$\boldsymbol{E}^{(m)} = \begin{cases} \frac{1}{2m} \left(\boldsymbol{C}^m - \boldsymbol{I} \right) & , m \neq 0 \\ \frac{1}{2} \ln(\boldsymbol{C}) & , m = 0 \end{cases} \tag{3.123}$$

where $m \in \mathbb{R}$. For the special cases $m = 1$ the Green-Lagrange strain tensor $\boldsymbol{E} \coloneqq \boldsymbol{E}^{(1)}$ as well as $m = 0$ the (logarithmic) Hencky strain tensor $\boldsymbol{\varepsilon} \coloneqq \boldsymbol{E}^{(0)}$ are obtained. In order to obtain the transformation formula from the logarithmic to the Lagrangian strain space, the

stress power is expressed as

$$\boldsymbol{S} : \frac{1}{2}\dot{\boldsymbol{C}} = \boldsymbol{S} : \dot{\boldsymbol{E}} = \boldsymbol{T} : \dot{\boldsymbol{\varepsilon}} \tag{3.124}$$

and further

$$\dot{\boldsymbol{\varepsilon}} = \underbrace{2\frac{\partial \boldsymbol{\varepsilon}}{\partial \boldsymbol{C}}}_{=:\mathbb{Q}} : \frac{1}{2}\dot{\boldsymbol{C}} \tag{3.125}$$

where $\mathbb{Q}$ possesses both minor and major symmetry, i.e. $Q_{ijkl} = Q_{jikl} = Q_{ijlk} = Q_{klij}$. Taking Equation (3.124) into account, the second Piola-Kirchhoff stress tensor can be expressed as

$$\boldsymbol{S} = \boldsymbol{T} : \mathbb{Q}. \tag{3.126}$$

as well as its rate

$$\dot{\boldsymbol{S}} = \frac{\partial \boldsymbol{S}}{\partial \boldsymbol{E}} : \dot{\boldsymbol{E}} + \frac{\partial \boldsymbol{S}}{\partial \bar{\mathbf{d}}} \cdot \dot{\bar{\mathbf{d}}} = \mathbb{C} : \frac{1}{2}\dot{\boldsymbol{C}} + \frac{\partial \boldsymbol{S}}{\partial \bar{\mathbf{d}}} \cdot \dot{\bar{\mathbf{d}}}. \tag{3.127}$$

Combining Equation (3.125) and (3.126), the stress rate can be rewritten as

$$\dot{\boldsymbol{S}} = \dot{\boldsymbol{T}} : \mathbb{Q} + \boldsymbol{T} : \dot{\mathbb{Q}} = \underbrace{\left(\mathbb{Q} : \frac{\partial \boldsymbol{T}}{\partial \boldsymbol{\varepsilon}} : \mathbb{Q} + \boldsymbol{T} : 4\frac{\partial^2 \boldsymbol{\varepsilon}}{\partial \boldsymbol{C} \partial \boldsymbol{C}}\right)}_{=\mathbb{C}} : \frac{1}{2}\dot{\boldsymbol{C}} + \underbrace{\left(\mathbb{Q} : \frac{\partial \boldsymbol{T}}{\partial \bar{\mathbf{d}}}\right)}_{=\mathscr{K}_{\bar{d}}} \cdot \dot{\bar{\mathbf{d}}} \tag{3.128}$$

from which a relation between the material tangent $\mathbb{C}$ and its counterpart in the logarithmic strain space can be deduced. Note that the above results are in line with the ones provided by Miehe and Lambrecht [2001]. However, they directly assumed to obtain the stress tensor $\boldsymbol{T}$ following the Coleman-Noll procedure (see Coleman and Noll [1961]) derived from the Helmholtz free energy ψ. Then, by making use of Faà di Bruno's formula the above results can also be derived. Furthermore, the straightforward numerical implementation of $\mathbb{Q}$, $\overset{6}{\mathbb{L}} \coloneqq 4\,\partial^2 \boldsymbol{\varepsilon} / \partial \boldsymbol{C} \partial \boldsymbol{C}$ as well as the transformation to $\boldsymbol{S}$ and $\mathbb{C}$ based either on the eigenvalue bases or eigenprojections is provided by Miehe and Lambrecht [2001] or Schröder et al. [2002].

3.8.12 Implicit integration scheme at local Gaussian point level

For a better understanding, Algorithm 1 provides a pseudo-code of the implicit time integration scheme as well as the transformation between Lagrangian and logarithmic strain spaces. Following the notation introduced by Korelc [2009], $\hat{\delta}(\bullet)/\hat{\delta}(\bullet)$ defines an algorithmic differentiation operator. These derivatives are obtained using *AceGen*. A more detailed explanation of the active-set search strategy and the trial active-set $\mathfrak{J}_{\text{act}}^{tr}$ can be found, for instance, in Simo and Hughes [2006] and Brepols et al. [2017].

Algorithm 1 Implicit integration scheme

Input: $\boldsymbol{C}_{n+1}$, $\bar{\mathrm{d}}_{n+1}$, $\hat{\boldsymbol{\varepsilon}}_{p_n}$, κ_{p_n}, $\hat{\boldsymbol{D}}_{r_n}$, κ_{d_n}

- **Logarithmic strain space**

$\boldsymbol{\varepsilon}_{n+1} \leftarrow \frac{1}{2}\ln\left(\boldsymbol{C}_{n+1}\right)$; $\quad \mathbb{Q}_{n+1} \leftarrow 2\frac{\partial \boldsymbol{\varepsilon}_{n+1}}{\partial \boldsymbol{C}_{n+1}}$; $\quad \overset{6}{\mathbb{L}}_{n+1} \leftarrow 4\frac{\partial^2 \boldsymbol{\varepsilon}_{n+1}}{\partial \boldsymbol{C}_{n+1}\partial \boldsymbol{C}_{n+1}}$

- **Trial state**

$\boldsymbol{\varepsilon}_{p_{n+1}} \leftarrow \boldsymbol{\varepsilon}_{p_n}$; $\quad \kappa_{p_{n+1}} \leftarrow \kappa_{p_n}$; $\quad \boldsymbol{D}_{r_{n+1}} \leftarrow \boldsymbol{D}_{r_n}$; $\quad \kappa_{d_{n+1}} \leftarrow \kappa_{d_n}$

$\bar{\boldsymbol{\varepsilon}}_{e_{n+1}} \leftarrow \boldsymbol{\varepsilon}_{n+1} - \boldsymbol{\varepsilon}_{p_{n+1}}$

▷ Compute $\boldsymbol{T}_{n+1}$, $\boldsymbol{X}_{n+1}$, $R_{p_{n+1}}$, $\boldsymbol{Y}_{n+1}$, and $R_{d_{n+1}}$ based on Equations (3.24), (3.43), (3.46)-(3.52)

$\Phi_p^{tr} \leftarrow \sqrt{\frac{3}{2}}\sqrt{\mathrm{tr}\left(\mathrm{dev}\left(\boldsymbol{T}_{n+1} - \boldsymbol{X}_{n+1}\right)^2\right)} - \left(\sigma_{y0} - R_{p_{n+1}}\right)$

$\Phi_d^{tr} \leftarrow \sqrt{3}\sqrt{\boldsymbol{Y}_{+_{n+1}} : \mathbb{A}_{d_{n+1}} : \boldsymbol{Y}_{+_{n+1}}} - \left(Y_0 - R_{d_{n+1}}\right)$ ▷ cf. Equations (3.31) and (3.33)

- **Check onset criteria**

if $\Phi_p^{tr} > 0$ or $\Phi_d^{tr} > 0$ **then**

$\mathfrak{J}_{\text{act}}^{tr} \coloneqq \{\alpha \in \{p, d\} \mid \Phi_\alpha^{tr} > 0\}$ ▷ Define trial active-set

▷ Set $\hat{\mathbf{r}}_{loc}$ and $\mathbf{x}_{loc}$ according to $\mathfrak{J}_{\text{act}}^{tr}$ (cf. Table 3.1 and Equation (3.74))

$k \leftarrow 1$

while $\|\hat{\mathbf{r}}_{loc}^{(k)}\| > tol$ **do** ▷ Start local Newton-Raphson iterations (k)

$$\mathbf{x}_{loc}^{(k+1)} \leftarrow \mathbf{x}_{loc}^{(k)} - \left(\frac{\hat{\delta}\hat{\mathbf{r}}_{loc}^{(k)}}{\hat{\delta}\mathbf{x}_{loc}^{(k)}}\right)^{-1} \hat{\mathbf{r}}_{loc}^{(k)}$$

$k \leftarrow k + 1$

end while

if $\Delta\gamma_\alpha < 0$ for any $\alpha \in \mathfrak{J}_{\text{act}}^{tr}$ **then**

▷ Drop α from the active-set. Restart Newton-Raphson iterations with new $\mathfrak{J}_{\text{act}}^{tr}$

else

▷ State is admissible. Solution has been found

▷ Update $\boldsymbol{\varepsilon}_{p_{n+1}}$, $\kappa_{p_{n+1}}$, $\boldsymbol{D}_{r_{n+1}}$, $\kappa_{d_{n+1}}$ depending on $\mathfrak{J}_{\text{act}}^{tr}$

▷ Update $\boldsymbol{T}_{n+1}$

$$\nabla\mathbf{x}_{loc} \leftarrow -\left(\frac{\hat{\delta}\hat{\mathbf{r}}_{loc}^{(k)}}{\hat{\delta}\mathbf{x}_{loc}^{(k)}}\right)^{-1} \frac{\hat{\delta}\hat{\mathbf{r}}_{loc}^{(k)}}{\hat{\delta}\mathbf{x}_{glo_{n+1}}}$$

end if

end if

- **Compute constitutively dependent quantities and tangents**

$\mathbf{d}_{n+1} \leftarrow \left(\mathrm{tr}\left(\boldsymbol{D}_{r_{n+1}}\right), \mathrm{tr}\left(\boldsymbol{D}_{r_{n+1}}^2\right), \mathrm{tr}\left(\boldsymbol{D}_{r_{n+1}}^3\right)\right)^T$

$\Delta\hat{\boldsymbol{T}}_{n+1}^{(6\times9)} \leftarrow \left.\frac{\hat{\delta}\hat{\boldsymbol{T}}_{n+1}}{\hat{\delta}\mathbf{x}_{glo_{n+1}}}\right|_{\frac{D\mathbf{x}_{loc}}{D\mathbf{x}_{glo}} = \nabla\mathbf{x}_{loc}}$; $\quad \Delta\mathbf{d}_{n+1}^{(3\times9)} \leftarrow \left.\frac{\hat{\delta}\mathbf{d}_{n+1}}{\hat{\delta}\mathbf{x}_{glo_{n+1}}}\right|_{\frac{D\mathbf{x}_{loc}}{D\mathbf{x}_{glo}} = \nabla\mathbf{x}_{loc}}$

- **Transform to Lagrangian space**

▷ Get $\mathbb{C}_{n+1}^{LOG}$, $\mathscr{K}_{\bar{d}_{n+1}}^{LOG}$ from $\Delta\hat{\boldsymbol{T}}_{n+1}$ and $\mathscr{G}_{u_{n+1}}^{LOG}$, $\mathbf{G}_{\bar{d}_{n+1}}$ from $\Delta\mathbf{d}_{n+1}$

$\boldsymbol{S}_{n+1} \leftarrow \boldsymbol{T}_{n+1} : \mathbb{Q}_{n+1}$

$\mathbb{C}_{n+1} \leftarrow \mathbb{Q}_{n+1} : \mathbb{C}_{n+1}^{LOG} : \mathbb{Q}_{n+1} + \boldsymbol{T}_{n+1} : \overset{6}{\mathbb{L}}_{n+1}$

$\mathscr{K}_{\bar{d}_{n+1}} \leftarrow \mathbb{Q}_{n+1} : \mathscr{K}_{\bar{d}_{n+1}}^{LOG}$

$\mathscr{G}_{u_{n+1}} \leftarrow \mathscr{G}_{u_{n+1}}^{LOG} : \mathbb{Q}_{n+1}$

3.8.13 Stress invariants

In order to describe the stress state of the material, different invariants of the Cauchy stress tensor $\boldsymbol{\sigma} = 1/J\ \boldsymbol{F}\boldsymbol{S}\boldsymbol{F}^T$ are utilized, with $J = \det(\boldsymbol{F}) = \sqrt{\det(\boldsymbol{C})}$ being the determinant of the deformation gradient. Under consideration of

$$\begin{aligned}\operatorname{dev}(\boldsymbol{\sigma}) &= \left(\boldsymbol{\sigma} - \frac{\operatorname{tr}(\boldsymbol{\sigma})}{3}\boldsymbol{I}\right) \\ &= \frac{1}{J}\boldsymbol{F}^{-T}\left(\boldsymbol{C}\boldsymbol{S} - \frac{\operatorname{tr}(\boldsymbol{C}\boldsymbol{S})}{3}\boldsymbol{I}\right)\boldsymbol{F}^T \\ &= \frac{1}{J}\boldsymbol{F}^{-T}\operatorname{dev}(\boldsymbol{C}\boldsymbol{S})\boldsymbol{F}^T\end{aligned} \tag{3.129}$$

these invariants can be expressed in terms of Lagrangian quantities as follows

$$I_1^{\boldsymbol{\sigma}} = \operatorname{tr}(\boldsymbol{\sigma}) = \frac{\operatorname{tr}(\boldsymbol{C}\boldsymbol{S})}{J} \tag{3.130}$$

$$J_2^{\boldsymbol{\sigma}} = \frac{1}{2}\operatorname{tr}\left(\operatorname{dev}(\boldsymbol{\sigma})^2\right) = \frac{1}{2\,J^2}\operatorname{tr}\left(\operatorname{dev}(\boldsymbol{C}\boldsymbol{S})^2\right) \tag{3.131}$$

$$J_3^{\boldsymbol{\sigma}} = \det(\operatorname{dev}(\boldsymbol{\sigma})) = \frac{\det(\operatorname{dev}(\boldsymbol{C}\boldsymbol{S}))}{J^3}. \tag{3.132}$$

With the latter equations at hand, the stress state invariants can be calculated as

$$\sigma_{eq} \coloneqq \sqrt{3\,J_2^{\boldsymbol{\sigma}}} = \frac{1}{J}\sqrt{\frac{3}{2}\operatorname{tr}\left(\operatorname{dev}(\boldsymbol{C}\boldsymbol{S})^2\right)} \tag{3.133}$$

$$\rho \coloneqq \frac{\frac{I_1^{\boldsymbol{\sigma}}}{3}}{\sigma_{eq}} = \frac{\frac{\operatorname{tr}(\boldsymbol{C}\boldsymbol{S})}{3}}{\sqrt{\frac{3}{2}\operatorname{tr}\left(\operatorname{dev}(\boldsymbol{C}\boldsymbol{S})^2\right)}} \tag{3.134}$$

$$r \coloneqq \cos(3\theta_c) = \frac{J_3^{\boldsymbol{\sigma}}}{2}\sqrt{\left(\frac{3}{J_2^{\boldsymbol{\sigma}}}\right)^3} = \frac{\det(\operatorname{dev}(\boldsymbol{C}\boldsymbol{S}))}{2}\sqrt{\left(\frac{6}{\operatorname{tr}\left(\operatorname{dev}(\boldsymbol{C}\boldsymbol{S})^2\right)}\right)^3} \tag{3.135}$$

where θ_c denotes Lode's angle in line with Han and Chen [1985].

3.8.14 Convergence study for cruciform specimen

See Figures 3.32-3.35 for the convergence study and Figure 3.36 for damage contour plots.

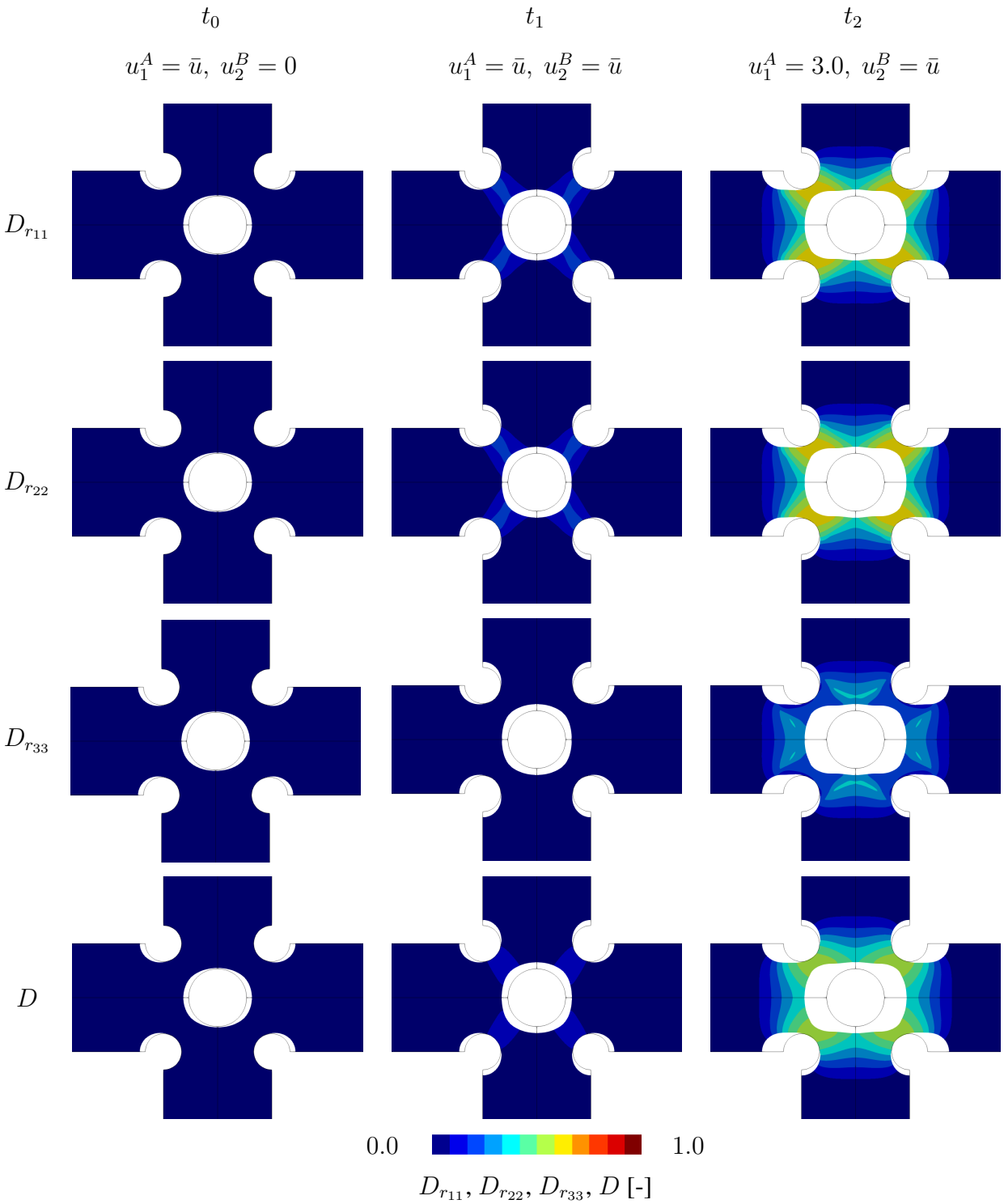

Figure 3.24: Damage contour plots for $\bar{u} = 0.8$ [mm] of main diagonal components of $\boldsymbol{D}_r$ in case of anisotropic damage and D for isotropic damage (41836 elements). The first two columns correspond to the time of load change while the third column is during further increase of u_1^A (cf. Figure 3.20).

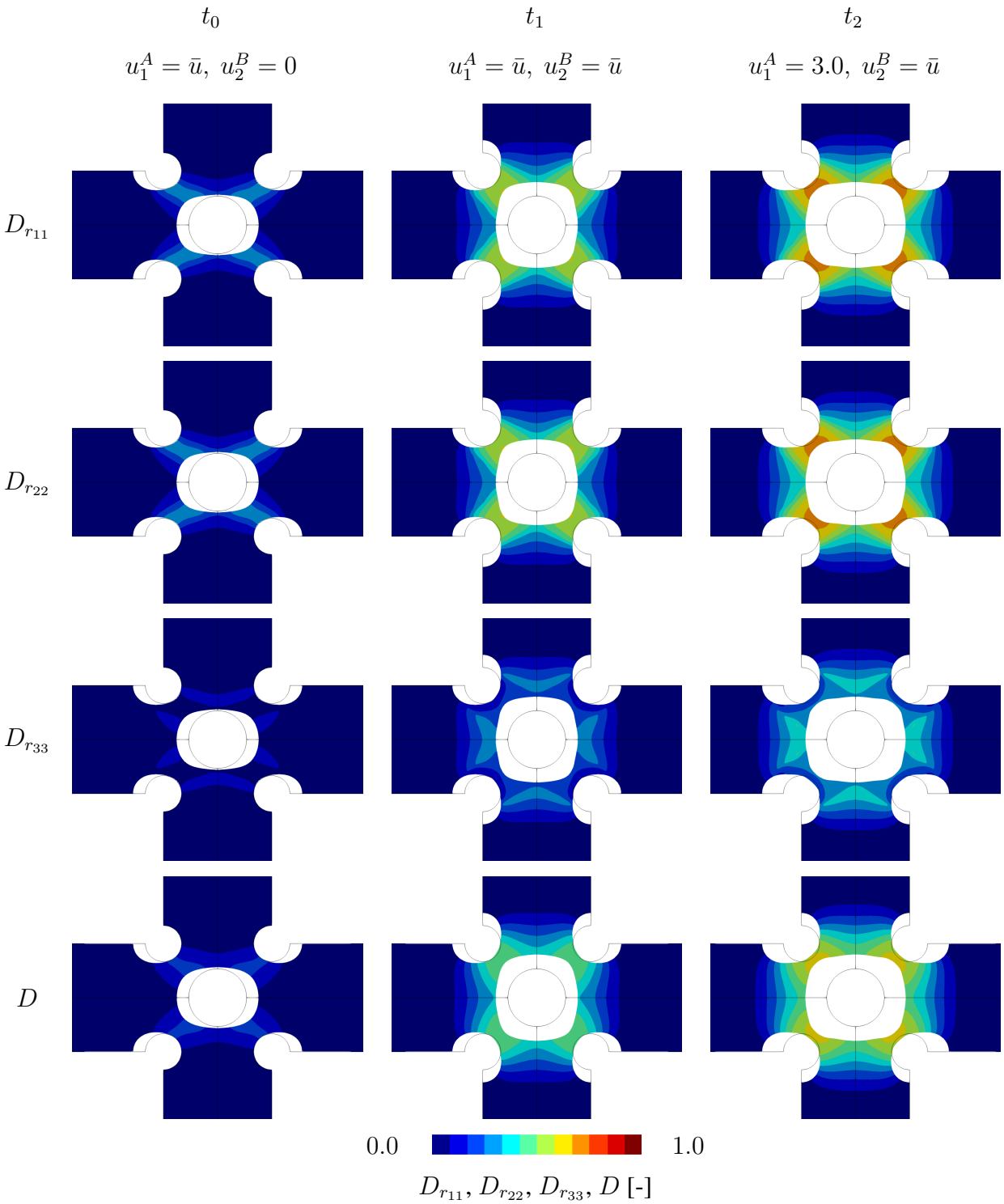

Figure 3.25: Damage contour plots for $\bar{u} = 1.75$ [mm] of main diagonal components of $\boldsymbol{D}_r$ in case of anisotropic damage and D for isotropic damage (41836 elements). The first two columns correspond to the time of load change while the third column is during further increase of u_1^A (cf. Figure 3.20).

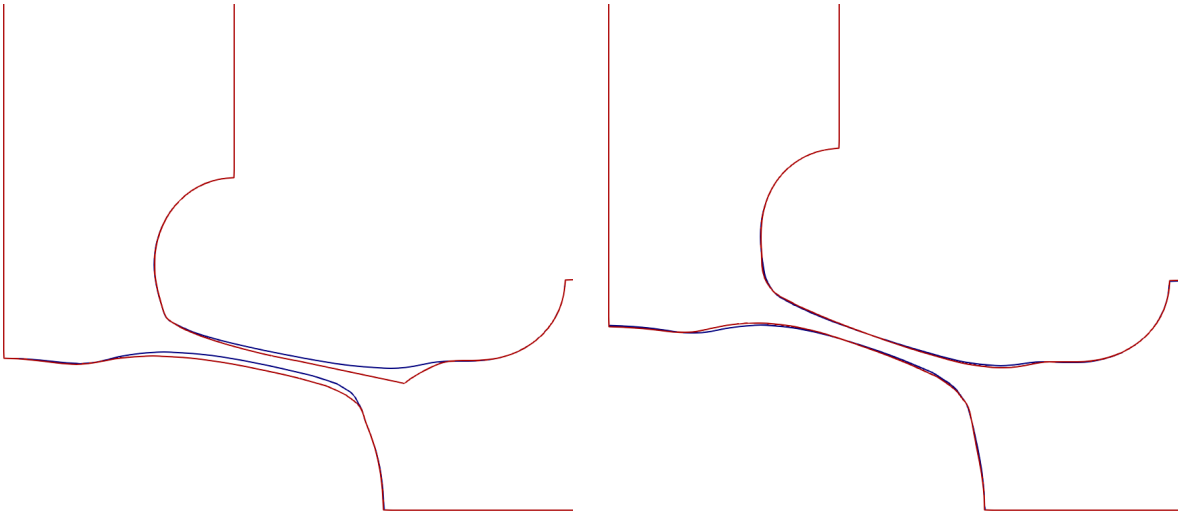

Figure 3.26: Comparison between isotropic (blue) and anisotropic (red) crack shapes at $u_1^A = 8.25$ [mm] (t_3) for different $\bar{u}$ using 41836 finite elements.

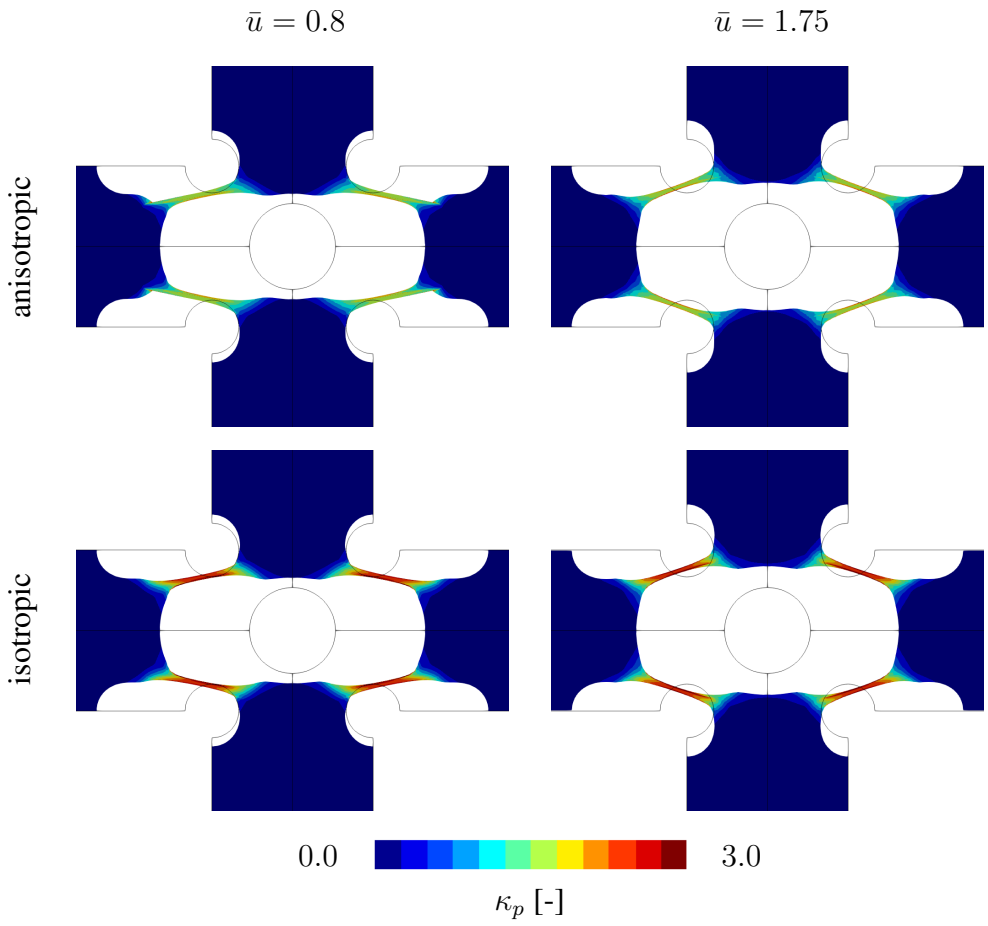

Figure 3.27: Accumulated plastic strain in case of anisotropic and isotropic damage at $u_1^A = 8.25$ [mm] (t_3) for different $\bar{u}$ using 41836 finite elements.

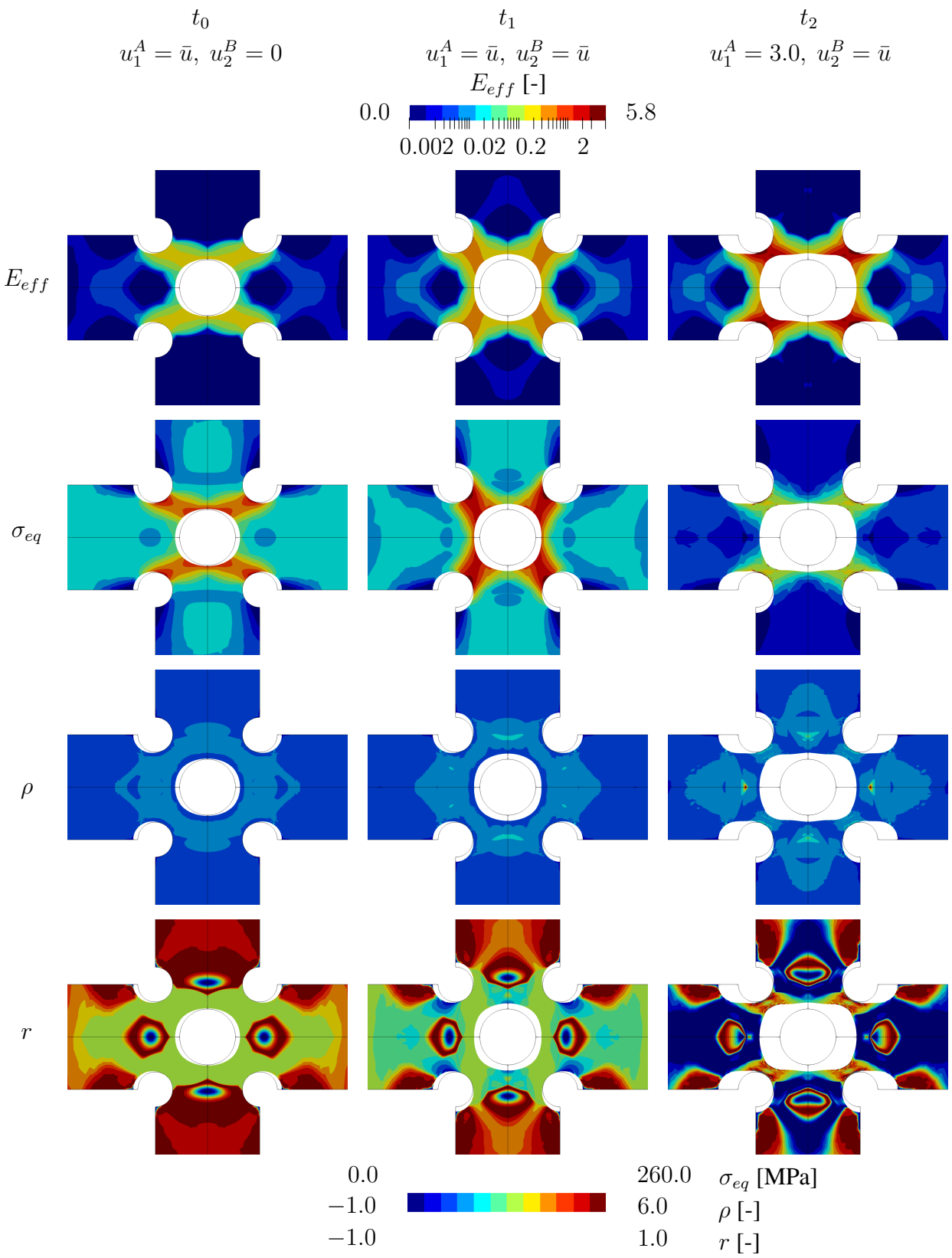

Figure 3.28: Stress-strain states for anisotropic damage and $\bar{u} = 0.8$ [mm] (cf. Figure 3.20). First column: Effective Green-Lagrange strain E_{eff} (logarithmic scale), second column: Von Mises stress σ_{eq}, third column: Lode parameter r.

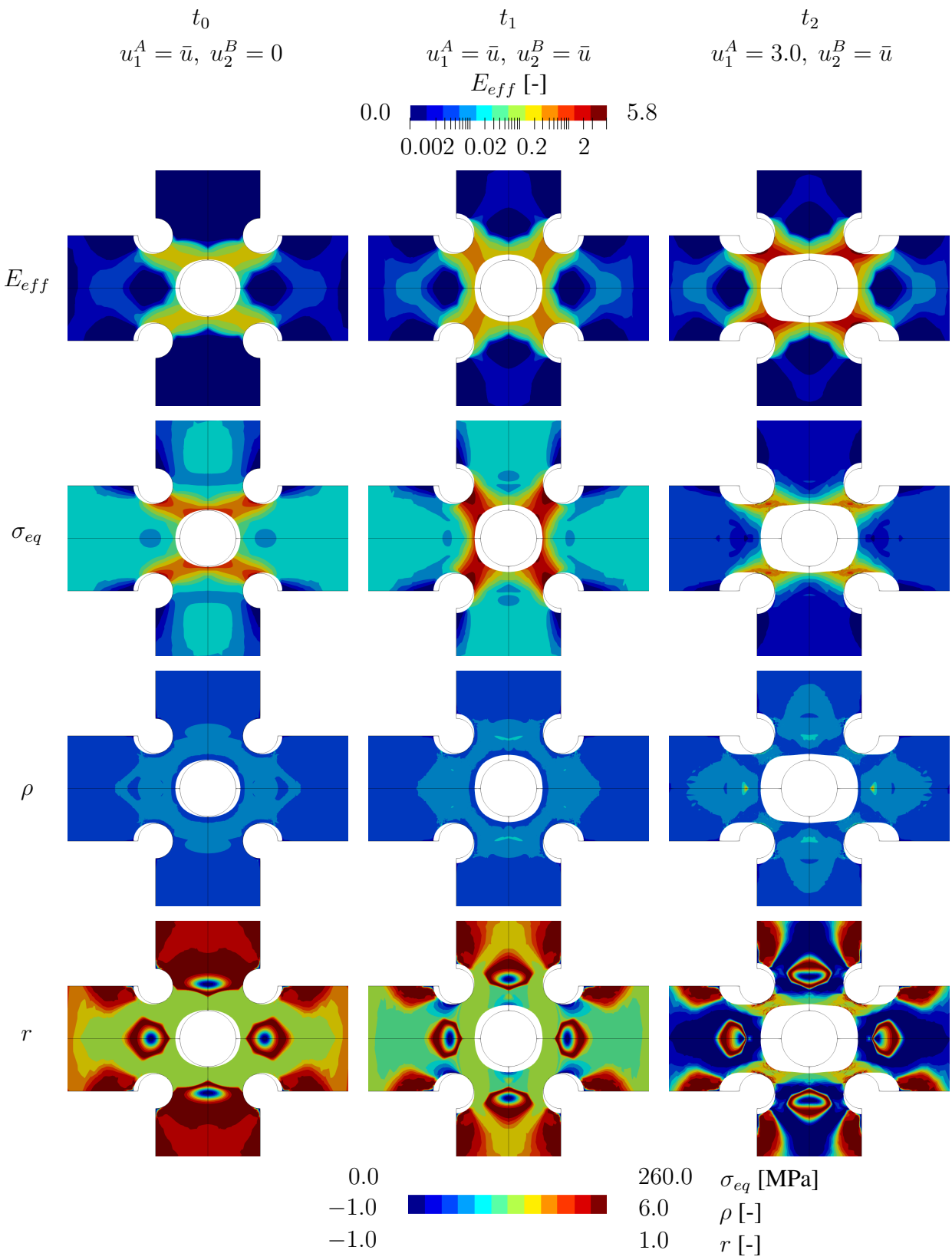

Figure 3.29: Stress-strain states for isotropic damage and $\bar{u} = 0.8$ [mm] (cf. Figure 3.20). First column: Effective Green-Lagrange strain E_{eff}, second column: Von Mises stress σ_{eq}, third column: Lode parameter r.

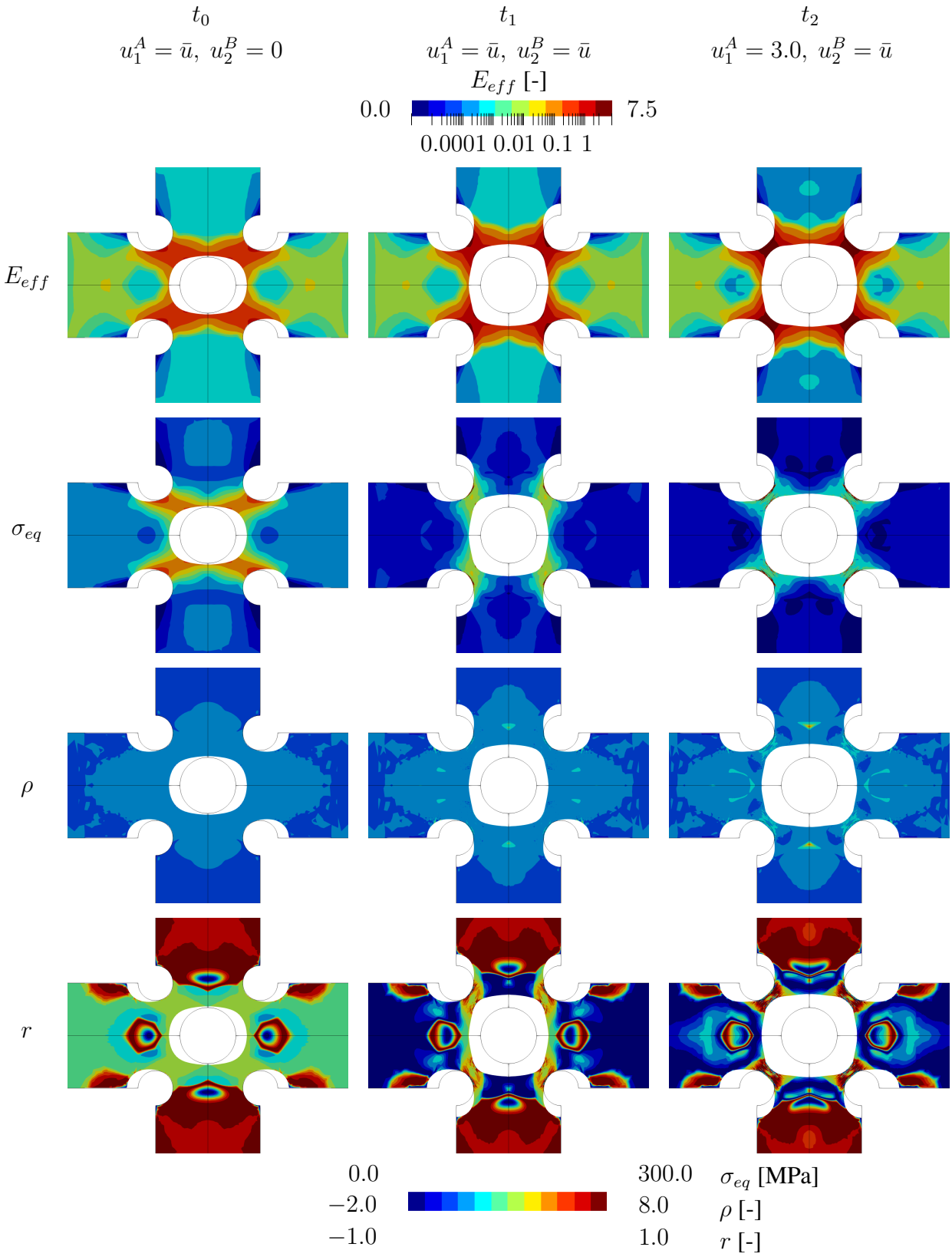

Figure 3.30: Stress-strain states for anisotropic damage and $\bar{u} = 1.75$ [mm] (cf. Figure 3.20). First column: Effective Green-Lagrange strain E_{eff}, second column: Von Mises stress σ_{eq}, third column: Lode parameter r.

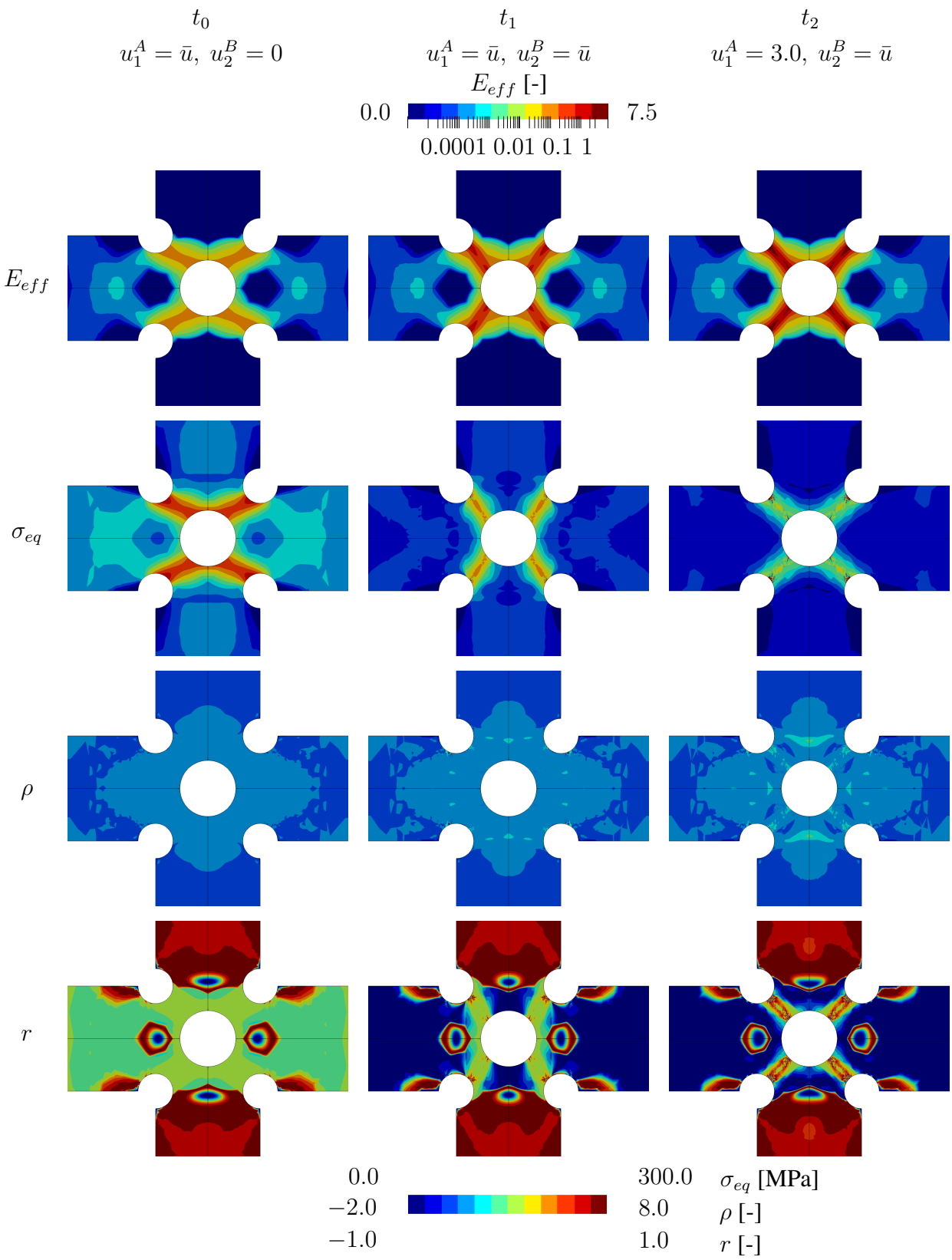

Figure 3.31: Stress-strain states for isotropic damage and $\bar{u} = 1.75$ [mm] (cf. Figure 3.20). First column: Effective Green-Lagrange strain E_{eff}, second column: Von Mises stress σ_{eq}, third column: Lode parameter r.

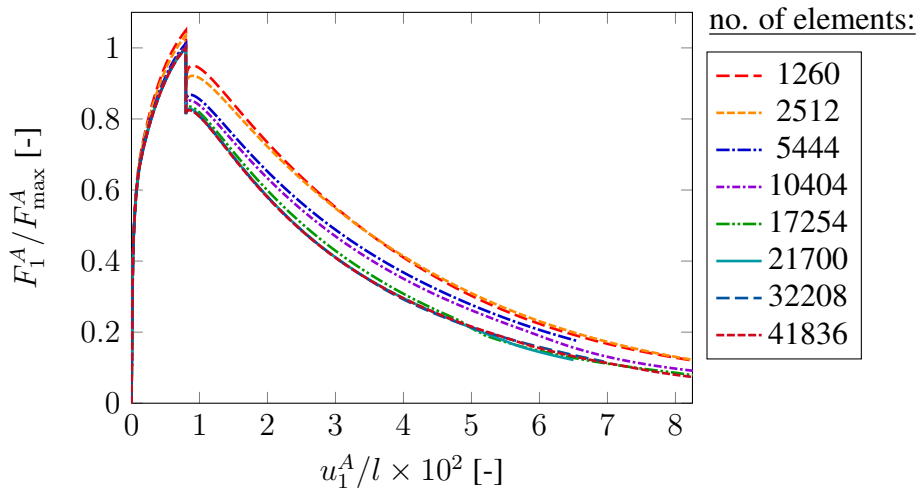

Figure 3.32: Normalized load-displacement curves ($u_{max} = 0.8$ [mm], edge A, $F^A_{max} = 1.5294$ [kN], anisotropic, finest mesh)

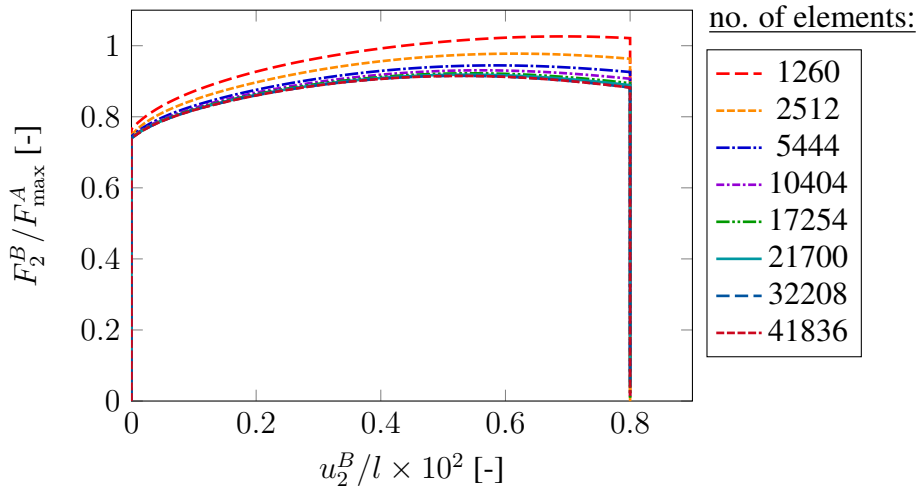

Figure 3.33: Normalized load-displacement curves ($u_{max} = 0.8$ [mm], edge B, $F^A_{max} = 1.5294$ [kN], anisotropic, finest mesh)

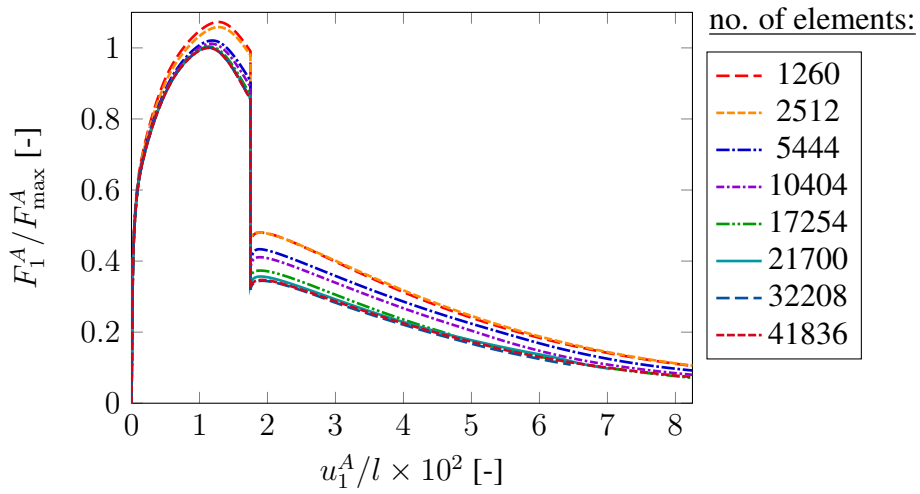

Figure 3.34: Normalized load-displacement curves ($u_{max} = 1.75$ [mm], edge A, $F_{max}^A = 1.5912$ [kN], anisotropic, finest mesh)

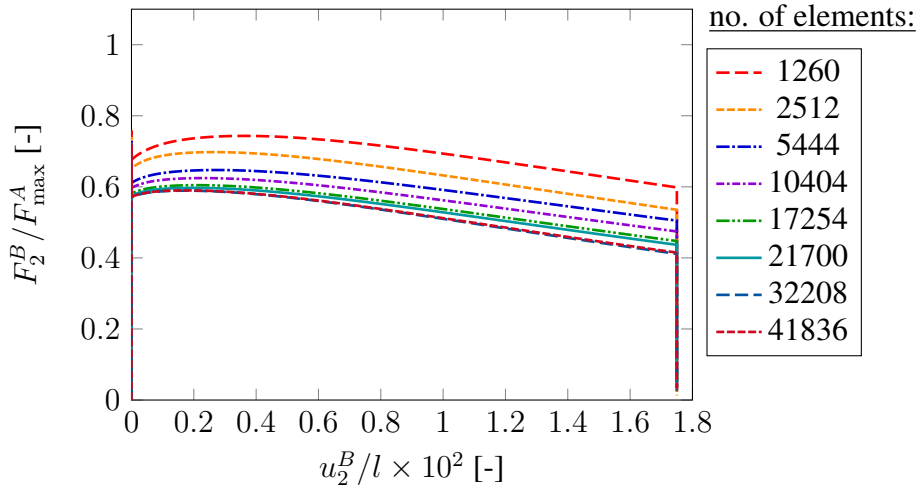

Figure 3.35: Normalized load-displacement curves ($u_{max} = 1.75$ [mm], edge B, $F_{max}^A = 1.5912$ [kN], anisotropic, finest mesh)

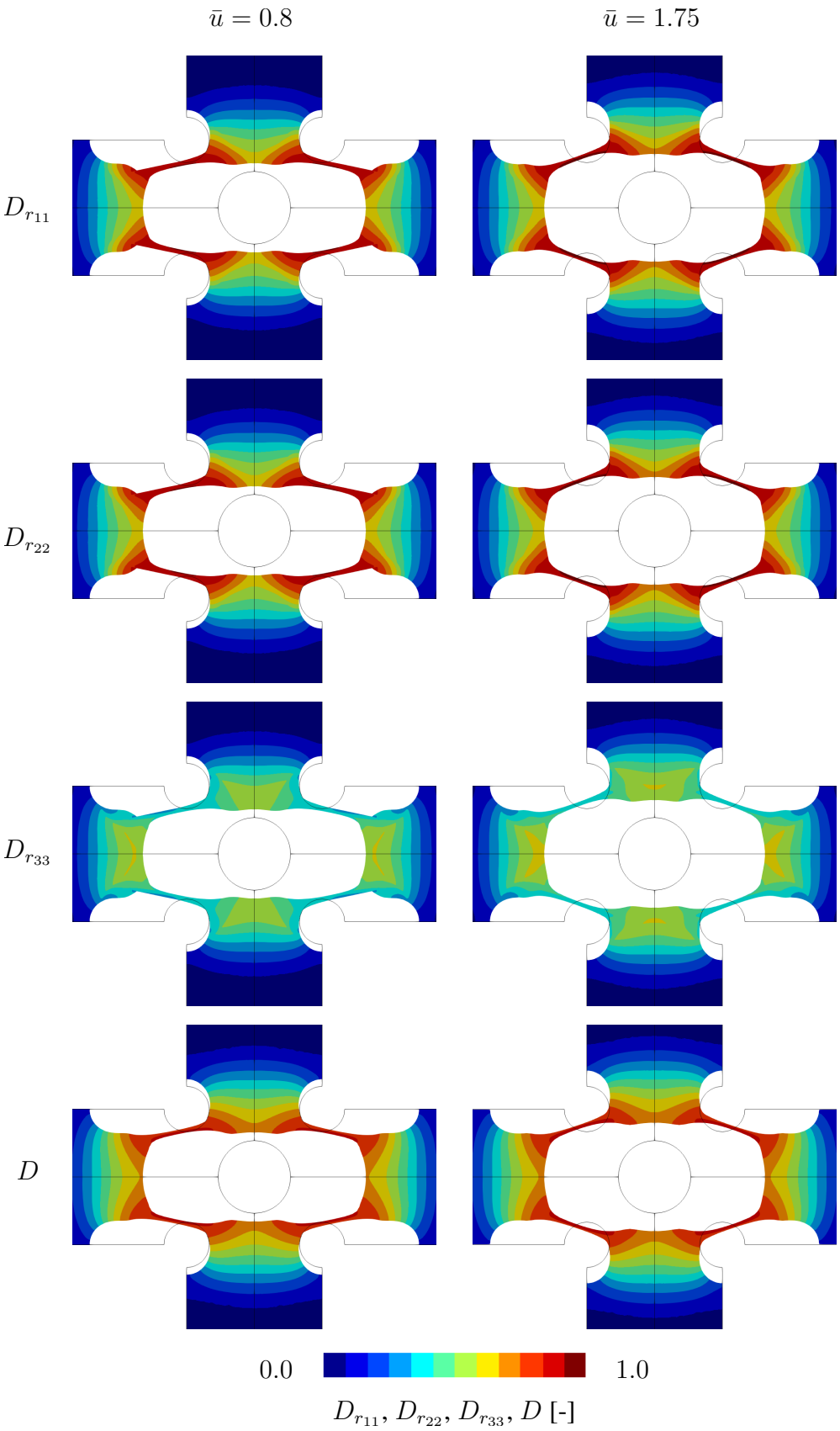

Figure 3.36: Damage contours at $u_1^A = 8.25$ [mm] (t_3) for different $\bar{u}$ (41836 elements)

4 Article 3: A novel gradient-extended anisotropic two-surface damage-plasticity model for finite deformations

This article was published as:

Holthusen, H., Brepols, T., Reese, S., and Simon, J.-W. [2022], 'A novel gradient-extended anisotropic two-surface damage-plasticity model for finite deformations', In: *XVI International Conference on Computational Plasticity. Fundamentals and Application (COMPLAS 2021)*, 1-12.

Disclosure of the individual authors' contributions to the article:

H. Holthusen reviewed the relevant existing literature, derived the constitutive framework and implemented the material model and the element routine into the finite element software *FEAP*. He set up and performed all simulations, interpreted the results and wrote the preliminary version of the article. It was his idea to employ the finite strain elasto-plasticity framework coupled to gradient-extended damage by Brepols et al. [2020] and the anisotropic damage model at small strains by Fassin et al. [2019*b*] as the basis for the model development. Moreover, T. Brepols, S. Reese, and J.-W. Simon gave conceptual advice, contributed to the discussion of the results, read the current version of the article, and gave valuable suggestions for improvement. All authors approved the preliminary publication of the article in the present dissertation.

4.1 Abstract

A novel 'two-surface' gradient-extended damage-plasticity model taking into account damage anisotropy in the logarithmic strain space is derived in a thermodynamically consistent manner. In addition, the concept of an additive split is followed, while the weak form of the linear momentum is stated with respect to Lagrangian quantities. Hence, the mapping between these two spaces is additionally addressed here. Moreover, in order to overcome mesh-dependency, the invariants of the second order damage tensor are gradient-enhanced using the micromorphic approach. In addition, some aspects of the numerical implementation are discussed. A numerical example considering an asymmetrically notched specimen illustrates the model's behavior as well as its ability to deliver mesh-independent results.

4.2 Introduction

For several decades, much research has been conducted in the field of anisotropic damage from both an experimental and a modeling point of view. Since experimental studies have shown that, for instance, in the case of non-proportional loading paths isotropic damage models reach their limitations, there is an enormous need of anisotropic damage models. Further, if one considers forming processes, besides non-proportional load paths also large deformations occur. Especially in the field of metal forming, coupled models for damage with plasticity at finite deformations are of utmost importance to better understand these processes and to predict local phenomena such as stress peaks.

The field of Continuum Damage Mechanics (CDM) is a well established modeling approach to counteract these problems by means of phenomenological material models. In fact, CDM is still an active field of research and led to coupled anisotropic models at large deformations in the recent past, for instance, for initially isotropic materials using a damage tensor (e.g. Badreddine et al. [2015]) or anisotropic materials using several scalar damage variables (e.g. Holthusen et al. [2020]). Moreover, while for the infinitesimal theory the kinematics in connection with a second order damage tensor are relatively clear, the finite strain theory offers way more conceptual ways to deal with finite elasto-plasticity combined with anisotropic damage.

In addition to the modeling difficulties, it is known that so-called local damage models suffer from severe mesh-dependency when considering structural examples. A possible solution technique is to take additional length scales into account by means of e.g. gradient-extended material model formulations. A certain subclass of those approaches is the micromorphic

approach Forest [2009, 2016], which has proven to avoid mesh-dependency for different cases of damage models (see e.g. Brepols et al. [2020], Fassin et al. [2019*b*]).
To this end, a coupled damage-plasticity model using a second order damage tensor in the sense of CDM is discussed. For this purpose, the material formulation takes place in the logarithmic strain space and further assumes the elastic strain to be additively decomposable. Following the micromorphic approach, a novel gradient-extension of the damage tensor's invariants is discussed to counteract mesh-dependency. First, several fundamental aspects for the constitutive framework are presented (Sec. 4.3), followed by the thermodynamically consistent derivation of the material model in Sec. 4.4. In Sec. 4.5, some remarks on the numerical implementation are given, also including a brief description of the transformation of constitutively dependent quantities between logarithmic and Lagrangian space. Finally, a numerical example investigates the proposed gradient-extended material model in Sec. 4.6.

4.3 Governing equations

Logarithmic strain measures. As widely accepted in the field of finite elasto-plasticity, the total deformation gradient can be multiplicatively decomposed into an elastic and plastic part $\boldsymbol{F} = \boldsymbol{F}_e\boldsymbol{F}_p$. In addition, the polar decomposition of $\boldsymbol{F}_p = \boldsymbol{R}_p\boldsymbol{U}_p$ into a proper orthogonal part and a positive definite stretch part is introduced.
Since the aim of this contribution is to state the material model formulation in terms of logarithmic strain measures, the elastic logarithmic strain is introduced as $\breve{\boldsymbol{\varepsilon}}_e \coloneqq 1/2\ln(\boldsymbol{F}_e^T\boldsymbol{F}_e)$. However, in order to express the rate of $\breve{\boldsymbol{\varepsilon}}_e$ depending on total and inelastic deformations, the rate of $\boldsymbol{U}_p$ has to be considered rather than its logarithmic counterpart $\ln(\boldsymbol{U}_p)$. To circumvent this problem, the concept of an additive split of the deformation is followed, which is *'surprisingly close'* to the multiplicative version according to Miehe et al. [2002]. With this approach at hand, the elastic strain is defined as

$$\boldsymbol{\varepsilon}_e \coloneqq \underbrace{\frac{1}{2}\ln(\boldsymbol{C})}_{=:\,\boldsymbol{\varepsilon}} - \underbrace{\frac{1}{2}\ln(\boldsymbol{C}_p)}_{=:\,\boldsymbol{\varepsilon}_p} \tag{4.1}$$

with the total and plastic right Cauchy-Green tensors $\boldsymbol{C}_{(p)} = \boldsymbol{F}_{(p)}^T\boldsymbol{F}_{(p)}$. Noteworthy, the elastic logarithmic strains $\breve{\boldsymbol{\varepsilon}}_e$ and $\boldsymbol{\varepsilon}_e$ are only equal if and only if $\boldsymbol{C}$ and $\boldsymbol{C}_p$ commute and further $\boldsymbol{F}_p = \boldsymbol{U}_p$ holds. Nevertheless, the split (4.1) is very well tested for quite different material behaviors in the literature and shows good agreement with experimental observations, even for

anisotropic plasticity.

Mapping of second order damage tensor. In the case of a purely elasto-plastic material behavior, the energy ψ is usually assumed as an isotropic function of $\boldsymbol{F}_e^T \boldsymbol{F}_e$ or, in the case of logarithmic strains, as an isotropic function of $\breve{\boldsymbol{\varepsilon}}_e$. In contrast, the damage tensor is usually stated with respect to the current or reference configuration and further is assumed to be positive semi-definite. Here, the latter assumption is followed and the referential second order damage tensor $\boldsymbol{D}_r$ is introduced. However, this means that a mapping to the intermediate configuration is required.
Two mapping strategies are considered here, namely symmetry-preserving (e.g. Reese et al. [2021]) and mixed-variant mappings (e.g. Murakami [1988]). While the latter prevent undesired inelastic scaling effects, only the former preserve the symmetry of the damage tensor $\boldsymbol{D}$ in the intermediate configuration in general, which is beneficial for the formulation of ψ in terms of its integrity basis. Each advantage is desirable in the case of damage, which is why a mapping combining both is preferable. Thus, the following mapping is stated

$$\boldsymbol{D} = \boldsymbol{R}_p \boldsymbol{D}_r \boldsymbol{R}_p^T = \boldsymbol{R}_p \boldsymbol{D}_r \boldsymbol{R}_p^{-1} \tag{4.2}$$

which will be used within this work. For further derivations, please note that the eigenvectors of $\boldsymbol{D}$ and $\boldsymbol{D}_r$ transform according to $\boldsymbol{n}_i^{\boldsymbol{D}} = \boldsymbol{R}_p \, \boldsymbol{n}_i^{\boldsymbol{D}_r}$.

Micromorphic approach. To overcome the severe mesh-dependency, an additional internal length scale is introduced. In this context, the micromorphic approach suggested in Forest [2009, 2016] offers a quite general way to account for additional gradient influences within the formulation of (local) material models. For this purpose, n additional unknowns - summarized within $\bar{\mathbf{d}} \coloneqq (\bar{d}_1, \dots, \bar{d}_n)$, which is referred to here and in the following as the micromorphic damage vector - are introduced in general. These additional so-called nonlocal variables are strongly coupled to the local variables of the material model, for instance, the damage variable D in the case of scalar isotropic damage models (see e.g. Brepols et al. [2020]). The gradient influence is then taken into account by an additional field equation - similar to the strong form of linear momentum - introduced for the micromorphic field. In case of damage, this field equation is given as (cf. Brepols et al. [2020])

$$\mathrm{Div}(\boldsymbol{\Xi}_{0_i}) - \boldsymbol{\xi}_{0_i} = \boldsymbol{0} \quad \text{in } B_0 \tag{4.3}$$

$$\boldsymbol{\Xi}_{0_i} \cdot \boldsymbol{n}_0 = \boldsymbol{0} \quad \text{on } \partial B_0 \tag{4.4}$$

with the Lagrangian divergence operator denoted by $\mathrm{Div}(\bullet)$, the 'generalized' stresses $\boldsymbol{\Xi}_{0_i}$ and $\boldsymbol{\xi}_{0_i}$ as well as the outward normal vector $\boldsymbol{n}_0$ with respect to the reference configuration. The domain of the body in the reference configuration is denoted by B_0.

Invariant-based gradient-extension. Several approaches based on the micromorphic one exist in the literature to gradient-enhance local damage material models. While for scalar isotropic damage models it seems natural to gradient-extend the scalar damage variable D, several possibilities exist in the case of anisotropic damage. Besides the approach to extend the components of the damage tensor (e.g. Langenfeld and Mosler [2020]), also the gradient-extension of the damage hardening variable is possible (see Fassin et al. [2019*b*]). The latter one is beneficial from a computational point of view, since only one additional degree of freedom has to be considered. However, as discussed in the just mentioned work, this leads to problems for the formulation of the damage yield criterion. To circumvent this situation, the invariants of the second order damage tensor are used for the gradient-extension. Hence, the local damage vector $\mathbf{d} \coloneqq (d_1, d_2, d_3)$ containing the local counterparts to $\bar{d}_i$ is introduced here as

$$d_1 = \mathrm{tr}(\boldsymbol{D}), \quad d_2 = \mathrm{tr}(\boldsymbol{D}^2), \quad d_3 = \mathrm{tr}(\boldsymbol{D}^3). \tag{4.5}$$

Noteworthy, due to the mapping in Eq. (4.2), it holds true that $\mathrm{tr}(\boldsymbol{D}^i) = \mathrm{tr}(\boldsymbol{D}_r^i)$ with $i \in \{1, 2, 3\}$. As a consequence, three micromorphic degrees of freedom $\bar{d}_1$, $\bar{d}_2$, $\bar{d}_3$ have to be considered in addition to the displacement field. To the best knowledge of the authors, such an approach based on the invariants of the damage tensor in connection with the micromorphic approach has not yet been used in the literature.

Weak forms. For the numerical implementation, the weak form of both the displacement field and the micromorphic field have to be solved, which read under consideration of Eqs. (4.3) and (4.4) in the reference configuration

$$g_u(\boldsymbol{u}, \bar{\mathbf{d}}, \delta\boldsymbol{u}) \coloneqq \int_{B_0} \boldsymbol{S} : \delta\boldsymbol{E} \, \mathrm{d}V - \int_{B_0} \boldsymbol{f}_0 \cdot \delta\boldsymbol{u} \, \mathrm{d}V - \int_{\partial_t B_0} \boldsymbol{t}_0 \cdot \delta\boldsymbol{u} \, \mathrm{d}A = 0 \tag{4.6}$$

$$g_{\bar{d}}(\boldsymbol{u}, \bar{\mathbf{d}}, \delta\bar{\mathbf{d}}) \coloneqq \int_{B_0} \boldsymbol{\xi}_{0_i} \cdot \delta\bar{\mathbf{d}} \, \mathrm{d}V + \int_{B_0} \boldsymbol{\Xi}_{0_i} : \mathrm{Grad}\left(\delta\bar{\mathbf{d}}\right) \, \mathrm{d}V = 0 \tag{4.7}$$

with the second Piola-Kirchhoff stress tensor $\boldsymbol{S}$, the short hand notation $\delta\boldsymbol{E} \coloneqq \mathrm{sym}(\boldsymbol{F}^T \mathrm{Grad}(\delta\boldsymbol{u}))$, the volume force $\boldsymbol{f}_0$, the traction $\boldsymbol{t}_0$ and the test functions $\delta\boldsymbol{u}$ and $\delta\bar{\mathbf{d}}$, respectively. Further, the Lagrangian gradient operator is denoted by $\mathrm{Grad}(\bullet)$.

4.4 Constitutive framework

For the constitutive modeling, the plastic logarithmic strain with respect to the intermediate configuration is defined as $\boldsymbol{\eta}_p \coloneqq 1/2\ln(\boldsymbol{F}_p\boldsymbol{F}_p^T) = \boldsymbol{R}_p\,\boldsymbol{\varepsilon}_p\,\boldsymbol{R}_p^T$. With this quantity at hand, the Helmholtz free energy is assumed to be additively decomposed as

$$\psi = \psi_{\check{e}}(\check{\boldsymbol{\varepsilon}}_e, \boldsymbol{D}) + \psi_p(\boldsymbol{\eta}_p, \kappa_p, \boldsymbol{D}) + \psi_d(\kappa_d) + \psi_h(\boldsymbol{D}) + \psi_{\bar{d}}(\mathbf{d}, \bar{\mathbf{d}}, \mathrm{Grad}(\bar{\mathbf{d}})). \tag{4.8}$$

Within the assumed form of the energy, $\psi_{\check{e}}$ represents the elastic energy contribution and ψ_p the plastic contribution due to kinematic as well as isotropic hardening with the accumulated plastic strain κ_p. Both are affected by the damage tensor $\boldsymbol{D}$. Furthermore, damage hardening is captured by the damage hardening variable κ_d within the energy ψ_d. The energy associated with ψ_h can be seen as a penalty energy preventing the eigenvalues of $\boldsymbol{D}$ (and thus also $\boldsymbol{D}_r$) from exceeding the value one. Such an approach was already used in the case of anisotropic damage in Fassin et al. [2019*b*] at small strains. In contrast to the other energies, the integrity basis is not expressed in terms of invariants but rather the eigenvalues of $\boldsymbol{D}$ are used for ψ_h, i.e. $\psi_h = \bar{\psi}_h(D_1, D_2, D_3)$. Nevertheless, this still means that ψ_h is an isotropic function of the second order damage tensor. The last term, namely $\psi_{\bar{d}}$, accounts for the gradient-extension and further ensures the strong coupling between $\mathbf{d}$ and $\bar{\mathbf{d}}$. This general format can be further specified, having Eq. (4.5) in mind, since $\mathbf{d}$ is only a function of $\boldsymbol{D}$. Hence, the formulation of this energy contribution can be rewritten as $\psi_{\bar{d}} = \bar{\psi}_{\bar{d}}(\boldsymbol{D}, \bar{\mathbf{d}}, \mathrm{Grad}(\bar{\mathbf{d}}))$.

4.4.1 Derivation based on the isothermal Clausius-Duhem inequality

For the derivation of thermodynamic driving forces, the micromorphically extended Clausius-Duhem inequality is used

$$-\dot{\psi} + \boldsymbol{T} : \dot{\boldsymbol{\varepsilon}} + \underbrace{\boldsymbol{\xi}_{0_i} \cdot \dot{\bar{\mathbf{d}}} + \boldsymbol{\Xi}_{0_i} : \mathrm{Grad}\left(\dot{\bar{\mathbf{d}}}\right)}_{\text{micromorphic extension}} \geq 0 \tag{4.9}$$

with the stress power expressed in terms of $\dot{\boldsymbol{\varepsilon}}$ and its stress-like conjugated driving force $\boldsymbol{T}$. Before inserting the total time derivative of ψ into the inequality, one has to note that due to the additive split (4.1) the elastic strain is defined with respect to the reference configuration. Thus, the elastic energy part in Eq. (4.8) is no longer a function of $\check{\boldsymbol{\varepsilon}}_e$ but rather $\boldsymbol{\varepsilon}_e$. Since $\boldsymbol{D}$ is located in the intermediate configuration, $\boldsymbol{D}_r$ is utilized in connection with $\boldsymbol{\varepsilon}_e$. Consequently, the elastic energy contribution $\psi_{\check{e}}$ in Eq. (4.8) is replaced by $\psi_e(\boldsymbol{\varepsilon}_e, \boldsymbol{D}_r)$.
After several mathematical operations, which are omitted here for brevity, the evaluated time

derivative of ψ yields the following

$$\begin{aligned}&\left(\boldsymbol{T}-\frac{\partial\psi_e}{\partial\boldsymbol{\varepsilon}_e}\right):\dot{\boldsymbol{\varepsilon}}+(\boldsymbol{T}-\boldsymbol{X}):\dot{\boldsymbol{\varepsilon}}_p+\overbrace{(\boldsymbol{Y}_e+\boldsymbol{Y}_p-\boldsymbol{Y}_h-\boldsymbol{Y}_{\bar{d}})}^{=:\boldsymbol{Y}}:\dot{\boldsymbol{D}}_r\\&+R_p\,\dot{\kappa}_p+R_d\,\dot{\kappa}_d+\left(\boldsymbol{\xi}_{0_i}-\frac{\partial\psi_{\bar{d}}}{\partial\bar{\mathbf{d}}}\right)\cdot\dot{\bar{\mathbf{d}}}+\left(\boldsymbol{\Xi}_{0_i}-\frac{\partial\psi_{\bar{d}}}{\partial\mathrm{Grad}(\bar{\mathbf{d}})}\right):\mathrm{Grad}\left(\dot{\bar{\mathbf{d}}}\right)\geq 0.\end{aligned}\tag{4.10}$$

Following the well-known Coleman-Noll procedure for the stress tensor $\boldsymbol{T}$ as well as similar relations for the 'generalized' stresses in order to fulfill the inequality for arbitrary processes, one may find

$$\boldsymbol{T}=\frac{\partial\psi_e}{\partial\boldsymbol{\varepsilon}_e},\quad \boldsymbol{\xi}_{0_i}=\frac{\partial\psi_{\bar{d}}}{\partial\bar{\mathbf{d}}},\quad \boldsymbol{\Xi}_{0_i}=\frac{\partial\psi_{\bar{d}}}{\partial\mathrm{Grad}(\bar{\mathbf{d}})}.\tag{4.11}$$

Furthermore, the kinematic backstress tensor and the driving force associated with plastic isotropic hardening are defined as

$$\boldsymbol{X}\coloneqq\boldsymbol{R}_p^T\frac{\partial\psi_p}{\partial\boldsymbol{\eta}_p}\boldsymbol{R}_p,\quad R_p\coloneqq-\frac{\partial\psi_p}{\partial\kappa_p}.\tag{4.12}$$

Analogously, the damage hardening force is introduced as $R_d\coloneqq-\partial\psi_d/\partial\kappa_d$. The remaining driving forces associated with the rate of the second order damage tensor $\boldsymbol{D}_r$ are defined as

$$\boldsymbol{Y}_e\coloneqq-\frac{\partial\psi_e}{\partial\boldsymbol{D}_r},\quad \boldsymbol{Y}_p\coloneqq-\boldsymbol{R}_p^T\frac{\partial\psi_p}{\partial\boldsymbol{D}}\boldsymbol{R}_p,\quad \boldsymbol{Y}_h\coloneqq\boldsymbol{R}_p^T\frac{\partial\psi_h}{\partial\boldsymbol{D}}\boldsymbol{R}_p,\quad \boldsymbol{Y}_{\bar{d}}\coloneqq\boldsymbol{R}_p^T\frac{\partial\psi_{\bar{d}}}{\partial\boldsymbol{D}}\boldsymbol{R}_p.\tag{4.13}$$

Noteworthy, the driving forces introduced all have in common that they are defined with respect to the reference configuration. It is further important to note that, since all energies are isotropic functions of their arguments, one can show that the plastic rotation tensor $\boldsymbol{R}_p$ is not needed to compute any of these forces. Moreover, the rate of $\boldsymbol{R}_p$ does not occur within the Clausius-Duhem inequality. Hence, this tensor plays no role in the actual model and remains undetermined, which is considered as an advantage.
To guarantee the non-negativeness of the remaining dissipation inequality, a set of evolution equations for the plastic and damage related quantities are presented in the following. For both processes, associative laws are assumed.

Plastic evolution equations. For simplicity, but without loss of generality, a von Mises-type yield criterion in the so-called effective continuum is assumed which reads

$$\Phi_p=\sqrt{3\tilde{J}_2}-(\sigma_{y0}-\tilde{R}_p)\leq 0\tag{4.14}$$

with $J_2 := 1/2\ \mathrm{tr}(\mathrm{dev}(\boldsymbol{T}-\boldsymbol{X})^2)$ being the second invariant of the deviator of the driving force and $\tilde{(\bullet)} = (\bullet)|_{\boldsymbol{D}=\boldsymbol{0}}$ refers to effective quantities. The initial yield stress is denoted by σ_{y0}. Based on this criterion, the evolution equations are as follows

$$\dot{\boldsymbol{\varepsilon}}_p = \dot{\gamma}_p \frac{\partial \Phi_p}{\partial \boldsymbol{T}} = \dot{\gamma}_p \frac{3}{\sqrt{12 \tilde{J}_2}}\, \mathrm{dev}(\tilde{\boldsymbol{T}} - \tilde{\boldsymbol{X}}) : \mathbb{M}^{-1}, \quad \dot{\kappa}_p = \dot{\gamma}_p \frac{\partial \Phi_p}{\partial R_p} = \frac{\dot{\gamma}_p}{f_d} \tag{4.15}$$

with the plastic multiplier $\dot{\gamma}_p$. In the above, invertible mappings in terms of a fourth order tensor $\mathbb{M}$ and the scalar degradation function f_d are introduced, which relate effective and damaged quantities, i.e. $\boldsymbol{T} = \mathbb{M} : \tilde{\boldsymbol{T}}$ and $R_p = f_d\, \tilde{R}_p$. Finally, the set of plastic constitutive equations is closed by the Karush-Kuhn-Tucker (KKT) conditions $\Phi_p \leq 0$, $\dot{\gamma}_p \geq 0$ and $\Phi_p \dot{\gamma}_p = 0$.

Damage evolution equations. The damage criterion for the onset of damage is denoted by (cf. Fassin et al. [2019*b*])

$$\Phi_d = \sqrt{3}\sqrt{\boldsymbol{Y}_+ : \mathbb{A}_d : \boldsymbol{Y}_+} - (Y_0 - R_d) \leq 0. \tag{4.16}$$

Here, Y_0 denotes the initial damage threshold and further $\boldsymbol{Y}_+ = \sum_{i=1}^{3} \langle Y_i \rangle_M\, \boldsymbol{n}_i^{\boldsymbol{Y}} \otimes \boldsymbol{n}_i^{\boldsymbol{Y}}$ refers to the positive part of the driving force, where Y_i and $\boldsymbol{n}_i^{\boldsymbol{Y}}$ are the eigenvalues and eigenvectors of $\boldsymbol{Y}$, respectively. The Macaulay brackets are given as $\langle(\bullet)\rangle_M = ((\bullet) + |(\bullet)|)/2$. In addition, and in line with Reese et al. [2021], the damage yield criterion is extended by a fourth order damage tensor $\mathbb{A}_d$ in order to provide more flexibility for the modeling of damage evolution. Different choices for this tensor are possible, while for the time being the components with respect to the Cartesian basis system are given as $A_{d_{ijkl}} = (\delta_{ik} - D_{r_{ik}})(\delta_{jl} - D_{r_{jl}})$, where δ_{ij} denotes the Kronecker delta. Following again the associative concept, the evolution equations for the damage quantities read as follows

$$\dot{\boldsymbol{D}}_r = \dot{\gamma}_d \frac{\partial \Phi_d}{\partial \boldsymbol{Y}} = \dot{\gamma}_d \frac{3}{Y_0 - R_d} \boldsymbol{Q}_+ (\boldsymbol{I} - \boldsymbol{D}_r) \boldsymbol{Y}_+ (\boldsymbol{I} - \boldsymbol{D}_r) \boldsymbol{Q}_+, \quad \dot{\kappa}_d = \dot{\gamma}_d \frac{\partial \Phi_d}{\partial R} = \dot{\gamma}_d \tag{4.17}$$

where $\dot{\gamma}_d$ denotes the damage multiplier and $\boldsymbol{Q}_+ = \sum_{i=1}^{3} \langle Y_i \rangle_H\, \boldsymbol{n}_i^{\boldsymbol{Y}} \otimes \boldsymbol{n}_i^{\boldsymbol{Y}}$ with $\langle(\bullet)\rangle_H$ denoting the Heaviside step function. Thus, $\boldsymbol{Y}_+$ can be alternatively expressed as $\boldsymbol{Y}_+ = \boldsymbol{Q}_+ \boldsymbol{Y} \boldsymbol{Q}_+$. In analogy to plasticity, the KKT conditions are introduced as $\Phi_d \leq 0, \dot{\gamma}_d \geq 0$ and $\Phi_d \dot{\gamma}_d = 0$. Please note that in Eq. $(4.17)_1$ it was used that $\sqrt{\boldsymbol{Y}_+ : \mathbb{A}_d : \boldsymbol{Y}_+} = (Y_0 - R_d)/\sqrt{3}$ follows from the KKT conditions for a damage step ($\dot{\gamma}_d > 0$). Although this reformulation does, of course, not change the solution, a division by zero is avoided, which may occur using $\sqrt{\boldsymbol{Y}_+ : \mathbb{A}_d : \boldsymbol{Y}_+}$ within the local Newton iteration.

4.4.2 Particular choices of Helmholtz free energy terms

While the derivation of the model has been kept quite general so far, in what follows particular choices will be made for the terms in Eq. (4.8). For the elastic energy, a quadratic form with respect to $\boldsymbol{\varepsilon}_e$ is chosen. Furthermore, as pointed out for instance in Desmorat [2016], the isochoric response of the Helmholtz free energy is assumed to be affected by the anisotropic nature of damage. In contrast, the volumetric part is assumed to be only affected by isotropic damage. Thus, it is influenced by the degradation function f_d already introduced in Eq. $(4.15)_2$, which is an isotropic function of $\boldsymbol{D}$ (and so of $\boldsymbol{D}_r$). In this regard, a great benefit of logarithmic strains becomes evident, since their decomposition into deviatoric and spherical parts is directly related to the decomposition into distortion and dilatation (see e.g. Criscione et al. [2000]). Hence, the elastic energy is provided as

$$\psi_e = \mu_e \operatorname{tr}\left(\operatorname{dev}(\boldsymbol{\varepsilon}_e)^2(\boldsymbol{I} - \boldsymbol{D}_r)\right) + f_d \, \frac{K_e}{2} \operatorname{tr}\left(\boldsymbol{\varepsilon}_e\right)^2 . \tag{4.18}$$

In the above, μ_e and K_e denote the shear modulus and bulk modulus, respectively. Similarly, the plastic energy combining kinematic and nonlinear isotropic hardening is denoted by

$$\psi_p = \mu_p \operatorname{tr}\left(\operatorname{dev}(\boldsymbol{\eta}_p)^2(\boldsymbol{I} - \boldsymbol{D})\right) + f_d \, r_p \left(\kappa_p + \frac{\exp(-s_p \, \kappa_p) - 1}{s_p}\right) \tag{4.19}$$

with μ_p, r_p and s_p being the plastic material parameters. Since a von Mises-type yield criterion is used here, no volumetric response for the backstress needs to be considered. Further, the degradation function is specified as $f_d = 1 - \operatorname{tr}(\boldsymbol{D})/3$. The remaining energies associated with damage are given as

$$\psi_d = r_d \left(\kappa_d + \frac{\exp(-s_d \, \kappa_d) - 1}{s_d}\right) + \frac{1}{2} H_d \, \kappa_d^2, \; \psi_h = K_h \sum_{i=1}^{3} \left(-2\sqrt{1 - D_i} - D_i + 2\right) \tag{4.20}$$

where the material parameters r_d, s_d, H_d and K_h are introduced and both linear and nonlinear isotropic hardening are considered. Finally, the micromorphic contribution to the overall Helmholtz free energy is assumed to be of quadratic type and reads as follows

$$\psi_{\bar{d}} = \frac{1}{2} \sum_{i=1}^{3} \left(H_i \, (d_i - \bar{d}_i)^2\right) + \frac{1}{2} \sum_{i=1}^{3} \left(A_i \operatorname{Grad}(\bar{d}_i) \cdot \operatorname{Grad}(\bar{d}_i)\right) \tag{4.21}$$

with the material parameters H_i and A_i with $i \in \{1,2,3\}$. While for sufficient large H_i the strong couplings between d_i and $\bar{d}_i$ are ensured, A_i introduce additional length scales into the material model accounting for the nonlocal character of damage.

4.5 Remarks on the numerical implementation

The weak forms provided in Eqs. (4.6) and (4.7) are solved using the finite element method with standard Q1 elements and are therefore discretized in both space and time. To solve the resulting system of nonlinear equations, the Newton scheme is used on a global level, which requires the material sensitivities $\partial \boldsymbol{S}/\partial \boldsymbol{E}$, $\partial \boldsymbol{S}/\partial \bar{\mathbf{d}}$, $\partial \mathbf{d}/\partial \boldsymbol{E}$, $\partial \mathbf{d}/\partial \bar{\mathbf{d}}$ (more precisely: their algorithmically consistent counterparts are needed), where $\boldsymbol{E}$ denotes the Green-Lagrange strain tensor. Since the material model is derived in the logarithmic strain space, the material sensitivities with respect to the logarithmic strains are obtained first and then transformed to their Lagrangian counterparts. With the relation $\boldsymbol{S} = \boldsymbol{T} : 2\, \partial \boldsymbol{\varepsilon}/\partial \boldsymbol{C}$ at hand, one can find

$$\frac{\partial \boldsymbol{S}}{\partial \boldsymbol{E}} = 4\, \frac{\partial \boldsymbol{\varepsilon}}{\partial \boldsymbol{C}} : \frac{\partial \boldsymbol{T}}{\partial \boldsymbol{\varepsilon}} : \frac{\partial \boldsymbol{\varepsilon}}{\partial \boldsymbol{C}} + \boldsymbol{T} : 4\, \frac{\partial^2 \boldsymbol{\varepsilon}}{\partial \boldsymbol{C} \partial \boldsymbol{C}}, \quad \frac{\partial \boldsymbol{S}}{\partial \bar{\mathbf{d}}} = 2\, \frac{\partial \boldsymbol{\varepsilon}}{\partial \boldsymbol{C}} : \frac{\partial \boldsymbol{T}}{\partial \bar{\mathbf{d}}}, \quad \frac{\partial \mathbf{d}}{\partial \boldsymbol{E}} = 2\, \frac{\partial \mathbf{d}}{\partial \boldsymbol{\varepsilon}} : \frac{\partial \boldsymbol{\varepsilon}}{\partial \boldsymbol{C}} \tag{4.22}$$

where it was utilized that $\partial \boldsymbol{\varepsilon}/\partial \boldsymbol{C}$ possess both minor and major symmetry. For the derivation of the transformation - at least for the purely mechanical part - the reader is kindly referred to Miehe and Lambrecht [2001]. Noteworthy, the sensitivity $\partial \mathbf{d}/\partial \bar{\mathbf{d}}$ does not need to be transformed.

The local residual functions are obtained by the discretized evolution Eqs. (4.15) and (4.17) within a time interval $t \in [t_n, t_{n+1}]$ using the backward Euler method and additionally the yield criteria (4.14) and (4.16). Thus, the internal variables which have to be solved are $\Delta t \dot{\gamma}_{p_{n+1}}$, $\boldsymbol{\varepsilon}_{p_{n+1}}$, $\Delta t \dot{\gamma}_{d_{n+1}}$, $\boldsymbol{D}_{r_{n+1}}$. Note that this is sufficient to ensure plastic incompressibility. However, in order to avoid a division by zero for the local Jacobian, the (modified) damage criterion solved on a material point level reads: $\bar{\Phi}_d = 3\, \boldsymbol{Y}_+ : \mathbb{A}_d : \boldsymbol{Y}_+ - (Y_0 - R_d)^2 = 0$. It is worth noting that, if damage is active ($\dot{\gamma}_d > 0$), $\bar{\Phi}_d$ can be obtained by means of an equivalence transformation of Φ_d. For the solution strategy, a combination of the classical trial step procedure in combination with an active-set search strategy is pursued. The local Jacobian as well as the material sensitivities within the logarithmic space are obtained with the help of the implicit function theorem and the algorithmic differentiation tool *AceGen*. Thus, the four tangent operators for the finite element method can be computed automatically in a consistent manner.

4.6 Numerical example

In order to investigate the model's behavior as well as its ability to deliver mesh-independent results, an asymmetrically notched specimen is studied. The computation is conducted under plane strain conditions using 2D quadrilateral finite elements. The boundary value problem is taken from the literature Brepols et al. [2017] and is illustrated in Fig. 4.1. The specimen is clamped at its left side and loaded by a concentrated force at the node in the middle of the right edge. In addition, the horizontal displacement degrees of freedom at this very edge are constrained in such a way that they deform in the same way as the node loaded by the single load does.

The material parameters for this example are partly taken from Brepols et al. [2020], otherwise chosen as: $\mu_e = 55000$ [MPa], $K_e = 61666.\bar{6}$ [MPa], $\mu_p = 62.5$ [MPa], $r_p = 125$ [MPa], $s_p = 5$ [-], $\sigma_{y0} = 100$ [MPa], $H_d = 1$ [MPa], $r_d = 5$ [MPa], $s_d = 100$ [-], $K_h = 0.1$ [MPa], $Y_0 = 2.5$ [MPa] as well as $A_i = 75$ [MPa mm^2] and $H_i = 10^5$ [MPa] with $i \in \{1, 2, 3\}$.

A mesh convergence study using 1624, 3592, 9667, 12704 and 13955 finite elements is conducted and shown in Fig. 4.2, where u_1 corresponds to the displacement of the right edge. A clear trend towards a solution with a finite amount of energy dissipation can be observed. Noteworthy, mesh refinement is strongly performed between the two notches.

In the process, damage starts to evolve at both notches and from that on progresses towards the interior of the specimen. Three stages during this process are shown in Fig. 4.3 for the damage component $D_{r_{11}}$, where these stages are indicated by black rectangles in Fig. 4.2. The corresponding accumulated plastic strain is shown as well. The remaining damage components of interest ($D_{r_{22}}$, $D_{r_{33}}$, $D_{r_{12}}$) are not shown here for brevity, however, $D_{r_{22}}$ evolves quite similar to $D_{r_{11}}$, whereas $D_{r_{33}}$ reaches merely a value of approximately 0.9 due to the plane strain conditions. This is also the reason why the load-displacement curve only drops to slightly less than ten percent of the maximum load achieved. Nevertheless, this can be considered as a 'fully broken' state, since a clear crack path can be observed.

Furthermore, in Fig. 4.4 the convergence of the damage contour plots of two exemplary meshes at the end of the simulation is shown. Although there are slight differences in the area of the upper notch visible, these can be considered as negligibly small.

4.7 Conclusion

In this work, a thermodynamically consistent damage-plasticity model accounting for the anisotropic nature of damage by means of a second order damage tensor was presented. More-

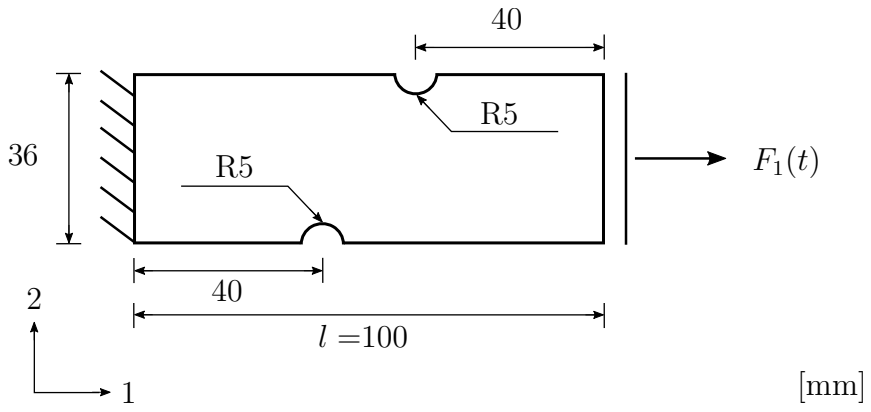

Figure 4.1: Geometry and boundary value problem.

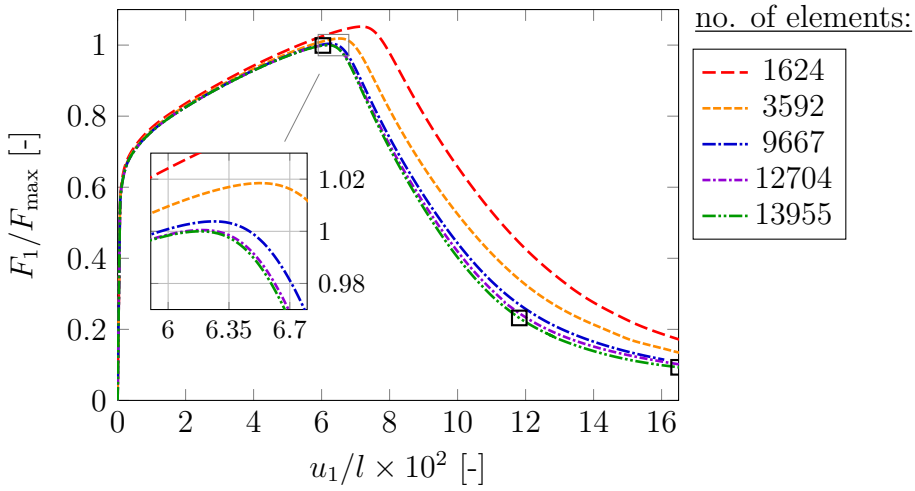

Figure 4.2: Normalized load-displacement curves ($F_{\max} = 5.4631$ [kN]).

over, a novel gradient-enhanced framework based on the invariants of the second order damage tensor and the micromorphic approach was discussed, in order to tackle mesh-sensitivities caused by damage localization. Hence, three degrees of freedom in addition to the displacement field have to be considered within the finite element method.

Based on the extended Clausius-Duhem inequality, expressions for the conjugated forces associated with the gradient-extension and the stress tensor were derived. Within this modeling approach, both logarithmic strains and an additive split of the elastic strain were utilized for the kinematics. The remaining dissipation inequality is fulfilled for arbitrary processes by means of associative evolution equations for the damage and plastic variables, respectively. In order to be applicable in standard finite element formulations based on Lagrangian quantities, the transformation from the logarithmic strain space was additionally addressed, in particular the transformation of the (algorithmic consistent) tangent operators. Finally, a numerical example

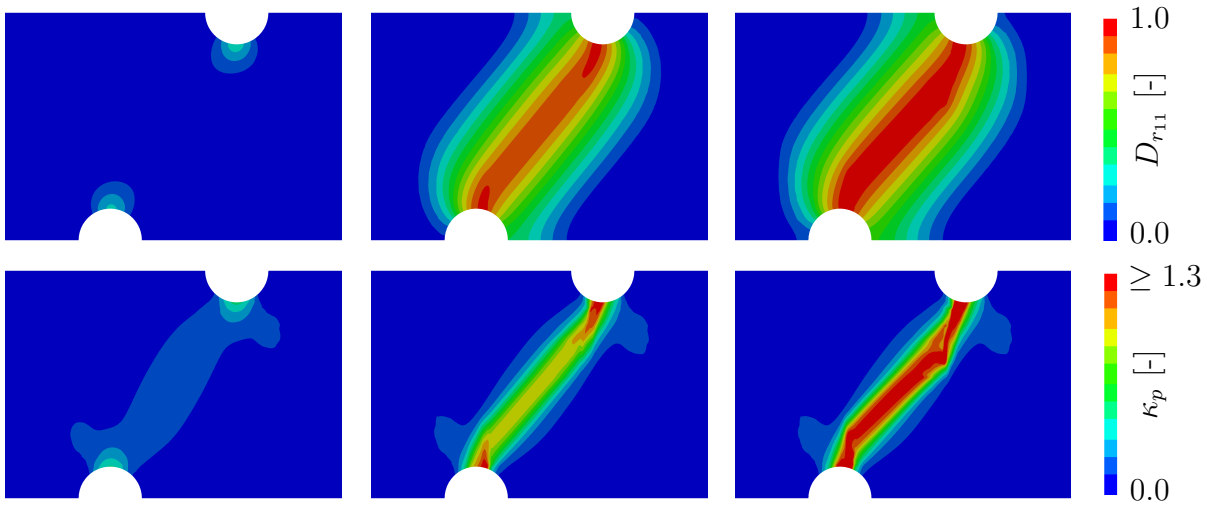

Figure 4.3: Three different stages of damage component $D_{r_{11}}$ and accumulated plastic strain κ_p for the finest mesh (13955 elements). The stages are indicated by black rectangles within Fig. 4.2.

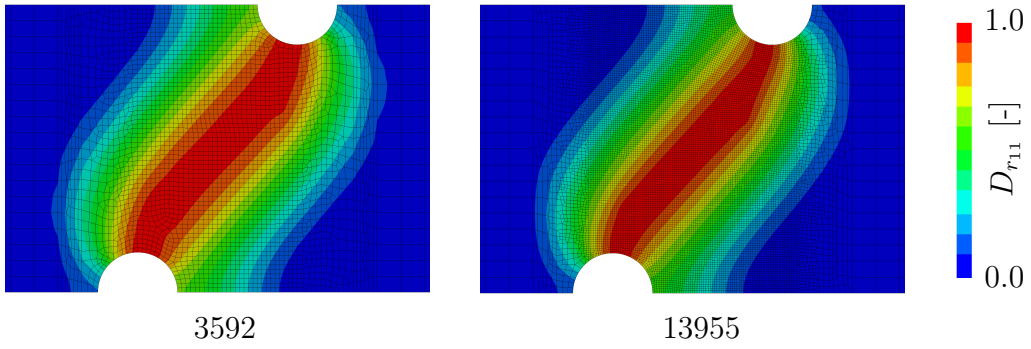

Figure 4.4: Exemplary comparison of damage contour plots $D_{r_{11}}$ for different mesh refinements at the end of the simulation ($u_1 = 16.5$ [mm]) plotted with the corresponding mesh.

demonstrated the behavior of the proposed model on a structural level as well as the ability to cure the mesh-dependency. It may be mentioned that a much more detailed study is currently in progress. In addition, the consideration of finite element technology could be interesting in order to reduce the computational effort (e.g. Barfusz, van der Velden, Brepols, Holthusen and Reese [2021]).

5 Article 4: A gradient-extended anisotropic damage-plasticity model in the logarithmic strain space

This article was published as:

Holthusen, H., Brepols, T., Simon, J.-W., and Reese, S. [2022], 'A gradient-extended anisotropic damage-plasticity model in the logarithmic strain space', In: *The 8th European Congress on Computational Methods in Applied Sciences and Engineering (ECCOMAS Congress 2022)*, 1-12.

Disclosure of the individual authors' contributions to the article:

H. Holthusen reviewed the relevant existing literature, derived the constitutive framework and implemented the material model and the element routine into the finite element software *FEAP*. He set up and performed all simulations, interpreted the results and wrote the preliminary version of the article. It was his idea to employ the finite strain elasto-plasticity framework coupled to gradient-extended damage by Brepols et al. [2020] and the anisotropic damage model at small strains by Fassin et al. [2019*b*] as the basis for the model development. Moreover, T. Brepols, J.-W. Simon, and S. Reese gave conceptual advice, contributed to the discussion of the results, read the current version of the article, and gave valuable suggestions for improvement. All authors approved the preliminary publication of the article in the present dissertation.

5.1 Abstract

Within this contribution, we discuss additional theoretical as well as numerical aspects of the material model developed in Holthusen, Brepols, Reese and Simon [2022*b*,*a*], where a 'two-surface' damage-plasticity model is proposed accounting for induced damage anisotropy by means of a second order damage tensor. The constitutive framework is stated in terms of logarithmic strain measures, while the total strain is additively decomposed into elastic and plastic parts. Moreover, a novel gradient-extension based on the damage tensor's invariants is presented using the micromorphic approach introduced in Forest [2009]. Finally, going beyond the numerical examples presented in Holthusen, Brepols, Reese and Simon [2022*b*,*a*], we study the model's ability to cure mesh-dependency in a three-dimensional setup.

5.2 Introduction

The defects observed on the microstructure can be classified into microvoids and microcracks, the former degrading the material more or less directionally independent. The latter, on the other hand, induce a strong anisotropy even in initially isotropic materials. Continuum mechanical models that take this anisotropy into account are essential for estimating the stiffness, and thus, the load-bearing capacity of structures that are damaged. In this context, non-proportional load paths, such as those occurring in forming processes, are also known to trigger this kind of induced anisotropy.

Within this contribution, in line with Continuum Damage Mechanics (CDM), we account for damage anisotropy by means of a second order damage tensor (see Murakami [1988]) in a phenomenological and smeared sense. The CDM modeling approach is used for a wide range of materials and damage behaviors, ranging from initially isotropic materials (e.g. Badreddine et al. [2015]) to initially anisotropic materials with different constituents (e.g. Holthusen et al. [2020]), and further, is employed in the context of scale transitions (e.g. Poggenpohl et al. [2022]). In this regard, Reese et al. [2021] recently formulated a finite strain framework that interprets the second order damage tensor in terms of structural tensors. This approach is also followed in Holthusen, Brepols, Reese and Simon [2022*b*,*a*], but in the logarithmic strain space, where additionally a novel gradient-extension is introduced. The latter extension is necessary to overcome mesh-dependency, a well-known problem of so-called local damage models, to which the class of CDM models belongs. In view of the many possibilities known in the literature for introducing a gradient-extension, the latter authors decided to use the micromorphic approach Forest [2009, 2016], which provides a rather flexible and general framework

for introducing additional length scales into the material formulation.
In this contribution, we first consider various aspects of the model developed in Holthusen, Brepols, Reese and Simon [2022*b*], discussing here in further detail the invariance to superimposed rotations of the intermediate configuration. In addition, the assumption of an additive decomposition of the total strain and the choice of local variables for the gradient extension are briefly discussed (Sec. 5.3). In Sec. 5.4, the transformation from logarithmic strain space to the Lagrangian one is presented, where a numerically more efficient calculation method is addressed. Finally, the model is investigated in a three-dimensional context using a tensile specimen (Sec. 5.5).

5.3 Constitutive framework

Additive decomposition. In finite elasto-plasticity modeling, the multiplicative decomposition $\boldsymbol{F} = \boldsymbol{F}_e \boldsymbol{F}_p$ into elastic and plastic parts is well established, which introduces an intermediate configuration in addition to the reference and current configuration. Further, both parts possess their polar decompositions into a rotational and stretch tensor, i.e. $\boldsymbol{F}_e = \boldsymbol{R}_e \boldsymbol{U}_e$ and $\boldsymbol{F}_p = \boldsymbol{R}_p \boldsymbol{U}_p$ with $\boldsymbol{R}_{e/p} \in \mathrm{SO}(3)$. Since both stretch tensors are defined with respect to different configurations, we make further use of the polar decomposition $\boldsymbol{F}_p = \boldsymbol{V}_p \boldsymbol{R}_p$. These stretch tensors are suitable to define the following logarithmic strain measures

$$\boldsymbol{\varepsilon} \coloneqq \ln(\boldsymbol{U}), \quad \boldsymbol{\varepsilon}_p \coloneqq \ln(\boldsymbol{U}_p), \quad \boldsymbol{\eta}_e \coloneqq \ln(\boldsymbol{U}_e), \quad \boldsymbol{\eta}_p \coloneqq \ln(\boldsymbol{V}_p) = \boldsymbol{R}_p \, \boldsymbol{\varepsilon}_p \, \boldsymbol{R}_p^T \tag{5.1}$$

where the polar decomposition of the deformation gradient $\boldsymbol{F} = \boldsymbol{R}\boldsymbol{U}$ with $\boldsymbol{R} \in \mathrm{SO}(3)$ is utilized. Considering both the property of the logarithm $\ln(\boldsymbol{A}) = 1/2 \ln(\boldsymbol{A}^2)$ for any positive definite tensor $\boldsymbol{A}$ and $\boldsymbol{U}_e^2 = \boldsymbol{F}_p^{-T} \boldsymbol{U}^2 \boldsymbol{F}_p^{-1}$, one may rewrite the elastic logarithmic strain as

$$\boldsymbol{\eta}_e = \frac{1}{2} \ln\left(\boldsymbol{U}_e^2\right) = \boldsymbol{R}_p \, \frac{1}{2} \ln\left(\boldsymbol{U}_p^{-1} \boldsymbol{U}^2 \boldsymbol{U}_p^{-1}\right) \boldsymbol{R}_p^T =: \boldsymbol{R}_p \, \boldsymbol{\varepsilon}_e \, \boldsymbol{R}_p^T \tag{5.2}$$

where $\boldsymbol{\varepsilon}_e$ is the elastic strain measure with respect to the reference configuration, which is pushed to the intermediate one by $\boldsymbol{R}_p$. Having further the properties $\ln(\boldsymbol{A}^{-1}) = -\ln(\boldsymbol{A})$ as well as $\ln(\boldsymbol{A}\boldsymbol{B}) = \ln(\boldsymbol{A}) + \ln(\boldsymbol{B})$ if and only if $\boldsymbol{A}$ and $\boldsymbol{B}$ commute in mind, the additive decomposition of the strain is motivated

$$\bar{\boldsymbol{\eta}}_e \coloneqq \boldsymbol{R}_p \left(\boldsymbol{\varepsilon} - \boldsymbol{\varepsilon}_p\right) \boldsymbol{R}_p^T =: \boldsymbol{R}_p \, \bar{\boldsymbol{\varepsilon}}_e \, \boldsymbol{R}_p^T. \tag{5.3}$$

Obviously, $\boldsymbol{\eta}_e$ and $\bar{\boldsymbol{\eta}}_e$, and thus also $\boldsymbol{\varepsilon}_e$ and $\bar{\boldsymbol{\varepsilon}}_e$, are only equal in case of coaxial loading. However, assuming small elastic strains, the additive decomposition is suitable to capture the elastic strains within the material (cf. Miehe et al. [2002]). Noteworthy, Friedlein et al. [2022] investigated the additive split in the context of excessive strains for coaxial and non-coaxial loading coupled to damage and provided interesting results on the structural performance.

Mapping of damage tensor. In line with Reese et al. [2021], we assume a symmetric and semi-positive definite referential damage tensor $\boldsymbol{D}_r$, which is pushed to the intermediate configuration in analogy to $\boldsymbol{\varepsilon}_e$, $\bar{\boldsymbol{\varepsilon}}_e$ and $\boldsymbol{\varepsilon}_p$

$$\boldsymbol{D} = \boldsymbol{R}_p \, \boldsymbol{D}_r \, \boldsymbol{R}_p^T. \tag{5.4}$$

Hence, the eigenvalues of both tensors remain the same, while their eigenvectors are transformed by $\boldsymbol{R}_p$. Further, the mapping (5.4) prevents undesired inelastic scaling effects. Besides these properties, a virgin material is characterized by $\boldsymbol{D}_r = \boldsymbol{D} = \boldsymbol{0}$, while a 'fully broken' state corresponds to $\boldsymbol{D}_r = \boldsymbol{D} = \boldsymbol{I}$.

Rotational non-uniqueness. The multiplicative decomposition of the deformation gradient suffers from an inherent problem of rotational non-uniqueness. Hence, a decomposition including superimposed rotations of the intermediate configuration in the sense of

$$\boldsymbol{F} = \boldsymbol{F}_e \boldsymbol{F}_p = \boldsymbol{F}_e \boldsymbol{Q}^T \boldsymbol{Q} \boldsymbol{F}_p =: \boldsymbol{F}_e^* \boldsymbol{F}_p^*, \quad \boldsymbol{Q} \in \mathrm{SO}(3) \tag{5.5}$$

can be equivalently stated. Considering the polar decomposition of $\boldsymbol{F}_p^* = \boldsymbol{Q}\boldsymbol{F}_p = \boldsymbol{Q}\boldsymbol{R}_p\boldsymbol{U}_p = \boldsymbol{R}_p^*\boldsymbol{U}_p$ where $\boldsymbol{R}_p^* \in \mathrm{SO}(3)$, one recognizes that this non-uniqueness only affects $\boldsymbol{R}_p$, while $\boldsymbol{U}_p$ is uniquely defined. In further consequence, for the mapping chosen in Equation (5.4), one must ensure that the Helmholtz free energy ψ is independent of the rotational non-uniqueness, in order to obtain a physically reasonable material formulation, i.e.

$$\psi\left(\bar{\boldsymbol{\eta}}_e, \boldsymbol{\eta}_p, \boldsymbol{D}\right) = \psi\left(\bar{\boldsymbol{\eta}}_e^*, \boldsymbol{\eta}_p^*, \boldsymbol{D}^*\right) \tag{5.6}$$

with $\bar{\boldsymbol{\eta}}_e^* = \boldsymbol{R}_p^* \, (\boldsymbol{\varepsilon} - \boldsymbol{\varepsilon}_p) \, \boldsymbol{R}_p^{*^T}$, $\boldsymbol{\eta}_p^* = \boldsymbol{R}_p^* \, \boldsymbol{\varepsilon}_p \, \boldsymbol{R}_p^{*^T}$, and $\boldsymbol{D}^* = \boldsymbol{R}_p^* \, \boldsymbol{D}_r \, \boldsymbol{R}_p^{*^T}$. Therefore, we assume the Helmholtz free energy to be a *scalar-valued isotropic function* of its arguments. Since the

following relations hold true

$$\begin{gathered}\operatorname{tr}\left(\left(\bar{\boldsymbol{\eta}}_e^*\right)^a\right)=\operatorname{tr}\left(\left(\bar{\boldsymbol{\eta}}_e\right)^a\right),\ \operatorname{tr}\left(\left(\boldsymbol{\eta}_p^*\right)^a\right)=\operatorname{tr}\left(\left(\boldsymbol{\eta}_p\right)^a\right),\ \operatorname{tr}\left(\left(\boldsymbol{D}^*\right)^a\right)=\operatorname{tr}\left(\left(\boldsymbol{D}\right)^a\right),\quad a\in\{1,2,3\}\\ \operatorname{tr}\left(\left(\bar{\boldsymbol{\eta}}_e\right)^b\left(\boldsymbol{\eta}_p\right)^c\left(\boldsymbol{D}\right)^d\right)=\operatorname{tr}\left(\left(\bar{\boldsymbol{\eta}}_e^*\right)^b\left(\boldsymbol{\eta}_p^*\right)^c\left(\boldsymbol{D}^*\right)^d\right),\quad b,c,d\in\{0,1,2\}\end{gathered} \tag{5.7}$$

the presented framework using the mapping (5.4) indeed is invariant with respect to superimposed rotations of the intermediate configuration.

Choice of local variables for gradient-extension. The micromorphic approach introduced in Forest [2009, 2016] introduces a set of 'non-local' variables $\bar{\mathbf{d}}$ on a global level. These variables are strongly coupled to the same number of inherent variables of the material formulation, which will be referred as 'local' variables $\mathbf{d}$. Noteworthy, the latter mentioned should not be understood as additional constitutive variables rather than the constitutive variables themselves or functions of those. Here, three 'local' variables are introduced, which are chosen as the invariants of the damage tensor

$$\mathbf{d}=\left(\operatorname{tr}\left(\boldsymbol{D}\right),\operatorname{tr}\left(\boldsymbol{D}^2\right),\operatorname{tr}\left(\boldsymbol{D}^3\right)\right). \tag{5.8}$$

Besides the invariant-based gradient-extension, several other possibilities are known in the literature, for instance, enhancing the damage hardening variable (see Fassin et al. [2019*b*]) or the components of the damage tensor (see e.g. Langenfeld and Mosler [2020]). Although the invariant-based approach is quite general, the question arises whether it is possible to reduce the number of variables. Having in mind that the volumetric part of the damage tensor represents isotropic damage, while the remaining deviatoric part is responsible for the anisotropic nature, one might use the following set

$$\mathbf{d}=\left(\frac{\operatorname{tr}\left(\boldsymbol{D}\right)}{3},\operatorname{tr}\left(\operatorname{dev}\left(\boldsymbol{D}\right)^2\right)\right) \tag{5.9}$$

which is a novel approach in gradient-extended anisotropic damage. A further benefit of this latter choice is that it reduces to the gradient-extension proposed by Brepols et al. [2020] in case of isotropic damage. However, investigating this kind of approach in further detail is out of the scope of this contribution.

5.3.1 Helmholtz free energy

In the following, the Helmholtz free energy is assumed to be additively decomposable

$$\psi = \psi_e\left(\bar{\boldsymbol{\eta}}_e, \boldsymbol{D}\right) + \psi_p\left(\boldsymbol{\eta}_p, \boldsymbol{D}, \kappa_p\right) + \psi_d\left(\boldsymbol{D}, \kappa_d\right) + \psi_{\bar{d}}\left(\mathrm{d}, \bar{\mathrm{d}}, \mathrm{Grad}\left(\bar{\mathrm{d}}\right)\right) \tag{5.10}$$

where ψ_e represents the elastically stored energy, ψ_p takes kinematic and isotropic plastic hardening into account, damage hardening is given by ψ_d, and $\psi_{\bar{d}}$ is a 'coupling' or 'non-local' energy term ensuring both a strong coupling between d and $\bar{\mathrm{d}}$ as well as introduces an internal length scale into the material formulation. Moreover, ψ_d prevents the eigenvalues of $\boldsymbol{D}$ and $\boldsymbol{D}_r$ to exceed the value one and is in line with Fassin et al. [2019*b*]. Additionally, κ_p and κ_d represent scalar hardening variables for plasticity and damage, respectively.

5.3.2 Micromorphically extended Clausius-Duhem inequality

Evaluating the micromorphically extended Clasuius-Duhem inequality in the logarithmic strain space

$$-\dot{\psi} + \boldsymbol{T} : \dot{\boldsymbol{\varepsilon}} + \underbrace{\boldsymbol{\xi}_{0_i} \cdot \dot{\bar{\mathrm{d}}} + \boldsymbol{\Xi}_{0_i} : \mathrm{Grad}\left(\dot{\bar{\mathrm{d}}}\right)}_{\text{micromorphic extension}} \geq 0 \tag{5.11}$$

by inserting the assumed Helmholtz free energy in Equation (5.10), the following reduced dissipation inequality is obtained

$$\left(\boldsymbol{T} - \boldsymbol{X}\right) : \dot{\boldsymbol{\varepsilon}}_p + R_p\, \dot{\kappa}_p + \boldsymbol{Y} : \dot{\boldsymbol{D}}_r + R_d\, \dot{\kappa}_d \geq 0 \tag{5.12}$$

under consideration of the state laws

$$\boldsymbol{T} = \boldsymbol{R}_p^T \frac{\partial \psi}{\partial \bar{\boldsymbol{\eta}}_e} \boldsymbol{R}_p, \quad \boldsymbol{\xi}_{0_i} = \frac{\partial \psi}{\partial \bar{\mathrm{d}}}, \quad \boldsymbol{\Xi}_{0_i} = \frac{\partial \psi}{\partial \mathrm{Grad}\left(\bar{\mathrm{d}}\right)}. \tag{5.13}$$

In Equation (5.11), $\boldsymbol{T}$ is the 'material' stress work-conjugated to the logarithmic strain rate, while both $\boldsymbol{\xi}_{0_i}$ and $\boldsymbol{\Xi}_{0_i}$ are so-called 'generalized' stresses. The thermodynamically consistent driving forces occurring in Equation (5.12) can be clearly distinguished into plastic and damage parts. First, we introduce the following plastic driving forces

$$\boldsymbol{X} \coloneqq \boldsymbol{R}_p^T \frac{\partial \psi}{\partial \boldsymbol{\eta}_p} \boldsymbol{R}_p, \quad R_p \coloneqq -\frac{\partial \psi}{\partial \kappa_p} \tag{5.14}$$

with $\boldsymbol{X}$ being the plastic backstress tensor and R_p the plastic isotropic hardening force. Furthermore, the damage driving forces are obtained as

$$\boldsymbol{Y} \coloneqq -\boldsymbol{R}_p^T \frac{\partial \psi}{\partial \boldsymbol{D}} \boldsymbol{R}_p, \quad R_d \coloneqq -\frac{\partial \psi}{\partial \kappa_d} \tag{5.15}$$

where $\boldsymbol{Y}$ is the damage driving force and R_d being a damage hardening force. It should be noted that $\boldsymbol{Y}$ is composed out of four individual contribution, which result from the elastic, plastic, damage hardening, and 'non-local' energy terms. For the latter, it is important to note that $\mathbf{d}$ is a function that depends solely on $\boldsymbol{D}$. Hence, the arguments of the 'non-local' energy in Equation (5.10) can be written as $\psi_{\bar{d}} = \bar{\psi}_{\bar{d}} \left(\boldsymbol{D}, \bar{\mathbf{d}}, \mathrm{Grad}\left(\bar{\mathbf{d}}\right)\right)$. Moreover, it is worth noted that the plastic rotation tensor $\boldsymbol{R}_p$ remains undetermined in the present framework, which is considered an advantage. In order to guarantee that the dissipation inequality is fulfilled for arbitrary processes, meaningful evolution equations are chosen in the following, whereby a 'two-surface' approach is followed. These particular choices, however, do not restrict the generality of the model in any way.

Plastic regime. For the plastic regime, a von Mises-type yield criterion is chosen with respect to the so-called effective continuum

$$\Phi_p \coloneqq \sqrt{3\,\tilde{J}_2} - (\sigma_{y0} - \tilde{R}_p) \leq 0, \quad \tilde{J}_2 \coloneqq \left(\frac{1}{2} \mathrm{tr}\left(\mathrm{dev}\left(\boldsymbol{T} - \boldsymbol{X} \right)^2 \right) \right) \Big|_{\boldsymbol{D}=\boldsymbol{0}}, \quad \tilde{R}_p = R_p \Big|_{\boldsymbol{D}=\boldsymbol{0}} \tag{5.16}$$

with σ_{y0} denoting the plastic onset. For the evolution equations, the principle of maximum dissipation is followed, i.e.

$$\dot{\boldsymbol{\varepsilon}}_p = \dot{\gamma}_p \frac{\partial \Phi_p}{\partial \boldsymbol{T}} = \dot{\gamma}_p \, \mathbb{M}^{-1} : \frac{\partial \Phi_p}{\partial \tilde{\boldsymbol{T}}}, \quad \dot{\kappa}_p = \dot{\gamma}_p \frac{\partial \Phi_p}{\partial R_p} = \frac{\dot{\gamma}_p}{f_d}, \quad \mathbb{M} \coloneqq \frac{\partial \boldsymbol{T}}{\partial \tilde{\boldsymbol{T}}} \tag{5.17}$$

where $\mathbb{M}$ is a fourth order damage mapping tensor, which transforms the constitutively dependent variables from the effective to the 'damaged' space. Further, $\dot{\gamma}_p$ is the plastic multiplier, while f_d denotes the scalar degradation function and will be introduced in Section 5.3.3. Karush-Kuhn-Tucker (KKT) conditions close the set of plastic constitutive equations.

Damage regime. In analogy to the plastic regime, the onset of damage is characterized by

$$\Phi_d \coloneqq \sqrt{3\,\boldsymbol{Y}_+ : \mathbb{A}_d : \boldsymbol{Y}_+} - (Y_0 - R_d) \leq 0 \tag{5.18}$$

with the damage threshold Y_0 and

$$\boldsymbol{Y}_+ = \sum_{i=1}^{3} \langle Y_i \rangle \, \boldsymbol{n}_i^{\boldsymbol{Y}} \otimes \boldsymbol{n}_i^{\boldsymbol{Y}}, \quad \mathbb{A}_{d_{ijkl}} = \left(\delta_{ik} - D_{r_{ik}}\right) \left(\delta_{jl} - D_{r_{jl}}\right). \tag{5.19}$$

In the latter equation, Y_i and $\boldsymbol{n}_i$ denote the eigenvalues and eigenvectors of $\boldsymbol{Y}$, respectively. Additionally, $\langle \bullet \rangle$ defines the Macaulay brackets and the fourth order tensor $\mathbb{A}_d$ equips the model with greater flexibility, whereby the definition in Equation (5.19) is given with respect to the Cartesian basis system. Similar to the plastic regime, the evolution equations are obtained by following the principle of maximum dissipation

$$\dot{\boldsymbol{D}}_r = \dot{\gamma}_d \frac{\partial \Phi_d}{\partial \boldsymbol{Y}} = \dot{\gamma}_d \, \boldsymbol{Q}_+ \frac{\partial \Phi_d}{\partial \boldsymbol{Y}_+} \boldsymbol{Q}_+, \quad \dot{\kappa}_d = \dot{\gamma}_d \frac{\partial \Phi_d}{\partial R_d} = \dot{\gamma}_d \tag{5.20}$$

with the definition of the mapping tensor $\boldsymbol{Q}_+ = \sum_{i=1}^{3} \langle Y_i \rangle_H \, \boldsymbol{n}_i^{\boldsymbol{Y}} \otimes \boldsymbol{n}_i^{\boldsymbol{Y}}$, where $\langle \bullet \rangle_H$ is the Heaviside step function. The damage set of constitutive equations is closed by individual KKT conditions with the damage multiplier $\dot{\gamma}_d$.

5.3.3 Specific choices of energy terms

So far, the derivation of the model was kept quite general, in order not to restrict the model to a particular choice of energy terms. However, to study the model in a more detailed manner, the following energies are chosen

- Elastic energy: It is assumed that anisotropic damage results from isochoric deformations, while isotropic damage is associated with volumetric deformations (cf. e.g. Desmorat [2016]). In case of logarithmic strains, the energy can be easily decomposed into volumetric and isochoric deformations (cf. e.g. Criscione et al. [2000])

$$\psi_e = \mu_e \operatorname{tr}\left(\operatorname{dev}\left(\bar{\boldsymbol{\eta}}_e\right)^2 \left(\boldsymbol{I} - \boldsymbol{D}\right)\right) + f_d \, \frac{K_e}{2} \operatorname{tr}\left(\bar{\boldsymbol{\eta}}_e\right)^2 \tag{5.21}$$

- Plastic energy: Chosen in line with the previous one but extended by an exponential hardening term

$$\psi_p = \mu_p \operatorname{tr}\left(\operatorname{dev}\left(\boldsymbol{\eta}_p\right)^2 \left(\boldsymbol{I} - \boldsymbol{D}\right)\right) + f_d \, \frac{K_p}{2} \operatorname{tr}\left(\boldsymbol{\eta}_p\right)^2 + f_d \, r_p \left(\kappa_p + \frac{\exp\left(-s_p \, \kappa_p\right) - 1}{s_p}\right) \tag{5.22}$$

- Damage energy: Includes exponential and linear hardening, and moreover, a limit func-

tion for the eigenvalues D_i of $\boldsymbol{D}$ is involved

$$\psi_d = r_d \left(\kappa_d + \frac{\exp\left(-s_d\,\kappa_d\right) - 1}{s_d} \right) + \frac{H_d}{2}\,\kappa_d^2 + K_h \sum_{i=1}^{3} \left(-2\sqrt{1 - D_i} - D_i + 2 \right) \tag{5.23}$$

- Micromorphic energy: Ensures a strong coupling of the 'local' variables with their 'non-local' counterparts, and further, introduces an internal length scale by taking the Lagrangian gradient of $\bar{\mathbf{d}}$ into account (cf. e.g. Brepols et al. [2020])

$$\psi_{\bar{d}} = \frac{H}{2} \sum_{i=1}^{3} \left(d_i - \bar{d}_i \right)^2 + \frac{A}{2} \sum_{i=1}^{3} \mathrm{Grad}\left(\bar{d}_i\right) \cdot \mathrm{Grad}\left(\bar{d}_i\right) \tag{5.24}$$

In the above, μ_e and K_e are the elastic shear and bulk modulus, μ_p and K_p can be interpreted analogously, while r_p, s_p, r_d, and s_d describe exponential hardening of plasticity and damage. Additionally, linear damage hardening is described by H_d and the eigenvalue limitation by K_h, while H is a penalty factor and A characterizes the internal length scale. The degradation function is given by $f_d = 1 - \frac{\mathrm{tr}(\boldsymbol{D})}{3}$.

5.3.4 Weak forms

The weak forms which need to be solved on a global level read as follows

$$g_u(\boldsymbol{u}, \bar{\mathbf{d}}, \delta\boldsymbol{u}) \coloneqq \int_{B_0} \boldsymbol{S} : \delta\boldsymbol{E}\, \mathrm{d}V - \int_{B_0} \boldsymbol{f}_0 \cdot \delta\boldsymbol{u}\, \mathrm{d}V - \int_{\partial_t B_0} \boldsymbol{t}_0 \cdot \delta\boldsymbol{u}\, \mathrm{d}A = 0 \tag{5.25}$$

$$g_{\bar{d}}(\boldsymbol{u}, \bar{\mathbf{d}}, \delta\bar{\mathbf{d}}) \coloneqq \int_{B_0} \boldsymbol{\xi}_{0_i} \cdot \delta\bar{\mathbf{d}}\, \mathrm{d}V + \int_{B_0} \boldsymbol{\Xi}_{0_i} : \mathrm{Grad}\left(\delta\bar{\mathbf{d}}\right)\, \mathrm{d}V = 0 \tag{5.26}$$

with the test functions $\delta\boldsymbol{u}$ and $\delta\bar{\mathbf{d}}$, the second Piola-Kirchhoff stress tensor $\boldsymbol{S}$, the virtual Green-Lagrange strain $\delta\boldsymbol{E} \coloneqq \mathrm{sym}\left(\boldsymbol{F}^T \mathrm{Grad}\left(\delta\boldsymbol{u}\right)\right)$, the referential body force vector $\boldsymbol{f}_0$, and the referential traction vector $\boldsymbol{t}_0$. Both weak forms are nonlinear functions of their arguments, and thus, need to be solved using Newton-Raphson's method.

5.4 Transformation of algorithmic tangent operators

To be applicable in standard finite element formulations, the weak form of linear momentum (5.25) is stated in terms of Lagrangian quantities. In contrast, the entire constitutive framework is expressed in terms of logarithmic strain measures, and thus, the constitutively dependent

variables as well as the material tangent operators need to be transformed to the Lagrangian space. Employing both that $\boldsymbol{\varepsilon}$ solely depends on $\boldsymbol{C} \coloneqq \boldsymbol{U}^2$ and the fact that the stress power in logarithmic and Lagrangian space has to be equal, the transformation of the second Piola-Kirchhoff stress is found

$$\dot{\boldsymbol{\varepsilon}} = \underbrace{2\frac{\partial \boldsymbol{\varepsilon}}{\partial \boldsymbol{C}}}_{=:\mathbb{Q}} : \frac{1}{2}\dot{\boldsymbol{C}}, \quad \boldsymbol{T} : \dot{\boldsymbol{\varepsilon}} \overset{!}{=} \boldsymbol{S} : \frac{1}{2}\dot{\boldsymbol{C}} \quad \rightarrow \quad \boldsymbol{S} = \boldsymbol{T} : \mathbb{Q}. \tag{5.27}$$

Since the evolution equations introduced in Section 5.3.2 are discretized in time within a time interval $t \in [t_n, t_{n+1}]$, the unknown variables which have to be solved on a local level are $\dot{\gamma}_{p_{n+1}}$, $\boldsymbol{\varepsilon}_{p_{n+1}}$, $\dot{\gamma}_{d_{n+1}}$, and $\boldsymbol{D}_{r_{n+1}}$. All of them being discretized using the backward Euler method. Algorithmically, these variables are implicit functions of $\boldsymbol{C}_{n+1}$ and $\bar{\mathbf{d}}_{n+1}$. Hence, in an algorithmic sense, one may write $\boldsymbol{S}_{n+1} = \bar{\boldsymbol{S}}_{n+1}\left(\boldsymbol{C}_{n+1}, \bar{\mathbf{d}}_{n+1}\right)$ as well as $\mathbf{d}_{n+1} = \breve{\mathbf{d}}_{n+1}\left(\boldsymbol{C}_{n+1}, \bar{\mathbf{d}}_{n+1}\right)$. In analogy, the logarithmic stress reads $\boldsymbol{T}_{n+1} = \bar{\boldsymbol{T}}_{n+1}\left(\boldsymbol{\varepsilon}_{n+1}, \bar{\mathbf{d}}_{n+1}\right)$. A straightforward incrementation of these latter equations leads to the following expressions

$$\Delta\boldsymbol{S} = 2\frac{\partial \boldsymbol{S}_{n+1}}{\partial \boldsymbol{C}_{n+1}} : \frac{1}{2}\Delta\boldsymbol{C} + \frac{\partial \boldsymbol{S}_{n+1}}{\partial \bar{\mathbf{d}}_{n+1}} \cdot \Delta\bar{\mathbf{d}}, \quad \Delta\mathbf{d} = 2\frac{\partial \mathbf{d}_{n+1}}{\partial \boldsymbol{C}_{n+1}} : \frac{1}{2}\Delta\boldsymbol{C} + \frac{\partial \mathbf{d}_{n+1}}{\partial \bar{\mathbf{d}}_{n+1}} \cdot \Delta\bar{\mathbf{d}} \tag{5.28}$$

with the global increments $\Delta\boldsymbol{C}$ and $\Delta\bar{\mathbf{d}}$. Following a similar procedure for $\boldsymbol{T}_{n+1}$ and $\mathbb{Q}_{n+1}$, the increments of $\boldsymbol{S}_{n+1}$ and $\mathbf{d}_{n+1}$, taking into account Equation (5.27), can also be written as

$$\begin{aligned}\Delta\boldsymbol{S} = \Delta\boldsymbol{T}_{n+1} : \mathbb{Q}_{n+1} + \boldsymbol{T}_{n+1} : \Delta\mathbb{Q}_{n+1} = \left(\mathbb{Q}_{n+1} : \frac{\partial \boldsymbol{T}_{n+1}}{\partial \boldsymbol{\varepsilon}_{n+1}} : \mathbb{Q}_{n+1} + \boldsymbol{T}_{n+1} : \overset{6}{\mathbb{L}}_{n+1}\right) : \frac{1}{2}\Delta\boldsymbol{C} \\ + \mathbb{Q}_{n+1} : \frac{\partial \boldsymbol{T}_{n+1}}{\partial \bar{\mathbf{d}}_{n+1}} \cdot \Delta\bar{\mathbf{d}}\end{aligned} \tag{5.29}$$

$$\Delta\mathbf{d} = \frac{\partial \mathbf{d}_{n+1}}{\partial \boldsymbol{\varepsilon}_{n+1}} : \mathbb{Q}_{n+1} : \frac{1}{2}\Delta\boldsymbol{C} + \frac{\partial \mathbf{d}_{n+1}}{\partial \bar{\mathbf{d}}_{n+1}} \cdot \Delta\bar{\mathbf{d}} \tag{5.30}$$

with the sixth order tensor $\overset{6}{\mathbb{L}} \coloneqq 4\frac{\partial^2 \boldsymbol{\varepsilon}}{\partial \boldsymbol{C} \partial \boldsymbol{C}}$. Both $\mathbb{Q}$ and $\overset{6}{\mathbb{L}}$ can be determined analytically (cf. Miehe and Lambrecht [2001]), but require both eigenvalues and eigenvectors, and thus, are numerically expensive to determine. However, if one considers that $\boldsymbol{C}$ has no complex eigenvalues, the calculation can be implemented numerically extremely efficient by means of algorithmic differentiation using the trigonometric solution of the eigenvalue problem. A technique based on this type of approach to compute the matrix logarithm as well as its derivatives is presented in Hudobivnik and Korelc [2016] using *generating functions*, which is not only very efficient but also quite accurate in terms of numerics. The material tangent

operators in the logarithmic space are obtained using the algorithmic differentiation tool *AceGen*.

5.5 Numerical example

In this numerical example, a tensile specimen is considered in a three-dimensional setting, whose boundary value problem is taken from the literature Felder et al. [2022] and is depicted in Figure 5.1. Hexahedral finite elements with trilinear shape functions are used for discretization. The tensile specimen is uniaxially constrained, while the displacement in y direction is increased over time. Furthermore, due to symmetry, only one eighth of the entire geometry is simulated. Noteworthy, only Neumann boundary conditions are considered for the micromorphic boundary value problem, which are set to zero.
The material parameters for this example are taken from Holthusen, Brepols, Reese and Simon [2022*b*]; Brepols et al. [2020]: $\mu_e = 55000$ [MPa], $K_e = 61666.\bar{6}$ [MPa], $\mu_p = 62.5$ [MPa], $K_p = 0$ [MPa], $r_p = 125$ [MPa], $s_p = 5$ [-], $\sigma_{y0} = 100$ [MPa], $H_d = 1$ [MPa], $r_d = 5$ [MPa], $s_d = 100$ [-], $K_h = 0.1$ [MPa], $Y_0 = 2.5$ [MPa] as well as $A = 75$ [MPa mm^2] and $H = 10^5$ [MPa]. It should be noted that an additional parameter used for a Taylor expansion of damage hardening is $a_d = 0.9999999$ [-] (cf. Holthusen, Brepols, Reese and Simon [2022*b*]).
The specimen is loaded in a monotonic way, where the displacements at the outer edges are steadily increased. A careful mesh convergence is performed using 580, 4113, 13660, and 18510 finite elements, which is shown in Figure 5.2. The finite element mesh of the finest discretization is shown in Figure 5.3. It is appealing to recognize convergence in both the onset of damage and the amount of dissipation. At the end of the simulation, the structural specimen can be considered 'fully broken', since the final value of the load is about two percent of the maximum value reached during the loading and a clear crack going through the specimen can be observed.
Moreover, Figure 5.3 provides the contour plots of the main damage components as well as the accumulated plastic strain at the end of simulation using the finest mesh. A strong necking is clearly visible in the middle of the specimen. In this context, $D_{r_{yy}}$ can be interpreted as cracks in the plane perpendicular to the loading direction, which is why this plane is the most degraded. Slightly less degraded is the component $D_{r_{zz}}$, while the component $D_{r_{xx}}$ merely reaches a value of 0.8 [-]. In addition, the accumulated plastic strain κ_p can be understood as a measure of plasticity evolved, which is most pronounced in the region of necking.
Overall, it can be concluded that the developed material model is capable of providing plausible results even in a three-dimensional context.

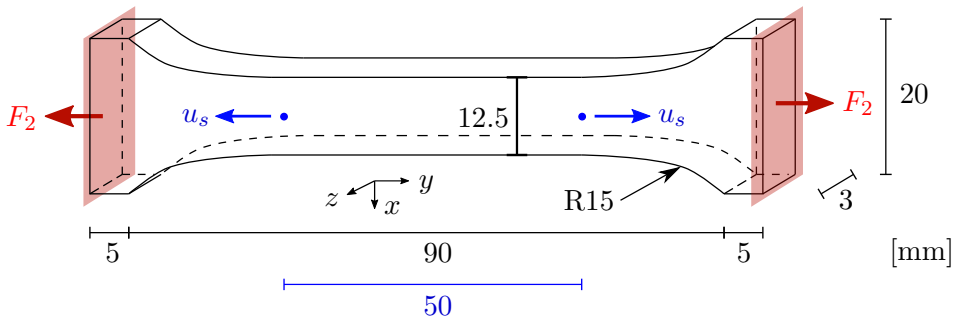

Figure 5.1: Geometry and boundary value problem. The specimen is loaded uniaxially, while the red edges remain perpendicular to the red forces. The displacements u_s (blue) are measured halfway between the center and the outer (red) edges of the specimen. The forces (red) are measured at the outer edges. Due to symmetry, only one eighth of the geometry is simulated.

5.6 Conclusion

Within this contribution, the model of Holthusen, Brepols, Reese and Simon [2022*b*], which couples elasto-plasticity to anisotropic damage for initially isotropic materials, was discussed in further detail. In addition, pathological mesh-dependency was cured by gradient-extended invariants of the second order damage tensor, resulting in three global unknowns in addition to the displacement field.

First of all, it was shown that the mapping for the damage tensor chosen in Holthusen, Brepols, Reese and Simon [2022*b*] indeed is invariant with respect to superimposed rotations of the intermediate configuration. Noteworthy, assuming an additive decomposition of the total strain does not harm the findings made in any way. As a consequence, it is not necessary to make any assumptions about, for instance, the plastic spin. Moreover, an alternative choice of the invariants used for gradient-extension was discussed here, which is based on the volumetric-deviatoric decoupling of the second order damage tensor.

For the numerical implementation, the weak form of linear momentum was expressed in terms of Lagrangian quantities, in order to be able to use the proposed model in standard finite element formulation. Therefore, the Lagrangian strains must be transformed to the logarithmic space and both the constitutively dependent variables as well as their algorithmic consistent tangent operators vice versa. In order to decrease the numerical effort required, it might be suitable to work with a combination of *generating functions* and algorithmic differentiation.

Lastly, the material model was examined in a three-dimensional numerical example to assess the ability of the proposed gradient-extension to cure mesh-dependency. Since coupled damage-plasticity simulations generally are very expensive in terms of numerical computation

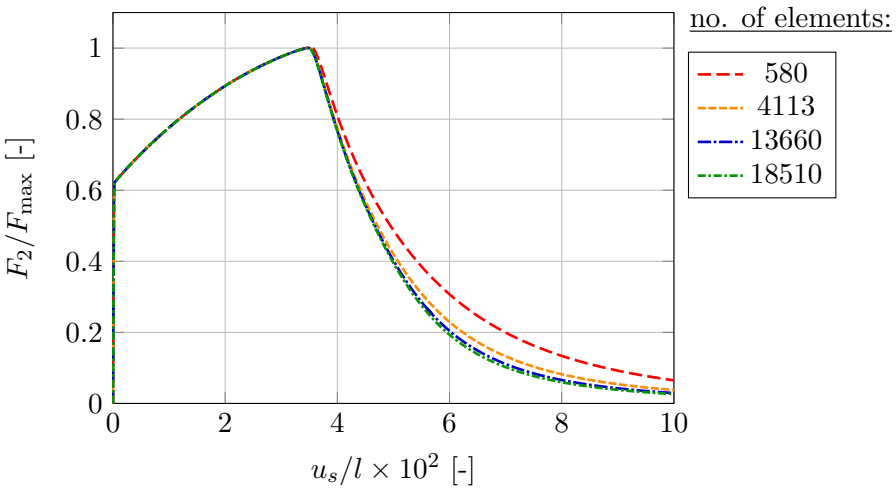

Figure 5.2: Normalized force-displacement curves with maximum load $F_{\max} = 6.044$ [kN]. Note that this value corresponds to the value of the whole geometry and not to the eighth, if symmetry is exploited. The latter corresponds to a quarter of $F_{\max}$. The displacement is normalized to the total length of the specimen $l = 100$ [mm]. For 18510 finite elements, the final value is about 0.02 [-]. The displacement u_s is indicated in Figure 5.1.

time, future works should focus on how to decrease the numerical effort, for instance, using adaptive mesh refinement or reduced integration (see e.g. Barfusz, van der Velden, Brepols, Holthusen and Reese [2021]).

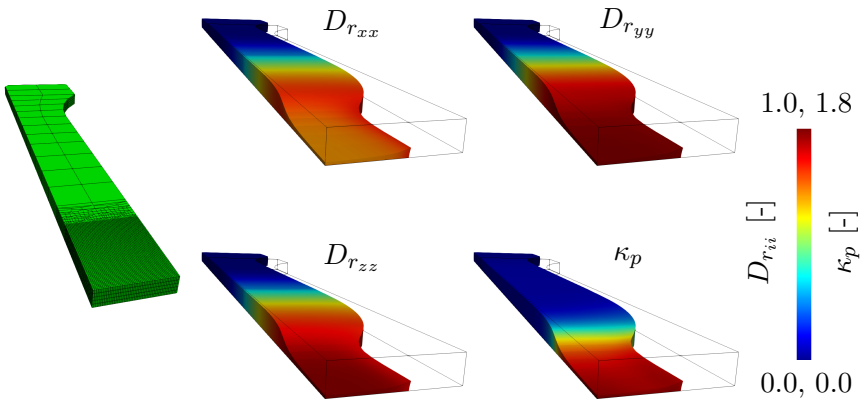

Figure 5.3: Left: Finite element mesh with 18510 elements, five layers are used in thickness direction. Middle: Contour plots of damage components $D_{r_{xx}}$, $D_{r_{yy}}$, $D_{r_{zz}}$, and accumulated plastic strain κ_p at the end of simulation ($u_s = 10$ [mm]). The maximum value of 1.0 [-] corresponds to the damage values, while 1.8 [-] is the maximum plastic strain value. Thin black lines illustrate the initial geometry.

6 Article 5: Inelastic material formulations based on a co-rotated intermediate configuration – Application to bioengineered tissues

This article was published as:

Holthusen, H., Rothkranz, C., Lamm, L., Brepols, T., and Reese, S. [2023], 'Inelastic material formulations based on a co-rotated intermediate configuration – Application to bioengineered tissues', *Journal of the Mechanics and Physics of Solids* **172**, 105174.

Disclosure of the individual authors' contributions to the article:

H. Holthusen reviewed the relevant existing literature, derived the entire theoretical framework and it was his idea to derive the co-rotated intermediate configuration in connection with algorithmic differentiation as well as to employ it for the kinematic growth and remodeling model. Further, he implemented the element routine used for the structural simulations. C. Rothkranz implemented the material routines, carried out all structural computations and fitted the corresponding parameters. L. Lamm gave valuable conceptual advice regarding the modeling of soft biological tissues. It was the original idea of L. Lamm to introduce homeostatic surfaces, while L. Lamm and H. Holthusen developed the concept of homeostatic surfaces proposed in Lamm et al. [2022] and used in this contribution. Moreover, C. Rothkranz, L. Lamm, T. Brepols, and S. Reese gave conceptual advice, contributed to the discussion of the results, read the current version of the article, and gave valuable suggestions for improvement. All authors approved the preliminary publication of the article in the present dissertation.

6.1 Abstract

In the field of material modeling, there is a general trend to include more and more complex phenomena in the modeling, making the models' theoretical derivation and numerical implementation extremely difficult. In particular, modeling inelastic material behavior under finite deformations in a continuum mechanical manner, e.g. to simulate soft biological tissues, remains one of the most challenging tasks. Unfortunately, the multiplicative decomposition of the deformation gradient usually utilized in this context suffers from an inherent rotational non-uniqueness, making it not straightforward to combine this approach with algorithmic differentiation (AD) – a very helpful tool in modern computational mechanics. To address this issue in the growth and remodeling model proposed herein, a novel co-rotated intermediate configuration is introduced. This configuration shares essential characteristics with the intermediate one, but is uniquely defined and applicable to a wide range of inelastic materials. In this regard, the concept of structural tensors, hardening effects, and a thermodynamically consistent derivation are discussed as well. Since the stress-driven growth model presented is based on the approach of homeostatic surfaces by Lamm et al. [2022], a large number of derivatives of potentials and energies are required, which can be elegantly implemented using AD due to the co-rotated formulation. Moreover, fiber remodeling of collagen fibers is taken into account in a stress-driven manner using AD. Finally, qualitative comparisons are made with recently published experiments by Eichinger et al. [2020] in uniaxial and multiaxial settings, revealing the efficient combination of the proposed framework and the material model.

Nomenclature

a, A	Scalar	$\times$	Cross product
$\boldsymbol{a}$	First order tensor	$\mid \boldsymbol{a} \mid$	$\sqrt{\boldsymbol{a} \cdot \boldsymbol{a}}$
$\boldsymbol{e}_i$	Cartesian basis	$\|\boldsymbol{A}\|$	$\sqrt{\mathrm{tr}\left(\boldsymbol{A}^T \boldsymbol{A}\right)}$
$\mathbf{a}$	Tuple $n \times 1$	$\sphericalangle\left(\boldsymbol{a}, \boldsymbol{b}\right)$	$\arccos\left(\dfrac{\boldsymbol{a} \cdot \boldsymbol{b}}{\mid \boldsymbol{a} \mid \mid \boldsymbol{b} \mid}\right)$
$\boldsymbol{A}$	Second order tensor	$\boldsymbol{A}^T$	Transpose of $\boldsymbol{A}$
$\mathbf{A}$	Matrix $n \times m$	$\boldsymbol{A}^{-1}$	Inverse of $\boldsymbol{A}$
$\mathbb{A}$	Fourth order tensor	$\mathrm{sym}\left(\boldsymbol{A}\right)$	$\frac{1}{2}\left(\boldsymbol{A} + \boldsymbol{A}^T\right)$
$\mathrm{SO}(3)$	Special orthogonal group	$\mathrm{tr}\left(\boldsymbol{A}\right)$	Trace of $\boldsymbol{A}$

$\cdot$	Single contraction	$\det(\boldsymbol{A})$	Determinant of $\boldsymbol{A}$
$\boldsymbol{AB}$	$\boldsymbol{A} \cdot \boldsymbol{B} = A_{ik} B_{kj} \boldsymbol{e}_i \otimes \boldsymbol{e}_j$	$\exp(\boldsymbol{A})$	Exponential of $\boldsymbol{A}$
$:$	Double contraction	$\mathrm{Grad}\,(\bullet)$	Lagrangian gradient
$\otimes$	Dyadic product	$\mathrm{Div}\,(\bullet)$	Lagrangian divergence
$\hat{\boldsymbol{A}}$	Nye notation of $\boldsymbol{A}$		

6.2 Introduction

Multiplicative decomposition. For modeling inelastic material behavior under finite deformations, the multiplicative decomposition of the deformation gradient into an elastic and an inelastic part has gained widespread in the continuum mechanics community and various application fields. Due to this decomposition, an intermediate configuration is introduced into the material formulation. Over the last decades, an enormous number of papers have been published based on this concept, which underlines a still high research interest in this regard. In the following, only a few that are of particular interest are named. Starting from finite elasto-plasticity (see e.g. Eckart [1948], Kröner [1959], Lee [1969], Mandel [1973], Lubarda et al. [1996]), the idea of a multiplicative decomposition to separate elastic and inelastic material behaviors was used in case of visco-elasticity (see e.g. Sidoroff [1974], Lubliner [1985], Holmes et al. [2006], Reese and Govindjee [1998], Lion [1997], Latorre and Montáns [2015]), visco-elasto-plastic models (see e.g. Haupt and Sedlan [2001], Nedjar [2002], Felder et al. [2020]) as well as in the field of biomechanics (Rodriguez et al. [1994], Lubarda and Hoger [2002]).

Noteworthy, the decompositions arising within the latter mentioned fields can also be interpreted in the sense of material isomorphism (see Bertram [1999], Svendsen [1998, 2001]), which naturally preserves the material's elastic behavior. Furthermore, the deformation gradient might be also decomposed in case of finite thermo-elasticity or thermo-elasto-plasticity (see Stojanović et al. [1964], Vujosevic and Lubarda [2002], Felder et al. [2022]). However, the thermal part is mainly determined by temperature and not by the pure mechanical problem. Moreover, Bammann and Solanki [2010*b*] decompose the deformation gradient into an elastic and damage part in case of brittle damage. Shanthraj et al. [2017] capture cleavage by a three factor decomposition, where the inelastic part is decomposed into plastic and damage parts. In addition, the idea of intermediate configurations was extended to finite damage mechanics,

for instance, by Menzel et al. [2005] using fictional configurations.
Apart from the theoretical considerations of the multiplicative split as well as the material models based on it, its numerical implementation is the subject of a wide range of research. Significant contributions to the application of return mapping algorithms based on the exponential map integrator scheme were made, among others, by Weber and Anand [1990], Eterovic and Bathe [1990], Cuitiño and Ortiz [1992], Simo and Miehe [1992] and Miehe [1996].
Unfortunately, all classical multiplicative decompositions, regardless the specific material behavior, have in common that the elastic and inelastic part suffer from an essential arbitrariness. Thus, it is neither possible to compute the elastic nor inelastic part, unless additional information about the substructure, for instance, about the slip systems involved in crystal plasticity (see e.g. Asaro [1983]) is known. Nevertheless, in order to be able to calculate the two parts, the inelastic material spin tensor is often set to zero, which implies that inelastic isotropy is assumed a priori (see Dafalias [1984, 1985]). Although this assumption may be valid for e.g. some classes of metals, its general applicability is questionable. Concerning the nature of the inelastic material spin tensor, reference is made to the work of Dafalias [1987, 2011], in which extensive discussions of the kinematics for finite elasto-plasticity can be found. The lack of a unified solution to the arbitrariness leads to the inability to calculate any stress- or strain-like quantity defined in the intermediate configuration, which must be considered a drawback. Since this is the natural configuration for specifying the constitutive framework, a solution to the problems that arise is highly desirable. For instance, the three-factor decompositions proposed by Bammann and Johnson [1987] and Casey [2017] might be employed. In contrast to the usual two-factor decomposition, all three factors are uniquely defined in these approaches. Nevertheless, the question remains to what extent a uniquely defined configuration similar to the intermediate configuration can be formulated. This configuration should have the same symmetry properties and physical interpretation as the intermediate configuration, since the conjugate driving forces of the latter have a sound physical interpretation.

Algorithmic differentiation. Since the numerical implementation of models is an essential part in computational mechanics, an efficient and robust implementation technique is crucial. Often, partial differential equations are coupled with each other, involving a large number of derivatives, which would be extremely time-consuming and error-prone if computed by hand. To counteract these problems, algorithmic differentiation (see e.g. Wengert [1964], Bartholomew-Biggs et al. [2000], Griewank and Walther [2008]) has emerged as an extremely powerful tool that solves the drawbacks of classical methods such as symbolic or numerical differentiation. Therefore, a huge number of AD tools for various programming

languages were developed in the past, e.g. for *FORTRAN* (Bischof et al. [1992], Hascoet and Pascual [2013]), *C/C++* codes (Griewank et al. [1996]) or *Mathematica* (Korelc [2002]), to name only a few.
These tools have already found their way into computational solid mechanics, both on a structural finite element level (see e.g. Zwicke et al. [2016], Vigliotti and Auricchio [2021]) and on a material point level (see e.g. Hudobivnik and Korelc [2016]) and have proven to be quite helpful and robust even in case of complex simulations. Unfortunately, because of the rotational non-uniqueness, for instance, the elastic Cauchy-Green tensor is not unique in general. Thus, while it is possible to calculate, for example, the Helmholtz free energy as a function of the invariants of the elastic strain tensor, the derivative with respect to the elastic Cauchy-Green tensor is again not unique. Therefore, it is not possible to calculate this derivative in an algorithmic way, especially not using AD. Hence, it is not straightforward to combine AD with inelastic and/or anisotropic materials under finite strains in general – at least not performed in the (physically sound) intermediate configuration – which must be considered a strong drawback and needs further development.

Biomechanics. Being an intensively studied domain of continuum mechanical modeling in the recent past, biomechanics is a highly interesting field and very challenging from a modeling point of view. Aiming to improve patient healthcare through *in silico*-based medical therapy, various mechanical properties of living organisms such as soft biological tissues need to be well understood. This requires novel approaches in order to predict the lifespan of bioengineered implants. A characteristic property of biological tissues, both soft and hard ones, is their ability to flexibly adapt to mechanical forces acting on them, which was already observed in the early work of Wolff [1870].
In this context, the process of growth, referring to a change in mass or volume, and remodeling, which takes into account the change in internal structure, are nowadays distinguished (see e.g. Thomson [1917], Ambrosi et al. [2019]) and are of particular interest for the constitutive modeling of tissues. Additionally, it is well known that both phenomena are mainly mechanically-driven (see e.g. Cyron and Humphrey [2016], Erlich et al. [2019]), as tissues, from a physiological point of view, exhibit an optimal load-bearing capacity under a preferred stress state, the so-called (tensional) homeostasis. In this regard, bridging the mechanical loading across the scales from the tissue to the cellular level is an important topic and has recently been investigated by Stracuzzi et al. [2022] in a comparative study between continuum and discrete fiber models.
Depending on the loading applied, tissues dynamically grow and remodel themselves to es-

tablish this state, and further, also restore this state after loading has changed (see e.g. Brown et al. [1998], Eichinger et al. [2020]). As a result of this continuous or long-term loading, soft tissues may be damaged (see e.g. Dong et al. [2020]) but have the ability to heal, the modeling of which is part of current research (Zuo et al. [2022]). Noteworthy, since a purely phenomenological model is proposed within this contribution, growth and remodeling are not explicitly differentiated, rather both phenomena are considered in a smeared sense.

In the literature, the existing models for volumetric growth can be roughly divided into isotropic models, such as the model of Lubarda and Hoger [2002], which assume the same growth in all spatial directions, and anisotropic models with direction-specific growth, such as the models of Menzel [2005] and Soleimani et al. [2020]. It should be noted that the terminology 'isotropic' and 'anisotropic' should not be misunderstood with the underlying or initial material behavior, i.e., anisotropic growth can also be observed in materials that are initially directionally independent.

Besides this classification and the resulting assumption about the nature of growth, most models are based on heuristic assumptions chosen in line with the conducted experiment. As a result, the inelastic part of the deformation gradient, which is also multiplicatively decomposed in biomechanics, is defined a priori. Thus, predictions in case of other loading scenarios is almost impossible, as also investigated in the work of Braeu et al. [2017] in the context of isotropic models compared to experimental observations.

In order to overcome these limitations of continuum growth modeling, two different approaches are widely used in the literature. These approaches are capable to flexibly adapt to different boundary value problems using the same model and circumvent heuristic assumptions about the growth part. The first one is the so-called 'constraint mixture approach', which considers the material as a mixture of different constituents with individual masses. In a biomechanical context, this theory is adapted by Cyron et al. [2016] and Cyron and Humphrey [2016] in a homogenized sense, describing growth and remodeling by a continuous removal and deposition of mass increments and therefore by introducing, for example, a deposition stretch. Contrary to classical constraint mixture models, their approach does not suffer from a relatively high computational cost. Further, Braeu et al. [2019] improved the approach insofar as no assumptions have to be made about the growth-related part of the deformation gradient a priori.

Alongside this promising approach, the 'original' two-factor decomposition of the deformation gradient into an elastic part and a growth-related part mentioned above (Rodriguez et al. [1994]), referred to as kinematic growth, receives renewed attention. Vastmans et al. [2022] compare the results of a kinematic growth model as well as a constraint mixture model using the same experimental data. Further, the models of, for instance, Soleimani et al. [2020] and

Lamm et al. [2022] belong to the kinematic growth approach, where growth is constantly influenced by the mechanical stress state and is able to change its principal directions. The latter authors introduce a novel concept of so-called 'homeostatic surfaces', similar to yield surfaces known from plasticity, which define the homeostatic state in the principal stress space. While growth and remodeling take place, the tissue seeks in a (non-)associative manner to achieve this state described by the homeostatic surface. Thus, the direction of growth is determined by the derivative of a growth potential with respect to the corresponding driving force. The great advantage of this appealing framework is that a variety of conceptual modeling approaches of plasticity are already known, both theoretically and numerically. For example, the concepts of isotropic, kinematic and distortional hardening or visco-plasticity can be easily adapted to growth modeling.

Although both consider anisotropic growth, the models of Soleimani et al. [2020] and Lamm et al. [2022] are restricted to initially isotropic materials. However, soft tissues, such as those found in tendons, arteries, fascia, or muscles, behave in a significantly anisotropic manner due to collagen fibers. Collagen is one of the main components of the extracellular matrix, along with elastin and the ground substance. The microfibrils formed from collagen are characterized by extremely stiff behavior, which then results in mostly transversally isotropic behavior of the overall tissue. The interested reader may find a deeper insight into the basic biological, but also mechanical principles, e.g. in the textbooks of Holzapfel and Ogden [2003] and Humphrey and Delange [2004]. In contrast to 'classical' transversally isotropic materials such as fiber-reinforced plastics, the preferred direction in soft tissue can change according to the loading as well. This remodeling of collagen fibers (see e.g. Taber [1995]), which should not be confused with growth and remodeling at the beginning, was already observed experimentally by Stopak and Harris [1982] under mechanical stimuli. The underlying mechanisms are a complex interplay of resorption and production of collagen, but are often described in a continuum mechanical sense as a rotation towards the main loading direction (see Menzel [2005] and Kuhl et al. [2005]), hence the term 'reorientation' is loosely associated with it. Suitable modeling of these complex constituents within soft tissues is still a current research topic in its own (see e.g. Miller and Gasser [2021]), where also the modeling of muscles can be mentioned in this context of anisotropic constitutive modeling (see e.g. Ehret et al. [2011], Böl et al. [2014]).

This overview of the literature on biomechanical modeling does not claim to be complete and reveals only a small insight into the current biomechanical modeling approaches as well as the various challenges associated with them. Due to the immense knowledge and research that has been conducted in recent years, the authors are pleased to refer the interested reader to

various review articles and textbooks on biomechanics, e.g. Menzel and Kuhl [2012], Kuhl [2014], de Rooij and Kuhl [2016], Goriely [2017], Ambrosi et al. [2011, 2019] and Budday et al. [2020].
As a result, it becomes clear that mechanical modeling of soft tissues is far from being complete and requires advanced and sophisticated models that combine the various characteristics of growth, remodeling, homeostasis and reorientation, which is a big challenge.

Outline. The symbiosis of above challenges is essential for modern material modeling. For example, biomechanics cannot be handled without computer-aided models, which, however, are far from simple – for this gap AD proves to be an indispensable tool. However, without any assumptions, the inelastic part of the deformation gradient cannot be determined. Consequently, no quantity in the intermediate configuration is calculable. Thus, equations stated in this very configuration cannot be implemented into AD. To solve this, a novel co-rotated framework of the intermediate configuration is introduced in Section 6.3. This configuration is uniquely defined and shares some essential properties with the intermediate one.
The proposed framework serves then as the theoretical foundation for the stress-driven kinematic growth model, which accounts for initially anisotropic behavior and fiber reorientation, developed in Section 6.4. Within this model, two different strategies for facing the tensional homeostasis based on homeostatic surfaces (Section 6.4.3) are presented. Its numerical implementation in a fully implicit manner is discussed in Section 6.5 with particular attention paid to the application of AD. Finally, several numerical examples illustrate the model's ability to adequately capture growth and remodeling as well as reorientation (Section 6.6). Moreover, the model is compared in a qualitative manner with recent experimental data of Eichinger et al. [2020] in a uniaxial as well as multiaxial setting. Section 6.7 provides a conclusion of the work.

6.3 Co-rotated intermediate configuration

In this section, the concept of a co-rotated intermediate configuration cic in the context of the multiplicative decomposition of the deformation gradient

$$\boldsymbol{F} = \boldsymbol{F}_e \boldsymbol{F}_i \tag{6.1}$$

into inelastic $\boldsymbol{F}_i$ and elastic parts $\boldsymbol{F}_e$ as well as its application in constitutive modeling are briefly presented.

Before discussing the main aspects of the cic framework, the most common approaches for modeling inelastic material behavior based on Equation (6.1) are shortly summarized. In this regard, it is crucial to note that for these approaches, the starting point for stating the constitutive framework – e.g. the choice of the Helmholtz free energy or evolution equations – is typically the intermediate configuration ic. These approaches can be roughly classified into four different categories, viz.:

1. The inelastic velocity gradient $\boldsymbol{L}_i \coloneqq \dot{\boldsymbol{F}}_i \boldsymbol{F}_i^{-1}$ is determined by the underlying microstructure. For instance, in crystal plasticity $\boldsymbol{L}_i$ is defined by n_{act} active slip systems, i.e. $\boldsymbol{L}_i = \sum_{\alpha=1}^{n_{act}} \left(\dot{\gamma}_\alpha \, \boldsymbol{s}_\alpha \otimes \boldsymbol{m}_\alpha\right)$ with $\boldsymbol{s}_\alpha$ and $\boldsymbol{m}_\alpha$ being the unit vectors of the slip system and $\dot{\gamma}_\alpha$ being a multiplier. Thus, the evolution equation is obtained as $\dot{\boldsymbol{F}}_i = \sum_{\alpha=1}^{n_{act}} \left(\dot{\gamma}_\alpha \, \boldsymbol{s}_\alpha \otimes \boldsymbol{m}_\alpha\right) \boldsymbol{F}_i$.

2. The inelastic material spin tensor $\boldsymbol{\Omega}_i \coloneqq \boldsymbol{L}_i - \operatorname{sym}\left(\dot{\boldsymbol{F}}_i \boldsymbol{F}_i^{-1}\right)$ is assumed to be zero (inelastic isotropy). Hence, $\boldsymbol{L}_i$ is equal to its symmetric part in general. Thus, the evolution equation reduces to $\dot{\boldsymbol{F}}_i = \boldsymbol{Z}_i \boldsymbol{F}_i$ with $\boldsymbol{Z}_i$ denoting the rate and direction of inelastic evolution. Although this approach seems to be similar to the latter, it should not be confused with it, as there might be no evidence to set $\boldsymbol{\Omega}_i$ equal to zero.

3. The inelastic part $\boldsymbol{F}_i$ of the deformation gradient or its evolution is set a priori, for example, proportional to the identity. In the latter case, the evolution equation results in $\dot{\boldsymbol{F}}_i = \dot{\vartheta} \boldsymbol{I}$ with $\dot{\vartheta}$ being the rate of inelastic evolution. Such models may be found in biomechanics, see e.g. Lubarda and Hoger [2002].

4. The Helmholtz free energy as well as all yield criteria and inelastic potentials are assumed to be *scalar-valued isotropic functions*. In combination with suitable pull-back operations to the reference configuration, it can be shown that neither $\boldsymbol{F}_e$ nor $\boldsymbol{F}_i$ need to be calculated. In the following, this approach will be abbreviated $pbic$. A short summary is presented in Appendix 6.8.1. For a deeper insight into the theoretical background of the $pbic$ framework, the interested reader is kindly referred to the works of e.g. Simo and Miehe [1992] and Dettmer and Reese [2004].

A brief overview can also be found in Lubarda [2004]. Unless further knowledge of the underlying microstructure is available, the latter $pbic$ framework is advantageous since no further assumptions need to be made about the nature of inelastic evolution. In this context, it is appealing to note that most of the equations given in the ic have a sound physical interpretation, as they can be related to the current configuration (see e.g. Dettmer and Reese [2004] and Appendix 6.8.1).

Therefore, only the $pbic$ and the cic frameworks will be compared in the following. Besides all the advantages of the $pbic$ framework, the question remains how to avoid the required pull-back operations. On the one hand, these make the physical interpretation more complicated, and on the other hand, they prevent the equations related to the ic from being entered directly into AD tools. Therefore, the $pbic$ framework is extend to a co-rotated formulation (cic) in the following.

Rotational non-uniqueness. The inherent problem of the decomposition (6.1) is that both parts suffer from a rotational non-uniqueness, i.e.

$$\boldsymbol{F} = \boldsymbol{F}_e \boldsymbol{Q}_1^T \boldsymbol{Q}_1 \boldsymbol{F}_i =: \boldsymbol{F}_e^* \boldsymbol{F}_i^* \tag{6.2}$$

is a possible decomposition as well, with $\boldsymbol{Q}_1 \in \mathrm{SO}(3)$. Considering the polar decompositions $\boldsymbol{F}_e = \boldsymbol{V}_e \boldsymbol{R}_e$ and $\boldsymbol{F}_i = \boldsymbol{R}_i \boldsymbol{U}_i$, where $\boldsymbol{R}_e,\ \boldsymbol{R}_i \in \mathrm{SO}(3)$ as well as $\boldsymbol{V}_e$ and $\boldsymbol{U}_i$ are positive definite stretch tensors, respectively. Further, with the following equations at hand

$$\boldsymbol{F}_e^* = \boldsymbol{V}_e \boldsymbol{R}_e \boldsymbol{Q}_1^T =: \boldsymbol{V}_e \boldsymbol{R}_e^* \tag{6.3}$$

$$\boldsymbol{F}_i^* = \boldsymbol{Q}_1 \boldsymbol{R}_i \boldsymbol{U}_i =: \boldsymbol{R}_i^* \boldsymbol{U}_i \tag{6.4}$$

it becomes clear that the rotational non-uniqueness affects only $\boldsymbol{R}_e$ and $\boldsymbol{R}_i$, while $\boldsymbol{V}_e$ and $\boldsymbol{U}_i$ are uniquely defined[1]. In order to derive a continuum mechanical material model, the following Cauchy-Green-like tensors with respect to the ic (see Figure 6.1) are introduced[2]

$$\boldsymbol{C}_e^* = \boldsymbol{F}_e^{*T} \boldsymbol{F}_e^* = \boldsymbol{Q}_1 \boldsymbol{F}_e^T \boldsymbol{F}_e \boldsymbol{Q}_1^T =: \boldsymbol{Q}_1 \boldsymbol{C}_e \boldsymbol{Q}_1^T \tag{6.5}$$

$$\boldsymbol{B}_i^* = \boldsymbol{F}_i^* \boldsymbol{F}_i^{*T} = \boldsymbol{Q}_1 \boldsymbol{F}_i \boldsymbol{F}_i^T \boldsymbol{Q}_1^T =: \boldsymbol{Q}_1 \boldsymbol{B}_i \boldsymbol{Q}_1^T \tag{6.6}$$

$$\boldsymbol{C}_i^* = \boldsymbol{F}_i^{*T} \boldsymbol{F}_i^* = \boldsymbol{F}_i^T \boldsymbol{F}_i =: \boldsymbol{C}_i. \tag{6.7}$$

Regarding the rotational non-uniqueness, Bammann and Johnson [1987] and Casey [2017] proposed two different three-factor decompositions of $\boldsymbol{F}$, where all parts are uniquely defined. Especially the latter mentioned was successfully applied by Ulz and Celigoj [2021] in the recent past and shares a few similarities with the framework proposed here. Since the aforementioned work deals with this topic in a mathematically more detailed manner, and further discusses a change of observer, the interested reader is kindly referred to this work as well as the literature cited therein.

[1] $\boldsymbol{R}_e^*,\ \boldsymbol{R}_i^* \in \mathrm{SO}(3)$

[2] A second order tensor $\breve{\boldsymbol{A}}$ in the intermediate configuration affected by the rotational non-uniqueness in the following manner $\breve{\boldsymbol{A}}^* = \boldsymbol{Q}_1 \breve{\boldsymbol{A}} \boldsymbol{Q}_1^T$ will be called $\boldsymbol{C}_e$-like hereinafter.

Additional inelastic decomposition. Within the present framework, an additional decomposition

$$\boldsymbol{F}_i = \boldsymbol{F}_{i_b}\boldsymbol{F}_{i_a} \tag{6.8}$$

is discussed, as might be of interest in modeling nonlinear kinematic hardening (see Lion [2000], Vladimirov et al. [2008] and Christ and Reese [2009]). As in case of Equation (6.2), the decomposition (6.8) is not unique as well, since $\boldsymbol{F}_i = \boldsymbol{F}_{i_b}\boldsymbol{Q}_2^T\boldsymbol{Q}_2\boldsymbol{F}_{i_a}$ with $\boldsymbol{Q}_2 \in \mathrm{SO}(3)$ can be stated. Further, again having Equation (6.2) in mind, one might define $\boldsymbol{F}_{i_b}^* := \boldsymbol{Q}_1\boldsymbol{F}_{i_b}\boldsymbol{Q}_2^T$ and $\boldsymbol{F}_{i_a}^* := \boldsymbol{Q}_2^T\boldsymbol{F}_{i_a}$, such that $\boldsymbol{F}_i^* = \boldsymbol{F}_{i_b}^*\boldsymbol{F}_{i_a}^*$ holds. However, in this regard, it is interesting to note that

$$\boldsymbol{B}_{i_b}^* = \boldsymbol{F}_{i_b}^*\boldsymbol{F}_{i_b}^{*^T} = \boldsymbol{Q}_1\boldsymbol{F}_{i_b}\boldsymbol{F}_{i_b}^T\boldsymbol{Q}_1^T =: \boldsymbol{Q}_1\boldsymbol{B}_{i_b}\boldsymbol{Q}_1^T \tag{6.9}$$

behaves $\boldsymbol{C}_e$-like.

Structural tensors. Moreover, in order to account for initially anisotropic behavior, for instance in the context of fiber-reinforced plastics (e.g. Mehdipour et al. [2019], Holthusen et al. [2020], Poggenpohl et al. [2021]) and thermoplastics (e.g. Dean et al. [2016, 2017]) or anisotropic phenomena that may induce a certain kind of anisotropy such as damage (see e.g. Hansen and Schreyer [1994], Badreddine et al. [2015], Reese et al. [2021], Holthusen, Brepols, Reese and Simon [2022*b*]), structural tensors are considered (see e.g. Spencer [1971, 1984], Boehler [1979], Zhang and Rychlewski [1990], Schröder and Neff [2003]). For simplicity, the structural tensor $\boldsymbol{H}$ in the reference configuration is assumed to be symmetric and is mapped to its intermediate counterpart $\breve{\boldsymbol{H}}$ according to[3]

$$\breve{\boldsymbol{H}}^* = \boldsymbol{F}_i^*\boldsymbol{H}\boldsymbol{F}_i^{*^T} = \boldsymbol{Q}_1\boldsymbol{F}_i\boldsymbol{H}\boldsymbol{F}_i^T\boldsymbol{Q}_1^T =: \boldsymbol{Q}_1\breve{\boldsymbol{H}}\boldsymbol{Q}_1^T \tag{6.10}$$

which behaves $\boldsymbol{C}_e$-like. Noteworthy, if $\boldsymbol{H}$ is not symmetric, $\breve{\boldsymbol{H}}$ is generally not symmetric, regardless of the mapping chosen. As a consequence, the integrity basis of ψ might contain both the symmetric and skew-symmetric part of $\breve{\boldsymbol{H}}$ (cf. Zheng [1994]), which would also influence the evaluation of the Clausius-Duhem inequality.
For a better understanding, Figure 6.1 illustrates the different decompositions and the mapping of a material point and its local neighborhood of a referential body $\mathscr{B}_0$ to the current body $\mathscr{B}_t$.

Helmholtz free energy. The tensorial quantities introduced above are suitable to describe

[3] Also other mappings are possible. The results for three important ones are presented in Appendix 6.8.2.

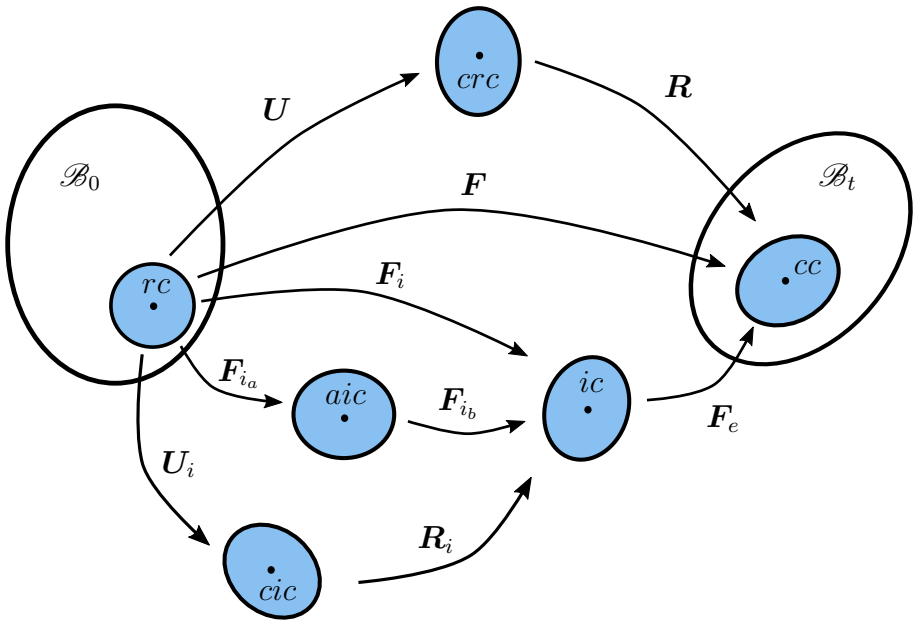

Figure 6.1: Decomposition of the deformation gradient $\boldsymbol{F} = \boldsymbol{F}_e\boldsymbol{F}_i$ into inelastic and elastic parts as well as the additional decomposition $\boldsymbol{F}_i = \boldsymbol{F}_{i_b}\boldsymbol{F}_{i_a}$. Moreover, $\boldsymbol{F} = \boldsymbol{R}\boldsymbol{U}$ and $\boldsymbol{F}_i = \boldsymbol{R}_i\boldsymbol{U}_i$ possess their polar decompositions. Configurations: rc – reference configuration, crc – co-rotated configuration, cc – current configuration, ic – intermediate configuration, aic – additional intermediate configuration, cic – co-rotated intermediate configuration.

different material behaviors in a phenomenological and smeared sense. Thus, and in line with material isomorphism (cf. Bertram [1999], Svendsen [1998, 2001]), the Helmholtz free energy per unit reference volume is assumed to be an *isotropic function* depending on the following arguments (cf. e.g. Green and Naghdi [1971])

$$\psi = \psi^* \left(\boldsymbol{C}_e, \boldsymbol{B}_i, \boldsymbol{B}_{i_b}, \breve{\boldsymbol{H}} \right) = \psi^* \left(\boldsymbol{C}_e^*, \boldsymbol{B}_i^*, \boldsymbol{B}_{i_b}^*, \breve{\boldsymbol{H}}^* \right) . \tag{6.11}$$

It is important to note that, since ψ is assumed to be an *isotropic function* of its arguments, and further due to Equations (6.5), (6.6), (6.9) and (6.10), the formulation is invariant with respect to superimposed rotations of $\boldsymbol{F}_i$ (cf. e.g. Sansour et al. [2007]).
Unfortunately, it is not possible to calculate any of the arguments of Equation (6.11), since the push-forwards to the ic of all arguments involve $\boldsymbol{F}_i$. Therefore, neither the Helmholtz free energy ψ can be calculated in its assumed form ψ^* nor the derivatives with respect to those arguments[4].

Remark 16. *Although the Helmholtz free energy is unique, since it is assumed to be an*

[4]Noteworthy, the invariants of the arguments of Equation (6.11) can be calculated without knowing $\boldsymbol{F}_i$ but $\boldsymbol{U}_i$.

isotropic function and thus not affected by the rotational non-uniqueness, the derivatives are not unique with respect to arguments defined in the intermediate configuration. For simplicity, assume an energy depending only on the elastic variables, i.e., $\psi = \psi'(\boldsymbol{C}_e) = \psi'(\boldsymbol{C}_e^*)$*. Thus, the derivatives read*

$$\frac{\partial \psi'}{\partial \boldsymbol{C}_e} = \alpha_1 \boldsymbol{I} + \alpha_2 \boldsymbol{C}_e + \alpha_3 \boldsymbol{C}_e^2, \quad \frac{\partial \psi'}{\partial \boldsymbol{C}_e^*} = \alpha_1 \boldsymbol{I} + \alpha_2 \boldsymbol{C}_e^* + \alpha_3 \boldsymbol{C}_e^{*^2} \tag{6.12}$$

where $\alpha_i = i \frac{\partial \psi'}{\partial \mathrm{tr}(\boldsymbol{C}_e^i)}$*. Hence, the derivative is affected by the non-uniqueness. Similar observations can be made for the remaining arguments.*

Co-rotated pull-back. As seen so far, the non-uniqueness is strongly related to the rotation tensor $\boldsymbol{R}_i$. A first step to circumvent this non-uniqueness is to note that ψ, as a *scalar-valued isotropic function*, can be expressed in terms of (mixed) invariants (see Spencer [1971], Boehler [1979], Zheng [1994])[5]. The second step, which is the main idea of the co-rotated intermediate configuration cic, is to pull-back all quantities in Equation (6.11) to this very configuration (cf. Figure 6.1)

$$\bar{\boldsymbol{C}}_e \coloneqq \boldsymbol{R}_i^{-1} \boldsymbol{C}_e \boldsymbol{R}_i = \boldsymbol{R}_i^T \boldsymbol{C}_e \boldsymbol{R}_i = \boldsymbol{U}_i^{-1} \boldsymbol{C} \boldsymbol{U}_i^{-1} \tag{6.13}$$

$$\bar{\boldsymbol{B}}_i \coloneqq \boldsymbol{R}_i^{-1} \boldsymbol{B}_i \boldsymbol{R}_i = \boldsymbol{R}_i^T \boldsymbol{B}_i \boldsymbol{R}_i \equiv \boldsymbol{C}_i = \boldsymbol{U}_i^2 \tag{6.14}$$

$$\bar{\boldsymbol{B}}_{i_b} \coloneqq \boldsymbol{R}_i^{-1} \boldsymbol{B}_{i_b} \boldsymbol{R}_i = \boldsymbol{R}_i^T \boldsymbol{B}_{i_b} \boldsymbol{R}_i = \boldsymbol{U}_i \boldsymbol{C}_{i_a}^{-1} \boldsymbol{U}_i = \boldsymbol{U}_i \boldsymbol{U}_{i_a}^{-2} \boldsymbol{U}_i \tag{6.15}$$

$$\bar{\boldsymbol{H}} \coloneqq \boldsymbol{R}_i^{-1} \breve{\boldsymbol{H}} \boldsymbol{R}_i = \boldsymbol{R}_i^T \breve{\boldsymbol{H}} \boldsymbol{R}_i = \boldsymbol{U}_i \boldsymbol{H} \boldsymbol{U}_i \tag{6.16}$$

with $\boldsymbol{C} \coloneqq \boldsymbol{F}^T \boldsymbol{F}$ and $\boldsymbol{F}_{i_a} = \boldsymbol{R}_{i_a} \boldsymbol{U}_{i_a}$, where $\boldsymbol{R}_{i_a} \in \mathrm{SO}(3)$ and $\boldsymbol{U}_{i_a}$ being uniquely defined[6]. In this way, the eigenvalues as well as the symmetry properties between the ic arguments and their cic counterparts, e.g. $\boldsymbol{C}_e$ and $\bar{\boldsymbol{C}}_e$, remain the same. Additionally, in line with finite elasto-plasticity and the assumption of an unstressed intermediate configuration (see Lee and Liu [1967] and Lee [1969]), the cic can also be considered unstressed. Nevertheless, all quantities in Equations (6.13)-(6.16) can be directly computed, i.e. they are uniquely defined. Therefore, the Helmholtz free energy can be equivalently expressed as[7] (cf. Appendix 6.8.3)

$$\psi = \psi^* \left(\bar{\boldsymbol{C}}_e, \boldsymbol{C}_i, \bar{\boldsymbol{B}}_{i_b}, \bar{\boldsymbol{H}} \right) = \psi^* \left(\boldsymbol{C}_e, \boldsymbol{B}_i, \boldsymbol{B}_{i_b}, \breve{\boldsymbol{H}} \right). \tag{6.17}$$

[5] Due to simplicity, the derivation is restricted to the three distinct invariants of each tensor and mixed invariants for up to two tensors.

[6] $\boldsymbol{R}_i^{-1} = \boldsymbol{R}_i^T$ since $\boldsymbol{R}_i \in \mathrm{SO}(3)$.

[7] Instead of $\boldsymbol{C}_i$, one may use $\boldsymbol{C}_i^{-1}$ to model the inelastic strains in the sense of an Euler-Almansi strain measure, see Appendix 6.8.4

Clausius-Duhem inequality. Next, it is the aim to derive the conjugated driving forces in a thermodynamically consistent manner. Therefore, the (isothermal) Clausius-Duhem inequality $-\dot{\psi} + \frac{1}{2}\,\boldsymbol{S} : \dot{\boldsymbol{C}} \geq 0$, with the second Piola-Kirchhoff stress tensor $\boldsymbol{S}$, must be evaluated and requires the time derivative of the Helmholtz free energy

$$\dot{\psi} \overset{\text{def}}{=} \dot{\psi}^* = \frac{\partial \psi^*}{\partial \bar{\boldsymbol{C}}_e} : \dot{\bar{\boldsymbol{C}}}_e + \frac{\partial \psi^*}{\partial \boldsymbol{C}_i} : \dot{\boldsymbol{C}}_i + \frac{\partial \psi^*}{\partial \bar{\boldsymbol{B}}_{i_b}} : \dot{\bar{\boldsymbol{B}}}_{i_b} + \frac{\partial \psi^*}{\partial \bar{\boldsymbol{H}}} : \dot{\bar{\boldsymbol{H}}} \tag{6.18}$$

with the rates

$$\dot{\bar{\boldsymbol{C}}}_e = \boldsymbol{U}_i^{-1}\dot{\boldsymbol{C}}\boldsymbol{U}_i^{-1} - \overbrace{\boldsymbol{U}_i^{-1}\boldsymbol{C}\boldsymbol{U}_i^{-1}}^{=\bar{\boldsymbol{C}}_e}\overbrace{\dot{\boldsymbol{U}}_i\boldsymbol{U}_i^{-1}}^{=:\bar{\boldsymbol{L}}_i} - \bar{\boldsymbol{L}}_i^T\bar{\boldsymbol{C}}_e \tag{6.19}$$

$$\dot{\boldsymbol{C}}_i = \dot{\boldsymbol{U}}_i\boldsymbol{U}_i + \boldsymbol{U}_i\dot{\boldsymbol{U}}_i = \bar{\boldsymbol{L}}_i\boldsymbol{C}_i + \boldsymbol{C}_i\bar{\boldsymbol{L}}_i^T = \boldsymbol{U}_i\left(\bar{\boldsymbol{L}}_i + \bar{\boldsymbol{L}}_i^T\right)\boldsymbol{U}_i \tag{6.20}$$

$$\dot{\bar{\boldsymbol{B}}}_{i_b} = -\boldsymbol{U}_i\boldsymbol{C}_{i_a}^{-1}\dot{\boldsymbol{C}}_{i_a}\boldsymbol{C}_{i_a}^{-1}\boldsymbol{U}_i + \bar{\boldsymbol{L}}_i\bar{\boldsymbol{B}}_{i_b} + \bar{\boldsymbol{B}}_{i_b}\bar{\boldsymbol{L}}_i^T \tag{6.21}$$

$$\dot{\bar{\boldsymbol{H}}} = \boldsymbol{U}_i\dot{\boldsymbol{H}}\boldsymbol{U}_i + \bar{\boldsymbol{L}}_i\bar{\boldsymbol{H}} + \bar{\boldsymbol{H}}\bar{\boldsymbol{L}}_i^T. \tag{6.22}$$

In the above equations, the relation $\dot{\boldsymbol{C}}_{i_a}^{-1} = -\boldsymbol{C}_{i_a}^{-1}\dot{\boldsymbol{C}}_{i_a}\boldsymbol{C}_{i_a}^{-1}$ was utilized. Moreover, all inelastic rotational parts, i.e. $\boldsymbol{R}_i$ and $\boldsymbol{R}_{i_a}$, remain undetermined, which is considered an advantage. Inserting the results for the different rates (6.19)-(6.22) into Equation (6.18), and following the procedure of Coleman and Noll [1961], the state law for the second Piola-Kirchhoff stress reads after rearranging

$$\boldsymbol{S} = 2\,\boldsymbol{U}_i^{-1}\frac{\partial \psi^*}{\partial \bar{\boldsymbol{C}}_e}\boldsymbol{U}_i^{-1}. \tag{6.23}$$

With this last equation at hand, the reduced dissipation inequality in terms of conjugated driving forces is obtained as

$$\begin{aligned}\mathscr{D}_{\text{red}} \coloneqq &\underbrace{\left(\overbrace{2\,\bar{\boldsymbol{C}}_e\frac{\partial \psi^*}{\partial \bar{\boldsymbol{C}}_e}}^{=:\bar{\boldsymbol{\Sigma}}} - \overbrace{2\,\frac{\partial \psi^*}{\partial \boldsymbol{C}_i}\boldsymbol{C}_i}^{=:\bar{\boldsymbol{X}}} - \overbrace{2\,\frac{\partial \psi^*}{\partial \bar{\boldsymbol{B}}_{i_b}}\bar{\boldsymbol{B}}_{i_b}}^{=:\bar{\boldsymbol{\chi}}} - \overbrace{2\,\frac{\partial \psi^*}{\partial \bar{\boldsymbol{H}}}\bar{\boldsymbol{H}}}^{=:\bar{\boldsymbol{\Upsilon}}}\right)}_{=:\bar{\boldsymbol{\Gamma}}} : \bar{\boldsymbol{L}}_i \\ &\underbrace{-\boldsymbol{U}_i\frac{\partial \psi^*}{\partial \bar{\boldsymbol{H}}}\boldsymbol{U}_i}_{=:\boldsymbol{G}} : \dot{\boldsymbol{H}} + \underbrace{\boldsymbol{C}_{i_a}^{-1}\boldsymbol{U}_i\frac{\partial \psi^*}{\partial \bar{\boldsymbol{B}}_{i_b}}\boldsymbol{U}_i\boldsymbol{C}_{i_a}^{-1}}_{=:\boldsymbol{\Theta}} : \dot{\boldsymbol{C}}_{i_a} \geq 0.\end{aligned} \tag{6.24}$$

where $\bar{\boldsymbol{X}}$ and $\bar{\boldsymbol{\chi}}$ are back-stress tensors. Although the stress-like tensors $\bar{\boldsymbol{\Sigma}}$, $\bar{\boldsymbol{X}}$, $\bar{\boldsymbol{\chi}}$ and $\bar{\boldsymbol{\Upsilon}}$ are not generally symmetric, it is interesting to note that $\bar{\boldsymbol{\Gamma}}$ is indeed symmetric (cf. Svendsen

[2001], Reese [2003]). The same holds for $\boldsymbol{G}$ and $\boldsymbol{\Theta}$. Thus, the last inequality reduces to

$$\mathscr{D}_{\mathrm{red}} \coloneqq \bar{\boldsymbol{\Gamma}} : \bar{\boldsymbol{D}}_i + \boldsymbol{G} : \dot{\boldsymbol{H}} + \boldsymbol{\Theta} : \dot{\boldsymbol{C}}_{i_a} \geq 0 \tag{6.25}$$

with $\bar{\boldsymbol{D}}_i \coloneqq \mathrm{sym}\left(\bar{\boldsymbol{L}}_i\right) = \frac{1}{2}\boldsymbol{U}_i^{-1}\dot{\boldsymbol{C}}_i\boldsymbol{U}_i^{-1}$. In addition, it is easy to show that all thermodynamic driving forces in Inequality (6.25) are the co-rotated expressions of their ic counterparts, e.g. $\bar{\boldsymbol{\Sigma}} = \boldsymbol{R}_i^{-1}\left(2\,\boldsymbol{C}_e\frac{\partial\psi}{\partial\boldsymbol{C}_e}\right)\boldsymbol{R}_i$ (cf. Appendix 6.8.1), such that their physical interpretation is the same[8]. It remains to choose sufficient onset criteria and potentials for the inelastic evolutions, typically in terms of their conjugated forces, to ensure the fulfillment of Inequality (6.25) for arbitrary processes. For instance, assuming a potential $g_i^*\left(\bar{\boldsymbol{\Gamma}}\right) = g_i^*\left(\breve{\boldsymbol{\Gamma}}\right)$ to be an *isotropic function* and following (non)-associative evolution laws, one obtains

$$\bar{\boldsymbol{D}}_i = \dot{\gamma}\,\frac{\partial g_i^*}{\partial\bar{\boldsymbol{\Gamma}}} = \dot{\gamma}\,\boldsymbol{R}_i^{-1}\frac{\partial g_i^*}{\partial\breve{\boldsymbol{\Gamma}}}\boldsymbol{R}_i \quad \rightarrow \quad \dot{\boldsymbol{C}}_i = 2\dot{\gamma}\,\boldsymbol{U}_i\,\frac{\partial g_i^*}{\partial\bar{\boldsymbol{\Gamma}}}\,\boldsymbol{U}_i \tag{6.26}$$

with $\dot{\gamma}$ denoting some rate quantity and the thermodynamic driving force $\breve{\boldsymbol{\Gamma}} = \boldsymbol{R}_i^{-1}\bar{\boldsymbol{\Gamma}}\boldsymbol{R}_i$ conjugated to $\mathrm{sym}\left(\boldsymbol{L}_i\right)$[9]. With these equations at hand, the set of constitutive equations is closed.

Summary of the cic framework. Contrary to the $pbic$ framework, the cic is uniquely defined. Further, $\boldsymbol{F}_i$ is required in the $pbic$ framework to compute quantities in the ic in their tensorial form. Within the cic framework, the latter is not the case. The fundamental idea is to pull-back all strain-like quantities in the ic by the rotation tensor $\boldsymbol{R}_i$. Thereby, it is observed that all thermodynamically conjugated driving forces are nothing but the co-rotated counterparts of the ic driving forces. Thus, a few subtle issues of the $pbic$ are overcome. In summary, it is appealing to recognize some of the cic advantages, namely:

- The framework is easily comprehensible, since all equations 'look' the same as in the $pbic$ framework.
- Due to the orthogonal pull-back, the physical interpretation between the $pbic$ and cic pairs remains the same, i.e. their invariants are equal, and further, properties such as symmetry are preserved.
- For example, yield criteria with a physical interpretation in the ic have the same interpretation in the cic. Only the ic quantities have to be 'interchanged' in the equations with their cic equivalents.

[8] They share the same eigenvalues, but their eigenvectors are rotated by $\boldsymbol{R}_i$.
[9] For $\dot{\boldsymbol{H}}$ and $\dot{\boldsymbol{C}}_{i_a}$ one may proceed similarly.

- In contrast to $pbic$ models, within the cic framework all strain- and stress-like quantities are uniquely defined.
- Thus, spectral decompositions of all quantities are possible.
- Moreover, all derivatives can be computationally obtained. For example, $\frac{\partial \psi}{\partial \boldsymbol{C}_e}$ depends on $\boldsymbol{C}_e$. Thus, the derivative could theoretically be written down, but in general it cannot be computed numerically as $\boldsymbol{C}_e$ is not known (cf. Equation (6.5), Remark 16 and Appendix 6.8.1). In contrast, since $\bar{\boldsymbol{C}}_e$ is known, $\frac{\partial \psi}{\partial \bar{\boldsymbol{C}}_e}$ is unique and can be calculated.
- The latter makes the whole framework very attractive in context of AD. In simple terms, the cic framework allows equations derived on a sheet of paper to be implemented directly into the AD tool. In particular, the derivatives required to develop a constitutive framework for inelastic materials can all be determined using AD.

Overall, these advantages enable the development of highly complex material models, which usually involve challenging derivatives and error-prone numerical implementations. In this regard, the following sections address a novel biomechanical material model based on the proposed framework, which is implemented into an AD software.

Remark 17. *For instance, Vladimirov et al. [2008] and Brepols et al. [2020] express the dissipation resulting from the additional split of* $\boldsymbol{F}_i$ *in terms of* $\boldsymbol{D}_{i_a} \coloneqq \operatorname{sym}\left(\dot{\boldsymbol{F}}_{i_a}\boldsymbol{F}_{i_a}^{-1}\right)$. *Since* $\boldsymbol{F}_{i_a}$ *possesses its polar decomposition, one might rewrite the last term in Inequality* (6.25) *as* $2\,\boldsymbol{U}_{i_a}\boldsymbol{\Theta}\boldsymbol{U}_{i_a} : \check{\boldsymbol{D}}_{i_a}$ *with* $\check{\boldsymbol{D}}_{i_a} \coloneqq \operatorname{sym}\left(\dot{\boldsymbol{U}}_{i_a}\boldsymbol{U}_{i_a}^{-1}\right) = \boldsymbol{R}_{i_a}^{-1}\boldsymbol{D}_{i_a}\boldsymbol{R}_{i_a} = \frac{1}{2}\boldsymbol{U}_{i_a}^{-1}\dot{\boldsymbol{C}}_{i_a}\boldsymbol{U}_{i_a}^{-1}$. *Thus, the driving force* $\check{\boldsymbol{\Theta}} \coloneqq 2\,\boldsymbol{U}_{i_a}\boldsymbol{\Theta}\boldsymbol{U}_{i_a}$ *can be seen as the 'additional' co-rotated counterpart to the driving force in the mentioned works.*

Remark 18. *The interested reader may find the essential equations to derive an elasto-plasticity model and a visco-elasticity model taken from the literature in the context of the* cic *framework in Appendix 6.8.5.*

6.4 Constitutive modeling of soft biological tissues

First, it is assumed that a change in mass of the system takes place on a much longer time scale than the change in shape, a common assumption which is referred to as the *slow-growth assumption* (see e.g. Goriely [2017]). Thus, the balance of mass is implicitly satisfied, while the balance of linear momentum can be reduced to the quasi-static case. Consequently, any mass production or flux is neglected. Moreover, in the context of growth and remodeling at

finite strains, the multiplicative decomposition (6.1) into elastic $\boldsymbol{F}_e$ and growth-remodeling $\boldsymbol{F}_g$ related parts is well-known (Rodriguez et al. [1994]) and was widely used in the past by several authors (see e.g. Garikipati et al. [2004], Ambrosi and Guana [2007], Grytsan et al. [2017], Braeu et al. [2017], Truster and Masud [2017]). For instance, the (active) addition or removal of mass can cause the stress state of the material to be different compared to its referential stress state. This kind of deformation associated with the stress state is characterized by the growth-remodeling related part of $\boldsymbol{F}$. The elastic part ensures compatibility with the total deformation field. Thus, if a volume element is cut out of the body, its deformation is completely characterized by $\boldsymbol{F}_g$. A more detailed explanation can be found in the just mentioned literature.

Since soft biological tissues are considered in a phenomenological and smeared sense within this contribution, two decompositions of the deformation gradient are employed, the first summarizing mostly direction-independent constituents (e.g. elastin, smooth muscle cells etc.), which will collectively be referred to as 'matrix' (m), and the second accounting for strongly direction-dependent constituents (mainly collagen co), i.e.

$$\boldsymbol{F} = \boldsymbol{F}_{e_m}\boldsymbol{F}_{g_m} = \boldsymbol{F}_{e_{co}}\boldsymbol{F}_{g_{co}}. \tag{6.27}$$

Obviously, this choice is mainly influenced by the effects of the individual constituents on the overall mechanical behavior and does not resolve the individual constituents in detail. However, this is sufficient for the present stage of model development and can be easily extended in future work. An additional decomposition of the inelastic parts, as for example used by Braeu et al. [2017] to decouple growth and remodeling, is not taken into account here, but could be easily implemented (cf. Equation (6.8)).

6.4.1 Helmholtz free energy

For the subsequent derivation of the material model, the following dependency of the *scalar-valued isotropic* Helmholtz free energy *function* is assumed, and additionally, a widely used *rule of mixtures* approach into 'matrix' and collagen parts is applied

$$\psi = \psi_m\left(\bar{\boldsymbol{C}}_{e_m}\right) + \psi_{co}\left(\bar{\boldsymbol{C}}_{e_{co}}, \bar{\boldsymbol{M}}\right) \tag{6.28}$$

with $\bar{\boldsymbol{C}}_{e_m} \coloneqq \boldsymbol{U}_{g_m}^{-1}\boldsymbol{C}\boldsymbol{U}_{g_m}^{-1}$ and $\bar{\boldsymbol{C}}_{e_{co}} \coloneqq \boldsymbol{U}_{g_{co}}^{-1}\boldsymbol{C}\boldsymbol{U}_{g_{co}}^{-1}$. Here, ψ_m represents the elastic stored energy within the 'matrix', while ψ_{co} accounts for the collagen fibers' energy contribution. For the time being, no further energy contribution directly counteracting growth processes is

assumed, as for instance done by Braeu et al. [2019] and Lamm et al. [2022]. However, this might be incorporated by assuming an energy depending also on $\boldsymbol{C}_{g_m}$ and/or $\boldsymbol{C}_{g_{co}}$, respectively. Noteworthy, no further assumptions on the energy itself are made. Thus, the model presented hereafter is derived in a quite general manner. Further, the structural tensor $\boldsymbol{M} \equiv \boldsymbol{H}$ takes the fiber orientation of collagen fibers into account and is specified as[10]

$$\boldsymbol{M} = \boldsymbol{n} \otimes \boldsymbol{n} \tag{6.29}$$

where $\boldsymbol{n}$ is the normalized structural vector in the rc. This vector is parallel to the averaged main direction of collagen in the referential configuration. In line with Reese [2003] and the previous section, the tensor is mapped to the cic via

$$\bar{\boldsymbol{M}} = \frac{\boldsymbol{U}_{g_{co}}\boldsymbol{n}}{\mid \boldsymbol{U}_{g_{co}}\boldsymbol{n} \mid} \otimes \frac{\boldsymbol{U}_{g_{co}}\boldsymbol{n}}{\mid \boldsymbol{U}_{g_{co}}\boldsymbol{n} \mid} = \frac{1}{\boldsymbol{C}_{g_{co}} : \boldsymbol{M}}\, \boldsymbol{U}_{g_{co}}\boldsymbol{M}\boldsymbol{U}_{g_{co}} \tag{6.30}$$

while its cc counterpart is defined analogously

$$\boldsymbol{M}_{cc} = \frac{1}{\boldsymbol{C} : \boldsymbol{M}}\boldsymbol{F}\boldsymbol{M}\boldsymbol{F}^T = \frac{1}{\bar{\boldsymbol{C}}_{e_{co}} : \bar{\boldsymbol{M}}}\boldsymbol{F}_{e_{co}}\boldsymbol{R}_{g_{co}}\bar{\boldsymbol{M}}\boldsymbol{R}^T_{g_{co}}\boldsymbol{F}^T_{e_{co}} = \boldsymbol{n}_{cc} \otimes \boldsymbol{n}_{cc} \tag{6.31}$$

and describes the fiber orientation with respect to the cc. For completeness, the ic structural tensor can be obtained by

$$\breve{\boldsymbol{M}} = \frac{\boldsymbol{F}_{g_{co}}\boldsymbol{n}}{\mid \boldsymbol{F}_{g_{co}}\boldsymbol{n} \mid} \otimes \frac{\boldsymbol{F}_{g_{co}}\boldsymbol{n}}{\mid \boldsymbol{F}_{g_{co}}\boldsymbol{n} \mid} = \boldsymbol{R}_{g_{co}}\bar{\boldsymbol{M}}\boldsymbol{R}^T_{g_{co}}. \tag{6.32}$$

Note that the traces of all structural tensors are equal to one.

6.4.2 Derivation based on the isothermal Clausius-Duhem inequality for open systems

In contrast to most materials, biological tissues can not be seen as a ‘closed’ system, since they constantly interact with their surroundings. For instance, growth and remodeling imply the inflow of e.g. nutritions and hormones. However, the scope of this contribution is stress-driven remodeling rather than the additional field equations describing diffusion processes. Thus, and in accordance with Kuhl and Steinmann [2003a], the isothermal Clausius-Duhem inequality

[10] The recent work of Bauer and Böhlke [2022] discusses the usage of a fourth order tensor to account for fiber orientations.

for open systems is employed

$$-\dot{\psi}+\frac{1}{2}\boldsymbol{S}:\dot{\boldsymbol{C}}+\mathcal{S}_0\geq 0 \tag{6.33}$$

where $\mathcal{S}_0$ summarizes both the contribution of entropy flux and entropy source, which can be understood as the exchange or interaction with the 'outside world' (e.g. human body)[11]. Following the derivation from the previous section, the state law is obtained as

$$\boldsymbol{S}=2\left(\boldsymbol{U}_{g_m}^{-1}\frac{\partial\psi}{\partial\bar{\boldsymbol{C}}_{e_m}}\boldsymbol{U}_{g_m}^{-1}+\boldsymbol{U}_{g_{co}}^{-1}\frac{\partial\psi}{\partial\bar{\boldsymbol{C}}_{e_{co}}}\boldsymbol{U}_{g_{co}}^{-1}\right). \tag{6.34}$$

The framework of Section 6.3 applied to Equation (6.28) leads under consideration of Equation (6.34) to the following reduced dissipation inequality

$$\mathscr{D}_{\mathrm{red}}\coloneqq\underbrace{\bar{\boldsymbol{\Sigma}}_m}_{=:\bar{\boldsymbol{\Gamma}}_m}:\bar{\boldsymbol{D}}_{g_m}+\underbrace{\left(\bar{\boldsymbol{\Sigma}}_{co}-\bar{\boldsymbol{\Upsilon}}_{co}+\bar{\boldsymbol{\Pi}}_{co}\right)}_{=:\bar{\boldsymbol{\Gamma}}_{co}}:\bar{\boldsymbol{D}}_{g_{co}}+\boldsymbol{G}_{co}:\dot{\boldsymbol{M}}+\mathcal{S}_0\geq 0. \tag{6.35}$$

where $\bar{\boldsymbol{\Sigma}}_j\coloneqq 2\,\bar{\boldsymbol{C}}_{e_j}\frac{\partial\psi}{\partial\bar{\boldsymbol{C}}_{e_j}}$ and $\bar{\boldsymbol{D}}_{g_j}\coloneqq\operatorname{sym}\left(\dot{\boldsymbol{U}}_{g_j}\boldsymbol{U}_{g_j}^{-1}\right)$ with $j\in\{m,co\}$, $\bar{\boldsymbol{\Upsilon}}_{co}\coloneqq 2\frac{\partial\psi}{\partial\bar{\boldsymbol{M}}}\bar{\boldsymbol{M}}$ as well as $\bar{\boldsymbol{\Pi}}_{co}\coloneqq 2\frac{\partial\psi}{\partial\bar{\boldsymbol{M}}}:\left(\bar{\boldsymbol{M}}\otimes\bar{\boldsymbol{M}}\right)$. Furthermore, the driving force $\boldsymbol{G}_{co}\coloneqq\frac{1}{\boldsymbol{C}_g:\boldsymbol{M}}\left(-\boldsymbol{U}_g\frac{\partial\psi}{\partial\bar{\boldsymbol{M}}}\boldsymbol{U}_g+\frac{\partial\psi}{\partial\bar{\boldsymbol{M}}}:\left(\bar{\boldsymbol{M}}\otimes\boldsymbol{C}_g\right)\right)$ is introduced. Comparing the expressions for the driving forces in Equation (6.35) with (6.24), one notices some additional terms in $\bar{\boldsymbol{\Gamma}}_{co}$ and $\boldsymbol{G}_{co}$. These result from the rate of $\bar{\boldsymbol{M}}$ (cf. Appendix 6.8.6). Nevertheless, both $\bar{\boldsymbol{\Gamma}}_{co}$ and $\boldsymbol{G}_{co}$ are still symmetric.

6.4.3 Evolution equations based on homeostatic surfaces

In order to close the set of constitutive equations, it remains to choose appropriate evolution equations for $\bar{\boldsymbol{D}}_{g_m}$ as well as $\bar{\boldsymbol{D}}_{g_{co}}$. For this purpose, homeostatic surfaces Φ_i as proposed by Lamm et al. [2022] are utilized, describing the preferred (homeostatic) stress to be reached within the entire tissue. These surfaces can be interpreted similar to plastic yield criteria, i.e. they define a surface in the principal stress space. However, contrary to plasticity, these surfaces do not distinguish the purely elastic and elasto-plastic regime, rather the tissue growths and remodels until the stress state lies on this particular surface. Slightly more mathematically spoken, this means that both $\Phi_i<0$ and $\Phi_i>0$ are possible, but $\Phi_i\to 0$ is reached after a finite amount of time. In order to account for the time dependency, visco-plastic concepts are employed.

[11] Note that $\mathcal{S}_0$ is introduced for mathematical convenience, however, it is never computed here.

In the present contribution, two different approaches are pursued, viz.

- One-surface approach: A single homeostatic surface based on the total stress, i.e. the sum of all constituents, is introduced (Section 6.4.3.1).
- Two-surface approach: Two different surfaces are used to account for different preferred stresses of both constituents (Section 6.4.3.2).

While the latter approach is more flexible and takes into account that not all constituents of the tissue may share the same material properties, i.e. they try to reach different homeostatic stresses, the former is advantageous when considering the experimental determination of the homeostatic surface, since only the tissue's overall behavior must be measured. Since two-surface approaches are frequently used today, e.g. in coupled damage-plasticity models (see e.g. Kiefer et al. [2012], Brepols et al. [2017]), a variety of insights into their efficient implementation can be found in the literature.
The evolution equations are defined in either an associative manner based on the surface or a non-associative manner derived from a growth potential. Noteworthy, the latter equips the model with greater flexibility in general. Besides, fiber remodeling of collagen fibers is modeled based on the total stress within the tissue (Section 6.4.3.3) and is the same for both the 'one-surface' and 'two-surface' approach.

6.4.3.1 Model I: 'One-surface' approach

For the definition of the 'one-surface' approach, the most reasonable stress measure to express the homeostatic surface Φ_g and growth potential g_g is the Cauchy stress tensor $\boldsymbol{\sigma} = \frac{1}{J}\boldsymbol{\tau} = \frac{1}{J}\boldsymbol{F}\boldsymbol{S}\boldsymbol{F}^T$ with J denoting the deformation gradient's determinant. In order to derive the evolution equations, $\boldsymbol{\sigma}$ has to be related to the thermodynamic driving forces $\bar{\boldsymbol{\Gamma}}_m$ and $\bar{\boldsymbol{\Gamma}}_{co}$. Therefore, considering Equation (6.34), the following relations can be found

$$\boldsymbol{S} = \boldsymbol{C}^{-1}\left(\boldsymbol{U}_{g_m}\bar{\boldsymbol{\Sigma}}_m\boldsymbol{U}_{g_m}^{-1} + \boldsymbol{U}_{g_{co}}\bar{\boldsymbol{\Sigma}}_{co}\boldsymbol{U}_{g_{co}}^{-1}\right) \tag{6.36}$$

$$\boldsymbol{\tau} = \boldsymbol{F}^{-T}\left(\boldsymbol{U}_{g_m}\bar{\boldsymbol{\Sigma}}_m\boldsymbol{U}_{g_m}^{-1} + \boldsymbol{U}_{g_{co}}\bar{\boldsymbol{\Sigma}}_{co}\boldsymbol{U}_{g_{co}}^{-1}\right)\boldsymbol{F}^{T}. \tag{6.37}$$

Although these relations are sufficient for the formulation of homeostatic surfaces, it is important for the next steps to keep in mind that AD utilizes the chain rule to derive derivatives. In the case that the homeostatic surface is expressed in terms of the eigenvalues σ_i of $\boldsymbol{\sigma}$, e.g. using a Rankine-type surface, i.e. $\Phi_g = \max\left(\sigma_i, \sigma_{\text{hom}}\right) - \sigma_{\text{hom}}$ with homeostatic stress σ_{hom} (cf. Soleimani et al. [2020]), not only the invariants of $\boldsymbol{\sigma}$ are required, but also the tensor itself

to compute $\frac{\partial \sigma_i}{\partial \boldsymbol{\sigma}}$[12]. Since the proposed framework is expressed with respect to the cic and later fully implemented with respect to the rc, no dependence on $\boldsymbol{F}$ is desired, which is needed to compute $\boldsymbol{\sigma}$[13].

Therefore, the so-called co-rotated Kirchhoff stress $\tilde{\boldsymbol{\tau}} = \boldsymbol{R}^{-1}\boldsymbol{\tau}\boldsymbol{R} = \boldsymbol{U}\boldsymbol{S}\boldsymbol{U}$ defined with respect to the crc (see Figure 6.1) is introduced[14], being symmetric and sharing the same eigenvalues with the Kirchhoff stress[15]. Inserting the latter into Equation (6.37), the following is obtained

$$\tilde{\boldsymbol{\tau}} = \boldsymbol{U}\boldsymbol{S}\boldsymbol{U} = \boldsymbol{U}^{-1} \underbrace{\left(\boldsymbol{U}_{g_m}\bar{\boldsymbol{\Sigma}}_m\boldsymbol{U}_{g_m}^{-1} + \boldsymbol{U}_{g_{co}}\bar{\boldsymbol{\Sigma}}_{co}\boldsymbol{U}_{g_{co}}^{-1}\right)}_{=:\boldsymbol{Y}_g} \boldsymbol{U} \tag{6.38}$$

where $\boldsymbol{Y}_g$ is generally non-symmetric, but shares the same eigenvalues with $\boldsymbol{\tau}$. Hence, it is suitable to define a homeostatic surface as a *scalar-valued isotropic function* in the following manner

$$\Phi_g \coloneqq \Phi_g^*\left(\boldsymbol{\sigma}\right) = \Phi_g^*\left(\frac{1}{J}\boldsymbol{\tau}\right) = \Phi_g^*\left(\frac{1}{J}\tilde{\boldsymbol{\tau}}\right) = \Phi_g^*\left(\frac{1}{J}\boldsymbol{Y}_g\right). \tag{6.39}$$

In contrast to Lamm et al. [2022], the homeostatic surface in this contribution is described by a smoothed Rankine-like surface that intersects with the principal stress axes only in the positive regime and, moreover, is not defined within the eighth octant[16] to account for the *hypothesis of tensile homeostasis*. This hypothesis represents a fundamental difference of living tissue from classical materials, since a preferred state of stress rather than a stress-free state is desired (cf. e.g. Cyron and Aydin [2017] and Eichinger, Haeusel, Paukner, Aydin, Humphrey and Cyron [2021]). The corresponding homeostatic surface reads

$$\Phi_g \coloneqq \begin{cases} \frac{2}{J}\mathrm{tr}\left(\boldsymbol{Y}_g\right) - 2\,\sigma_g & , \frac{1}{J^2}\mathrm{tr}\left(\boldsymbol{Y}_g^2\right) + \beta_g = 0 \\ \frac{1}{J}\mathrm{tr}\left(\boldsymbol{Y}_g\right) + \sqrt{\frac{1}{J^2}\mathrm{tr}\left(\boldsymbol{Y}_g^2\right) + \beta_g} - 2\,\sigma_g & , \text{else} \end{cases} \tag{6.40}$$

where the surface described by the second case is illustrated in Figure 6.2. The case differentiation is mainly done for numerical reasons to ensure a well-defined evolution for all possible stress states, since the term under the square root may tend towards zero. As a consequence, the growth and remodeling direction (cf. Equation (6.41)) would tend towards infinity.

For simplicity, but without loss of generality, an associative evolution equation is chosen, i.e.

[12] As will be seen in Section 6.4.3.3, also the eigenvector $\boldsymbol{n}_{\boldsymbol{\sigma}_i}$ of $\boldsymbol{\sigma}$, and thus, also the derivative $\frac{\partial \boldsymbol{n}_{\boldsymbol{\sigma}_i}}{\partial \boldsymbol{\sigma}}$ is required.

[13] Moreover, the material sensitivity $2\,\frac{\partial \boldsymbol{S}}{\partial \boldsymbol{C}}$ can not be calculated, since the mapping between $\boldsymbol{C}$ and $\boldsymbol{F}$ is surjective. Thus, $\frac{\partial \boldsymbol{F}}{\partial \boldsymbol{C}}$ can not be obtained in general.

[14] $\boldsymbol{F} = \boldsymbol{R}\boldsymbol{U}$ with $\boldsymbol{R} \in \mathrm{SO}(3)$.

[15] The co-rotated Kirchhoff stress also plays an important role for the fiber reorientation in Section 6.4.3.3. Further, $\frac{\partial \boldsymbol{U}}{\partial \boldsymbol{C}}$ is unique.

[16] $\sigma_1, \sigma_2, \sigma_3 \leq 0$ with σ_i denoting the Cauchy stress tensor's eigenvalues.

$g_g = \Phi_g + 2\sigma_g$. Hence, the growth and remodeling direction for both constituents is derived from this potential by[17]

$$\boldsymbol{N}_{g_m} := \frac{\partial g_g}{\partial \bar{\boldsymbol{\Gamma}}_m} = \mathrm{sym}\left(\frac{\partial g_g}{\partial \bar{\boldsymbol{\Sigma}}_m}\right) \equiv \frac{\partial g_g}{\partial \bar{\boldsymbol{\Sigma}}_m}, \quad \boldsymbol{N}_{g_{co}} := \frac{\partial g_g}{\partial \bar{\boldsymbol{\Gamma}}_{co}} = \mathrm{sym}\left(\frac{\partial g_g}{\partial \bar{\boldsymbol{\Sigma}}_{co}}\right). \tag{6.41}$$

With the latter equations at hand, the normalized evolution equations are obtained as

$$\bar{\boldsymbol{D}}_{g_m} = \dot{\gamma}_g \frac{\boldsymbol{N}_{g_m}}{\|\boldsymbol{N}_{g_m}\|}, \quad \bar{\boldsymbol{D}}_{g_{co}} = \dot{\gamma}_g \frac{\boldsymbol{N}_{g_{co}}}{\|\boldsymbol{N}_{g_{co}}\|} \tag{6.42}$$

with the growth multiplier $\dot{\gamma}_g$. Due to the normalization, the multiplier is ensured to be a rate quantity, independent of the specific potential. Note that the evolution equations can be pulled-back to the rc in line with Equation (6.26). Furthermore, as mentioned above, the growth and remodeling evolution is accomplished using visco-plastic concepts. Here, the approach of Perzyna [1966, 1971] is adopted, such that the rate of growth and remodeling depends on the over- and under-stress from the homeostatic surface and tends to zero as the state of homeostasis is reached

$$\dot{\gamma}_g = \frac{1}{\eta_g}\left(\frac{\Phi_g}{2\sigma_g}\right)^{\frac{1}{\nu_g}}. \tag{6.43}$$

In the latter equation, η_g is the 'growth and remodeling' time, while ν_g describes the degree of non-linearity. To be capable to capture the limit of rate independent growth and for numerical stability reasons, Equation (6.43) is reformulated (cf. de Souza Neto et al. [2011])

$$\Phi_g - 2\sigma_g \left(\eta_g \dot{\gamma}_g\right)^{\nu_g} = 0. \tag{6.44}$$

6.4.3.2 Model II: 'Two-surface' approach

As already mentioned, the 'one-surface' approach is easier to be experimentally determined. However, the accuracy to model the complex behavior of soft tissues might not be sufficient. Hence, a 'two-surface' model is introduced in the following. To this end, it is important to note that the overall Kirchhoff stress $\boldsymbol{\tau}$ is the sum of both the 'matrix-Kirchhoff stress' $\boldsymbol{\tau}_m := 2\boldsymbol{F}_{e_m}\frac{\partial \psi}{\partial \boldsymbol{C}_{e_m}}\boldsymbol{F}_{e_m}^T$ and 'collagen-Kirchhoff stress' $\boldsymbol{\tau}_{co} := 2\boldsymbol{F}_{e_{co}}\frac{\partial \psi}{\partial \boldsymbol{C}_{e_{co}}}\boldsymbol{F}_{e_{co}}^T$, whereby the eigenvalues of $\bar{\boldsymbol{\Gamma}}_m$ are the same as the ones of $\boldsymbol{\tau}_m$. In addition, as shown by Reese [2003], the

[17] $\bar{\boldsymbol{\Sigma}}_m \equiv \bar{\boldsymbol{\Gamma}}_m, \bar{\boldsymbol{\Gamma}}_m = \bar{\boldsymbol{\Gamma}}_m^T, \bar{\boldsymbol{\Sigma}}_{co} = \bar{\boldsymbol{\Gamma}}_{co} + \bar{\boldsymbol{\Upsilon}}_{co} - \bar{\boldsymbol{\Pi}}_{co}, \bar{\boldsymbol{\Gamma}}_{co} = \bar{\boldsymbol{\Gamma}}_{co}^T$

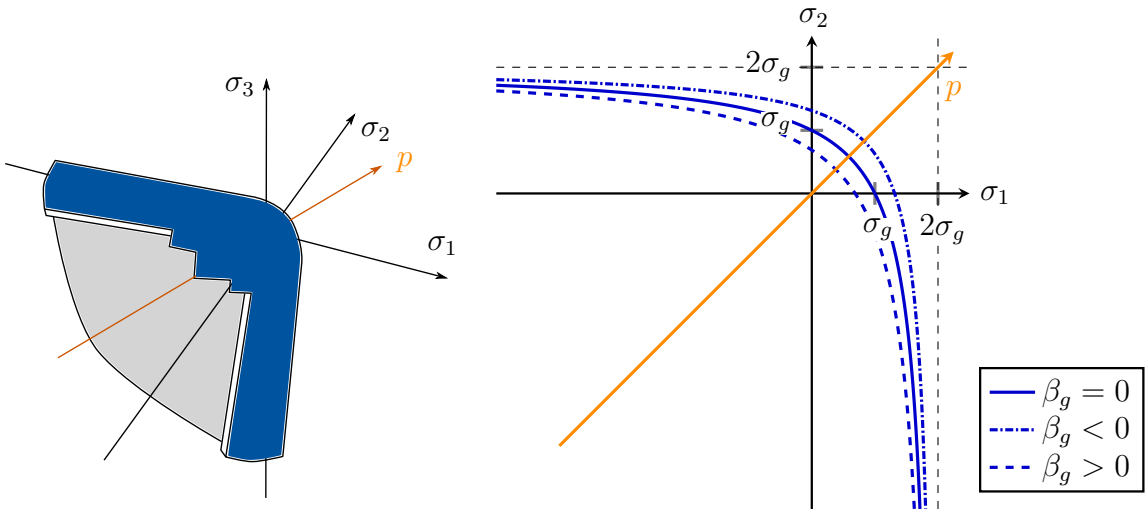

(a) Perspective view

(b) Intersection with $\sigma_3 = 0$ plane

Figure 6.2: Rankine-like homeostatic surface defined with respect to the eigenvalues σ_i of the Cauchy stress tensor. The hydrostatic axis is denoted by p. The surface's intersection with the principal axes for $\beta_g = 0$ is defined by the stress-like material parameter σ_g, while β_g describes the distance to the apex.

following relation holds true

$$\boldsymbol{\tau}_{co} : \boldsymbol{M}_{cc} = \frac{1}{\boldsymbol{C}_{e_{co}} : \breve{\boldsymbol{M}}} \boldsymbol{\Gamma}_{co} : \operatorname{sym}\left(\boldsymbol{C}_{e_{co}} \breve{\boldsymbol{M}}\right) \tag{6.45}$$

which describes the 'collagen-Kirchhoff stress' in fiber direction with respect to the cc. Hence, it is straightforward to prove that

$$\boldsymbol{\tau}_{co} : \boldsymbol{M}_{cc} = \frac{1}{\boldsymbol{C}_{e_{co}} : \breve{\boldsymbol{M}}} \boldsymbol{\Gamma}_{co} : \operatorname{sym}\left(\boldsymbol{C}_{e_{co}} \breve{\boldsymbol{M}}\right) = \frac{1}{\bar{\boldsymbol{C}}_{e_{co}} : \bar{\boldsymbol{M}}} \bar{\boldsymbol{\Gamma}}_{co} : \operatorname{sym}\left(\bar{\boldsymbol{C}}_{e_{co}} \bar{\boldsymbol{M}}\right) \tag{6.46}$$

holds also true. With these preliminaries at hand, the following homeostatic surfaces per constituent are defined as

$$\Phi_m := \begin{cases} \frac{2}{J}\operatorname{tr}\left(\bar{\boldsymbol{\Gamma}}_m\right) - 2\,\sigma_m & , \frac{1}{J^2}\operatorname{tr}\left(\bar{\boldsymbol{\Gamma}}_m^2\right) + \beta_m = 0 \\ \frac{1}{J}\operatorname{tr}\left(\bar{\boldsymbol{\Gamma}}_m\right) + \sqrt{\frac{1}{J^2}\operatorname{tr}\left(\bar{\boldsymbol{\Gamma}}_m^2\right) + \beta_m} - 2\,\sigma_m & , \text{else} \end{cases} \tag{6.47}$$

$$\Phi_{co} := \frac{1}{J}\frac{1}{\bar{\boldsymbol{C}}_{e_{co}} : \bar{\boldsymbol{M}}} \bar{\boldsymbol{\Gamma}}_{co} : \operatorname{sym}\left(\bar{\boldsymbol{C}}_{e_{co}} \bar{\boldsymbol{M}}\right) - \sigma_{co} \tag{6.48}$$

where Φ_m is chosen in analogy to Φ_g (6.40), but refers only to the 'matrix' part. Both Φ_m and Φ_{co} are described by individual preferred stresses σ_m and σ_{co}, and further, are scaled by J in

order to be defined in Cauchy's principal stress space. The following steps are quite similar to the previous section, i.e.

$$\boldsymbol{N}_{g_m} \coloneqq \frac{\partial g_m}{\partial \bar{\boldsymbol{\Gamma}}_m} = \operatorname{sym}\left(\frac{\partial g_m}{\partial \bar{\boldsymbol{\Sigma}}_m}\right) \equiv \frac{\partial g_g}{\partial \bar{\boldsymbol{\Sigma}}_m}, \quad \boldsymbol{N}_{g_{co}} \coloneqq \frac{\partial g_{co}}{\partial \bar{\boldsymbol{\Gamma}}_{co}} = \operatorname{sym}\left(\frac{\partial g_{co}}{\partial \bar{\boldsymbol{\Sigma}}_{co}}\right) \tag{6.49}$$

with $g_m = \Phi_m + 2\sigma_m$ and $g_{co} = \Phi_{co} + \sigma_{co}$. Consequently, the evolution equations read as follows

$$\bar{\boldsymbol{D}}_{g_m} = \dot{\gamma}_m \frac{\boldsymbol{N}_{g_m}}{\|\boldsymbol{N}_{g_m}\|}, \quad \bar{\boldsymbol{D}}_{g_{co}} = \dot{\gamma}_{co} \frac{\boldsymbol{N}_{g_{co}}}{\|\boldsymbol{N}_{g_{co}}\|} \tag{6.50}$$

with individual growth multipliers $\dot{\gamma}_m$ and $\dot{\gamma}_{co}$ per constituent. Lastly, in analogy to Equation (6.43), the following is stated

$$\dot{\gamma}_m = \frac{1}{\eta_m}\left(\frac{\Phi_m}{2\sigma_m}\right)^{\frac{1}{\nu_m}}, \quad \dot{\gamma}_{co} = \frac{1}{\eta_{co}}\left(\frac{\Phi_{co}}{\sigma_{co}}\right)^{\frac{1}{\nu_{co}}} \tag{6.51}$$

both of which are similarly rewritten as Equation (6.44) for reasons like those mentioned in Section 6.4.3.1.

6.4.3.3 Fiber reorientation

In contrast to most 'standard' transversely isotropic materials, collagen fibers within soft tissues are able to be remodeled by the cells, in order to optimally carry mechanical loading. Due to this remodeling, which will be called reorientation hereafter to distinguish it from remodeling processes described above, soft tissues can adapt their mechanical resistance to varying loading scenarios. In the literature, two different approaches are widely used, namely either a strain- or stress-driven approach. The latter is followed by, for instance, Hariton et al. [2007*a*] and Zahn and Balzani [2017], and will also be utilized within this contribution. As a stress-driven approach, the only physically meaningful stress measure to describe this particular phenomenon is again the Cauchy stress, where an optimal state is reached when $\boldsymbol{M}_{cc}$ (6.31) and $\boldsymbol{\sigma}$ are coaxial. In line with this kind of approach, an evolution equation for $\boldsymbol{n}_{cc}$ (cf. Equation (6.31)) should tend towards zero the more $\boldsymbol{n}_{cc}$ becomes collinear with some target vector $\boldsymbol{n}_{\text{target}}$, which is usually chosen as one of the eigenvectors of $\boldsymbol{\sigma}$. However, considering an evolution equation for $\boldsymbol{n}_{cc}$, one has to deal with objective rates, which is not desired. To avoid this issue, one can pull $\boldsymbol{n}_{\text{target}}$ back to the rc by means of $\boldsymbol{F}^{-1}$, which is similar to the approach of Zahn and Balzani [2018]. Nevertheless, as already mentioned in Section 6.4.3.1, this would then generally require the derivative $\frac{\partial \boldsymbol{n}_{\text{target}}}{\partial \boldsymbol{\sigma}}$, which is not desired as the formulation

should be independent of $\boldsymbol{F}$[18]. Thus, the evolution equation is prescribed with respect to the crc and the following auxiliary vector is introduced

$$\tilde{\boldsymbol{n}} = \frac{1}{\sqrt{\boldsymbol{n}\cdot\boldsymbol{C}\cdot\boldsymbol{n}}}\,\boldsymbol{U}\boldsymbol{n} \quad \rightarrow \quad \boldsymbol{n} = \frac{1}{\sqrt{\tilde{\boldsymbol{n}}\cdot\boldsymbol{C}^{-1}\cdot\tilde{\boldsymbol{n}}}}\,\boldsymbol{U}^{-1}\tilde{\boldsymbol{n}} \tag{6.52}$$

with respect to the crc and $\tilde{\boldsymbol{n}}\cdot\tilde{\boldsymbol{n}} = 1$. It is also worth mentioning that $\tilde{\boldsymbol{n}}$ and $\tilde{\boldsymbol{M}} \coloneqq \tilde{\boldsymbol{n}}\otimes\tilde{\boldsymbol{n}}$ are related to the cc as follows

$$\boldsymbol{n}_{cc} = \boldsymbol{R}\,\tilde{\boldsymbol{n}}, \quad \boldsymbol{M}_{cc} = \boldsymbol{R}\,\tilde{\boldsymbol{M}}\,\boldsymbol{R}^{-1}. \tag{6.53}$$

Consequently, the structural tensor $\boldsymbol{M}$ in the rc can be calculated according to

$$\boldsymbol{M} = \frac{1}{\boldsymbol{C}^{-1}:\tilde{\boldsymbol{M}}}\,\boldsymbol{U}^{-1}\tilde{\boldsymbol{M}}\boldsymbol{U}^{-1}. \tag{6.54}$$

In line with the approach suggested by Menzel [2005], which is adopted by e.g. Kuhl et al. [2005] and Himpel et al. [2008], the following evolution of $\tilde{\boldsymbol{n}}$ is assumed

$$\dot{\tilde{\boldsymbol{n}}} = \underbrace{\frac{\pi}{2\eta_s}\,(\tilde{\boldsymbol{n}}\times\tilde{\boldsymbol{n}}_{\text{target}})}_{=:\tilde{\boldsymbol{\omega}}}\times\tilde{\boldsymbol{n}} \tag{6.55}$$

such that the rate decreases as the angle $\sphericalangle\,(\tilde{\boldsymbol{n}},\tilde{\boldsymbol{n}}_{\text{target}})$ becomes smaller ($\boldsymbol{n}_{\text{target}} = \boldsymbol{R}\,\tilde{\boldsymbol{n}}_{\text{target}}$). The parameter η_s can be considered as the remodeling time of fiber reorientation. Note that this particular evolution equation was originally introduced in the context of a strain-driven approach, but can also be used for a stress-driven approach. Additionally, the latter equation can be reformulated

$$\dot{\tilde{\boldsymbol{n}}} = \tilde{\boldsymbol{\Omega}}\,\tilde{\boldsymbol{n}} \tag{6.56}$$

with $\tilde{\boldsymbol{\Omega}} = \sum_{i=1}^{3}(\tilde{\boldsymbol{\omega}}\times\boldsymbol{e}_i)\otimes\boldsymbol{e}_i$ being skew-symmetric, and thus, fulfilling the orthogonality condition $\dot{\tilde{\boldsymbol{n}}}\cdot\tilde{\boldsymbol{n}} = 0$.

So far, $\boldsymbol{n}_{\text{target}}$ is not further specified, except that Cauchy's eigenvectors are most reasonable when expressing the evolution with respect to the cc. Since $\boldsymbol{\sigma}$ and $\boldsymbol{\tau}$ share the same eigenvectors, one may also go for the latter one. In this regard, the spectral decompositions

$$\boldsymbol{\tau} = \sum_{i=1}^{3}\tau_i\,\boldsymbol{n}_{\boldsymbol{\tau}_i}\otimes\boldsymbol{n}_{\boldsymbol{\tau}_i}, \quad \tilde{\boldsymbol{\tau}} = \sum_{i=1}^{3}\tau_i\,\boldsymbol{n}_{\tilde{\boldsymbol{\tau}}_i}\otimes\boldsymbol{n}_{\tilde{\boldsymbol{\tau}}_i} \tag{6.57}$$

[18] Further, the issue of the derivative $\frac{\partial\boldsymbol{F}}{\partial\boldsymbol{C}}$ arises again (cf. Footnote 13). A solution for this might be the so-called *first elasticity tensor* $\frac{\partial\boldsymbol{F}\boldsymbol{S}}{\partial\boldsymbol{F}}$ and its pull-back to the rc (see Ogden [1984]).

are introduced with the same eigenvalues τ_i for both tensors, but different eigenvectors $\boldsymbol{n}_{\boldsymbol{\tau}_i}$ and $\boldsymbol{n}_{\tilde{\boldsymbol{\tau}}_i}$, which are related by $\boldsymbol{n}_{\boldsymbol{\tau}_i} = \boldsymbol{R}\,\boldsymbol{n}_{\tilde{\boldsymbol{\tau}}_i}$. It is appealing to recognize that $\sphericalangle\left(\tilde{\boldsymbol{n}}, \boldsymbol{n}_{\tilde{\boldsymbol{\tau}}_i}\right) = \sphericalangle\left(\boldsymbol{n}_{cc}, \boldsymbol{n}_{\boldsymbol{\tau}_i}\right)$, which substantiates Equation (6.55) with a physical meaning, since the angle in the crc remains the same as in the cc. Based on the maximum eigenvalue τ_i, $\tilde{\boldsymbol{n}}_{\text{target}}$ is chosen the same as the corresponding eigenvector $\boldsymbol{n}_{\tilde{\boldsymbol{\tau}}_i}$, which is described in detail in Appendix 6.8.7. In case of several maximum eigenvalues, the smallest angle between the eigenvectors and the current direction of $\tilde{\boldsymbol{n}}$ is calculated and serves as a decision-making aid.

Remark 19. *A more mathematical treatment of Equation* (6.55) *and its derivation based on a pull-back from the* cc *as well as the associated objective rate can be found in Appendix 6.8.8. It is shown that the evolution described by Equation* (6.55) *follows from an evolution equation for* $\boldsymbol{n}_{cc}$.

6.4.4 Particular choice of Helmholtz free energy

The material model presented so far was derived in a general manner without specifying the Helmholtz free energy. Hence, the material model is independent of the chosen form. However, in order to study the model in a more detailed manner, a suitable energy must be chosen. For the time being, a compressible Neo-Hookean-type energy is chosen for the 'matrix' part

$$\psi_m = \frac{\mu_m}{2}\left(\operatorname{tr}\left(\bar{\boldsymbol{C}}_{e_m}\right) - 3 - \ln\left(\det\left(\bar{\boldsymbol{C}}_{e_m}\right)\right)\right) + \frac{\Lambda_m}{4}\left(\det\left(\bar{\boldsymbol{C}}_{e_m}\right) - 1 - \ln\left(\det\left(\bar{\boldsymbol{C}}_{e_m}\right)\right)\right) \tag{6.58}$$

with the Lamé constants Λ_m and μ_m of the 'matrix' part. Additionally, an energy originally introduced by Holzapfel et al. [2000] is adopted for the collagen part, and further, the common assumption is made that collagen fibers cannot carry compressive loads, i.e.

$$\psi_{co} = \begin{cases} \frac{K_1}{2\,K_2}\left(\exp\left[K_2\left(\operatorname{tr}\left(\bar{\boldsymbol{C}}_{e_{co}}\bar{\boldsymbol{M}}\right) - 1\right)^2\right] - 1\right) & , \operatorname{tr}\left(\bar{\boldsymbol{C}}_{e_{co}}\bar{\boldsymbol{M}}\right) \geq 1 \\ 0 & , \operatorname{tr}\left(\bar{\boldsymbol{C}}_{e_{co}}\bar{\boldsymbol{M}}\right) < 1 \end{cases} \tag{6.59}$$

where K_1 and K_2 denote material parameters. It should be noted that fiber dispersion might be included in line with Gasser et al. [2006], but it is not considered at the current stage of development. Nevertheless, the interested reader may find experimental studies on the determination of the dispersion parameter in Schriefl, Reinisch, Sankaran, Pierce and Holzapfel [2012] and Schriefl, Zeindlinger, Pierce, Regitnig and Holzapfel [2012]. With these energies at hand, the model will be investigated in Section 6.6, however, it should be noted that due to the cic framework combined with AD, it is quite easy to change the expressions for the energy.

6.5 Algorithmic implementation

In the following, both the algorithmic implementation of the material model is presented as well as the essential steps of the element formulation are summarized. Since the element formulation used within this contribution is not the focus, the interested reader is kindly referred to the works cited below. Both the material model as well as the element routine are implemented with the help of the algorithmic differentiation tool *AceGen* (Korelc [2002], Korelc and Wriggers [2016]). Further, in line with Korelc [2009], $\frac{\hat{\delta}(\bullet)}{\hat{\delta}(\bullet)}$ denotes an algorithmic differentiation operator, indicating that the derivative is obtained by means of *AceGen*.
Moreover, a single Gaussian point concept for continuum elements (Q1STc) by Barfusz, Brepols, van der Velden, Frischkorn and Reese [2021] is employed, which is based on the Enhanced Assume Strain (EAS) method introduced by Simo and Armero [1992]. The former carry out a Taylor expansion of both the element's geometry and the constitutively dependent quantities with respect to the element's center. As studied by Holthusen et al. [TBA], omitting the Taylor series of geometry while using only a Taylor series expansion of the constitutively dependent variables leads to increased performance and more accurate results. The interested reader may find a short summary of the enhanced Q1STc element using AD in Appendix 6.8.9.

6.5.1 Implicit time integration and corresponding local residuals

On the local level, a fully implicit time integration scheme is employed, where all evolution equations are discretized within a time interval $t \in [t_n, t_{n+1}]$ ($\Delta t := t_{n+1} - t_n$). Values from the last converged time step are indicated by an index n, whereas the index $n+1$ denoting values from the next time step is omitted in the following. Regardless of the choice of the model with one or two homeostatic surfaces, evolution equations for $\bar{\boldsymbol{D}}_{g_m}$ and $\bar{\boldsymbol{D}}_{g_{co}}$ have to be solved, which both can be represented as follows, considering Equation (6.26)

$$\dot{\boldsymbol{C}}_i = 2\,\boldsymbol{U}_i \boldsymbol{T}_i \boldsymbol{U}_i, \quad \boldsymbol{T}_i = \boldsymbol{T}_i^T. \tag{6.60}$$

Originally suggested by Dettmer and Reese [2004] and further improved by Christ and Reese [2009] and Vladimirov et al. [2008], their formulation of an exponential integrator scheme for the time discretization is used, i.e.

$$\boldsymbol{C}_i = \exp\left(2\,\Delta t\,\boldsymbol{U}_i \boldsymbol{T}_i \boldsymbol{U}_i^{-1}\right) \boldsymbol{C}_{i_n}. \tag{6.61}$$

Having in mind that the exponential satisfies the identities $\exp(\boldsymbol{A})^{-1} = \exp(-\boldsymbol{A})$ and $\exp(\boldsymbol{B}\boldsymbol{A}\boldsymbol{B}^{-1}) = \boldsymbol{B}\exp(\boldsymbol{A})\boldsymbol{B}^{-1}$ if $\boldsymbol{B}$ is invertible, the following residual form is obtained

$$\boldsymbol{U}_{i_n}^2 - \boldsymbol{U}_i \exp(-2\,\Delta t\,\boldsymbol{T}_i)\,\boldsymbol{U}_i = \boldsymbol{0}. \tag{6.62}$$

Additionally, it is appealing to note that Equation (6.62) naturally ensures the symmetry of $\boldsymbol{U}_i$. Unfortunately, calculating the exponential of $-2\,\Delta t\,\boldsymbol{T}_i$ usually requires a spectral decomposition or truncated series representation, in order to be able to also calculate the derivative $\frac{\partial \exp(\boldsymbol{A})}{\partial \boldsymbol{A}}$. However, this leads to an undesired increase in numerical effort. To circumvent this, the approach proposed by Korelc and Stupkiewicz [2014] is followed, who compute the exponential function based on a *generating function* (see Lu [2004]) by means of AD. Noteworthy, Arghavani, Auricchio and Naghdabadi [2011]; Arghavani, Auricchio, Naghdabadi and Reali [2011] investigated a reformulated residual of Equation (6.62) using the logarithm instead of an exponential integrator with considerable success in terms of numerical efficiency. Moreover, the calculation of $\tilde{\boldsymbol{\tau}}$ requires the determination of the stretch tensor $\boldsymbol{U}$ and its derivative with respect to $\boldsymbol{C}$. However, it should be mentioned that this must be calculated only once before the local Newton-Raphson iteration and does not need to be updated. Similar to the exponential, this tensor is obtained by means of a *generating function* $\mathscr{F}(\boldsymbol{C})$ combined with AD (see Hudobivnik and Korelc [2016]).

For time discretization of Equation (6.56) describing the fiber reorientation, an exponential integrator scheme is utilized, i.e.

$$\tilde{\boldsymbol{n}} - \exp\left(\Delta t\,\tilde{\boldsymbol{\Omega}}\right)\tilde{\boldsymbol{n}}_n = \boldsymbol{0}. \tag{6.63}$$

Note that the index $n+1$ is omitted again. Since $\tilde{\boldsymbol{\Omega}}$ is skew-symmetric, the following closed-form expression, which is known as Rodrigues' formula, is employed

$$\exp\left(\Delta t\,\tilde{\boldsymbol{\Omega}}\right) = \boldsymbol{I} + \frac{\sin\left(\Delta t\sqrt{\tilde{\boldsymbol{\omega}}\cdot\tilde{\boldsymbol{\omega}}}\right)}{\sqrt{\tilde{\boldsymbol{\omega}}\cdot\tilde{\boldsymbol{\omega}}}}\,\tilde{\boldsymbol{\Omega}} + \frac{1-\cos\left(\Delta t\sqrt{\tilde{\boldsymbol{\omega}}\cdot\tilde{\boldsymbol{\omega}}}\right)}{\left(\sqrt{\tilde{\boldsymbol{\omega}}\cdot\tilde{\boldsymbol{\omega}}}\right)^2}\,\tilde{\boldsymbol{\Omega}}^2. \tag{6.64}$$

The evolution of fiber reorientation is thus implemented in an efficient manner. Moreover, since $\exp\left(\Delta t\,\tilde{\boldsymbol{\Omega}}\right) \in \mathrm{SO}(3)$, the (time discretized) evolution equation does indeed describes a rotation.

The number of local unknown variables depends on the chosen material model with one or two homeostatic surfaces. Under consideration of the symmetry of both $\boldsymbol{U}_{g_m}$ and $\boldsymbol{U}_{g_{co}}$, the unknowns reduce to 16 for Model I and 17 for Model II. Appendix 6.8.10 provides two pseudo-

codes, Algorithms 3 and 4, in order to make the material models' implementation easier to understand.

6.5.2 Algorithmic consistent tangent operator

To achieve quadratic convergence within the global Newton-Raphson iteration, it is necessary to derive the (algorithmic) tangent operator consistently with the local time integration introduced in the previous section. Therefore, the implicit (algorithmic) dependency of the local variables with respect to the displacement field must be taken into account. Although already presented in Algorithms 3 and 4, the derivation of the tangent operator is briefly shown in the following. Since this derivation is more or less the same for both models, the derivation is restricted to Model I.

Under consideration of all previous constitutive equations, one can identify the following dependence $\boldsymbol{S} = \boldsymbol{S}^* \left(\boldsymbol{C}, \boldsymbol{U}, \tilde{\boldsymbol{n}}, \boldsymbol{U}_{g_m}, \boldsymbol{U}_{g_{co}}\right)$. Thus, the algorithmic consistent tangent operator $\mathbb{C}$ can be calculated

$$\mathbb{C} = 2 \left(\frac{\partial \boldsymbol{S}}{\partial \boldsymbol{C}} + \frac{\partial \boldsymbol{S}}{\partial \boldsymbol{U}} : \frac{\partial \boldsymbol{U}}{\partial \boldsymbol{C}} + \frac{\partial \boldsymbol{S}}{\partial \tilde{\boldsymbol{n}}} \cdot \frac{\partial \tilde{\boldsymbol{n}}}{\partial \boldsymbol{C}} + \frac{\partial \boldsymbol{S}}{\partial \boldsymbol{U}_{g_m}} : \frac{\partial \boldsymbol{U}_{g_m}}{\partial \boldsymbol{C}} + \frac{\partial \boldsymbol{S}}{\partial \boldsymbol{U}_{g_{co}}} : \frac{\partial \boldsymbol{U}_{g_{co}}}{\partial \boldsymbol{C}} \right) \tag{6.65}$$

where the index $n+1$ is again omitted. Since $\boldsymbol{U}$ depends solely on $\boldsymbol{C}$, $\frac{\partial \boldsymbol{U}}{\partial \boldsymbol{C}}$ can be directly calculated as, for instance, described in the previous section. The algorithmic dependence of the local variables is obtained using the *implicit function theorem*. In this regard, let $\mathbf{h}_{\mathrm{I}} = \mathbf{h}_{\mathrm{I}}^* \left(\hat{\boldsymbol{U}}_{g_m}, \tilde{\boldsymbol{n}}, \hat{\boldsymbol{U}}_{g_{co}} \right)$ denote the local variables, and further, $\mathbf{r}_{\mathrm{I}} \left(\hat{\boldsymbol{C}}, \mathbf{h}_{\mathrm{I}} \right) = \mathbf{0}$ being a converged local residual. Hence, $\mathbf{K}_{loc}$ defined via

$$\frac{\partial \mathbf{h}_{\mathrm{I}}}{\partial \hat{\boldsymbol{C}}} = \underbrace{- \left(\frac{\partial \mathbf{r}_{\mathrm{I}}}{\partial \mathbf{h}_{\mathrm{I}}} \right)^{-1} \frac{\partial \mathbf{r}_{\mathrm{I}}}{\partial \hat{\boldsymbol{C}}}}_{=: \mathbf{K}_{loc}} \tag{6.66}$$

contains all desired implicit derivatives appearing in Equation (6.65) .

6.6 Numerical examples

In the following, the models' response in an academic setting as well as their capability to reproduce experimental observations are investigated. Section 6.6.1 examines the models while undergoing temporary changing boundary conditions. Afterwards, in Section 6.6.2 the material models are compared with recently published experimental data taken from Eichinger

et al. [2020] in a qualitative manner. The different material sets used within the latter mentioned studies are summarized within Table 6.1. Both the element routine as well as the material models with Model I and II are implemented into the finite element program *FEAP* (see Taylor [2020]), the open-source package *ParaView* (see Ahrens et al. [2005]) is utilized for visualization and the finite element meshes are generated using the commercial software *HyperMesh*.

Table 6.1: Material parameter sets. The parameters belonging to the Helmholtz energy and fiber reorientation may vary in set 2 and set 3, depending on whether Model I or Model II is used. Moreover, the homeostatic stresses in set 3 depend on which experiment ('dog-bone' or cross specimen) is simulated. However, the ratio $\frac{\sigma_m^{\text{'dog-bone'}}}{\sigma_{co}^{\text{'dog-bone'}}} = \frac{\sigma_m^{\text{cross}}}{\sigma_{co}^{\text{cross}}} \approx 0.69$ is kept constant.

Symbol	Numerical Example Material parameter	6.6.1 Set 1	6.6.2.1 Set 2	6.6.2.2 Set 3	Unit
Helmholtz free energy					
Λ_m	Lamé constant of 'matrix'	50	I: 50 II: 40	I: 818 II: 999	$\frac{\mu\text{N}}{\text{mm}^2}$
μ_m	Shear modulus of 'matrix'	100	I: 80 II: 70	I: 982 II: 426	$\frac{\mu\text{N}}{\text{mm}^2}$
K_1	Stiffness parameter of collagen	200	I: 220 II: 250	I: 3351 II: 5565	$\frac{\mu\text{N}}{\text{mm}^2}$
K_2	Exponential parameter of collagen	20	I: 120 II: 100	I: 14996 II: 14428	–
Model I					
σ_g	Homeostatic stress	20	11.6	'dog-bone': 13.3 cross: 22.9	$\frac{\mu\text{N}}{\text{mm}^2}$
β_g	Stress-like apex parameter	1	1	1	$\frac{\mu\text{N}}{\text{mm}^2}$
η_g	Relaxation time	150	400	658	h
ν_g	Perzyna exponent	1	1	1	–
Model II					
σ_m	Homeostatic stress of 'matrix'	10	4	'dog-bone': 5.72 cross: 10.6	$\frac{\mu\text{N}}{\text{mm}^2}$
β_m	Stress-like apex parameter of 'matrix'	1	1	1	$\frac{\mu\text{N}}{\text{mm}^2}$
η_m	Relaxation time of 'matrix'	75	250	280	h
ν_m	Perzyna exponent of 'matrix'	1	1	1	–
σ_{co}	Homeostatic stress of collagen	10	7.6	'dog-bone': 8.28 cross: 15.3	$\frac{\mu\text{N}}{\text{mm}^2}$
η_{co}	Relaxation time of collagen	75	100	381	h
ν_{co}	Perzyna exponent of collagen	1	1	1	–
Fiber reorientation					
η_S	Relaxation time of reorientation	5	I: 5 II: 10	I: 50 II: 37	h

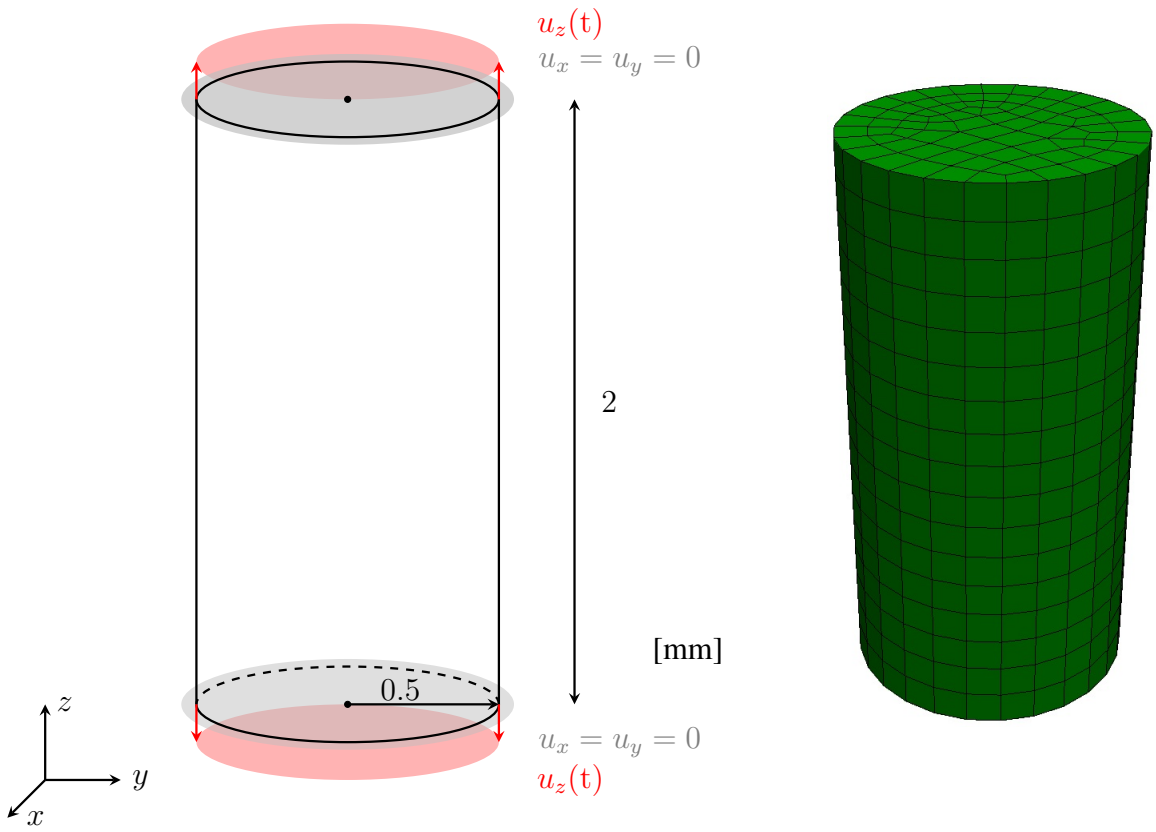

Figure 6.3: Left: Geometry and boundary value problem of cylindrical specimen. Both bottom and top surfaces are clamped. At the top, the displacement in longitudinal direction is prescribed, while the same displacement is prescribed in negative direction at the bottom edge. Right: Finite element mesh with 1377 elements used for the cylindrical specimen.

6.6.1 Cylindrical specimen

In order to study the ability of both achieving the prescribed homeostatic stress as well as reorient collagen fibers, a cylindrical specimen is fully clamped at the top and bottom surface, while the displacement perpendicular to these surfaces varies with time. Figure 6.3 illustrates the corresponding boundary value problem as well as the finite element mesh used for these studies. The material parameters are arbitrarily chosen and correspond to 'set 1' listed in Table 6.1. The displacement is prescribed in a stepwise manner over time, where certain values are held constant for a time period of 20 [h] (see Figure 6.4). Both stretching and compression of the cylindrical specimen are investigated.

Homeostatic stress. To begin with, the fibers are initially aligned with the z axis. Since the

stress state in the middle of the specimen is almost uniaxial, the fibers do not have to reorient themselves, expect for the region near the clamping. Hence, the effect of remodeling can studied in a more detailed manner. In Figure 6.5, the obtained Cauchy stress as well as the reaction force in z direction are shown. Up to $t = 20$ [h], both the Cauchy stresses and reaction forces for Model I as well as Model II rise up to the desired homeostatic stress. Noteworthy, due to the additive decomposition of $\boldsymbol{S}$ (cf. Equation (6.34)) also the Cauchy stress is the sum of both constituents. Thus, for Model II, the observed Cauchy stress must be equal to the sum of σ_m and σ_{co} in a uniaxial setup, which is the case here. The specimen is then loaded at three different intervals with different specified displacements. In each interval, both model versions are able to regain the homeostatic stress state, where Model II reaches the state within a shorter time period. It should be noted that the reaction forces in each interval are not necessarily the same, since the homeostatic stress is given in terms of Cauchy's stress, which is defined per unit current area. Since the current areas are not the same in each interval, the reaction forces are also not the same. Moreover, Figure 6.6 illustrates the radial displacement of the cylinder. As expected, the specimen contracts itself during the first interval to achieve a tensile stress state. Stretching the specimen within the second step increases the tensile stress, which is why the specimen relaxes afterwards. The remaining steps can be analogously interpreted.

Fiber reorientation. It remains to investigate the models' capability to align the fibers with the eigenvector associated with the principal stress direction. Contrary to the previous study, the initial fibers are therefore randomly orientated in each element. Nevertheless, the specimen is subjected to the same loading conditions as before. However, only up to a value of $t = 40$ [h]. In Figure 6.7, the fiber vector $\tilde{\boldsymbol{n}}$ is illustrated. It can be readily observed that, in addition to remodeling to achieve a homeostatic stress state, the fibers in both model versions reorient and align with the principal stress direction. Even after immediately increasing the load at $t = 20$ [h], the fibers are still able to align with the principal direction. In addition, the expansion and contraction already observed in Figure 6.6 can be well seen in Figure 6.7 between $t = 0 - 20$ [h] and $t = 20 - 40$ [h], respectively.

6.6.2 Qualitative comparison with experimental data

In the following, the two model versions are qualitatively compared with recent experiments of equivalent tissues conducted by Eichinger et al. [2020], who provided the authors with both the experimental data and the geometry for the specimens. In the mentioned study, two different geometries are examined, one is a 'dog bone' specimen to examine the equivalent tissues under a nearly uniaxial stress state, and the other is a cross specimen to examine multiaxial stress

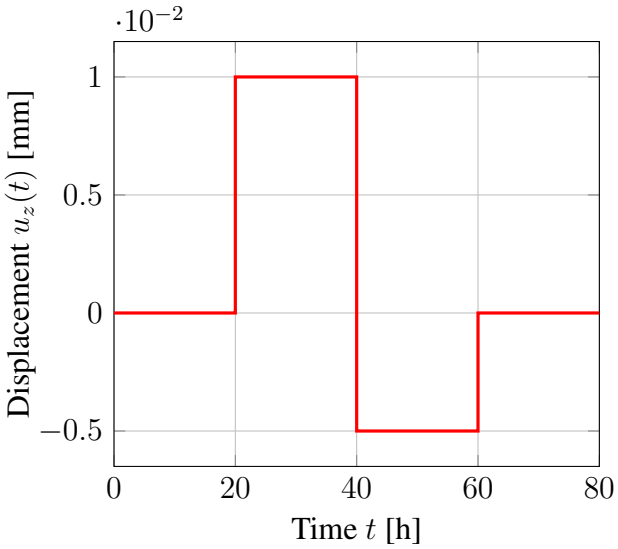

Figure 6.4: Stepwise loading procedure applied to the boundary value problem depicted in Figure 6.3.

states. A cell-seeded collagen gel is used, which is clamped directly into the testing device with the end of gelation. The subsequent experiment starts immediately, ensuring a stress-free state at the beginning. For more details of the manufacturing and testing procedure, the interested reader is kindly referred to the work of Eichinger et al. [2020].

6.6.2.1 'Dog-bone' specimen (uniaxial constraint)

In this section, a 'dog-bone' shaped specimen is investigated. Figure 6.8 illustrates the geometry as well as the finite element meshed used for simulation. Due to the force transducers in the experimental setup, the right and left edges are considered to be clamped and not simulated. The aim is to investigate to what extent the model versions are able to reproduce the homeostatic state compared to experimental data. For this purpose, the 'dog-bone' specimen is held fixed for 17 [h] until a tensile state is reached by growth and remodeling. Subsequently, the reaction force obtained after 17 [h] is perturbed by $\pm 10\%$. Note that this perturbation is applied in a displacement-driven manner, which is held constant up to 27 [h] (cf. Figures 6.11 and 6.12).

For both Model I and Model II, the material parameters are fitted to the experimental data using nonlinear optimization with the help of the *Matlab* build-in function *patternsearch*. The obtained parameters correspond to 'set 2' listed in Table 6.1. It is important to mention that in both cases only the experimental data of $+10\%$ up to 17 [h] are used for optimization.

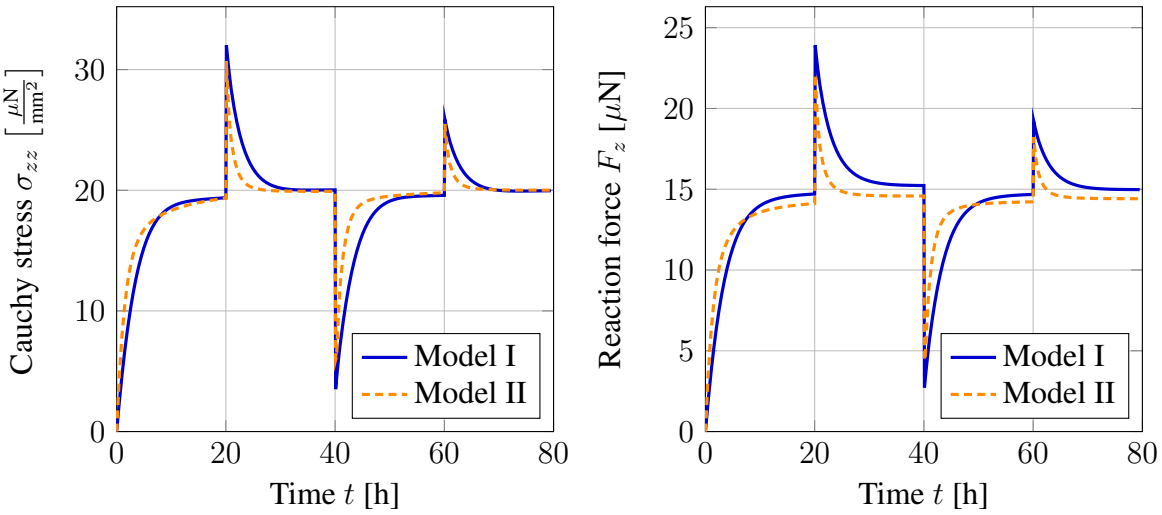

Figure 6.5: Cauchy stress σ_{zz} and reaction force F_z in longitudinal direction obtained with Model I and II. The homeostatic stress for Model I is chosen as $\sigma_g = 20\ \left[\frac{\mu N}{mm^2}\right]$, while the sum of σ_m and σ_{co} is equal to $20\ \left[\frac{\mu N}{mm^2}\right]$ for Model II. The loading conditions are depicted in Figure 6.3 and 6.4. The Cauchy stress is evaluated at the node closest to the center of the cylinder.

Hence, the response of the model is not adjusted for neither perturbation nor compression, which means that these results are predictive. However, due to a current lack of experimental data, the material parameters differ per model version, and further, are not necessarily the only solution possible, i.e. they might be not unique. A more detailed analysis of the individual constituents as well as more information about the displacement field, e.g. using digital image correlation, are required to optimally determine the parameters. In this regard, it should be noted that the Perzyna exponents ν_i and the stress-like parameters β_i were not optimized to restrict the solution.

Before the numerical observations are discussed, a careful mesh convergence study is performed using 280, 663, 2112 and 4580 finite elements. The obtained force-time curves are depicted in Figure 6.9, while the corresponding meshes are shown in Figure 6.10. A very good convergence behavior can already be observed with coarse meshes. For the following investigations, the mesh with 2112 elements is used.

As mentioned above, the testing procedure is divided into two parts, where the boundary conditions are kept constant for the first 17 hours, followed by a rapid increase in displacement to achieve a force perturbation. Both the experimental data including the standard error of the mean (SEM) as well as the numerical results are shown in Figure 6.11 for Model I and Fig-

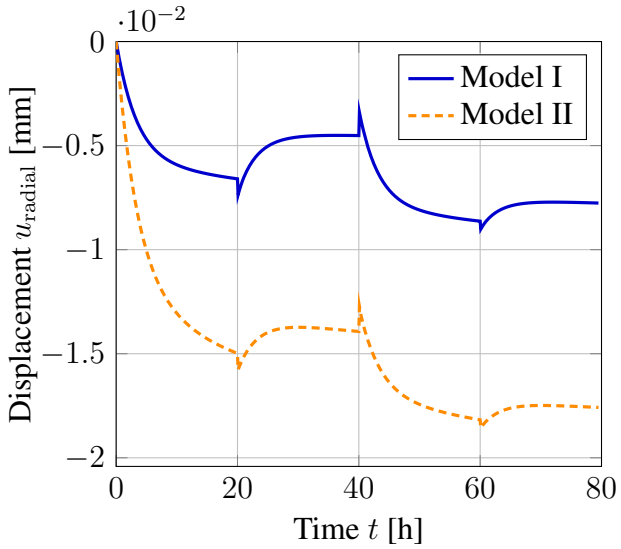

Figure 6.6: Displacement in radial direction of the cylinder on the side surface at half the height of the cylinder. Positive values would mean that the cylinder is expanding compared to the initial configuration.

ure 6.12 for Model II. One can observe that the equivalent tissues seek a tensional homeostatic state, independent of whether a positive or negative perturbation is applied, which is consistent with other experiments available in the literature (see, for instance, Brown et al. [1998] and Ezra et al. [2010]).

The 'one-surface' approach reveals the S-shaped increase within the first 17 hours slightly more accurately, while the 'two-surface' approach re-establishes homeostasis within a shorter period of time. However, both do not establish the homeostatic state as fast as observed in the experiments. Nevertheless, with both versions it is possible to reproduce the experimental curves in a very good way, which is especially pleasant for Model I considering that only the overall behavior is specified. Thus, it becomes evident that only specifying the Helmholtz free energy and the assumption of homeostatic surfaces leads to reliable results. But it must be emphasized that a more precise investigation in the future is essential.
Furthermore, in Figure 6.13, the Cauchy stress in longitudinal direction for the $+10\%$ loading is shown at the beginning, just before (17^-) and right after (17^+) the perturbation as well as at the end of the simulation[19]. A homeostatic state is achieved mainly within the entire specimen before the perturbation, increases with stretching and is re-established in the following. In line with the previous observations, Model II is slightly more rapid.

[19]The results for the -10% loading procedure are similar.

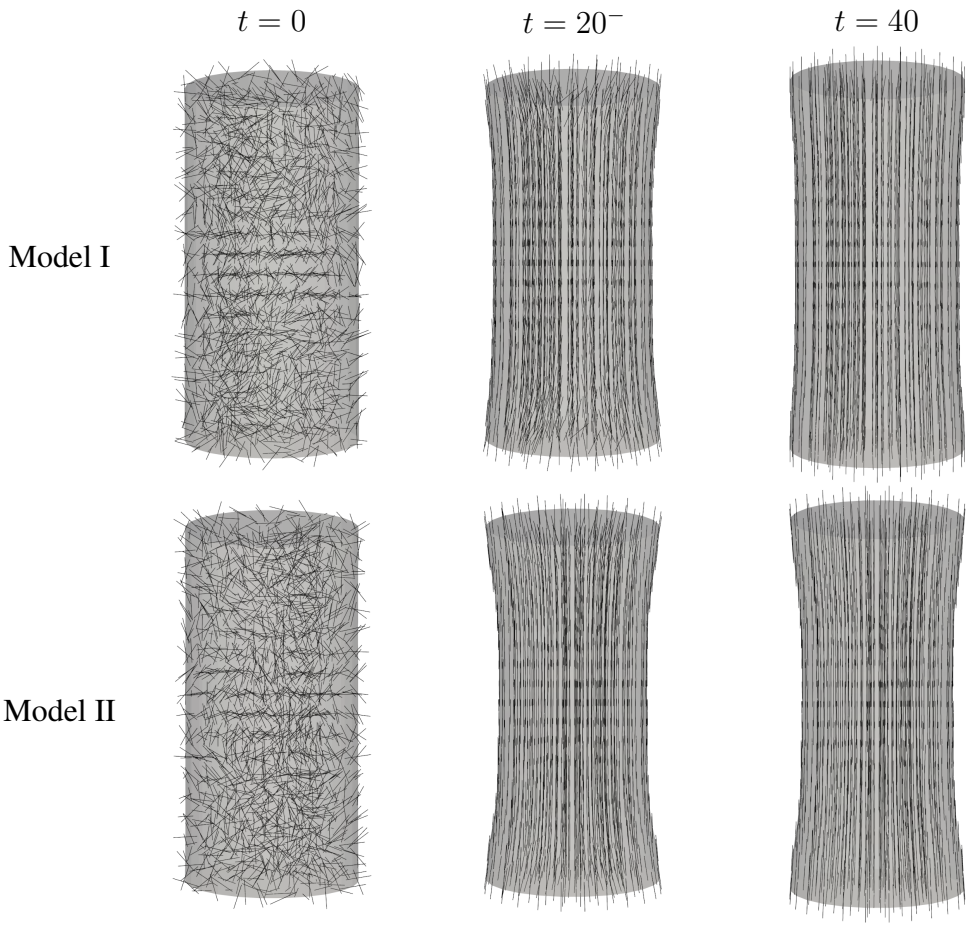

Figure 6.7: Fiber reorientation of Model I and II. The structural vector $\tilde{\boldsymbol{n}}$ is illustrated. The initial fiber orientations are randomly chosen in each element. The loading procedure prescribed in Figure 6.4 is applied up to $t = 40$ [h]. The snapshot at $t = 20^-$ [h] corresponds to the state immediately before the perturbation is applied. The deformed geometry is not to scale.

Besides these promising results, a remark should be made on the experimental results only for the $+10\%$ loading procedure. Although the simulation clearly re-establishes homeostasis, the experimental results seem to slightly differ from this particular state. An explanation for this phenomenon was already given by Eichinger et al. [2020], who concluded that the cells may exceed a certain threshold and re-enter the cell cycle increasing the number of cells. An increased number of cells would explain a change in the preferred homeostatic state. Since cell proliferation is out of the scope of this work, this phenomenon cannot be modeled with the presented models. Noteworthy, the experimental setup is slightly changed in the following section, where Mitomycin C is used in order to minimize proliferation.

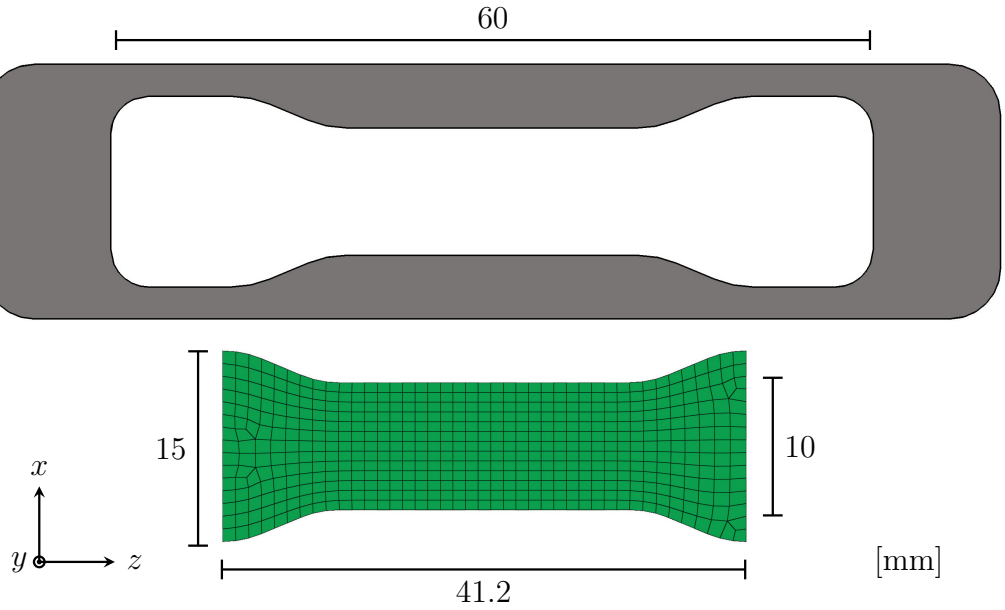

Figure 6.8: Geometry for 'dog-bone' specimen. The thickness is four millimeters. Top: Mold used for manufacturing. Bottom: Finite element mesh with 2112 element in total (four elements over the thickness, see Figure 6.10c). The edges are considered to be clamped, and thus, are not simulated.

It remains to investigate the reorientation of collagen fibers, which is depicted in Figure 6.14. Since the equivalent tissues did not undergo any mechanical loading during manufacturing, a random distribution of collagen fibers is assumed at the beginning. The fibers are aligned with the principal stress direction after 17 hours and align themselves also after the perturbation is applied. Only in the region near the clamping no clear fiber direction can be identified, but this can be explained by a very complex stress state in this area, which is not surprising.

Lastly, attention should be paid to the numerical performance. Therefore, the residual norms of the global Newton-Raphson iterations at three different time steps are shown in Table 6.2. Regardless of the used model, the convergence rate is perfectly quadratic throughout the whole simulation and converges towards the solution in a few iterations. Even after the perturbation is applied, which is a strong discontinuity in the displacement, the convergence is very satisfying.

6.6.2.2 Cross and 'dog-bone' specimen (multiaxial constraint)

In order to study the models undergoing multiaxial boundary conditions, a cross specimen is investigated in the following. As already mentioned in the previous section, with the

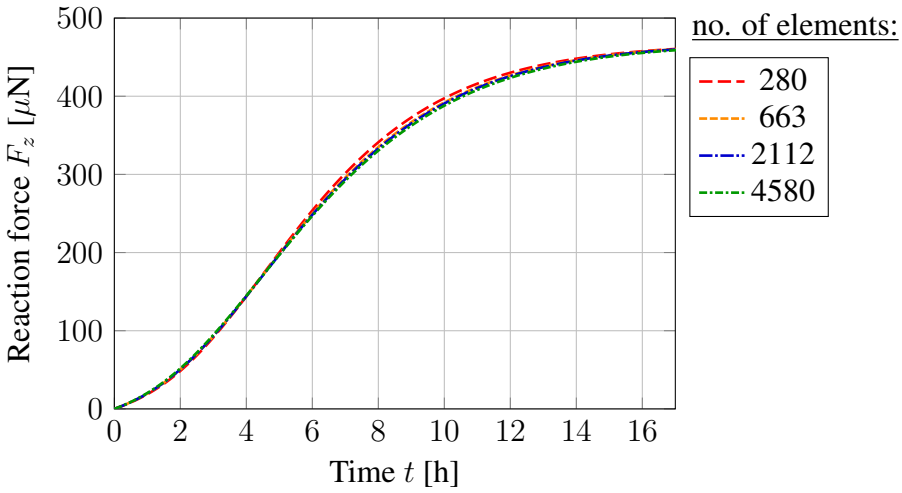

Figure 6.9: Force-time curves with four different mesh refinements for the 'dog-bone' specimen.

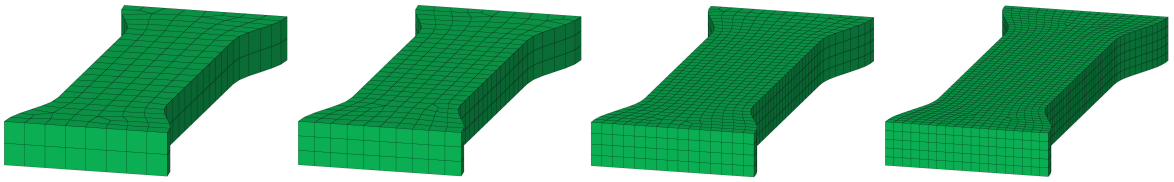

(a) 280 elements (b) 663 elements (c) 2112 elements (d) 4580 elements

Figure 6.10: Finite element meshes with four different mesh refinements for the 'dog-bone' specimen. The refinement is performed in all three spatial directions.

experimental setup used by Eichinger et al. [2020] for the 'dog-bone' specimen, it cannot be ensured that cell proliferation is avoided, which is why they treated the cells with Mitomycin C preventing a re-entering of the cell cycle. Hence, also the 'dog-bone' specimen is investigated once more in the following. The mold utilized for manufacturing as well as the boundary value problem used for the cross specimen are depicted in Figure 6.15. As in the previous example, the outer edges are considered to be fully clamped. Similarly, the loading is prescribed in a two-step manner, however, contrary to Section 6.6.2.1, the state of homeostasis is reached within a period of 27 hours, while the total time taken by the experiment is 42 hours. Moreover, the homeostatic forces achieved in both the cross- and 'dog-bone'-setup are perturbed again after 27 hours, but with $\pm 20\%$ of their values.

Due to a more sophisticated experimental study, let us briefly summarize the setups investigated in this section

- 'Dog-bone': Same experimental setup as in Section 6.6.2.1, but with a perturbation of

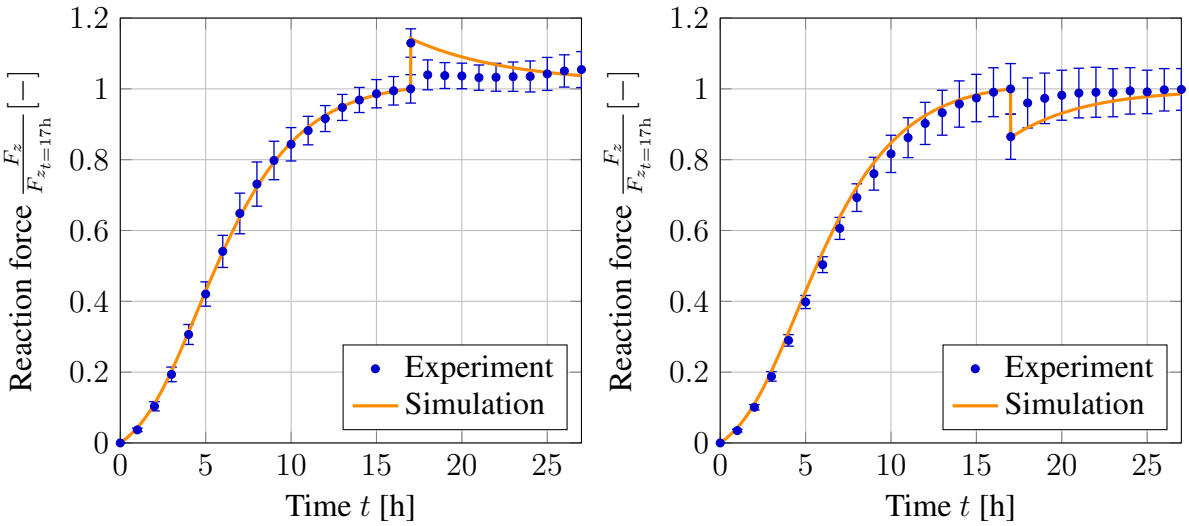

Figure 6.11: Model I - Comparison of simulation with experimental data of 'dog-bone' tissue stripe. Left: Perturbation at $t = 17$ [h] with $+10\%$ of the homeostatic reaction force. Right: Perturbation at $t = 17$ [h] with -10% of the homeostatic reaction force, experimental data is plotted as the mean value of all experiments with error bars denoting the SEM.

$\pm 20\%$ of the homeostatic force. With this kind of setup, a uniaxially constraint problem is investigated in the middle of the specimen (see Figures 6.16a and 6.17a).

- Biaxially constraint – semi-biaxially loaded: A cross-like specimen is investigated. The force perturbation is applied in a semi-biaxial manner, i.e. only the displacements of the horizontal arms in z direction is changed after 27 hours (see Figures 6.16b and 6.17b).
- Biaxially constraint – biaxially loaded: The same cross specimen is investigated as before, but this time both the horizontal (z) and vertical (x) arms are stretched by $+20\%$ as well as compressed by -20% of their homeostatic forces (see Figures 6.16c and 6.17c).

Thus, a total of ten independent experimental curves are available, since the forces in both directions were measured for each of the cross-like setups.

To begin with, the same parameters as in the previous section ('set 2') are used. Unfortunately, it was even not possible to reproduce the experimental observations made for the 'dog-bone' specimen shown in Figure 6.16a and 6.17a. However, this could be expected, having in mind that neither the parameters are uniquely determined with certainty as already discussed in Section 6.6.2.1, nor that the specimens can be considered to be the same as in the previous section

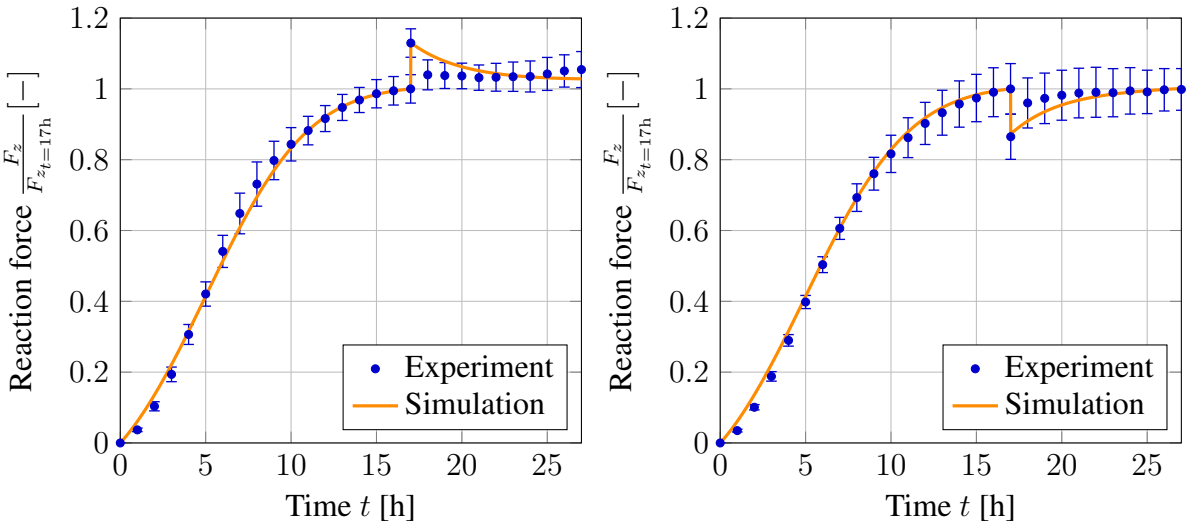

Figure 6.12: Model II - Comparison of simulation with experimental data of 'dog-bone' tissue stripe. Left: Perturbation at $t = 17$ [h] with $+10\%$ of the homeostatic reaction force. Right: Perturbation at $t = 17$ [h] with -10% of the homeostatic reaction force, experimental data is plotted as the mean value of all experiments with error bars denoting the SEM.

due to the Mitocymin C. Hence, the material parameters must be fitted to the experimental data once more, where nonlinear optimization tools are utilized to determine the material parameters. For optimization, only the experimental data of the 'dog-bone' and the semi-biaxially loaded cross specimen with $+20\%$ in both directions perturbation were used, but only up to the time step just before the perturbation is applied ($t = 27^{-}$ [h]). Thus, only three out of ten experimental curves are used for fitting, which means that the remaining results are predictive. However, it was not possible to determine a suitable set of preferred stresses which fit to both 'dog-bone' as well as cross specimen. Hence, it was decided to use the same parameters for both 'dog-bone' and cross specimen, but let the preferred stresses differ from each other (see 'set 3' in Table 6.1). Nevertheless, it should be mentioned that for Model II at least the ratio $\frac{\sigma_m^{\text{'dog-bone'}}}{\sigma_{co}^{\text{'dog-bone'}}} = \frac{\sigma_m^{\text{cross}}}{\sigma_{co}^{\text{cross}}} \approx 0.69$ is kept constant. Of course, it would be desirable to determine a single set of parameters, but given the arbitrary choice of homeostatic surfaces, which is mechanically motivated but requires a much more sophisticated experimental determination, the assumption of different homeostatic stresses is acceptable. A more precise determination would require further experiments, which is beyond the scope of this contribution.

A careful mesh convergence study in analogy to Section 6.6.2.1 was carried out using 626, 1032 and 3132 finite elements. The results are not shown here for brevity. However, a similar

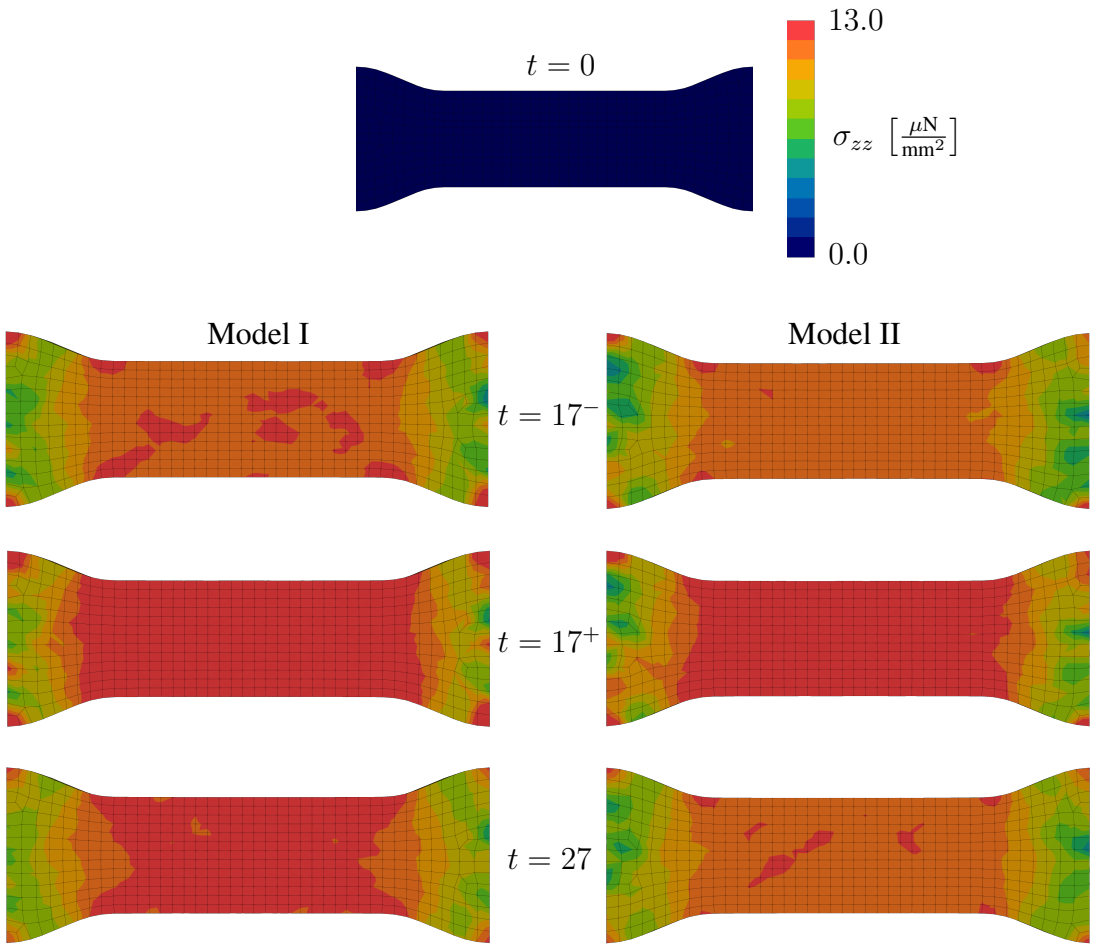

Figure 6.13: Cauchy stress in z direction at different time steps for the $+10\%$ loading procedure. Here, 17^- denotes the time step right before the perturbation is applied, while 17^+ corresponds to the time step right afterwards.

behavior as in Figure 6.9 was observed. The results presented in the following correspond to the solution with 3132 finite elements in total, where four elements over the thickness are used.

Regardless both semi-biaxial or biaxial loading and stretching or compression, the results up to the perturbation ($t = 27^-$ [h]) should be the same for all cross investigations. Indeed, the simulation clearly shows this kind of behavior, except for some minor deviations due to randomly chosen initial directions of the fibers. Contrary, the experimental results show significant deviations, which might be explained by the inherently very large variability in biological tissues. In addition, the different slopes at the beginning between the 'dog-bone' and cross specimen raise questions. As mentioned by Eichinger et al. [2020] themselves, replacing the cross specimen with a 'dog bone'-like one should not affect the results, which is consistent

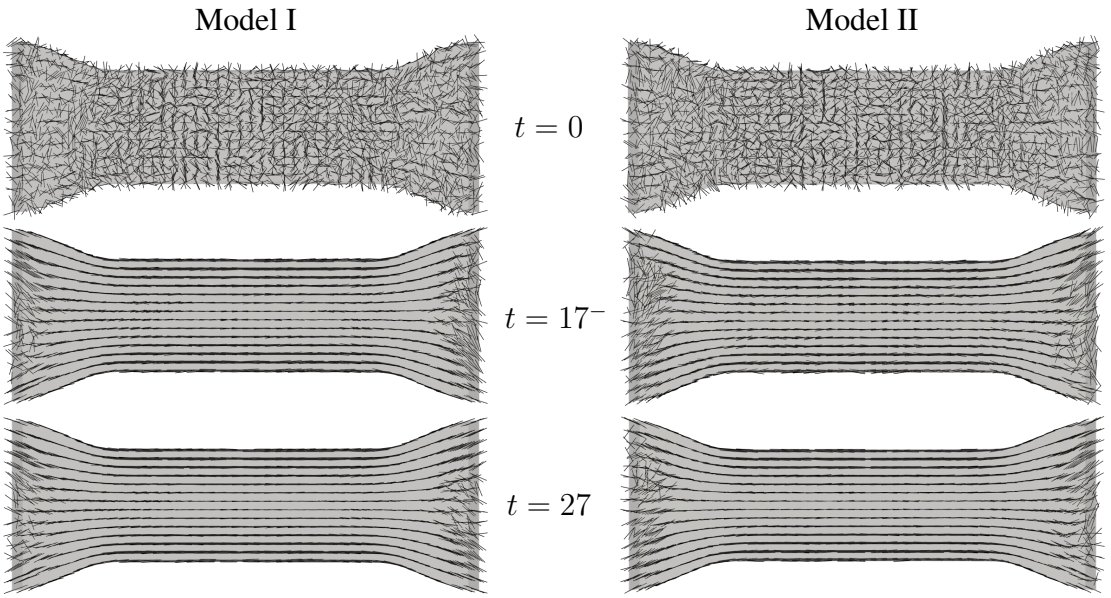

Figure 6.14: Fiber reorientation of Model I and Model II for the 'dog-bone' specimen. The structural vector $\tilde{\boldsymbol{n}}$ is illustrated. The results correspond to the $+10\%$ loading procedure.

with observations made in the simulation. However, the experimental data strongly differ from each other. With the approach of equal parameters for all specimens, it was not possible to determine a more suitable parameter set.

Both model versions are able to reproduce the experimental studies in a surprisingly close way. However, compared with Model I (see Figure 6.16), Model II (see Figure 6.17) performs better in terms of both recovery of the homeostasis as well as less deviation for the entire time period investigated. Therefore, the following discussion focuses on the results obtained using Model II, but the corresponding results of Model I are shown in Appendix 6.8.11. Additionally, the results for the 'dog-bone' specimen are qualitatively the same as in Section 6.6.2.1, and thus, are also not discussed below.

In Figure 6.18, the Cauchy stresses in x and z direction are shown for both the semi-biaxially and biaxially loaded cross specimen undergoing stretching. As desired, right before loading ($t = 27^-$ [h]), the component σ_{xx} in the vertical arms tends to the homeostatic tensile stress while in the horizontal arms the stress component σ_{zz} behaves similarly. This is independent of the subsequent semi-biaxial or biaxial loading. Perturbing the homeostatic force by $+20\%$ generally increases the observed stresses, whereby the increase in the vertical arm is higher in case of biaxial loading ($t = 27^+$ [h]).

For the case of compression by -20% of the homeostatic force, the Cauchy stress components

Table 6.2: Global convergence rates of the 'dog-bone' specimen at three different time steps (see Figure 6.11 and 6.12). Listed are the global residual norms, where $t = 17.01$ [h], also referred to as $t = 17^{+}$ [h], corresponds to the first iteration after applying the perturbation of $+10\%$.

	$t = 8.5$ [h]		$t = 17.0$ [h]		$t = 17.01$ (17^{+}) [h]	
Iteration	Model I	Model II	Model I	Model II	Model I	Model II
0	1.117E+00	2.096E+00	5.617E-01	1.064E+00	1.707E+02	1.500E+02
1	1.842E-03	3.255E-03	5.191E-04	1.243E-03	4.876E-01	1.828E-01
2	6.231E-08	8.186E-08	8.039E-10	7.286E-09	1.217E-03	9.959E-05
3	8.115E-11	6.893E-11	-	-	1.649E-08	1.061E-10

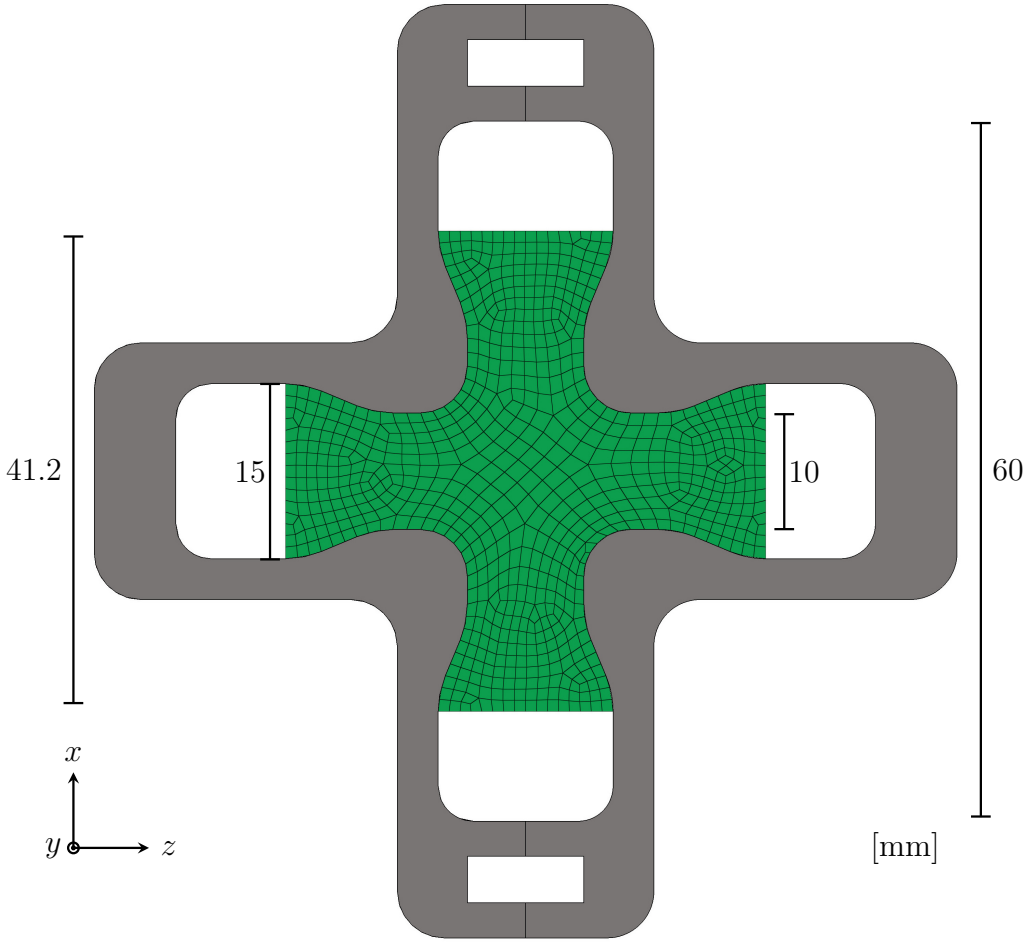

Figure 6.15: Geometry for cross specimen. The thickness is four millimeters. The mold used for manufacturing is highlighted in grey. The edges are considered to be clamped, and thus, are not simulated.

immediately before and after perturbation are shown in Figure 6.19. Due to the same exper-

imental setup up to $t = 27^{-}$ [h], there is nearly no difference between the semi- and biaxial loading, and moreover, the results are quite similar as in Figure 6.18. Noteworthy, the small deviation result from the randomly chosen fiber directions at the beginning. In contrast to stretching, a decrease in the stress components is observed for compression, whereby, however, the results concerning the vertical and horizontal arms for both semi-biaxial and biaxial loading can be interpreted analogously to the previous results made for stretching.
Finally, Figure 6.20 illustrates the reorientation of fibers during the simulation. At the beginning, the fibers are randomly orientated. While the specimens grow and remodel themselves in order to reach a tensile homeostatic state, the fibers within the arms align with the principal stress direction. Contrary, the fibers in the center of the specimens are orientated rather randomly. Compared with Figure 6.18, these behaviors are quite good understandable, as there is a main tensile stress within the arms, while both σ_{xx} and σ_{zz} are positive and almost equal in the specimen's center resulting in a more complex stress state. Both observations are in line with experimental findings made by Hu et al. [2009]. At the end of the simulation, an even clearer alignment can be noticed, which can be explained on the one hand by the extra stimulus due to the perturbation and on the other hand by the additional time for the reorientation.

6.7 Conclusion and outlook

The main objective of this work were, to introduce a novel constitutive framework based on a co-rotated intermediate configuration for various types of inelastic material behaviors,which is used in the context of a stress-driven growth model for materials behaving initially anisotropically. This general framework and the material model excellently synergize with each other, since modeling of biomechanical processes is usually associated with a high degree of complexity.

The co-rotated intermediate configuration shares the same physical interpretation with the intermediate configuration, which is the starting point for most inelastic material models. However, contrary to the intermediate one, the co-rotated one is uniquely defined, i.e. all strain- and stress-like quantities can be determined within this configuration. Thus, all derivations required to derive the constitutively dependent or thermodynamically consistent variables can be obtained using algorithmic differentiation. Moreover, the derivation of evolution equations using dissipation potentials that depend on these constitutively dependent variables can also be computed using algorithmic differentiation. Due to the latter steps as well as due to the fact that the calculation of the (algorithmic) consistent tangent is known to be very error-

prone, the co-rotated framework significantly simplifies the development of new continuum mechanical models.

The stress-driven growth model can be considered the initially anisotropic version of the model proposed by Lamm et al. [2022]. Hence, biological fibers such as collagen can be taken into account. As presented by the latter mentioned authors, the growth and remodeling process in order to achieve a state of tensile homeostasis is modeled using homeostatic surfaces. Thus, the inelastic part of the deformation gradient does not have to be specified a priori. The model seeks to achieve the preferred stress state described by the surfaces in the principal stress space of Cauchy's stress. Within this contribution, two versions of the model were presented. The first version assumes one homeostatic surface in terms of the overall Cauchy stress, the second assumes two surfaces expressed in terms of the stresses of the individual constituents. While the former is easier to be experimentally determined, the second one is more flexible in modeling the behavior of soft tissues. In addition to growth and remodeling, stress-driven fiber reorientation was also taken into account. It was assumed that fibers align with the main principal stress eigenvector.

Finally, the model versions were implemented in an efficient way using an algorithmic differentiation tool. Computational examples were performed to study the models' ability to reach a homeostatic state under several loading conditions, their reorientation behavior as well as their numerical performance. The models were qualitatively in good accordance with the experimental data of Eichinger et al. [2020] even for complex multiaxial setups.

Despite these promising results, a more comprehensive determination of the model versions' material parameters is of high interest as well as further validation. For this purpose, digital image correlation should be employed to obtain high resolution of the deformation field. Additionally, more experimental evidence on the usage of homeostatic surfaces is necessary. Besides these topics, cell-cell interactions such as cell aggregates (see e.g. Firooz et al. [2022]) as well as diffusion of nutrients and hormones should be considered in future work, as done for instance by Manjunatha et al. [2022*b*] – all these factors influence and limit growth and remodeling in addition to the mechanical stimuli considered in this contribution.

6.8 Appendix

6.8.1 Summary of $pbic$ framework

For simplicity, the influences of structural tensors as well as an additional split of $\boldsymbol{F}_i$ are neglected in the following. Further, no dependence on $\boldsymbol{B}_i$ is assumed. Thus, the Helmholtz free energy reads

$$\psi = \breve{\psi}\left(\boldsymbol{C}_e\right). \tag{6.67}$$

Inserting the above energy into the dissipation inequality $-\dot{\psi} + \frac{1}{2}\boldsymbol{S} : \dot{\boldsymbol{C}} \geq 0$ leads to the following expression

$$\left(\boldsymbol{S} - 2\,\boldsymbol{F}_i^{-1}\frac{\partial\breve{\psi}}{\partial\boldsymbol{C}_e}\boldsymbol{F}_i^{-T}\right) : \frac{1}{2}\dot{\boldsymbol{C}} + \underbrace{2\,\boldsymbol{C}_e\frac{\partial\breve{\psi}}{\partial\boldsymbol{C}_e}}_{=:\breve{\boldsymbol{\Sigma}}} : \boldsymbol{D}_i \geq 0. \tag{6.68}$$

Following the arguments of Coleman and Noll [1961] and under consideration of $\breve{\psi}$ being an *isotropic function*, the general expression for $\boldsymbol{S}$ and $\breve{\boldsymbol{\Sigma}}$ are obtained as

$$\boldsymbol{S} = 2\left(\alpha_1\,\boldsymbol{C}_i^{-1} + \alpha_2\,\boldsymbol{C}_i^{-1}\boldsymbol{C}\boldsymbol{C}_i^{-1} + \alpha_3\,\boldsymbol{C}_i^{-1}\left(\boldsymbol{C}\boldsymbol{C}_i^{-1}\right)^2\right) \tag{6.69}$$

$$\breve{\boldsymbol{\Sigma}} = 2\left(\alpha_1\,\boldsymbol{F}_i^{-T}\boldsymbol{C}\boldsymbol{F}_i^{-1} + \alpha_2\,\boldsymbol{F}_i^{-T}\boldsymbol{C}\boldsymbol{C}_i^{-1}\boldsymbol{C}\boldsymbol{F}_i^{-1} + \alpha_3\,\boldsymbol{F}_i^{-T}\left(\boldsymbol{C}\boldsymbol{C}_i^{-1}\right)^2\boldsymbol{C}\boldsymbol{F}_i^{-1}\right) \tag{6.70}$$

with $\alpha_i = i\,\frac{\partial\breve{\psi}}{\partial\mathrm{tr}(\boldsymbol{C}_e^i)}$. The Mandel-like stress tensor $\breve{\boldsymbol{\Sigma}}$ can be related to the Kirchhoff stress tensor $\boldsymbol{\tau} = \boldsymbol{F}\boldsymbol{S}\boldsymbol{F}^T = 2\,\boldsymbol{F}_e\frac{\partial\breve{\psi}}{\partial\breve{\boldsymbol{C}}_e}\boldsymbol{F}_e^T$ by $\breve{\boldsymbol{\Sigma}} = \boldsymbol{F}_e^T\boldsymbol{\tau}\boldsymbol{F}_e^{-T}$. Hence, both share the same eigenvalues. Consequently, a *scalar-valued isotropic function* of $\breve{\boldsymbol{\Sigma}}$ can be interpreted analogously in terms of $\boldsymbol{\tau}$.

It is obvious that $\boldsymbol{F}_i$ is required in order to compute $\breve{\boldsymbol{\Sigma}}$, however, $\boldsymbol{F}_i$ is not unique. As common practice in elasto-plasticity or visco-elasticity, the evolution law is derived from a potential g_i depending on the invariants of the thermodynamic driving force. This potential itself is assumed to be an *isotropic function*, resulting in the following expression for the inelastic rate

$$\boldsymbol{D}_i = \dot{\gamma}\,\frac{\partial g_i}{\partial\breve{\boldsymbol{\Sigma}}} = \dot{\gamma}\,\left(\beta_1\,\boldsymbol{I} + \beta_2\,\breve{\boldsymbol{\Sigma}} + \beta_3\,\breve{\boldsymbol{\Sigma}}^2\right) \tag{6.71}$$

with $\dot{\gamma}$ being some rate quantity and $\beta_i = i\,\frac{\partial g_i}{\partial\mathrm{tr}(\boldsymbol{\Sigma}^i)}$. Hence, the computation of $\boldsymbol{D}_i$ requires $\boldsymbol{F}_i$ as well. In order to stay within this 'classical' framework, several pull-backs are necessary, which will be briefly presented in the following. At first, one notices the relation $\breve{\boldsymbol{\Sigma}} = \boldsymbol{C}_e\boldsymbol{F}_i\boldsymbol{S}\boldsymbol{F}_i^T$.

With this at hand, it is easy to show that the invariants of $\breve{\boldsymbol{\Sigma}}$ can be expressed as

$$\operatorname{tr}\left(\breve{\boldsymbol{\Sigma}}^k\right) = \operatorname{tr}\left(\left(\boldsymbol{F}_i^T \boldsymbol{C}_e \boldsymbol{F}_i \boldsymbol{S}\right)^k\right) = \operatorname{tr}\left((\boldsymbol{C}\boldsymbol{S})^k\right), \quad k \in \{1,2,3\} \tag{6.72}$$

which do not require $\boldsymbol{F}_i$. Next, having the relation $\dot{\boldsymbol{C}}_i = 2\boldsymbol{F}_i^T \boldsymbol{D}_i \boldsymbol{F}_i$ in mind, the evolution law can be pulled-back and rewritten as

$$\dot{\boldsymbol{C}}_i = 2\dot{\gamma}\, \boldsymbol{F}_i^T \frac{\partial g_i}{\partial \breve{\boldsymbol{\Sigma}}} \boldsymbol{F}_i = 2\dot{\gamma}\, \left(\beta_1\, \boldsymbol{C}_i + \beta_2\, \boldsymbol{F}_i^T \breve{\boldsymbol{\Sigma}} \boldsymbol{F}_i + \beta_3\, \boldsymbol{F}_i^T \breve{\boldsymbol{\Sigma}}^2 \boldsymbol{F}_i\right) \tag{6.73}$$

with

$$\boldsymbol{F}_i^T \breve{\boldsymbol{\Sigma}} \boldsymbol{F}_i = 2\left(\alpha_1\, \boldsymbol{C} + \alpha_2\, \boldsymbol{C}\boldsymbol{C}_i^{-1}\boldsymbol{C} + \alpha_3\, \left(\boldsymbol{C}\boldsymbol{C}_i^{-1}\right)^2 \boldsymbol{C}\right). \tag{6.74}$$

The latter can be expressed in terms of $\boldsymbol{C}$ and $\boldsymbol{C}_i$. Note that a similar result can be found for $\boldsymbol{F}_i^T \breve{\boldsymbol{\Sigma}}^2 \boldsymbol{F}_i$. Thus, the rate of $\boldsymbol{C}_i$ does not require $\boldsymbol{F}_i$.

6.8.2 Different mappings of structural tensor

In the following, three different mappings of the structural tensor $\boldsymbol{H}$ in addition to the one presented in Equation (6.10) from the reference configuration to the cic are considered (cf. Dafalias [1987]). Therefore, the Helmholtz free energy is assumed as follows

$$\psi = \psi'(\bar{\boldsymbol{C}}_e, \bar{\boldsymbol{H}}). \tag{6.75}$$

The corresponding reduced dissipation inequalities (cf. Equation (6.24)) are obtained as:

1. $\bar{\boldsymbol{H}} = \boldsymbol{U}_i^{-1} \boldsymbol{H} \boldsymbol{U}_i^{-1}$ ($\breve{\boldsymbol{H}} = \boldsymbol{F}_i^{-T} \boldsymbol{H} \boldsymbol{F}_i^{-1}$):

$$\mathscr{D}_{\mathrm{red}} := \left(2\,\bar{\boldsymbol{C}}_e \frac{\partial \psi'}{\partial \bar{\boldsymbol{C}}_e} + 2\,\bar{\boldsymbol{H}} \frac{\partial \psi'}{\partial \bar{\boldsymbol{H}}}\right) : \bar{\boldsymbol{D}}_i - \boldsymbol{U}_i^{-1} \frac{\partial \psi'}{\partial \bar{\boldsymbol{H}}} \boldsymbol{U}_i^{-1} : \dot{\boldsymbol{H}} \geq 0 \tag{6.76}$$

2. $\bar{\boldsymbol{H}} = \boldsymbol{U}_i \boldsymbol{H} \boldsymbol{U}_i^{-1}$ ($\breve{\boldsymbol{H}} = \boldsymbol{F}_i \boldsymbol{H} \boldsymbol{F}_i^{-1}$):

$$\mathscr{D}_{\mathrm{red}} := \left(2\,\bar{\boldsymbol{C}}_e \frac{\partial \psi'}{\partial \bar{\boldsymbol{C}}_e} - \frac{\partial \psi'}{\partial \bar{\boldsymbol{H}}} \bar{\boldsymbol{H}}^T + \bar{\boldsymbol{H}}^T \frac{\partial \psi'}{\partial \bar{\boldsymbol{H}}}\right) : \bar{\boldsymbol{L}}_i - \boldsymbol{U}_i \frac{\partial \psi'}{\partial \bar{\boldsymbol{H}}} \boldsymbol{U}_i^{-1} : \dot{\boldsymbol{H}} \geq 0 \tag{6.77}$$

3. $\bar{\boldsymbol{H}} = \boldsymbol{U}_i^{-1}\boldsymbol{H}\boldsymbol{U}_i$ ($\breve{\boldsymbol{H}} = \boldsymbol{F}_i^{-T}\boldsymbol{H}\boldsymbol{F}_i^{T}$):

$$\mathscr{D}_{\text{red}} := \left(2\,\bar{\boldsymbol{C}}_e\frac{\partial\psi'}{\partial\bar{\boldsymbol{C}}_e} + \bar{\boldsymbol{H}}\left(\frac{\partial\psi'}{\partial\bar{\boldsymbol{H}}}\right)^T - \left(\frac{\partial\psi'}{\partial\bar{\boldsymbol{H}}}\right)^T\bar{\boldsymbol{H}}\right) : \bar{\boldsymbol{L}}_i - \boldsymbol{U}_i^{-1}\frac{\partial\psi'}{\partial\bar{\boldsymbol{H}}}\boldsymbol{U}_i : \dot{\boldsymbol{H}} \geq 0 \tag{6.78}$$

6.8.3 Invariants

The invariants in the intermediate configuration can be expressed in terms of cic quantities as follows

$$\operatorname{tr}\left(\boldsymbol{C}_e^k\right) = \operatorname{tr}\left(\bar{\boldsymbol{C}}_e^k\right),\ \operatorname{tr}\left(\boldsymbol{B}_i^k\right) = \operatorname{tr}\left(\boldsymbol{C}_i^k\right),\ k \in \{1,2,3\} \tag{6.79}$$

$$\operatorname{tr}\left(\boldsymbol{B}_{i_b}^k\right) = \operatorname{tr}\left(\bar{\boldsymbol{B}}_{i_b}^k\right),\ \operatorname{tr}\left(\breve{\boldsymbol{H}}^k\right) = \operatorname{tr}\left(\bar{\boldsymbol{H}}^k\right),\ k \in \{1,2,3\} \tag{6.80}$$

$$\operatorname{tr}\left(\boldsymbol{C}_e^a\boldsymbol{B}_i^b\boldsymbol{B}_{i_b}^c\breve{\boldsymbol{H}}^d\right) = \operatorname{tr}\left(\bar{\boldsymbol{C}}_e^a\boldsymbol{C}_i^b\bar{\boldsymbol{B}}_{i_b}^c\bar{\boldsymbol{H}}^d\right),\quad a,b,c,d \in \{0,1,2\} \tag{6.81}$$

where the 'structure' of the invariants is maintained. Alternatively, one may investigate the characteristic polynomial, for instance,

$$p_1(\lambda_A) = \det\left(\boldsymbol{C}_e - \lambda_A\boldsymbol{I}\right) = \det\left(\boldsymbol{R}_i\left[\bar{\boldsymbol{C}}_e - \lambda_A\boldsymbol{I}\right]\boldsymbol{R}_i^{-1}\right) = \det\left(\bar{\boldsymbol{C}}_e - \lambda_A\boldsymbol{I}\right) \tag{6.82}$$

or

$$p_2(\lambda_B) = \det\left(\boldsymbol{C}_e\boldsymbol{B}_p - \lambda_B\boldsymbol{I}\right) = \det\left(\boldsymbol{R}_i\left[\bar{\boldsymbol{C}}_e\boldsymbol{C}_p - \lambda_B\boldsymbol{I}\right]\boldsymbol{R}_i^{-1}\right) = \det\left(\bar{\boldsymbol{C}}_e\boldsymbol{C}_p - \lambda_B\boldsymbol{I}\right) \tag{6.83}$$

and so forth.

6.8.4 Modeling inelastic strains Euler-Almansi-like

The Green-Lagrange strain tensor $\boldsymbol{E} := \frac{1}{2}\left(\boldsymbol{C} - \boldsymbol{I}\right)$ is pushed to the Euler-Almansi strain tensor by $\boldsymbol{A} := \boldsymbol{F}^{-T}\boldsymbol{E}\boldsymbol{F}^{-1} = \frac{1}{2}\left(\boldsymbol{I} - \boldsymbol{B}^{-1}\right)$. Hence, its counterpart in the intermediate configuration $\boldsymbol{F}_i^{-T}\boldsymbol{E}\boldsymbol{F}_i^{-1} = \frac{1}{2}\left(\boldsymbol{C}_e - \boldsymbol{I}\right) + \frac{1}{2}\left(\boldsymbol{I} - \boldsymbol{B}_i^{-1}\right) =: \boldsymbol{E}_e + \boldsymbol{A}_i$ additively decouples elastic and inelastic strains. Here, the inelastic strains are modeled Euler-Almansi-like. In this regard, the cic strains read $\boldsymbol{R}_i^{-1}\boldsymbol{E}_e\boldsymbol{R}_i = \frac{1}{2}\left(\bar{\boldsymbol{C}}_e - \boldsymbol{I}\right)$ as well as $\boldsymbol{R}_i^{-1}\boldsymbol{A}_i\boldsymbol{R}_i = \frac{1}{2}\left(\boldsymbol{I} - \boldsymbol{C}_i^{-1}\right)$. Thus, it is more convenient to express the Helmholtz free energy as

$$\psi = \tilde{\bar{\psi}}\left(\bar{\boldsymbol{C}}_e, \boldsymbol{C}_i^{-1}\right). \tag{6.84}$$

With the relation $\dot{\boldsymbol{C}}_i^{-1} = -\boldsymbol{C}_i^{-1}\dot{\boldsymbol{C}}_i\boldsymbol{C}_i^{-1}$ at hand and in comparison with Equations (6.24) and (6.25), the following is found

$$\mathscr{D}_{\mathrm{red}} \coloneqq \left(2\,\bar{\boldsymbol{C}}_e \frac{\partial \bar{\tilde{\psi}}}{\partial \bar{\boldsymbol{C}}_e} + 2\,\boldsymbol{C}_i^{-1} \frac{\partial \bar{\tilde{\psi}}}{\partial \boldsymbol{C}_i^{-1}} \right) : \bar{\boldsymbol{D}}_i \geq 0 \tag{6.85}$$

where the term in brackets is still symmetric (cf. the first mapping presented in Appendix 6.8.2).

6.8.5 Elasto-plastic and visco-elastic model in the cic framework

Elasto-plasticity. In the following, the equations to derive the model presented by Vladimirov et al. [2008] in the context of the cic framework shortly summarized. For all material parameters occurring in the following, reference is made to the latter mentioned work. Moreover, due to brevity, the effect of isotropic hardening is neglected, however, this is straightforward to add. Vladimirov et al. [2008] account for nonlinear kinematic hardening, thus, the additional decomposition of $\boldsymbol{F}_i$ is required (cf. Equation (6.8)). The Helmholtz free energy reads

$$\begin{aligned} \psi = \frac{\mu}{2}\left(\mathrm{tr}\left(\bar{\boldsymbol{C}}_e\right) - 3 - \ln\left(\det\left(\bar{\boldsymbol{C}}_e\right)\right)\right) + \frac{\Lambda}{4}\left(\det\left(\bar{\boldsymbol{C}}_e\right) - 1 - \ln\left(\det\left(\bar{\boldsymbol{C}}_e\right)\right)\right) \\ + \frac{c}{2}\left(\mathrm{tr}\left(\bar{\boldsymbol{B}}_{i_b}\right) - 3 - \ln\left(\det\left(\bar{\boldsymbol{B}}_{i_b}\right)\right)\right). \end{aligned} \tag{6.86}$$

In addition, the following yield criterion Φ as well as the potential g_{kin}, which describes the evolution of nonlinear kinematic hardening are prescribed

$$\Phi \coloneqq \sqrt{\frac{3}{2}}\,\|\mathrm{dev}\left(\bar{\boldsymbol{\Gamma}}\right)\| - \sigma_y \leq 0, \quad \bar{\boldsymbol{\Gamma}} \coloneqq \bar{\boldsymbol{\Sigma}} - \bar{\boldsymbol{\chi}} \tag{6.87}$$

$$g_{kin} \coloneqq \frac{b}{2\,c}\,\mathrm{tr}\left(\mathrm{dev}\left(\check{\boldsymbol{\Theta}}\right)^2\right). \tag{6.88}$$

Thus, the evolution equations for both $\bar{\boldsymbol{D}}_i$ and $\check{\boldsymbol{D}}_{i_a}$ are obtained as

$$\bar{\boldsymbol{D}}_i = \dot{\gamma}\,\frac{\partial \Phi}{\partial \bar{\boldsymbol{\Gamma}}} \tag{6.89}$$

$$\check{\boldsymbol{D}}_{i_a} = \dot{\gamma}\,\frac{\partial g_{kin}}{\partial \check{\boldsymbol{\Theta}}} \tag{6.90}$$

with the plastic multiplier $\dot{\gamma}$.

Visco-elasticity. In addition, the equations needed to derive the model of Reese and Govindjee [1998] in the cic context are briefly provided. For the Helmholtz free energy, the model of

Ogden and Hill [1972] is utilized, i.e.

$$\psi = \sum_{r=1}^{3} \frac{(\mu_m)_r}{(\alpha_m)_r} \left(\omega_{e_1}^{\frac{(\alpha_m)_r}{2}} + \omega_{e_2}^{\frac{(\alpha_m)_r}{2}} + \omega_{e_3}^{\frac{(\alpha_m)_r}{2}} - 3 \right) + \frac{K_m}{4} \left(\det\left(\bar{\boldsymbol{C}}_e\right) - 1 - \ln\left(\det\left(\bar{\boldsymbol{C}}_e\right)\right) \right)$$
$$+ \sum_{r=1}^{3} \frac{(\mu)_r}{(\alpha)_r} \left(\omega_1^{\frac{(\alpha)_r}{2}} + \omega_2^{\frac{(\alpha)_r}{2}} + \omega_3^{\frac{(\alpha)_r}{2}} - 3 \right) + \frac{K}{4} \left(\det\left(\boldsymbol{C}\right) - 1 - \ln\left(\det\left(\boldsymbol{C}\right)\right) \right) \tag{6.91}$$

where again reference is made to the original work for material parameters' meaning. Further, ω_{e_i} denote the eigenvalues of $\left(\det\left(\bar{\boldsymbol{C}}_e\right)^{-\frac{1}{3}}\right)\bar{\boldsymbol{C}}_e$ and ω_i the eigenvalues of $\left(\det\left(\boldsymbol{C}\right)^{-\frac{1}{3}}\right)\boldsymbol{C}$. The set of constitutive equations is closed by the definition of a dissipative potential

$$\bar{g}_i = \frac{1}{4\,\mu_m} \operatorname{tr}\left(\operatorname{dev}\left(\bar{\boldsymbol{\Gamma}}\right)^2\right) + \frac{1}{18\,K_m} \operatorname{tr}\left(\bar{\boldsymbol{\Gamma}}\right)^2, \quad \bar{\boldsymbol{\Gamma}} \equiv \bar{\boldsymbol{\Sigma}} \tag{6.92}$$

as well as the evolution equation

$$\bar{\boldsymbol{D}}_i = \frac{1}{\tau} \frac{\partial \bar{g}_i}{\partial \bar{\boldsymbol{\Gamma}}} \tag{6.93}$$

with the relaxation time τ and $\mu_m = \frac{1}{2}\sum_{r=1}^{3}(\mu_m)_r\,(\alpha_m)_r$.

6.8.6 Rate of $\bar{\boldsymbol{M}}$

The rate of $\bar{\boldsymbol{M}}$ (6.30) reads

$$\dot{\bar{\boldsymbol{M}}} = \frac{1}{\boldsymbol{C}_{g_{co}} : \boldsymbol{M}} \boldsymbol{U}_{g_{co}} \dot{\boldsymbol{M}} \boldsymbol{U}_{g_{co}} + \underbrace{\dot{\boldsymbol{U}}_{g_{co}} \boldsymbol{U}_{g_{co}}^{-1}}_{=:\bar{\boldsymbol{L}}_{g_{co}}} \underbrace{\boldsymbol{U}_{g_{co}} \boldsymbol{M} \boldsymbol{U}_{g_{co}} \frac{1}{\boldsymbol{C}_{g_{co}} : \boldsymbol{M}}}_{=\bar{\boldsymbol{M}}} + \bar{\boldsymbol{M}} \bar{\boldsymbol{L}}_{g_{co}}^T$$
$$+ \overline{\left(\frac{1}{\boldsymbol{C}_{g_{co}} : \boldsymbol{M}} \right)^{\cdot}} \boldsymbol{U}_{g_{co}} \boldsymbol{M} \boldsymbol{U}_{g_{co}} \tag{6.94}$$

with

$$\overline{\left(\frac{1}{\boldsymbol{C}_{g_{co}} : \boldsymbol{M}} \right)^{\cdot}} = -\frac{1}{\left(\boldsymbol{C}_{g_{co}} : \boldsymbol{M}\right)^2} \left(\dot{\boldsymbol{C}}_{g_{co}} : \boldsymbol{M} + \boldsymbol{C}_{g_{co}} : \dot{\boldsymbol{M}} \right). \tag{6.95}$$

The term in brackets can be rewritten using Equation (6.20) as

$$\left(\dot{\boldsymbol{C}}_{g_{co}} : \boldsymbol{M} + \boldsymbol{C}_{g_{co}} : \dot{\boldsymbol{M}} \right) = \left(2\bar{\boldsymbol{L}}_{g_{co}} : \boldsymbol{U}_{g_{co}} \boldsymbol{M} \boldsymbol{U}_{g_{co}} + \boldsymbol{C}_{g_{co}} : \dot{\boldsymbol{M}} \right) \tag{6.96}$$

with $2\bar{\boldsymbol{L}}_{g_{co}} : \boldsymbol{U}_{g_{co}}\boldsymbol{M}\boldsymbol{U}_{g_{co}} = 2\bar{\boldsymbol{D}}_{g_{co}} : \boldsymbol{U}_{g_{co}}\boldsymbol{M}\boldsymbol{U}_{g_{co}}$. Hence, the final result is obtained as

$$\dot{\bar{\boldsymbol{M}}} = \frac{1}{\boldsymbol{C}_{g_{co}} : \boldsymbol{M}}\boldsymbol{U}_{g_{co}}\dot{\boldsymbol{M}}\boldsymbol{U}_{g_{co}} + \bar{\boldsymbol{L}}_{g_{co}}\bar{\boldsymbol{M}} + \bar{\boldsymbol{M}}\bar{\boldsymbol{L}}_{g_{co}}^{T} - \left(2\bar{\boldsymbol{L}}_{g_{co}} : \bar{\boldsymbol{M}} + \frac{\boldsymbol{C}_{g_{co}} : \dot{\boldsymbol{M}}}{\boldsymbol{C}_{g_{co}} : \boldsymbol{M}}\right)\bar{\boldsymbol{M}}. \quad (6.97)$$

6.8.7 Choice of $\tilde{n}_{\text{target}}$ and its derivative

Algorithm 2 describes the procedure to decide which eigenvector of $\tilde{\boldsymbol{\tau}}$ is chosen. Moreover, the derivative of the eigenvector $\boldsymbol{n}_{\tilde{\boldsymbol{\tau}}_i}$, and thus, also the derivative of $\tilde{\boldsymbol{n}}_{\text{target}}$ with respect to $\tilde{\boldsymbol{\tau}}$ is defined in Equation (6.98). Since this derivative tends to infinity if $\tau_a = \tau_b$, a small perturbation is included in order to avoid numerical instabilities. Noteworthy, the chosen perturbation is in analogy to Miehe [1993].

Algorithm 2 Set $\tilde{\boldsymbol{n}}_{\text{target}}$

Input: $\tilde{\boldsymbol{\tau}}$, $\tilde{\boldsymbol{n}}$
Output: $\tilde{\boldsymbol{n}}_{target}$
▷ calculate spectral decomposition of $\tilde{\boldsymbol{\tau}}$ into eigenvalues $\tau_1 \leq \tau_2 \leq \tau_3$ and eigenvectors $\boldsymbol{n}_{\tilde{\boldsymbol{\tau}}_1}$, $\boldsymbol{n}_{\tilde{\boldsymbol{\tau}}_2}$, $\boldsymbol{n}_{\tilde{\boldsymbol{\tau}}_3}$
if $\tau_1 \leq \tau_2 \leq \tau_3 < 0$ **then**
  ▷ no maximal eigenvalue, stress state under compression
  $\tilde{\boldsymbol{n}}_{target} \leftarrow \tilde{\boldsymbol{n}}$
else if $\tau_1 \leq \tau_2 < \tau_3$ and $\tau_3 > 0$ **then**
  ▷ one maximal eigenvalue, stress state under tension
  if $\sphericalangle(\tilde{\boldsymbol{n}}, \boldsymbol{n}_{\tilde{\boldsymbol{\tau}}_3}) < \sphericalangle(\tilde{\boldsymbol{n}}, -\boldsymbol{n}_{\tilde{\boldsymbol{\tau}}_3})$ **then**
    $\tilde{\boldsymbol{n}}_{target} \leftarrow \boldsymbol{n}_{\tilde{\boldsymbol{\tau}}_3}$
  else
    ▷ enclosed angle is obtuse
    $\boldsymbol{n}_{\tilde{\boldsymbol{\tau}}_3} \leftarrow -\boldsymbol{n}_{\tilde{\boldsymbol{\tau}}_3}$
    $\tilde{\boldsymbol{n}}_{target} \leftarrow \boldsymbol{n}_{\tilde{\boldsymbol{\tau}}_3}$
  end if
else if $\tau_1 = \tau_3$ or $\tau_2 = \tau_3$ or $\tau_1 = \tau_2 = \tau_3$ and $\tau_3 > 0$ **then**
  ▷ several maximal eigenvalues, stress state under tension
  ▷ find smallest angle α_i for all $\tau_i > 0$ between eigenvector and structural vector
  $\alpha_i = \sphericalangle(\tilde{\boldsymbol{n}}, \boldsymbol{n}_{\tilde{\boldsymbol{\tau}}_i})$
  if $\sphericalangle(\tilde{\boldsymbol{n}}, \boldsymbol{n}_{\tilde{\boldsymbol{\tau}}_i}) > \sphericalangle(\tilde{\boldsymbol{n}}, -\boldsymbol{n}_{\tilde{\boldsymbol{\tau}}_i})$ **then**
    ▷ enclosed angle is obtuse
    $\boldsymbol{n}_{\tilde{\boldsymbol{\tau}}_i} \leftarrow -\boldsymbol{n}_{\tilde{\boldsymbol{\tau}}_i}$
    $\alpha_i = \sphericalangle(\tilde{\boldsymbol{n}}, \boldsymbol{n}_{\tilde{\boldsymbol{\tau}}_i})$
  end if
  $\tilde{\boldsymbol{n}}_{target} \leftarrow \boldsymbol{n}_{\tilde{\boldsymbol{\tau}}_i}(\min \alpha_i)$
end if

$$\frac{\partial \boldsymbol{n}_{\tilde{\tau}_a}}{\partial \tilde{\boldsymbol{\tau}}} = \frac{1}{2}\sum_{\substack{b=1 \\ b\neq a}}^{3} \frac{1}{\tau_a(1+\epsilon)-\tau_b(1-\epsilon)} \boldsymbol{n}_{\tilde{\tau}_b} \otimes (\boldsymbol{n}_{\tilde{\tau}_a} \otimes \boldsymbol{n}_{\tilde{\tau}_b} + \boldsymbol{n}_{\tilde{\tau}_b} \otimes \boldsymbol{n}_{\tilde{\tau}_a}) \tag{6.98}$$

with

$$\epsilon = \begin{cases} 0 & , \tau_a \neq \tau_b \\ 10^{-8} & , \tau_a = \tau_b \end{cases}. \tag{6.99}$$

6.8.8 Evolution equation of current structural vector

As mentioned in Section 6.4.3.3, a physically reasonable evolution equation of the structural vector should be stated in terms of $\boldsymbol{n}_{cc}$. Since the latter is defined with respect to the cc, an objective rate must be considered for its evolution equation. Therefore, the following Green-Naghdi-like rate is introduced between the crc and cc

$$\mathring{\boldsymbol{n}}_{cc} = \boldsymbol{R}\left[\frac{\mathrm{d}}{\mathrm{d}t}\left(\underbrace{\boldsymbol{R}^{-1}\boldsymbol{n}_{cc}}_{=\tilde{\boldsymbol{n}}}\right)\right] = \dot{\boldsymbol{n}}_{cc} - \dot{\boldsymbol{R}}\boldsymbol{R}^{-1}\,\boldsymbol{n}_{cc} = \boldsymbol{R}\,\dot{\tilde{\boldsymbol{n}}}. \tag{6.100}$$

It should be noted that in contrast to the classical Green-Naghdi rate, one does not have to assume $\boldsymbol{U} = \boldsymbol{I}$. With this latter objective rate at hand, the following evolution equation is introduced

$$\mathring{\boldsymbol{n}}_{cc} = \underbrace{\frac{\pi}{2\eta_s}\left(\boldsymbol{n}_{cc} \times \boldsymbol{n}_{\text{target}}\right)}_{=:\boldsymbol{\omega}} \times \boldsymbol{n}_{cc}. \tag{6.101}$$

In analogy to Section 6.4.3.3, the skew-symmetric tensor $\boldsymbol{\Omega} = \sum_{i=1}^{3}(\boldsymbol{\omega} \times \boldsymbol{e}_i) \otimes \boldsymbol{e}_i$ is defined. The latter evolution equation is rewritten as

$$\dot{\boldsymbol{n}}_{cc} = \left(\boldsymbol{\Omega} + \dot{\boldsymbol{R}}\boldsymbol{R}^{-1}\right)\boldsymbol{n}_{cc} \tag{6.102}$$

which fulfills the orthogonality condition $\boldsymbol{n}_{cc} \cdot \dot{\boldsymbol{n}}_{cc} = 0$, since $\dot{\boldsymbol{R}}\boldsymbol{R}^{-1}$ is skew-symmetric as well. In order to derive the evolution equation of $\tilde{\boldsymbol{n}}$ (6.55), Equations (6.100) and (6.101) are combined

$$\dot{\tilde{\boldsymbol{n}}} = \frac{\pi}{2\eta_s}\,\boldsymbol{R}^{-1}\left(\left(\boldsymbol{n}_{cc} \times \boldsymbol{n}_{\text{target}}\right) \times \boldsymbol{n}_{cc}\right). \tag{6.103}$$

Since the cross product obeys the following identity $\boldsymbol{Q}\,(\boldsymbol{a} \times \boldsymbol{b}) = ((\boldsymbol{Q}\boldsymbol{a}) \times (\boldsymbol{Q}\boldsymbol{b}))$ for any $\boldsymbol{Q} \in \mathrm{SO}(3)$, and considering $\tilde{\boldsymbol{n}} = \boldsymbol{R}^{-1}\boldsymbol{n}_{cc}$ as well as $\tilde{\boldsymbol{n}}_{\text{target}} = \boldsymbol{R}^{-1}\boldsymbol{n}_{\text{target}}$, Equation (6.55) is

regained

$$\dot{\tilde{\boldsymbol{n}}} = \frac{\pi}{2\eta_s}\left((\boldsymbol{R}^{-1}\boldsymbol{n}_{cc}) \times (\boldsymbol{R}^{-1}\boldsymbol{n}_{\text{target}})\right) \times (\boldsymbol{R}^{-1}\boldsymbol{n}_{cc}) = \frac{\pi}{2\eta_s}\left(\tilde{\boldsymbol{n}} \times \tilde{\boldsymbol{n}}_{\text{target}}\right) \times \tilde{\boldsymbol{n}}. \tag{6.104}$$

6.8.9 Single Gaussian point concept (enhanced Q1STc)

To begin with, the two-field functional solved during the iterative solution procedure is denoted by

$$g_u^c\left(\boldsymbol{u}, \boldsymbol{w}, \delta\boldsymbol{u}\right) \coloneqq \int_{\mathcal{B}_0} \boldsymbol{S}(\boldsymbol{E}) : \delta\boldsymbol{E}_c \,\mathrm{d}V - \int_{\mathcal{B}_0} \boldsymbol{f}_0 \cdot \delta\boldsymbol{u} \,\mathrm{d}V - \int_{\partial_t\mathcal{B}_0} \boldsymbol{t}_0 \cdot \delta\boldsymbol{u} \,\mathrm{d}A = 0 \tag{6.105}$$

$$g_w\left(\boldsymbol{u}, \boldsymbol{w}, \delta\boldsymbol{u}\right) \coloneqq \int_{\mathcal{B}_0} \boldsymbol{S}(\boldsymbol{E}) : \delta\boldsymbol{E}_e \,\mathrm{d}V = 0 \tag{6.106}$$

with the incompatible displacement field $\boldsymbol{w}$. Moreover, the (total) Green-Lagrange strain tensor $\boldsymbol{E} = \boldsymbol{E}_c + \boldsymbol{E}_e$ is assumed to be additively decomposable into a compatible part $\boldsymbol{E}_c(\boldsymbol{u}) = \frac{1}{2}\left(\boldsymbol{F}^{e^T}\boldsymbol{F}^e - \boldsymbol{I}\right)$ as well as an incompatible part $\boldsymbol{E}_e(\boldsymbol{w})$. The deformation gradient at the element level $\boldsymbol{F}^e$ is obtained using AD (cf. Equation (6.111)).
For discretization, the problem's approximated domain $\mathcal{B}_0^h$ is divided into n_{el} elements

$$\mathcal{B}_0 \approx \mathcal{B}_0^h = \bigcup_{e=1}^{n_{el}} \mathcal{B}_0^e \tag{6.107}$$

where an isoparametric approach is followed for the (initial) geometry ($\boldsymbol{x}^e$) and displacement ($\boldsymbol{u}^e$) of the eight-node hexahedral elements, i.e.

$$\boldsymbol{u}^e = \mathbf{N}\left(\boldsymbol{\xi}\right)\mathbf{u}^e, \quad \boldsymbol{x}^e = \mathbf{N}\left(\boldsymbol{\xi}\right)\mathbf{x}^e. \tag{6.108}$$

In the latter equation, $\mathbf{u}^e$ contains the element nodal values of displacement and $\mathbf{x}^e$ its nodal positions, respectively. Additionally, $\boldsymbol{\xi} = (\xi, \eta, \zeta)^T$ contains the natural coordinates with respect to the isoparameteric space, while the trilinear shape functions N_i are arranged within the shape function matrix

$$\mathbf{N} = \left(N_1\,\boldsymbol{I}, \ldots, N_8\,\boldsymbol{I}\right). \tag{6.109}$$

With these formulas at hand, the Jacobian matrices with respect to the referential and current positions are obtained as

$$\mathbf{J} = \frac{\hat{\delta}\boldsymbol{x}^e}{\hat{\delta}\boldsymbol{\xi}}, \quad \mathbf{J}_{cur} = \frac{\hat{\delta}\left(\boldsymbol{x}^e + \boldsymbol{u}^e\right)}{\hat{\delta}\boldsymbol{\xi}} \tag{6.110}$$

which allow to compute the deformation according to

$$\boldsymbol{F}^e = \mathbf{J}_{cur}\,\mathbf{J}^{-1}. \tag{6.111}$$

It remains to define the incompatible part of the Green-Lagrange strain tensor, which is given in Nye's notation by

$$\hat{\boldsymbol{E}}^e = \mathbf{T}\Big|_{\boldsymbol{\xi}=\mathbf{0}}\,\mathbf{B}^e\,\mathbf{w}^e \tag{6.112}$$

where $\mathbf{w}^e = (w_1, w_2, w_3, w_4, w_5, w_6)^T$ contains the six enhanced degrees of freedom and $\mathbf{T}$ transforms from the isoparametric to the Lagrangian space[20], which is evaluated at the element's center for reasons discussed in Barfusz, Brepols, van der Velden, Frischkorn and Reese [2021]. Furthermore, the enhanced B-Operator is defined as

$$\mathbf{B}^e \coloneqq \begin{pmatrix} 0 & 0 & 0 & 0 & 0 & 0 \\ 0 & 0 & 0 & 0 & 0 & 0 \\ 0 & 0 & 0 & 0 & 0 & 0 \\ \eta & \xi & 0 & 0 & 0 & 0 \\ 0 & 0 & \zeta & \eta & 0 & 0 \\ 0 & 0 & 0 & 0 & \xi & \zeta \end{pmatrix}. \tag{6.113}$$

In order to eliminate various locking phenomena, which are widely known for low-order finite element formulations in the literature, as well as to increase the efficiency enormously by using only one instead of eight Gaussian points, and moreover, not having to store the enhanced degrees of freedom as history variables, $\boldsymbol{S}(\boldsymbol{E})$ is obtained by a Taylor series expansion up to bilinear terms with respect to the element center

$$\boldsymbol{S}(\boldsymbol{E}) \approx \boldsymbol{S}\Big|_{\boldsymbol{\xi}=\mathbf{0}} + \mathbb{C}^{hg}\left(\sum_{i=1}^{3}\frac{\hat{\delta}\boldsymbol{E}}{\hat{\delta}\xi_i}\Big|_{\boldsymbol{\xi}=\mathbf{0}}\xi_i + \frac{1}{2}\sum_{i=1}^{3}\sum_{\substack{j=1\\ j\neq i}}^{3}\left(\frac{\hat{\delta}}{\hat{\delta}\xi_j}\left(\frac{\hat{\delta}\boldsymbol{E}}{\hat{\delta}\xi_i}\right)\right)\Big|_{\boldsymbol{\xi}=\mathbf{0}}\xi_i\,\xi_j\right). \tag{6.114}$$

[20] Note that some rows and columns must be interchanged compared with the expression provided by Barfusz, Brepols, van der Velden, Frischkorn and Reese [2021], since they do not use Nye's notation.

Noteworthy, the 'correct' material tangent $\mathbb{C}$ was already substituted with its hourglass counterpart $\mathbb{C}^{hg}$ in the latter equation, which is expressed as

$$\mathbb{C}^{hg} = \frac{\mu^{hg}}{3}\begin{pmatrix} 4 & -2 & -2 & 0 & 0 & 0 \\ -2 & 4 & -2 & 0 & 0 & 0 \\ -2 & -2 & 4 & 0 & 0 & 0 \\ 0 & 0 & 0 & 3 & 0 & 0 \\ 0 & 0 & 0 & 0 & 3 & 0 \\ 0 & 0 & 0 & 0 & 0 & 3 \end{pmatrix}, \quad \mu^{hg} = \frac{1}{2}\sqrt{\frac{\mathrm{tr}\left(\mathrm{dev}\left(\boldsymbol{S}|_{\boldsymbol{\xi}=\boldsymbol{0}}\right)^2\right)}{\mathrm{tr}\left(\mathrm{dev}\left(\boldsymbol{E}|_{\boldsymbol{\xi}=\boldsymbol{0}}\right)^2\right)}}. \tag{6.115}$$

Contrary to Barfusz, Brepols, van der Velden, Frischkorn and Reese [2021], but in line with Holthusen et al. [TBA], the values of the current time step are used to calculate μ^{hg}. For solving the global Newton-Raphson scheme, the element residual as well as the element stiffness matrix are required, however, since both are consistent with the formulas in Barfusz, Brepols, van der Velden, Frischkorn and Reese [2021], they are omitted here for brevity. Nevertheless, it should be mentioned that the (algorithmic) material tangent of $\boldsymbol{S}$ with respect to $\boldsymbol{C}$ is still required for the enhanced Q1STc formulation.

6.8.10 Pseudo-codes of Models I and II

Algorithm 3 provides the pseudo-code of Model I, while the pseudo-code of Model II can be found in Algorithm 4. Note that $\frac{\hat{\delta}(\bullet)}{\hat{\delta}(\bullet)}\big|_{\boldsymbol{0}}$ is equivalent to a 'standard' partial derivative. For instance, $\frac{\hat{\delta}\,\mathrm{tr}\left(\bar{\boldsymbol{C}}_e\right)}{\hat{\delta}\boldsymbol{C}}\big|_{\boldsymbol{0}} = \boldsymbol{0}$, while $\frac{\hat{\delta}\,\mathrm{tr}\left(\bar{\boldsymbol{C}}_e\right)}{\hat{\delta}\boldsymbol{C}} = \boldsymbol{C}_i^{-1}$.

6.8.11 'One-surface' contour plots for cross specimen

See Figures 6.21-6.23

Algorithm 3 Implementation of Model I

Input: $\boldsymbol{C}, \hat{\boldsymbol{U}}_{g_{m_n}}, \hat{\boldsymbol{U}}_{g_{co_n}}, \tilde{\boldsymbol{n}}_n$
Output: $\boldsymbol{S}, \hat{\boldsymbol{U}}_{g_m}, \hat{\boldsymbol{U}}_{g_{co}}, \tilde{\boldsymbol{n}}, \hat{\mathbb{C}}$
$\boldsymbol{U} \leftarrow \frac{\hat{\delta}\mathscr{F}(\boldsymbol{C})}{\hat{\delta}\boldsymbol{C}}; \quad \boldsymbol{U}_{g_m} \leftarrow \hat{\boldsymbol{U}}_{g_{m_n}}; \quad \boldsymbol{U}_{g_{co}} \leftarrow \hat{\boldsymbol{U}}_{g_{co_n}}; \quad \tilde{\boldsymbol{n}} \leftarrow \tilde{\boldsymbol{n}}_n; \quad \dot{\gamma}_g \leftarrow 0$
• **Local Newton-Raphson iteration** (k)
$k \leftarrow 1$
$\mathbf{h}_{\mathrm{I}}^{(k)} \leftarrow (\hat{\boldsymbol{U}}_{g_m}, \tilde{\boldsymbol{n}}, \hat{\boldsymbol{U}}_{g_{co}}, \dot{\gamma}_g)$
while $\|\mathbf{r}_{\mathrm{I}}^{(k)}\| > tol$ **do**
$\bar{\boldsymbol{C}}_{e_m} \leftarrow \boldsymbol{U}_{g_m}^{-1}\boldsymbol{C}\boldsymbol{U}_{g_m}^{-1}; \qquad \bar{\boldsymbol{C}}_{e_{co}} \leftarrow \boldsymbol{U}_{g_{co}}^{-1}\boldsymbol{C}\boldsymbol{U}_{g_{co}}^{-1}$
$\tilde{\boldsymbol{M}} \leftarrow \tilde{\boldsymbol{n}} \otimes \tilde{\boldsymbol{n}}; \qquad \boldsymbol{M} \leftarrow \frac{1}{\boldsymbol{C}^{-1}:\tilde{\boldsymbol{M}}}\boldsymbol{U}^{-1}\tilde{\boldsymbol{M}}\boldsymbol{U}^{-1}; \qquad \bar{\boldsymbol{M}} \leftarrow \frac{1}{\boldsymbol{C}_{g_{co}}:\boldsymbol{M}}\boldsymbol{U}_{g_{co}}\boldsymbol{M}\boldsymbol{U}_{g_{co}}$
▷ Define Helmholtz free energy $\bar{\psi}$, see Equations (6.58) and (6.59)
$\bar{\boldsymbol{\Sigma}}_m \leftarrow 2\,\bar{\boldsymbol{C}}_{e_m}\frac{\hat{\delta}\bar{\psi}}{\hat{\delta}\bar{\boldsymbol{C}}_{e_m}}\Big|_{\mathbf{0}}; \qquad \bar{\boldsymbol{\Sigma}}_{co} \leftarrow 2\,\bar{\boldsymbol{C}}_{e_{co}}\frac{\hat{\delta}\bar{\psi}}{\hat{\delta}\bar{\boldsymbol{C}}_{e_{co}}}\Big|_{\mathbf{0}}$
▷ Define Φ_g and g_g, cf. Equation (6.40)
$\boldsymbol{N}_{g_m} \leftarrow \mathrm{sym}\left(\frac{\hat{\delta}g_g}{\hat{\delta}\bar{\boldsymbol{\Sigma}}_m}\Big|_{\mathbf{0}}\right); \qquad \boldsymbol{R}_{\mathrm{I}_m} \leftarrow \boldsymbol{U}_{g_{m_n}}^2 - \boldsymbol{U}_{g_m}\exp\left(-2\,\Delta t\,\dot{\gamma}_g\frac{\boldsymbol{N}_{g_m}}{\|\boldsymbol{N}_{g_m}\|}\right)\boldsymbol{U}_{g_m}$
$\boldsymbol{N}_{g_{co}} \leftarrow \mathrm{sym}\left(\frac{\hat{\delta}g_g}{\hat{\delta}\bar{\boldsymbol{\Sigma}}_{co}}\Big|_{\mathbf{0}}\right); \qquad \boldsymbol{R}_{\mathrm{I}_{co}} \leftarrow \boldsymbol{U}_{g_{co_n}}^2 - \boldsymbol{U}_{g_{co}}\exp\left(-2\,\Delta t\,\dot{\gamma}_g\frac{\boldsymbol{N}_{g_{co}}}{\|\boldsymbol{N}_{g_{co}}\|}\right)\boldsymbol{U}_{g_{co}}$
$r_{\mathrm{I}\Phi_g} \leftarrow \Phi_g - 2\sigma_g\left(\eta_g\dot{\gamma}_g\right)^{\nu_g}$
$\boldsymbol{S} \leftarrow 2\,\boldsymbol{U}_{g_m}^{-1}\frac{\hat{\delta}\bar{\psi}}{\hat{\delta}\bar{\boldsymbol{C}}_{e_m}}\Big|_{\mathbf{0}}\boldsymbol{U}_{g_m}^{-1} + 2\,\boldsymbol{U}_{g_{co}}^{-1}\frac{\hat{\delta}\bar{\psi}}{\hat{\delta}\bar{\boldsymbol{C}}_{e_{co}}}\Big|_{\mathbf{0}}\boldsymbol{U}_{g_{co}}^{-1}$
$\tilde{\boldsymbol{\tau}} \leftarrow \boldsymbol{U}\boldsymbol{S}\boldsymbol{U}$
▷ Spectral decomposition of $\tilde{\boldsymbol{\tau}}$ and define $\tilde{\boldsymbol{n}}_{target}$, see Appendix 6.8.7
$\tilde{\boldsymbol{\omega}} \leftarrow \frac{\pi}{2\eta_s}(\tilde{\boldsymbol{n}} \times \tilde{\boldsymbol{n}}_{target}); \qquad \tilde{\boldsymbol{\Omega}} \leftarrow \sum_{i=1}^{3}(\tilde{\boldsymbol{\omega}} \times \boldsymbol{e}_i) \otimes \boldsymbol{e}_i$
$\boldsymbol{r}_{\mathrm{I}n} \leftarrow \tilde{\boldsymbol{n}} - \left(\boldsymbol{I} + \frac{\sin\left(\Delta t\sqrt{\tilde{\boldsymbol{\omega}}\cdot\tilde{\boldsymbol{\omega}}}\right)}{\sqrt{\tilde{\boldsymbol{\omega}}\cdot\tilde{\boldsymbol{\omega}}}}\,\tilde{\boldsymbol{\Omega}} + \frac{1-\cos\left(\Delta t\sqrt{\tilde{\boldsymbol{\omega}}\cdot\tilde{\boldsymbol{\omega}}}\right)}{\left(\sqrt{\tilde{\boldsymbol{\omega}}\cdot\tilde{\boldsymbol{\omega}}}\right)^2}\,\tilde{\boldsymbol{\Omega}}^2\right)\tilde{\boldsymbol{n}}_n$
$\mathbf{r}_{\mathrm{I}}^{(k)} \leftarrow \left(\hat{\boldsymbol{R}}_{\mathrm{I}_m}, \hat{\boldsymbol{R}}_{\mathrm{I}_{co}}, \boldsymbol{r}_{\mathrm{I}n}, r_{\mathrm{I}\Phi_g}\right)$
$\mathbf{h}_{\mathrm{I}}^{(k+1)} \leftarrow \mathbf{h}_{\mathrm{I}}^{(k)} - \left(\frac{\hat{\delta}\mathbf{r}_{\mathrm{I}}^{(k)}}{\hat{\delta}\mathbf{h}_{\mathrm{I}}^{(k)}}\right)^{-1}\mathbf{r}_{\mathrm{I}}^{(k)}$
$k \leftarrow k+1$
end while
$\nabla\mathbf{h}_{\mathrm{I}} \leftarrow -\left(\frac{\hat{\delta}\mathbf{r}_{\mathrm{I}}^{(k)}}{\hat{\delta}\mathbf{h}_{\mathrm{I}}^{(k)}}\right)^{-1}\frac{\hat{\delta}\mathbf{r}_{\mathrm{I}}^{(k)}}{\hat{\delta}\hat{\boldsymbol{C}}}\Big|_{\frac{D\hat{\boldsymbol{U}}}{D\hat{\boldsymbol{C}}}=\frac{\hat{\delta}\hat{\boldsymbol{U}}}{\hat{\delta}\hat{\boldsymbol{C}}}}$
• **Calculate stress state and tangent operator**
$\boldsymbol{S} \leftarrow 2\,\boldsymbol{U}_{g_m}^{-1}\frac{\hat{\delta}\bar{\psi}}{\hat{\delta}\bar{\boldsymbol{C}}_{e_m}}\Big|_{\mathbf{0}}\boldsymbol{U}_{g_m}^{-1} + 2\,\boldsymbol{U}_{g_{co}}^{-1}\frac{\hat{\delta}\bar{\psi}}{\hat{\delta}\bar{\boldsymbol{C}}_{e_{co}}}\Big|_{\mathbf{0}}\boldsymbol{U}_{g_{co}}^{-1}$
$\hat{\mathbb{C}} \leftarrow \frac{\hat{\delta}\hat{\boldsymbol{S}}}{\hat{\delta}\hat{\boldsymbol{C}}}\Big|_{\frac{D\mathbf{h}_{\mathrm{I}}^{(k)}}{D\hat{\boldsymbol{C}}}=\nabla\mathbf{h}_{\mathrm{II}};\ \frac{D\hat{\boldsymbol{U}}}{D\hat{\boldsymbol{C}}}=\frac{\hat{\delta}\hat{\boldsymbol{U}}}{\hat{\delta}\hat{\boldsymbol{C}}}}$

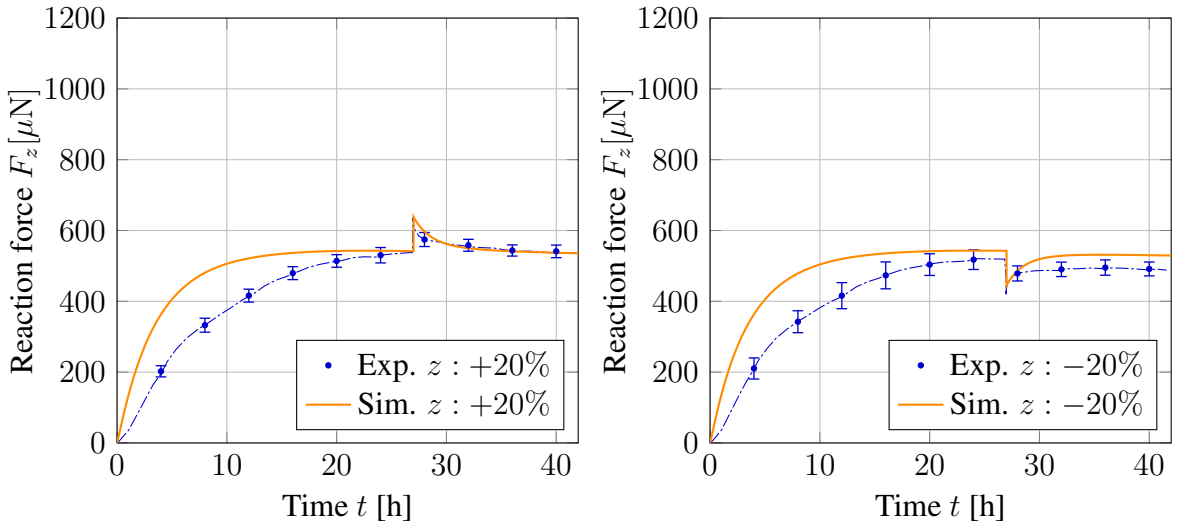

(a) 'Dog-bone' – uniaxially constraint – uniaxially loaded in one (z) direction

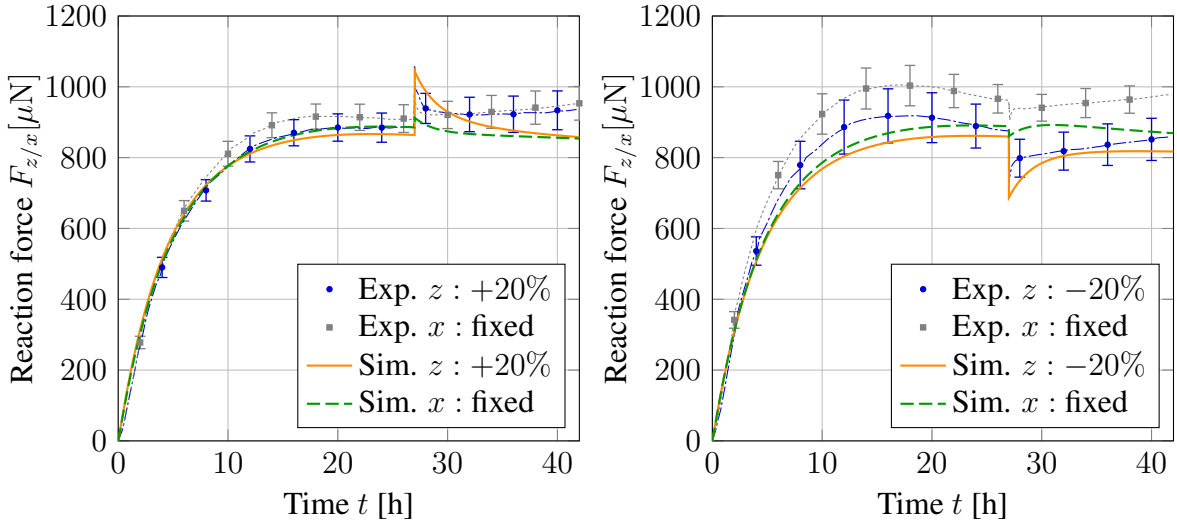

(b) Cross – biaxially constraint – semi-biaxially loaded in one (z) direction

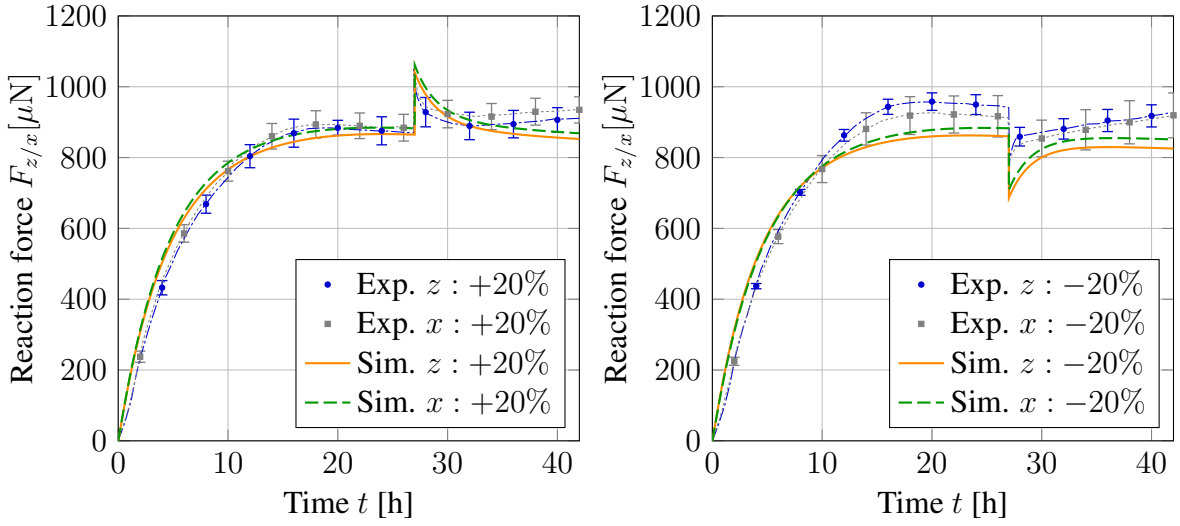

(c) Cross – biaxially constraint – biaxially loaded in both (x and z) directions

Figure 6.16: Model I – Comparison of simulation results with experimental data under multi-axial constraint. Perturbation at $t = 27$ [h] with $\pm 20\%$ of the homeostatic reaction force. Experimental data is plotted as the mean value of all experiments with error bars denoting the SEM.

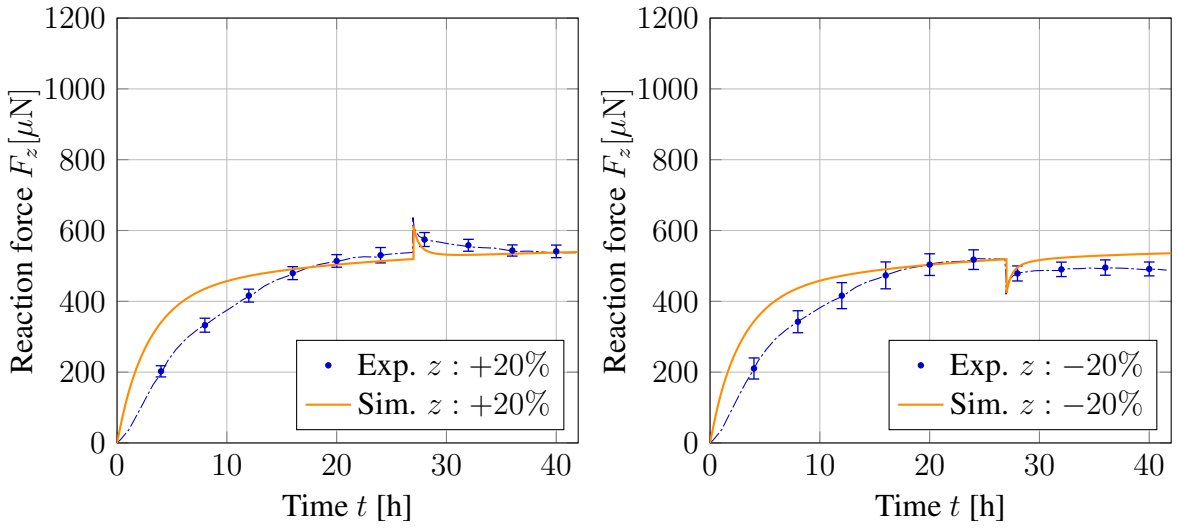

(a) 'Dog-bone' – uniaxially constraint – uniaxially loaded in one (z) direction

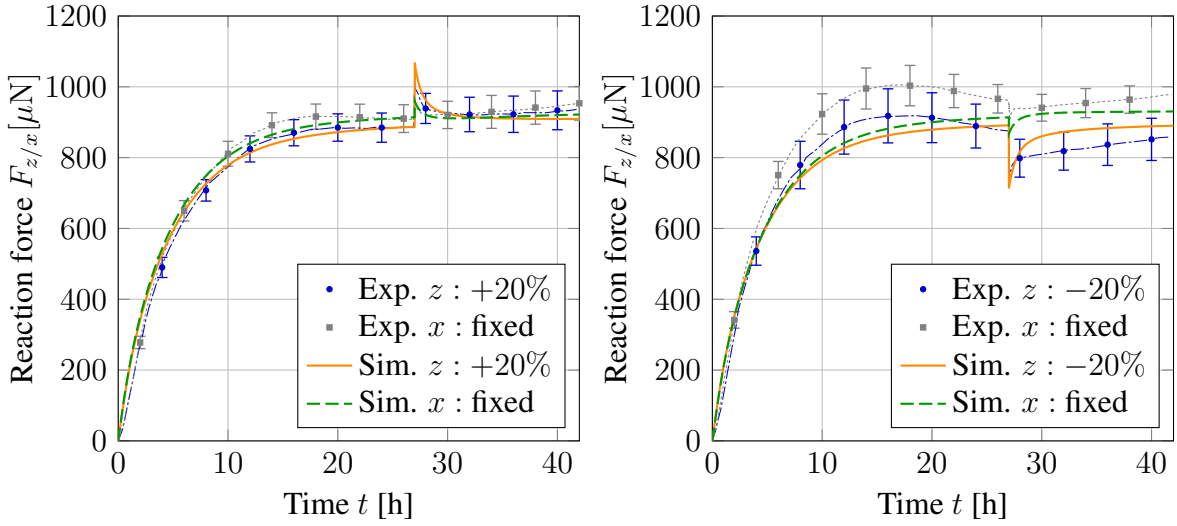

(b) Cross – biaxially constraint – semi-biaxially loaded in one (z) direction

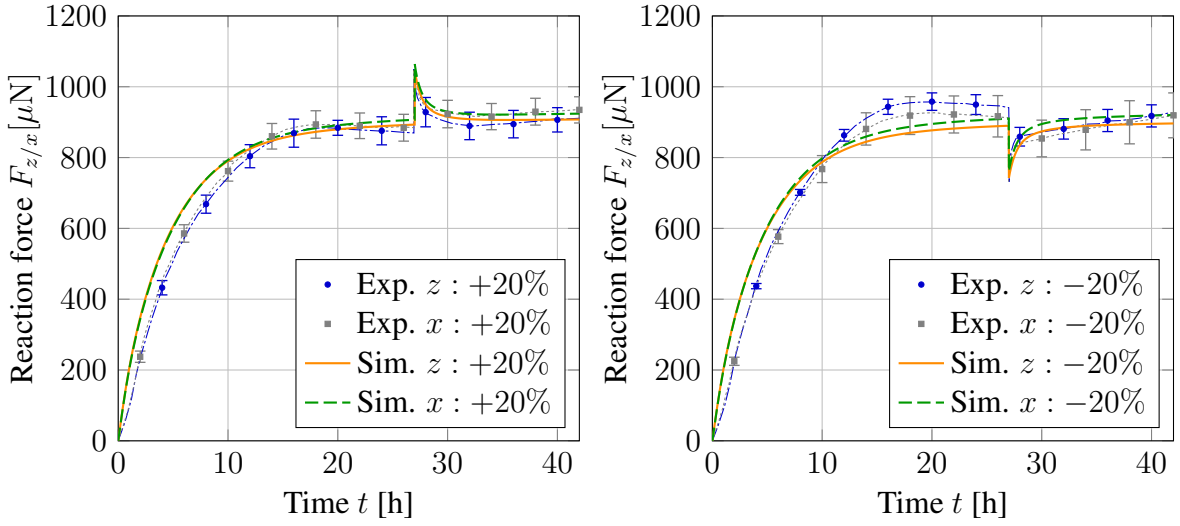

(c) Cross – biaxially constraint – biaxially loaded in both (x and z) directions

Figure 6.17: Model II – Comparison of simulation results with experimental data under multi-axial constraint. Perturbation at $t = 27$ [h] with $\pm 20\%$ of the homeostatic reaction force. Experimental data is plotted as the mean value of all experiments with error bars denoting the SEM.

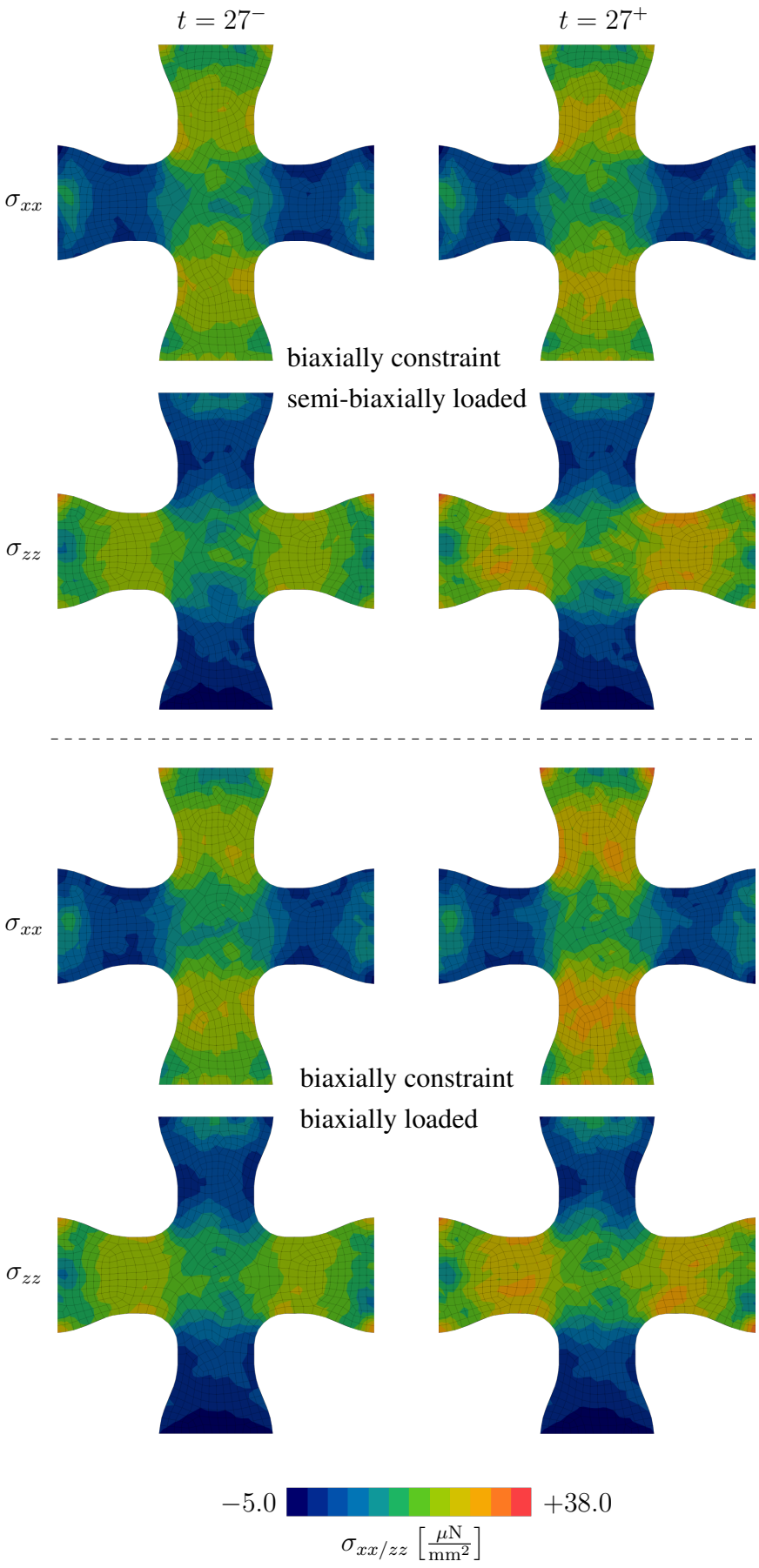

Figure 6.18: Model II – Cauchy stress in both x and z direction right before ($t = 27^-$ [h]) and after ($t = 27^+$ [h]) the perturbation of $+20\%$ is applied.

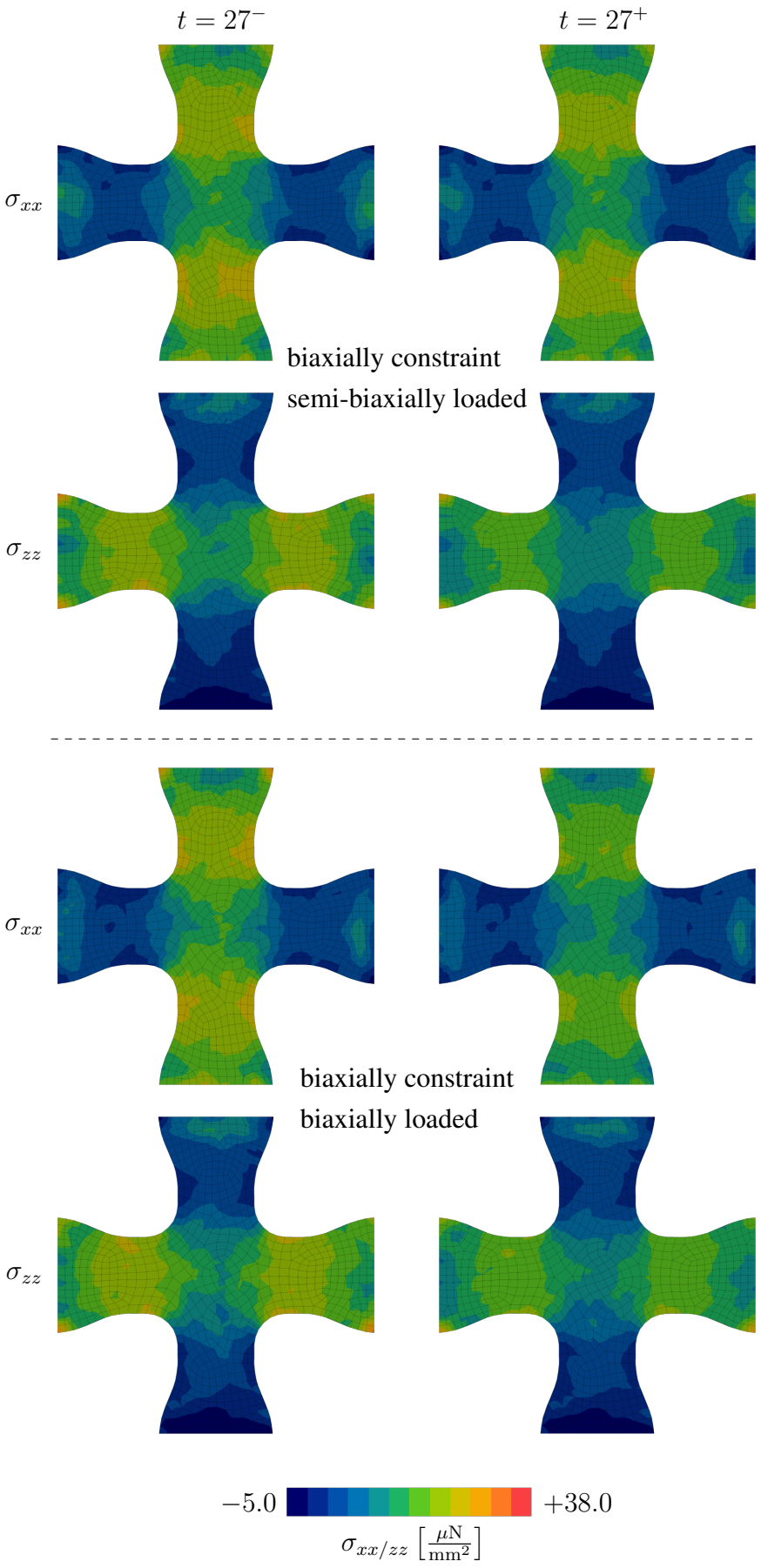

Figure 6.19: Model II – Cauchy stress in both x and z direction right before ($t = 27^-$ [h]) and after ($t = 27^+$ [h]) the perturbation of -20% is applied.

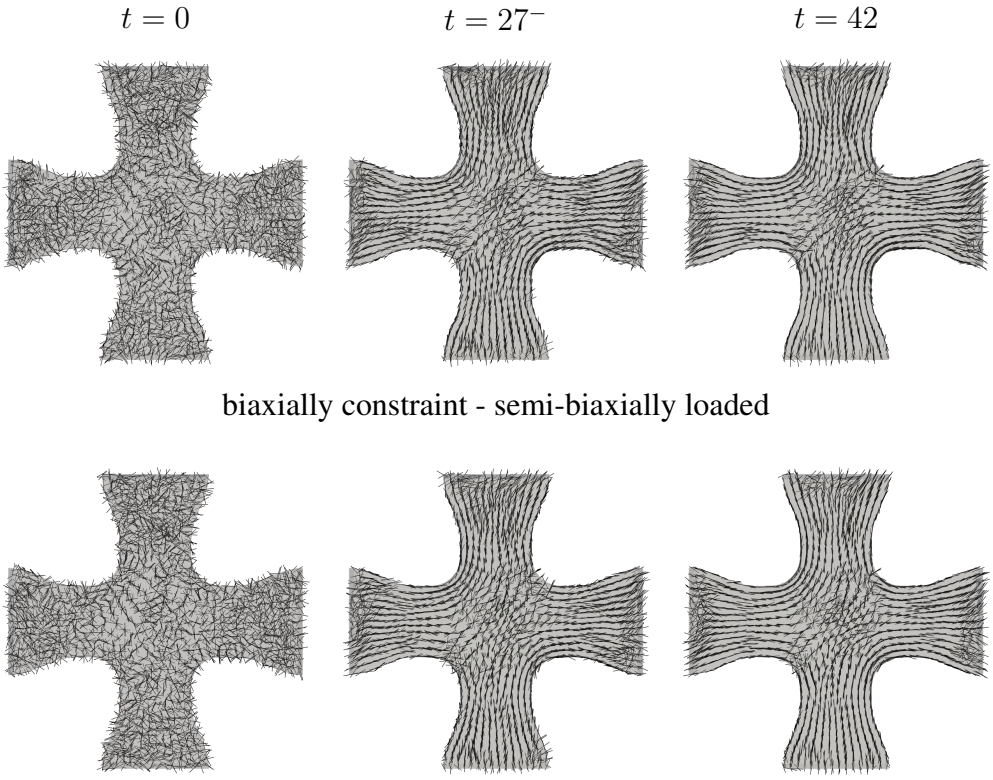

Figure 6.20: Model II – Fiber reorientation of $\tilde{\boldsymbol{n}}$ at the beginning, right before perturbation and at the end of the simulation. Both loading scenarios (semi-biaxial and biaxial) are shown. The results correspond to an increase of $+20\%$ of the homeostatic force at $t = 27$ [h].

Algorithm 4 Implementation of Model II

Input: $\boldsymbol{C}, \hat{\boldsymbol{U}}_{g_{m_n}}, \hat{\boldsymbol{U}}_{g_{co_n}}, \tilde{\boldsymbol{n}}_n$
Output: $\boldsymbol{S}, \hat{\boldsymbol{U}}_{g_m}, \hat{\boldsymbol{U}}_{g_{co}}, \tilde{\boldsymbol{n}}, \hat{\mathbb{C}}$
$\boldsymbol{U} \leftarrow \frac{\hat{\delta}\mathscr{F}(\boldsymbol{C})}{\hat{\delta}\boldsymbol{C}}; \quad \boldsymbol{U}_{g_m} \leftarrow \hat{\boldsymbol{U}}_{g_{m_n}}; \quad \boldsymbol{U}_{g_{co}} \leftarrow \hat{\boldsymbol{U}}_{g_{co_n}}; \quad \tilde{\boldsymbol{n}} \leftarrow \tilde{\boldsymbol{n}}_n; \quad \dot{\gamma}_m \leftarrow 0; \quad \dot{\gamma}_{co} \leftarrow 0$
• **Local Newton-Raphson iteration** (k)
$k \leftarrow 1$
$\mathbf{h}_{\mathrm{II}}^{(k)} \leftarrow (\hat{\boldsymbol{U}}_{g_m},\, \tilde{\boldsymbol{n}},\, \hat{\boldsymbol{U}}_{g_{co}},\, \dot{\gamma}_m,\, \dot{\gamma}_{co})$
while $\|\mathbf{r}_{\mathrm{II}}^{(k)}\| > tol$ **do**
$\bar{\boldsymbol{C}}_{e_m} \leftarrow \boldsymbol{U}_{g_m}^{-1}\boldsymbol{C}\boldsymbol{U}_{g_m}^{-1}; \qquad \bar{\boldsymbol{C}}_{e_{co}} \leftarrow \boldsymbol{U}_{g_{co}}^{-1}\boldsymbol{C}\boldsymbol{U}_{g_{co}}^{-1}$
$\tilde{\boldsymbol{M}} \leftarrow \tilde{\boldsymbol{n}} \otimes \tilde{\boldsymbol{n}}; \qquad \boldsymbol{M} \leftarrow \frac{1}{\boldsymbol{C}^{-1}:\tilde{\boldsymbol{M}}}\boldsymbol{U}^{-1}\tilde{\boldsymbol{M}}\boldsymbol{U}^{-1}; \qquad \bar{\boldsymbol{M}} \leftarrow \frac{1}{\boldsymbol{C}_{g_{co}}:\boldsymbol{M}}\boldsymbol{U}_{g_{co}}\boldsymbol{M}\boldsymbol{U}_{g_{co}}$
▷ Define Helmholtz free energy $\bar{\psi}$, see Equations (6.58) and (6.59)
$\bar{\boldsymbol{\Gamma}}_m \leftarrow 2\,\bar{\boldsymbol{C}}_{e_m}\frac{\hat{\delta}\bar{\psi}}{\hat{\delta}\bar{\boldsymbol{C}}_{e_m}}\Big|_{\mathbf{0}}$
▷ Define Φ_m and g_m for 'matrix' part, cf. Equation (6.47)
$\boldsymbol{N}_{g_m} \leftarrow \frac{\hat{\delta}g_m}{\hat{\delta}\bar{\boldsymbol{\Gamma}}_m}\Big|_{\mathbf{0}}; \qquad \boldsymbol{R}_{\mathrm{II}_m} \leftarrow \boldsymbol{U}_{g_{m_n}}^2 - \boldsymbol{U}_{g_m}\exp\left(-2\,\Delta t\,\dot{\gamma}_g\frac{\boldsymbol{N}_{g_m}}{\|\boldsymbol{N}_{g_m}\|}\right)\boldsymbol{U}_{g_m}$
$r_{\mathrm{II}\Phi_m} \leftarrow \Phi_m - 2\sigma_m\left(\eta_m\dot{\gamma}_m\right)^{\nu_m}$
$\bar{\boldsymbol{\Gamma}}_{co} \leftarrow 2\,\bar{\boldsymbol{C}}_{e_{co}}\frac{\hat{\delta}\bar{\psi}}{\hat{\delta}\bar{\boldsymbol{C}}_{e_{co}}}\Big|_{\mathbf{0}} - 2\,\frac{\hat{\delta}\bar{\psi}}{\hat{\delta}\bar{\boldsymbol{M}}}\Big|_{\mathbf{0}}\bar{\boldsymbol{M}} + 2\,\mathrm{tr}\left(\frac{\hat{\delta}\bar{\psi}}{\hat{\delta}\bar{\boldsymbol{M}}}\Big|_{\mathbf{0}}\bar{\boldsymbol{M}}\right)\bar{\boldsymbol{M}}$
▷ Define Φ_{co} and g_{co} for 'collagen' part, cf. Equation (6.48)
$\boldsymbol{N}_{g_{co}} \leftarrow \frac{\hat{\delta}g_{co}}{\hat{\delta}\bar{\boldsymbol{\Gamma}}_{co}}\Big|_{\mathbf{0}}; \qquad \boldsymbol{R}_{\mathrm{II}_{co}} \leftarrow \boldsymbol{U}_{g_{co_n}}^2 - \boldsymbol{U}_{g_{co}}\exp\left(-2\,\Delta t\,\dot{\gamma}_g\frac{\boldsymbol{N}_{g_{co}}}{\|\boldsymbol{N}_{g_{co}}\|}\right)\boldsymbol{U}_{g_{co}}$
$r_{\mathrm{II}\Phi_{co}} \leftarrow \Phi_{co} - \sigma_{co}\left(\eta_{co}\dot{\gamma}_{co}\right)^{\nu_{co}}$
$\boldsymbol{S} \leftarrow 2\,\boldsymbol{U}_{g_m}^{-1}\frac{\hat{\delta}\bar{\psi}}{\hat{\delta}\bar{\boldsymbol{C}}_{e_m}}\Big|_{\mathbf{0}}\boldsymbol{U}_{g_m}^{-1} + 2\,\boldsymbol{U}_{g_{co}}^{-1}\frac{\hat{\delta}\bar{\psi}}{\hat{\delta}\bar{\boldsymbol{C}}_{e_{co}}}\Big|_{\mathbf{0}}\boldsymbol{U}_{g_{co}}^{-1}$
$\tilde{\boldsymbol{\tau}} \leftarrow \boldsymbol{U}\boldsymbol{S}\boldsymbol{U}$
▷ Spectral decomposition of $\tilde{\boldsymbol{\tau}}$ and define $\tilde{\boldsymbol{n}}_{target}$, see Appendix 6.8.7
$\tilde{\boldsymbol{\omega}} \leftarrow \frac{\pi}{2\eta_s}(\tilde{\boldsymbol{n}} \times \tilde{\boldsymbol{n}}_{target}); \qquad \tilde{\boldsymbol{\Omega}} \leftarrow \sum_{i=1}^{3}(\tilde{\boldsymbol{\omega}} \times \boldsymbol{e}_i) \otimes \boldsymbol{e}_i$
$\boldsymbol{r}_{\mathrm{II}n} \leftarrow \tilde{\boldsymbol{n}} - \left(\boldsymbol{I} + \frac{\sin\left(\Delta t\sqrt{\tilde{\boldsymbol{\omega}}\cdot\tilde{\boldsymbol{\omega}}}\right)}{\sqrt{\tilde{\boldsymbol{\omega}}\cdot\tilde{\boldsymbol{\omega}}}}\,\tilde{\boldsymbol{\Omega}} + \frac{1-\cos\left(\Delta t\sqrt{\tilde{\boldsymbol{\omega}}\cdot\tilde{\boldsymbol{\omega}}}\right)}{\left(\sqrt{\tilde{\boldsymbol{\omega}}\cdot\tilde{\boldsymbol{\omega}}}\right)^2}\,\tilde{\boldsymbol{\Omega}}^2\right)\tilde{\boldsymbol{n}}_n$
$\mathbf{r}_{\mathrm{II}}^{(k)} \leftarrow \left(\hat{\boldsymbol{R}}_{\mathrm{II}_m},\, \hat{\boldsymbol{R}}_{\mathrm{II}_{co}},\, \boldsymbol{r}_{\mathrm{II}n},\, r_{\mathrm{II}\Phi_m},\, r_{\mathrm{II}\Phi_{co}}\right)$
$\mathbf{h}_{\mathrm{II}}^{(k+1)} \leftarrow \mathbf{h}_{\mathrm{II}}^{(k)} - \left(\frac{\hat{\delta}\mathbf{r}_{\mathrm{II}}^{(k)}}{\hat{\delta}\mathbf{h}_{\mathrm{II}}^{(k)}}\right)^{-1}\mathbf{r}_{\mathrm{II}}^{(k)}$
$k \leftarrow k+1$
end while
$\nabla\mathbf{h}_{\mathrm{II}} \leftarrow -\left(\frac{\hat{\delta}\mathbf{r}_{\mathrm{II}}^{(k)}}{\hat{\delta}\mathbf{h}_{\mathrm{II}}^{(k)}}\right)^{-1}\frac{\hat{\delta}\mathbf{r}_{\mathrm{II}}^{(k)}}{\hat{\delta}\hat{\boldsymbol{C}}}\Big|_{\frac{D\hat{\boldsymbol{U}}}{D\hat{\boldsymbol{C}}}=\frac{\hat{\delta}\hat{\boldsymbol{U}}}{\hat{\delta}\hat{\boldsymbol{C}}}}$
• **Calculate stress state and tangent operator**
$\boldsymbol{S} \leftarrow 2\,\boldsymbol{U}_{g_m}^{-1}\frac{\hat{\delta}\bar{\psi}}{\hat{\delta}\bar{\boldsymbol{C}}_{e_m}}\Big|_{\mathbf{0}}\boldsymbol{U}_{g_m}^{-1} + 2\,\boldsymbol{U}_{g_{co}}^{-1}\frac{\hat{\delta}\bar{\psi}}{\hat{\delta}\bar{\boldsymbol{C}}_{e_{co}}}\Big|_{\mathbf{0}}\boldsymbol{U}_{g_{co}}^{-1}$
$\hat{\mathbb{C}} \leftarrow \frac{\hat{\delta}\hat{\boldsymbol{S}}}{\hat{\delta}\hat{\boldsymbol{C}}}\Big|_{\frac{D\mathbf{h}_{\mathrm{II}}^{(k)}}{D\hat{\boldsymbol{C}}}=\nabla\mathbf{h}_{\mathrm{II}};\ \frac{D\hat{\boldsymbol{U}}}{D\hat{\boldsymbol{C}}}=\frac{\hat{\delta}\hat{\boldsymbol{U}}}{\hat{\delta}\hat{\boldsymbol{C}}}}$

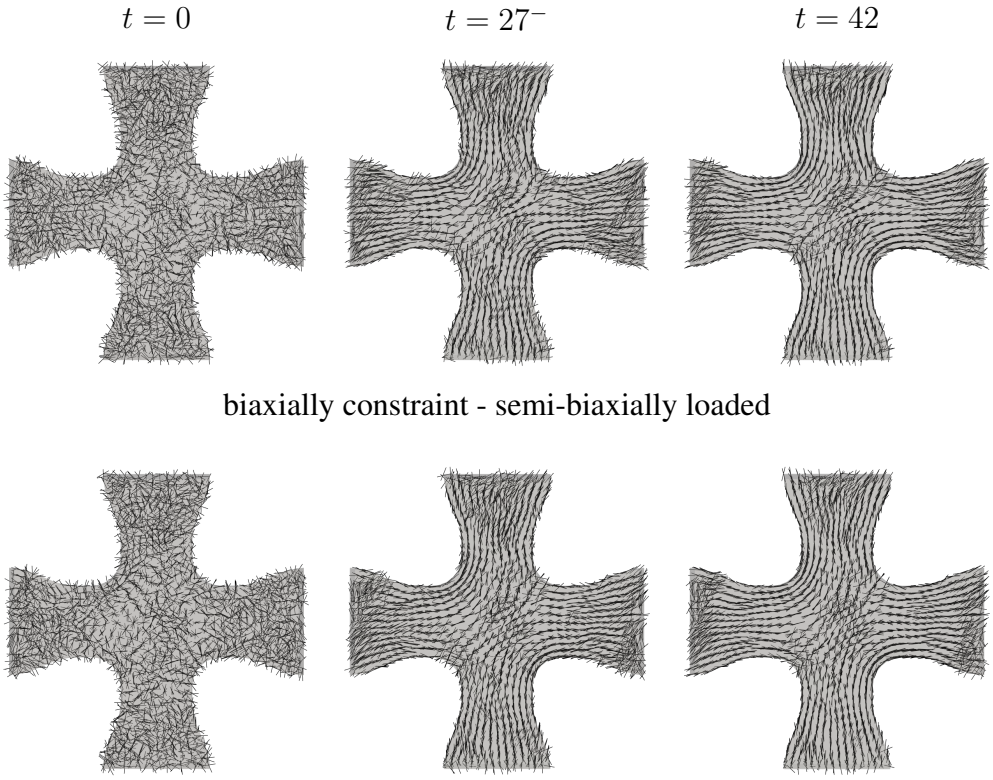

Figure 6.21: Model I – Fiber reorientation of $\tilde{\boldsymbol{n}}$ at the beginning, right before perturbation and at the end of the simulation. Both loading scenarios (semi-biaxial and biaxial) are shown. The results correspond to an increase of $+20\%$ of the homeostatic force at $t = 27$ [h].

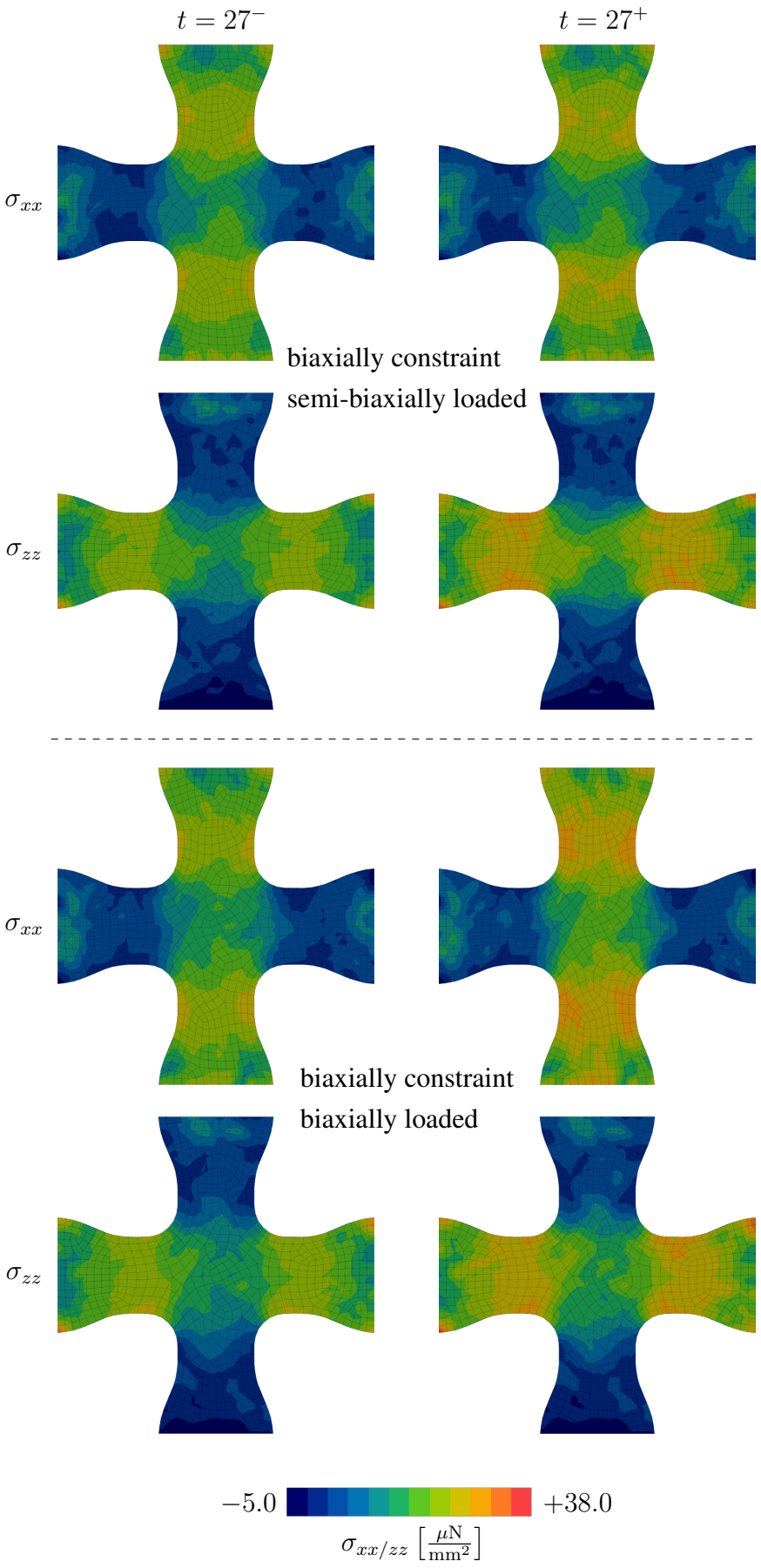

Figure 6.22: Model I – Cauchy stress in both x and z direction right before ($t = 27^-$ [h]) and after ($t = 27^+$ [h]) the perturbation of $+20\%$ is applied.

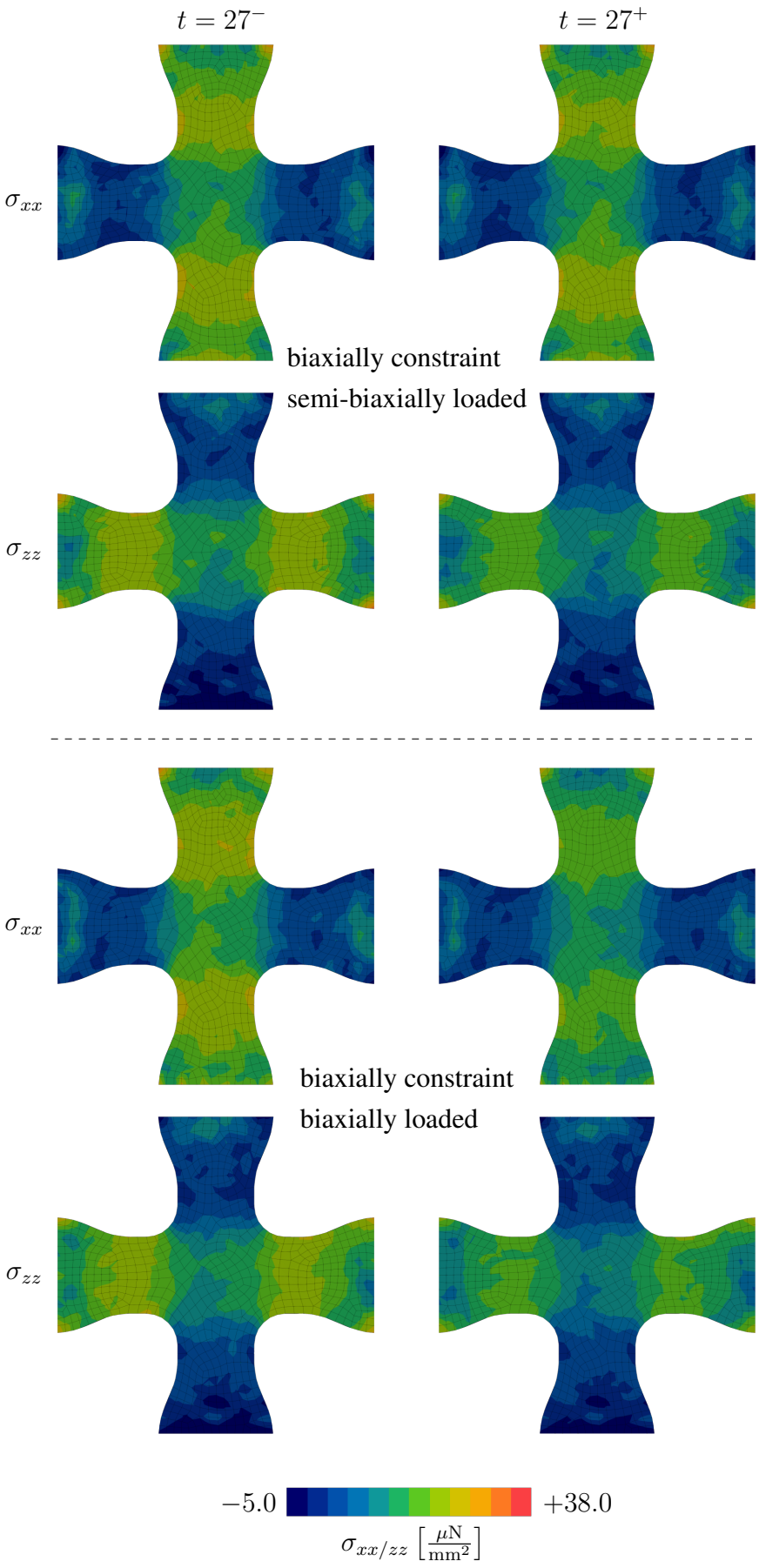

Figure 6.23: Model I – Cauchy stress in both x and z direction right before ($t = 27^-$ [h]) and after ($t = 27^+$ [h]) the perturbation of -20% is applied.

7 Article 6: A novel anisotropic stress-driven model for bioengineered tissues accounting for remodeling and reorientation based on homeostatic surfaces

This article was published as:

Holthusen, H., Rothkranz, C., Lamm, L., Brepols, T., and Reese, S. (*accepted*), 'A novel anisotropic stress-driven model for bioengineered tissues accounting for remodeling and reorientation based on homeostatic surfaces', In: *Proceedings in Applied Mathematics and Mechanics (PAMM 2022)*, 1-6.

Disclosure of the individual authors' contributions to the article:

H. Holthusen reviewed the relevant existing literature, derived the entire theoretical framework and it was his idea to derive the co-rotated intermediate configuration in connection with algorithmic differentiation as well as to employ it for the kinematic growth and remodeling model. Further, he implemented the element routine used for the structural simulations and carried out all structural examples. C. Rothkranz implemented the material routines. L. Lamm gave valuable conceptual advice regarding the modeling of soft biological tissues. It was the original idea of L. Lamm to introduce homeostatic surfaces, while L. Lamm and H. Holthusen developed the concept of homeostatic surfaces proposed in Lamm et al. [2022] and used in this contribution. Moreover, C. Rothkranz, L. Lamm, T. Brepols, and S. Reese gave conceptual advice, contributed to the discussion of the results, read the current version of the article, and

gave valuable suggestions for improvement. All authors approved the preliminary publication of the article in the present dissertation.

7.1 Abstract

A co-rotated formulation of the intermediate configuration is derived in a thermodynamically consistent manner. As a result of this formulation, algorithmic differentiation (AD) and the equations of the material model can be combined directly, i.e., the equations can be implemented into the AD tool and the corresponding derivatives can be calculated using AD. This is not possible when the equations are given in terms of the intermediate configuration, since the multiplicative decomposition suffers from an inherent rotational non-uniqueness. Moreover, a novel stress-driven kinematic growth model is presented that takes homeostasis and fiber reorientation into account and is based on the co-rotated formulation. A numerical example reveals the promising potential of both the co-rotated formulation and the stress-driven growth model.

7.2 Introduction

In the last decades, the modeling of finite inelastic material behavior has become more and more advanced. In this regard, the multiplicative decomposition of the deformation gradient has emerged as an extremely powerful continuum mechanical approach. This approach is used in various disciplines reaching from elasto-plasticity coupled with damage (e.g. Holthusen, Brepols, Reese and Simon [2022*b*]) to the modeling of soft tissues' growth and remodeling (e.g. Soleimani et al. [2020]). To tackle the challenging and error-prone numerical implementation of such models, AD has proven to be a handy tool, which unfortunately cannot be easily combined with models based on the multiplicative decomposition. The reason lies in the involved rotational non-uniqueness of the decomposition.

One of the currently most challenging tasks of material modeling is the simulation of soft biological tissues. Soft tissues are known to seek for a certain state of homeostasis (see e.g. Eichinger, Haeusel, Paukner, Aydin, Humphrey and Cyron [2021]). In order to achieve this state, which is characterized by a preferred stress state to be reached throughout the tissue, the tissue growths and remodels itself until this state is reached. In the literature, different approaches exist to describe these phenomena, for instance, constraint mixture approaches. In this regard, Lamm et al. [2022] recently published an approach based on so-called homeostatic surfaces. These surfaces prescribe the preferred state in the principal stress space, such that growth and remodeling is considered in a smeared and phenomenological sense until the current stress state coincides with the surface. Additionally, soft tissue are able to remodel collagen fibers – often referred to as reorientation – in order to increase their mechanical

resistance to changing loading conditions.
Within this contribution, a novel co-rotated formulation of the intermediate configuration is presented at first. This configuration is unique, but shares the same physical interpretation with the intermediate one. Hence, contrary to equations stated with respect to the intermediate configuration, material model equations in the co-rotated configuration can be directly implemented into an AD tool. This enables an efficient and easy numerical implementation of a wide class of materials.
Second, a new stress-driven growth and remodeling model is discussed. Its theoretical backbone is the co-rotated intermediate configuration. Furthermore, the approach of homeostatic surfaces is followed and the preferred stress state is prescribed in terms of the overall Cauchy stress in the principal stress state. Here, the hypothesis of tensile homeostasis is followed. Moreover, reorientation of collagen fibers is taken into account such that these fibers align with the principal tensile direction.
Section 7.3 presents the co-rotated formulation, and further, discusses the influence of structural tensors. Subsequently, in Section 7.4, a novel stress-driven growth and remodeling model is developed. Further, the evolution equations of the different inelastic phenomena are discussed. Finally, the models is investigated in a three-dimensional setting in Section 7.5.

7.3 Co-rotational formulation of the intermediate configuration

Within this contribution, the well-established multiplicative decomposition of the deformation gradient $\boldsymbol{F}$ into its elastic $\boldsymbol{F}_e$ and growth-related part $\boldsymbol{F}_g$ is employed (see Rodriguez et al. [1994]). For the time being, the Helmholtz free energy ψ is assumed to be a *scalar-valued isotropic function* of the elastic Cauchy-Green tensor $\boldsymbol{C}_e := \boldsymbol{F}_e^T \boldsymbol{F}_e = \boldsymbol{F}_g^{-T} \boldsymbol{C} \boldsymbol{F}_g^{-1}$ with $\boldsymbol{C} := \boldsymbol{F}^T \boldsymbol{F}$ and some structural tensor $\breve{\boldsymbol{M}} := \boldsymbol{F}_g \boldsymbol{M} \boldsymbol{F}_g^T / \mathrm{tr}(\boldsymbol{C}_g \boldsymbol{M})$ with $\boldsymbol{C}_g := \boldsymbol{F}_g^T \boldsymbol{F}_g$ and $\boldsymbol{M}$ being a (symmetric) structural tensor in the reference configuration. Its purpose is to take into account the orientation of the fibers. The mapping of $\boldsymbol{M}$ from the reference to the intermediate configuration is chosen in line with Reese [2003].
Unfortunately, the multiplicative decomposition of $\boldsymbol{F}$ suffers from an inherent non-uniqueness, i.e.

$$\boldsymbol{F} = \boldsymbol{F}_e \boldsymbol{F}_g = \boldsymbol{F}_e \boldsymbol{Q}^T \boldsymbol{Q} \boldsymbol{F}_g =: \boldsymbol{F}_e^* \boldsymbol{F}_g^*, \quad \boldsymbol{Q} \in \mathrm{SO}(3) \tag{7.1}$$

is an equivalent decomposition as well. Due to this non-uniqueness, neither $\boldsymbol{C}_e$ nor $\breve{\boldsymbol{M}}$ can be determined, and thus, also $\psi = \bar{\psi}(\boldsymbol{C}_e, \breve{\boldsymbol{M}})$ cannot be calculated[1]. Hence, it is not straightforward to implement the material model's equations derived with respect to the intermediate configuration directly into an AD tool. To solve this, additional pull-back operations of all constitutively dependent variables are necessary (cf. Dettmer and Reese [2004]). However, besides the additional effort, the thermodynamic driving forces might lose their physical meaning as well as their symmetry properties.

Therefore, the aim is to present a co-rotated formulation of the intermediate configuration in the following. Contrary to the latter, this co-rotated configuration is uniquely defined, but at the same time has the same physical interpretation as the intermediate configuration. Further, all symmetry properties are preserved. To begin with, using the polar decomposition $\boldsymbol{F}_g = \boldsymbol{R}_g \boldsymbol{U}_g$ with $\boldsymbol{R}_g \in \mathrm{SO}(3)$, it can be seen that only the rotation tensor $\boldsymbol{R}_g$ is affected by the non-uniqueness, while the growth-related stretch tensor $\boldsymbol{U}_g$ is uniquely defined. Thus, the co-rotated quantities $\bar{\boldsymbol{C}}_e \coloneqq \boldsymbol{R}_g^T \boldsymbol{C}_e \boldsymbol{R}_g = \boldsymbol{U}_g^{-1} \boldsymbol{C} \boldsymbol{U}_g^{-1}$ and $\bar{\boldsymbol{M}} \coloneqq \boldsymbol{R}_g^T \breve{\boldsymbol{M}} \boldsymbol{R}_g = \boldsymbol{U}_g \boldsymbol{M} \boldsymbol{U}_g / \mathrm{tr}(\boldsymbol{C}_g \boldsymbol{M})$ are introduced. Since these quantities are *similar* with their intermediate counterparts, the same Helmholtz free energy can be used, i.e. $\psi = \bar{\psi}(\boldsymbol{C}_e, \breve{\boldsymbol{M}}) = \bar{\psi}(\bar{\boldsymbol{C}}_e, \bar{\boldsymbol{M}})$. Inserting this Helmholtz free energy into the Clausius-Planck inequality $-\dot{\psi} + 1/2\, \boldsymbol{S} : \dot{\boldsymbol{C}} \geq 0$, the following state law for the second Piola-Kirchhoff stress $\boldsymbol{S}$ as well as the thermodynamic driving forces are obtained

$$\boldsymbol{S} = 2\, \boldsymbol{U}_g^{-1} \frac{\partial \psi}{\partial \bar{\boldsymbol{C}}_e} \boldsymbol{U}_g^{-1}, \quad \bar{\boldsymbol{\Sigma}} \coloneqq 2\, \bar{\boldsymbol{C}}_e \frac{\partial \psi}{\partial \bar{\boldsymbol{C}}_e}, \quad \bar{\boldsymbol{\Pi}} \coloneqq 2 \frac{\partial \psi}{\partial \bar{\boldsymbol{M}}} \bar{\boldsymbol{M}} - 2 \frac{\partial \psi}{\partial \bar{\boldsymbol{M}}} : (\bar{\boldsymbol{M}} \otimes \bar{\boldsymbol{M}}), \quad \bar{\boldsymbol{\Gamma}} \coloneqq \bar{\boldsymbol{\Sigma}} - \bar{\boldsymbol{\Pi}} \tag{7.2}$$

where the relative stress $\bar{\boldsymbol{\Gamma}}$ is conjugated to $\bar{\boldsymbol{D}}_g \coloneqq \mathrm{sym}(\dot{\boldsymbol{U}}_g \boldsymbol{U}_g^{-1})$. Furthermore, the conjugated driving forces in the latter equation can be considered the co-rotated quantities of their intermediate counterparts, e.g. $\bar{\boldsymbol{\Sigma}} = \boldsymbol{R}_g^T (2\, \boldsymbol{C}_e (\partial \psi / \partial \boldsymbol{C}_e)) \boldsymbol{R}_g$. It should be mentioned that the driving force associated with $\dot{\boldsymbol{M}}$ is unique as well and can also be computed using AD. However, since this driving force is not needed in the model presented hereafter, it is omitted at this point.

Since all quantities in Equation (7.2) are uniquely defined as well, all of them can be implemented into an AD tool without further pull-back operations. Moreover, all derivatives of the Helmholtz free energy can be calculated using AD, which is considered a major advantage, since these might be challenging when computed 'by hand'. With this framework of a co-rotated intermediate configuration at hand, the following Section 7.4 considers a novel

[1] Since ψ is an *isotropic function*, changing the arguments $\psi = \psi^{\#}(\boldsymbol{C}, \boldsymbol{C}_g, \boldsymbol{M})$ allows to determine ψ depending on referential quantities (cf. Dettmer and Reese [2004]).

stress-driven kinematic growth model, which is based on the proposed co-rotated framework, and thus, fully implemented using AD.

Note on numerical implementation. Since an AD tool is utilized for the numerical implementation, only some scalar-valued inelastic potentials as well as the Helmholtz free energy need to be prescribed. All derivatives appeared so far are uniquely defined, and thus, can be calculated by AD. The same holds for the derivatives of the material model proposed hereafter. For the time discretized evolution equation of $\bar{\boldsymbol{D}}_g$, an exponential integrator scheme similar to Dettmer and Reese [2004] is utilized. Thus, an efficient and flexible implementation of the overall model is enabled.

7.4 Stress-driven growth model

This sections deals with a novel stress-driven growth and remodeling model for soft tissues as well as the reorientation of collagen fibers in a stress-driven manner. In this regards, soft tissues are considered in a smeared sense. Hence, for modeling growth and remodeling, two parallel decomposition of the deformation gradient into 'matrix' (m) and 'fibers' (f) parts are utilized, i.e.

$$\boldsymbol{F} = \boldsymbol{F}_{e_m}\boldsymbol{F}_{g_m} = \boldsymbol{F}_{e_f}\boldsymbol{F}_{g_f}. \tag{7.3}$$

Direction-independent constituents such as elastin are summarized within the first decomposition, while the second decomposition accounts for direction-dependent constituents like collagen. The Helmholtz free energy is assumed to be additively decomposed, i.e. $\psi = \psi_m(\bar{\boldsymbol{C}}_{e_m}) + \psi_f(\bar{\boldsymbol{C}}_{e_f}, \bar{\boldsymbol{M}})$ where the contribution of the 'matrix' is given by ψ_m and ψ_f accounts for the 'fibers' contribution. Moreover, the structural tensor in the reference configuration is defined by $\boldsymbol{M} = \boldsymbol{n} \otimes \boldsymbol{n}$ with $\boldsymbol{n}$ being the structural vector in the reference configuration, which is parallel to the (major) collagen direction. Similar to the procedure described in the previous section, and as a result of the parallel decomposition in Equation (7.3), the driving forces and the second Piola-Kirchhoff stress read

$$\boldsymbol{S} = 2\,\boldsymbol{U}_{g_m}^{-1}\frac{\partial\psi}{\partial\bar{\boldsymbol{C}}_{e_m}}\boldsymbol{U}_{g_m}^{-1} + 2\,\boldsymbol{U}_{g_f}^{-1}\frac{\partial\psi}{\partial\bar{\boldsymbol{C}}_{e_f}}\boldsymbol{U}_{g_f}^{-1}, \quad \bar{\boldsymbol{\Gamma}}_m \coloneqq 2\,\bar{\boldsymbol{C}}_{e_m}\frac{\partial\psi}{\partial\bar{\boldsymbol{C}}_{e_m}}, \quad \bar{\boldsymbol{\Gamma}}_f \coloneqq 2\,\bar{\boldsymbol{C}}_{e_f}\frac{\partial\psi}{\partial\bar{\boldsymbol{C}}_{e_f}} - \bar{\boldsymbol{\Pi}} \tag{7.4}$$

with $\bar{\boldsymbol{C}}_{e_m} \coloneqq \boldsymbol{U}_{g_m}^{-1}\boldsymbol{C}\boldsymbol{U}_{g_m}^{-1}$ and $\bar{\boldsymbol{C}}_{e_f} \coloneqq \boldsymbol{U}_{g_f}^{-1}\boldsymbol{C}\boldsymbol{U}_{g_f}^{-1}$. The stretch tensors $\boldsymbol{U}_{g_m}$ and $\boldsymbol{U}_{g_f}$ result from the polar decompositions of $\boldsymbol{F}_{g_m}$ and $\boldsymbol{F}_{g_f}$, respectively. Moreover, it is important to note that both $\bar{\boldsymbol{\Gamma}}_m$ and $\bar{\boldsymbol{\Gamma}}_f$ are symmetric (cf. Svendsen [2001]). It remains to choose suitable evolution

equations for growth and remodeling as well as fiber reorientation, which will be presented in the following.

7.4.1 Evolution equations

Soft biological tissues are known to prefer a state of homeostasis, i.e. a homeostatic stress is tried to reach throughout the whole tissue. Within this contribution, the approach suggested in Lamm et al. [2022] for modeling growth and remodeling is followed. A so-called 'homeostatic surface' in the principal stress space similar to plasticity is introduced, which describes the preferred or homeostatic stress. Due to growth and remodeling, the tissues seeks to achieve this preferred state. The direction of growth may be described in an associative way by taking the derivative of the homeostatic surface with respect to the thermodynamic driving forces.
Besides growth and remodeling, collagen fibers are produced and absorbed by cells in order to optimally carry mechanical loading. In a smeared sense, this can be described by a reorientation of the structural vector associated with the direction of collagen fibers. Here, it is assumed that an optimal state is reached when the structural vector is collinear with the eigenvector associated with the principal eigenvalue of Cauchy's stress tensor $\boldsymbol{\sigma} = 1/J\,\boldsymbol{\tau} = 1/J\,\boldsymbol{F}\boldsymbol{S}\boldsymbol{F}^T$. In the latter equation, J is the determinate of $\boldsymbol{F}$ and $\boldsymbol{\tau}$ the Kirchhoff stress tensor.

Growth and remodeling. The homeostatic surface proposed herein is assumed to be a *scalar-valued isotropic function* of the overall Cauchy stress $\boldsymbol{\sigma}$. To account for the hypothesis of tensile homeostasis, i.e. a tensile stress state is preferred (cf. Eichinger, Haeusel, Paukner, Aydin, Humphrey and Cyron [2021]), the following smoothed Rankine-like surface is introduced

$$\Phi = \mathrm{tr}\,(\boldsymbol{\sigma}) + \sqrt{\mathrm{tr}\,(\boldsymbol{\sigma}^2) + \beta} - 2\,\sigma_{hom} \tag{7.5}$$

where σ_{hom} is the homeostatic stress and β is a stress-like parameter for shifting the surface in the principal stress space. Further, having in mind that $\boldsymbol{\tau} = 2\left(\boldsymbol{F}_{e_m}(\partial\psi/\partial\boldsymbol{C}_{e_m})\boldsymbol{F}_{e_m}^T + \boldsymbol{F}_{e_f}(\partial\psi/\partial\boldsymbol{C}_{e_f})\boldsymbol{F}_{e_f}^T\right)$ with $\boldsymbol{C}_{e_m} \coloneqq \boldsymbol{F}_{e_m}^T\boldsymbol{F}_{e_m}$ and $\boldsymbol{C}_{e_f} \coloneqq \boldsymbol{F}_{e_f}^T\boldsymbol{F}_{e_f}$, the following relation is important to note

$$\boldsymbol{\tau} = \boldsymbol{F}^{-T}\left(\boldsymbol{U}_{g_m}\bar{\boldsymbol{\Gamma}}_m\boldsymbol{U}_{g_m}^{-1} + \boldsymbol{U}_{g_f}\left(\bar{\boldsymbol{\Gamma}}_f + \bar{\boldsymbol{\Pi}}\right)\boldsymbol{U}_{g_f}^{-1}\right)\boldsymbol{F}^T. \tag{7.6}$$

The term in brackets is generally non-symmetric, but shares the same eigenvalues with $\boldsymbol{\tau}$. Hence, the following evolution equations for the co-rotated symmetric parts of the inelastic

velocity gradients $\bar{\boldsymbol{D}}_{g_m} \coloneqq \mathrm{sym}\left(\dot{\boldsymbol{U}}_{g_m}\boldsymbol{U}_{g_m}^{-1}\right)$ and $\bar{\boldsymbol{D}}_{g_f} \coloneqq \mathrm{sym}\left(\dot{\boldsymbol{U}}_{g_f}\boldsymbol{U}_{g_f}^{-1}\right)$ are introduced

$$\bar{\boldsymbol{D}}_{g_m} = \dot{\gamma}\frac{\partial\Phi}{\partial\bar{\boldsymbol{\Gamma}}_m}\Bigg/\,\|\frac{\partial\Phi}{\partial\bar{\boldsymbol{\Gamma}}_m}\|, \quad \bar{\boldsymbol{D}}_{g_f} = \dot{\gamma}\frac{\partial\Phi}{\partial\bar{\boldsymbol{\Gamma}}_f}\Bigg/\,\|\frac{\partial\Phi}{\partial\bar{\boldsymbol{\Gamma}}_f}\|. \tag{7.7}$$

In the latter equations, $\dot{\gamma}$ is a kind of growth multiplier that describes the rate of growth and remodeling. The multiplier is determined by a Perzyna-type law (see Perzyna [1966]): $\dot{\gamma} = 1/\eta\,(\Phi/2\,\sigma_{hom})$. Here, η is the growth and remodeling time.

Reorientation. As mentioned above, fiber reorientation is considered in a stress-driven manner. Therefore, a physically reasonable evolution equation of the structural vector is stated in the current configuration. More precisely, an optimal state is reached if the structural vector in the current configuration is parallel to Cauchy's principal eigenvector. Unfortunately, in this case objective rates must be taken into account. To avoid this issue, the polar decomposition $\boldsymbol{F} = \boldsymbol{R}\boldsymbol{U}$ with $\boldsymbol{R} \in \mathrm{SO}(3)$ is employed. Based on this decomposition, the so-called co-rotated Cauchy stress $\boldsymbol{R}^T\boldsymbol{\sigma}\boldsymbol{R}$ as well as the (normalized) stretched structural vector $\boldsymbol{n}' \coloneqq (1/\sqrt{\boldsymbol{n}\cdot\boldsymbol{C}\cdot\boldsymbol{n}})\,\boldsymbol{U}\boldsymbol{n}$ are introduced. Noteworthy, it can be shown that an optimal state is also reached if the principal eigenvector of the co-rotated Cauchy stress and $\boldsymbol{n}'$ are collinear. It should be noted that it is assumed that the collagen fibers always align with the principal tensile direction. In the case of a fully compressive state, no reorientation takes place.
The evolution equation is chosen in line with Menzel [2005]

$$\dot{\boldsymbol{n}}' = \frac{\pi}{2\tau}\,(\boldsymbol{n}' \times \boldsymbol{n}_t) \times \boldsymbol{n}' \tag{7.8}$$

with the reorientation time τ. Note that the latter equation can be reformulated in terms of a skew-symmetric tensor contracted with $\boldsymbol{n}'$. Hence, if an exponential integrator scheme is utilized for the time discretized evolution equation, this can be solved in closed-form using Rodrigues' formula. Further, $\boldsymbol{n}_t$ is the principal eigenvector of Cauchy's stress tensor.

7.4.2 Specific choices for energy terms

For studying the material model's response, the following Helmholtz free energy terms are chosen. For the 'matrix' part, a compressible Neo-Hookean energy is used

$$\psi_m = \frac{\mu_m}{2}\left(\mathrm{tr}\left(\bar{\boldsymbol{C}}_{e_m}\right) - 3 - \ln\left(\det\left(\bar{\boldsymbol{C}}_{e_m}\right)\right)\right) + \frac{\Lambda_m}{4}\left(\det\left(\bar{\boldsymbol{C}}_{e_m}\right) - 1 - \ln\left(\det\left(\bar{\boldsymbol{C}}_{e_m}\right)\right)\right) \tag{7.9}$$

while the energy for the 'fibers' part is in line with Holzapfel et al. [2000]

$$\psi_f = \frac{K_1}{2\,K_2}\,\left(\exp\left(K_2\langle \mathrm{tr}\left(\bar{\boldsymbol{C}}_{e_f}\bar{\boldsymbol{M}}\right)-1\rangle^2\right)-1\right). \tag{7.10}$$

In the latter, the Macaulay brackets are used, since collagen fibers are assumed to be not able to carry compressive loadings. The material parameters are μ_m, Λ_m, K_1 and K_2.

7.5 Numerical example

In this contribution, the boundary value problem considered is chosen in accordance with the example presented e.g. in Himpel et al. [2008]. The corresponding geometry as well as the loading applied are illustrated in Figure 7.1. Here, the radial displacement loading is described by $u_r(z) = 0.3\,\sin(\pi/4\,z)$ [mm] such that the maximum displacement is 0.3 [mm]. Both the top and bottom surfaces are considered clamped.

The material parameters are either taken from the literature Himpel et al. [2008] or arbitrarily chosen: $\Lambda_m = 4.285$ [MPa], $\mu_m = 1.071$ [MPa], $K_1 = 2.0$ [MPa], $K_2 = 1.0$ [-], $\sigma_{hom} = 1.0$ [MPa], $\eta = 10.0$ [h], $\beta = 0.1$ [MPa], $\tau = 10.0$ [h]. The initial collagen fiber directions are randomly chosen per element. Furthermore, a reduced integrated finite element formulation with a single Gaussian point per element Barfusz, van der Velden, Brepols, Holthusen and Reese [2021] is utilized for discretization to avoid locking effects.

The loading is increased in a monotonic way within the first hour, i.e. the load is linearly increased until the maximum displacement of 0.3 [mm] is reached at $t = 1$ [h]. Subsequently, the loading is hold constant until the end of the simulation. Furthermore, the force-time curve obtained throughout the simulation up to $t = 40$ [h] is shown in Figure 7.2. As can be seen, due to growth and remodeling as well as fiber reorientation, a tensile state is observed at the beginning, while a compressive state is reached in the longitudinal direction at the end. Moreover, since the slope is decreasing at the end, it can concluded that a state of homeostasis is reached. In order to give a better understanding of the processes, Figure 7.3 provides the contour plots of the Cauchy stress in longitudinal direction σ_{zz} and the value of the growth multiplier $\dot{\gamma}$. Noteworthy, the multiplier is always non-zero if the current stress state does not lie on the homeostatic surface, i.e. homeostasis is not reached.

At the beginning ($t = 1$ [h]), the fibers are randomly orientated. Further, the stress state is far from lying on the chosen homeostatic, since the rate of $\dot{\gamma}$ is relatively high and mainly depends on the over- and under-stress, respectively. With time, the collagen fibers orient themselves towards the principal tensile direction of stress, which is the circumferential one. At the end

of the simulation, nearly all fibers are aligned with this particular direction.
Since the rate of growth and remodeling is highest in the middle of the specimen, growth and remodeling are most pronounced in this region. However, at the end of the simulation homeostasis is reached throughout the whole specimen. Similarly, stress is initially quite heterogeneous in the longitudinal direction, but becomes more homogeneous as homeostasis is reached and collagen fibers are aligned in circumferential direction.
In summary, it can be concluded that the model is able to provide plausible results in terms of homeostasis and fiber reorientation for complex loading scenarios.

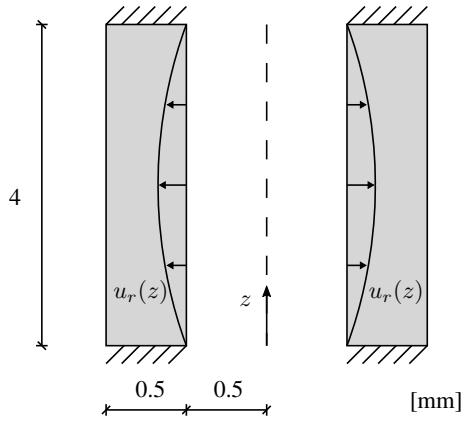

Figure 7.1: Geometry and boundary value problem. The geometry and loading are axisymmetric with z being the axis of symmetry. The displacement in radial direction is sine-shaped. For meshing, 4 elements in thickness direction, 16 elements over the height and 32 elements in circumferential direction are used.

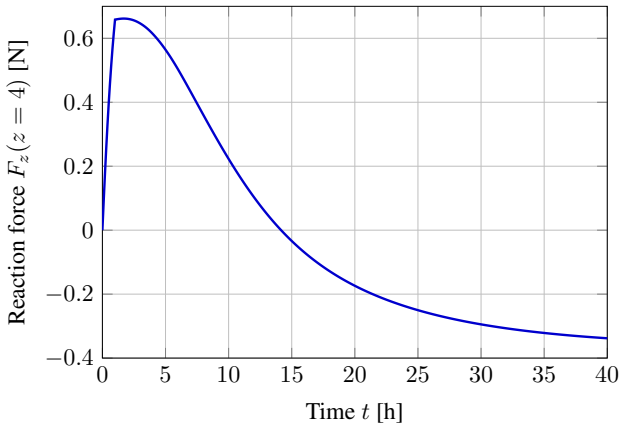

Figure 7.2: Force-time curve at the top surface ($z = 4$ [mm]). Within the first hour, the sine-shaped loading is linearly increased and then hold constant throughout the rest of the simulation.

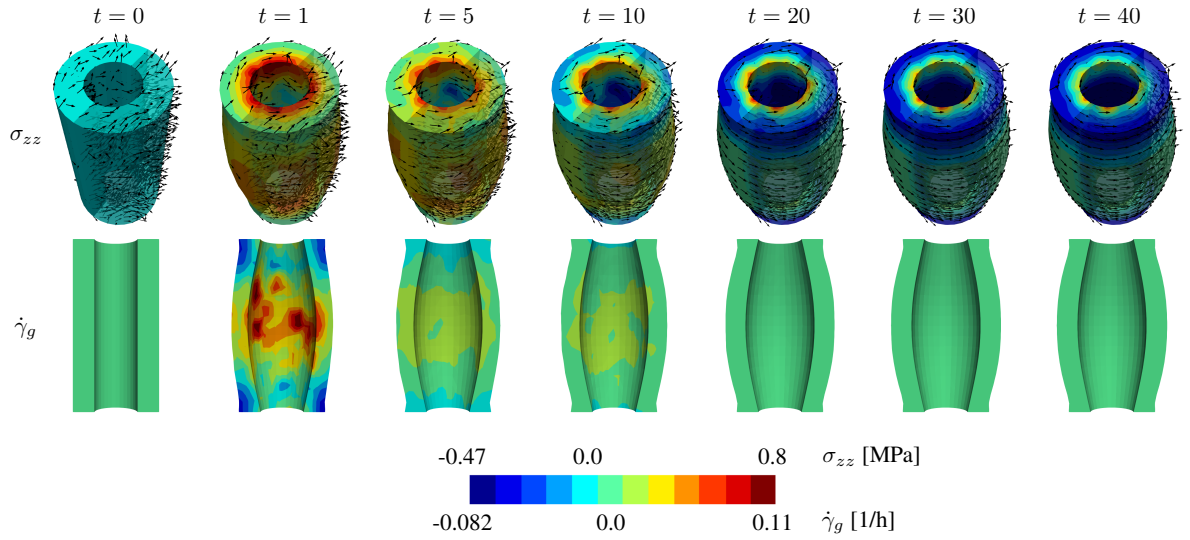

Figure 7.3: Top: Cauchy stress σ_{zz} in longitudinal (z) direction at different time steps. Further, the reorientation of collagen fibers is visualized. Bottom: Growth multiplier $\dot{\gamma}$ at different time steps. A zero value corresponds to a stress state lying on the homeostatic surface.

7.6 Conclusion and outlook

This work has addressed both a novel co-rotated formulation of the intermediate configuration and a stress-driven growth model based on this formulation. The former is extremely advantageous when it comes to the application of AD tools for the implementation of material models based on the multiplicative decomposition of the deformation gradient.

The soft tissue material model derived from the latter takes into account both reorientation of collagen fibers and homeostasis. The latter is described by homeostatic surfaces. These surfaces are similar to yield criteria in plasticity, i.e. they describe a surface in the principal stress state. Contrary to plasticity, growth and remodeling always takes place until the current stress state lies on this surface. Here, a surface in terms of the overall Cauchy stress was chosen for this purpose.

Collagen fibers are assumed to align with the principal eigenvector of the Cauchy stress tensor. To avoid objective rates of the corresponding evolution equation, a polar decomposition of the deformation gradient was used.

Finally, the material model was examined on the basis of a structural example. It was shown that both the state of homeostasis and an orientation of the fibers in the main tensile direction can be simulated. Future work should focus on the determination of the homeostatic area, as well as the comparison with experiments.

8 Conclusions and Outlook

The present dissertation was concerned with different modeling approaches for anisotropic material behavior under consideration of various inelastic effects. Particular attention was paid to the phenomena of plasticity, damage and growth in a theoretical and continuum mechanical framework. Both initially anisotropic materials and anisotropy induced by inelastic effects were investigated.

The first article presented in Chapter 2 dealt with initially anisotropic materials, in particular transversal isotropy was taken into account. Based on the second law of thermodynamics, the model was derived consistently. Structural tensors were used to account for initial anisotropy, the matrix was modeled elasto-plastically with isotropic and kinematic hardening, and three scalar damage variables were introduced. Noteworthy, a so-called 'two-surface' approach was used to treat damage and plasticity as independent but strongly coupled mechanisms. Hence, several inelastic phenomena were considered. First, kinematic hardening leads to a natural plastic anisotropy due to the translational motion of the yield surface in the principal stress space. Second, three significant failure mechanisms are accounted for using three damage variables, namely fiber breakage under tensile loading, kinking under compression, and (isotropic) matrix failure. The first two result in an asymmetry of the fibers under tensile and compressive loading. Moreover, in order to guarantee mesh-insensitive results, each of these variables were gradient-extended using the micromorphic approach. Therefore, the theoretical development, approximation, linearization, and algorithmic implementation of the associated weak forms and the local residuals were derived and solved using a monolithic solution strategy. The proposed model was examined using single element tests as well as structural examples. The former revealed the effect of tension-compression asymmetry of the fibers under uniaxial cyclic loading tests. Subsequently, the structural examples were concerned with the overall influence of the orientation of fibers on the direction of both fiber and matrix damage. Furthermore, the accumulated plastic strain was investigated and compared with experimental observations reported in literature. For this purpose, the proposed model was subjected to several plate with a hole examples under different fiber angles. It was shown that the evolution of inelastic phenomena is strongly influenced by the fibers' direction.

Additionally, the performance of the developed gradient-extension was investigated and it was shown that this approach can handle high degrees of damage up to complete failure.

By introducing several scalar damage variables, a certain kind of damage anisotropy has already been taken into account within this contribution. However, it is known that damage is inherently an anisotropic phenomenon resulting from underlying microdefects, especially microcracks. Consequently, at least the matrix constituent should be modeled anisotropically with respect to its damage behavior.

Hence, in Chapter 3 a general geometrically nonlinear theory was developed for initially isotropic materials undergoing plastic deformations coupled to anisotropic damage. To this end, a symmetric second order damage tensor was introduced. The entire theoretical framework was systematically developed with respect to the logarithmic strain space, where the local part of the Helmholtz free energy depends on the logarithmic elastic strains, logarithmic plastic strains, the damage tensor, and the accumulated variables of plasticity and damage. For the kinematics, an additive decomposition was assumed. Since the energy was assumed to be an *isotropic function*, the principal invariants of the damage tensor result in isotropic damage, while mixed invariants of strains and damage induce damage anisotropy. With this assumed energy at hand, the model was derived in a thermodynamically consistent manner, where kinematic and isotropic hardening effects of each dissipative mechanism were taken into account. A 'two-surface' approach was again employed for the evolution of these phenomena. It should be emphasized that the model satisfies the *damage growth criterion*, which prevents artificial stiffening during progressive damage and is violated by some models in the literature. In addition to these local modeling related considerations, pathological mesh dependence must be addressed in the case of damage and material degradation. For this purpose, the micromorphic approach was utilized once again and a novel gradient-extension of the damage tensor's invariants was proposed. Additionally, to be applicable in standard finite element formulations, the transformation of all constitutively dependent variables as well as all tangent operators to the Lagrangian strain space was presented. For the numerical implementation, both the local residuals and the global weak forms were solved in a monolithic scheme using Newton-Raphson's method, while algorithmic differentiation was used on a local level. The element formulation used is similar to the one presented in Chapter 2. The effect of damage-induced anisotropy, the coupling between plasticity and damage anisotropy, and the limitation of the eigenvalues of the damage tensor to the value of one were studied under various loading conditions using single element tests. In representative structure examples, the invariant-based regularization was studied at first. For this purpose, an asymmetrical notched specimen and brittle material behavior were investigated in order to exclude any effects resulting from

plasticity. Even at high degrees of damage and severe snapback, the framework was able to achieve mesh-insensitive results. Furthermore, the difference between isotropic and anisotropic damage was examined under monotonic and non-proportional loading paths by means of a 'dog-bone' and cruciform specimen. Especially the latter showed significant differences in terms of both overall stiffness and remaining load-bearing capacity after degradation.

In Chapters 4 and 5, further aspects of the formulation from Chapter 3 were addressed. For example, more simplistic Helmholtz free energies were used and the expressions for the evolution equations were simplified. In addition, other theoretical aspects were discussed. It was shown that the mapping of the damage tensor does not violate the independence of the rotational non-uniqueness of the intermediate configuration, and a reduced set of invariants for the regularization was proposed. This time, the asymmetrically notched specimen was investigated using a ductile material, and moreover, a three-dimensional example was studied. The formulation was able to handle both simulations in a robust and stable manner.

Despite these promising results and the insights revealed into coupled elasto-plasticity coupled to anisotropic damage, there is still the need for further research. One major aspect is for sure to avoid an additive decomposition of the total strain into elastic and plastic parts. Although this assumption might be valid in case of small elastic strains and coaxial loadings, its general application in structural simulations remains questionable.

Modeling inelastic material behavior at large deformations is – as can be seen, for example, from the models discussed in the previous chapters – a highly complex and challenging task. In engineering applications, this always involves numerical implementations of these models, which is known to be a time-consuming and error-prone process.

Therefore, Chapter 6 presented an elegant way of how to generally formulate inelastic materials based on the multiplicative decomposition of the deformation gradient in order to enable an easy, physically sound and straightforward implementation using algorithmic differentiation. Within this thermodynamically consistent framework, the constitutive variables defined with respect to the intermediate configuration are pulled back by the rotational part of the inelastic part of the deformation gradient. Due to this orthogonal pull-back, the physical interpretation remains the same, thus the arguments defined in the intermediate configuration of any *isotropic function* need only to be interchanged with their co-rotated counterparts. As a result, the inelastic rotation remains undetermined, which is considered an advantage. In the second part of this chapter, the proposed co-rotated formulations serves as a theoretical framework for a novel stress-driven kinematic growth model for soft biological tissues. Here, growth and remodeling are modeled in a phenomenological sense using two parallel decompositions of the deformations gradient to treat growth and remodeling of direction-dependent

and -independent constituents separately. In line with the hypothesis of *tensional homeostasis*, homeostatic surfaces were introduced to prescribe the preferred stress state in the principal stress space. Two approaches were investigated: (i) a 'one-surface' model which prescribes the overall Cauchy stress and (ii) a 'two-surface' model accounting for different preferred stresses of each constituent. Further, collagen fibers, the major direction-dependent component of soft tissues, are remodeled or reoriented by cells to optimally carry mechanical loads. In this contribution, it was assumed that this takes place in a stress-driven manner, i.e. an optimal state is reached if the structural tensor describing the direction of collagen fibers is coaxial with the overall Cauchy stress tensor. To avoid objective rates for the associated evolution equation, the polar decomposition of the deformation gradient was employed and the equations were stated in the co-rotated current configuration. The material model was fully implemented implicitly, while only the Helmholtz free energy and the homeostatic surfaces were defined, and, thanks to the co-rotated formulation, all the numerics were obtained with the help of algorithmic differentiation. For structural simulations, a reduced integration-based solid element with only one Gaussian point was used, which was improved by using algorithmic differentiation, to obtain accurate structural results and eliminate locking. The model's capability and numerical performance was revealed by three structural examples. In the first example, a clamped cylindrical specimen was utilized to compare the 'one-' and 'two-surface' approach with each other. Both model versions were able to achieve homeostasis and restore it under altering loading conditions. Besides, the collagen fibers were initially oriented randomly, but with time they aligned towards the principal stress direction. Despite this highly anisotropic boundary value problem, it could be well recognized on the basis of the global convergence behavior that a numerically extremely stable model was developed and quadratic convergence was achieved throughout the simulation. Subsequently, a qualitative comparison was carried out with experimental data from the literature. For this purpose, the model was subjected to (nearly) uniaxial boundary conditions in a second and to (nearly) biaxial boundary conditions in a third example. Noteworthy, not all of the measured experimental data were used to characterize the material parameters, allowing the remaining data to be used to assess the prediction of the model.

Although these comparisons were only qualitative, the results of the model were very promising and showed the main properties of soft tissue to be expected in terms of homeostasis and alignment of collagen fibers in the direction of principal stress, even under biaxial loading.

The last Chapter 7 was concerned with a more detailed investigation of the 'one-surface' model from the previous chapter. To this end, a hollow cylinder was subjected to sinusoidal internal pressure. Due to growth and remodeling, the reaction force in longitudinal direction shifted from tension to compression. In addition, the collagen fibers aligned with the

circumferential direction, since this is the principal (tensile) stress direction.

In the present thesis, different continuum mechanical approaches for a variety of anisotropic materials with inelastic effects have been discussed and their reliability was validated by sophisticated numerical studies. Nevertheless, there is an ongoing demand for research in this field in general.

As one of the most challenging fields of continuum mechanics nowadays (cf. Maugin [2013]), biomechanics is ideally suited to combine the different approaches presented here in an application-oriented way. In this regard, it is important to note that soft tissues are not only undergoing growth and remodeling, but may also be affected by irreversible deformations or even degradation. This can, of course, refer to typical degradation caused by excessive loading of the tissue, but a common disease is calcification, where calcium is abnormally deposited in soft tissues. Due to the resulting hardening, the tissue may behave more brittle and – given its complex microstructure – damage may progress in an anisotropic manner. More generally, almost all organs in living organisms are subject to cyclic loading, the most famous of which is certainly the heart. Detailed digital twins of these organs, as implemented for example in Baillargeon et al. [2014], allow the simulation of several cycles. Since cyclic loading is always accompanied by fatigue, the combination of irreversible deformations (plasticity), anisotropic damage as well as growth and remodeling is of extraordinary interest also here. While these are only exemplary combinations of the inelastic effects discussed in this thesis, it clearly reveals an absolutely desirable task for modern continuum mechanical challenges and needs further research. Particularly at the theoretical level, in order to better understand the complex interactions between different inelasticities.

Apart from these local modeling questions, various field equations on a global level need to be taken into account, which may cause the material to behave significantly differently locally. The thermo-mechanical coupling of dissipative mechanisms in a finite element simulation is a common problem in engineering applications, for example the heat production of plastic deformations (see e.g. Canadija and Mosler [2011]) and damage (see e.g. Felder et al. [2022]) plays a crucial role, but also the temperature-dependent mechanical properties. With regard to biomechanical problems, the incorporation of diffusion equations is essential, which describe, among other things, the concentration of nutrients and hormones (see e.g. Escuer et al. [2019], Manjunatha et al. [2022*a*] and Rahman et al. [2023]). For instance, homeostasis and growth rate are strongly dependent on the current concentration of these fields. In contrast to plasticity and damage, growth and remodeling are active processes, i.e. additional energy must be added to the system and/or its entropy must be reduced. The related transformation of chemical energy into mechanical energy, also to contract muscles, involves mechano-electro-chemical

coupling in living organisms (see e.g. Kojic et al. [2019]), also highly relevant in the context of the heart (see e.g. Dal et al. [2013]).

The coupling of these fields is a challenging task in its own and can only be accomplished by algorithmic differentiation. To this end, the proposed co-rotated framework is ideally suited as a counterpart at the local material point level when it comes to the numerical implementation. It is worth noting that the micromorphic approach used for gradient-extended damage is already a fairly general multi-field problem.

A novel and popular approach to materials modeling is the use of data science methods from computer science and related techniques such as machine learning and neural networks. Instead of developing a constitutive material model, the mechanical response is in a sense calculated directly from the data used. Besides, there are also approaches that bypass both the constitutive modeling and the construction of neural networks, but directly use the experimental data in a so-called data-driven manner (see Kirchdoerfer and Ortiz [2016], Eggersmann et al. [2021] and Prume et al. [2023]).

The disadvantage of all these computer techniques is that they ignore in their basic principles the knowledge of several centuries of material modeling and thermodynamics. As a result, unphysical predictions can occur, especially for materials that do not behave in a purely elastic material manner, which must be considered a drawback. To solve this issue, there is a growing tendency to incorporate physics into computer science, for instance, through the use of physics-augmented (see Klein et al. [2022]) or physics-informed (see Raissi et al. [2018, 2019] and Rezaei et al. [2022]) neural networks as well as constitutive artificial neural networks (see Linka and Kuhl [2023]). While the physical restrictions of field equations are more or less clear and can be directly incorporated into computer science approaches, the thermodynamic restrictions of complex material modeling are by no means a trivial task, especially when inelastic effects or anisotropic behavior are involved. Thus, the investigation of these challenging material behaviors in a macroscopic and phenomenological sense based on the principles of continuum mechanics as well as the design of new approaches for anisotropic and inelastic materials remains of outstanding interest – not only to be used in the classical sense as material models for finite element simulations, but also to ensure the physical plausibility of novel modeling approaches and to support the development of those in a systematic way.

List of Figures

List of Tables

Bibliography

Abu Al-Rub, R. K. and Voyiadjis, G. Z. [2003], 'On the coupling of anisotropic damage and plasticity models for ductile materials', *International Journal of Solids and Structures* **40**(11), 2611–2643.

Ahrens, J., Geveci, B. and Law, C. [2005], 'Paraview: An end-user tool for large data visualization', *The visualization handbook* **717**(8).

Alliche, A. [2016], 'A continuum anisotropic damage model with unilateral effect', *Mechanical Sciences (MS)* **7**(1), 61–68.

Altenbach, H. [2015], *Kontinuumsmechanik - Einführung in die materialunabhängigen und materialabhängigen Gleichungen*, 3. aufl. edn, Springer Verlag, Berlin Heidelberg New York.

Ambati, M., Kruse, R. and Lorenzis, L. [2016], 'A phase-field model for ductile fracture at finite strains and its experimental verification', *Comput. Mech.* **57**(1), 149–167.

Ambrosi, D., Ateshian, G., Arruda, E., Cowin, S., Dumais, J., Goriely, A., Holzapfel, G., Humphrey, J., Kemkemer, R., Kuhl, E., Olberding, J., Taber, L. and Garikipati, K. [2011], 'Perspectives on biological growth and remodeling', *Journal of the Mechanics and Physics of Solids* **59**(4), 863–883.

Ambrosi, D., Ben Amar, M., Cyron, C. J., DeSimone, A., Goriely, A., Humphrey, J. D. and Kuhl, E. [2019], 'Growth and remodelling of living tissues: perspectives, challenges and opportunities', *Journal of The Royal Society Interface* **16**(157), 20190233.

Ambrosi, D. and Guana, F. [2007], 'Stress-modulated growth', *Mathematics and Mechanics of Solids* **12**(3), 319–342.

Andrade Pires, F., César de Sá, J., Costa Sousa, L. and Natal Jorge, R. [2003], 'Numerical modelling of ductile plastic damage in bulk metal forming', *International Journal of Mechanical Sciences* **45**(2), 273–294.

Arghavani, J., Auricchio, F. and Naghdabadi, R. [2011], 'A finite strain kinematic hardening constitutive model based on hencky strain: General framework, solution algorithm and application to shape memory alloys', *International Journal of Plasticity* **27**(6), 940–961.

Arghavani, J., Auricchio, F., Naghdabadi, R. and Reali, A. [2011], 'On the robustness and efficiency of integration algorithms for a 3d finite strain phenomenological sma constitutive model', *International Journal for Numerical Methods in Engineering* **85**(1), 107–134.

Asaro, R. J. [1983], 'Crystal Plasticity', *Journal of Applied Mechanics* **50**(4b), 921–934.

Aslan, O., Cordero, N., Gaubert, A. and Forest, S. [2011], 'Micromorphic approach to single crystal plasticity and damage', *International Journal of Engineering Science* **49**(12), 1311–1325. Advances in generalized continuum mechanics.

Aslan, O. and Forest, S. [2009], 'Crack growth modelling in single crystals based on higher order continua', *Computational Materials Science* **45**(3), 756–761. Proceedings of the 17th International Workshop on Computational Mechanics of Materials.

Ateshian, G. A. and Ricken, T. [2010], 'Multigenerational interstitial growth of biological tissues', *Biomechanics and Modeling in Mechanobiology* **9**(6), 689–702.

Baaser, H. [2014], *Development and Application of the Finite Element Method Based on MatLab*, Springer Publishing Company, Incorporated.

Badreddine, H. and Saanouni, K. [2015], 'Advanced anisotropic damage model fully coupled with anisotropic plasticity', *Applied Mechanics and Materials* **784**, 153–160.

Badreddine, H. and Saanouni, K. [2017], 'On the full coupling of plastic anisotropy and anisotropic ductile damage under finite strains', *International Journal of Damage Mechanics* **26**(7), 1080–1123.

Badreddine, H., Saanouni, K. and Dogui, A. [2010], 'On non-associative anisotropic finite plasticity fully coupled with isotropic ductile damage for metal forming', *International Journal of Plasticity* **26**(11), 1541 – 1575.

Badreddine, H., Saanouni, K. and Nguyen, T. D. [2015], 'Damage anisotropy and its effect on the plastic anisotropy evolution under finite strains', *International Journal of Solids and Structures* **63**, 11 – 31.

Badreddine, H., Yue, Z. and Saanouni, K. [2017], 'Modeling of the induced plastic anisotropy fully coupled with ductile damage under finite strains', *International Journal of Solids and Structures* **108**, 49 – 62.

Baillargeon, B., Rebelo, N., Fox, D. D., Taylor, R. L. and Kuhl, E. [2014], 'The living heart project: A robust and integrative simulator for human heart function', *European Journal of Mechanics - A/Solids* **48**, 38–47. Frontiers in Finite-Deformation Electromechanics.

Balieu, R. and Kringos, N. [2015], 'A new thermodynamical framework for finite strain multiplicative elastoplasticity coupled to anisotropic damage', *International Journal of Plasticity* **70**, 126 – 150.

Balzani, D. [2006], Polyconvex anisotropic energies and modeling of damage applied to arterial walls, PhD thesis, Universität Duisburg-Essen (Institute für Mechanik).

Bammann, D. J. and Johnson, G. C. [1987], 'On the kinematics of finite-deformation plasticity', *Acta Mechanica* **70**(1), 1–13.

Bammann, D. and Solanki, K. [2010*a*], 'On kinematic, thermodynamic, and kinetic coupling of a damage theory for polycrystalline material', *International Journal of Plasticity* **26**(6), 775–793.

Bammann, D. and Solanki, K. [2010*b*], 'On kinematic, thermodynamic, and kinetic coupling of a damage theory for polycrystalline material', *International Journal of Plasticity* **26**(6), 775–793.

Barbero, E. J. [2013], *Finite Element Analysis of Composite Materials using AbaqusTM* -, 1. aufl. edn, CRC Press, Boca Raton, Fla.

Barenblatt, G. [1962], The mathematical theory of equilibrium cracks in brittle fracture, Vol. 7 of *Advances in Applied Mechanics*, Elsevier, pp. 55–129.

Barfusz, O., Brepols, T., van der Velden, T., Frischkorn, J. and Reese, S. [2021], 'A single gauss point continuum finite element formulation for gradient-extended damage at large deformations', *Computer Methods in Applied Mechanics and Engineering* **373**, 113440.

Barfusz, O., van der Velden, T., Brepols, T., Holthusen, H. and Reese, S. [2021], 'A reduced integration-based solid-shell finite element formulation for gradient-extended damage', *Computer Methods in Applied Mechanics and Engineering* **382**, 113884.

Barsoum, I. and Faleskog, J. [2011], 'Micromechanical analysis on the influence of the lode parameter on void growth and coalescence', *International Journal of Solids and Structures* **48**(6), 925–938.

Bartholomew-Biggs, M., Brown, S., Christianson, B. and Dixon, L. [2000], 'Automatic differentiation of algorithms', *Journal of Computational and Applied Mathematics* **124**(1), 171–190. Numerical Analysis 2000. Vol. IV: Optimization and Nonlinear Equations.

Basu, S., Waas, A. M. and Ambur, D. R. [2006], 'Compressive failure of fiber composites under multi-axial loading', *Journal of the Mechanics and Physics of Solids* **54**(3), 611 – 634.

Bauer, J. K. and Böhlke, T. [2022], 'Fiber orientation distributions based on planar fiber orientation tensors of fourth order', *Mathematics and Mechanics of Solids* **0**(0), 10812865221093958.

Bayat, H. R., Rezaei, S., Brepols, T. and Reese, S. [2020], 'Locking-free interface failure modeling by a cohesive discontinuous galerkin method for matching and nonmatching meshes', *International Journal for Numerical Methods in Engineering* **121**(8), 1762–1790.

Bažant, Z., Belytschko, T. and Chang, T. [1984], 'Continuum theory for strain-softening', *Journal of Engineering Mechanics - ASCE* **110**(12), 1666–1692. Copyright: Copyright 2015 Elsevier B.V., All rights reserved.

Bažant, Z. and Ožbolt, J. [1990], 'Nonlocal microplane model for fracture, damage, and size effect in structures', *Journal of Engineering Mechanics - ASCE* **116**(11), 2485–2505. Copyright: Copyright 2015 Elsevier B.V., All rights reserved.

Bažant, Z. P. [1982], Crack band model for fracture of geomaterials., *in* 'Proceedings of the 4th International Conference on Numerical Methods in Geomechanics', AA Balkema, pp. 1137–1152.

Bažant, Z. P. [1985], *Mechanics of fracture and progressive cracking in concrete structures*, Springer Netherlands, Dordrecht, pp. 1–94.

Bazant, Z. P. [1991], 'Why continuum damage is nonlocal: Micromechanics arguments', *Journal of Engineering Mechanics* **117**(5), 1070–1087.

Bažant, Z. P. and Pijaudier-Cabot, G. [1988], 'Nonlocal continuum damage, localization instability and convergence', *Journal of Applied Mechanics* **55**(2), 287–293.

Bažant, Z. P. and Gambarova, P. G. [1984], 'Crack shear in concrete: Crack band microflane model', *Journal of Structural Engineering* **110**(9), 2015–2035.

Bažant, Z. P. and Jirásek, M. [2002], 'Nonlocal integral formulations of plasticity and damage: Survey of progress', *Journal of Engineering Mechanics* **128**(11), 1119–1149.

Bažant, Z. P. and Oh, B. H. [1985], 'Microplane model for progressive fracture of concrete and rock', *Journal of Engineering Mechanics* **111**(4), 559–582.

Bednarcyk, B. A., Stier, B., Simon, J.-W., Reese, S. and Pineda, E. J. [2015], 'Meso- and micro-scale modeling of damage in plain weave composites', *Composite Structures* **121**, 258 – 270.

Belytschko, T. and Black, T. [1999], 'Elastic crack growth in finite elements with minimal remeshing', *International Journal for Numerical Methods in Engineering* **45**(5), 601–620.

Benzerga, A., Besson, J. and Pineau, A. [2004], 'Anisotropic ductile fracture', *Acta Materialia* **52**(15), 4623–4638.

Bertram, A. [1999], 'An alternative approach to finite plasticity based on material isomorphisms', *International Journal of Plasticity* **15**(3), 353–374.

Bertram, A. [2012], *Elasticity and Plasticity of Large Deformations*, Springer Berlin Heidelberg.

Besson, J. [2010], 'Continuum models of ductile fracture : A review', *International Journal of Damage Mechanics* **19**, 3–52.

Betten, J. [1987], 'Irreducible invariants of fourth-order tensors', *Mathematical Modelling* **8**, 29–33.

Bischof, C., Carle, A., Corliss, G., Griewank, A. and Hovland, P. [1992], 'Adifor–generating derivative codes from fortran programs', *Scientific Programming* **1**, 717832.

Boehler, J.-P. [1979], 'A simple derivation of representations for non-polynomial constitutive equations in some cases of anisotropy', *ZAMM - Journal of Applied Mathematics and Mechanics / Zeitschrift für Angewandte Mathematik und Mechanik* **59**(4), 157–167.

Böl, M., Ehret, A. E., Leichsenring, K., Weichert, C. and Kruse, R. [2014], 'On the anisotropy of skeletal muscle tissue under compression', *Acta Biomaterialia* **10**(7), 3225–3234.

Borino, G., Failla, B. and Parrinello, F. [2003], 'A symmetric nonlocal damage theory', *International Journal of Solids and Structures* **40**(13), 3621–3645.

Bouchard, P.-O., Bourgeon, L., Fayolle, S. and Mocellin, K. [2011], 'An enhanced lemaitre model formulation for materials processing damage computation', *International Journal of Material Forming* **4**(3), 299–315.

Bourdin, B., Francfort, G. and Marigo, J.-J. [2000], 'Numerical experiments in revisited brittle fracture', *Journal of the Mechanics and Physics of Solids* **48**(4), 797–826.

Braeu, F. A., Aydin, R. C. and Cyron, C. J. [2019], 'Anisotropic stiffness and tensional homeostasis induce a natural anisotropy of volumetric growth and remodeling in soft biological tissues', *Biomechanics and Modeling in Mechanobiology* **18**(2), 327–345.

Braeu, F. A., Seitz, A., Aydin, R. C. and Cyron, C. J. [2017], 'Homogenized constrained mixture models for anisotropic volumetric growth and remodeling', *Biomechanics and Modeling in Mechanobiology* **16**(3), 889–906.

Brepols, T., Wulfinghoff, S. and Reese, S. [2017], 'Gradient-extended two-surface damage-plasticity: Micromorphic formulation and numerical aspects', *International Journal of Plasticity* **97**, 64 – 106.

Brepols, T., Wulfinghoff, S. and Reese, S. [2018*a*], 'A flexible two-surface gradient-extended damage-plasticity model for large deformations with nonlinear kinematic hardening', *PAMM* **18**(1).

Brepols, T., Wulfinghoff, S. and Reese, S. [2018*b*], *A Micromorphic Damage-Plasticity Model to Counteract Mesh Dependence in Finite Element Simulations Involving Material Softening*, Springer International Publishing, Cham, pp. 235–255.

Brepols, T., Wulfinghoff, S. and Reese, S. [2020], 'A gradient-extended two-surface damage-plasticity model for large deformations', *International Journal of Plasticity* **129**, 102635.

Brown, R. A., Prajapati, R., McGrouther, D. A., Yannas, I. V. and Eastwood, M. [1998], 'Tensional homeostasis in dermal fibroblasts: Mechanical responses to mechanical loading in three-dimensional substrates', *Journal of Cellular Physiology* **175**(3), 323–332.

Brünig, M. [2003], 'An anisotropic ductile damage model based on irreversible thermodynamics', *International Journal of Plasticity* **19**(10), 1679–1713.

Brünig, M., Chyra, O., Albrecht, D., Driemeier, L. and Alves, M. [2008], 'A ductile damage criterion at various stress triaxialities', *International Journal of Plasticity* **24**(10), 1731–1755. Special Issue in Honor of Jean-Louis Chaboche.

Brünig, M. and Gerke, S. [2011], 'Simulation of damage evolution in ductile metals undergoing dynamic loading conditions', *International Journal of Plasticity* **27**(10), 1598–1617. Conventional and Emerging Materials.

Brünig, M., Gerke, S. and Hagenbrock, V. [2013], 'Micro-mechanical studies on the effect of the stress triaxiality and the lode parameter on ductile damage', *International Journal of Plasticity* **50**, 49–65.

Brünig, M., Gerke, S. and Schmidt, M. [2018], 'Damage and failure at negative stress triaxialities: Experiments, modeling and numerical simulations', *International Journal of Plasticity* **102**, 70–82.

Brünig, M., Gerke, S. and Zistl, M. [2019], 'Experiments and numerical simulations with the h-specimen on damage and fracture of ductile metals under non-proportional loading paths', *Engineering Fracture Mechanics* **217**, 106531.

Budday, S., Nay, R., de Rooij, R., Steinmann, P., Wyrobek, T., Ovaert, T. C. and Kuhl, E. [2015], 'Mechanical properties of gray and white matter brain tissue by indentation', *Journal of the Mechanical Behavior of Biomedical Materials* **46**, 318–330.

Budday, S., Ovaert, T. C., Holzapfel, G. A., Steinmann, P. and Kuhl, E. [2020], 'Fifty shades of brain: A review on the mechanical testing and modeling of brain tissue', *Archives of Computational Methods in Engineering* **27**(4), 1187–1230.

Budday, S., Sommer, G., Birkl, C., Langkammer, C., Haybaeck, J., Kohnert, J., Bauer, M., Paulsen, F., Steinmann, P., Kuhl, E. and Holzapfel, G. [2017], 'Mechanical characterization of human brain tissue', *Acta Biomaterialia* **48**, 319–340.

Buganza Tepole, A., Joseph Ploch, C., Wong, J., Gosain, A. K. and Kuhl, E. [2011], 'Growing skin: A computational model for skin expansion in reconstructive surgery', *Journal of the Mechanics and Physics of Solids* **59**(10), 2177–2190.

Burgio, V., Civera, M., Reinoso, M. R., Pizzolante, E., Prezioso, S., Bertuglia, A. and Surace, C. [2022], 'Mechanical properties of animal tendons: A review and comparative study for the identification of the most suitable human tendon surrogates', *Processes* **10**(3), 485.

Böl, M., Ehret, A. E., Leichsenring, K. and Ernst, M. [2015], 'Tissue-scale anisotropy and compressibility of tendon in semi-confined compression tests', *Journal of Biomechanics* **48**(6), 1092–1098.

Canadija, M. and Mosler, J. [2011], 'On the thermomechanical coupling in finite strain plasticity theory with non-linear kinematic hardening by means of incremental energy minimization', *International Journal of Solids and Structures* **48**(7), 1120–1129.

Cannon, W. B. [1929], 'ORGANIZATION FOR PHYSIOLOGICAL HOMEOSTASIS', *Physiological Reviews* **9**(3), 399–431.

Carol, I., Rizzi, E. and Willam, K. [2002], 'An 'extended' volumetric/deviatoric formulation of anisotropic damage based on a pseudo-log rate', *European Journal of Mechanics - A/Solids* **21**(5), 747–772.

Casey, J. [2017], 'A convenient form of the multiplicative decomposition of the deformation gradient', *Mathematics and Mechanics of Solids* **22**(3), 528–537.

Celentano, D. J. and Chaboche, J.-L. [2007], 'Experimental and numerical characterization of damage evolution in steels', *International Journal of Plasticity* **23**(10-11), 1739–1762.

Chaboche, J. [1984], 'Anisotropic creep damage in the framework of continuum damage mechanics', *Nuclear Engineering and Design* **79**(3), 309–319.

Chaboche, J.-L. [1978], Description thermodynamique et phénoménologique de la viscoplasticité cyclique avec endommagement, PhD thesis, University Pierre and Marie Curie (Paris VI).

Chaboche, J.-L. [1981], 'Continuous damage mechanics — a tool to describe phenomena before crack initiation', *Nuclear Engineering and Design* **64**(2), 233–247.

Chaboche, J.-L. [1992], 'Damage induced anisotropy: On the difficulties associated with the active/passive unilateral condition', *International Journal of Damage Mechanics* **1**(2), 148–171.

Chaboche, J.-L. [1993], 'Development of continuum damage mechanics for elastic solids sustaining anisotropic and unilateral damage', *International Journal of Damage Mechanics* **2**(4), 311–329.

Chaboche, J. L., Lesne, P. M. and Maire, J. F. [1995], 'Continuum damage mechanics, anisotropy and damage deactivation for brittle materials like concrete and ceramic composites', *International Journal of Damage Mechanics* **4**(1), 5–22.

Chaboche, J.-L. and Maire, J.-F. [2002], 'A new micromechanics based cdm model and its application to cmc's', *Aerospace Science and Technology* **6**(2), 131 – 145.

Challamel, N., Lanos, C. and Casandjian, C. [2005], 'Strain-based anisotropic damage modelling and unilateral effects', *International Journal of Mechanical Sciences* **47**(3), 459 – 473.

Chen, F., Balieu, R. and Kringos, N. [2017], 'Thermodynamics-based finite strain viscoelastic-viscoplastic model coupled with damage for asphalt material', *International Journal of Solids and Structures* **129**, 61 – 73.

Chen, S., Chen, H., Mitsume, N., Morita, N., Bui, T. Q., Gao, W. and Yoshimura, S. [2021], 'A nodal-based lagrange multiplier/cohesive zone approach for dynamic interfacial cracking analysis of thin-walled laminated composite structures', *Composite Structures* **256**, 113112.

Chow, C. L. and Wei, Y. [1999], 'Constitutive modeling of material damage for fatigue failure prediction', *International Journal of Damage Mechanics* **8**(4), 355–375.

Christ, D. and Reese, S. [2009], 'A finite element model for shape memory alloys considering thermomechanical couplings at large strains', *International Journal of Solids and Structures* **46**(20), 3694–3709.

Chung, I. and Weitsman, Y. [1995], 'On the buckling/kinking compressive failure of fibrous composites', *International Journal of Solids and Structures* **32**(16), 2329 – 2344.

Ciambella, J., Lucci, G., Nardinocchi, P. and Preziosi, L. [2022], 'Passive and active fiber reorientation in anisotropic materials', *International Journal of Engineering Science* **176**, 103688.

Ciambella, J. and Nardinocchi, P. [2019], 'Torque-induced reorientation in active fibre-reinforced materials', *Soft Matter* **15**(9), 2081–2091.

Ciambella, J. and Nardinocchi, P. [2022], 'Non-affine fiber reorientation in finite inelasticity', *Journal of Elasticity* .

Coleman, B. D. and Gurtin, M. E. [1967], 'Thermodynamics with internal state variables', *The Journal of Chemical Physics* **47**(2), 597–613.

Coleman, B. D. and Noll, W. [1961], 'Foundations of linear viscoelasticity', *Rev. Mod. Phys.* **33**, 239–249.

Coleman, B. D. and Noll, W. [1963], 'The thermodynamics of elastic materials with heat conduction and viscosity', *Archive for Rational Mechanics and Analysis* **13**(1), 167–178.

Comi, C. [2001], 'Non-local model with tension and compression damage mechanisms', *European Journal of Mechanics - A/Solids* **20**, 1–22.

Comi, C. and Perego, U. [2001], 'Fracture energy based bi-dissipative damage model for concrete', *International Journal of Solids and Structures* **38**(36-37), 6427–6454.

Cordebois, J. P. and Sidoroff, F. [1982], Damage induced elastic anisotropy, *in* J.-P. Boehler, ed., 'Mechanical Behavior of Anisotropic Solids / Comportment Méchanique des Solides Anisotropes', Springer Netherlands, Dordrecht, pp. 761–774.

Cowin, S. C. [1984], 'Mechanical modeling of the stress adaptation process in bone', *Calcified Tissue International* **36**(S1), S98–S103.

Cowin, S. C. [1999], 'Bone poroelasticity', *Journal of Biomechanics* **32**(3), 217–238.

Cowin, S. C. [2004], 'Tissue growth and remodeling', *Annual Review of Biomedical Engineering* **6**(1), 77–107.

Cowin, S. C. and Doty, S. B., eds [2007], *Tissue Mechanics*, Springer New York.

Cowin, S. C., ed. [2001], *Bone Mechanics Handbook*, CRC Press.

Cowin, S. C. and Hegedus, D. H. [1976], 'Bone remodeling i: theory of adaptive elasticity', *Journal of Elasticity* **6**(3), 313–326.

Cowin, S. C. and Nachlinger, R. R. [1978], 'Bone remodeling III: uniqueness and stability in adaptive elasticity theory', *Journal of Elasticity* **8**(3), 285–295.

Creane, A., Maher, E., Sultan, S., Hynes, N., Kelly, D. J. and Lally, C. [2011], 'Prediction of fibre architecture and adaptation in diseased carotid bifurcations', *Biomechanics and Modeling in Mechanobiology* **10**(6), 831–843.

Criscione, J. C., Humphrey, J. D., Douglas, A. S. and Hunter, W. C. [2000], 'An invariant basis for natural strain which yields orthogonal stress response terms in isotropic hyperelasticity', *Journal of the Mechanics and Physics of Solids* **48**(12), 2445–2465.

Cuitiño, A. and Ortiz, M. [1992], 'A material-independent method for extending stress update algorithms from small-strain plasticity to finite plasticity with multiplicative kinematics', *Engineering Computations* **9**(4), 437–451.

Cuntze, R. G. [2006], 'Failure conditions for isotropic materials, unidirectional composites, woven fabrics- their visualization and links-'.

Cyron, C. J. and Aydin, R. C. [2017], 'Mechanobiological free energy: a variational approach to tensional homeostasis in tissue equivalents', *ZAMM - Journal of Applied Mathematics and Mechanics / Zeitschrift für Angewandte Mathematik und Mechanik* **97**(9), 1011–1019.

Cyron, C. J., Aydin, R. C. and Humphrey, J. D. [2016], 'A homogenized constrained mixture (and mechanical analog) model for growth and remodeling of soft tissue', *Biomechanics and Modeling in Mechanobiology* **15**(6), 1389–1403.

Cyron, C. J. and Humphrey, J. D. [2016], 'Growth and remodeling of load-bearing biological soft tissues', *Meccanica* **52**(3), 645–664.

Dafalias, Y. F. [1984], 'The plastic spin concept and a simple illustration of its role in finite plastic transformations', *Mechanics of Materials* **3**(3), 223–233.

Dafalias, Y. F. [1985], 'The Plastic Spin', *Journal of Applied Mechanics* **52**(4), 865–871.

Dafalias, Y. F. [1987], 'Issues on the constitutive formulation at large elastoplastic deformations, part 1: Kinematics', *Acta Mechanica* **69**(1), 119–138.

Dafalias, Y. F. [2011], 'Finite elastic-plastic deformations: Beyond the plastic spin', *Theoretical and Applied Mechanics* **38**(4), 321–345.

Dal, H., Göktepe, S., Kaliske, M. and Kuhl, E. [2013], 'A fully implicit finite element method for bidomain models of cardiac electromechanics', *Computer Methods in Applied Mechanics and Engineering* **253**, 323–336.

Davison, L. and Stevens, A. L. [1973], 'Thermomechanical constitution of spalling elastic bodies', *Journal of Applied Physics* **44**(2), 668–674.

de Borst, R. [1991], 'Simulation of strain localization: A reappraisal of the cosserat continuum', *Engineering Computations* **8**(4), 317–332.

de Borst, R. [1996], Softening, damage, and higher order continua, *in* 'ed.). FH Wittmann, AEDIFICATIO Publishers, Freiburg (Germany) Proc. 2nd Conf on Fracture Mech. of Concrete Struc', pp. 1631–1640.

de Borst, R., Sluys, L., Muhlhaus, H. and Pamin, J. [1993], 'Fundamental issues in finite element analyses of localization of deformation', *Engineering Computations* **10**(2), 99–121.

de Rooij, R. and Kuhl, E. [2016], 'Constitutive Modeling of Brain Tissue: Current Perspectives', *Applied Mechanics Reviews* **68**(1). 010801.

de Souza Neto, E. A., Perić, D. and Owen, D. R. J. [1998], 'Continuum modelling and numerical simulation of material damage at finite strains', *Archives of Computational Methods in Engineering* **5**(4), 311.

de Souza Neto, E. A., Peric, D. and Owen, D. R. J. [2011], *Computational Methods for Plasticity: Theory and Applications*, John Wiley & Sons, New York.

Dean, A., Asur Vijaya Kumar, P., Reinoso, J., Gerendt, C., Paggi, M., Mahdi, E. and Rolfes, R. [2020], 'A multi phase-field fracture model for long fiber reinforced composites based on the puck theory of failure', *Composite Structures* **251**, 112446.

Dean, A., Reinoso, J., Sahraee, S. and Rolfes, R. [2016], 'An invariant-based anisotropic material model for short fiber-reinforced thermoplastics: Coupled thermo-plastic formulation', *Composites Part A: Applied Science and Manufacturing* **90**, 186–199.

Dean, A., Safdar, N. and Rolfes, R. [2019], 'A co-rotational based anisotropic elasto-plastic model for geometrically non-linear analysis of fibre reinforced polymer composites: Formulation and finite element implementation', *Materials (Basel, Switzerland)* **12**(11).

Dean, A., Sahraee, S., Reinoso, J. and Rolfes, R. [2017], 'A new invariant-based thermo-plastic model for finite deformation analysis of short fibre reinforced composites: Development and numerical aspects', *Composites Part B: Engineering* **125**, 241–258.

Desmorat, R. [2016], 'Anisotropic damage modeling of concrete materials', *International Journal of Damage Mechanics* **25**(6), 818–852.

Desmorat, R. and Cantournet, S. [2008], 'Modeling microdefects closure effect with isotropic/anisotropic damage', *International Journal of Damage Mechanics* **17**(1), 65–96.

Dettmer, W. and Reese, S. [2004], 'On the theoretical and numerical modelling of armstrong–frederick kinematic hardening in the finite strain regime', *Computer Methods in Applied Mechanics and Engineering* **193**(1), 87 – 116.

Dimitrijevic, B. J. and Hackl, K. [2008], 'A method for gradient enhancement of continuum damage models', *Technische Mechanik-European Journal of Engineering Mechanics* **28**(1), 43–52.

Dimitrijevic, B. J. and Hackl, K. [2011], 'A regularization framework for damage–plasticity models via gradient enhancement of the free energy', *International Journal for Numerical Methods in Biomedical Engineering* **27**(8), 1199–1210.

Dittmann, M., Aldakheel, F., Schulte, J., Schmidt, F., Krüger, M., Wriggers, P. and Hesch, C. [2020], 'Phase-field modeling of porous-ductile fracture in non-linear thermo-elasto-plastic solids', *Computer Methods in Applied Mechanics and Engineering* **361**, 112730.

Dittmann, M., Aldakheel, F., Schulte, J., Wriggers, P. and Hesch, C. [2018], 'Variational phase-field formulation of non-linear ductile fracture', *Computer Methods in Applied Mechanics and Engineering* **342**, 71–94.

Dong, H., Liu, M., Martin, C. and Sun, W. [2020], 'A residual stiffness-based model for the fatigue damage of biological soft tissues', *Journal of the Mechanics and Physics of Solids* **143**, 104074.

Dorn, C. and Wulfinghoff, S. [2021], 'A gradient-extended large-strain anisotropic damage model with crack orientation director', *Computer Methods in Applied Mechanics and Engineering* **387**, 114123.

Dow, N. and Gruntfest, T. [1960], 'Determination of most needed potentially possible improvements', *Materials for Ballastic and Space Vehicles* .

Dragon, A. and Mróz, Z. [1979], 'A continuum model for plastic-brittle behaviour of rock and concrete', *International Journal of Engineering Science* **17**(2), 121–137.

Driessen, N. J. B., Cox, M. A. J., Bouten, C. V. C. and Baaijens, F. P. T. [2008], 'Remodelling of the angular collagen fiber distribution in cardiovascular tissues', *Biomechanics and Modeling in Mechanobiology* **7**(2), 93–103.

Driessen, N., Wilson, W., Bouten, C. and Baaijens, F. [2004], 'A computational model for collagen fibre remodelling in the arterial wall', *Journal of Theoretical Biology* **226**(1), 53–64.

Dugdale, D. [1960], 'Yielding of steel sheets containing slits', *Journal of the Mechanics and Physics of Solids* **8**(2), 100–104.

Eastwood, M., Mudera, V., Mcgrouther, D. and Brown, R. [1998], 'Effect of precise mechanical loading on fibroblast populated collagen lattices: Morphological changes', *Cell Motility and the Cytoskeleton* **40**(1), 13–21.

Eckart, C. [1948], 'The thermodynamics of irreversible processes. iv. the theory of elasticity and anelasticity', *Phys. Rev.* **73**, 373–382.

Eggersmann, R., Stainier, L., Ortiz, M. and Reese, S. [2021], 'Model-free data-driven computational mechanics enhanced by tensor voting', *Computer Methods in Applied Mechanics and Engineering* **373**, 113499.

Ehret, A. E., Böl, M. and Itskov, M. [2011], 'A continuum constitutive model for the active behaviour of skeletal muscle', *Journal of the Mechanics and Physics of Solids* **59**(3), 625–636.

Eichinger, J. F. [2021], Micromechanical Foundations of Mechanobiology in Soft Tissues, PhD thesis, Technische Universität München.

Eichinger, J. F., Grill, M. J., Kermani, I. D., Aydin, R. C., Wall, W. A., Humphrey, J. D. and Cyron, C. J. [2021], 'A computational framework for modeling cell–matrix interactions in soft biological tissues', *Biomechanics and Modeling in Mechanobiology* **20**(5), 1851–1870.

Eichinger, J. F., Haeusel, L. J., Paukner, D., Aydin, R. C., Humphrey, J. D. and Cyron, C. J. [2021], 'Mechanical homeostasis in tissue equivalents: a review', *Biomechanics and Modeling in Mechanobiology* **20**(3), 833–850.

Eichinger, J. F., Paukner, D., Aydin, R. C., Wall, W. A., Humphrey, J. D. and Cyron, C. J. [2021], 'What do cells regulate in soft tissues on short time scales?', *Acta Biomaterialia* **134**, 348–356.

Eichinger, J. F., Paukner, D., Szafron, J. M., Aydin, R. C., Humphrey, J. D. and Cyron, C. J. [2020], 'Computer-Controlled Biaxial Bioreactor for Investigating Cell-Mediated Homeostasis in Tissue Equivalents', *Journal of Biomechanical Engineering* **142**(7). 071011.

Ekh, M., Lillbacka, R. and Runesson, K. [2004], 'A model framework for anisotropic damage coupled to crystal (visco)plasticity', *International Journal of Plasticity* **20**(12), 2143–2159.

Erlich, A., Moulton, D. E. and Goriely, A. [2019], 'Are homeostatic states stable? dynamical stability in morphoelasticity', *Bulletin of Mathematical Biology* **81**(8), 3219–3244.

Escuer, J., Martínez, M. A., McGinty, S. and Peña, E. [2019], 'Mathematical modelling of the restenosis process after stent implantation', *Journal of The Royal Society Interface* **16**(157), 20190313.

Eterovic, A. L. and Bathe, K.-J. [1990], 'A hyperelastic-based large strain elasto-plastic constitutive formulation with combined isotropic-kinematic hardening using the logarithmic stress and strain measures', *International Journal for Numerical Methods in Engineering* **30**(6), 1099–1114.

Evans, A. and Adler, W. [1978], 'Kinking as a mode of structural degradation in carbon fiber composites', *Acta Metallurgica* **26**(5), 725 – 738.

Ezra, D. G., Ellis, J. S., Beaconsfield, M., Collin, R. and Bailly, M. [2010], 'Changes in Fibroblast Mechanostat Set Point and Mechanosensitivity: An Adaptive Response to Mechanical Stress in Floppy Eyelid Syndrome', *Investigative Ophthalmology & Visual Science* **51**(8), 3853–3863.

Fassin, M., Eggersmann, R., Wulfinghoff, S. and Reese, S. [2019*a*], 'Efficient algorithmic incorporation of tension compression asymmetry into an anisotropic damage model', *Computer Methods in Applied Mechanics and Engineering* **354**, 932 – 962.

Fassin, M., Eggersmann, R., Wulfinghoff, S. and Reese, S. [2019*b*], 'Gradient-extended anisotropic brittle damage modeling using a second order damage tensor – theory, implementation and numerical examples', *International Journal of Solids and Structures* **167**, 93 – 126.

Fassin, M., Wulfinghoff, S. and Reese, S. [2017], A gradient-extended elastic isotropic damage model considering crack-closure, *in* 'Proceedings of the 7th GACM Colloquium on Computational Mechanics', pp. 305–311.

Fausten, S., Balzani, D. and Schröder, J. [2016], 'An algorithmic scheme for the automated calculation of fiber orientations in arterial walls', *Computational Mechanics* **58**(5), 861–878.

Felder, S., Holthusen, H., Hesseler, S., Pohlkemper, F., Gries, T., Simon, J.-W. and Reese, S. [2020], 'Incorporating crystallinity distributions into a thermo-mechanically coupled constitutive model for semi-crystalline polymers', *International Journal of Plasticity* **135**, 102751.

Felder, S., Kopic-Osmanovic, N., Holthusen, H., Brepols, T. and Reese, S. [2022], 'Thermo-mechanically coupled gradient-extended damage-plasticity modeling of metallic materials at finite strains', *International Journal of Plasticity* **148**, 103142.

Fiedler, B., Hojo, M., Ochiai, S., Schulte, K. and Ando, M. [2001], 'Failure behavior of an epoxy matrix under different kinds of static loading', *Composites Science and Technology* **61**(11), 1615 – 1624.

Firooz, S., Kaessmair, S., Zaburdaev, V., Javili, A. and Steinmann, P. [2022], 'On continuum modeling of cell aggregation phenomena', *Journal of the Mechanics and Physics of Solids* **167**, 105004.

Floerkemeier, T., Lutz, A., Nackenhorst, U., Thorey, F., Waizy, H., Windhagen, H. and von Lewinski, G. [2010], 'Core decompression and osteonecrosis intervention rod in osteonecrosis of the femoral head: clinical outcome and finite element analysis', *International Orthopaedics* **35**(10), 1461–1466.

Flory, P. [1961], 'Thermodynamic relations for high elastic materials', *Transactions of the Faraday Society* **57**, 829–838.

Forest, S. [2009], 'Micromorphic approach for gradient elasticity, viscoplasticity, and damage', *Journal of Engineering Mechanics* **135**(3), 117–131.

Forest, S. [2016], 'Nonlinear regularization operators as derived from the micromorphic approach to gradient elasticity, viscoplasticity and damage', *Proceedings of the Royal Society A: Mathematical, Physical and Engineering Sciences* **472**(2188), 20150755.

Francfort, G. and Marigo, J.-J. [1998], 'Revisiting brittle fracture as an energy minimization problem', *Journal of the Mechanics and Physics of Solids* **46**(8), 1319–1342.

Friedlein, J., Mergheim, J. and Steinmann, P. [2021], A finite plasticity gradient-damage model for sheet metals during forming and clinching, *in* 'Sheet Metal 2021', Vol. 883 of *Key Engineering Materials*, Trans Tech Publications Ltd, pp. 57–64.

Friedlein, J., Mergheim, J. and Steinmann, P. [2022], 'Observations on additive plasticity in the logarithmic strain space at excessive strains', *International Journal of Solids and Structures* **239-240**, 111416.

Friedlein, J., Mergheim, J. and Steinmann, P. [2023], 'Efficient gradient enhancements for plasticity with ductile damage in the logarithmic strain space', *European Journal of Mechanics - A/Solids* **99**, 104946.

Ganghoffer, J., Sluys, L. and de Borst, R. [1999], 'A reappraisal of nonlocal mechanics', *European Journal of Mechanics - A/Solids* **18**(1), 17–46.

Ganjiani, M., Naghdabadi, R. and Asghari, M. [2013], 'An elastoplastic damage-induced anisotropic constitutive model at finite strains', *International Journal of Damage Mechanics* **22**(4), 499–529.

Garikipati, K., Arruda, E., Grosh, K., Narayanan, H. and Calve, S. [2004], 'A continuum treatment of growth in biological tissue: the coupling of mass transport and mechanics', *Journal of the Mechanics and Physics of Solids* **52**(7), 1595–1625.

Gasser, T. C., Ogden, R. W. and Holzapfel, G. A. [2006], 'Hyperelastic modelling of arterial layers with distributed collagen fibre orientations', *Journal of The Royal Society Interface* **3**(6), 15–35.

Geers, M. [2004], 'Finite strain logarithmic hyperelasto-plasticity with softening: a strongly non-local implicit gradient framework', *Computer Methods in Applied Mechanics and Engineering* **193**(30), 3377–3401. Computational Failure Mechanics.

Geers, M., de Borst, R., Brekelmans, W. and Peerlings, R. [1998], 'Strain-based transient-gradient damage model for failure analyses', *Computer Methods in Applied Mechanics and Engineering* **160**(1), 133 – 153.

Geers, M., Kouznetsova, V. and Brekelmans, W. [2010], 'Multi-scale computational homogenization: Trends and challenges', *Journal of Computational and Applied Mathematics* **234**(7), 2175–2182. Fourth International Conference on Advanced COmputational Methods in ENgineering (ACOMEN 2008).

Gerke, S., Zistl, M. and Brünig, M. [2020], 'Experiments and numerical simulation of damage and fracture of the x0-specimen under non-proportional loading paths', *Engineering Fracture Mechanics* **224**, 106795.

Germain, N., Besson, J. and Feyel, F. [2007], 'Composite layered materials: Anisotropic nonlocal damage models', *Computer Methods in Applied Mechanics and Engineering* **196**(41), 4272 – 4282.

Germain, P., Nguyen, Q. S. and Suquet, P. [1983], 'Continuum Thermodynamics', *Journal of Applied Mechanics* **50**(4b), 1010–1020.

Gierden, C., Kochmann, J., Waimann, J., Svendsen, B. and Reese, S. [2022], 'A review of fe-fft-based two-scale methods for computational modeling of microstructure evolution and macroscopic material behavior', *Archives of Computational Methods in Engineering* **29**(6), 4115–4135.

González, C. and LLorca, J. [2007], 'Mechanical behavior of unidirectional fiber-reinforced polymers under transverse compression: Microscopic mechanisms and modeling', *Composites Science and Technology* **67**(13), 2795 – 2806.

Goriely, A. [2017], *The Mathematics and Mechanics of Biological Growth*, Springer New York.

Goriely, A. [2018], 'Five ways to model active processes in elastic solids: Active forces, active stresses, active strains, active fibers, and active metrics', *Mechanics Research Communications* **93**, 75–79. Mechanics from the 20th to the 21st Century: The Legacy of Gérard A. Maugin.

Govindjee, S., Kay, G. J. and Simo, J. C. [1995], 'Anisotropic modelling and numerical simulation of brittle damage in concrete', *International Journal for Numerical Methods in Engineering* **38**(21), 3611–3633.

Green, A. and Naghdi, P. [1971], 'Some remarks on elastic-plastic deformation at finite strain', *International Journal of Engineering Science* **9**(12), 1219–1229.

Griewank, A., Juedes, D. and Utke, J. [1996], 'Algorithm 755: Adol-c: A package for the automatic differentiation of algorithms written in c/c++', *ACM Trans. Math. Softw.* **22**(2), 131–167.

Griewank, A. and Walther, A. [2008], *Evaluating Derivatives*, Society for Industrial and Applied Mathematics.

Grytsan, A., Eriksson, T. S. E., Watton, P. N. and Gasser, T. C. [2017], 'Growth description for vessel wall adaptation: A thick-walled mixture model of abdominal aortic aneurysm evolution', *Materials (Basel, Switzerland)* **10**(9), 994. 28841196[pmid].

Guccione, J. M. and McCulloch, A. D. [1993], 'Mechanics of Active Contraction in Cardiac Muscle: Part I—Constitutive Relations for Fiber Stress That Describe Deactivation', *Journal of Biomechanical Engineering* **115**(1), 72–81.

Gurson, A. L. [1977], 'Continuum theory of ductile rupture by void nucleation and growth: Part i—yield criteria and flow rules for porous ductile media', *Journal of Engineering Materials and Technology* **99**(1), 2–15.

Göktepe, S., Abilez, O. J. and Kuhl, E. [2010], 'A generic approach towards finite growth with examples of athlete's heart, cardiac dilation, and cardiac wall thickening', *Journal of the Mechanics and Physics of Solids* **58**(10), 1661–1680.

Han, D. and Chen, W. [1985], 'A nonuniform hardening plasticity model for concrete materials', *Mechanics of Materials* **4**(3), 283–302.

Hansen, N. and Schreyer, H. [1994], 'A thermodynamically consistent framework for theories of elastoplasticity coupled with damage', *International Journal of Solids and Structures* **31**(3), 359 – 389.

Hao, L., Ke, P. and June, W. [1985], 'An anisotropic damage criterion for deformation instability and its application to forming limit analysis of metal plates', *Engineering Fracture Mechanics* **21**(5), 1031–1054.

Harich, J., Lapusta, Y. and Wagner, W. [2009], '3d fe-modeling of surface and anisotropy effects during micro-buckling in fiber composites', *Composite Structures* **89**(4), 551 – 555.

Hariton, I., deBotton, G., Gasser, T. C. and Holzapfel, G. A. [2007*a*], 'Stress-driven collagen fiber remodeling in arterial walls', *Biomechanics and Modeling in Mechanobiology* **6**(3), 163–175.

Hariton, I., deBotton, G., Gasser, T. and Holzapfel, G. [2007*b*], 'Stress-modulated collagen fiber remodeling in a human carotid bifurcation', *Journal of Theoretical Biology* **248**(3), 460–470.

Harris, B. [1999], *Engineering composite materials*, The Institute of Materials; 673, 2nd edn, IOM Communications, London.

Hascoet, L. and Pascual, V. [2013], 'The tapenade automatic differentiation tool', *ACM Transactions on Mathematical Software* **39**(3), 1–43.

Hashin, Z. and Rotem, A. [1973], 'A fatigue failure criterion for fiber reinforced materials', *Journal of Composite Materials* **7**(4), 448–464.

Haupt, P. [2002], *Continuum Mechanics and Theory of Materials*, Springer Berlin Heidelberg.

Haupt, P. and Sedlan, K. [2001], 'Viscoplasticity of elastomeric materials: experimental facts and constitutive modelling', *Archive of Applied Mechanics* **71**(2), 89–109.

He, G. [2019], 'Development of an elastothermoviscoplasticity damage model for injection molded short fiber reinforced thermoplastics with anisotropic damage evolutions', *Mechanics of Advanced Materials and Structures* **26**(22), 1889–1901.

Hegedus, D. H. and Cowin, S. C. [1976], 'Bone remodeling II: small strain adaptive elasticity', *Journal of Elasticity* **6**(4), 337–352.

Hill, R. [1968], 'On constitutive inequalities for simple materials—i', *Journal of the Mechanics and Physics of Solids* **16**(4), 229 – 242.

Hill, R. and Orowan, E. [1948], 'A theory of the yielding and plastic flow of anisotropic metals', *Proceedings of the Royal Society of London. Series A. Mathematical and Physical Sciences* **193**(1033), 281–297.

Hillerborg, A., Modéer, M. and Petersson, P.-E. [1976], 'Analysis of crack formation and crack growth in concrete by means of fracture mechanics and finite elements', *Cement and Concrete Research* **6**(6), 773–781.

Himpel, G., Kuhl, E., Menzel, A. and Steinmann, P. [2005], 'Computational modelling of isotropic multiplicative growth', *Computer Modeling in Engineering & Sciences* **8**(2), 119–134.

Himpel, G., Menzel, A., Kuhl, E. and Steinmann, P. [2008], 'Time-dependent fibre reorientation of transversely isotropic continua—finite element formulation and consistent linearization', *International Journal for Numerical Methods in Engineering* **73**(10), 1413–1433.

Holmes, D. W., Loughran, J. G. and Suehrcke, H. [2006], 'Constitutive model for large strain deformation of semicrystalline polymers', *Mechanics of Time-Dependent Materials* **10**(4), 281–313.

Holthusen, H., Awad, A., Barfusz, O., Brepols, T. and Reese, S. [TBA], 'An enhanced single gaussian point continuum finite element formulation using algorithmic differentiation', *TBA* .

Holthusen, H., Brepols, T., Reese, S. and Simon, J.-W. [2020], 'An anisotropic constitutive model for fiber-reinforced materials including gradient-extended damage and plasticity at finite strains', *Theoretical and Applied Fracture Mechanics* **108**, 102642.

Holthusen, H., Brepols, T., Reese, S. and Simon, J.-W. [2022*a*], A novel gradient-extended anisotropic two-surface damage-plasticity model for finite deformations, *in* '16th edition of the International Conference on Computational Plasticity', CIMNE.

Holthusen, H., Brepols, T., Reese, S. and Simon, J.-W. [2022*b*], 'A two-surface gradient-extended anisotropic damage model using a second order damage tensor coupled to additive plasticity in the logarithmic strain space', *Journal of the Mechanics and Physics of Solids* **163**, 104833.

Holthusen, H., Brepols, T., Simon, J. and Reese, S. [2022], A gradient-extended anisotropic damage-plasticity model in the logarithmic strain space, *in* '8th European Congress on Computational Methods in Applied Sciences and Engineering', CIMNE.

Holthusen, H., Rothkranz, C., Lamm, L., Brepols, T. and Reese, S. [2023], 'Inelastic material formulations based on a co-rotated intermediate configuration—application to bioengineered tissues', *Journal of the Mechanics and Physics of Solids* **172**, 105174.

Holzapfel, G. A. [2010], *Nonlinear solid mechanics*, repr. edn, Wiley, Chichester ; Weinheim [u.a.].

Holzapfel, G. A., Gasser, T. C. and Ogden, R. W. [2000], 'A new constitutive framework for arterial wall mechanics and a comparative study of material models', *Journal of elasticity and the physical science of solids* **61**(1), 1–48.

Holzapfel, G. A. and Ogden, R. W., eds [2003], *Biomechanics of Soft Tissue in Cardiovascular Systems*, Springer Vienna.

Holzapfel, G. and Ogden, R. [2010], 'Constitutive modelling of arteries', *Proceedings of The Royal Society A Mathematical Physical and Engineering Sciences* **466**, 1551–1597.

Hoskins, P. R., Lawford, P. V. and Doyle, B. J., eds [2017], *Cardiovascular Biomechanics*, Springer International Publishing.

Hu, J.-J., Humphrey, J. D. and Yeh, A. T. [2009], 'Characterization of engineered tissue development under biaxial stretch using nonlinear optical microscopy', *Tissue Engineering Part A* **15**(7), 1553–1564. PMID: 19063662.

Hudobivnik, B. and Korelc, J. [2016], 'Closed-form representation of matrix functions in the formulation of nonlinear material models', *Finite Elements in Analysis and Design* **111**, 19–32.

Humphrey, J. D. [2002], *Cardiovascular Solid Mechanics*, Springer New York.

Humphrey, J. D. and Delange, S. L. [2004], *An Introduction to Biomechanics*, Springer New York.

Humphrey, J. D., Dufresne, E. R. and Schwartz, M. A. [2014], 'Mechanotransduction and extracellular matrix homeostasis', *Nature Reviews Molecular Cell Biology* **15**(12), 802–812.

Humphrey, J. D. and Rajagopal, K. R. [2002], 'A constrained mixture model for growth and remodeling of soft tissues', *Mathematical Models and Methods in Applied Sciences* **12**(03), 407–430.

Imatani, S. and Maugin, G. [2002], 'A constitutive model for material growth and its application to three-dimensional finite element analysis', *Mechanics Research Communications* **29**(6), 477–483.

Itskov, M. [2004], 'On the application of the additive decomposition of generalized strain measures in large strain plasticity', *Mechanics Research Communications* **31**(5), 507–517.

Javili, A., McBride, A. and Steinmann, P. [2019], 'Continuum-kinematics-inspired peridynamics. mechanical problems', *Journal of the Mechanics and Physics of Solids* **131**, 125–146.

Jha, N.-K., Reinoso, J., Dehghani, H. and Merodio, J. [2019], 'A computational model for fiber-reinforced composites: hyperelastic constitutive formulation including residual stresses and damage', *Computational Mechanics* **63**(5), 931–948.

Ji, W., Waas, A., Gustafson, P., Ng, W., Pineda, E., Prabhakar, P. and Raveendra, R. [2011], 'Computational modeling of failure in composite structures including uncertainties in material and geometrical properties'.

Jin, W. and Arson, C. [2018], 'Anisotropic nonlocal damage model for materials with intrinsic transverse isotropy', *International Journal of Solids and Structures* **139-140**, 29 – 42.

Jirásek, M. and Grassl, P. [2008], 'Evaluation of directional mesh bias in concrete fracture simulations using continuum damage models', *Engineering Fracture Mechanics* **75**(8), 1921–1943.

Johansson, G., Menzel, A. and Runesson, K. [2005], 'Modeling of anisotropic inelasticity in pearlitic steel at large strains due to deformation induced substructure evolution', *European Journal of Mechanics - A/Solids* **24**(6), 899–918.

Ju, J. [1989], 'On energy-based coupled elastoplastic damage theories: Constitutive modeling and computational aspects', *International Journal of Solids and Structures* **25**(7), 803–833.

Juhre, D. and Reese, S. [2010], 'A reduced integration finite element technology based on a thermomechanically consistent stabilisation for 3d problems', *Computer Methods in Applied Mechanics and Engineering* **199**(29), 2050 – 2058.

Kachanov, L. M. [1958], 'Time of the rupture process under creep conditions, izy akad', *Nank SSR Otd Tech Nauk* **8**, 26–31.

Kachanov, M. [1987], 'Elastic solids with many cracks: A simple method of analysis', *International Journal of Solids and Structures* **23**(1), 23–43.

Karush, W. [1939], Minima of functions of several variables with inequalities as side conditions, Master's thesis, Department of Mathematics, University of Chicago, Chicago, IL, USA.

Kawai, M., Yajima, S., Hachinohe, A. and Takano, Y. [2001], 'Off-axis fatigue behavior of unidirectional carbon fiber-reinforced composites at room and high temperatures', *Journal of Composite Materials* **35**(7), 545–576.

Kerschbaum, M. and Hopmann, C. [2016], 'A progressive damage model for unidirectional fibre reinforced composites with application to impact and penetration simulation', *Applied Composite Materials* **23**(3), 495–522.

Kiefer, B., Bartel, T. and Menzel, A. [2012], 'Implementation of numerical integration schemes for the simulation of magnetic SMA constitutive response', *Smart Materials and Structures* **21**(9), 094007.

Kiefer, B., Waffenschmidt, T., Sprave, L. and Menzel, A. [2018], 'A gradient-enhanced damage model coupled to plasticity—multi-surface formulation and algorithmic concepts', *International Journal of Damage Mechanics* **27**(2), 253–295.

Kirchdoerfer, T. and Ortiz, M. [2016], 'Data-driven computational mechanics', *Computer Methods in Applied Mechanics and Engineering* **304**, 81–101.

Klein, D. K., Ortigosa, R., Martínez-Frutos, J. and Weeger, O. [2022], 'Finite electro-elasticity with physics-augmented neural networks', *Computer Methods in Applied Mechanics and Engineering* **400**, 115501.

Klingbeil, D., Svendsen, B. and Reusch, F. [2016], 'Gurson-based modelling of ductile damage and failure during cyclic loading processes at large deformation', *Engineering Fracture Mechanics* **160**, 95–123.

Klinkel, S. and Reichel, R. [2019], 'A finite element formulation in boundary representation for the analysis of nonlinear problems in solid mechanics', *Computer Methods in Applied Mechanics and Engineering* **347**, 295 – 315.

Kloppenburg, G., Walther, E., Holthusen, H., Czibula, C., Hirn, U. and Simon, J.-W. [2023], 'Using numerical homogenization to determine the representative volume element size of paper', *PAMM* **22**(1), e202200226.

Kojic, M., Milosevic, M., Simic, V., Milicevic, B., Geroski, V., Nizzero, S., Ziemys, A., Filipovic, N. and Ferrari, M. [2019], 'Smeared multiscale finite element models for mass transport and electrophysiology coupled to muscle mechanics', *Frontiers in Bioengineering and Biotechnology* **7**.

Korelc, J. [2002], 'Multi-language and multi-environment generation of nonlinear finite element codes', *Engineering with Computers* **18**(4), 312–327.

Korelc, J. [2009], 'Automation of primal and sensitivity analysis of transient coupled problems', *Computational Mechanics* **44**(5), 631–649.

Korelc, J. and Stupkiewicz, S. [2014], 'Closed-form matrix exponential and its application in finite-strain plasticity', *International Journal for Numerical Methods in Engineering* **98**(13), 960–987.

Korelc, J. and Wriggers, P. [2016], *Automation of Finite Element Methods*, Springer.

Krajcinovic, D. and Fonseka, G. U. [1981], 'The continuous damage theory of brittle materials, part 1: General theory', *Journal of Applied Mechanics* **48**(4), 809–815.

Kröner, E. [1959], 'Allgemeine kontinuumstheorie der versetzungen und eigenspannungen', *Archive for Rational Mechanics and Analysis* **4**(1), 273.

Kuhl, E. [2014], 'Growing matter: A review of growth in living systems', *Journal of the Mechanical Behavior of Biomedical Materials* **29**, 529–543.

Kuhl, E., Garikipati, K., Arruda, E. M. and Grosh, K. [2005], 'Remodeling of biological tissue: Mechanically induced reorientation of a transversely isotropic chain network', *Journal of the Mechanics and Physics of Solids* **53**(7), 1552–1573.

Kuhl, E., Maas, R., Himpel, G. and Menzel, A. [2007], 'Computational modeling of arterial wall growth', *Biomechanics and Modeling in Mechanobiology* **6**(5), 321–331.

Kuhl, E., Ramm, E. and de Borst, R. [2000], 'An anisotropic gradient damage model for quasi-brittle materials', *Computer Methods in Applied Mechanics and Engineering* **183**(1), 87–103.

Kuhl, E. and Steinmann, P. [2003*a*], 'Mass– and volume–specific views on thermodynamics for open systems', *Proceedings of the Royal Society of London. Series A: Mathematical, Physical and Engineering Sciences* **459**(2038), 2547–2568.

Kuhl, E. and Steinmann, P. [2003*b*], 'Theory and numerics of geometrically non-linear open system mechanics', *International Journal for Numerical Methods in Engineering* **58**(11), 1593–1615.

Kuhl, E., Steinmann, P. and Carol, I. [2001], 'A thermodynamically consistent approach to microplane theory. part ii. dissipation and inelastic constitutive modeling', *International Journal of Solids and Structures* **38**(17), 2933–2952.

Kuhn, H. W. and Tucker, A. W. [1951], Nonlinear programming, *in* 'Proceedings of the Second Berkeley Symposium on Mathematical Statistics and Probability', University of California Press, Berkeley, Calif., pp. 481–492.

Kulawinski, D., Nagel, K., Henkel, S., Hübner, P., Fischer, H., Kuna, M. and Biermann, H. [2011], 'Characterization of stress–strain behavior of a cast trip steel under different biaxial planar load ratios', *Engineering Fracture Mechanics* **78**(8), 1684–1695. Multiaxial Fracture.

Kuna-Ciskał, H. and Skrzypek, J. J. [2004], 'CDM based modelling of damage and fracture mechanisms in concrete under tension and compression', *Engineering Fracture Mechanics* **71**(4-6), 681–698.

Ladeveze, P. and Lemaitre, J. [1984], Damage effective stress in quasi unilateral conditions, *in* 'ICTAM'.

Lamm, L., Holthusen, H., Brepols, T., Jockenhövel, S. and Reese, S. [2022], 'A macroscopic approach for stress-driven anisotropic growth in bioengineered soft tissues', *Biomechanics and Modeling in Mechanobiology* **21**(2), 627–645.

Lamm, L., Holthusen, H., Böhm, C., Jockenhövel, S. and Reese, S. [2021], 'Macroscopic modelling of stress driven anisotropic growth in bioengineered tissues', *PAMM* **21**(1), e202100046.

Langenfeld, K., Junker, P. and Mosler, J. [2018], 'Quasi-brittle damage modeling based on incremental energy relaxation combined with a viscous-type regularization', *Continuum Mechanics and Thermodynamics* **30**(5), 1125–1144.

Langenfeld, K. and Mosler, J. [2020], 'A micromorphic approach for gradient-enhanced anisotropic ductile damage', *Computer Methods in Applied Mechanics and Engineering* **360**, 112717.

Latorre, M. and Montáns, F. J. [2015], 'Anisotropic finite strain viscoelasticity based on the sidoroff multiplicative decomposition and logarithmic strains', *Computational Mechanics* **56**(3), 503–531.

Latorre, M. and Montáns, F. J. [2016], 'Stress and strain mapping tensors and general work-conjugacy in large strain continuum mechanics', *Applied Mathematical Modelling* **40**(5), 3938 – 3950.

Läufer, J. [2018], Entwicklung eines gradientenbasierten Modells zur netzunabhängigen Schädigungssimulation geschichteter Faserverbundstrukturen, PhD thesis, Karlsruher Institut für Technologie (KIT).

Lauraitis, K. [1981], *Fatigue of Fibrous Composite Materials*, ASTM International.

Laurien, M., Javili, A. and Steinmann, P. [2023], 'Peridynamic modeling of nonlocal degrading interfaces in composites', *Forces in Mechanics* **10**, 100124.

Lee, E. H. [1969], 'Elastic-Plastic Deformation at Finite Strains', *Journal of Applied Mechanics* **36**(1), 1–6.

Lee, E. H. and Liu, D. T. [1967], 'Finite-strain elastic—plastic theory with application to plane-wave analysis', *Journal of Applied Physics* **38**(1), 19–27.

Lehmann, T. [1989], 'Some thermodynamical considerations on inelastic deformations including damage processes', *Acta Mechanica* **79**(1), 1–24.

Lehmann, T. [1991], 'Thermodynamical foundations of large inelastic deformations of solid bodies including damage', *International Journal of Plasticity* **7**(1), 79–98.

Lemaitre, J. [1971], Evalution of dissipation and damage in metals submitted to dynamic loading, *in* 'Proceedings of International Conference of Mechanical Behavior of Materials'.

Lemaitre, J. [1984], A three-dimensional ductile damage model applied to deep-drawing forming limits, *in* J. CARLSSON and N. OHLSON, eds, 'Mechanical Behaviour of Materials', Pergamon, pp. 1047–1053.

Lemaitre, J. [1985*a*], 'A Continuous Damage Mechanics Model for Ductile Fracture', *Journal of Engineering Materials and Technology* **107**(1), 83–89.

Lemaitre, J. [1985*b*], 'Coupled elasto-plasticity and damage constitutive equations', *Computer Methods in Applied Mechanics and Engineering* **51**(1), 31–49.

Lemaitre, J. and Chaboche, J.-L. [1978], 'Aspect phenomenologique de la rupture par edommagement', *J. MEC. APPL.; FRA; DA. 1978; VOL. 2; NO 3; PP. 317-365; ABS. ENG; BIBL. 57 REF.* .

Lemaitre, J. and Desmorat, R. [2006], *Engineering Damage Mechanics - Ductile, Creep, Fatigue and Brittle Failures*, Springer Science & Business Media, Berlin Heidelberg.

Lemaitre, J., Desmorat, R. and Sauzay, M. [2000], 'Anisotropic damage law of evolution', *European Journal of Mechanics - A/Solids* **19**(2), 187 – 208.

Lemaitre, J. and Dufailly, J. [1987], 'Damage measurements', *Engineering Fracture Mechanics* **28**(5-6), 643–661.

Li, H., Fu, M., Lu, J. and Yang, H. [2011], 'Ductile fracture: Experiments and computations', *International Journal of Plasticity* **27**(2), 147–180.

Li, Y., Stier, B., Bednarcyk, B., Simon, J.-W. and Reese, S. [2016], 'The effect of fiber misalignment on the homogenized properties of unidirectional fiber reinforced composites', *Mechanics of Materials* **92**, 261 – 274.

Lian, J., Feng, Y. and Münstermann, S. [2014], 'A modified lemaitre damage model phenomenologically accounting for the lode angle effect on ductile fracture', *Procedia Materials Science* **3**, 1841–1847.

Linka, K. and Kuhl, E. [2023], 'A new family of constitutive artificial neural networks towards automated model discovery', *Computer Methods in Applied Mechanics and Engineering* **403**, 115731.

Lion, A. [1997], 'On the large deformation behaviour of reinforced rubber at different temperatures', *Journal of the Mechanics and Physics of Solids* **45**(11), 1805–1834.

Lion, A. [2000], 'Constitutive modelling in finite thermoviscoplasticity: a physical approach based on nonlinear rheological models', *International Journal of Plasticity* **16**(5), 469–494.

Littell, J. D., Ruggeri, C. R., Goldberg, R. K., Roberts, G. D., Arnold, W. A. and Binienda, W. K. [2008], 'Measurement of epoxy resin tension, compression, and shear stress–strain curves over a wide range of strain rates using small test specimens', *Journal of Aerospace Engineering* **21**(3), 162–173.

Liu, H., Zhang, M., Liu, M., Martin, C., Cai, Z. and Sun, W. [2019], 'Finite element simulation of three dimensional residual stress in the aortic wall using an anisotropic tissue growth model', *Journal of the Mechanical Behavior of Biomedical Materials* **92**, 188–196.

Liu, J., Huang, M., Li, Z., Zhao, L. and Zhu, Y. [2021], 'Microvoid growth mechanism in fcc polycrystals and a statistical damage model', *International Journal of Plasticity* **137**, 102888.

Lodygowski, A., Voyiadjis, G., Deliktas, B. and Palazotto, A. [2011], 'Non-local and numerical formulations for dry sliding friction and wear at high velocities', *International Journal of Plasticity* **27**(7), 1004–1024.

Lu, J. [2004], 'Exact expansions of arbitrary tensor functions f(a) and their derivatives', *International Journal of Solids and Structures* **41**(2), 337–349.

Lubarda, V. A. [2004], 'Constitutive theories based on the multiplicative decomposition of deformation gradient: Thermoelasticity, elastoplasticity, and biomechanics', *Applied Mechanics Reviews* **57**(2), 95–108.

Lubarda, V. and Hoger, A. [2002], 'On the mechanics of solids with a growing mass', *International Journal of Solids and Structures* **39**(18), 4627–4664.

Lubarda, V., Mastilovic, S. and Knap, J. [1996], 'Some comments on plasticity postulates and non-associative flow rules', *International Journal of Mechanical Sciences* **38**(3), 247 – 258.

Lubliner, J. [1985], 'A model of rubber viscoelasticity', *Mechanics Research Communications* **12**(2), 93–99.

Macek, D., Holthusen, H., Rjosk, A., Ritzert, S., Lautenschläger, T., Neinhuis, C., Simon, J.-W. and Reese, S. [2023], 'Mechanical investigations of the peltate leaf of stephania japonica (menispermaceae): Experiments and a continuum mechanical material model', *Frontiers in Plant Science* **13**.

Maimí, P., Camanho, P., Mayugo, J. and Dávila, C. [2007], 'A continuum damage model for composite laminates: Part i – constitutive model', *Mechanics of Materials* **39**(10), 897 – 908.

Malcher, L., Andrade Pires, F. and César de Sá, J. [2014], 'An extended gtn model for ductile fracture under high and low stress triaxiality', *International Journal of Plasticity* **54**, 193–228.

Mandel, J. [1973], 'Equations constitutives et directeurs dans les milieux plastiques et viscoplastiques', *International Journal of Solids and Structures* **9**(6), 725–740.

Manjunatha, K., Behr, M., Vogt, F. and Reese, S. [2022*a*], 'A multiphysics modeling approach for in-stent restenosis: Theoretical aspects and finite element implementation', *Computers in Biology and Medicine* **150**, 106166.

Manjunatha, K., Behr, M., Vogt, F. and Reese, S. [2022*b*], 'A multiphysics modeling approach for in-stent restenosis: Theoretical aspects and finite element implementation', *arXiv* .

Marenzana, M., Wilson-Jones, N., Mudera, V. and Brown, R. A. [2006], 'The origins and regulation of tissue tension: Identification of collagen tension-fixation process in vitro', *Experimental Cell Research* **312**(4), 423–433.

Marquis, D. and Lemaitre, J. [1988], 'Constitutive equations for the coupling between elasto-plasticity damage and aging', *Revue de Physique Appliquee* **23**(4), 615–624.

Matouš, K., Geers, M. G., Kouznetsova, V. G. and Gillman, A. [2017], 'A review of predictive nonlinear theories for multiscale modeling of heterogeneous materials', *Journal of Computational Physics* **330**, 192–220.

Matzenmiller, A., Lubliner, J. and Taylor, R. [1995], 'A constitutive model for anisotropic damage in fiber-composites', *Mechanics of Materials* **20**(2), 125 – 152.

Maugin, G. A. [2013], *Continuum Mechanics Through the Twentieth Century*, Springer Netherlands.

Mazars, J., Berthaud, Y. and Ramtani, S. [1990], 'The unilateral behaviour of damaged concrete', *Engineering Fracture Mechanics* **35**(4), 629 – 635.

McClintock, F. A. [1968], 'A criterion for ductile fracture by the growth of holes', *Journal of Applied Mechanics* **35**(2), 363–371.

Mehdipour, H., Camanho, P. and Belingardi, G. [2019], 'Elasto-plastic constitutive equations for short fiber reinforced polymers', *Composites Part B: Engineering* **165**, 199 – 214.

Melro, A., Camanho, P., Andrade Pires, F. and Pinho, S. [2012], 'Numerical simulation of the non-linear deformation of 5-harness satin weaves', *Computational Materials Science* **61**, 116 – 126.

Melro, A., Camanho, P., Andrade Pires, F. and Pinho, S. [2013], 'Micromechanical analysis of polymer composites reinforced by unidirectional fibres: Part i – constitutive modelling', *International Journal of Solids and Structures* **50**(11), 1897 – 1905.

Menzel, A. [2005], 'Modelling of anisotropic growth in biological tissues', *Biomechanics and Modeling in Mechanobiology* **3**(3), 147–171.

Menzel, A. [2007], 'A fibre reorientation model for orthotropic multiplicative growth', *Biomechanics and Modeling in Mechanobiology* **6**(5), 303–320.

Menzel, A., Ekh, M., Runesson, K. and Steinmann, P. [2005], 'A framework for multiplicative elastoplasticity with kinematic hardening coupled to anisotropic damage', *International Journal of Plasticity* **21**(3), 397–434.

Menzel, A. and Kuhl, E. [2012], 'Frontiers in growth and remodeling', *Mechanics Research Communications* **42**, 1–14. Recent Advances in the Biomechanics of Growth and Remodeling.

Menzel, A. and Steinmann, P. [2003], 'Geometrically non-linear anisotropic inelasticity based on fictitious configurations: Application to the coupling of continuum damage and multiplicative elasto-plasticity', *International Journal for Numerical Methods in Engineering* **56**(14), 2233–2266.

Mester, L., Klarmann, S. and Klinkel, S. [2021], 'A homogenisation approach for shell structures using scaled boundary isogeometric analysis on rve-level', *PAMM* **21**(1), e202100157.

Mester, L., Klarmann, S. and Klinkel, S. [2023], 'Homogenisation for macroscopic shell structures with application to textile-reinforced mesostructures', *PAMM* **22**(1), e202200137.

Miehe, C. [1993], 'Computation of isotropic tensor functions', *Communications in Numerical Methods in Engineering* **9**(11), 889–896.

Miehe, C. [1996], 'Exponential map algorithm for stress updates in anisotropic multiplicative elastoplasticity for single crystals', *International Journal for Numerical Methods in Engineering* **39**(19), 3367–3390.

Miehe, C. [2014], 'Variational gradient plasticity at finite strains. part i: Mixed potentials for the evolution and update problems of gradient-extended dissipative solids', *Computer Methods in Applied Mechanics and Engineering* **268**, 677–703.

Miehe, C., Aldakheel, F. and Teichtmeister, S. [2017], 'Phase-field modeling of ductile fracture at finite strains: A robust variational-based numerical implementation of a gradient-extended theory by micromorphic regularization', *International Journal for Numerical Methods in Engineering* **111**(9), 816–863.

Miehe, C., Apel, N. and Lambrecht, M. [2002], 'Anisotropic additive plasticity in the logarithmic strain space: modular kinematic formulation and implementation based on incremental

minimization principles for standard materials', *Computer Methods in Applied Mechanics and Engineering* **191**(47), 5383 – 5425.

Miehe, C., Göktepe, S. and Méndez Diez, J. [2009], 'Finite viscoplasticity of amorphous glassy polymers in the logarithmic strain space', *International Journal of Solids and Structures* **46**(1), 181 – 202.

Miehe, C. and Lambrecht, M. [2001], 'Algorithms for computation of stresses and elasticity moduli in terms of seth–hill's family of generalized strain tensors', *Communications in Numerical Methods in Engineering* **17**(5), 337–353.

Miehe, C., Méndez Diez, J., Göktepe, S. and Schänzel, L.-M. [2011], 'Coupled thermoviscoplasticity of glassy polymers in the logarithmic strain space based on the free volume theory', *International Journal of Solids and Structures* **48**(13), 1799 – 1817.

Miehe, C., Welschinger, F. and Hofacker, M. [2010*a*], 'Thermodynamically consistent phase-field models of fracture: Variational principles and multi-field fe implementations', *International Journal for Numerical Methods in Engineering* **83**(10), 1273–1311.

Miehe, C., Welschinger, F. and Hofacker, M. [2010*b*], 'Thermodynamically consistent phase-field models of fracture: Variational principles and multi-field FE implementations', *International Journal for Numerical Methods in Engineering* **83**(10), 1273–1311.

Mihai, L. A., Budday, S., Holzapfel, G. A., Kuhl, E. and Goriely, A. [2017], 'A family of hyperelastic models for human brain tissue', *Journal of the Mechanics and Physics of Solids* **106**, 60–79.

Miller, C. and Gasser, T. C. [2021], 'A microstructurally motivated constitutive description of collagenous soft biological tissue towards the description of their non-linear and time-dependent properties', *Journal of the Mechanics and Physics of Solids* **154**, 104500.

Mindlin, R. [1964], 'Micro-structure in linear elasticity'.

Mirone, G. and Corallo, D. [2010], 'A local viewpoint for evaluating the influence of stress triaxiality and lode angle on ductile failure and hardening', *International Journal of Plasticity* **26**(3), 348–371.

Mogilner, A., Allard, J. and Wollman, R. [2012], 'Cell polarity: Quantitative modeling as a tool in cell biology', *Science* **336**(6078), 175–179.

Morin, L., Leblond, J.-B. and Kondo, D. [2015], 'A gurson-type criterion for plastically anisotropic solids containing arbitrary ellipsoidal voids', *International Journal of Solids and Structures* **77**, 86–101.

Moulton, D. E., Lessinnes, T., O'Keeffe, S., Dorfmann, L. and Goriely, A. [2016], 'The elastic secrets of the chameleon tongue', *Proceedings of the Royal Society A: Mathematical, Physical and Engineering Sciences* **472**(2188), 20160030.

Moës, N. and Belytschko, T. [2002], 'Extended finite element method for cohesive crack growth', *Engineering Fracture Mechanics* **69**(7), 813–833.

Murakami, S. [1981], 'A continuum theory of creep damage', *Creep in Structures* pp. 422–444.

Murakami, S. [1988], 'Mechanical Modeling of Material Damage', *Journal of Applied Mechanics* **55**(2), 280–286.

Murakami, S. [2012], *Continuum damage mechanics: a continuum mechanics approach to the analysis of damage and fracture*, Springer Science & Business Media.

Murakami, S. and Kamiya, K. [1997], 'Constitutive and damage evolution equations of elastic-brittle materials based on irreversible thermodynamics', *International Journal of Mechanical Sciences* **39**(4), 473 – 486.

Nackenhorst, U. and Hartung, C. [2001], 'Numerische simulation des beanspruchungsadaptiven knochenwachstums mit hilfe der finite elemente methode', **46**(s1), 284–285.

Nasab, A. S. and Mashayekhi, M. [2019], 'Application of an efficient anisotropic damage model to the prediction of the failure of metal forming processes', *International Journal of Damage Mechanics* **28**(10), 1556–1579.

Nedjar, B. [2002], 'Frameworks for finite strain viscoelastic-plasticity based on multiplicative decompositions. part i: Continuum formulations', *Computer Methods in Applied Mechanics and Engineering* **191**(15), 1541–1562.

Needleman, A. [1988], 'Material rate dependence and mesh sensitivity in localization problems', *Computer Methods in Applied Mechanics and Engineering* **67**(1), 69–85.

Neff, P. and Ghiba, I.-D. [2016], 'Loss of ellipticity for non-coaxial plastic deformations in additive logarithmic finite strain plasticity', *International Journal of Non-Linear Mechanics* **81**, 122–128.

Neff, P., Ghiba, I.-D. and Lankeit, J. [2015], 'The exponentiated hencky-logarithmic strain energy. part i: Constitutive issues and rank-one convexity', *Journal of Elasticity* **121**(2), 143–234.

Neilsen, M. and Schreyer, H. [1993], 'Bifurcations in elastic-plastic materials', *International Journal of Solids and Structures* **30**(4), 521–544.

Niazi, M. S., Wisselink, H. H. and Meinders, T. [2013], 'Viscoplastic regularization of local damage models: revisited', *Computational Mechanics* **51**(2), 203–216.

Ogden, R. [1984], *Non-linear Elastic Deformations*, Ellis Horwood series in mathematics and its applications, E. Horwood.

Ogden, R. W. and Hill, R. [1972], 'Large deformation isotropic elasticity – on the correlation of theory and experiment for incompressible rubberlike solids', *Proceedings of the Royal Society of London. A. Mathematical and Physical Sciences* **326**(1567), 565–584.

Ortiz, M. [1985], 'A constitutive theory for the inelastic behavior of concrete', *Mechanics of Materials* **4**(1), 67–93.

Papa, E. [1996], 'A unilateral damage model for masonry based on a homogenisation procedure', *Mechanics of Cohesive-frictional Materials* **1**(4), 349–366.

Papadopoulos, P. and Lu, J. [1998], 'A general framework for the numerical solution of problems in finite elasto-plasticity', *Computer Methods in Applied Mechanics and Engineering* **159**(1), 1 – 18.

Papadopoulos, P. and Lu, J. [2001], 'On the formulation and numerical solution of problems in anisotropic finite plasticity', *Computer Methods in Applied Mechanics and Engineering* **190**(37), 4889–4910.

Pawlina, W. and Ross, M. H. [2018], *Histology: a text and atlas: with correlated cell and molecular biology*, Lippincott Williams & Wilkins.

Peerlings, R., De Borst, R., Brekelmans, W. and De Vree, J. [1995], Computational modelling of gradient-enhanced damage for fracture and fatigue problems, *in* 'Computational Plasticity, Fundamentals and Applications: Proceedings of the 4th International Conference', Pineridge Press: Swansea, pp. 975–986.

Peerlings, R., Geers, M., de Borst, R. and Brekelmans, W. [2001], 'A critical comparison of nonlocal and gradient-enhanced softening continua', *International Journal of Solids and Structures* **38**(44), 7723–7746.

Peerlings, R. H. J., de Borst, R., Brekelmans, W. A. M. and de Vree, J. H. P. [1996], 'Gradient enhanced damage for quasi-brittle materials', *International Journal for Numerical Methods in Engineering* **39**(19), 3391–3403.

Perzyna, P. [1966], Fundamental problems in viscoplasticity, Vol. 9 of *Advances in Applied Mechanics*, Elsevier, pp. 243–377.

Perzyna, P. [1971], 'Thermodynamic theory of viscoplasticity', *Advances in Applied Mechanics* **11**, 313–354.

Pijaudier-Cabot, G. and Bažant, Z. P. [1987], 'Nonlocal damage theory', *Journal of Engineering Mechanics* **113**(10), 1512–1533.

Pipes, R. B. and Cole, B. [1973], 'On the off-axis strength test for anisotropic materials1', *Journal of Composite Materials* **7**(2), 246–256.

Pituba, J. J. C. and Fernandes, G. R. [2011], 'Anisotropic damage model for concrete', *Journal of Engineering Mechanics* **137**(9), 610–624.

Poggenpohl, L., Brepols, T., Holthusen, H., Wulfinghoff, S. and Reese, S. [2021], 'Towards brittle damage in carbon fiber reinforced plastics: A gradient extended approach', *Composite Structures* **255**, 112911.

Poggenpohl, L., Holthusen, H. and Simon, J.-W. [2022], 'Failure zone homogenization for modeling damage- and debonding-induced softening in composites including gradient-extended damage at finite strains', *International Journal of Plasticity* **154**, 103277.

Praster, M., Klassen, M. and Klinkel, S. [2019], 'An adaptive fe^2 approach for fiber–matrix composites', *Computational Mechanics* **63**(6), 1333–1350.

Prume, E., Reese, S. and Ortiz, M. [2023], 'Model-free data-driven inference in computational mechanics', *Computer Methods in Applied Mechanics and Engineering* **403**, 115704.

Puck, A. [1996], *Festigkeitsanalyse von Faser-Matrix-Laminaten*, Carl Hanser Verlag Munich.

Puck, A. and Schürmann, H. [2002], 'Failure analysis of frp laminates by means of physically based phenomenological models', *Composites Science and Technology* **62**(12), 1633 – 1662.

Quarteroni, A., Manzoni, A. and Vergara, C. [2017], 'The cardiovascular system: mathematical modelling, numerical algorithms and clinical applications', *Acta Numerica* **26**, 365–590.

Rabotnov, Y. N. [1963], 'Paper 68: On the equation of state of creep', *Proceedings of the Institution of Mechanical Engineers, Conference Proceedings* **178**(1), 2–117–2–122.

Rabotnov, Y. N. [1969], Creep rupture, *in* M. Hetényi and W. G. Vincenti, eds, 'Applied Mechanics', Springer Berlin Heidelberg, Berlin, Heidelberg, pp. 342–349.

Rahman, M. M., Watton, P. N., Neu, C. P. and Pierce, D. M. [2023], 'A chemo-mechano-biological modeling framework for cartilage evolving in health, disease, injury, and treatment', *Computer Methods and Programs in Biomedicine* p. 107419.

Raina, A. and Linder, C. [2014], 'A homogenization approach for nonwoven materials based on fiber undulations and reorientation', *Journal of the Mechanics and Physics of Solids* **65**, 12–34.

Raissi, M., Perdikaris, P. and Karniadakis, G. [2019], 'Physics-informed neural networks: A deep learning framework for solving forward and inverse problems involving nonlinear partial differential equations', *Journal of Computational Physics* **378**, 686–707.

Raissi, M., Wang, Z., Triantafyllou, M. S. and Karniadakis, G. E. [2018], 'Deep learning of vortex-induced vibrations', *Journal of Fluid Mechanics* **861**, 119–137.

Reese, S. [2003], 'Meso-macro modelling of fibre-reinforced rubber-like composites exhibiting large elastoplastic deformation', *International Journal of Solids and Structures* **40**(4), 951 – 980.

Reese, S. [2005], 'On a physically stabilized one point finite element formulation for three-dimensional finite elasto-plasticity', *Computer Methods in Applied Mechanics and Engineering* **194**(45), 4685 – 4715.

Reese, S., Brepols, T., Fassin, M., Poggenpohl, L. and Wulfinghoff, S. [2021], 'Using structural tensors for inelastic material modeling in the finite strain regime – a novel approach to anisotropic damage', *Journal of the Mechanics and Physics of Solids* **146**, 104174.

Reese, S. and Christ, D. [2008], 'Finite deformation pseudo-elasticity of shape memory alloys – constitutive modelling and finite element implementation', *International Journal of Plasticity* **24**(3), 455 – 482.

Reese, S. and Govindjee, S. [1998], 'A theory of finite viscoelasticity and numerical aspects', *International Journal of Solids and Structures* **35**(26), 3455 – 3482.

Reese, S., Raible, T. and Wriggers, P. [2001], 'Finite element modelling of orthotropic material behaviour in pneumatic membranes', *International Journal of Solids and Structures* **38**(52), 9525 – 9544.

Reifsnider, K. L. and Lauraitis, K. N., eds [1977], *Fatigue of Filamentary Composite Materials*, ASTM International, West Conshohocken, PA.

Reinoso, J., Blázquez, A., Estefani, A., París, F., Cañas, J., Arévalo, E. and Cruz, F. [2012], 'Experimental and three-dimensional global-local finite element analysis of a composite component including degradation process at the interfaces', *Composites Part B: Engineering* **43**(4), 1929–1942.

Reinoso, J., Catalanotti, G., Blázquez, A., Areias, P., Camanho, P. and París, F. [2017], 'A consistent anisotropic damage model for laminated fiber-reinforced composites using the 3d-version of the puck failure criterion', *International Journal of Solids and Structures* **126-127**.

Reiter, N., Roy, B., Paulsen, F. and Budday, S. [2021], 'Insights into the microstructural origin of brain viscoelasticity', *Journal of Elasticity* **145**(1-2), 99–116.

Rezaei, S., Harandi, A., Moeineddin, A., Xu, B.-X. and Reese, S. [2022], 'A mixed formulation for physics-informed neural networks as a potential solver for engineering problems in heterogeneous domains: Comparison with finite element method', *Computer Methods in Applied Mechanics and Engineering* **401**, 115616.

Rezaei, S., Mianroodi, J. R., Brepols, T. and Reese, S. [2021], 'Direction-dependent fracture in solids: Atomistically calibrated phase-field and cohesive zone model', *Journal of the Mechanics and Physics of Solids* **147**, 104253.

Rice, J. [1971], 'Inelastic constitutive relations for solids: An internal-variable theory and its application to metal plasticity', *Journal of the Mechanics and Physics of Solids* **19**(6), 433–455.

Rice, J. and Tracey, D. [1969], 'On the ductile enlargement of voids in triaxial stress fields∗', *Journal of the Mechanics and Physics of Solids* **17**(3), 201–217.

Ricker, A., Gierig, M. and Wriggers, P. [2023], 'Multiplicative, non-newtonian viscoelasticity models for rubber materials and brain tissues: Numerical treatment and comparative studies', *Archives of Computational Methods in Engineering* .

Rocha, I., van der Meer, F., Raijmaekers, S., Lahuerta, F., Nijssen, R. and Sluys, L. [2019], 'Numerical/experimental study of the monotonic and cyclic viscoelastic/viscoplastic/fracture behavior of an epoxy resin', *International Journal of Solids and Structures* **168**, 153 – 165.

Rodriguez, E. K., Hoger, A. and McCulloch, A. D. [1994], 'Stress-dependent finite growth in soft elastic tissues', *Journal of Biomechanics* **27**(4), 455–467.

Rolfes, R., Ernst, G., Hartung, D. and Teßmer, J. [2006], Strength of textile composites — a voxel based continuum damage mechanics approach, *in* C. A. Motasoares, J. A. C. Martins, H. C. Rodrigues, J. A. C. Ambrósio, C. A. B. Pina, C. M. Motasoares, E. B. R. Pereira and J. Folgado, eds, 'III European Conference on Computational Mechanics', Springer Netherlands, Dordrecht, pp. 32–32.

Saanouni, K. [2013], *Damage Mechanics in Metal Forming - Advanced Modeling and Numerical Simulation*, John Wiley & Sons, New York.

Saanouni, K. and Hamed, M. [2013], 'Micromorphic approach for finite gradient-elastoplasticity fully coupled with ductile damage: Formulation and computational aspects', *International Journal of Solids and Structures* **50**(14), 2289 – 2309.

Saanouni, K. and Lestriez, P. [2009], 'Modelling and numerical simulation of ductile damage in bulk metal forming', *steel research international* **80**(9), 645–657.

Sáez, P., Peña, E., Martínez, M. A. and Kuhl, E. [2014], 'Computational modeling of hypertensive growth in the human carotid artery', *Computational Mechanics* **53**(6), 1183–1196.

Sansour, C., Karšaj, I. and Sorić, J. [2007], 'On a formulation for anisotropic elastoplasticity at finite strains invariant with respect to the intermediate configuration', *Journal of the Mechanics and Physics of Solids* **55**(11), 2406 – 2426.

Sansour, C. and Wagner, W. [2003], 'Viscoplasticity based on additive decomposition of logarithmic strain and unified constitutive equations: Theoretical and computational considerations with reference to shell applications', *Computers & Structures* **81**(15), 1583–1594.

Saroukhani, S., Vafadari, R. and Simone, A. [2013], 'A simplified implementation of a gradient-enhanced damage model with transient length scale effects', *Computational Mechanics* **51**(6), 899–909.

Schemmann, M., Lang, J., Helfrich, A., Seelig, T. and Böhlke, T. [2018], 'Cruciform specimen design for biaxial tensile testing of SMC', *Journal of Composites Science* **2**(1), 12.

Scheyvaerts, F., Onck, P., Tekogˇlu, C. and Pardoen, T. [2011], 'The growth and coalescence of ellipsoidal voids in plane strain under combined shear and tension', *Journal of the Mechanics and Physics of Solids* **59**(2), 373–397.

Schriefl, A. J., Reinisch, A. J., Sankaran, S., Pierce, D. M. and Holzapfel, G. A. [2012], 'Quantitative assessment of collagen fibre orientations from two-dimensional images of soft biological tissues', *Journal of The Royal Society Interface* **9**(76), 3081–3093.

Schriefl, A. J., Zeindlinger, G., Pierce, D. M., Regitnig, P. and Holzapfel, G. A. [2012], 'Determination of the layer-specific distributed collagen fibre orientations in human thoracic and abdominal aortas and common iliac arteries', *Journal of The Royal Society Interface* **9**(71), 1275–1286.

Schröder, J., Gruttmann, F. and Löblein, J. [2002], 'A simple orthotropic finite elasto–plasticity model based on generalized stress–strain measures', *Computational Mechanics* **30**(1), 48–64.

Schröder, J. and Neff, P. [2003], 'Invariant formulation of hyperelastic transverse isotropy based on polyconvex free energy functions', *International Journal of Solids and Structures* **40**(2), 401 – 445.

Sénac, C., Hure, J. and Tanguy, B. [2023], 'Void growth yield criteria for intergranular ductile fracture', *Journal of the Mechanics and Physics of Solids* **172**, 105167.

Seth, B. [1961], Generalized strain measure with applications to physical problems, Technical report, Wisconsin Univ-Madison Mathematics Research Center.

Seymen, Y., Güler, B. and Efe, M. [2016], 'Large strain and small-scale biaxial testing of sheet metals', *Experimental Mechanics* **56**(9), 1519–1530.

Sgarra, C. and Vianello, M. [1997], 'Rotations which make strain and stress coaxial', *Journal of Elasticity* **47**(3), 217–224.

Shang, X., Zhang, H., Cui, Z., Fu, M. and Shao, J. [2020], 'A multiscale investigation into the effect of grain size on void evolution and ductile fracture: Experiments and crystal plasticity modeling', *International Journal of Plasticity* **125**, 133–149.

Shanthraj, P., Svendsen, B., Sharma, L., Roters, F. and Raabe, D. [2017], 'Elasto-viscoplastic phase field modelling of anisotropic cleavage fracture', *Journal of the Mechanics and Physics of Solids* **99**, 19–34.

Sidoroff, F. [1974], 'Un modele viscoelastique non lineaire avec configuration intermediaire.', *J. MEC.; FR.; DA. 1974; VOL. 13; NO 4; PP. 679-713; ABS. ANGL.; BIBL. 18 REF.* .

Sielenkämper, M., Dittmann, J. and Wulfinghoff, S. [2022], 'Numerical strategies for variational updates in large strain inelasticity with incompressibility constraint', *International Journal for Numerical Methods in Engineering* **123**(1), 245–267.

Silver, F. H., Freeman, J. W. and Seehra, G. P. [2003], 'Collagen self-assembly and the development of tendon mechanical properties', *Journal of Biomechanics* **36**(10), 1529–1553. Bone Cell and Tissue Mechanics.

Simo, J. C. and Armero, F. [1992], 'Geometrically non-linear enhanced strain mixed methods and the method of incompatible modes', *International Journal for Numerical Methods in Engineering* **33**(7), 1413–1449.

Simo, J. C. and Hughes, T. J. [2006], *Computational inelasticity*, Vol. 7, Springer Science & Business Media.

Simo, J. and Ju, J. [1987], 'Strain- and stress-based continuum damage models—i. formulation', *International Journal of Solids and Structures* **23**(7), 821 – 840.

Simo, J. and Miehe, C. [1992], 'Associative coupled thermoplasticity at finite strains: Formulation, numerical analysis and implementation', *Computer Methods in Applied Mechanics and Engineering* **98**(1), 41 – 104.

Simon, J.-W., Höwer, D., Stier, B., Reese, S. and Fish, J. [2017], 'A regularized orthotropic continuum damage model for layered composites: intralaminar damage progression and delamination', *Computational Mechanics* **60**(3), 445–463.

Simon, J.-W., Stier, B. and Reese, S. [2015], 'Numerical analysis of layered fiber composites accounting for the onset of delamination', *Advances in Engineering Software* **80**, 4 – 11. Civil-Comp.

Skalak, R., Farrow, D. A. and Hoger, A. [1997], 'Kinematics of surface growth', *Journal of Mathematical Biology* **35**(8), 869–907.

Skrzypek, J. J. and Ganczarski, A. [1999], *Modeling of Material Damage and Failure of Structures*, Springer Berlin Heidelberg.

Soleimani, M., Muthyala, N., Marino, M. and Wriggers, P. [2020], 'A novel stress-induced anisotropic growth model driven by nutrient diffusion: Theory, fem implementation and applications in bio-mechanical problems', *Journal of the Mechanics and Physics of Solids* **144**, 104097.

Song, X., Leotoing, L., Guines, D. and Ragneau, E. [2017], 'Characterization of forming limits at fracture with an optimized cruciform specimen: Application to dp600 steel sheets', *International Journal of Mechanical Sciences* **126**, 35–43.

Spencer, A. [1971], 'Part iii. theory of invariants', *Continuum physics* **1**, 239–353.

Spencer, A. [1984], 'Constitutive theory for stringly anisotropic solids', *Continuum theory of the mechanics of fiber-reinforced composites* pp. 1–32.

Sprave, L. and Menzel, A. [2020], 'A large strain gradient-enhanced ductile damage model: finite element formulation, experiment and parameter identification', *Acta Mechanica* **231**(12), 5159–5192.

Stapleton, S. E., Moreira, R., Jockenhoevel, S., Mela, P. and Reese, S. [2015], 'Effect of reinforcement volume fraction and orientation on a hybrid tissue engineered aortic heart valve with a tubular leaflet design', *Advanced Modeling and Simulation in Engineering Sciences* **2**(1), 21.

Steinmann, P. [1999], 'Formulation and computation of geometrically non-linear gradient damage', *International Journal for Numerical Methods in Engineering* **46**(5), 757–779.

Stier, B., Simon, J.-W. and Reese, S. [2015], 'Finite element analysis of layered fiber composite structures accounting for the material's microstructure and delamination', *Applied Composite Materials* **22**.

Stojanović, R., Djurić, S. and Vujosević, L. [1964], 'On finite thermal deformations', *Arch. Mech. Stosow.* **16**, 103–108.

Stopak, D. and Harris, A. K. [1982], 'Connective tissue morphogenesis by fibroblast traction: I. tissue culture observations', *Developmental Biology* **90**(2), 383–398.

Stracuzzi, A., Britt, B. R., Mazza, E. and Ehret, A. E. [2022], 'Risky interpretations across the length scales: continuum vs. discrete models for soft tissue mechanobiology', *Biomechanics and Modeling in Mechanobiology* **21**(2), 433–454.

Svendsen, B. [1998], 'A thermodynamic formulation of finite-deformation elastoplasticity with hardening based on the concept of material isomorphism', *International Journal of Plasticity* **14**(6), 473 – 488.

Svendsen, B. [2001], 'On the modelling of anisotropic elastic and inelastic material behaviour at large deformation', *International Journal of Solids and Structures* **38**(52), 9579 – 9599.

Svendsen, B. and Bargmann, S. [2010], 'On the continuum thermodynamic rate variational formulation of models for extended crystal plasticity at large deformation', *Journal of the Mechanics and Physics of Solids* **58**(9), 1253–1271.

Taber, L. A. [1995], 'Biomechanics of Growth, Remodeling, and Morphogenesis', *Applied Mechanics Reviews* **48**(8), 487–545.

Taylor, R. L. [2020], 'FEAP - finite element analysis program'.

Thomson, J. A. [1917], 'On growth and form', *Nature* **100**(2498), 21–22.

Thon, M. P., Hemmler, A., Glinzer, A., Mayr, M., Wildgruber, M., Zernecke-Madsen, A. and Gee, M. W. [2017], 'A multiphysics approach for modeling early atherosclerosis', *Biomechanics and Modeling in Mechanobiology* **17**(3), 617–644.

Tikenoğulları, O. Z., Costabal, F. S., Yao, J., Marsden, A. and Kuhl, E. [2022], 'How viscous is the beating heart? insights from a computational study', *Computational Mechanics* **70**(3), 565–579.

Titscher, T., Oliver, J. and Unger, J. F. [2019], 'Implicit - explicit integration of gradient-enhanced damage models', *Journal of Engineering Mechanics* **145**(7), 04019040.

Totry, E., González, C. and LLorca, J. [2008], 'Failure locus of fiber-reinforced composites under transverse compression and out-of-plane shear', *Composites Science and Technology* **68**(3), 829 – 839.

Totry, E., Molina-Aldareguía, J. M., González, C. and LLorca, J. [2010], 'Effect of fiber, matrix and interface properties on the in-plane shear deformation of carbon-fiber reinforced composites', *Composites Science and Technology* **70**(6), 970 – 980.

Truster, T. J. and Masud, A. K. M. [2017], 'A unified mixture formulation for density and volumetric growth of multi-constituent solids in tissue engineering', *Computer Methods in Applied Mechanics and Engineering* **314**, 222–268.

Tsai, S. W. [1979], 'Composite materials: testing and design (fifth conference)'.

Tsai, S. W. and Wu, E. M. [1971], 'A general theory of strength for anisotropic materials', *Journal of Composite Materials* **5**(1), 58–80.

Tvergaard, V. [1981], 'Influence of voids on shear band instabilities under plane strain conditions', *International Journal of Fracture* **17**(4), 389–407.

Tvergaard, V. [1982*a*], 'Material failure by void coalescence in localized shear bands', *International Journal of Solids and Structures* **18**(8), 659–672.

Tvergaard, V. [1982*b*], 'On localization in ductile materials containing spherical voids', *International Journal of Fracture* **18**(4), 237–252.

Tvergaard, V. and Needleman, A. [1984], 'Analysis of the cup-cone fracture in a round tensile bar', *Acta Metallurgica* **32**(1), 157–169.

Ulz, M. H. and Celigoj, C. C. [2021], 'A uniquely defined multiplicative elasto-plasticity model with orthotropic yield function and plastic spin', *Computer Methods in Applied Mechanics and Engineering* **374**, 113565.

van der Velden, T., Ritzert, S., Reese, S. and Waimann, J. [2023], 'A novel numerical strategy for modeling the moving boundary value problem of electrochemical machining', *International Journal for Numerical Methods in Engineering* .

van der Velden, T., Rommes, B., Klink, A., Reese, S. and Waimann, J. [2021], 'A novel approach for the efficient modeling of material dissolution in electrochemical machining', *International Journal of Solids and Structures* **229**, 111106.

Vastmans, J., Maes, L., Peirlinck, M., Vanderveken, E., Rega, F., Kuhl, E. and Famaey, N. [2022], 'Growth and remodeling in the pulmonary autograft: Computational evaluation using kinematic growth models and constrained mixture theory', *International Journal for Numerical Methods in Biomedical Engineering* **38**(1), e3545.

Vigliotti, A. and Auricchio, F. [2021], 'Automatic differentiation for solid mechanics', *Archives of Computational Methods in Engineering* **28**(3), 875–895.

Vignjevic, R., Djordjevic, N. and Panov, V. [2012], 'Modelling of dynamic behaviour of orthotropic metals including damage and failure', *International Journal of Plasticity* **38**, 47–85.

Vladimirov, I. N., Pietryga, M. P. and Reese, S. [2008], 'On the modelling of non-linear kinematic hardening at finite strains with application to springback—comparison of time integration algorithms', *International Journal for Numerical Methods in Engineering* **75**(1), 1–28.

Vladimirov, I. N., Pietryga, M. P. and Reese, S. [2010], 'Anisotropic finite elastoplasticity with nonlinear kinematic and isotropic hardening and application to sheet metal forming', *International Journal of Plasticity* **26**(5), 659 – 687.

Voce, E. [1955], 'A practical strain-hardening function', *Metallurgia* **51**(307), 219–226.

Vogler, M., Rolfes, R. and Camanho, P. [2013], 'Modeling the inelastic deformation and fracture of polymer composites – part i: Plasticity model', *Mechanics of Materials* **59**, 50 – 64.

Voyiadjis, G. and Katten, P. [2005], *Damage Mechanics*, first edn, CRC Press Inc.

Voyiadjis, G. and Katten, P. [2006], *Advances in Damage Mechanics: Metals and Metal Matrix Composites With an Introduction to Fabric Tensors*, second edn, Elsevier.

Voyiadjis, G. Z., Jeong, J. and Kysar, J. W. [2021], 'Grain size dependence of polycrystalline plasticity modeling in cylindrical indentation', *Computational Mechanics* **68**(3), 499–543.

Voyiadjis, G. Z. and Kattan, P. I. [1992*a*], 'Finite Strain Plasticity and Damage in Constitutive Modeling of Metals With Spin Tensors', *Applied Mechanics Reviews* **45**(3S), S95–S109.

Voyiadjis, G. Z. and Kattan, P. I. [1992*b*], 'A plasticity-damage theory for large deformation of solids—i. theoretical formulation', *International Journal of Engineering Science* **30**(9), 1089–1108.

Voyiadjis, G. Z. and Song, Y. [2019], 'Strain gradient continuum plasticity theories: Theoretical, numerical and experimental investigations', *International Journal of Plasticity* **121**, 21–75.

Voyiadjis, G. Z., Taqieddin, Z. N. and Kattan, P. I. [2008], 'Anisotropic damage–plasticity model for concrete', *International Journal of Plasticity* **24**(10), 1946–1965. Special Issue in Honor of Jean-Louis Chaboche.

Vujosevic, L. and Lubarda, V. [2002], 'Finite-strain thermoelasticity based on multiplicative decomposition of deformation gradient', *Theoretical and Applied Mechanics* pp. 379–399.

Wang, J. H.-C., Goldschmidt-Clermont, P., Wille, J. and Yin, F. C.-P. [2001], 'Specificity of endothelial cell reorientation in response to cyclic mechanical stretching', *Journal of Biomechanics* **34**(12), 1563–1572.

Wcisło, B., Pamin, J. and Kowalczyk-Gajewska, K. [2013], 'Gradient-enhanced damage model for large deformations of elastic-plastic materials', *Archives of Mechanics* **65**, 407–428.

Weber, G. and Anand, L. [1990], 'Finite deformation constitutive equations and a time integration procedure for isotropic, hyperelastic-viscoplastic solids', *Computer Methods in Applied Mechanics and Engineering* **79**(2), 173–202.

Wells, R. G. [2013], 'Tissue mechanics and fibrosis', *Biochimica et Biophysica Acta (BBA) - Molecular Basis of Disease* **1832**(7), 884–890. Fibrosis: Translation of basic research to human disease.

Wengert, R. E. [1964], 'A simple automatic derivative evaluation program', *Commun. ACM* **7**(8), 463–464.

Wisdom, K. M., Delp, S. L. and Kuhl, E. [2014], 'Use it or lose it: multiscale skeletal muscle adaptation to mechanical stimuli', *Biomechanics and Modeling in Mechanobiology* **14**(2), 195–215.

Wolff, J. [1870], 'Ueber die innere architectur der knochen und ihre bedeutung für die frage vom knochenwachsthum', *Archiv für pathologische Anatomie und Physiologie und für klinische Medicin* **50**(3), 389–450.

Wolinsky, H. and Glagov, S. [1967], 'A lamellar unit of aortic medial structure and function in mammals', *Circulation Research* **20**(1), 99–111.

Wu, H., Xu, W., Shan, D. and Jin, B. C. [2019], 'An extended GTN model for low stress triaxiality and application in spinning forming', *Journal of Materials Processing Technology* **263**, 112–128.

Wulfinghoff, S. and Böhlke, T. [2012], 'Equivalent plastic strain gradient enhancement of single crystal plasticity: theory and numerics', *Proceedings of the Royal Society A: Mathematical, Physical and Engineering Sciences* **468**(2145), 2682–2703.

Wulfinghoff, S., Fassin, M. and Reese, S. [2017], 'A damage growth criterion for anisotropic damage models motivated from micromechanics', *International Journal of Solids and Structures* **121**, 21 – 32.

Yavari, A. and Goriely, A. [2014], 'The geometry of discombinations and its applications to semi-inverse problems in anelasticity', *Proceedings of the Royal Society A: Mathematical, Physical and Engineering Sciences* **470**(2169), 20140403.

Yin, B., Zreid, I., Lin, G., Bhashyam, G. and Kaliske, M. [2020], 'An anisotropic damage formulation for composite materials based on a gradient-enhanced approach: Formulation and implementation at small strain', *International Journal of Solids and Structures* **202**, 631 – 645.

Yoshihara, L., Coroneo, M., Comerford, A., Bauer, G., Klöppel, T. and Wall, W. A. [2014], 'A combined fluid–structure interaction and multi–field scalar transport model for simulating mass transport in biomechanics', *International Journal for Numerical Methods in Engineering* **100**(4), 277–299.

Zahn, A. and Balzani, D. [2017], 'Modeling of anisotropic growth and residual stresses in aterial walls', *Acta Polytechnica CTU Proceedings* **7**, 85.

Zahn, A. and Balzani, D. [2018], 'A combined growth and remodeling framework for the approximation of residual stresses in arterial walls', *ZAMM - Journal of Applied Mathematics and Mechanics / Zeitschrift für Angewandte Mathematik und Mechanik* **98**(12), 2072–2100.

Zhang, J. and Rychlewski, J. [1990], 'Structural tensors for anisotropic solids', *Archives of Mechanics* **42**, 267–277.

Zheng, Q.-S. [1994], 'Theory of representations for tensor functions—a unified invariant approach to constitutive equations', *Applied Mechanics Reviews* **47**(11), 545–587.

Zhu, Y. and Cescotto, S. [1995], 'A fully coupled elasto-visco-plastic damage theory for anisotropic materials', *International Journal of Solids and Structures* **32**(11), 1607–1641.

Zuo, D., He, Y., Avril, S., Yang, H. and Hackl, K. [2022], 'A thermodynamic framework for unified continuum models for the healing of damaged soft biological tissue', *Journal of the Mechanics and Physics of Solids* **158**, 104662.

Zwicke, F., Knechtges, P., Behr, M. and Elgeti, S. [2016], 'Automatic implementation of material laws: Jacobian calculation in a finite element code with tapenade', *Computers & Mathematics with Applications* **72**(11), 2808–2822.